University College London

Insight into the Surface Structure of Iron (-Nickel) Sulfides in Aqueous Environments for CO_2 Reduction Applications using In-situ Spectroelectrochemistry

Thesis submitted for the degree of Doctor of Philosophy (PhD) by

Siti Nurul Azian binti Zakaria

Supervisor:

Dr Katherine Holt

December 2017

Declaration

I, Siti Nurul Azian binti Zakaria, confirm that the work presented in this thesis is my own. Where information has been derived from other sources, I confirm that this has been indicated in the thesis.

_____

Abstract

Iron sulfides and iron nickel sulfides, specifically greigite, (Fe_3S_4), and violarite, ($FeNi_2S_4$), have been shown to reduce CO_2 on application of low electrode potentials (up to −1.3 V vs AgCl|Ag). However, at such low potentials, metal sulfides are predicted to undergo reductive decomposition and competing reactions such as water reduction may also take place. The aim of the work in this thesis was to determine the stability of the iron (-nickel) sulfides under conditions where CO_2 reduction has been demonstrated to take place. In-situ Attenuated Total Reflectance Fourier Transformed Infrared Spectroscopy (ATR-FTIR) and X-ray Absorption Spectroscopy (XAS) techniques were used to monitor and characterise the structural transformations of iron and iron-nickel sulfides in aqueous solutions on application of an external potential. Additional iron (-nickel) sulfides investigated in this work include pyrrhotite (Fe_7S_8) and pentlandite ($(Fe,Ni)_9S_8$). Pourbaix diagrams were used to preliminarily assign the redox features in the cyclic voltammograms of these iron and iron-nickel sulfides. These assignments were then correlated with the spectroscopic data to verify the assignments. Iron hydroxide / oxyhydroxide was detected on applying negative potentials on both the iron and iron-nickel sulfides, which was not predicted by the Pourbaix diagrams at constant solution pH. The formation of the iron hydroxide / oxyhydroxide was proposed to be instigated by water reduction occurring at low electrode potentials, causing an increase in the local pH. The XAS spectra showed the transformation to iron hydroxide / oxyhydroxide was surface confined as a high percentage of sulfide character remained within the nanoparticles. The significant shift in the local pH near the electrode, due to water reduction, contributed to the stability of the iron hydroxide / oxyhydroxide formed at pH 4 and 7. On introduction of CO_2, the formation of iron hydroxide / oxyhydroxide was halted. This was attributed to the adsorption of CO_2 and its dissolved species HCO_3^-, based on the spectroscopic evidence collected. Current suppression was observed in the voltammograms of the iron sulfides, while current enhancement was observed in the voltammograms of the iron-nickel sulfides. These differences were linked to the different nature and transformations of the electrode surface of the iron and iron-nickel sulfides on application of potential with electrolyte media. On variation of the Fe:S and Fe:Ni stoichiometries of the iron and iron-nickel sulfides, the voltammetric responses remained similar with small differences in the anodic currents attributed to different amounts of sulfates and elemental sulfur produced. The work described in this thesis provides a new insight into the stability and potential thermodynamic transformations of iron (-nickel) sulfides, on application of an applied electrode potential, in aqueous environments essential for future CO_2 reduction applications.

Acknowledgements

I would like to thank my supervisor, Katherine Holt, for her guidance, support, knowledge and encouragement throughout this journey. I would also like to thank Daren Caruana for his contagious curiosity. Thanks also go to my sponsors, the Ministry of Education Brunei and Universiti Brunei Darussalam, for funding my PhD.

I would like to particularly thank Nathan Hollingsworth, Anna Roffey and Husn-Ubayda Islam from the CO_2 consortium for their invaluable help, conversation, time and enthusiasm while working on the same project. I would also like to thank all members of the electrochemistry group, past and present, who are always beaming with positivity in the lab and office everyday. Thank you also to everyone I have met and worked with in the past eight years in UCL! Your friendships have enriched my experience at UCL immensely.

Finally, thank you to my parents and siblings for their encouragement and patience with me, and to FXG for everything.

List of Figures

List of Appendix Figures

List of Tables

List of Symbols

Symbol	Meaning	Unit
A	Absorbance	
a	Unit cell	Å
c	Speed of light	m s^{-1}
c	Concentration	mol L^{-1}
d	Density of target	kg m^{-3}
D	Diffusion coefficient	cm^2 s^{-1}
DP	Depth of penetration	m
e	Elementary charge	C
E	Energy	eV
E_0	Standard potential	V
E_{el}	Electronic energy	J
ei	Atomic charges	C
E_{ocp}	Open circuit potential	V
E_p	Peak potential	V
Ep	Photon energy	J
E_{rot}	Rotational energy	J
E_{vib}	Vibrational energy	J
F	Faraday's constant	C mol^{-1}
F	Fourier frequency of interferogram	Hz
$f_j(k)$	Atomic scattering amplitude	Å
ΔG°	Gibbs energy change	kJ mol^{-1}
ΔG_f	Gibbs energy of formation	kJ mol^{-1}
h	Planck's constant	J s
I	Current	A

I	Sample spectrum intensity	
I_0	Background spectrum intensity	
j	Current density	mA cm^{-2}
j	Scattering path	Å
kH	Henry's Law constant	mol L^{-1} kPa^{-1}
k	Force constant	kg s^{-2}
k	Wavenumber of photoelectron	cm^{-1}
l	Path length	cm
L	Libration vibration	
m	Atomic mass	kg
n	Refractive index	
n_c	Crystal refractive index	
n_s	Sample refractive index	
n_{sc}	Ratio of refractive index of sample to crystal	
N	Number of atoms	
N_j	Number of neighbouring atoms	
P	Pressure	Pa
Q	Charge	C
Q_p	Charge under peak	C
R	Real space	Å
r_i	Atomic positions	m
R_j	Bond distance of neighbouring atoms	Å
T	Transmittance	
T	Temperature	K, °C
t	Time	s
v	Velocity	cm s^{-1}
ν	Frequency	Hz

Z	Atomic number	
$\delta_j(k)$	Atomic phase shift	Å
δ	Optical path difference	cm
δ	Diffusion layer thickness	cm
δ	Bending vibration	
δ_d	Deformation	
θ_R	Angle of refraction	°
θ_c	Critical angle	°
θ_i	Angle of incidence	°
σ_j^2	Static and thermal disordering of atoms	$Å^2$
ε	Absorptivity	L mol^{-1} cm^{-1}
λ	Wavelength	nm
μ	Dipole moment	D
μ	Reduced mass	kg
μ(E)	X-ray absorption coefficient	
ν_{asym}	Asymmetric stretching vibration	
ν_{sym}	Symmetric stretching vibration	
ν	Stretching vibration	
$\bar{\nu}$	Wavenumber	cm^{-1}
$\chi(k)$	Mean free path of photoelectron	Å

List of Abbreviations

ATR	Attenuated total reflectance
BDD	Boron-doped diamond
CE	Counter electrode
CV	Cyclic voltammetry
DFT	Density Functional Theory
DP	Depth of penetration
EXAFS	Extended x-ray absorption fine structure
GR	Green rust
HER	Hydrogen evolution reaction
HRTEM	High-Resolution Transmission Electron Microscopy
ICDD	International Centre for Diffraction Data
LCF	Linear Combination Fitting
MSA	Mineralogical Society of America
OCP	Open circuit potential
PBS	Phosphate buffer
PEM	Proton exchange membrane
RDE	Rotating Disk Electrode
SCE	Saturated Calomel Electrode
SEIRAS	Surface Enhanced Infrared Absorption Spectroscopy
SHE	Standard Hydrogen Electrode
WE	Working electrode
XAFS	X-ray Absorption Fine Structure
XANES	X-ray absorption near-edge structure
XAS	X-ray Absorption
XRD	X-ray Diffraction
ZPD	Zero path difference

Chapter 1 Introduction

Iron and iron-nickel sulfides have garnered interest for their potential use as carbon dioxide reduction catalysts[1,2]. Of particular interest in this thesis are iron sulfide greigite, (Fe_3S_4) and iron-nickel sulfide violarite, ($FeNi_2S_4$). The cubic structure of greigite and violarite has been likened to the cubane structure found in iron-sulfur proteins ferredoxins (Fe_4S_4) and the iron-nickel active sites, Ni-[Fe_4S_4] or $NiFeS_5$, cubane clusters of carbon monoxide dehydrogenase (CODH). Given these structural similarities, iron and iron-nickel sulfides have been proposed to have the potential to perform similar CO/CO_2 interconversion efficiently carried out by CODH enzyme.

The work in this thesis was also motivated by the iron sulphide membrane origin of life theory where greigite and violarite present in deep sea hydrothermal vents, under high temperature and pressure, were proposed to be catalytic for CO_2 reduction. Aside from this proposed theory, greigite has been proven to reduce CO_2 under ambient conditions, while violarite was shown to reduce CO_2 under high CO_2 pressures[2,3]. However, in these published studies, no in-situ characterisation of the electrodes were carried out to verify the nature of the greigite and violarite electrodes during the catalysis and the possible redox or thermodynamics transformations of these iron and iron-nickel sulfides that may occur. CO_2 reduction efficiency on both greigite and violarite will most likely depend on the nature and transformation of the electrode during catalysis. Additionally, the redox chemistry of greigite and violarite has not been well established in literature, with published electrochemical studies lacking in in-situ characterisation to verify the assigned redox reactions.

Also of interest in this work are the iron sulfide, pyrrhotite (Fe_7S_8) and the iron-nickel sulfide, pentlandite ($(Fe,Ni)_9S_8$). These additional materials were considered to compare the effect of differing the Fe:S and Fe:Ni ratios of the iron and iron-nickel sulfides on the electrochemical behaviour, as well as the effect of the introduction of CO_2 on their electrochemical responses.

1.1. Project aims, objectives and tasks

Iron and iron-nickel sulfides, specifically greigite and violarite, have been proven to reduce CO_2 on application of negative potentials (up to −1.3 V vs AgCl|Ag).[2,3] However, at such low potentials, metal sulfides are predicted to undergo reductive decomposition and competing reactions such as water reduction may also take place. The aim of the work described in this thesis is to determine the stability of the iron (-nickel) sulfides under conditions where CO_2 reduction has been demonstrated to take place.

To meet the aim of this project, this thesis has the following objectives:

i) To define redox potentials of the FeS and FeNiS materials in aqueous solutions under ambient conditions under both argon and CO_2 atmospheres.

ii) To deterine if changes to the oxidation state and coordination environments of the metal ions (Fe or Ni) in the bulk structure or surface of the FeS and FeNiS electrodes take place at the potentials used for previous CO_2 reduction studies.

iii) To meausre if changes in the IR-active groups present within the interfacial layer between the electrode and electrolyte that could affect the stability of the nanoparticles.

iv) To develop in-situ IR and XAS spectro-electrochemical cells to study the electrode surface in-situ using In-situ Attenuated Total Reflectance Fourier Transformed Infrared (ATR-FTIR) and X-ray Absorption Spectroscopy (XAS) techniques.

The following tasks were set to achieve the aim and objectives of the project:

i) A systematic pH study of the voltammetric responses of the nanoparticles under both argon and CO_2 atmospheres. This systematic pH study will allow:
   a. Comparison of the electrochemical behaviour of the nanoparticles under both argon and CO_2.
   b. Comparison of the electrochemical behaviour of the iron sulfides (greigite and pyrrhotite) vs. the iron-nickel sulfides (violarite and pentlandite) to understand the effect of Ni on the electrochemical behaviour of iron sulfides.
   c. Comparison of the electrochemical behaviour of the iron and iron-nickel sulfides on varying the stoichiometric ratios of Fe:S and Fe:Ni (greigite vs. pyrrhotite and violarite vs. pentlandite).
   d. Examining the effect of the electrolyte species and pH on the electrochemical response of the nanoparticles
   e. Predicting the possible redox transformations occurring on the electrodes based on the redox features recorded.

ii) Development of an in-situ spectro-electrochemical cell suitable for investigating the electrode surface in-situ using FTIR and XAS techniques. This will allow:
   a. Determination of the IR-active species present within the interfacial layer of the electrode and electrolyte produced on application of an applied electrode potential.
   b. Detection of the formation of solid-state redox products, if any, using XAS on application of an applied electrode potential.
   c. Monitoring of the absence or presence of CO_2 and its dissolved species on introduction of CO_2 under the experimental conditions tested on application of an applied electrode potential.
   d. Correlation of the transformation of the electrodes to the observed voltammetric responses under both argon and CO_2.
   e. Correlation and comparison of the transformation and the nature of the electrodes to the published CO_2 reduction efficiencies.

1.2. Thesis outline

The structure of this thesis is as follows. A brief introduction on the structures and properties of the iron and iron-nickel sulfides studied are detailed in chapter one. A discussion on the speculative role of iron (-nickel) sulfides in origins of life theories, which was one of the motivations of this work, the role of iron (-nickel) sulfides in nature, as well as their potential use for CO_2 reduction applications will be presented in the same chapter. The principles behind the main techniques used in this work are discussed in Chapter 2. Chapter 3 presents the cyclic voltammetry studies of greigite under both argon and CO_2 atmospheres. The implications of the findings in this chapter on the hypothesised role of greigite in the origins of life theory, as well as its potential for CO_2 reduction are discussed. The effect of the electrolyte species and pH used on the electrochemical response of greigite was also investigated in this chapter. To verify the assignments of the redox features made in Chapter 3, in-situ spectroscopic evidence of the transformations of greigite, collected using FTIR and XAS techniques, are presented in Chapter 4. The addition of Ni in the nickel-analogue of greigite, violarite, on its electrochemical properties is explored in Chapter 5. A comparison between greigite and violarite and the significance of incorporating nickel in greigite structure is reviewed in this chapter. Additional spectroscopic evidence were collected and presented in Chapter 6 to understand and correlate the transformations of the violarite electrode to its electrochemical behaviour reported in Chapter 5. The data in chapters 5 and 6 were used to compare the CO_2 reduction efficiencies published in literature of violarite compared to greigite. Chapter 7 investigates the effect of the variation in stoichiometry of Fe:S and Fe:Ni ratios of the iron and iron-nickel sulfides on their electrochemical behaviour. The final chapter highlights the findings in this work which provides new information into the field of iron and iron-nickel sulfides and suggested further work on iron (-nickel) sulfides to consider in the future.

1.3. Literature review

1.3.1. Iron sulfides

Iron sulfides are the most widely occurring metal sulfides in the Earth's crust, existing in various phases leading to diverse physical properties (detailed in Table 1). Iron sulfides can be classed into a group of solids / minerals and aqueous complexes / clusters, many of which play important roles in geology, marine systems and key biochemical reactions[4].

Table 1.1 Selected iron sulfides and their properties[4,5]. Reprinted with permission from ACS and Science Reviews 2000. Copyright 2007 American Chemical Society and 1987 Science Reviews 2000.

Composition / mineral	Structure	Electrical and magnetic properties
FeS / mackinawite	Tetragonal, *P*4/*nmm*	Metallic conductor, paramagnet (above 234 K)
FeS_2 / pyrite	Cubic, *Pa*3	Semiconductor, diamagnet
FeS_2 / marcasite	Orthorhombic, *Pnnm*	Semiconductor, diamagnet
Fe_3S_4 / greigite	Spinel-type, cubic, *Fd*3*m*	Metallic conductor, ferrimagnet
$Fe_{1-x}S$, x > 0.2 / pyrrhotite	NiAs-type; monoclinic *A*2/*a* or hexagonal *P*6/*mmc*	Monoclinic: Metallic conductor, ferrimagnet Hexagonal: metallic conductor, antiferromagnet
FeS / troilite	NiAs-type, hexagonal, *P*2*c*	Metallic conductor, antiferromagnet

Solid iron sulfides are further divided into stable high temperature and metastable low temperature phases. The extremely stable pyrite and pyrrhotite phases dominate above 350°C. In addition to these stable iron sulfide phases, metastable phases such as greigite, mackinawite, troilite and marcasite exist below 350°C.

This thesis will concentrate upon the iron sulfides: greigite and pyrrhotite. As mentioned previously, greigite was chosen as the material of interest for CO_2 reduction applications based on its proposed role in the iron sulphide membrane theory as well as published CO_2 reduction studies on greigite. Pyrrhotite, which has a different Fe:S stoichiometry compared to greigite, was chosen in this work to study the effect of the variation in Fe:S ratios on the electrochemical properties of both greigite and pyrrhotite.

1.3.1.1. Greigite

Greigite is an iron thiospinel, Fe_3S_4 and has a structure analogous to iron oxide magnetite, Fe_3O_4[16]. The valence electrons in greigite are localised and it has ferromagnetic and semiconducting properties[43]. The Mössbauer spectrum of greigite suggests that its inverse spinel structure contains high-spin Fe^{2+} and Fe^{3+} cations[43]. Greigite is a metastable sulfide as demonstrated by its rare existence in nature and is one of the less studied iron sulfides[43]. It occurs in aquatic environments[2-6] and soils, and is present inside the chimneys of deep sea alkaline hydrothermal vents.

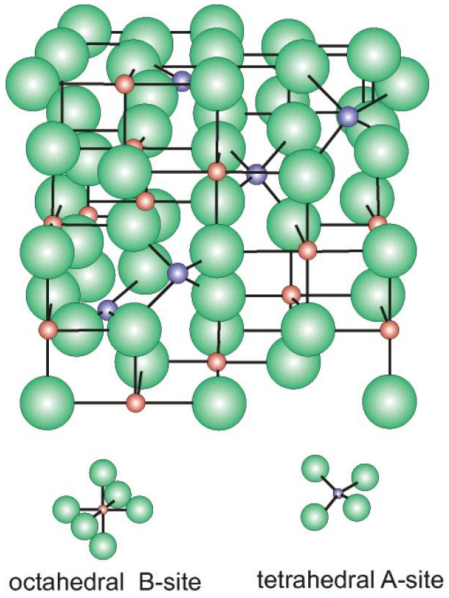

Figure 1.1 Structure of greigite. Inverse spinel structure: $A(AB)_2S_4$, where Fe(II) atoms occupy tetrahedral A sites and mixed Fe(III) and Fe(II) occur in octahedral B sites[4]. Reprinted with permission from ACS. Copyright 2007 American Chemical Society.

Greigite has a cubic unit cell of a = 9.876 Å. The unit cell, shown in Figure 1.1, contains a cluster of eight Fe_3S_4 moieties, with eight and 16 Fe atoms occurring in tetrahedral A-sites and octahedral B-sites respectively. Molecular orbital calculations suggest a mixture of Fe(III) and Fe(II) occurring in octahedral B sites, thus its structure tends towards an inverse spinel, suggesting nonstoichiometry in greigite.

The cubic structure of greigite occurs in FeS active centres of iron sulfur proteins, known as ferredoxins, which are essential electron carriers in many key biochemical pathways. This similarity in structure and greigite's presence in deep sea hydrothermal vents has resulted in greigite proposed in the Iron Sulphide Membrane theory as a catalyst for CO_2 reduction in the ocean to produce organic molecules (see section 1.3.4)[42]. In anoxic marine environments and lake sedimentary systems, greigite is produced through biotic mineralisation by magnetotactic bacteria[6]. This bacteria produces greigite to achieve directional sensing using magnetosomes, which are chains of ferromagnetic crystals.

Recent applications of greigite include; electrocatalyst for PEM Water electrolysis[7], a cathode material for magnesium batteries[8] and an anode material in lithium ion batteries[9].

1.3.1.2. Pyrrhotite

The iron-deficient phase pyrrhotite, $Fe_{(1-x)}S$ (where $x > 0.2$), is the most abundant iron sulfide on Earth, solar system and universe, but is rare in marine systems. Pyrrhotite minerals appear dark and rusty brown and are often found in basic igneous or ultrabasic rocks, hydrothermal mineral deposits, and contact-metasomatic sediments[10].

The formula of pyrrhotite minerals can also be expressed as $Fe_{n-1}S_n$ with $n \geq 8$ to give structures ranging from Fe_7S_8 to $Fe_{11}S_{12}$[11]. As a result of this, different possible arrangements of iron vacancies in pyrrhotites exist leading to monoclinic, hexagonal and orthorhombic structures. The most Fe-deficient end member, Fe_7S_8, has a monoclinic symmetry. This thesis investigates the

monoclinic pyrrhotite, Fe_7S_8, hence this section focuses more on the monoclinic structure.

The monoclinic structure of pyrrhotite contains alternating layers of full Fe sites and layers of Fe sites with vacancies, thus has a lower symmetry than the hexagonal structure. The monoclinic structure is regarded as a slightly distorted hexagonal structure, in which the c axis is tilted with respect to the ab-plane[10].

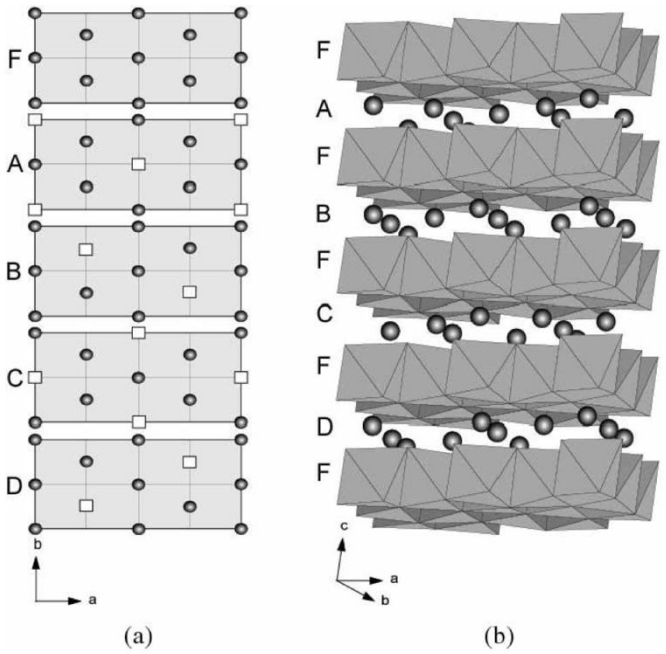

Figure 1.2 The 4C monoclinic superstructure of pyrrhotite[10]. (a) Four different vacancy arrangements in cation layers, A, B, C and D, and F represents a layer with no Fe vacancies. (b) Stacking sequence of vacancy layers and vacancy free layers. Reprinted with permission from Taylor & Francis. Copyright 2005 Taylor & Francis.

The 4C monoclinic superstructure of pyrrhotite can be expressed as (. . . FAFBFCFDF . . .), where F represents a layer with no Fe vacancies Figure 1.2a. Fe vacancies occur in alternate rows (A, B, C, D) and are confined to every other site (see Figure 1.2b).

In Fe_7S_8, Fe atoms are octahedrally coordinated, but S is both five- and six-fold coordinated due to Fe vacancies. Due to the common sulfur deficiency nature of pyrrhotites, Fe atoms exist in both Fe^{2+} and Fe^{3+} states, with Fe^{3+} ions found in vacancy bearing layers. The 4C pyrrhotite can thus be formulated as $(Fe_2^{3+}Fe^{2+})(Fe_4^{2+})S_8$[10].

Both the monoclinic and hexagonal pyrrhotite are metallic conductors. However they have contrasting magnetic properties; monoclinic pyrrhotite is ferrimagnetic, while hexagonal pyrrhotite is antiferromagnetic.

Magnetism in pyrrhotites is dependent on the ordering of Fe atoms and vacancies in the vacancy bearing layers[10]. The ferrimagnetism in monoclinic pyrrhotite is attributed to the antiparallel orientations of magnetic moments in the vacancy bearing layers (A, B, C, D) and vacancy free layer (F) (see Figure 1.3). Due to the presence of vacancies in alternate layers, an overall net magnetic moment > 0 is produced resulting in ferrimagnetism.

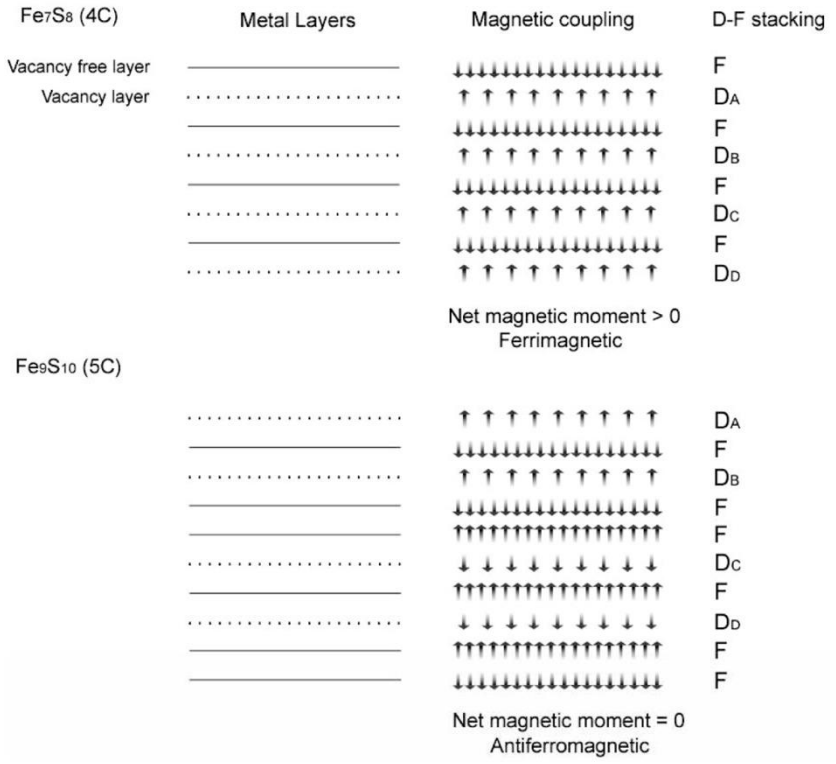

Figure 1.3 Stacking sequence of the metal vacancy layer and vacancy free layer for 4C Fe_7S_8 and 5C Fe_9S_{10} hexagonal structures[10]. Reprinted with permission from Taylor & Francis. Copyright 2005 Taylor & Francis.

In terms of applications, pyrrhotite is of interest in mineral processing as it is one of the major iron ores used as feedstock in flash smelting processes for metal extractions. Pyrrhotite has also been used in sulfuric acid production, mine waste remediation and wastewater treatment.

1.3.2. Iron-nickel sulfides

The iron-nickel sulfides studied in this thesis are violarite ($FeNi_2S_4$) and pentlandite $(Fe,Ni)_9S_8$. Iron-nickel sulfides were considered in this project to examine the effect of the addition of Ni in iron sulfides on its electrochemical properties and CO_2 reduction efficiencies. Similar to greigite, violarite was chosen as the material of interest in this thesis based on its proposed role in the iron sulphide membrane theory as well as published CO_2 reduction studies on violarite. Pentlandite, which has a different Fe:Ni ratio compared to violarite, was chosen in this work to study the effect of the variation in Fe:Ni ratios on the electrochemical properties of both iron-nickel sulfides.

Both violarite and pentlandite are major nickel-hosting sulfide minerals. Thus, industrial nickel recovery from both of these minerals are of economic importance. Additionally, pentlandite is an important carrier of cobalt and platinum group metals such as palladium and rhodium.

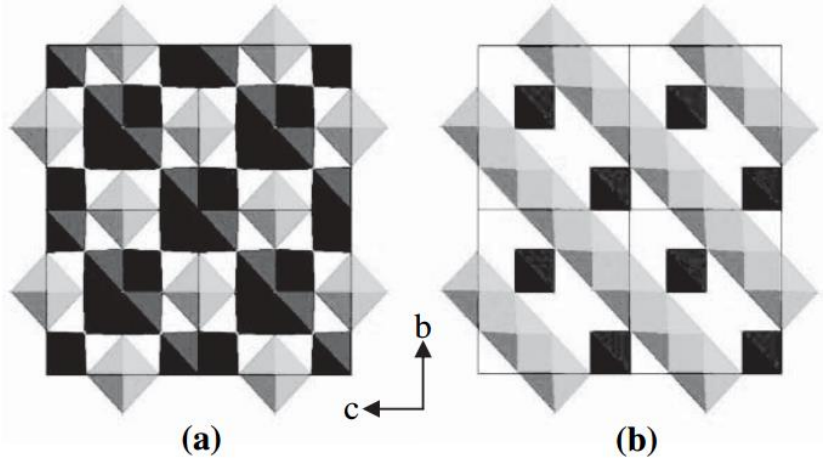

Figure 1.4 Schematic representations of (a) pentlandite and (b) violarite structures. MS_6 octahedra are grey while MS_4 tetrahedra are black[12]. Reprinted with permission from Mineralogical Society of America. Copyright 2006 MSA.

Both violarite and pentlandite have similar cubic close-packed sulfur lattices[13]. The main structural difference is in the arrangement of the metal cations in the tetrahedral and octahedral sites within the sulfur lattice (see Figure 1.4). In pentlandite, the Fe and Ni atoms occupy ½ of the tetrahedral sites and ⅛th of the

octahedral sites, whereas in the violarite structure they occupy ½ of the octahedral and ⅛th of the tetrahedral sites[12].

In this thesis, the iron-nickel core structure of pentlandite and violarite is of interest as it is comparable to the iron-nickel active centres of CO-hydrogenase. Thus, these iron-nickel sulfides may have the potential to perform the same chemistry as hydrogenases and ferredoxins. The section below details the structure and recent applications of violarite and pentlandite.

1.3.2.1. Violarite

Violarite is the nickel analogue of greigite. Similar to greigite, violarite has been suggested as an important precursor in the iron sulfide membrane theory and it may have played a more important catalytic role than greigite[14]. Violarite in nature forms via exosolution as hypogene product of pentlandite but more commonly as a supergene oxidation product of pentlandite[13]. Violarite is a normal thiospinel with extensively delocalised valence electrons[14]. It has unit cell of a = 9.465 Å and space group $Fd3m$[15]. The unit cell is composed of eight AB_2S_4 subunits with tetrahedral A-sites and octahedral B-sites. Nickel occurs in both the tetrahedral and octahedral sites[14]. The iron atom is most likely restricted to the octahedral site in low-spin state[14]. With respect to the charges on metal cations, violarite can be expressed as $[(Ni^{3+})(Fe^{2+},Ni^{3+})]S_4$[12].

1.3.2.2. Pentlandite

Pentlandite is the nickel analogue of pyrrhotite and is often present in pyrrhotite ores. Pentlandite forms with pyrrhotite as exsolution products from the breakdown of monosulfide solid solution[12]. Pentlandite has unit cell of a = 10.1075 Å and is associated with space group Fmm[12]. The tetrahedral and octahedral sites are each occupied by an equal mixture of Ni and Fe cations. Pentlandite is also a metallic conductor and shows high electronic conductivity[16]. Recently, a pentlandite ore was used as a hydrogen evolution reaction (HER) catalyst, echoing similar applications of greigite[16]. Advantages of using natural ore pentlandite as HER catalyst includes its low cost, high availability and

robustness in extremely acidic conditions where precious metal catalyst are often poisoned.

1.3.3. Iron (-Nickel) Sulfides in Nature

Iron sulfide minerals can be found over much of the Earth's surface, especially in ore deposits. They are also common in black sulfurous shales and mudstones[17]. Iron sulfides play an important role in Earth's biogeochemical sulfur cycle as well as the iron cycle[4]. This section highlights the role of iron sulfides in nature and key biochemical reactions.

Greigite, for example, is found in magnetotactic bacteria. These bacteria respond to magnetic fields and were first discovered by Blakemore in 1975[18]. Magnetotactic bacteria produce magnetosomes which are made of nanoscale ferrimagnetic crystals of greigite (Fe_3S_4) and magnetite (Fe_3O_4). This ferrimagnetism directs the bacteria along the Earth's geomagnetic fields towards sediments and anaerobic areas favourable to their growth[18].

Iron sulfides have also been observed in Martian meteorites and carbonaceous chondrites. Their discovery has led to the suggestion of iron sulfides as catalysts in possible organic synthesis on ancient Mars[19–22].

The cubane structure of greigite and violarite is also found in activation centres and electron transfer sites in several enzymes, in particular, Ni—X—Fe_4S_4 active centres of CO dehydrogenase and acetyl coenzyme-A synthase and the cubane type $[Fe_4S_4]^{2+}$ structure of the ferredoxins and nitrogenase found in both archaea and bacteria[17].

1.3.4. Iron (-Nickel) Sulfides in Origins of Life Theories

Iron(-nickel) sulfide minerals have been proposed to play a role in two origins of life theories: the Iron-Sulfur World theory[23] and the Iron-Sulfide Membrane theory[14]. Both theories have been subjected to experimental testing and reformed over time[1,19,24–32]. Both hypotheses propose CO_2 reduction taking place on iron (-nickel) sulfide minerals which is of interest in this thesis. This section will discuss key concepts in both theories and their significance to the project.

The Iron-Sulfur World theory[23], proposed by Wächtershäuser, suggests the oxidative formation of pyrite, in equation (1.1) and (1.2), from HS^- or H_2S and Fe^{2+} species, as a plausible source of reducing power for the origin of life:

$$FeS + HS^- \rightarrow FeS_2 + H^+ + 2e^- \quad (1.1)$$

$$FeS + H_2S \rightarrow FeS_2 + 2H^+ + 2e^- \quad (1.2)$$

In this hypothesis, the coupling of CO_2 fixation and pyrite formation, in reactions (1.3)and (1.4), was proposed to generate small organic molecules, leading to the emergence of life.[23]

$$4CO_2 + 7FeS + 7H_2S \rightarrow (CH_2COOH)_2 + 7FeS_2 + 4H_2O \quad \Delta G° = -420 \text{ kJ mol}^{-1} \quad (1.3)$$

$$HCO_3^- + FeS + H_2S \rightarrow HCOO^- + FeS_2 + H_2O \quad \Delta G° = -37.1 \text{ kJ mol}^{-1} \quad (1.4)$$

The thermodynamic constraint for the spontaneous reduction of CO_2 by FeS to occur requires $E_{CO_2/?} < E_{O/R,}$ where R is the reductant and ? is the CO_2 reduction product (see Table 1.2 for a list of products and thermodynamics of CO_2 reduction). There is a limited range of mixed potentials at which the spontaneous coupled redox reactions could take place, as shown by the black line in Fig A.20 in Appendix 7. Based on the thermodynamic calculations in Appendix 7 at pH 7, the redox potentials of most of these processes show that it is thermodynamically not feasible for the spontaneous reduction of CO_2 to take place. With the possible exception of that for the reduction of CO_2 to HCOOH, (E = −0.61 V) in Table 1.2, the standard equilibrium potentials do not appear to be sufficiently low to be

driven by the oxidation of FeS to FeS_2 (where E of reactions (1.6)-(1.8) > E of reaction (1.5)).

$$FeS_2 + H^+ + 2e^- \rightleftarrows FeS + H_2S \qquad E = -0.5780\ V\ @\ pH\ 7 \qquad (1.5)$$

$$CO_2(g) + 8H^+ + 8e^- \rightleftarrows CH_4 + 2H_2O \qquad E = -0.2447\ V\ @\ pH\ 7 \qquad (1.6)$$

$$CO_2(g) + H^+ + 2e^- \rightleftarrows HCOO^- \qquad E = -0.4319\ V\ @\ pH\ 7 \qquad (1.7)$$

$$2H^+ + 2e^- \rightleftarrows H_2 \qquad E = -0.4141\ V\ @\ pH\ 7 \qquad (1.8)$$

Wächtershäuser also did not specify under which conditions FeS reacts with HS^- or H_2S in reactions (1.1) and (1.2). The current author assumes that the reaction with H_2S proceeds at pH < 7, while the reaction with HS^- occurs at pH > 7. Additionally, there is also a kinetic constraint for reactions (1.1) and (1.2) where the reactions are only sustainable if the product were a fast ion conductor, which iron sulfides such as FeS_2 are not.

Separately, Russell and Hall developed the proposal for the Iron-Sulfide Membrane theory[14]. In this theory, a hypothetical system is proposed, where iron monosulfide (mackinawite) precipitated from the interface between iron-rich alkaline hot springs and sulfur-rich acidic ocean of the early Earth billions of years ago in deep hydrothermal vents[14]. The precipitate was proposed to form compartments containing an alkaline and highly reduced hydrothermal solution rich in Fe, Ni and Co. The iron sulfide membrane undergoes further geochemical transformations with the hydrothermal solution to form mixed valence catalytic phases such as greigite (Fe_3S_4) and violarite ($FeNi_2S_4$)[14]. In the presence of such membranes, it was suggested that electron transfer for reactions such as CO_2 reduction to organic compounds could occur[14]. The main source of electrons for CO_2 reduction in this theory was suggested to be from H_2 oxidation from serpentinization reactions, which involve hydration and transformation of the rocks in the Earth's mantle[14].

Clearly, both models described above are equally difficult to verify. Despite geochemical evidence of rock remnants hinting conditions of early Earth, it is difficult to be certain of which of these conditions existed, and hence were

favourable for formation of organics important for life. The main appealing aspect in both theories is the concept of CO_2 reduction on the surface of iron (-nickel) sulfides. For CO_2 reduction to be feasible, the kinetic and thermodynamic barriers must be considered and overcome. In the case of hydrothermal systems (proposed by Russell and Hall)[14], the absence of light in deep oceans excludes a photochemical mechanism for CO_2 reduction. However, if the geochemical setting billions of years ago was characterised by more extreme pressures and temperatures than those used in most aqueous CO_2 reduction experiments, these conditions may have aided the catalytic activation of carbon dioxide[14].

Given the thermodynamic and kinetic restraints discussed above, the Iron-Sulphur Theory proposed by Wachtershauser would seem an unlikely route to CO_2 reduction under the ambient conditions explored in this thesis. Therefore, this proposed model is not discussed any further in this work. However, the role of iron (-nickel) sulfides as catalytic surfaces, as proposed by Russell and Hall, may still be important, if a source of reducing electrons is made available (e.g. through application of a sufficiently negative applied potential). The stability of such a membrane under CO_2 reduction conditions is therefore considered briefly in the discussion of the results.

1.3.5. Electrochemical CO_2 reduction

The gradual depletion of fossil fuel reserves and an increasing concentration of CO_2 present in the atmosphere which contributes to global warming represent the two main energy crisis faced today[34]. The electrochemical reduction of CO_2 to useful chemical feedstock particularly when coupled with renewable electricity offers a promising means of storing electricity in chemical form[34]. This would decrease the dependence on fossil fuels and the negative impact of CO_2 emissions[34]. Electrochemical CO_2 reduction on iron and iron-nickel sulfides is of particular interest in this project. This section reviews the challenges in this field, and discusses reports on CO_2 reduction performed on iron (-nickel) sulfides. Reviews by Wu *et al*[34] and Taifan *et al*[35] have been referred to in constructing this section.

1.3.5.1. Structure and properties of CO_2

CO_2 is a linear triatomic molecule with a double bond between the carbon and oxygen atoms (O=C=O). The central carbon atom possesses sp hybridisation and a C-O distance of 116.3 pm, shorter than a C=O bond distance involving an sp^2 carbon centre[34]. The molecular orbital diagram of CO_2 is shown in Figure 1.5.

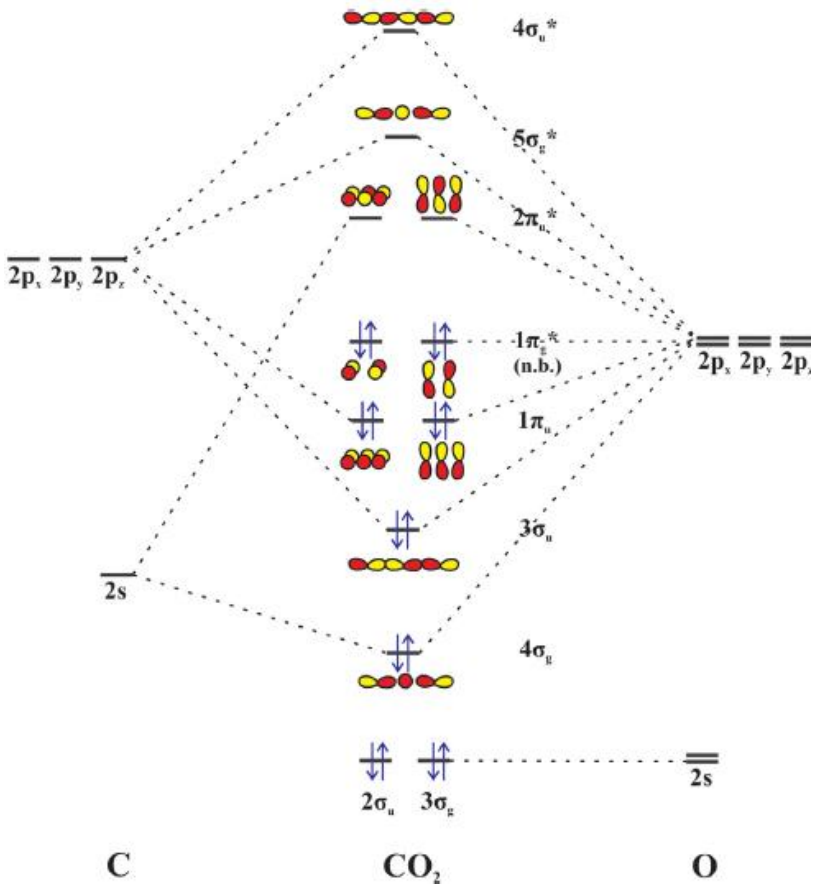

Figure 1.5 Molecular orbital diagram of linear CO_2 ($D_{\infty h}$ symmetry).[35] Reprinted with permission from Elsevier. Copyright 2016 Elsevier.

The 1s shells of the C and O atoms are non-bonding orbitals thus do not contribute to the bonding of CO_2. The $2p_x$ and $2p_y$ orbitals are located in the same plane forming three doubly degenerate molecular orbitals, $1\pi_g$ (non-bonding), $1\pi_u$ and $2\pi u^*$. The former does not contain a contribution from the C atom as the 2p orbitals of the O atoms are out of phase and contain lone pair electrons. The $2p_z$ and 2s atomic orbitals combine to form six σ molecular orbitals labelled as $3\sigma_g$, $2\sigma_u$, $4\sigma_g$, $5\sigma_g*$, $3\sigma_u$ and $4\sigma_u^*$. Excluding the core electrons, the CO_2 molecule shares 16

electrons in the molecular orbitals, with eight electrons occupying four σ orbitals, and the other eight in two π orbitals.

The carbon atom in a CO_2 molecule is electrophilic and hence may interact with an electron-rich surface via chemisorption resulting in the bending of the CO_2 molecule. In a bent CO_2 molecule, the oxygen atom is prone to attack by protons, while the C atom is prone to the reaction with the adsorbed H atoms that often requires a higher activation energy. A CO_2 molecule has no net electric dipole due to its symmetry. It has two IR-active vibrational bands (anti-symmetric stretching mode at 2349 cm^{-1} and a bending mode near 666 cm^{-1}) and one symmetric stretching Raman-active band at 1388 cm^{-1}.

1.3.5.2. Thermodynamics of electrochemical reduction of CO_2

CO_2 is a very stable molecule with Gibbs energy of formation $\Delta G_f = -394$ kJ mol^{-1} in gas phase. It is the most oxidised form of carbon and hence the only possible chemical transformation would be to reduce it. Upon one electron transfer, the geometry changes from linear to bent, resulting in an irreversible reduction.

Table 1.2 Gibbs energy change and standard potential for electrochemical reduction of CO_2. [34] Reprinted with permission from Elsevier. Copyright 2014 Dalian Institute Chemical Physics, the Chinese Academy of Sciences.

Reaction	ΔG^0 [a] (kJ/mol)	E^0 / V vs. SHE	$E^{0'}$ / V vs. SHE [b]
$CO_2 + e^- = CO_2^{\bullet-}$	183.32	−1.90	—
$CO_2 + 2H^+ + 2e^- = CO + H_2O$	19.88	−0.10	−0.52
$CO_2 + 2H^+ + 2e^- = HCOOH$	38.40	−0.20	−0.61
$CO_2 + 6H^+ + 6e^- = CH_3OH + H_2O$	−17.95	0.03	−0.38
$CO_2 + 8H^+ + 8e^- = CH_4 + 2H_2O$	−130.40	0.17	−0.24
$2CO_2 + 12H^+ + 12e^- = C_2H_4 + 4H_2O$	−40.52	0.07	−0.34
$2CO_2 + 12H^+ + 12e^- = C_2H_5OH + 3H_2O$	−49.21	0.085	−0.3287
$3CO_2 + 18H^+ + 18e^- = C_3H_7OH + 5H_2O$	−52.1	0.09	−0.3237

[a] Free Gibbs energy of reaction per mole of CO_2, at 25 °C.
[b] The apparent standard potential is calculated at pH = 7 and 25 °C.

Under mild conditions, CO_2 can be electrochemically reduced, but only with a very low energy conversion efficiency of ~ 30 – 40%[36]. The electrochemical method of reducing CO_2 has an advantage of using water as the proton source. CO_2 is

reduced by incoming electrons and protons to a variety of products depending on the catalysts[34]. Table 1.2 lists the possible products and thermodynamics of electrochemical CO_2 reduction.

The reduction of linear CO_2 to the bent anion radical $CO_2^{\bullet-}$ is difficult ($E^0 = -1.90$ vs SHE (Standard Hydrogen Electrode)) and is the rate determining step in the overall reduction reaction. CO_2 reduction via electrochemical methods has a number of disadvantages at the very negative reduction potentials often used in experiments including competition with Hydrogen Evolution Reaction (HER) when using aqueous solutions, high overpotentials and low Faradaic efficiencies. These problems have been partly resolved by selection of electrode material, pre-treatment of electrode, special construction of electrochemical cell and using non-aqueous solvents[14].

1.3.5.3. Factors affecting CO_2 reduction products

Products obtained from CO_2 reduction vary according to the catalyst material and electrolyte used. Heterogeneous catalysts tested for electrochemical CO_2 reduction reported in literature are categorised based on the products obtained listed in Table 1.3.

Metallic catalysts are classified based on their electronic configurations in the d orbital: sp and d metal electrodes. The "*sp* metals" group refer to metals with completely filled d orbitals (d^{10}) such as Hg, Pd, In, Sn, Cu, Zn, Ag, Au and Cd, while "*d* metal" electrodes refer to metals with partly filled d orbitals. The electrocatalytic activity of heterogeneous catalyst can be associated with their electronic configuration. CO_2 reduction products are highly dependent on binding energies of the intermediates on the metals. For example, Cu is the only metal that displays electrocatalytic activity for hydrocarbons, alcohols and aldehydes. However, Cu surfaces also suffer from deactivation. The reason for deactivation is still unclear, however, it has been proposed that over time the surface may be poisoned or is contaminated by Fe and Zn deposited from the electrolyte. D group metals such as Fe and Zn have very low activity for CO_2 reduction due to the

competing and dominant hydrogen evolution reaction. Thus, this would decrease catalytic activity of Cu if such deposition occurs.

Table 1.3 Productivity of CO_2 reduction on *sp* and *d* metals[34]. Reprinted with permission from Elsevier. Copyright 2014 Dalian Institute Chemical Physics, the Chinese Academy of Sciences.

Metal		Product	
		Aqueous electrolyte	Non-aqueous electrolyte
sp metals (d^{10} electronic configuration)	*sp* metals (Hg, In, Sn, Pb, Cd)	Formic acid	Oxalate (Tl, Pb, Hg)
	sp metals (Zn, Ag, Au)	CO	CO
	sp metals (Cu)	C_2H_3, CH_4, HCOOH, CO and alcohols	CO
d metals (partly filled with *d* orbitals)	*d* metals (e.g. Pt and Pd)	Adsorbed CO	CO (including Ni)
	d metals (e.g. Ru)	Low yield of hydrocarbons, alcohols, formaldehyde	
	d metals (Fe, Cr, Mo, Ti, Nb)	Weak performance	Oxalate and CO

Other factors which affect CO_2 reduction include surface orientation and morphology of material used as well as temperature and pressure. In some cases presence of an oxide layer on the surface or pretreatment of the electrode resulting in the formation of oxides seem to enhance catalytic activity for CO_2 reduction. Studies published in this field also report varying results in Faradaic efficiency of similar materials used which may arise from differences in the electrode used, electrolysis conditions, electrolyte and cell design.

1.3.5.4. Electrochemical CO_2 reduction on iron (-nickel) sulfides

Iron sulfides have been proven to promote a few synthesis and electron transfer reactions; more importantly they have been shown to promote the reduction of CO_2, CO and N_2[29,37]. CO_2 reduction on iron (-nickel) sulfides is dominated by the hydrogen evolution reaction (HER) occurring at negative potentials. Present literature on the electrochemistry of iron and iron-nickel sulfides are discussed in parallel with the results obtained in chapter 3 for greigite, chapter 5 for violarite and chapter 7 for pyrrhotite and pentlandite.

Successful CO_2 reduction on iron sulfides has been reported by Vladimirov *et al*[1], Roldan *et al*[2] and Yamagauchi *et al*[3]. Vladimirov *et al*[1] performed a high-pressure electrochemical reduction of CO_2 on a pyrite electrode, mimicking conditions in hydrothermal vents. Formate was detected at potentials more negative than −0.8 V (vs. AgCl|Ag) at pH 7 but no other organic products were present. The authors, however, did not consider the likely transformations of pyrite under these conditions. It is predicted that pyrite will undergo reductive decomposition to FeS at −0.8 V and to metallic Fe at −1.0 V.[38] The report also did not suggest the reaction mechanism of CO_2 reduction on pyrite and no in-situ characterisation of the electrode was performed.

Roldan *et al*[2] used synthetic iron sulfide greigite for CO_2 reduction under ambient conditions and recorded a range of organic products on application of negative electrode potentials up to −1.0 V (vs AgCl|Ag).[2] Similar to pyrite, greigite is likely to undergo reductive decomposition to FeS and Fe at negative electrode potentials.[4] It is important to highlight that synthetic greigite used in their work is the same material used and studied in this thesis as this project was part of a larger consortium involving synthetic chemists, computational modellers and electrochemists. The report concluded that CO_2 reduction was feasible and optimum at pH 7 based on binding energies of dissolved CO_2 species on iron sulfide greigite. However, it did not consider the possible changes in the surface structure of greigite under the reactions conditions used which may affect the binding of CO_2 and its dissolved species.

Yamaguchi *et al*[3] used a gas diffusion electrode system to test for CO_2 reduction on both greigite and violarite coated carbon electrodes in pH 5.5 phosphate buffer electrolyte under 760 Torr CO_2. An external potential of −1.3 V (vs AgCl|Ag) was applied for 1 hour and CO, CH_4 and H_2 were detected as gas phase products during electrolysis of both materials. At such a negative electrode potential of −1.3 V, greigite is predicted to undergo reductive decomposition to metallic Fe while violarite is predicted to reduce to metallic Fe and Ni.[4,39] Violarite was found to be more catalytic compared to greigite, but no explanation was offered by the authors. Similar to the work by Roldan *et al*[2] and Vladimirov *et al*[1], Yamaguchi *et al*[3] did not characterise the electrodes in-situ to monitor the likely transformation of the greigite and violarite electrodes under such reducing conditions.

1.4. References

1. Vladimirov, M. G. *et al.* Electrochemical Reduction of Carbon Dioxide on Pyrite as a Pathway for Abiogenic Formation of Organic Molecules. *Orig. Life Evol. Biosph.* **34,** 347–360 (2004).
2. Roldan, A. *et al.* Bio-inspired CO2 conversion by iron sulfide catalysts under sustainable conditions. *Chem. Commun.* **51,** 7501–7504 (2015).
3. Yamaguchi, A. *et al.* Electrochemical CO2 reduction by Ni-containing iron sulfides: How is CO2 electrochemically reduced at bisulfide-bearing deep-sea hydrothermal precipitates? *Electrochim. Acta* **141,** 311–318 (2014).
4. Rickard, D. & Luther, G. W. Chemistry of iron sulfides. *Chem. Rev.* **107,** 514-562 (2007).
5. Vaughan, D. J. & Lennie, A. R. The iron sulphide minerals: their chemistry and role in nature. *Sci. Prog. Sci. Rev.* **75,** 371–388 (1991).
6. Ly, M., Sfai, P., Buseck, P. R., Bazylinski, D. A. & Frankel, R. B. Iron sulfides from magnetotactic bacteria: Structure, composition, and phase transitions. *Am. Mineral.* **83,** 1469–1481 (1998).
7. Di Giovanni, C. *et al.* Low-Cost Nanostructured Iron Sulfide Electrocatalysts for PEM Water Electrolysis. *ACS Catal.* **6,** 2626–2631 (2016).
8. Zhang, R.-R., Wu, X.-M., Zeng, X.-Q., Zou, J.-X. & Ding, W.-J. Electrochemical Properties of Nanostructure Greigite (Fe3S4) as a Cathode Material in Rechargeable Magnesium Battery. *Chinese J. Inorg. Chem.* **31,** 1351–1356 (2015).
9. Li, T. *et al.* Colloidal synthesis of greigite nanoplates with controlled lateral size for electrochemical applications. *Nanoscale* **7,** 4171-4178 (2015).
10. Wang, H. & Salveson, I. A review on the mineral chemistry of the non-stoichiometric iron sulphide, Fe1-xS(0<x<0.125): polymorphs, phase

relations and transitions, electronic and magnetic structures. *Phase Transitions* **78,** 547–567 (2005).

11. Zhao, C. hua, Wu, B. zeng & Chen, J. hua. Electronic structure and flotation behavior of monoclinic and hexagonal pyrrhotite. *J. Cent. South Univ.* **22,** 466-471 (2015). doi:10.1007/s11771-015-2544-4

12. Tenailleau, C., Etschmann, B., Ibberson, R. M. & Pring, A. A neutron powder diffraction study of Fe and Ni distributions in synthetic pentlandite and violarite using 60Ni isotope. *Am. Mineral.* **91,** 1442–1447 (2006).

13. Misra, K. C. & Fleet, M. E. Chemical Composition and Stability of Violarite. *Econ. Geol.* **69,** 391–403 (1974).

14. Russell, M. J., Hall, A. J. & Daia, D. E. The Emergence of Life from FeS Bubbles at Alkaline Hot Springs in an Acid Ocean. in *Thermophiles: The Keys to the Molecular Evolution and the Origin of Life?* (eds. Adams, W. W. M. & Weigel, J.) 77–116 (Taylor & Francis e-Library, 2003).

15. Craig, J. R. VIOLARITE STABILITY RELATIONS. *Am. Mineral.* **56,** 1303–1311 (1971).

16. Konkena, B. *et al.* Pentlandite rocks as sustainable and stable efficient electrocatalysts for hydrogen generation. *Nat. Commun.* **7,** 12269 (2016).

17. White, L. M., Bhartia, R., Stucky, G. D., Kanik, I. & Russell, M. J. Mackinawite and greigite in ancient alkaline hydrothermal chimneys: Identifying potential key catalysts for emergent life. *Earth Planet. Sci. Lett.* **430,** 105–114 (2015).

18. Blakemore, R. Magnetotactic Bacteria. *Science.* **190,** 377–379 (1975).

19. Davis, W. L. & McKay, C. P. Origins of life: a comparison of theories and application to Mars. *Orig. life Evol. Biosph. J. Int. Soc. Study Orig. Life* **26,** 61–73 (1996).

20. Keller, L. P. *et al.* Identification of iron sulphide grains in protoplanetary disks. *Nature* **417,** 148–150 (2002).

21. Chatzitheodoridis, E., Haigh, S. & Lyon, I. A Conspicuous Clay Ovoid in Nakhla: Evidence for Subsurface Hydrothermal Alteration on Mars with Implications for Astrobiology. *Astrobiology* **14**, 651-693 (2014). doi:10.1089/ast.2013.1069

22. Schmitt-Kopplin, P. *et al.* High molecular diversity of extraterrestrial organic matter in Murchison meteorite revealed 40 years after its fall. *Proceedings of the National Academy of Sciences* **107**, 2763-2768 (2010) doi:10.1073/pnas.0912157107

23. Wächtershäuser, G. On the chemistry and evolution of the pioneer organism. *Chem. Biodivers.* **4,** 584–602 (2007).

24. Cody, G. D. *et al.* Geochemical roots of autotrophic carbon fixation: hydrothermal experiments in the system citric acid, H2O-(±FeS)–(±NiS). *Geochim. Cosmochim. Acta* **65,** 3557–3576 (2001).

25. Hazen, R. M. *et al.* High pressure and the origin of life. *J. Phys. Condens. Matter* **14,** 11489–11494 (2002).

26. Hazen, R. M. & Deamer, D. W. Hydrothermal reactions of pyruvic acid: synthesis, selection, and self-assembly of amphiphilic molecules. *Orig. life Evol. Biosph. J. Int. Soc. Study Orig. Life* **37,** 143–152 (2007).

27. Heinen, W. & Lauwers, A. The iron-sulfur world and the origins of life: abiotic thiol synthesis from metallic iron, H2S and CO2; a comparison of the thiol generating FeS/HCl(H2S)/CO2-system and its Fe-0/H2S/CO2-counterpart. *Proc. K. Ned. Akad. Van Wet* **100***,* 11–25 (1997).

28. Heinen, W. & Lauwers, A. M. Organic sulfur compounds resulting from the interaction of iron sulfide, hydrogen sulfide and carbon dioxide in an anaerobic aqueous environment. *Orig. life Evol. Biosph. J. Int. Soc. Study Orig. Life* **26,** 131–150 (1996).

29. Lindgren, P., Parnell, J., Holm, N. G. & Broman, C. A demonstration of an affinity between pyrite and organic matter in a hydrothermal setting. *Geochem. Trans.* **12:3,** 1–7 (2011).

30. Drobner, E., Huber, H., Wachtershauser, G., Rose, D. & Stetter, K. O. Pyrite formation linked with hydrogen evolution under anaerobic conditions. *Nature* **346,** 742–744 (1990).

31. Bada, J. L. *et al.* Debating evidence for the origin of life on Earth. *Science* **315,** 937-9-9 (2007).

32. Ross, D. S. A quantitative evaluation of the iron-sulfur world and its relevance to life's origins. *Astrobiology* **8,** 267–272 (2008).

33. Thauer, R. K., Jungermann, K. & Decker, K. Energy conservation in chemotrophic anaerobic bacteria. *Bacteriol. Rev.* **41,** 100–180 (1977).

34. Wu, J. & Zhou, X.-D. Current Status and perspective of rare earth catalytic materials and catalysis. *Chinese J. Catal.* **35,** 108–119 (2014).

35. Taifan, W., Boily, J.-F. & Baltrusaitis, J. Surface chemistry of carbon dioxide revisited. *Surf. Sci. Rep.* **71,** 595–671 (2016).

36. Hori, Y. Electrochemical CO2 Reduction on Metal Electrodes. in *Modern Aspects of Electrochemistry* (eds. Vayenas, C. G., White, R. E. & Gamboa-Aldeco, M. E.) 89–189 (Springer New York, 2008). doi:10.1007/978-0-387-49489-0_3

37. Schoonen, M., Smirnov, A. & Cohn, C. A perspective on the role of minerals in prebiotic synthesis. *Ambio* **33,** 539–551 (2004).

38. Marsland, S. D. Ph. D. Thesis. Non-oxidative dissolution of iron sulphide minerals - of relevance to inorganic chemical souring of oil reservoirs. (Imperial College London, 1992).

39. Warner, T. E., Rice, N. M. & Taylor, N. Thermodynamic stability of pentlandite and violarite and new EH-pH diagrams for the iron-nickel sulphur aqueous system. *Hydrometallurgy* **41,** 107–118 (1996).

Chapter 2

Electrochemical and Spectroscopic Methods: Theory

Electrochemical techniques such as cyclic voltammetry (CV) and multistep amperometry were used to investigate electrochemical behaviour of the iron (-nickel) sulfides of interest in this thesis and assign their redox reactions. The impact of CO_2 on the electrochemistry and structure of these iron (-nickel) sulfides were also investigated using the same techniques. Detailed surface and bulk structure characterisation were done by using in situ Attenuated Total Reflectance Fourier Transformed Infrared (ATR-FTIR) and in situ X-ray Absorption Spectroscopy (XAS). These techniques aided in understanding of the changes in IR-active groups present on the surface, the oxidation state and the coordination environment of the iron and nickel centres, in situ with applied potentials in aqueous solutions. The XAS experiments were performed by two students, one of whom is the author of this thesis. Detailed XAS analysis are attached in Appendix 3 – 6.

2.1 Synthesis of iron (-nickel) sulfides nanoparticles

The iron-nickel sulfide nanoparticles were synthesised via solvothermal decomposition method and characterised via XRD (X-ray Diffraction), TEM (Transmission Electron Microscopy) and HRTEM (High-Resolution Transmission Electron Microscopy) by Dr Anna Roffey and Dr Nathan Hollingsworth. The resulting synthesised samples were greigite, violarite, pyrrhotite and pentlandite. Description of the synthesis for each sample are outlined in Appendix 1 for reference[1].

2.2 Electrochemical techniques

Cyclic voltammetry (CV) and multistep amperometry are the two main electrochemical techniques used in this thesis to investigate redox properties of iron (-nickel) sulfides studied. A three-electrode-cell setup was used in both techniques and further details can be found in Chapter 3. The principles behind cyclic voltammetry and multistep amperometry are well established. This section briefly discusses the main concepts of cyclic voltammetry and multistep amperometry, and has been constructed from the works of Pletcher *et. al.*[2] in *Instrumental Methods in Electrochemistry*, Bard and Faulkner[3] in *Electrochemical Methods: Fundamentals and Applications* and Bontempelli and Toniolo[4] in *Measurements Methods: Electrochemical - Linear Sweep and Voltammetry*. The review by Scholz *et al*[5] in *Electrochemical Analysis of Solids* is also referred to.

CV is a potential sweep technique widely used to understand electrochemical surface reaction mechanisms occurring on the material of interest. Typically for CV measurements, the potential sweep is initiated at a desired start potential and reversed on reaching the second potential limit. In this technique, the cell current is recorded as a function of the applied potential, an example of a CV is shown in Figure 2.1.

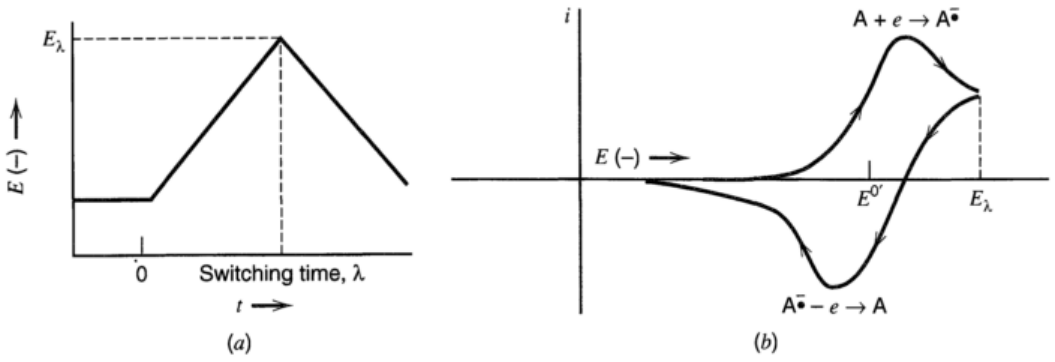

Figure 2.1 Cyclic voltammetry where (a) shows sweeping of potential as function of time and (b) resulting current versus potential cyclic voltammogram.[3] **Reprinted with permission from John Wiley & Sons. Copyright 2001 John Wiley & Sons.**

In contrast, the multistep amperometry is a potential-step technique where defined potential steps are applied consecutively for a set period of time. This

electrochemical technique was used in synchrony with the spectroscopy techniques to characterise the structure of iron (-nickel) sulfides in-situ. The amount of current passed as each potential is applied is recorded as a function of time as shown in the example in Figure 2.2.

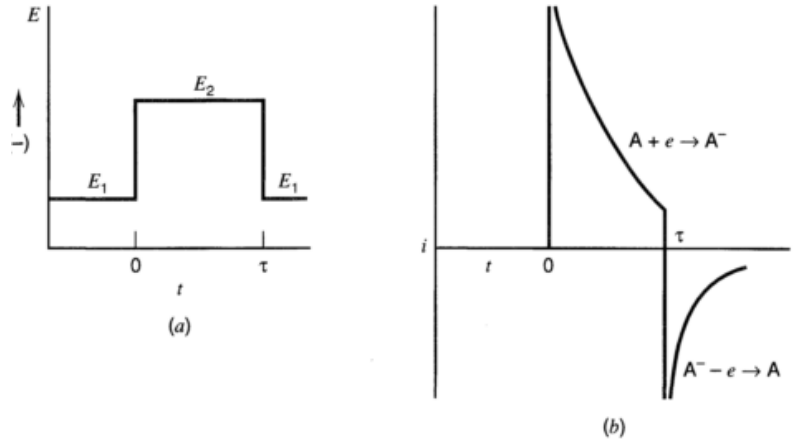

Figure 2.2 Multistep amperometry where (a) shows potential steps applied as function of time and (b) is the resulting current-time curve. [3] **Reprinted with permission from John Wiley & Sons. Copyright 2001 John Wiley & Sons.**

The standard three-electrode cell setup used in both cyclic voltammetry and multistep amperometry techniques consists of a working electrode, counter electrode and reference electrode immersed in an electrolyte media. A device known as the potentiostat controls the voltage between the working and counter electrodes while maintaining the potential difference between the working and reference electrodes. The working electrode is usually the site of the redox reaction of interest. The potential of the working electrode is controlled with respect to the reference electrode which acts as a standard. The potential is measured in volts (V), where 1 V = 1 joule/coulomb (J/C), is a measure of the energy available to force charge externally between the electrodes.

As electrons move between electrode/electrolyte interface, the number of electrons can be quantified in terms of total charge Q passed in the circuit. One unit of charge Q (one coulomb, 1 C) passed is equivalent to 6.24×10^{18} electrons. Faraday's law states that 96 485.4 C causes 1 equivalent of reaction. The rate of electron flow is the current, I and 1 ampere (A) of current is equivalent to 1 C/s. Plots of current versus potential can then be used to interpret electrochemical

properties of electrodes and electrolytes and predict reactions occuring at the interfaces.

2.2.1 Electrochemical analysis of solids

For solid electrodes, there are three types of reactions which may occur: i) electrodissolution, ii) topotactic solid-to-solid transformation, and iii) non-topotactic solid-to-solid transformation. Table 2.1 summarises the general redox peak analysis for each type of reaction. Electrodissolution is the conversion of solid species to soluble products on application of the electrode potential. This process may involve multi-step reactions including surface conditioning in the aqueous phase, redox change at the solid surface, and the diffusion of soluble products. For example, the interfacial redox chemistry of Fe_3O_4 involves: i) the reductive dissolution **(2.1)**, ii) the reduction to metallic iron **(2.2)**, or ii) catalytic hydrogen evolution **(2.3)**. These processes produced one separate and one multicomponent peak in the voltammogram of Fe_3O_4.

$$Fe_3O_4 + 2e^- + 8H^+ \rightarrow 3Fe^{2+} + 4H_2O \quad (2.1)$$

$$Fe_3O_4 + 8e^- + 8H^+ \rightarrow 3Fe + 4H_2O \quad (2.2)$$

$$2H^+ + 2e^- \rightarrow H_2 \quad (2.3)$$

For solid-to-solid transformations, the structural relationship between the reactant and products determines if the transformation is “topotactic” or non-topotactic. In topotactic transformations, both reactant and products have very similar structures, no recrystallisation is involved and the host lattice remained intact. For non-topotactic transformation, the process involves rearrangement of the host lattice during the redox process or recrystallation. Topotactic reactions are chemically reversible and produce stable cyclic voltammograms. Non-topotactic reactions, where the reactants and products are not structurally similar, include chemically reversible and irreversible transformations. The reversibility depends on the reaction rate, scan rate, temperature and particle size.

Table 2.1 Analysis of peak shapes of reactions occurring in voltammetry of solids.[5]

Type	Requirements for single peaks	Causes of splitting or complex peaks
Dissolution reactions	• Uniform particles of solids • Single dissolution mechanism	• Bimodal size distribution • Several kinetic regimes or reactions pathways • Highly anisotropic crystals
Topotactic solid-to-solid transformations	• One kind of redox centres in the solid • Reagent and products form solid solution	• More redox centres, amorphous fraction in reactants • Surface much more reactive than bulk
Non-topotactic solid-to-solid transformations	Single reaction mechanism and kinetic regime	• Poor conductivity of intermediates or products • Recrystallisation of thin films of amorphous intermediates on increasing reaction rate

2.2.2 Advantages and Limitations

Use of cyclic voltammetry to analyse the electrochemistry of solids has its advantages and limitations. Compared to traditional solution cyclic voltammetry, voltammetric data for solid-state transformations are more complex and challenging to interpret qualitatively. The voltammograms of solid electrodes are often characterised by non-conventional current responses and signal distortion may occur if the potential step used in the technique is too large (Figure 2.3). This can be resolved by using the smallest possible potential step in the cyclic potential sweep programme.

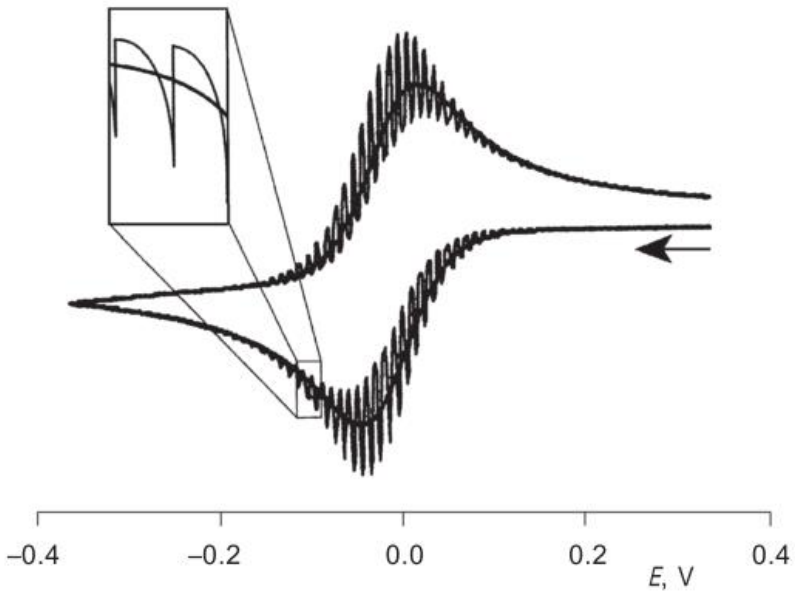

Figure 2.3 Distortion of voltammetric curve due to large potential step set in the parameters of the cyclic potential sweep programme.

Important features such as the peak position E_p, peak current I_p and the charge under the peak Q_p from the resulting current response can be used to analyse the voltammograms of the solid electrodes. The redox peaks observed in the voltammograms of solid electrodes are characteristic of the redox species involved. Materials with mixed compositions can be analysed if the E_p values of each element differ significantly. If the E_p values of the components in the mixed material are very similar, resulting in overlapping redox processes, pulsed techniques such as differential-pulse and square-wave voltammetry may be used to improve the peak separation. The potential at which the redox peaks occur, the peak potential E_p, is dependent on the experimental conditions, such as the scan rate and concentrations of ions involved in the reaction in supporting electrolyte. The physical and chemical properties of the solid, for example the particle size, uniformity and variation in stoichiometry may also affect the peak potential.

The amount of mixed compound solids transferred onto the electrode and the total amount of material adhered onto the electrode cannot usually be controlled since the materials may undergo dissolution upon immersion into the electrolyte. Thus, quantitative analysis of mixed compounds can only be carried out by analysing voltammograms of the mixed compounds with varying stoichiometries.

Considering the sum of peak currents recorded to be 100%, the percentage peak current for each peak observed in the voltammograms of the material with varying stoichiometries can be used to set up a calibration plot. Although it is possible to perform a quantitative analysis of the composition of the mixed compounds, the calibration method and very small sample amounts used in this technique can lead to standard deviations between 5 – 15%. Additionally, this technique can only be used for the relative quantification of the electroactive components. Non-active components will not appear in the voltammogram. Further to this, when the mixed compound has more than two components, the quantification becomes less accurate due to the use of signal ratios for quantification. The total charge passed through the working electrode is directly proportional to the actual amount of reactant involved. However, usually, not all of the bulk structure is involved in the reaction.

The peak potential I_p will be dependent on the peak shape. Thus, the reproducibility of both I_p and Q_p generally decreases going from pure redox active substances to mixtures of redox active substances in an inert matrix. Information on the reproducibility of electroanalysis of solid electrodes is also scarce. On performing CVs of solid electrodes, there is also a background charging current which is present throughout the experiment which is due to the capacitance of the interface at the working electrode. This restricts the detection limit to c.a. 10^{-5} M. The detection limits in voltammetry of solid reactants have also been published only in a few cases.

2.3 ATR-FTIR spectroscopy

Attenuated Total Reflectance-Fourier Transformed Infrared (ATR-FTIR) spectroscopy is an infrared technique based on measuring changes occurring in a totally internally reflected IR beam within an optically dense crystal. In this technique, the use of an ATR component in a FTIR spectrometer serves to increase the sensitivity of FTIR measurements and produce high quality IR spectra. This section outlines the fundamentals of infrared spectroscopy in particular FTIR spectroscopy, its advantages and limitations and how an ATR

crystal works in the FTIR spectrometer. The works of Barbara Stuart in *Infrared Spectroscopy: Fundamentals and Applications*[6], Peter Larkin in *IR and Raman Spectroscopy: Principles and Spectral Interpretation*[7] and Brian Smith in *Fundamentals of Fourier Transformed Infrared Spectroscopy*[8] have been referred to in constructing this section.

2.3.1 Infrared spectroscopy

An infrared spectrum is obtained by passing infrared radiation through a sample and calculating the amount of the incident radiation absorbed at a particular energy. All light (including infrared) is classified as electromagnetic radiation. Light is composed of alternating electric and magnetic fields. Absorbance of light arises from the interaction of the electric vector with matter. In IR spectroscopy the magnetic field component is neglected and only the electric field is considered. The amplitude and polarity (+ and – in Figure 2.4) of electric vector changes over time and has the form of a sine wave.

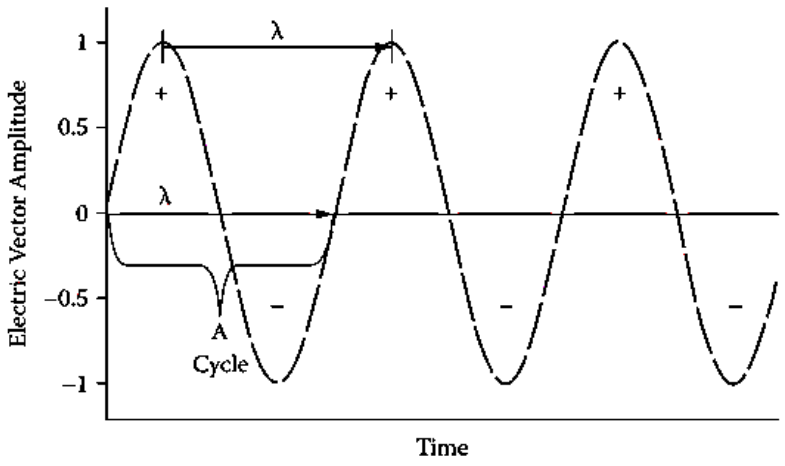

Figure 2.4 The amplitude of the electric vector of electromagnetic radiation as a function of time, where + and – indicate alternating polarity of electric vector and λ is one wavelength of one cycle.[8] Reprinted with permission from Taylor & Francis Group. Copyright 2011 Taylor & Francis Group.

The main parameters are wavelength (λ, length of 1 wave), frequency (ν, number cycles per unit time), and wavenumbers ($\bar{\nu}$, number of waves per unit length). These parameters are related by the following equation:

$$\bar{v} = \frac{\nu}{(c/n)} = \frac{1}{\lambda} \qquad (2.4)$$

where c is the speed of light and n is the refractive index of the medium it is passing through. Radiation is emitted from a source as quantized units (photons). The Bohr equation relates the photon energy, E_p and the photon frequency, ν as follows:

$$E_p = hv \qquad (2.5)$$

where h is Planck's constant (6.6256×10^{-27} J s). Photons may be absorbed (or emitted) by a molecule upon incident radiation resulting in a transfer of energy. Events such as vibration and rotation observed in infrared spectroscopy, can be characterised in terms of quantized energy levels E_0, E_1, E_2, etc., as shown in Figure 2.5. Each atom or molecule in a system must exist in one of these quantized levels. For an ensemble of molecules, all atoms or molecules will be spread among these various energy levels.

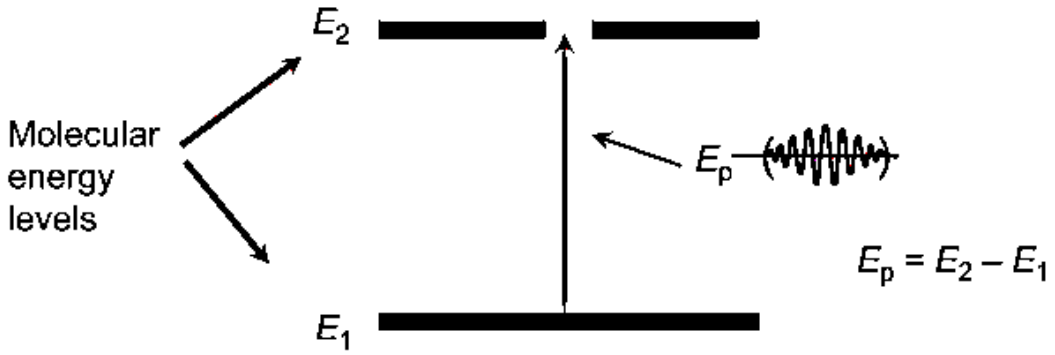

Figure 2.5 Absorption of radiation between discrete energy levels of a molecule.[7] **Reprinted with permission from Elsevier. Copyright 2011 Elsevier.**

A photon is either emitted or absorbed when a molecule interacts with radiation. In each case, the photon energy E_p must exactly fit the energy gap $E_1 - E_0$ or $E_2 - E_1$, etc. The photon energy is related to the frequency by the following:

$$\Delta E = E_p = h\nu = hc\bar{\nu} \qquad (2.6)$$

Hence, the frequency of emission or absorption of radiation for a transition between the energy states E_0 and E_1 is given by:

$$\nu = (E_1 - E_0)/h \qquad (2.7)$$

The energy of photon absorbed or emitted, ΔE, usually changes the rotational (E_{rot}), vibrational (E_{vib}), or electronic (E_{el}) energy of the molecule. To a first approximation, the rotational, vibrational, and electronic energies are additive:

$$E_T = E_{el} + E_{vib} + E_{rot} \qquad (2.8)$$

For IR spectroscopy only E_{vib} is considered for condensed phase measurements. However in gas-state IR measurements, both E_{vib} and E_{rot} are considered. Electronic transitions (E_{el}) occur at higher energy radiation and rotational transitions (E_{rot}) occur at lower energy radiation as summarised in the following figure:

>14,000 cm^{-1} Visible & UV	14,000 to 4000 cm^{-1} Near IR	4000 to 400 cm^{-1} Mid-Infrared	400 to 4 cm^{-1} Far Infrared	< 4 cm^{-1} Microwaves
Electronic Transitions	Molecular Vibrations	Molecular Vibrations	Molecular Vibrations	Molecular Rotations

Higher Wavenumber	**Lower Wavenumber**
Higher Frequency	**Lower Frequency**
Higher Energy	**Lower Energy**
Shorter Wavelength	**Longer Wavelength**

Figure 2.6 Electromagnetic spectrum between 14 000 and 4 cm^{-1} highlighting spread of relevant transitions.[8] Reprinted with permission from Taylor & Francis Group. Copyright 2011 Taylor & Francis Group.

2.3.1.1 Infrared absorption

IR spectrometers emit various IR frequencies; near-IR region (14000-4000 cm^{-1}), mid-IR region (4000-400 cm^{-1}) and far-IR region (400-10 cm^{-1}). An IR spectrum is a plot of intensity (absorbance or transmittance) versus the wavenumber, which is proportional to the energy difference between the ground and the excited vibrational states. The absorbance spectrum of a sample is calculated from the following equation:

$$A = \log(I_0/I) \qquad (2.9)$$

where A is absorbance and I_0 and I are the background and sample spectrum intensity respectively. Absorbance is also proportional to the concentration of molecules in a sample via the Beer's Law:

$$A = \varepsilon lc \qquad (2.10)$$

where ε is absorptivity, l is path length and c is concentration. IR spectra collection can be done in two modes: absorption and transmittance. Transmittance is a measure of percentage of light transmitted by sample, $\%T = 100 \times (I/I_0)$. However as absorbance is directly proportional to concentration, absorbance mode must be used for qualitative IR analyses.

For IR absorption to take place, the selection rule states that there must be a change in the dipole moment of the molecule during the vibration. The dipole moment, μ, for a molecule is defined as a function of the magnitude of the atomic charges (e_i) and their positions (r_i):

$$\mu = \sum e_i r_i \qquad (2.11)$$

As the bond in a molecule expands and contracts its dipole moment changes. The dipole moments of uncharged molecules arise from partial charges present on the atoms, which can be calculated using molecular orbital calculations. As a simple approximation, the atoms' partial charges can be estimated by comparing electronegativities of atoms on each end of the bond. Homonuclear diatomic

molecules (such as O_2, N_2, H_2) have no dipole moment and are IR-inactive while heteronuclear diatomic molecules (such as NO, CO) are IR-active as they possess dipole moments.

2.3.1.2 Degrees of freedom of vibrations

The number of vibrations a molecule produced upon interaction with IR radiation is dependent on the on its internal degrees of freedom. Table 2.2 lists the degrees of freedom for non-linear and linear molecules, where N is the number of atoms in a molecule.

Table 2.2 Degrees of freedom for polyatomic molecules.[6] Reprinted with permission from John Wiley & Sons. Copyright 2004 John Wiley & Sons.

Type of degrees of freedom	Linear	Non-linear
Translational	3	3
Rotational	2	3
Vibrational	$3N - 5$	$3N - 6$
Total	$3N$	$3N$

For example in Figure 2.7, non-linear molecule of H_2O has 3(3) – 6 = 3 degrees of freedom hence three vibrations and CO_2 has 3(3) – 5 = 4 degrees of freedom hence four vibrations. The molecular vibrations are shown in Figure 2.7. H_2O has the out-of-plane, in-plane and deformation (bending) vibrations, while CO_2 has an additional two deformation (bending) vibrations. However it is important to note that not all of these vibrations are infrared active.

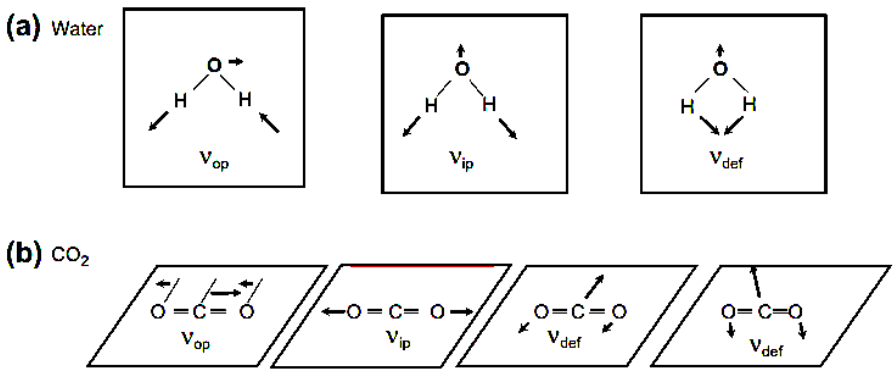

Figure 2.7 Vibrations of water and CO_2 molecules.[7] Reprinted with permission from Elsevier. Copyright 2011 Elsevier.

2.3.1.3 Symmetry of vibrations

The symmetry of a molecule will define which vibrations are IR active. For example the symmetric in-plane stretch of CO_2 is IR inactive because there is no net change in dipole moment. In contrast, the out-of-plane asymmetric stretch of CO_2 is IR active. Group theory allows classification of a molecule by its symmetry elements and predicts which vibrations will be IR active. Symmetry elements include planes of symmetry, axes of symmetry, and a centre of symmetry. Using group theory, symmetry elements of the molecule determine its point group and further vibrational analysis can be applied.

2.3.1.4 Frequency of vibrations

The frequency of vibrational modes is determined by the bond strength and the mass of atoms at each end of the bond. The bond strength is characterized by the force constant, k (derived from Hooke's law). The reduced mass, μ, combines the individual atomic masses expressed as follows:

$$\mu = \frac{m_1 m_2}{(m_1 + m_2)} \qquad (2.12)$$

where m_1 and m_2 are the masses of atoms at each end of the bond. The equation relating the force constant, reduced mass and absorption frequency is:

$$v = (1/2\pi)\sqrt{k/\mu}\,(1.8) \qquad (2.13)$$

which can be used to directly obtain wavenumber values of bond vibrational frequencies:

$$\bar{v} = (1/2\pi c)\sqrt{k/\mu} \qquad (2.14)$$

where c is the speed of light.

2.3.2 FTIR

FTIR (Fourier Transform Infrared) spectroscopy is a specific type of infrared spectroscopy. It was developed in order to overcome limitations encountered with slow dispersive infrared techniques. An optical device called an interferometer in a FTIR spectrometer measures the interference pattern between two light beams. Figure 2.8 depicts the pathways of light inside an interferometer. The light from an infrared source enters from one side of the interferometer and is split into two light beams by the interferometer. The two light beams then travel different paths.

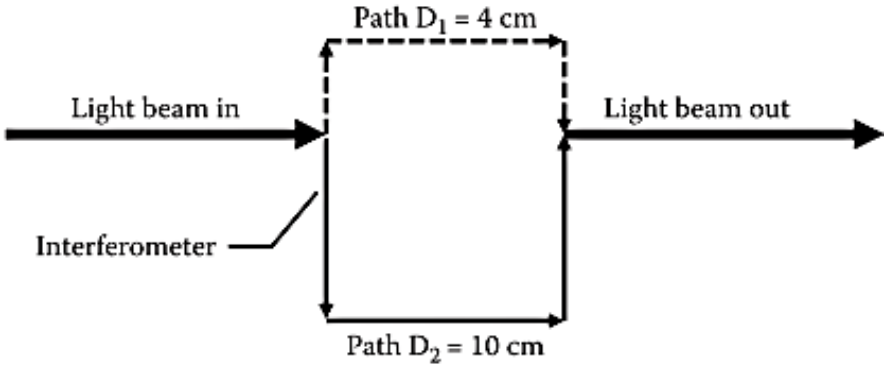

Figure 2.8 Simplified diagram of an interferometer.[8] Reprinted with permission from Taylor & Francis Group. Copyright 2011 Taylor & Francis Group.

The two light beams are recombined into one beam and the light beam leaves the interferometer. The two light beams may have different path lengths as shown in Figure 2.8. The optical path difference, δ, of an interferometer, is the difference in distance travelled by the two light beams. When the two light beams have identical path lengths then δ is equal to zero which is termed zero path difference (ZPD).

The most common type of interferometer in FTIR spectrometers is the Michelson interferometer. The Michelson interferometer measures an interferogram. An interferogram is a plot of light intensity versus optical path difference. It is the fundamental measurement obtained by an FTIR.

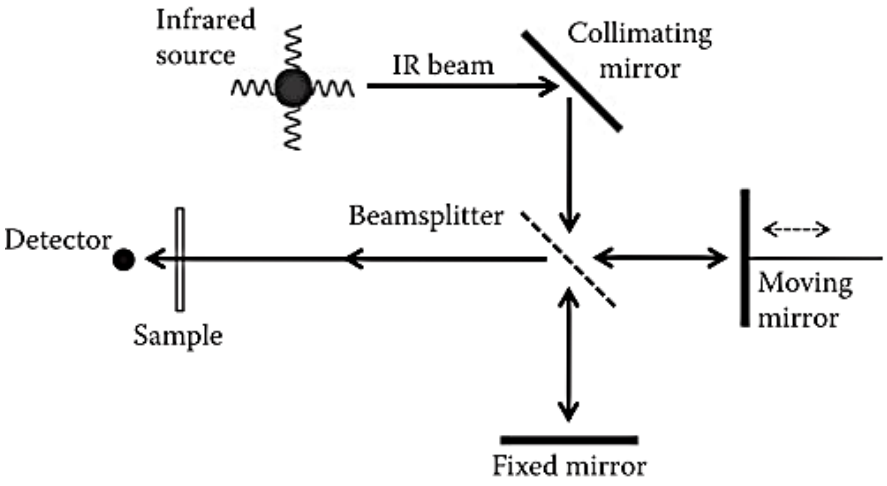

Figure 2.9 Optics inside a Michelson interferometer.[8] Reprinted with permission from Taylor & Francis Group. Copyright 2011 Taylor & Francis Group.

The Michelson interferometer consists of four arms as shown in Figure 2.9. The top arm holds the infrared source and a collimating mirror to collect the light from the source and make its rays parallel. The bottom arm of the Michelson interferometer contains a fixed mirror. The right arm contains a moving mirror and the left arm contains the sample and detector. In the centre of the interferometer is the beamsplitter. A beamsplitter is designed to transmit some of the light incident upon it and reflect some of the light incident upon it.

Once the light beams reflect from the fixed and moving mirrors, they travel back to the beamsplitter, where they are recombined (and undergo constructive or destructive interference) into a single light beam. This recombined beam leaves the interferometer, interacts with the sample, and reaches the detector.

An interferogram is measured by moving the mirror back and forth in the Michelson interferometer. However these interferograms cannot be interpreted directly. They are Fourier transformed to yield a spectrum, hence the term Fourier Transform Infrared (FTIR) spectroscopy.

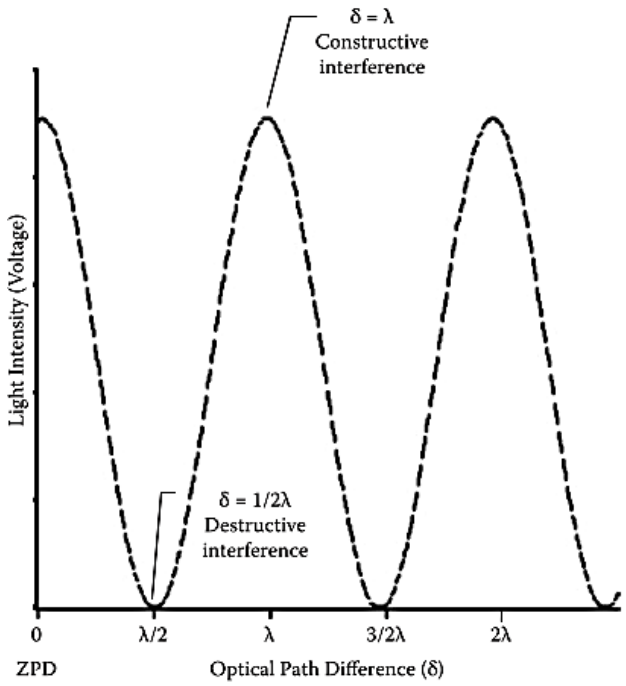

Figure 2.10 Light intensity versus optical path difference for a moving mirror in a Michelson interferometer.[8] Reprinted with permission from Taylor & Francis Group. Copyright 2011 Taylor & Francis Group.

The interferogram is received by the infrared detector as electrical signals and these signals have a cosine waveform as seen in Figure 2.10. The signal frequencies are measured in units of Hertz which can be converted into wavenumbers:

$$F = 2v\mathrm{v}/c \qquad (2.15)$$

where F is Fourier Frequency of the interferogram in Hertz, v is frequency of lightwave in Hertz, v is velocity of moving mirror (constant) in cm / sec and c is speed of light in cm / sec. This can be rewritten in terms of wavenumber ($\bar{v}$ is wavenumber in cm^{-1}) as follows:

$$F = 2\bar{v}\mathrm{v} \,/\, c \qquad (2.16)$$

$$\bar{v} = F/2\mathrm{v} \qquad (2.17)$$

In reality, the infrared source emits all wavenumbers of light through the interferometer where each wavenumber possess a unique Fourier frequency. Thus, the infrared detector measures the sum of interferograms produced. An

example of the resulting interferogram is shown in Figure 2.11. There is a large intensity peak at zero path difference termed the centreburst as all wavelengths of light at this point are in-phase and constructively interfere at ZPD. The height of the centreburst is correlated to the amount of infrared light reaching the detector. On both sides of the centreburst, the infrared intensity falls off quickly and termed as wings. The wings have low intensity because the various Fourier frequencies fall increasingly out of phase and destructively interfere as optical path difference increases.

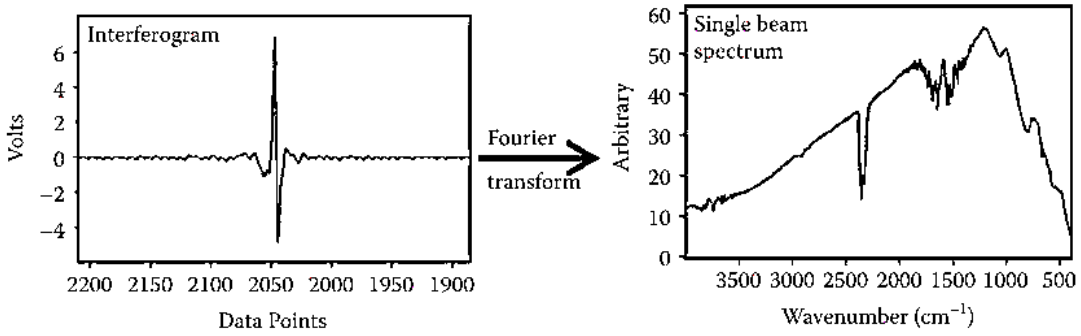

Figure 2.11 Applying Fourier transform to an interferogram produces a single beam spectrum.[8] Reprinted with permission from Taylor & Francis Group. Copyright 2011 Taylor & Francis Group.

There are several steps required to produce the final FTIR spectrum. The Fourier transform of any interferogram produces a single beam spectrum as shown in Figure 2.11. A single beam spectrum is a plot of arbitrary infrared intensity versus wavenumber. The term "single beam" is due to only one infrared beam being used in an FTIR spectrometer. If interferograms are measured with no sample present, the single beam spectrum produced is a background spectrum.

This background spectrum includes spectral contributions from the instrument and the environment (such as infrared absorbing gases such as water vapour and CO_2). Once the background spectrum is measured, the sample is placed in the infrared beam. Interferograms measured with a sample present produces a sample single beam spectrum containing contributions from the environment, instrument, and sample.

The final FTIR spectra is evaluated from the ratio of the background and sample single beam spectra. The difference between the background and sample spectra should be the presence of the sample if contributions from instrument and environment are constant in both spectra.

2.3.3 ATR

Attenuated total reflectance (ATR) is based upon internal reflectance of light within a crystal as depicted in Figure 2.12. The IR beam passes through a crystal of high refractive index n_c and encounters an interface region with a sample with lower refractive index n_s. The dotted line is the surface normal and θ_i is the incidence angle of the incoming beam to the surface normal. The angle of refraction, θ_R is the angle of the refracted beam to the surface normal.

At certain incidence angles, the refraction angle will be 90° resulting in the infrared beam not exiting the crystal thus remaining inside. This is termed total internal reflectance. The minimum incidence angle at which total internal reflectance takes place in a crystal is its critical angle θ_c. The critical angle is dependent on the refractive indices of both the crystal and sample. Total internal reflection occurs at $\theta_i \geq \theta_c$.

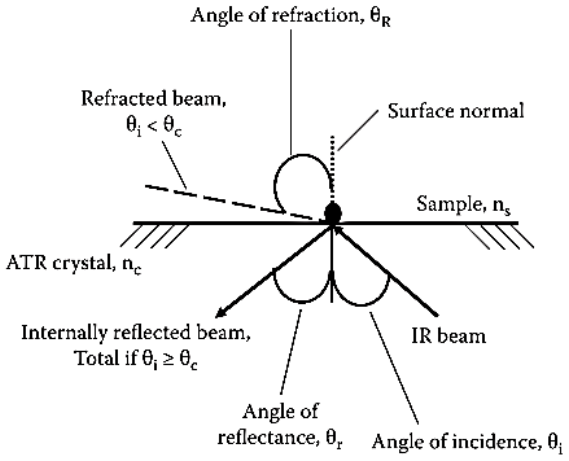

Figure 2.12 Principles of ATR. The infrared beam in a crystal of high refractive index, n_c encounters a sample of lower refractive index n_s. θ_i is the angle of incidence and refraction angle θ_R and critical angle θ_c above which total internal reflection takes place.[8] Reprinted with permission from Taylor & Francis Group. Copyright 2011 Taylor & Francis Group.

When total internal reflectance occurs, the two incident and refracted beams occupy the same environment. Under the right conditions (including $\theta_i \geq \theta_c$), these two beams will undergo constructive interference. Hence, the resulting infrared amplitude at the point of internal reflectance will be greater than the amplitude on either side. Since the beams meet on the crystal surface, the enhanced amplitude can only go upwards resulting in infrared light protruding into the space above the crystal surface and this is termed an evanescent wave or hotspot as illustrated in Figure 2.13.

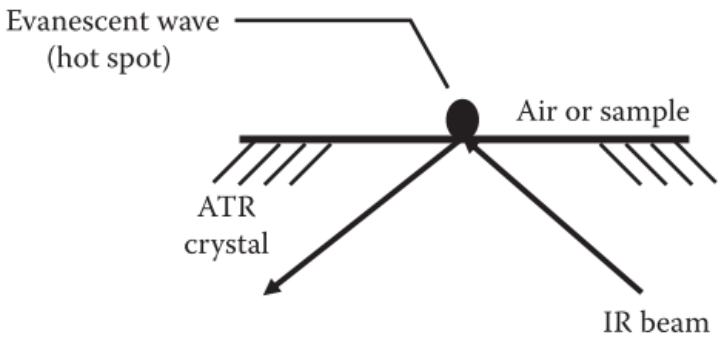

Figure 2.13 Production of an evanescent wave above ATR crystal when infrared beam undergoes total internal reflectance.[8] Reprinted with permission from Taylor & Francis Group. Copyright 2011 Taylor & Francis Group.

The evanescent wave penetrates above the crystal surface usually by less than a micron up to 10 microns. The evanescent wave will be attenuated or altered in the regions of the IR spectrum where the sample absorbs energy. The attenuated energy from each evanescent wave is directed back to the IR beam, which then exits the other end of the crystal and is passed to the detector in the IR spectrometer.

2.3.3.1 Depth of penetration

In an ATR experiment, the intensity of evanescent wave decreases exponentially with depth of penetration above the ATR crystal. The depth of penetration (DP) is the depth at which the evanescent wave intensity decreases to 36.8% (= $1/e$ where e is the base of natural logarithms) of its original value. The depth of penetration for an ATR experiment is given by:

$$DP = 1/[2\pi\bar{\nu}n_c(sin^2\theta - n_{sc}^2)^{\frac{1}{2}}] \qquad (2.18)$$

where DP is depth of penetration, $\bar{\nu}$ is wavenumber, n_c is refractive index of ATR crystal, θ is angle of incidence and n_{sc} is the ratio of refractive index of sample to refractive index of crystal.

Thus the dependence of ATR intensities on wavenumber, ratio of refractive indices of sample and crystal, angle of incidence has significant implications on interpreting an ATR spectra. It is difficult to compare ATR spectra to spectra measured using different ATR crystals as the infrared beams will penetrate at different depths as listed in Table 2.3. In addition to the crystal's refractive index, properties such as its useful wavenumber range, pH sensitivity, durability, and toughness also need to be considered.

Table 2.3 Properties of common ATR crystals.[8] Reprinted with permission from Taylor & Francis Group. Copyright 2011 Taylor & Francis Group.

Crystal Material	Refractive Index	Wavenumber Range(s) (cm^{-1})	Color	pH Range	Comments
KRS-5	2.37	20,000–250	Red	5–8	Soft, highly toxic, rarely used today
ZnSe	2.42	15,000–600	Yellow	5–9	Once very common, brittle, attacked by strong acids and bases
Si	3.42	8900–660	Grey	1–12	
Ge	4.0	5500–600	Grey	1–14	Shallow DP, durable
Diamond	2.42	30,000–2200, 2000–400	Clear	1–14	Tough, durable, absorbs in mid-infrared, $$$

2.3.4 Advantages and Limitations

Use of IR spectroscopy as a characterisation technique has its advantages but also limitations. IR vibrational bands are characterised by their frequency, intensity and band shapes. Since the vibrational energy levels are unique to each molecule, IR spectrum provides a fingerprint of a particular molecule. In particular, many molecules have strong absorbances in the mid-IR region. In an IR spectra the peak positions give the structures of the molecules in a sample, the peak intensities give the concentrations of molecules in a sample, and the peak widths are sensitive to the chemical matrix of the sample including pH and hydrogen bonding. Thus IR spectra provide information on molecular structure, dynamics and environment. IR measurements can also be done quickly which reduces exposure of sample and increases accuracy of measurements.

In particular for the ATR-FTIR technique, it is a reflectance technique hence it does not suffer from the opacity problems that arise in transmission methods. Sample preparation is also very minimal for ATR analysis making it a fast and easy technique. ATR can be used for diverse samples including liquids, semi-solids, polymers, powders and solids. It is also non-destructive technique where the sample is not altered, damaged or chemically modified by the analysis. ATR is also a qualitative technique as absorbance intensities are proportional to concentration in sample. The FTIR technique also has the ability to measure spectra with high signal-to-noise ratios compared to other infrared spectrometers which may have additional gratings and slits filtering and decreasing the light intensity reaching the detector. An added advantage of using FTIR is its wavenumber precision. Since FTIRs contain a laser that acts as an internal wavenumber reference, it allows the wavenumbers measured with a precision of ±0.01 cm^{-1} where the unique wavenumber of the laser source acts as a calibration point for the equipment.

Associated with its advantages, FTIR-ATR spectroscopy also has certain limitations as a characterisation technique. As an infrared technique, vibrations of homonuclear molecules cannot be detected due to no change in dipole moment in their symmetric stretch. Individual atoms such as noble gases are not

chemically bonded to anything thus have no vibrations. Monatomic ions may affect the spectrum of solvent molecules around them and may change the spectrum of liquid water, but the monatomic ions cannot be detected directly by infrared spectroscopy. Another challenge is the complex spectral interpretation for mixtures. Purification steps and control experiments are needed to analyse each component present in the mixture.

The biggest challenge in this technique is when working in aqueous solutions where sample spectral bands are masked by broad and intense infrared peaks of liquid water. Use of ionic liquids as an electrolyte may solve this problem. FTIRs suffer from other artefact features including water vapour and CO_2 peaks which arise due to different atmospheric environment of the background and sample spectra measured.

ATR-FTIR also cannot be used to analyse gases and the ATR crystal must be kept scratch free and clean. Every ATR crystal has its own useful wavenumber range. In the case of diamond used in this thesis, diamond absorbs between 2200 and 2000 cm^{-1} hence any sample infrared peaks within this region may be masked. Another issue with using ATR is lack of sensitivity associated with path-length and depth of penetration of the infrared beams. In general, ATR can only detect molecules present in concentrations greater than 0.1%.

2.3.5 Spectrometer details

The FTIR spectrometer used in this thesis was a Bruker Tensor 27 with Platinum Diamond ATR accessory. The ATR prism is a single reflection diamond prism with a spectral range of 4000-370 cm^{-1} with 4cm^{-1} resolution, refractive index of 2.4 and angle of incidence of 45°. The spectrometer used is equipped with a HeNe laser (laser class 2) which emits red light of wavelength 633 nm. The sample compartment is located on the ATR stage. Further experimental details are found in Chapter 3.

This technique was synchronised with multistep amperometry described in the previous section to probe infrared-active surface groups on iron (-nickel) sulfide

in-situ as a function of applied potential. It is important to note that the technique used in this thesis is not Surface Enhanced Infrared Absorption Spectroscopy (SEIRAS). Thus, a number of control experiments were performed to account for various interferences / discrepancies arising from the use of this in-situ ATR-FTIR technique.

2.4 X-ray absorption spectroscopy

X-ray Absorption (XAS) spectroscopy is an analytical technique used for studying the local structure around specific elements contained within a sample, at the atomic and molecular level. This technique is often used in the characterisation of solids, liquids, membranes, gases, crystalline or amorphous materials either in bulk or nanoscale form. This section aims to outline the basic principles of XAS and how it is used to aid characterisation of iron sulfides / iron-nickel sulfides studied in this work. Works of Schnohr and Ridgway in *XAS of semiconductors*[9], Scott Calvin in *XAFS for everyone*[10] and Grant Bunker in *Introduction to XAFS*[11] have been referred to in constructing this section.

Fundamentally, XAS is a quantum mechanical phenomenon that is based on the X-ray photoelectric effect, in which an atom absorbs an incident X-ray photon, liberating an electron from an inner atomic orbital (e.g. 1s). The "photoelectron" wave scatters from the atoms around the X-ray absorbing atom, resulting in constructive and destructive interferences between the outgoing and scattered parts of the photoelectron wavefunction. These quantum interference effects cause an energy-dependent variation in the X-ray absorption probability, which is proportional to the X-ray absorption coefficient. When analysed, these modulations provide information about the structure, atomic number, structural disorder and thermal motions of neighbouring atoms.

In a typical X-ray absorption experiment, a sample of interest is bombarded with x-rays of known photon energies. The atoms in the sample absorb some of these x-rays, causing the excitation or ejection of a core electron. This absorption can be quantified using the Beer Lambert law:

$$I_t(t) = I_0 e^{-\mu(E)t} \qquad (2.19)$$

where incident, I_0, and transmitted beam, I_t, can be measured from the fluorescence given off by the excited atoms as an electron fills the core hole, or by measuring the ejected electrons as the core hole is filled (Auger electrons). The X-ray absorption coefficient μ(E) which describes how strongly X-rays are absorbed as a function of X-ray energy E can then be quantified.

Once μ(E) is determined for one energy of incident x-rays, the energy is changed slightly. Thus by varying the range of X-ray energies, an X-ray absorption spectrum is created (Figure 2.14b).

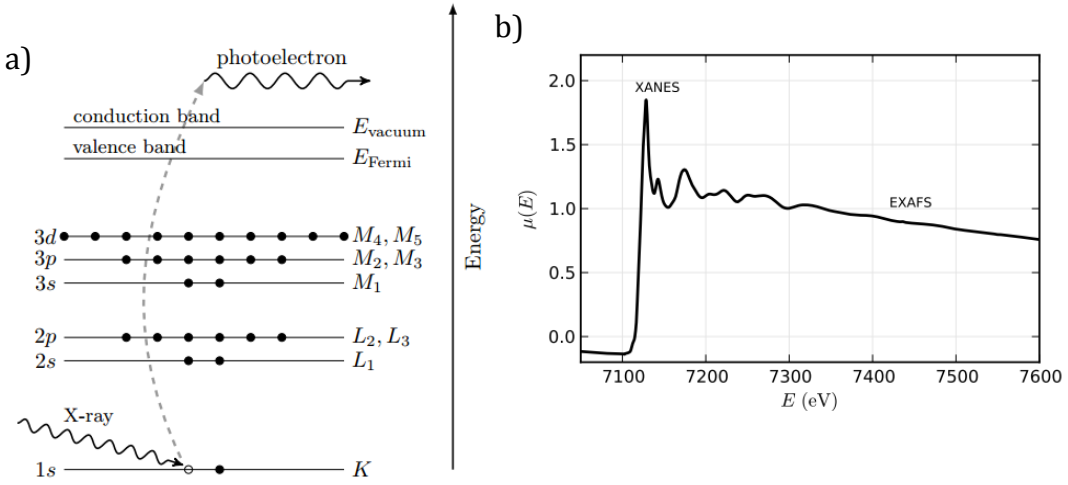

Figure 2.14 a) Schematic of the absorption process and b) example XAS spectra showing absorption coefficient μ(E) versus photon energy E including the fine structure above the edge divided into the XANES and EXAFS regions.[12] Reprinted with permission from Mineralogical Society of America (MSA). Copyright 2014 MSA.

In general the absorption coefficient μ(E) decreases as the photon energy increases (approximately as $\mu(E) \sim dZ^4/mE^3$ where d is density of target, Z is atomic number and m is atomic mass). However when the incident x-ray photon energy exceeds the core electron binding energy, a drastic gain in μ(E) termed the "edge" is observed (Figure 2.14b). The edge occurs because at energies below this value, x-ray photons do not have enough energy to excite electrons from some particular orbital, while above it they do. Above the edge, the difference between

the photon energy and the binding energy is converted into kinetic energy of the photoelectron and μ(E) continues to decrease with increasing photon energy.[9]

Taking iron as an example, 7112 eV is required to excite an electron in its 1s orbital, leading to a sharp increase in the absorption of iron-containing samples around 7112 eV, known as the iron K edge. (Excitations of orbitals from n = 1 states are assigned as K edges, n = 2, 3 states as L and M edges and so on)

Once an electron is ejected from an atom by the incident photon, this photoelectron can be treated as a wave radiating out in all directions, propagating outwards and scattered at neighbouring atoms. The photoelectron can either be excited to an unoccupied bound state of the absorbing atom (when incident photon energy is equal to that of core electron binding energy) or to the continuum at higher X-ray energies as depicted in Figure 2.14a. Constructive or destructive interferences resulting from the propagated and scattered waves thus increases or decreases the absorption probability, resulting in the fine structure of the absorption coefficient which is energy-dependent.

The XAS spectra can be split into two regions: the XANES and EXAFS regions. The features near or on the edge are known as x-ray absorption near-edge structure (XANES). The oscillations above the edge are known as extended x-ray absorption fine structure (EXAFS).

The XANES region is characterised by the photoelectron transitions to unoccupied bound states. Thus this region contains chemical bonding information, exhibiting distinct features for different oxidation states of the absorbing atom. The features in the XANES region are also affected by multiple scattering effects which depend on the geometry of the crystal structure, thus allowing us to distinguish between different crystal phases. Analysis of the XANES region is usually done by comparison of the measured spectra to those of known standards. Linear combination fitting can be applied to quantify the ratios of these standards present in the sample.

The EXAFS region in the XAS spectrum starts at ~30 eV above the edge where the photoelectron is promoted to a continuum state. This region is dependent on the

atomic arrangement around the atom. It contains information such as the coordination number, interatomic distances and structural and thermal disorder around the atomic species. This region is modelled using the EXAFS equation:

$$\chi(k) = \sum_j \left(\frac{N_j f_j(k) e^{-2k^2\sigma_j^2}}{kR_j^2} \sin[\,2kR_j + \delta_j(k)] \right) \quad (2.20)$$

where $\chi(k)$ is the mean free path of photoelectron, k is the wavenumber of photoelectron, j is a scattering path, N_j is the number of neighbouring atoms, R_j is the bond distance of neighbouring atoms, and σ_j^2 is the static and thermal disorder of neighbouring atoms, $f_j(k)$ the is scattering amplitude and $\delta_j(k)$ is the phase shift. N_j, R_j, and σ_j^2 can be determined from the EXAFS equation when scattering amplitude $f_j(k)$ and phase-shift $\delta_j(k)$are known.

In terms of analysis of XAS raw data, both XANES and EXAFS region are analysed separately. Firstly for the XANES region, the spectrum is usually normalised with the Edge jump to compare it to spectra of standards. The EXAFS region requires further manipulation as it contains oscillatory features and background subtraction is required. $\chi(E)$ is then converted to $\chi(k)$ using equation:

$$k = \frac{1}{\hbar}\sqrt{2m_e(E - E_o)} \quad (2.21)$$

k-weighting is then performed to achieve uniform amplitudes of $\chi(k)$ as shown in the figures below. Fourier transformation is usually applied to the k-weighted data to transform to real space R (Å).

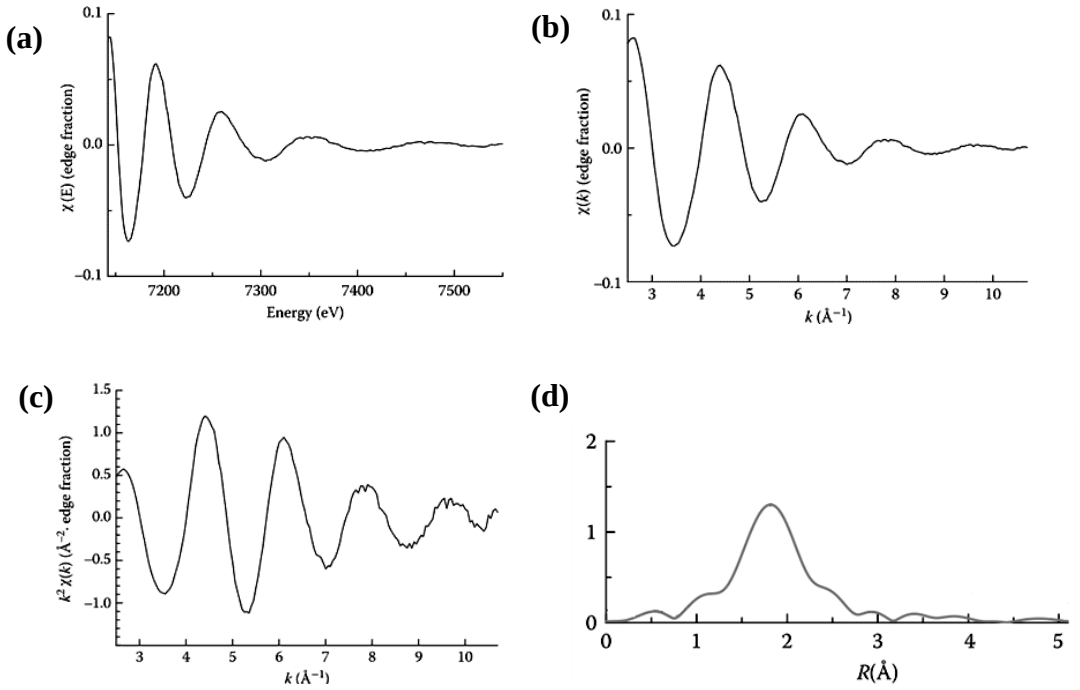

Figure 2.15(a) EXAFS raw data $\chi(E)$, (b) EXAFS raw data $\chi(E)$ converted to $\chi(k)$, (c) converted $\chi(k)$ weighted by k^2, (d) Fourier transformed data of (c).[10] **Reprinted with permission from Taylor & Francis Group. Copyright 2014 Taylor & Francis Group.**

2.4.1 Advantages and Limitations

XAS is an element specific technique hence it is able to focus on one element without interference from other elements present in the sample.[13] In the case of mixed metal materials, it is possible to study the structural environment of each metal atom selectively.

XAS is a bulk characterisation technique which enables probing of both surface and bulk structures of the element of interest simultaneously. Both oxidation states and coordination environment of the element can be investigated using XAS. Thus monitoring of oxidation states and coordination environment is possible when performing in-situ XAS.

Samples analysed using XAS are also not restricted to ordered crystals thus samples can be prepared as powder or solution.[13] Similar to infrared spectroscopy, XAS is a non-destructive technique however the user needs to be

cautious with selecting suitable energy of X-ray beams to prevent production of undesired free radicals and hydrated electrons.[13]

Analysis of XAS spectra relies heavily on comparison to sample standard XAS spectra. This limits interpretation of spectral data if there are not enough standards to compare with from XAS spectra libraries. As with bulk characterisation techniques, it is difficult to distinguish between surface and bulk proportions in the sample using XAS. Hence it is not possible associate percentage of surface or bulk structure which changed in oxidation state or coordination environment. Interpretation of XAS spectra is also limited to Linear Combination Analysis modelling, fitting spectra of standards to sample spectra.

2.5 References

1. Roffey, A. Ph. D. Thesis. Dithiocarbamate Complexes as Single Source Precursors to Metal Sulfide Nanoparticles for Applications in Catalysis. (University College London, 2014).

2. Pletcher, D Greff, R. P. & Peter, L. M. *Instrumental Methods in Electrochemistry*. (Woodhead Publishing, Oxford, 2001).

3. Bard, A. J. & Faulkner, L. R. *Electrochemical Methods: Fundamentals and Applications*. (Wiley, New York, 2001).

4. Bontempelli, G. & Toniolo, R. MEASUREMENT METHODS | Electrochemical: Linear Sweep and Cyclic Voltammetry. *Encycl. Electrochem. Power Sources* 643–654 (2009). doi:http://dx.doi.org/10.1016/B978-044452745-5.00069-1

5. Grygar, T., Marken, F., Schröder, U. & Scholz, F. Electrochemical Analysis of Solids. A Review. *Collect. Czechoslov. Chem. Commun.* **67,** 163–208 (2002).

6. Stuart, B. H. *Infrared Spectroscopy: Fundamentals and Applications*. *Methods* (Wiley, Chichester, 2004). doi:10.1002/0470011149

7. Larkin, P. *IR and Raman Spectroscopy: Principles and Spectral Interpretation*. (Elsevier, Amsterdam, 2011). doi:10.1016/B978-0-12-386984-5.10001-1

8. Smith, B. *Fundamentals of Fourier transform infrared spectroscopy*. (CRC Press, Boca Raton, 2011).

9. Schnohr, C. S. & Ridgway, M. C. in *X-ray Absorption Spectroscopy of Semiconductors* **190,** 1–26 (Springer, Berlin, 2015).

10. Calvin, S. *XAFS for Everyone*. (CRC Press, Boca Raton, 2013).

11. Bunker, G. *Introduction to XAFS*. (Cambridge University Press, Cambridge, 2010).

12. Newville, M. Fundamentals of XAFS. *Rev. Mineral. Geochemistry* **78,** 33–74 (2014).

13. Yano, J. & Yachandra, V. K. X-ray absorption spectroscopy. *Photosynth. Res.* **102,** 241–254 (2009).

Chapter 3 Electrochemistry of Greigite

3.1 Introduction

To investigate the changes in the surface structure of greigite on immersion into aqueous electrolytes, the dissolution pathway of greigite at each solution pH must be considered. The application of an external potential to test for CO_2 reduction on greigite may also have a significant impact on its structure. However, since the electrochemistry of iron sulfides such as greigite is not well established in the literature, the changes in the surface structure of greigite on applying an external potential with no CO_2 must be first investigated.

Published electrochemical studies on iron sulfides often lack surface characterisation to complement proposed redox reactions occurring. The following suggested mechanisms are present in literature: 1) dissolution of Fe(II) and Fe(III) ions upon contact with electrolyte leading to a metal-deficient/sulfur-rich surface,[1] 2) dissolution of sulfide ions forming H_2S or HS^-,[1] and 3) formation of a passivating layer assumed to be iron oxide or hydroxide.[2] The assignment of redox reactions is further complicated by the nature of the materials used in literature. Materials used are often composed of mixed minerals, not pure iron sulfides and may have different degrees of prior oxidation.

The dissolution, decomposition and redox reactions of iron sulfides at various experimental conditions used in this thesis are discussed by considering the relevant Pourbaix diagrams. The redox features observed in the cyclic voltammograms presented in this chapter were assigned based on the thermodynamic predictions in the relevant Pourbaix diagrams. Since the Pourbaix diagrams constructed do not consider the reaction kinetics, spectroscopic evidence is compared to the thermodynamic predictions to assess their validity in the next chapter. The impact of solution pH, electrolyte and external potential applied on the surface structure of greigite under CO_2 and its implications are discussed.

3.1.1 Pourbaix diagrams

Potential-pH diagrams, or Pourbaix diagrams, map the stability regions of a material and its thermodynamically stable redox products as a function of pH and potential. Pourbaix diagrams incorporate both chemical and electrochemical thermodynamics of a system of interest and are widely used to predict corrosion behaviour and active species. However, one of the limitations of these diagrams is that they do not consider reaction kinetics which may affect the stability regions in the diagram. Pourbaix diagrams are used in this thesis to initially assign redox features observed in the cyclic voltammograms, before verifying the predictions with spectroscopic evidence.

Relevant Pourbaix diagrams that are referred to in this thesis include: i) Fe-H_2O system (Figure 3.1), ii) Fe-H_2S-H_2O system (Figure 3.2), iii) Fe-S-H_2O system (Figure 3.3), and iv) S-H_2O system (Figure 3.4). For CV experiments under CO_2, the Pourbaix diagrams of Fe-CO_2-H_2O system (Figure 3.5) and Fe-S-C-H_2O system (Figure 3.6) were also considered.

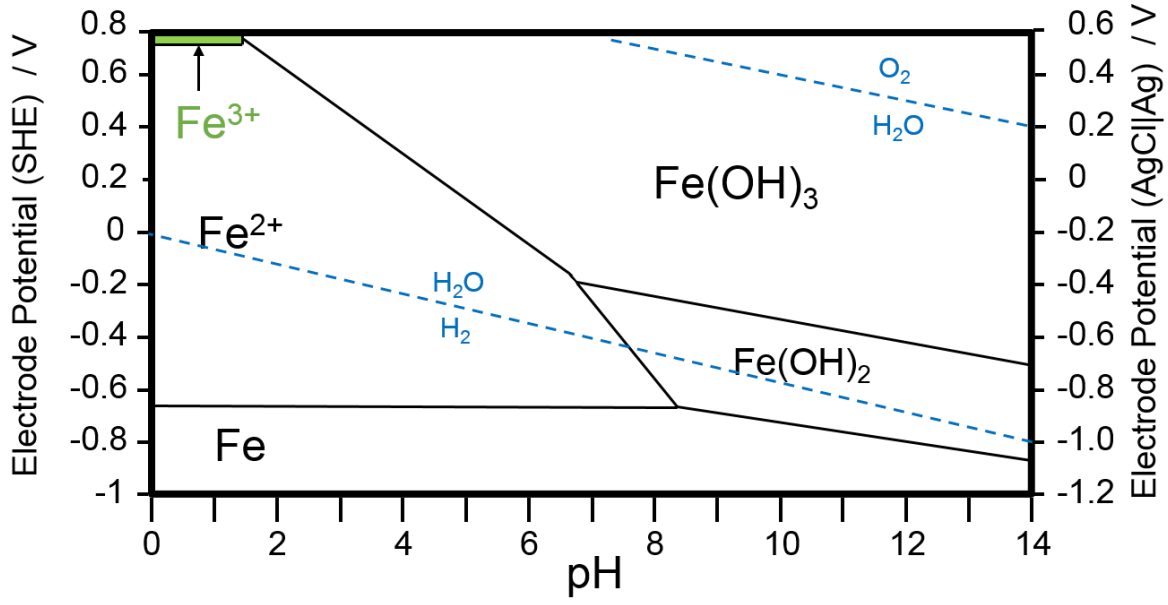

Figure 3.1 Pourbaix diagram for Fe-H_2O system, with $Fe(OH)_3$ as solid iron oxide phase at 25°C. Dissolved species = 10^{-5} M. Adapted from reference [3].

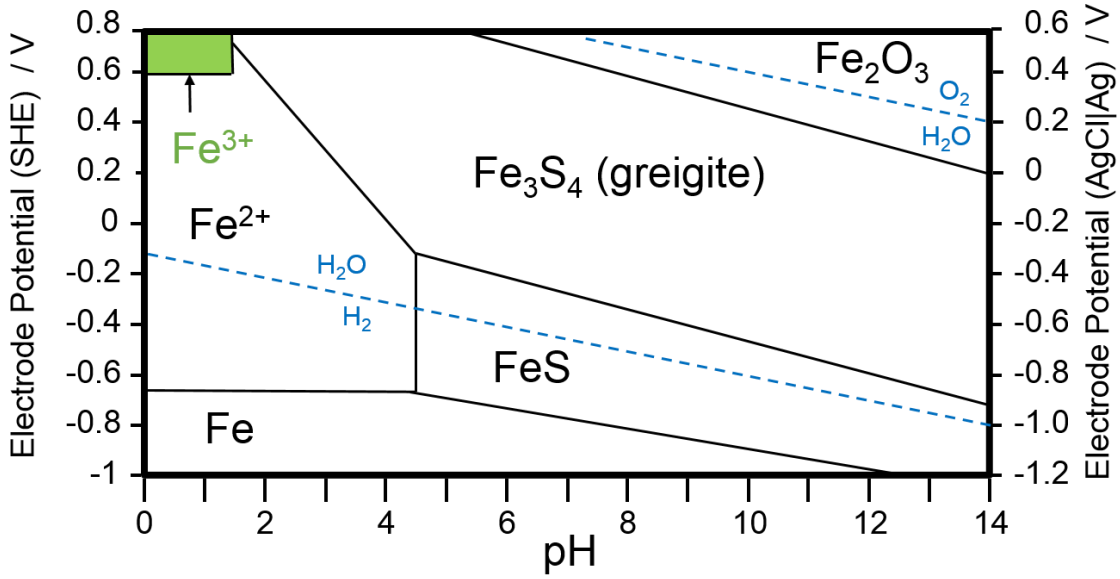

Figure 3.2 Pourbaix diagram for Fe-H_2S-H_2O system at 25°C. ([H_2S]aq = 10^{-3} M, [Fe^{2+}] = 10 ppm, [Fe^{3+}] = 10^{-6} M). Adapted from reference [10].

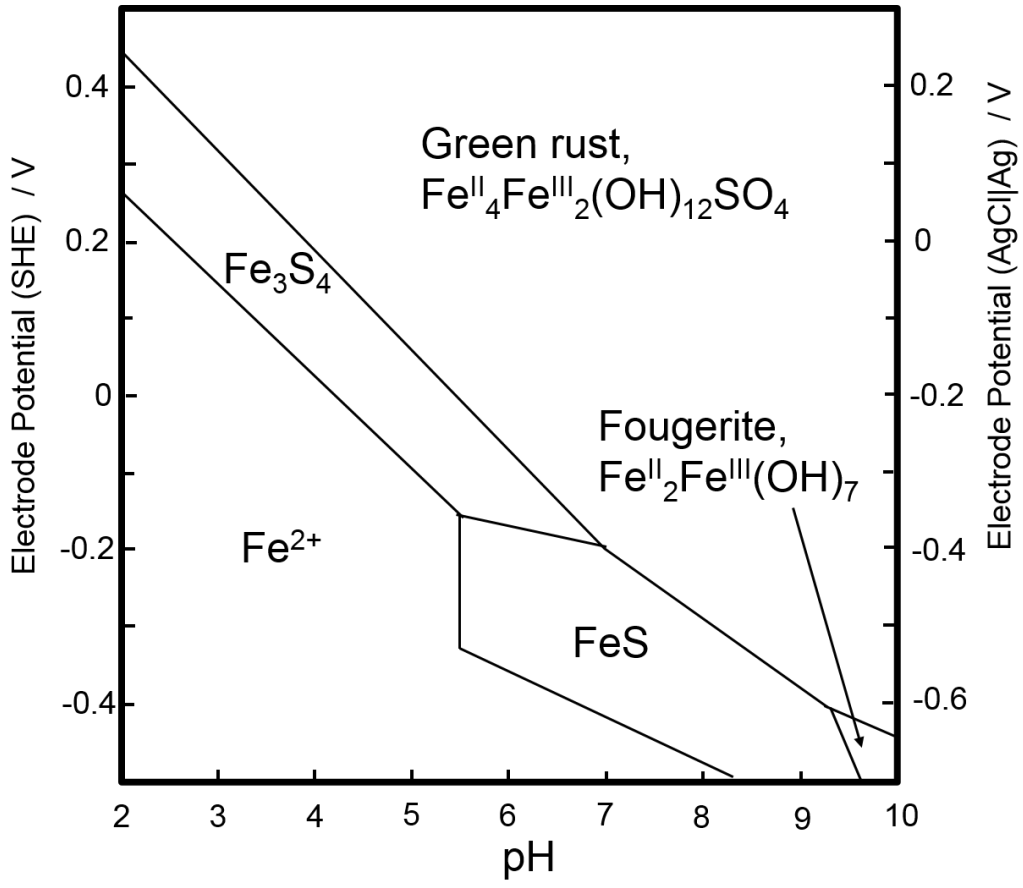

Figure 3.3 Pourbaix diagram of Fe-S-H_2O system, showing the mackinawite (FeS)-greigite (Fe_3S_4) boundary at 25°C, 1 bar total pressure. [Fe] =10^{-3} M and [S] =10^{-6} M. Adapted from reference [4].

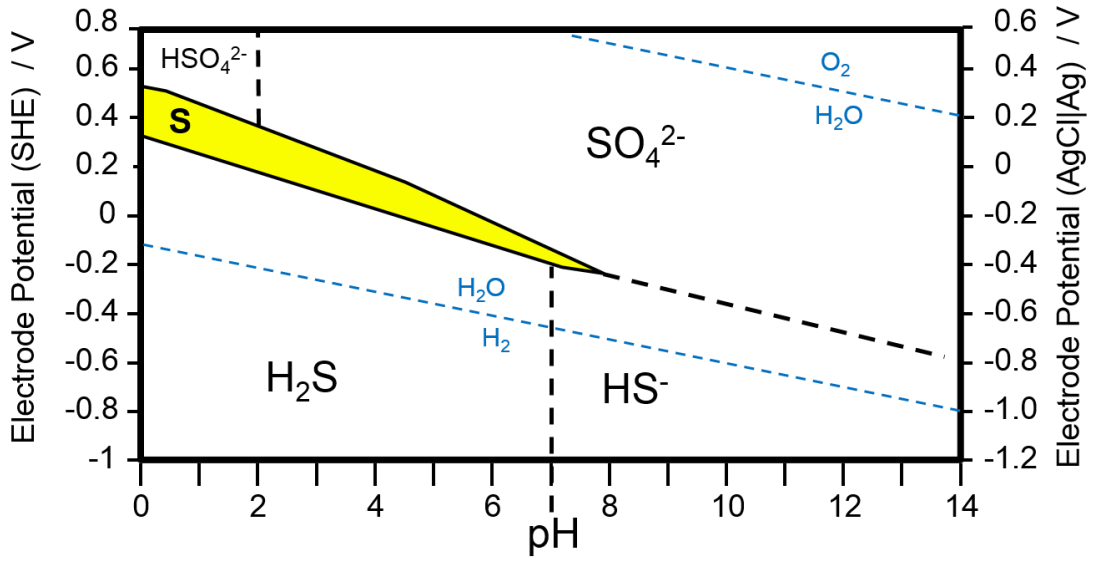

Figure 3.4 Potential-pH diagram for S-H_2O system at 298.15 K. Dissolved sulfur activity = 0.01. Adapted from reference [5].

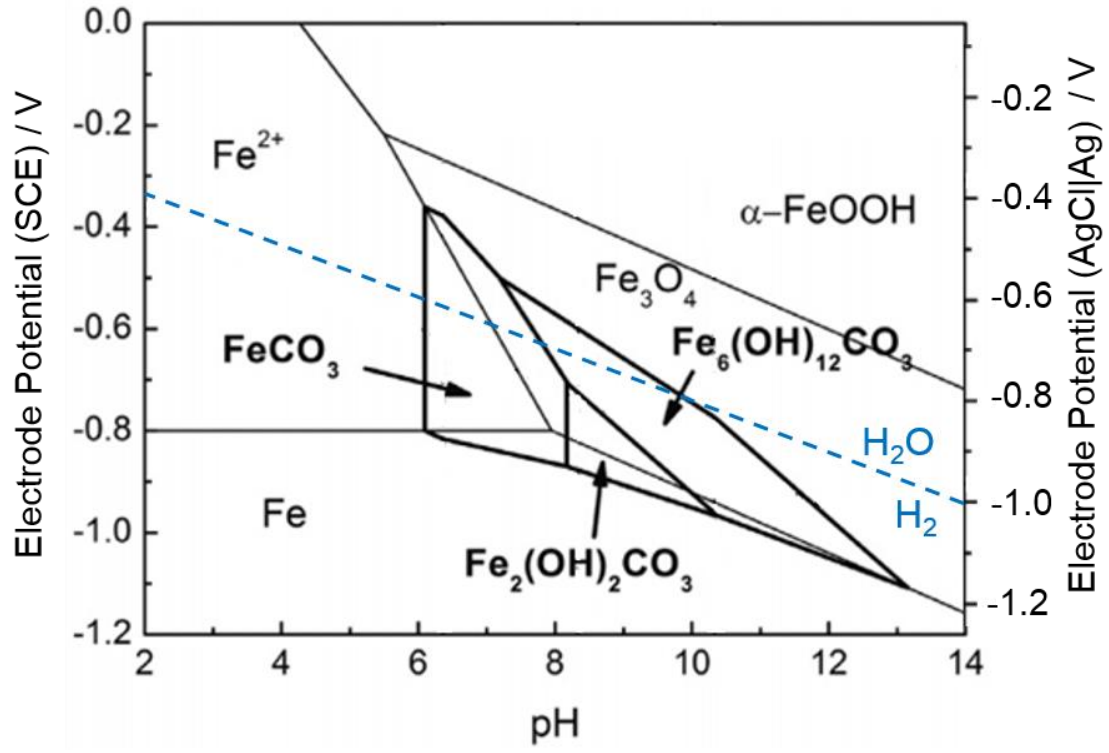

Figure 3.5 Pourbaix diagram of Fe-CO_2-H_2O system at 298 K ($[Fe^{2+}] = [Fe^{3+}] = 10^{-5}$ M, $[CO_2] = 10^{-1}$ M). Adapted from reference [6].

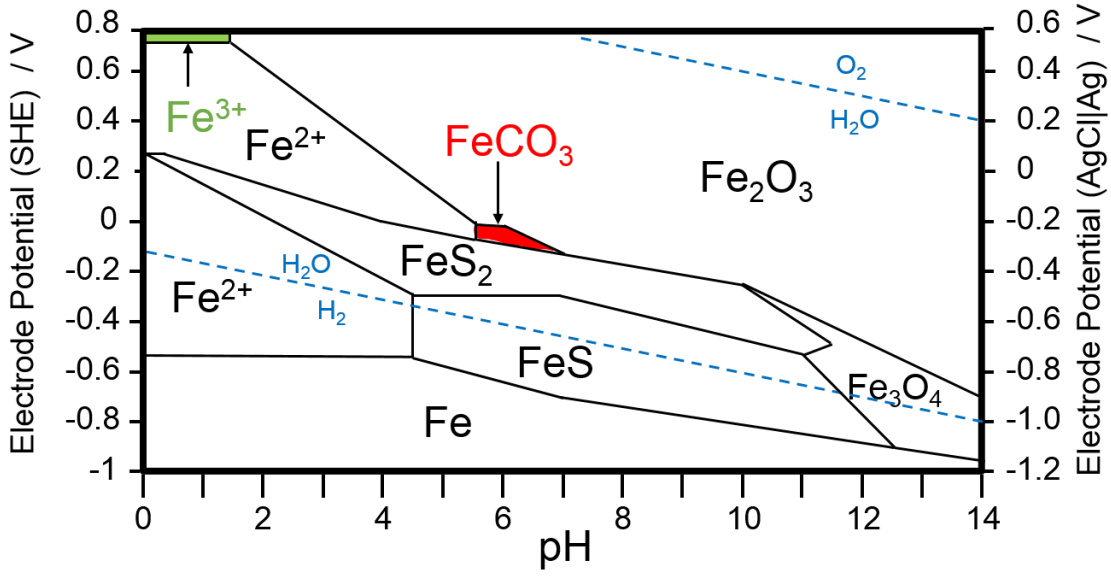

Figure 3.6 Pourbaix diagram of Fe-S-C-H_2O system at 298 K (Dissolved Fe^{2+}/Fe^{3+} activities = 10^{-3}, dissolved carbon species activities = 1, dissolved sulfur species activities = 10^{-4}). Adapted from reference [7].

The Pourbaix diagrams presented in this section were based on the compounds / solid phase and products considered in the thermodynamic calculations which were closest to those observed experimentally in this project. These diagrams were also selected based on their consensus with the transformations of the FeS / FeNiS nanoparticles observed in this work.

3.1.2 Reactions of iron sulfides

Based on the studies of chemistry of metal sulfides in the open literature, the following reactions are proposed to occur on iron sulfides such as greigite under various experimental conditions:

i) Under acidic conditions, non-oxidative dissolution of metal sulfides proceeds via protonation, releasing the metal cation and HS^- or H_2S via the following reactions:[8]

$$MS + H^+ \longrightarrow M^{2+} + HS^- \quad (3.1)$$

$$MS + 2H^+ \longrightarrow M^{2+} + H_2S \quad (3.2)$$

where M = metal.

ii) In alkaline solutions, the non-oxidative dissolution process proceeds via release of metal cations which undergo complexation with hydroxide ions and water:[9]

$$M^{z+} + xOH^- \rightarrow M(OH)_x^{z-x} \quad (3.3)$$

$$S^{2-} + H_2O \rightarrow HS^- + OH^- \quad (3.4)$$

iii) On the negative-going reduction potential sweep in the CV experiments in this thesis, iron sulfides may undergo reductive decomposition:

$$MS + 2H^+ + e^- \rightarrow M^{2+} + H_2S \quad (3.5)$$

iv) or reduction to metallic iron:

$$MS + 2H^+ + 2e^- \rightarrow M(0) + H_2S \quad (3.6)$$

Iron sulfides are also prone to aerial oxidation on exposure to air, forming iron oxide or hydroxide layers.[10] Thus, precautions must be taken during the synthesis of the iron sulfides used. The greigite materials used in this thesis were synthesised using the capping agent oleylamine ((Z)-octadec-9-enylamine)) which protects the surface from aerial oxidation.

$$FeS + 3O_2 + 2H_2O \rightarrow 4FeOOH + S \quad (3.7)$$

Figures 3.2 and 3.3 both show the Fe-S-H_2O system, yet predict regions of stability for greigite. In particular, Figure 3.2 predicts greigite to be stable to oxidation over a wider range than Figure 3.3. Such discrepancies arise from the difficulties in obtaining reliable experimental thermodynamic data for these compounds. In this work, Figure 3.2 is used for the initial interpretation of the CV data as the greigite stability region is more consistent with our experimental observations. However, the reduction transformations under consideration (e.g. greigite to FeS boundaries) are similar in both diagrams.

3.2 Methods and experimental conditions

The cyclic voltammetry experiments performed on greigite were performed in phosphate buffer solutions (PBS) pH 4.5 and 6.8, $KHCO_3$ pH 8.55 and K_2CO_3 pH 11.2. These pH values were selected based on the iron sulfide membrane theory where CO_2 reduction was proposed to occur between the interface of acidic ocean and alkaline hydrothermal vents comprised of greigite.[11] Additionally, phosphate buffer solutions pH 4.5 and 6.8 were chosen as the electrolyte for their buffering capacity on introduction of CO_2. $KHCO_3$ and K_2CO_3 electrolytes were also used to consider and contrast the possible formation of iron carbonate on the surface of greigite with and without CO_2 in solution. The electrochemical studies were performed by sweeping a cyclic potential sweep between 0.00 and −1.00 V (vs. AgCl|Ag). All potentials cited in this work are against AgCl|Ag electrode (+0.197 vs. SHE). This potential range was chosen to study CO_2 reduction on greigite since the reduction of CO_2 is known to have a large overpotential.

3.2.1 Equipment details

In the cyclic voltammetry experiments, a three-electrode cell was used. The working electrode (WE) chosen was a 3 mm diameter disk boron-doped-diamond (BDD) electrode, press fitted into a Teflon body (Windsor Scientific, Slough, United Kingdom). A coiled platinum wire served as a counter electrode (CE) and reference electrode (RE) used was an AgCl|Ag electrode (sat. KCl) (BASI, United Kingdom). The measurements were performed using a potentiostat (Bio-Logic VMP3) and were recorded using EC-Lab software (ver 10.10).

Electrolytes, 0.2 M phosphate buffer solutions (PBS), 0.2 M $KHCO_3$, and 0.2 M K_2CO_3, were prepared using deionised distilled water (Milli-Q pore system A10 water filter 18.2 MΩ cm at 25°C), K_2HPO_4 (Sigma Aldrich, 99%), KH_2PO_4 (Sigma Aldrich, 98+%), $KHCO_3$ (Sigma Aldrich, 99.7%) and K_2CO_3 (BDH Laboratories, 99.9%). Different concentrations of electrolytes were prepared to achieve the desired pH of electrolyte. The resulting pH of the electrolytes were 4.5 (0.2 M KH_2PO_4), 6.8 (0.1 M KH_2PO_4 + 0.1 M KH_2PO_4), 8.55 (0.2 M $KHCO_3$) and 11.2 (0.2 M K_2CO_3).

For measurements under Ar, 50 ml of the electrolyte was deoxygenated by bubbling Ar gas (99.998% purity, BOC Pureshield Argon) into the solution for 20 minutes. A flow of Ar was then maintained over the solution throughout the experiment. For measurements under CO_2, the deoxygenated electrolyte was further bubbled with CO_2 gas (> 99.995% purity, BOC) for 20 minutes to ensure CO_2 saturation of electrolyte. On introduction of CO_2, the pH was allowed to decrease to pH 4.3 in 0.2 M KH_2PO_4, pH 6.5 in 0.1 M KH_2PO_4 + 0.1 M KH_2PO_4, pH 7.1 in 0.2 M $KHCO_3$ and pH 10.1 in 0.2 M K_2CO_3.

The CE and RE were rinsed thoroughly with distilled water before the electrodes were immersed into the electrolyte. The WE was polished three times with alumina slurry, rinsed with distilled water and the electrode was left to dry before it was immersed into the electrolyte. A background CV measurement was taken each time to ensure the electrode was free of contaminants before drop-coating the electrode with the synthetic iron and iron-nickel sulfide samples.

The samples were prepared by suspension of the nanoparticles in 20 µl isopropanol in Eppendorf tubes. The tubes were then sonicated for 15 minutes to ensure an even dispersion of samples in the suspension. 2 µl of suspension was drop coated onto the working electrode and the electrode was left to dry for 2 minutes. The amount of nanoparticles drop coated on the electrode was not quantified due to an uneven coating of the nanoparticles on the electrode surface, which resulted in some of the nanoparticles to fall off the electrode on immersion into the electrolyte. The presence of a potentially insulating oleylamine capping agent layer meant that it was not possible to ensure a good low ohmic contact between the nanoparticles and the underlying electrode, however, the setup was clearly sufficient to obtain a clear voltammetry. Hence with these factors considered, there are limitations on analysing CV data.

The main parameters controlled in the CV experiment were the start and end potentials, scan rate and number of scans. The start and end potentials chosen were 0 and −1.0 V, then reversed back to 0 V. 0 V was chosen as an arbitrary starting potential since preliminary experiments showed that no redox features were present in this potential region. Each run was composed of three scans. The

CVs were performed with scan rates of 1, 10, 100 mV s^{-1}. The CVs performed at a scan rate of 10 mV s^{-1} were chosen for qualitative analysis in this project. Each measurement was repeated three times to ensure reproducibility of cyclic voltammograms of samples tested (see Appendix 3 for reproducibility of the CVs recorded).

3.2.2 Literature on electrochemistry of greigite

Greigite has been used as an electrode material in electrochemical studies such as proton exchange membrane (PEM) water electrolysis,[12] cathode material in magnesium batteries,[13] and an anode material in lithium ion batteries.[14] Most electrochemical studies of greigite that have been published focused on the production of hydrogen and the efficiency of batteries. These studies used linear sweep voltammetry which represents only the forward sweep in a cyclic voltammetry experiment. The study of the use of greigite in PEM water electrolysis by Giovanni *et al* is of most relevance to the investigations in this thesis.[12]

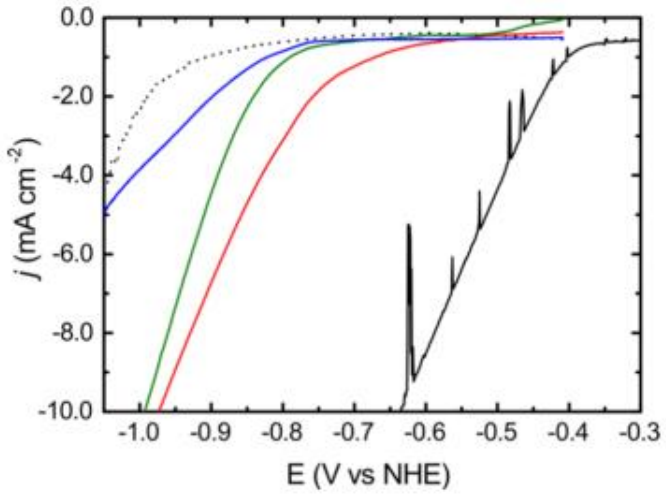

Figure 3.7 Linear sweep voltammograms of Fe_xS_y nanoparticles and Pt/C on a rotating disk glassy-carbon electrode recorded in 0.1 mol L^{-1} phosphate buffer solution at pH 7.0 at 20°C, scan rate 1 mV s^{-1}, rotation rate 4000 rpm. Pt/C (black line); pyrite/C (red line); greigite (green line); pyrrhotite (blue line); C (black dashed line).[12] Reprinted with permission from ACS Catalysis. Copyright 2016 American Chemical Society.

Giovanni *et al* tested greigite nanoparticles for activity towards molecular hydrogen evolution. [12] The linear sweep voltammetry of greigite (green trace) at pH 7 in Figure 3.7 shows the onset of hydrogen evolution, cited by the authors, to occur at ~ −0.55 V (vs. AgCl|Ag). The authors did not assign any redox reactions of greigite in the linear sweep voltammetry. Based on the Pourbaix diagram in Figure 3.2, greigite is predicted to be stable up to −0.55 V where it will undergo transition to FeS:

$$Fe_3S_4 + 2H^+ + 2e^- = 3FeS + H_2S \qquad (3.8)$$

This predicted conversion from greigite to FeS, however, was not suggested in their work, and may have contributed to the reduction currents observed at −0.55 V. No other reduction peaks were recorded which suggests that the greigite used by the authors was relatively stable. The reduction of greigite and FeS to metallic iron was also not considered in their study, predicted to occur at ~ −1.00 V in the Pourbaix diagram in Figure 3.2, which is within the potential range used in their work (Figure 3.7). The formation of metallic iron on the linear sweep voltammetry of greigite may contribute to the reduction current or provide active sites for catalysis of hydrogen evolution.

$$FeS + 2H^+ + 2e^- = Fe(0) + H_2S \qquad (3.9)$$
$$Fe_3S_4 + 8H^+ + 8e^- = 3Fe(0) + 4H_2S \qquad (3.10)$$

As there is limited published work on the electrochemistry of greigite, the electrochemistry of pyrite, FeS_2, which has a similar cubic structure to greigite is also reviewed here. Hamilton and Woods[15] investigated the surface oxidation of natural mineral pyrite by linear sweep voltammetry in electrolytes of pH 4.6, 9.2 and 13. The authors reported the presence of similar anodic and cathodic peaks across all the pHs tested as seen in Figure 3.8 and Figure 3.9. The authors constructed Pourbaix diagrams for the FeS_2-H_2O system as shown in Figure 3.10, which has a much larger stability region for Fe_2O_3 compared to the Pourbaix diagram for Fe-H_2S-H_2O system for greigite in Figure 3.2.

At pH 4.6, the sharp anodic current at *c.a.* +0.80 V (vs SHE) was assigned to the oxidation of the sulfur content of pyrite to sulfur or sulfate ((**3.11**) and (**3.12**)):

$$FeS_2 + 3H_2O \rightarrow Fe(OH)_3 + 2S + 3H^+ + 3e^- \quad (3.11)$$
$$FeS_2 + 11H_2O \rightarrow Fe(OH)_3 + 2SO_4^{2-} + 19H^+ + 15e^- \quad (3.12)$$

Comparing the stability regions of sulfur and sulfate in Figure 3.4, it is most likely that the oxidation reaction to produce sulfates will be favoured over sulfur. The step feature at +0.40 V (vs SHE) was assigned to the oxidation of Fe^{2+} species to form ferric hydroxide:

$$Fe^{2+} + 3H_2O \rightarrow Fe(OH)_3 + 3H^+ + e^- \quad (3.13)$$

with the reverse reaction occurring at the small cathodic peak at +0.25 V (vs SHE). This suggested redox transition between Fe^{2+} and $Fe(OH)_3$ is in agreement with the stability regions of Fe^{2+} and $Fe(OH)_3$ in the Pourbaix diagram in Figure 3.1 at pH 4.6. The cathodic peak at −0.15 V (vs SHE) was assigned to the reduction of sulfur (**3.14**):

$$S + 2H^+ + 2e^- \rightarrow H_2S \quad (3.14)$$

The reverse reaction of (**3.14**) was suggested to occur at the anodic peak at 0 V (vs SHE). The reduction of sulfate species was not considered by the authors, which although is thermodynamically predicted to contribute to reduction currents in this region is in reality likely to be kinetically too slow a process to occur at this potential.

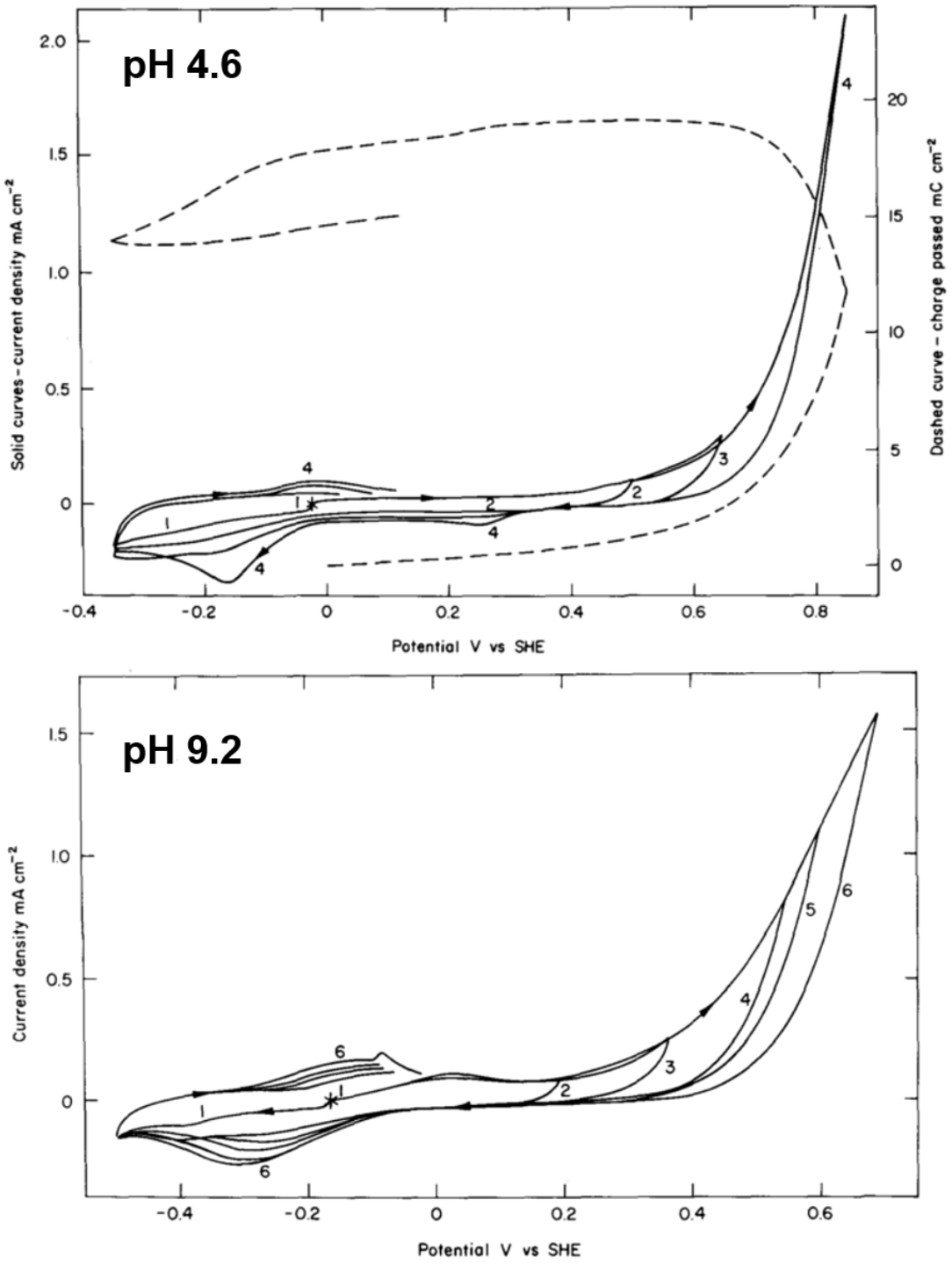

Figure 3.8 Cyclic voltammograms of stationary pyrite electrode at pH 4.6 and 9.2 at scan rate of 20 mV s^{-1} reversed at different upper potential limits. Dashed line in CV at pH 4.6 is the recorded charge on voltammogram curve 4. [15] **Reprinted with permission from Elsevier. Copyright 1981 Elsevier B.V.**

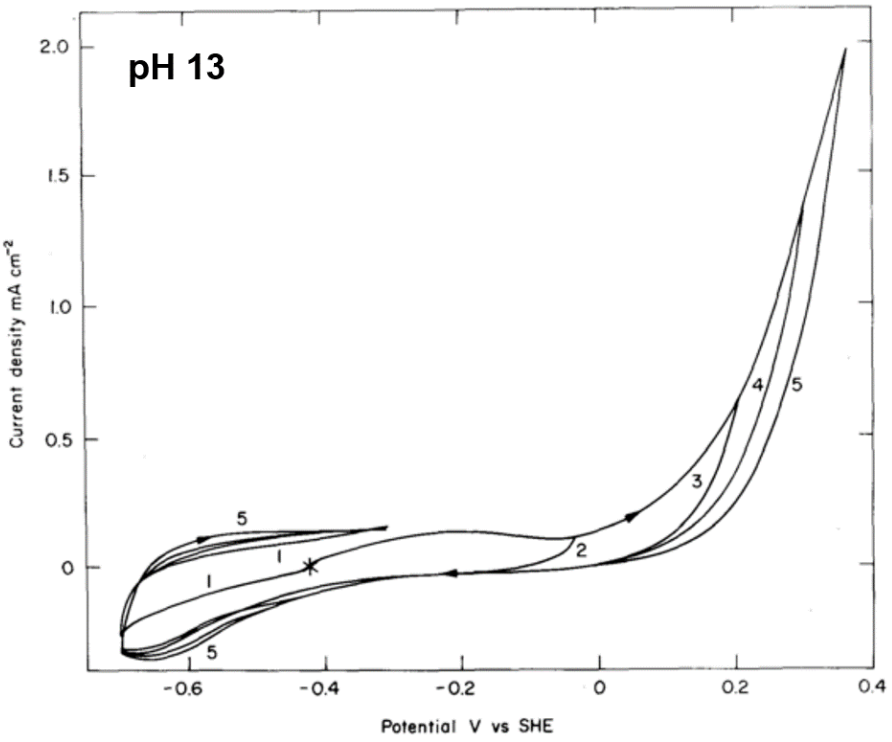

Figure 3.9 Cyclic voltammograms of stationary pyrite electrode at pH 13 at scan rate of 20 mVs^{-1} reversed at different upper potential limits. [15] **Reprinted with permission from Elsevier. Copyright 1981 Elsevier B.V.**

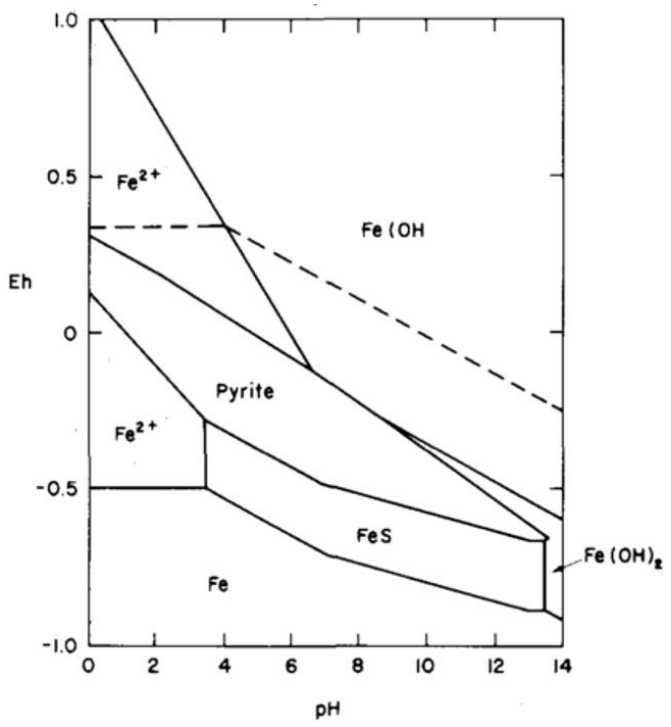

Figure 3.10 Pourbaix diagram for FeS_2-H_2O system at 25°C and 10^{-3} M dissolved species. [15] **Reprinted with permission from Elsevier. Copyright 1981 Elsevier B.V.**

In basic solutions (9.2 and 13), Hamilton and Woods suggested it was not possible for HS^- to be released from the pyrite surface due to the presence of iron oxides according to their Pourbaix diagram in Figure 3.10, which led to the absence of the cathodic peak at ~ −0.25 V at both pHs compared to pH 4.6. It seems that the authors implied that the sulfur formed on the positive-going potential sweep would be passivated / trapped by the iron oxide form, thus no reduction of sulfur to HS^- takes place. However, since the authors did not consider the presence of sulfates on the pyrite electrode on the positive-going potential sweep, it is also possible that the sulfates may have diffused away from the electrode surface.

The suggested passivation of an iron sulfide surface by iron oxides was also reported in works by Bura-Nakic, [2] Hunger [16] and Thornber. [1] Hamilton and Woods[15] further proposed the formation of iron sulfides via the reduction of sulfur, in the presence of iron oxides under basic conditions:

$$Fe(OH)_3 + S + 3e^- \rightarrow FeS + 3OH^- \quad (3.15)$$

$$Fe(OH)_3 + H^+ + e^- \rightarrow Fe(OH)_2 + H_2O \quad (3.16)$$

The formation of iron oxides on iron sulfide surfaces at positive potentials must be verified using characterisation techniques. In contrast to the potential range used by Hamilton and Woods (between −0.65 and +0.40 V vs SHE), it is not expected that greigite would undergo similar passivation by iron oxides, since the potential sweep used in this work is only between 0.00 and −1.00 V (vs AgCl|Ag).

3.3 Results

3.3.1 PBS pH 4.5 under argon

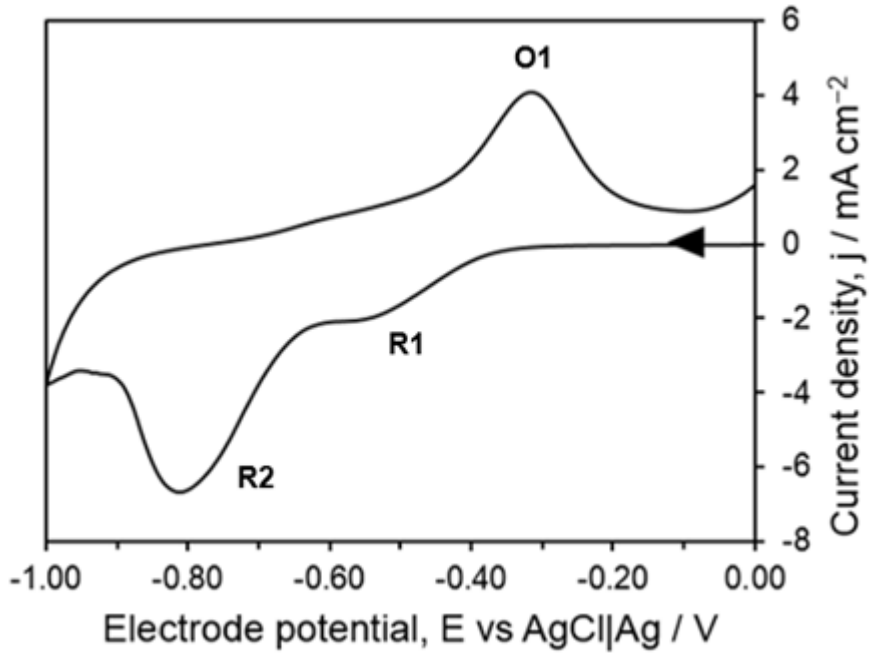

Figure 3.11 First scan of cyclic voltammogram of greigite in phosphate buffer solution (PBS) pH 4.5 under argon recorded at 10 mV s^{-1}. Start potential = 0.00 V.

The assignments of the redox features in the CVs of greigite in this chapter are based on thermodynamically feasible reactions predicted in the Pourbaix diagrams in Figure 3.1, Figure 3.2 and Figure 3.4, which show the stability regions of Fe_3S_4, FeS, Fe and S species at a range of electrode potential E and pH. In chapter 4, these thermodynamic predictions will be compared to the spectroscopic data obtained to confirm their validity.

Figure 3.11 displays the first CV scan of greigite recorded in phosphate buffer solution (PBS) pH 4.5 under argon. On the negative-going sweep, a reduction current was recorded at −0.35 V followed by two reduction peaks R1 (−0.50 V) and R2 (−0.82 V). In the potential region between 0 and −0.35 V, the current value appeared to be close to zero indicating no redox reactions occurred over this potential range.

According to the Pourbaix diagram in Figure 3.2, dissolution of greigite via **(3.17)** is predicted to occur at −0.35 V. Separately, the Pourbaix diagram in Figure 3.3 predicted that green rust, $Fe^{II}_4Fe^{III}_2(OH)_{12}SO_4$, will form on application of an electrode potential sweep between 0.00 and −0.10 V at pH 4.5. However, there was no distinct reduction peak recorded within this potential range in Figure 3.11 and additionally, there was no visible green precipitate observed on the greigite electrode. Therefore, the transformation of greigite to green rust may not have occurred due to slow kinetics or protection offered by the presence of the capping agent. Based on the close agreement between the redox features of greigite and the Pourbaix diagram in Figure 3.2, the predictions in Figure 3.2 will be used to compare the redox features of greigite.

Thus, based on the Pourbaix diagram in Figure 3.2, the reduction peak R1 is assigned to reductive decomposition (Equation 3.17). The flat current trace between 0.00 and −0.35 V in Figure 3.11 suggests that greigite is stable within this potential range, as predicted in Figure 3.2.

$$Fe_3S_4 + 8H^+ + 2e^- = 3Fe^{2+} + 4H_2S \qquad (3.17)$$

Greigite is predicted to undergo reduction to Fe^{2+} species on applying more negative potentials past −0.35 V, according to Figure 3.2. Between −0.35 V and −0.85 V at pH 4.5, greigite is also predicted to reduce to "FeS" where "FeS" denotes a general term for an iron sulfide. "FeS" here is most likely an iron-deficient iron sulfide or the reduced form of greigite Fe_3S_4.

$$Fe_3S_4 + 2H^+ + 2e^- = 3FeS + H_2S \qquad (3.18)$$

The above prediction for the reduction of Fe_3S_4 to "FeS" to occur between −0.35 V and −0.85 V is also close to the predicted transition of other iron-deficient iron sulfides such as Fe_7S_8 and FeS_2 to stoichiometric FeS which is expected to occur at −0.60 V at pH 4.5. [7] The peak current of the redox feature R1 in Figure 3.11 occurred at −0.52 V which suggests that the transition from greigite to "FeS" may have also contributed to peak R1. Therefore, it is proposed here that peak R1 is associated with the reductive decomposition of greigite to Fe^{2+} (reaction **(3.17)**) and the transition of greigite to "FeS" (reaction **(3.18)**). "FeS" will also be

susceptible to dissolution to Fe^{2+} at pH 4.5 (since the stability regions of Fe^{2+} and "FeS" coincide at pH 4.5 in Figure 3.2):

$$FeS + 2H^+ = Fe^{2+} + H_2S \qquad (3.19)$$

These thermodynamic predictions for peak R1 suggest a complete transformation of the bulk structure of greigite Fe_3S_4 to "FeS", followed by dissolution to soluble Fe^{2+} species. However, kinetically these processes may be slow and confined to the surface of the greigite particles since the greigite drop coat on the electrode was intact at the end of the experiment and suggests that greigite was more stable than predicted.

Peak R1 was followed by a second reduction peak R2 at −0.82 V. According to Figure 3.2, Fe^{2+} and "FeS" are predicted to be reduced to Fe(0) at −0.85 V, while Fe(0) is expected to remain stable on reaching the vertex potential of −1.00 V. It must also be considered that any remaining greigite present on the surface could also be reduced to Fe(0) at this point.

$$FeS + 2H^+ + 2e^- = Fe(0) + H_2S \qquad (3.20)$$
$$Fe^{2+} + 2e^- = Fe(0) \qquad (3.21)$$
$$Fe_3S_4 + 8H^+ + 8e^- = 3Fe(0) + 4H_2S \qquad (3.22)$$

Thus, the redox feature R2 (−0.82 V) in Figure 3.11 is assigned to the reduction of Fe_3S_4, FeS and Fe(II) species, produced from the process at R1, to Fe(0). At this point in the experiment (during potential sweep from −0.80 to −1.00 V), bubbles were evident on the electrode surface which implies that the formation of Fe(0) at peak R2 catalysed the reduction of protons or water to form hydrogen.

On reversing the potential sweep from −1.00 V to 0.00 V, only one distinct anodic peak O1 at −0.30 V was recorded followed by the onset of an oxidation peak at −0.05 V. According to Figure 3.2, Fe(0) formed at the end of the negative-going sweep is predicted to remain as the stable phase between E = −1.00 to −0.80 V on the positive-going sweep hence no redox feature is expected within this potential window.

Continuing the positive-going sweep above −0.80 V, the following thermodynamic transitions are predicted according to the Pourbaix diagrams in Figure 3.1 and Figure 3.2:

i) Fe(0) oxidised to Fe^{2+} at E = −0.80 V:

$$Fe = Fe^{2+} + 2e^- \quad (3.23)$$

ii) If H_2O only is present (no H_2S), Fe^{2+} formed at **(3.23)** will remain stable up to 0.00 V.

iii) If H_2S is present, Fe(0) and Fe^{2+} can react with H_2S to form "FeS" (if the local pH increases above pH 4.5 due to water and proton reduction).

$$Fe + H_2S = FeS + 2H^+ + 2e^- \quad E = -0.80\ V \quad (3.24)$$

$$Fe^{2+} + H_2S = FeS + 2H^+ \quad E = \text{between } -0.80 \text{ V to } -0.60\ V \quad (3.25)$$

iv) If H_2S is present, it can be oxidised to elemental sulfur or sulfate according to Figure 3.4:

$$H_2S = S + 2H^+ + 2e^- \quad E = -0.25\ V \quad (3.26)$$

$$S + 4H_2O = SO_4^{2-} + 8H^+ + 6e^- \quad E = -0.15\ V \quad (3.27)$$

$$H_2S + 4H_2O = SO_4^{2-} + 10H^+ + 8e^- \quad (3.28)$$

In contrast to the thermodynamic assessment above which predicted multiple oxidation events could take place, only one oxidation peak was observed in Figure 3.11 (peak O1 at −0.30 V). It is proposed here that peak O1 is assigned to the oxidation of Fe(0) to Fe^{2+} (reaction **(3.23)**) with a high overpotential, possibly due to catalysis of proton and water reduction by Fe(0) on the previous negative sweep, resulting in a surface covered by OH^-. According to the Pourbaix diagram in Figure 3.4, any H_2S present will also be oxidised to elemental sulfur (reaction **(3.26)**) at this potential and thus may also contribute towards peak O1. Peak O1 is not assigned to the formation of FeS (reactions **(3.24)**-**(3.25)**), as it is expected that the H_2S required for FeS formation will be oxidised to elemental sulfur (reaction **(3.26)**) at this potential.

The onset of an oxidation peak observed at −0.05 V in Figure 3.11 on the positive-going sweep is assigned to further oxidation of H_2S or elemental sulfur to sulfate (reactions **(3.27)** and **(3.28)**).

The effect of possible reduction of water and protons also needs to be considered on both the negative- and positive-going potential sweeps (see Figure 3.1, Figure 3.2 and Figure 3.4). The reduction of water is predicted to occur between 0.00 V and −0.45 V where the reduction of protons will take place:

$$2H_2O + 2e^- = H_2 + 2OH^- \qquad E = -0.45\ V \qquad (3.29)$$

$$2H^+ + 2e^- = H_2 \qquad E < -0.45\ V \qquad (3.30)$$

However, it is expected that the reduction of water and protons may be slow on greigite due to a high overpotential. If either reaction takes place, it will result in an increase of the local pH on the electrode due to consumption of protons or reduction of water generating OH^-. According to the Pourbaix diagram in Figure 3.2, an increase of the local pH to a pH value greater than 4.5 will favour the transition of greigite to "FeS" over the reductive decomposition of greigite to Fe^{2+} assigned at R1. It is also predicted in the Pourbaix diagram in Figure 3.1 that the formation of iron hydroxide is possible at −1.00 V, if the pH value shifted and was greater than 8.5.

There is prevalent information in the open literature regarding the formation of a passivating iron hydroxide layer on iron sulfide surfaces due to aerial oxidation.[10] The presence of an iron hydroxide layer on an iron sulfide surface has been suggested to passivate redox reactions on the iron sulfide surface. As previously stated, the greigite material used in this thesis was capped with a capping agent which prevents surface oxidation. Thus, it is not expected that any iron hydroxide will be present on greigite prior to immersion into the electrolyte. Hence, the presence of an iron hydroxide will not be considered in the redox assignments of greigite in this chapter.

However, for additional literature information, the potential redox reactions of iron hydroxide are discussed here. If an iron hydroxide layer was present on the greigite surface prior to immersion of the electrode, it must first be dissolved before the reductive decomposition of greigite current flows. According to Figure 3.1, iron hydroxide layers are expected to form soluble Fe^{2+} species at pH 4.5 below 0.00 V via dissolution (reactions **(3.31)**-**(3.32)**). The iron hydroxide layer

may also undergo reduction to form soluble Fe^{2+} species (reactions **(3.33)-(3.34)**). The iron hydroxide layers that may be present on greigite include $Fe(OH)_3$, α-FeOOH (goethite) and γ-FeOOH (lepidocrocite).

$$Fe(OH)_3 + 3H^+ = Fe^{3+} + 3H_2O \quad (3.31)$$
$$FeOOH + 3H^+ = Fe^{3+} + 2H_2O \quad (3.32)$$

$$FeOOH + 3H^+ + e^- = Fe^{2+} + 2H_2O \quad (3.33)$$
$$Fe(OH)_3 + 3H^+ + e^- = Fe^{2+} + 3H_2O \quad (3.34)$$

Based on the stability region of iron hydroxide ($Fe(OH)_3$) at pH 4.5 in Figure 3.1, it is expected that iron hydroxide will not be stable at 0.00 V. Thus, if any iron hydroxide was present on the greigite surface, it will be reduced to soluble Fe^{2+} species at 0.00 V at pH 4.5.

Figure 3.12 displays the subsequent scans of the CV of greigite at pH 4.5. The redox features on the first scan are clearly different compared to the subsequent scans which suggests a change in the electrode surface composition prior to the second scan. At the end of the first scan, it was assumed that Fe^{2+} and SO_4^{2-} species were present on the electrode surface. If the local pH increased above pH 4.5 at the onset of the second scan at 0.00 V, iron hydroxide will also be present on the electrode surface, according to the Pourbaix diagram in Figure 3.1.

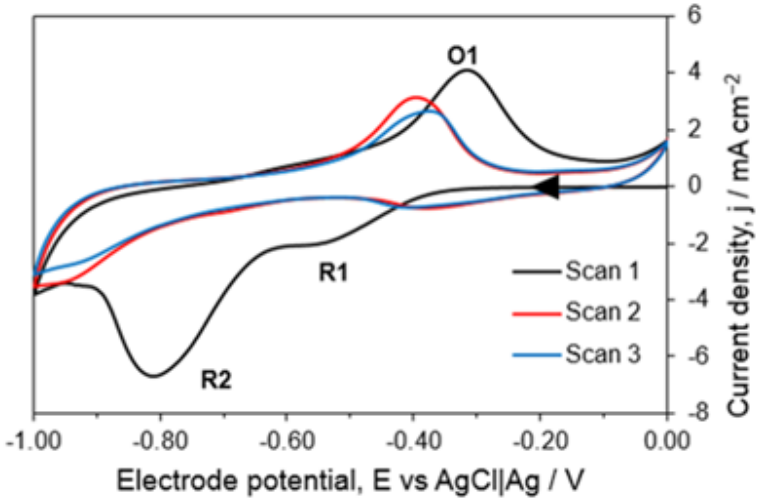

Figure 3.12 Cyclic voltammogram of greigite with three consecutive scans in phosphate buffer solution (PBS) pH 4.5 under argon recorded at 10 mV s^{-1}. Potential sweep started at 0.00 V.

Assuming the local pH maintained at pH 4.5 at the onset of the second scan, the following thermodynamic predictions, according to Figure 3.1, Figure 3.2 and Figure 3.4 at pH 4.5, are expected on the negative-going sweep of the second scan:

i) Fe^{2+} species will be reduced to Fe(0) at E = −0.80 V (reaction **(3.21)**)

ii) SO_4^{2-} species will be reduced to elemental sulfur and H_2S at −0.15 V and −0.25 V. The reduction of SO_4^{2-} species is thermodynamically feasible, however, kinetically it does not happen as it does not occur at measurable rates in aqueous solutions under ambient conditions without the presence of sulfate-reducing bacteria.

$$SO_4^{2-} + 8H^+ + 6e^- = S + 4H_2O \qquad E = -0.15\ V \qquad (3.35)$$

$$S + 2H^+ + 2e^- = H_2S \qquad E = -0.25\ V \qquad (3.36)$$

$$SO_4^{2-} + 10H^+ + 8e^- = H_2S + 4H_2O \qquad (3.37)$$

On the negative-going sweep of the second scan in Figure 3.12, there was a small reduction peak recorded at −0.30 V, followed by the onset of a reduction peak at −0.85 V. Based on the predictions above, the reduction peak at −0.30 V is assigned similarly to peak R1 on the first scan. It cannot be assigned to the reduction of SO_4^{2-} species due to slow kinetics. The reduction peak at −0.85 V is assigned to reduction of Fe^{2+} species to Fe(0), similar to peak R2 on the first scan. It is also predicted in Figure 3.2 that FeS can be formed chemically (reaction **(3.38)**) if there are sufficient amounts of Fe^{2+} and H_2S present. If FeS was formed, the reduction of FeS to Fe(0) (reaction **(3.20)**) may contribute to the reduction peak at −0.85 V.

$$Fe^{2+} + H_2S = FeS + 2H_2O \qquad (3.38)$$

On the reverse positive-going sweep of the second scan in Figure 3.12, only one oxidation peak was recorded at −0.40 V. This oxidation peak resembled peak O1 on the first scan and hence it is assigned similarly to Fe(0) oxidation to Fe^{2+}. This oxidation peak on the second scan is, however, smaller compared to peak O1 which suggests that there was less Fe(0) produced on the negative-going sweep of the second CV scan compared to the first CV scan. This was as expected considering there was no distinct reduction peak on the negative-going sweep of

the second scan compared to peaks R1 and R2 in the first scan. The subsequent third scan in the CV of greigite appears similar to the second scan and therefore similar reaction assignments are proposed.

Comparing the first and subsequent scans in the CV of greigite in Figure 3.12, the significantly reduced currents on the second and third scans show that repeated cycling affects the stability of the electrode composition. It is likely that there was a change in the electrode surface on the subsequent scans. It is possible that a passivating iron hydroxide layer may have formed on the surface of the electrode. Such formation of an iron hydroxide layer is not predicted in a Fe-H_2S-H_2O system as shown in the Pourbaix diagram in Figure 3.2. Thus, the formation of an iron hydroxide layer would only occur if there was no H_2S available near the electrode (see Pourbaix diagram in Figure 3.1). The formation of such layer on the greigite electrode, however, requires further evidence.

3.3.2 PBS pH 6.8 under argon

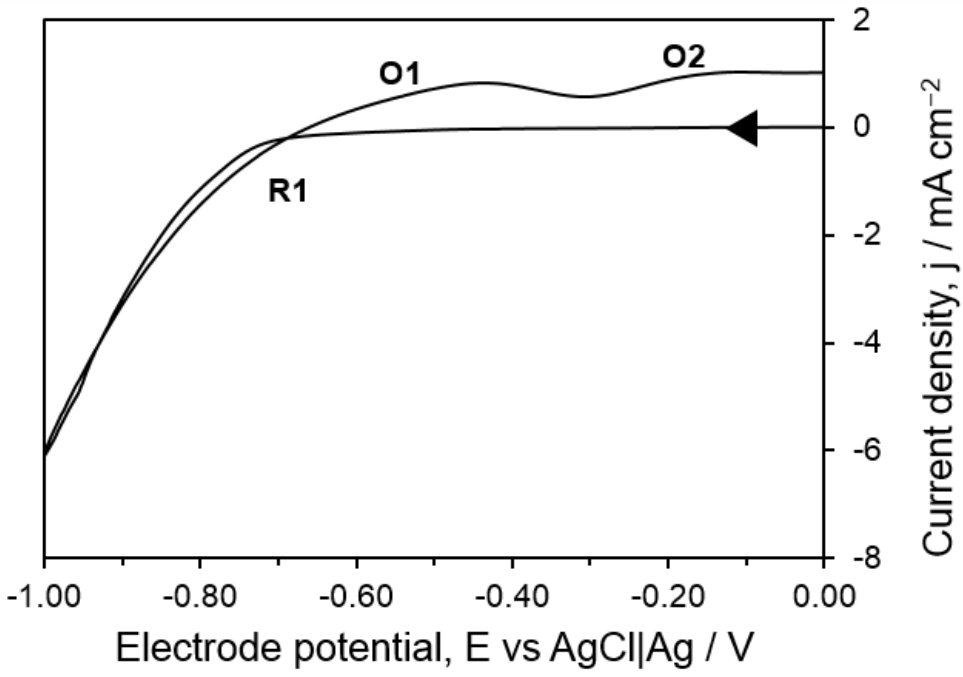

Figure 3.13 First scan of cyclic voltammogram of greigite in phosphate buffer solution (PBS) pH 6.8 under argon recorded at 10 mV s^{-1}. Potential sweep started at 0.00 V.

Figure 3.13 shows the first CV scan of greigite in phosphate buffer solution (PBS) pH 6.8 under argon. Similar to the CV of greigite in pH 4.5 in the previous section, there is a region in Figure 3.13 where the current appears to be close to zero (on the negative-going sweep from 0.00 V to −0.70 V). This flat current trace was previously assigned at pH 4.5 to the potential region where greigite is stable as predicted in Figure 3.2, hence no redox reactions are expected to occur. Alternatively, green rust, $Fe^{II}_4Fe^{III}_2(OH)_{12}SO_4$ is predicted to form between 0 and −0.38 V at pH 6.8 in the Pourbaix diagram in Figure 3.3, while greigite is predicted to be stable over a very narrow potential range between −0.38 and −0.40 V. Similar to the observation in pH 4.5, considering the absence of green precipitate on the electrode, the transformation to form green rust may not have occurred due to slow kinetics.

At pH 6.8, greigite is predicted to be stable between 0.00 to −0.55 V according to the Pourbaix diagram in Figure 3.2. However, the onset of reduction observed at pH 6.8 in Figure 3.13 was recorded at −0.70 V. This is also comparable to the results reported by Giovanni *et al*[12] detailed at the beginning of this chapter (−0.55 V). The more negative onset of the reduction current recorded at pH 6.8 compared to the predicted value in the Pourbaix diagram in Figure 3.2 and the study by Giovanni *et al*[12] may be associated with the capping agent present on the greigite surface. At pH 6.8, the amine group of the capping agent is neutral ($-RNH_2$) and uncharged. Due to the long carbon chain of the capping agent ($C_{18}H_{37}N$ or (Z)-octadec-9-enylamine) and its lack of charge at pH 6.8, it is likely to be water insoluble. It is plausible that an overpotential was required to repel the capping agent away from the the electrode surface before redox reactions can proceed.

It is assumed here that the use of the capping agent in the synthesis of the greigite material prevented aerial oxidation of greigite which could lead to the formation of iron hydroxide on the greigite surface. However, if an iron hydroxide layer was present on the surface of greigite, it needs to be dissolved before current flows. The presence of such iron hydroxide layer on greigite, however, must be characterised in-situ. Considering the potential redox reactions of iron hydroxide

which may occur at pH 6.8, according to Figure 3.1, any iron hydroxide present is predicted to be stable between 0.00 V up to −0.40 V where it will undergo dissolution (reactions **(3.31)**-**(3.32)**) or reduction (**(3.33)**-**(3.34)**) to form soluble Fe^{2+} species and may contribute to the reduction peak R1.

Assuming no iron hydroxide was present on the greigite surface, the following thermodynamic transitions of greigite, according to Figure 3.2, are expected at pH 6.8 when a negative-going potential sweep from 0.00 V to −1.00 V is applied:

i) greigite is predicted to remain stable between 0.00 to −0.55 V.

ii) at −0.55 V, greigite is predicted to be reduced to "FeS" phase, producing H_2S **(3.18)** or HS^- **(3.39)**.

$$Fe_3S_4 + H^+ + 2e^- = 3FeS + HS^- \qquad (3.39)$$

iii) water and proton reduction are predicted to occur from −0.50 V which will produce H_2 and OH^- (reactions **(3.29)** and **(3.30)**). However, as mentioned in the previous section at pH 4.5, the reaction kinetics of water and proton reduction are predicted to be slow on greigite and is therefore most likely to occur at a more negative potential than predicted.

iv) "FeS" produced in reaction **(3.18)** is expected to be stable up to −1.00 V, where "FeS" is reduced to Fe(0) and releases H_2S (reaction **(3.20)**) or HS^- (reaction **(3.40)**). At this pH, both H_2S and HS^- will exist in equilibrium (reaction **(3.41)**). Assuming water and proton reduction occurred, this will increase the pH at the electrode and will shift the equilibrium towards the production of HS^- in reaction **(3.41)**. Any remaining greigite present on the surface is also predicted to be reduced to Fe(0) and produce HS^- (reaction **(3.42)**).

$$FeS + 2H^+ + 2e^- = Fe(0) + HS^- \qquad E = -1.00\ V \qquad (3.40)$$

$$H_2S = HS^- + H^+ \qquad E = -0.40 \text{ to } -1.00V \qquad (3.41)$$

$$Fe_3S_4 + 4H^+ + 8e^- = 3Fe(0) + 4HS^- \qquad (3.42)$$

Additionally, according to Figure 3.1, any Fe^{2+} species produced from the dissolution of iron hydroxide present on the greigite surface as well as greigite itself will be stable within the potential range of −0.40 V to −0.90 V at which it will be reduced to Fe(0) (reaction **(3.21)**).

In the negative-going sweep in Figure 3.13, only one reduction peak R1 was recorded at −0.70 V. No redox features were observed at −0.50 V where the reduction of greigite to "FeS" is expected. This suggests that the predicted phase transition from greigite to "FeS" may have a higher overpotential. As previously stated, this overpotential may be associated with the water insoluble amine group of the capping agent at this pH. Therefore, the phase transition from greigite to "FeS" may have occurred at peak R1. Peak R1 may also be associated with the reduction of any Fe^{2+} species present on the electrode surface to Fe(0) which is predicted to occur at −0.90 V. According to Figure 3.2, "FeS" is expected to be reduced to Fe(0) at the vertex potential E = −1.00 V. Thus, the reduction of "FeS" to Fe(0) may also contribute to peak R1. Therefore, at the end of the negative-going sweep, it is expected that Fe(0), any unreacted "FeS" and HS^- species (assuming water and proton reduction occurred) will be present on the electrode surface.

On the reverse positive-going sweep from −1.00 to 0.00 V, two anodic peaks O1 and O2 were recorded at −0.45 V and −0.20 V in Figure 3.13. According to the Pourbaix diagrams in Figure 3.1, Figure 3.2 and Figure 3.4, the following thermodynamic transitions are predicted on positive-going potential sweep for Fe(0), "FeS" and HS^- species from −1.00 V to 0.00 V at pH 6.8:

i) If HS^- is present, Fe(0) can react to form "FeS" at −1.00 V.

$$Fe(0) + HS^- = FeS + 2H^+ + 2e^- \qquad (3.43)$$

ii) Fe(0) is oxidised to Fe^{2+} at −0.80 V (reaction **(3.23)**)

iii) Any unreacted "FeS" present or produced by reaction **(3.43)** will be stable up to −0.50 V where it can further react with HS^- to form greigite Fe_3S_4.

$$3FeS + HS^- = Fe_3S_4 + H^+ + 2e^- \qquad E = -0.50\ V \qquad (3.44)$$

iv) If H_2O only is present (no HS^-), Fe^{2+} formed at **(3.23)** will remain stable up to −0.40 V where it can react with H_2O to form iron hydroxide (according to Figure 3.1). The iron hydroxide will be stable at potentials above −0.40 V.

$$Fe^{2+} + 3H_2O = Fe(OH)_3 + 3H^+ + e^- \qquad (3.45)$$
$$Fe^{2+} + 2H_2O = FeOOH + 3H^+ + e^- \qquad (3.46)$$

v) If HS^- is present, it is predicted to be stable below −0.40 V. At potentials above −0.40 V, HS^- can be oxidised to elemental sulfur or sulfate according to Figure 3.4 (reactions **(3.47)**-**(3.48)**). The formation of sulfate is most likely favoured over elemental sulfur according to the size of their respective stability regions at pH 6.8 in Figure 3.4. Any elemental sulfur formed will most likely be oxidised to sulfate **(3.49)**.

$$HS^- + 4H_2O = SO_4^{2-} + 9H^+ + 8e^- \qquad (3.47)$$
$$HS^- = S + H^+ + 2e^- \qquad (3.48)$$
$$S + 4H_2O = SO_4^{2-} + 8H^+ + 6e^- \qquad (3.49)$$

Based on the predictions above, it is proposed that the anodic peak O1 at −0.45 V on the positive going-sweep in Figure 3.13 is assigned to the oxidation of Fe(0) to Fe^{2+} soluble species, occurring at a higher potential than predicted (−0.80 V). This is a similar assignment to the oxidation peak at pH 4.5 where the overpotential for Fe(0) oxidation was attributed to presence of OH^- produced by catalysis of proton and water reduction by Fe(0) on the previous negative-going sweep. The oxidation of "FeS" to greigite in the presence of HS^- species (see Figure 3.2) may also contribute to peak O1. Concurrently, the oxidation of HS^- to SO_4^{2-} may also contribute to this peak based on the predictions above. The presence of HS^- may be a limiting factor for the oxidation of "FeS" to proceed. It is likely that some "FeS" may remain unreacted. Once HS^- is consumed, according to Figure 3.1, the soluble Fe^{2+} species produced on Fe(0) oxidation can be further oxidised to iron hydroxide. Hence, Fe^{2+} oxidation is assigned to peak O2 in Figure 3.13.

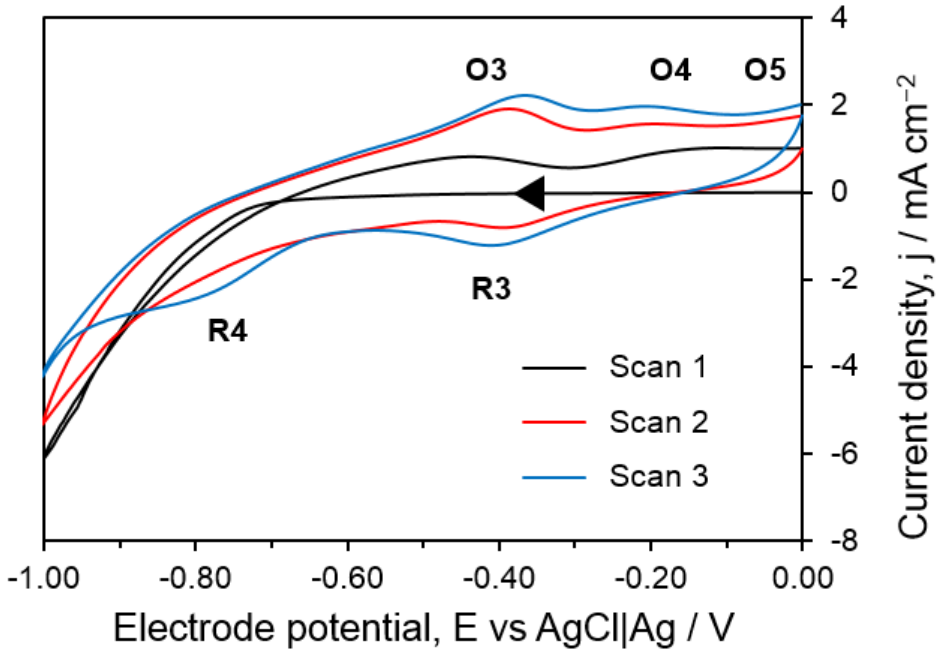

Figure 3.14 First, second and third scans of cyclic voltammogram of greigite in phosphate buffer solution (PBS) pH 6.8 under argon recorded at 10 mV s^{-1}. Potential sweep started at 0.00 V.

At the end of the first scan, it is assumed that an unreacted "FeS" surface with an iron hydroxide layer was present. Sulfate species are also predicted to be present near the electrode surface. Figure 3.14 show the subsequent CV scans of greigite at pH 6.8. Based on the Pourbaix diagrams at pH 6.8 in Figure 3.1, Figure 3.2 and Figure 3.4, the following thermodynamic transitions are expected on the negative-going sweep of the second scan in Figure 3.14:

i) If H_2O only is present (no HS^-), according to Figure 3.1, the iron hydroxide present on the electrode surface is predicted to reduce to Fe^{2+} species or Fe_3O_4 at −0.40 V (reactions **(3.33)-(3.34)**), depending on the local pH. It is most likely that the formation of Fe_3O_4 is favoured if the local pH increased due to water and proton reduction. The removal / dissolution of the iron hydroxide layer may expose any unreacted "FeS" or greigite on the electrode surface. This "FeS" surface will remain stable down to −1.00 V.

ii) If greigite is present on the electrode, it will be reduced to "FeS" and H_2S (pH < 7, reaction **(3.18)**) or "FeS" and HS^- (pH > 7, reaction **(3.39)**) at −0.40 V (see Figure 3.2).

iii) Any unreacted or newly formed "FeS" surface will remain stable down to −1.00 V where it is predicted to reduce to Fe(0) (reaction **(3.40)**).

iv) The sulfate species present near the electrode surface are predicted to reduce to elemental sulfur or HS^- at −0.40 V (reactions **(3.50)** - **(3.52)**, see Figure 3.4). As previously stated, the reduction of sulfate is kinetically hindered and thus will not occur.

$$SO_4^{2-} + 8H^+ + 6e^- = S + 4H_2O \quad (3.50)$$
$$S + H^+ + 2e^- = HS^- \quad (3.51)$$
$$SO_4^{2-} + 9H^+ + 8e^- = HS^- + 4H_2O \quad (3.52)$$

v) Fe^{2+} species produced at −0.40 V from the reduction of iron hydroxide will be stable down to −0.90 V where it is predicted to reduce to Fe(0).

In Figure 3.14, only two reduction peaks R3 and R4 at −0.40 and −0.75 V were present on the negative-going sweep of the second CV scan. Based on the thermodynamic predictions above, peak R3 is assigned to the reduction of greigite to "FeS" and HS^-. Consequently, on production of HS^-, the reduction of iron hydroxide layer on the electrode surface to Fe_3O_4 may be prevented as iron hydroxide may react with HS^- to form greigite or "FeS" (see Figure 3.2). Thus, the iron hydroxide layer may remain on the electrode surface up to −0.80 V where it is predicted to reduce to Fe(0). Therefore, peak R4 is assigned to the reduction of iron hydroxide layer, any unreacted "FeS" and greigite to Fe(0).

On the positive-going sweep of the second CV scan in Figure 3.14, three oxidation peaks O3, O4 and O5 at −0.40, −0.25 and −0.05 V were recorded. Peak O3 is assigned similarly to peak O1 on the first CV scan which is the Fe(0) oxidation to Fe^{2+} soluble species with an overpotential. If HS^- species are present, "FeS" can be formed via Fe(0) oxidation at peak O3. Any "FeS" present on the surface will remain stable and unreacted at potentials above peak O3. Peak O4 is assigned to

the formation of iron hydroxide species from Fe^{2+} soluble species (reactions **(3.45)** - **(3.46)**). Peak O5 is assigned to the oxidation of HS^- species to elemental sulfur or sulfate species (reactions **(3.47)**-**(3.48)**).

Comparing the second CV scan of greigite at pH 4.5 and pH 6.8, the redox features occurred at approximately similar electrode potentials at both pHs, with extra oxidation peaks and a more negative onset of reduction at pH 6.8. These extra features are associated with the presence of an iron hydroxide layer on the greigite surface at pH 6.8 formed on the second scan on the assumption that the local pH on the electrode may have increased (pH > 7) due to water and proton reduction. The iron hydroxide layer has a wide stability region at pH 6.8, as predicted by the Pourbaix diagram in Figure 3.1. Such iron hydroxide layer is not expected to form on greigite at pH 4.5 as iron hydroxide is not stable below 0.00 V. It is reiterated here and proposed that the greigite used in this thesis is not susceptible to aerial oxidation due to the capping agent used in the synthesis which protected the surface from oxidation.

Based on the thermodynamic predictions in the Pourbaix diagrams in Figure 3.1-Figure 3.4, the electrolyte pH is the main factor which determines the stability of the electrode surface as greigite is predicted to be stable over a wider potential window at pH 6.8 compared to pH 4.5. The Pourbaix diagrams also predict the redox reactions which will occur on greigite and determine the stable redox species at each pH condition. The redox assignments of greigite proposed in this chapter are based on the pH of the bulk electrolyte which was assumed to be constant throughout the experiment. However, it is important to consider that the local pH on the greigite electrode (pH within the diffusion layer near the electrode surface) itself may change during the CV experiments due to reactions such as water and proton reduction or adsorption of electrolyte species. Chapter 4 will assess the validity of these thermodynamic predictions, based on the bulk electrolyte pH, which suggest these changes in greigite composition at varying pHs with applied potentials.

3.3.3 **PBS pH 4.5 and 6.8 under CO_2**

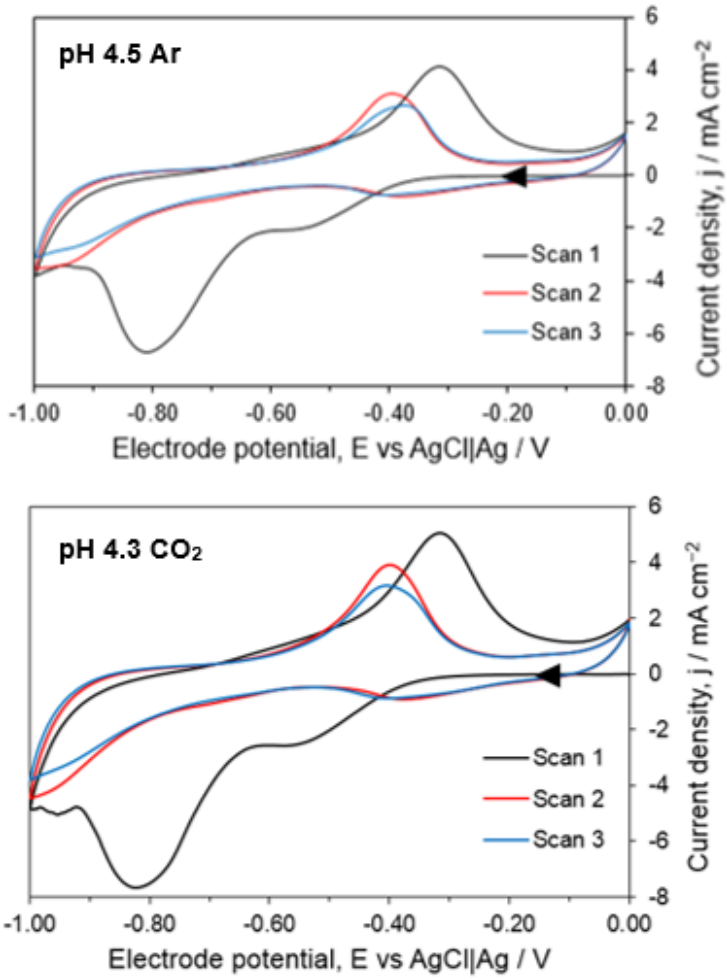

Figure 3.15 CVs of greigite in phosphate buffer solution (PBS) pH 4.5 under argon and pH 4.3 under CO_2 recorded at 10 mV s^{-1}. Potential sweep started at 0.00 V.

Figure 3.15 and Figure 3.16 compares the CVs of greigite recorded in phosphate buffers pH 4.5 and 6.8 under both argon and CO_2. The redox peaks recorded in pH 4.5 in argon remained unchanged when CO_2 was introduced (pH lowered to 4.3). The same was true for the CV of greigite in pH 6.8 under CO_2 (pH lowered to 6.5) where the peak positions remained unchanged under CO_2. However, the currents recorded were three orders of magnitude lower under CO_2 than under argon at pH 6.5.

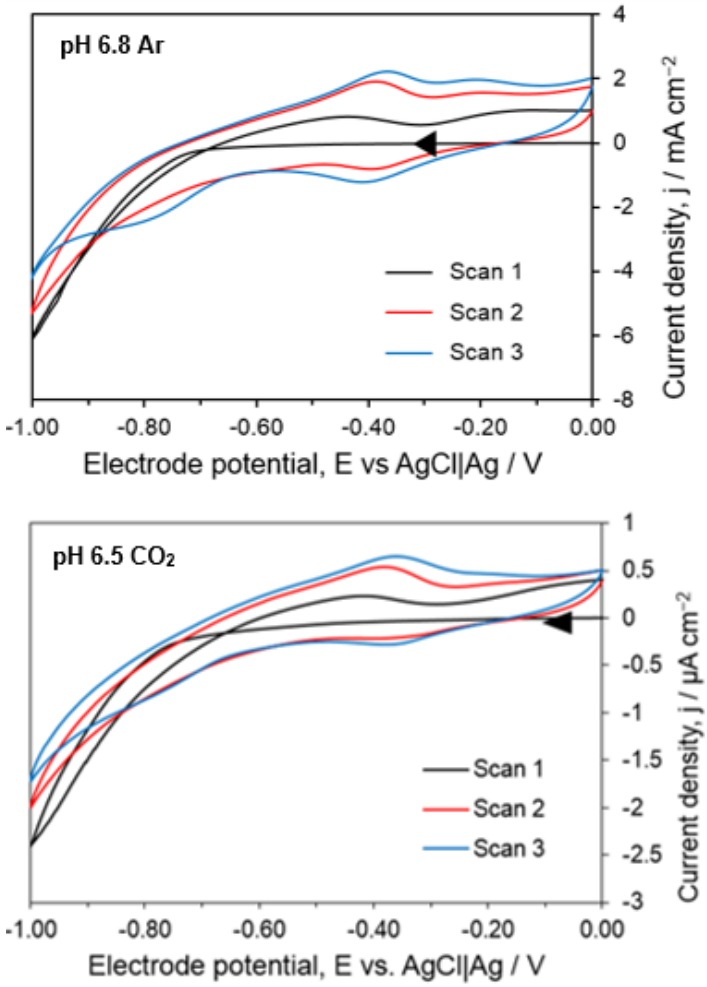

Figure 3.16 CVs of greigite in phosphate buffer solution (PBS) pH 6.8 under argon and pH 6.5 under CO_2 recorded at 10 mV s^{-1}. Potential sweep started at 0.00 V.

Upon bubbling CO_2 into solution, the dissolution of CO_2 occurs, **(3.53)-(3.56)**, forming an equilibrium of $CO_2(aq)$, HCO_3^- and CO_3^{2-} (Figure 3.17).

$$CO_2(g) \leftrightarrow CO_2(aq) \quad (3.53)$$
$$CO_2(aq) + H_2O(l) \leftrightarrow H_2CO_3(aq) \quad (3.54)$$
$$H_2CO_3(aq) \leftrightarrow H^+(aq) + HCO_3^-(aq) \quad (3.55)$$
$$HCO_3^-(aq) \leftrightarrow H^+(aq) + CO_3^{2-}(aq) \quad (3.56)$$

Figure 3.17 shows the speciation of dissolved CO_2 species over pH range 0 - 14. It is clear from Figure 3.17 that $CO_2(aq)$ dominates at pH < 5, HCO_3^- at pH > 6 and CO_3^{2-} at pH > 10. The total dissolved CO_2 concentration $[CO_2]_T$ is estimated by adding the concentrations of $CO_{2(aq)}$, HCO_3^- and CO_3^{2-}. The concentration of $CO_{2(aq)}$ is determined by Henry's law:

$$[CO_2]_l = k_H \times P_{CO2} \qquad (3.57)$$

where $[CO_2]_l$ is the concentration of dissolved CO_2, k_H is Henry's law constant (for CO_2 at 25°C, $k_H = 3.2 \times 10^{-4}$ mol dm^{-3} kPa^{-1}), P_{CO2} is the partial pressure of CO_2 (20 kPa in this work). At pH < 5, only $[CO_2]_{(aq)}$ will contribute towards $[CO_2]_T$ and this is determined by Henry's Law and was calculated to be 0.0066 mol dm^{-3}. At pH > 6, contributions from HCO_3^- and CO_3^{2-} need to be considered. Hence, $[CO_2]_T$ is estimated to increase at pH > 6. As $[CO_2]_T$ is estimated to be higher at pH 6.5 than at pH 4.3, the suppression in current observed in Figure 3.16 could be attributed to the contribution of HCO_3^- (aq). However, further evidence is required to confirm this association.

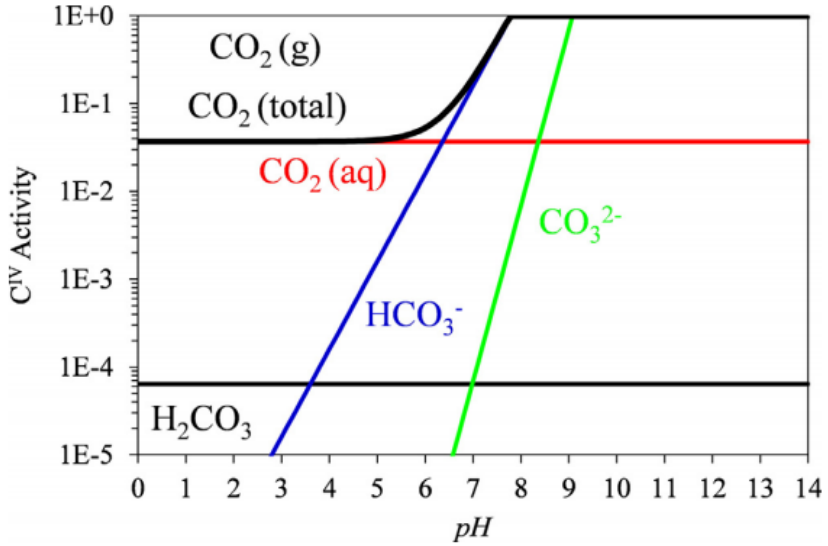

Figure 3.17 C^{IV} solubility and speciation for P(CO_2) = 105 Pa and dissolved activities limited to unity. Thick black line shows total dissolved activity. Reproduced with permission.[17]

However, since the redox peaks are identical under both argon (pH 6.8) and CO_2 (pH 6.5), the redox features recorded under CO_2 must still be associated with the same greigite redox reactions. The suppression of current at pH 6.5 under CO_2 may have also resulted from less surface area available for redox reactions, due to the formation of a passivating layer on the electrode surface or adsorption of CO_2, HCO_3^- or reaction intermediates.

According to the Pourbaix diagrams of Fe-CO_2-H_2O and Fe-S-C-H_2O systems (Figure 3.5 and Figure 3.6), the introduction of CO_2 may result in the formation of

iron carbonate and carbonate green rust, GR, (such as $Fe_2(OH)_2CO_3$ and $Fe_6(OH)_{12}CO_3$) on a metal iron or iron sulfide surface which may passivate the surface. The formation of iron carbonate and GR as well as their stability domains are dependent on the potential and pH condition.

Based on the stability regions of iron carbonate and GR in Figure 3.5 and Figure 3.6, the formation of both iron carbonate and GR is not expected at pH 4.5 when CO_2 is introduced. However, iron carbonate but not GR may form at pH 6.5 when CO_2 is introduced. At pH 6.5, iron carbonate is predicted to form within a narrow potential range of −0.30 to −0.35 V in the Fe-S-C-H_2O system, while in the Fe-CO_2-H_2O system, iron carbonate is predicted to be stable over a wider potential range of −0.50 to −0.90 V.

On the negative-going potential sweep initiated from 0.00 V at pH 6.5 under CO_2 in Figure 3.16, "FeS" such as greigite may react with CO_2 or HCO_3^- to form iron carbonate:

$$FeS + CO_2 + H_2O = FeCO_3 + H_2S \quad (3.58)$$
$$Fe^{2+} + CO_2 + H_2O = FeCO_3 + 2H^+ \quad (3.59)$$
$$Fe^{2+} + HCO_3^- = FeCO_3 + H^+ \quad (3.60)$$

Reactions **(3.58)**- **(3.60)** involve precipitation of iron carbonate on an FeS surface and are not redox reactions. On inspection of the Pourbaix diagram in Figure 3.2 at pH 6.5 for a negative-going potential sweep initiated at 0.00 V, it is predicted that greigite will be stable up to −0.50 V before it is reduced to "FeS", while in the Pourbaix diagram in Figure 3.6, iron carbonate is expected to form from the reduction of Fe_2O_3, within a narrow potential range of −0.30 to −0.35 V. Since it is assumed that no iron oxide / hydroxide is present on the greigite electrode (on immersion), it is proposed here that iron carbonate may have formed via precipitation (**(3.58)**- **(3.60)**) on the negative-going potential sweep. It is proposed here that the speculative reduction of CO_2 to CO may occur with a high overpotential, on the FeS surface via **(3.61)** and will induce a cathodic current. The CO_2 reduction may contribute to the reduction peak at ~

−0.70 V in CV under CO_2 in Figure 3.16. However, evidence for such CO_2 reduction on an FeS surface must be verified.

$$FeS + CO_2 + 4H^+ + 4e^- = Fe(0) + CO + H_2O + H_2S \quad \Delta G = +119.55 \text{ kJ mol}^{-1} \quad (3.61)$$

According to Figure 3.6, the iron carbonate formed on an FeS surface will be stable between −0.30 to −0.35 V and at potentials more negative than −0.35 V, the iron carbonate is predicted to be reduced back to "FeS" in the presence of (dissolved / excess) sulfur. However, it is not expected that dissolved sulfur species such as sulfate required for the conversion of $FeCO_3$ to FeS will be present near the electrode surface at this point in the negative-going potential sweep (since greigite is predicted to be stable up to −0.50 V thus no sulfate should be present, as discussed in the previous section (see Figure 3.2)). Instead, in the absence of dissolved sulfur species, according to Figure 3.5 for a Fe-C-H_2O system, any iron carbonate formed will remain stable up to −0.90 V. The presence and stability of iron carbonate within a large potential window may have contributed to the suppression of current when CO_2 was introduced at pH 6.5.

At the end of the negative-going sweep, metallic iron is expected to be formed on the electrode surface at pH 6.5 as discussed in the previous section. Thus, on the reverse positive-going sweep under CO_2, iron carbonate may be formed from the oxidation of the metal iron produced (reaction **(3.62)**), or precipitated via adsorption of CO_2 on Fe(0) (reaction **(3.63)**). Any "FeS" present may also contribute to the formation of iron carbonate on the positive-going sweep (reaction **(3.64)**). If any iron hydroxide was present prior to immersion of greigite into the electrolyte, this may also contribute to the formation of iron carbonate (reaction **(3.65)**).

$$Fe(0) + HCO_3^- = FeCO_3 + H^+ + 2e^- \quad (3.62)$$
$$Fe(0) + CO_2 + H_2O = FeCO_3 + 2H^+ + 2e^- \quad (3.63)$$
$$FeS + HCO_3^- + 4H_2O = FeCO_3 + SO_4^{2-} + 9H^+ + 6e^- \quad (3.64)$$
$$Fe(OH)_2 + HCO_3^- = FeCO_3 + H_2O + OH^- \quad (3.65)$$

The subsequent potential sweeps under CO_2 at pH 6.5 resembled those recorded under argon, but with suppressed currents. The predicted formation of iron

carbonate on an "FeS" surface when CO_2 was introduced may have resulted in the decrease in number of surface sites available for redox reactions.

The possibility of adsorption of electrolyte species and dissolved CO_2 species on the greigite electrode also need to be considered. Roldan *et al*[18] performed DFT calculations for the binding energies of water and dissolved CO_2 species including HCO_3^- and CO_3^- species, on an ideal greigite surface to calculate feasibility for CO_2 adsorption. As these calculations were performed on a perfect surface of greigite with H_2O only present, they are only used in this thesis to preliminarily assess the binding energies of CO_2 related species. These calculations did not account for phosphate ions which were also present in the CV experiments here. Phosphate ions are known to bind well on metallic surfaces affecting rates of surface reactions.[19]

The binding energies of CO_2 on greigite surfaces were calculated to be unfavourable at pH 4 (E_B = 0.00 eV on (001) and −0.62 eV on (111) surface) compared to the competing reaction which is water adsorption (E_B = −0.42 eV on (001) and −0.56 eV on (111) surface). Given the vast amount of water present, this implies that at pH 4, CO_2 less likely to affect surface reactions on greigite leading to no change in the CVs recorded at pH 4 under CO_2. At pH 6.5, the binding energies of HCO_3^- species on greigite surfaces were calculated to be E_B = −0.30 eV on (001) and E_B = −1.64 eV on (111) surface. Comparing this to the water adsorption binding energies, HCO_3^- species will preferentially adsorb on the (111) surface, while water molecules will adsorb on the (001) surface. This highlights the adsorption of HCO_3^- species is energetically feasible and may thus have led to suppressed currents in CV of greigite in pH 6.5 when CO_2 is introduced.

The plausible adsorption of HCO_3^- species as suggested by DFT calculations above and the presence of a passivating iron carbonate layer predicted by the Pourbaix diagrams in Figure 3.5 and Figure 3.6 will be dependent on the reaction kinetics and the concentrations of dissolved CO_2 and electrolyte species present on the greigite surface. Hence these predictions need to be further confirmed using in-situ characterisation techniques.

3.3.4 $KHCO_3$ pH 8.55 and K_2CO_3 pH 11.2 under argon

Figure 3.18 displays the CVs of greigite recorded in $KHCO_3$ pH 8.55 and K_2CO_3 pH 11.2 electrolyte solutions under argon. The CV recorded in $KHCO_3$ pH 8.55 closely resembles the previously detailed CV of greigite at pH 6.8 (Figure 3.14), with a sharp anodic peak at 0.00 V. Given the similarity in the CV response, the redox features at $KHCO_3$ pH 8.55 are assigned to similar reactions for the redox peaks at pH 6.8. Inspection of the Pourbaix diagrams in Figure 3.1, Figure 3.2 and Figure 3.4 shows that similar behaviour is predicted at pH 8.55. In contrast to all the CVs of greigite recorded, at pH 11.2 K_2CO_3 the CV response was relatively featureless.

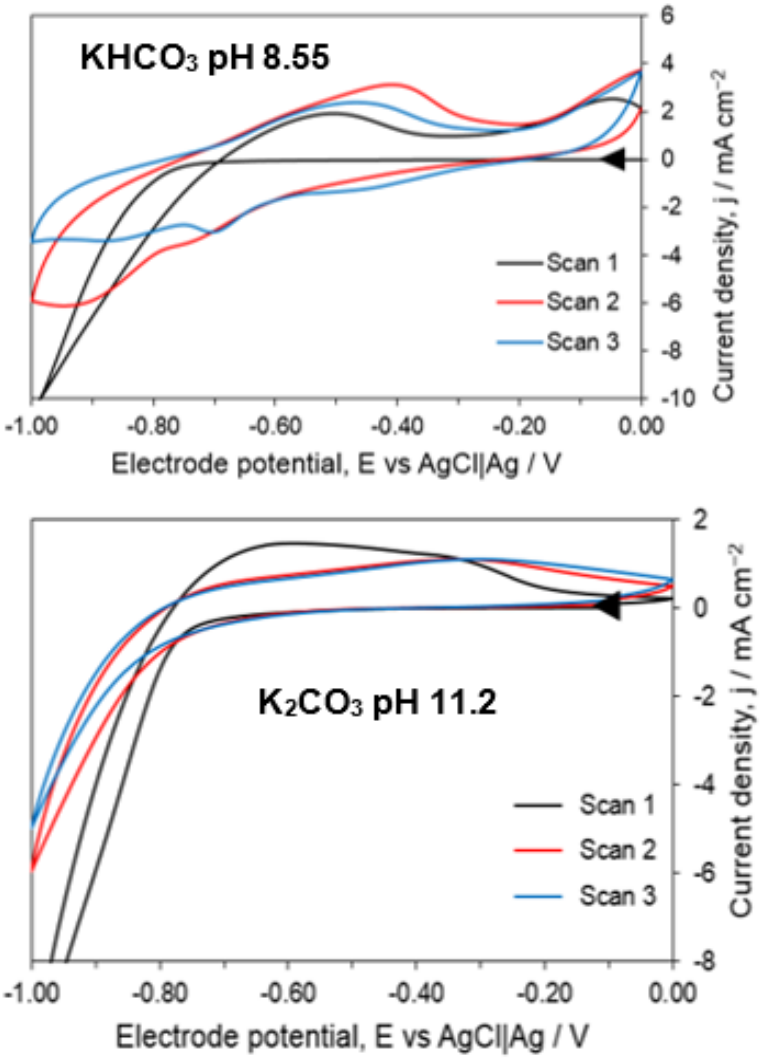

Figure 3.18 CVs of greigite recorded in $KHCO_3$ pH 8.55 and K_2CO_3 pH 11.2 under argon at 10 mV s^{-1}. Potential sweep started at 0.00 V.

According to the Pourbaix diagrams in Figure 3.1, Figure 3.2, Figure 3.4 - Figure 3.6, at pH 11.2, greigite is predicted to be stable up to −0.70 V while the formation of iron carbonate is not expected at this pH. Carbonate GR is predicted to form at −0.95 V but since it is metastable, it is not expected to form.

In contrast to these predictions, the Pourbaix diagram in Figure 3.3 predicted green rust, $Fe^{II}_4Fe^{III}_2(OH)_{12}SO_4$, to form between 0 and −0.50 V at pH 8.1 and between 0 and −0.60 V at pH > 10. Similar to previous observations at pH 4.5 and 6.8, the absence of green rust precipitate on the greigite electrode show that it does not form due to slow kinetics or due to the protective effect of the capping agent.

Another route where passivating layers such as iron carbonate, hydroxide could form is via dissolution of greigite. At alkaline conditions such as at pH 8.55 $KHCO_3$ and pH 11.2 K_2CO_3, soluble Fe^{2+} species released from the electrode surface may complex with OH^-, CO_3^{2-} and HCO_3^- species present. This may result in a competition between the formation of iron carbonate and hydroxides on greigite and may have led to the passivated CV response at pH 11.2.[20,21] However, the presence of such passivating layer needs to be confirmed and characterised in-situ. The adsorption of OH^-, CO_3^{2-} and HCO_3^- species present may also affect the number of surface sites available on greigite which could affect redox reactions.

3.3.5 $KHCO_3$ pH 8.55 and K_2CO_3 pH 11.2 under CO_2

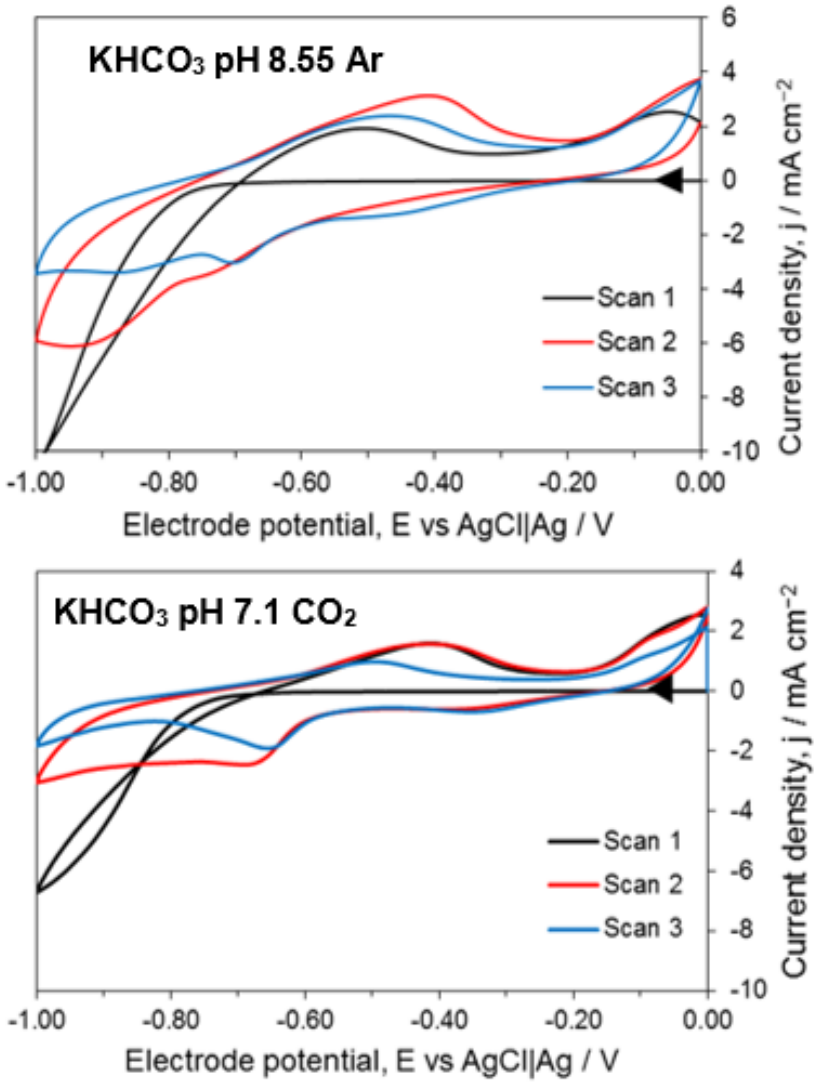

Figure 3.19 CVs of greigite in $KHCO_3$ pH 8.55 under argon and pH 7.1 under CO_2 recorded at 10 mV s^{-1}. Potential sweep started at 0.00 V.

Figure 3.19 and Figure 3.20 compare the CVs of greigite recorded in $KHCO_3$ and K_2CO_3 under both argon and CO_2. Upon introduction of CO_2 in $KHCO_3$ and K_2CO_3 electrolyte solutions, the pH of $KHCO_3$ and K_2CO_3 electrolyte solutions decreased to pH 7.1 and 10.1, respectively. These electrolytes are not strong buffer solutions compared to phosphate buffer solutions pH 4.5 and 6.8 used in the previous sections resulting in the decrease in pH.

For $KHCO_3$ under CO_2 at pH 7.1, the redox features appeared suppressed compared to the redox features recorded under argon. This was a similar trend

observed for the CV of greigite at pH 6.8 when CO_2 was introduced, which was attributed to the formation of iron carbonate which may have resulted in the decrease in surface area available for redox reactions. Therefore, the suppression of redox features for $KHCO_3$ on introduction of CO_2 may have also resulted from the decrease in electrolyte pH from pH 8.55 to 7.1. The shift in pH moves into the region where a narrow stability range of iron carbonate exists and thus may form on the greigite surface (Figure 3.6).

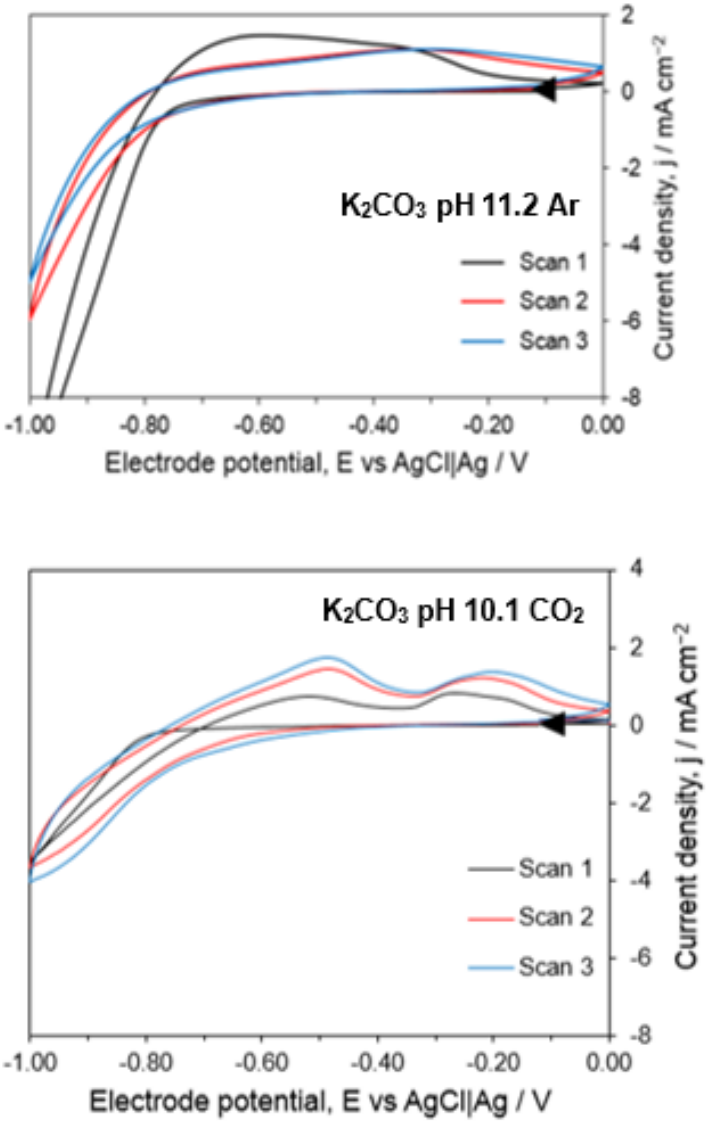

Figure 3.20 CVs of greigite in K_2CO_3 pH 11.2 under argon and pH 10 under CO_2 recorded at 10 mV s^{-1}. Potential sweep started at 0.00 V.

For the CV recorded in K_2CO_3 under CO_2, the broad oxidation feature on the positive-going potential sweep was split into two defined oxidation peaks on

introduction of CO_2 and the current magnitude increased with each scan. According to the Pourbaix diagram in Figure 3.6, iron carbonate is not expected to form at both pH 10.1 and 11.2. The increase in current magnitude with each scan in the CV recorded in K_2CO_3 when CO_2 was introduced may be associated with the shift in pH from 11.2 to 10.1. At the vertex potential of −1.00 V, prior to the positive-going potential sweep, according to the Pourbaix diagram in Figure 3.6, the shift in pH from 11.2 to 10.1 moves closer to a region where complex speciation is predicted. Within the pH window between 9.5 and 10.5 at −1.00 V, metallic iron and FeS are predicted to be the stable redox species. Therefore, the increased current magnitudes in K_2CO_3 on introduction of CO_2 may be attributed to the formation of metallic iron at −1.00 V on the negative-going potential sweep, which did not form under argon. Thus, the metallic iron produced on the negative-going potential sweep in K_2CO_3 under CO_2 may have increased the redox species available for oxidation on the positive-going potential sweep.

The introduction of CO_2 in both $KHCO_3$ and K_2CO_3 will result in an overall increase in the total concentration of dissolved CO_2 species in both electrolytes. On reaction with CO_2, for $KHCO_3$, there will be an increase in HCO_3^- species while for K_2CO_3, there will be an increase in CO_3^{2-} concentration. However, the increase in concentrations of HCO_3^- and CO_3^{2-} species will be small compared to amount of dissolved CO_2 introduced in both electrolytes. Thus, the changes in redox features observed in both $KHCO_3$ and K_2CO_3 in Figure 3.19 and Figure 3.20 may have resulted from the pH change or introduction of CO_2.

3.3.6 Influence of solution pH and electrolyte species

In the previous sections, the presence of different electrolyte species (including phosphates, CO_3^{2-}, HCO_3^- species and water molecules) under various solution pHs tested seem to affect the electrochemical response of greigite. Further investigation was carried out to verify the effects of solution pH and species present on the CV responses of greigite. This was done via two methods:

Method 1: A CV of greigite was recorded in phosphate buffer solution pH 6.8. With the same electrode still in place, the pH and composition of the electrolyte cell was altered by introducing an equal volume of K_2CO_3 into the phosphate buffer solution. This mixed electrolyte had an overall pH of 9.6 and consisted of phosphate, CO_3^{2-} and HCO_3^- species. Performing CV in this mixed electrolyte will show which redox features remain constant while altering the electrolyte species and pH. Lastly, the same electrode was taken out of the mixed electrolyte, the cell was emptied and replaced by fresh phosphate buffer solution pH 6.8 and a final CV of this electrode was recorded to investigate if the redox peaks were reversible on returning to the original pH condition and electrolyte species present.

Method 2: Similar to method 1 but the starting electrolyte was K_2CO_3 pH 11.2. A CV of greigite was first recorded in K_2CO_3 pH 11.2. An equal volume of phosphate buffer solution pH 6.8 was added into the electrolyte cell resulting in an overall pH 9.6 of the mixed electrolyte. A CV of the same electrode was then performed in this mixed solution. Lastly, the used electrode and mixed electrolyte were removed from the cell and a fresh solution of K_2CO_3 pH 11.2 was replaced as the electrolyte. A final CV of the used electrode was then recorded in the fresh K_2CO_3 pH 11.2 solution.

3.3.6.1 Method 1: starting electrolyte PBS pH 6.8

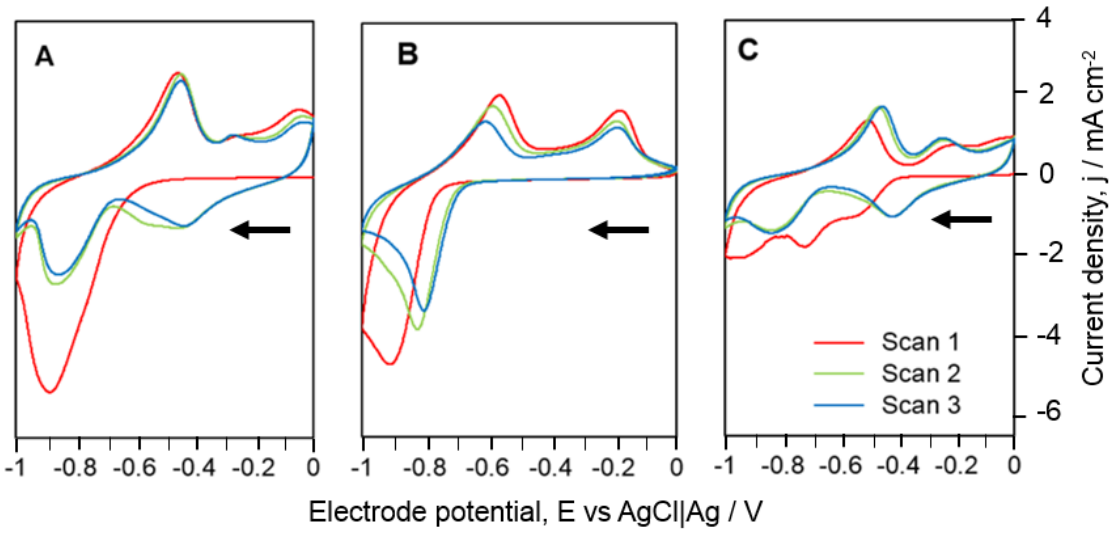

Figure 3.21 Cyclic voltammograms of greigite recorded under argon in A) starting solution phosphate buffer pH 6.8, B) mix of phosphate buffer pH 6.8 and K_2CO_3 pH 11.2 with overall pH 9.6 and C) final fresh phosphate buffer pH 6.8. All CVs started from 0.00 V and performed using the same greigite drop-coat on working electrode at scan rate 10 mVs^{-1}.

Figure 3.21 shows the variation in electrochemical response of greigite in different electrolytes via Method 1 with phosphate buffer pH 6.8 as the starting solution, followed by mixed electrolyte of phosphate buffer and K_2CO_3 with pH 9.6 and finally in fresh phosphate buffer pH 6.8. The electrochemical behaviour of greigite under argon at pH 6.8 has been previously detailed in previous sections.

When equal amounts of K_2CO_3 was added to phosphate buffer pH 6.8 (Figure 3.21 B), the electrolyte pH increased to 9.6 and a change in the CV response was recorded. At this pH, phosphate, CO_3^{2-} and HCO_3^- species will be present in the same electrolyte. The negative-going potential sweep in Figure 3.21 B appeared to be passivated compared to Figure 3.21 A where the reduction peak at ~ −0.40 V observed on the second scan in Figure 3.21 A was absent in Figure 3.21 B. This cathodic peak at ~ −0.40 V was previously assigned based on thermodynamic predictions to the reduction of sulfates to HS^- and reduction of greigite to "FeS". The absence of this peak may be associated with growth of a passivating layer

such as iron carbonate or adsorption of CO_3^{2-} and HCO_3^- species on the greigite surface, preventing the cathodic reaction at ~ −0.40 V from taking place. The formation of iron carbonate, however, is not predicted at pH 9.6 according to the Pourbaix diagrams in Figure 3.5 and Figure 3.6. Thus, the absence of the reduction peak at ~ −0.40 V in Figure 3.21 B when CO_3^{2-} and HCO_3^- species were introduced may also be associated with the absence of sulfate species near the electrode surface which may have diffused away from the electrode due to adsorption of CO_3^{2-} and HCO_3^- species, or rinsed away during the replacement of electrolyte.

Additionally, the peak positions of the two anodic peaks observed in Figure 3.21 A were shifted from ~−0.50 to −0.60 V and ~−0.30 to −0.20 V respectively in Figure 3.21 B. These two anodic peaks were assigned to the oxidation of Fe(0) to Fe^{2+} species at −0.50 V and the oxidation of HS^- to S(0) or sulfates at −0.30 V. The shift in the peak positions implies less energy was required for Fe(0) oxidation at −0.60 V and more energy required for HS^- oxidation at −0.20 V. Fe(0) oxidation may have occurred at more negative potentials due to the absence of sulfates near the electrode surface which would have been reduced to S(0) or HS^- and passivate the electrode surface. HS^- oxidation occurred at a more positive potential plausibly due to the adsorption of CO_3^{2-} and HCO_3^- species which may have decreased the surface area available for redox reactions and prevented the HS^- species from further oxidation.

When the mixed electrolyte pH 9.6 was replaced with a fresh solution of phosphate buffer pH 6.8 (Figure 3.21 C), the CV response was restored to the original response observed in Figure 3.21 A. The first negative-going potential sweep in Figure 3.21 C featured three reduction peaks at ~ −0.50, −0.70 and −0.90 V. These reduction peaks are assigned to the reduction of sulfates to HS^-, reduction of greigite, any "FeS", iron hydroxides to Fe^{2+} and Fe(0), respectively. The removal of adsorbed CO_3^{2-} and HCO_3^- species may have contributed to the restoration of the redox peaks in Figure 3.21 C.

Evidently, there seems to be competing surface reactions occurring on the electrode surface when K_2CO_3 was introduced to phosphate buffer pH 6.8, with the redox chemistry restored upon using a fresh solution of phosphate buffer pH

6.8. The passivated CV response in the mixed electrolyte suggest that CO_3^{2-} and HCO_3^- species have a significant impact on the CV features when introduced to phosphate buffer pH 6.8 (Figure 3.21 B), restricting the reduction peak at −0.4 V associated with reduction of sulfates and greigite. However, the CO_3^{2-} and HCO_3^- species do not adsorb strongly onto greigite surface, since replacing the electrolyte with fresh phosphate buffer pH 6.8 (Figure 3.21 C) reverted the electrochemical behaviour of greigite back to that observed initially in Figure 3.21 A.

3.3.6.2 Method 2: starting electrolyte K_2CO_3 pH 11.2

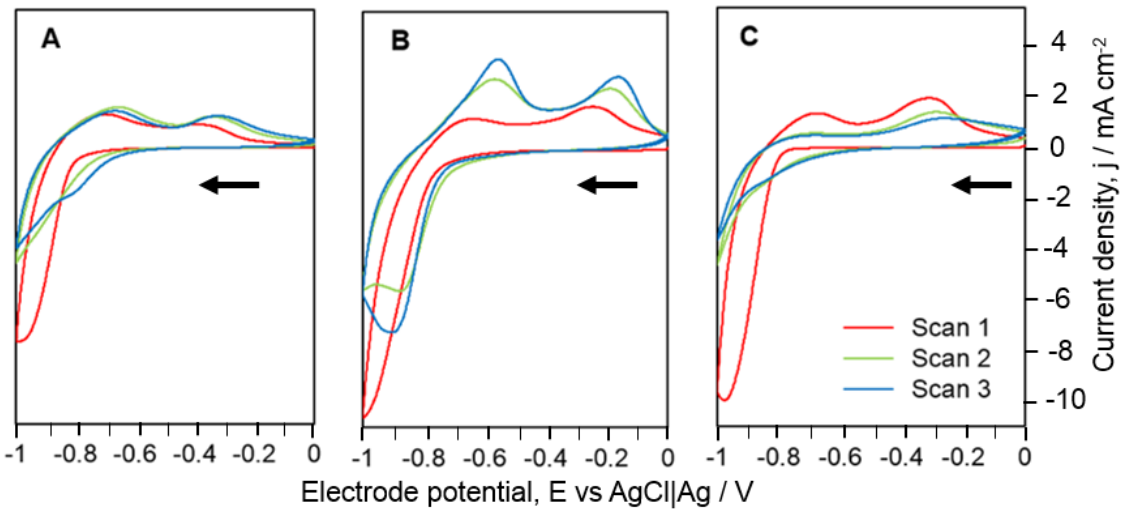

Figure 3.22 Cyclic voltammograms of greigite recorded in A) starting solution K_2CO_3 pH 11.2, B) mix of phosphate buffer pH 6.8 and K_2CO_3 pH 11.2 with overall pH 9.6 and C) final fresh K_2CO_3 pH 11.2. All CVs started from 0.00 V and performed using the same greigite drop-coat on working electrode at scan rate 10 mVs^{-1}.

Figure 3.22 shows the variation in CV responses of greigite recorded via Method 2 with K_2CO_3 pH 11.2 as the starting solution, followed by pH 9.6 mixed electrolyte of phosphate buffer and K_2CO_3, and lastly in fresh K_2CO_3 pH 11.2. The CV of greigite in K_2CO_3 pH 11.2 under argon (Figure 3.22 A) was previously detailed in previous sections. Similar to Method 1, on introducing phosphate buffer pH 6.8 to K_2CO_3 electrolyte, the pH lowered to 9.6. In this mixed electrolyte, phosphates and HCO_3^- species were also present compared to the starting solution K_2CO_3.

An increase in current magnitude with each scan was recorded when phosphate buffer pH 6.8 was added to K_2CO_3 (Figure 3.22 B). The CV in Figure 3.22 B resembled CV of greigite in K_2CO_3 when CO_2 was introduced. The increase in current magnitude with each scan in Figure 3.22 B in the mixed electrolyte may be attributed to decrease in pH from 11.2 to 9.6 as detailed previously for CV of greigite in K_2CO_3 on introduction of CO_2 where the pH shifted from 11.2 to 10.1. This was attributed to metallic iron produced at the end of the negative-going potential sweep at the lower pH (based on the Pourbaix diagram in Figure 3.6) and therefore, more redox species are available for oxidation on the positive-going sweep. Also, the peak positions of the two anodic peaks in Figure 3.22 A have shifted from ~ −0.70 to −0.60 V and −0.30 to −0.20 V in Figure 3.22 B. The new peak positions occurred at more positive potentials implying that more energy was required for the same redox reactions to proceed in the presence of phosphates. No additional redox peaks were recorded indicating that the addition of phosphates did not promote any other surface reactions other than those that were already occurring. These observations imply that CO_3^{2-} and HCO_3^- species and decrease in pH have a significant impact on the surface reactions of greigite compared to phosphate ions.

When the mixed electrolyte (K_2CO_3 with PBS pH 6.8 added) was replaced with a fresh solution of K_2CO_3 (Figure 3.22 C), the CV response was restored to the original response observed in Figure 3.22 A. The currents decreased in magnitude with each scan and the two anodic peaks returned to their initial peak positions. This may result from the removal of phosphate species from the surface, freeing surface sites on greigite for carbonates to adsorb and suppress currents.

In this section, it becomes more evident that CO_3^{2-} and HCO_3^- species as well as a change in pH are the dominant factors affecting the redox reactions occurring on greigite. A reduction peak recorded at −0.40 V in Figure 3.21 when performing the second scan in CV of greigite in PBS pH 6.8 was not observed in any of the CVs recorded in Figure 3.22. Thus, it may be deduced that CO_3^{2-} and HCO_3^- species have a greater influence on the redox chemistry of greigite compared to phosphate species. The binding energies of all these electrolyte species on greigite need to be considered to understand the changes in the CV responses.

3.4 Discussion

The redox features in the CVs of greigite presented in this section were assigned based on the Pourbaix diagrams in Figure 3.1 - Figure 3.6. Pourbaix diagrams are useful in aiding assignments of redox reactions occurring in a particular system, in this case the greigite electrode surface. However, the thermodynamic calculations used to construct Pourbaix diagrams do not consider the reaction kinetics of the redox reactions.

Often published electrochemical studies on iron sulfides begin with pre-treatment of iron sulfide electrodes to remove the iron hydroxide layer, either by applying a reduction potential or washing the material in acidic solution. In this work, a capping agent (oleylamine or (Z)-octadec-9-enylamine) was used in the greigite material synthesis which prevented surface aerial oxidation. Thus, in our prior discussion of the possible redox transformations using the Pourbaix diagrams, the possible prior presence of iron hydroxides was not considered. This novel synthesis of greigite material removes the pre-treatment required to remove iron hydroxides to analyse the electrochemical behaviour of greigite.

In general, greigite exhibited similar redox peaks across all the pHs tested, with the exception of pH 11.2 K_2CO_3. Based on the Pourbaix diagrams, the reduction peaks were assigned to the reduction of greigite to reduced "FeS", further reduction of greigite and "FeS" to Fe^{2+} and reduction of Fe^{2+} to Fe(0). The oxidation peaks were assigned to oxidation of Fe(0) to Fe^{2+}, and H_2S (pH < 7) or HS^- (pH > 7) oxidation to S(0) or sulfates. At pH 11.2 K_2CO_3, the CV response was featureless and this was attributed to the formation of a passivating iron carbonate layer. This was not predicted by the Pourbaix diagrams at this pH which suggests that the passivation of the surface is not a bulk transformation to iron carbonate. Rather, the passivation may have resulted from the surface adsorption of CO_3^{2-} or OH^-, given the pH.

When CO_2 was introduced, the CV response remained the same at PBS pH 4.3, decreased in current magnitude at PBS pH 6.5 and $KHCO_3$ pH 7.1, and increased in current magnitude at K_2CO_3 pH 10.1. Differences in the CV responses were

attributed to differing binding energies of CO_2 on greigite under each condition and the possible formation of iron carbonate. Upon mixing of electrolytes (PBS with K_2CO_3), there was a variation in the CV response of greigite which was dependent on the electrolyte species present. It was concluded that CO_3^{2-} and HCO_3^- species have a significant effect on greigite CV response compared to phosphate species.

Binding energies of relevant electrolyte / CO_2 species present can be used to explain the discrepancies in the CV responses observed when under argon, under CO_2 or upon mixing of electrolytes. The calculated binding energies of water, CO_3^{2-}, HCO_3^- and phosphate ions modelled on perfect greigite surfaces (001) and (111), the two major surfaces of greigite used in this thesis, are summarised in Table 3.1. [22] These calculations considered adsorption of electrolyte species separately and thus do not fully represent the experimental conditions tested here where there is often a mix of electrolyte species present at the same time. These calculations also do not consider the potential formation of iron hydroxide layer on the surface.

Table 3.1 Binding energies, E_B, of electrolyte species on greigite (001) and (111) surfaces. [22]

Electrolyte species	E_B (001) surface /eV	E_B (111) surface) /eV
$[H_2O]_{10}$	−0.66	−0.73
CO_2	0.00	−0.62
$HCO_3^- + H^+$	−0.30	−1.64
$CO_3^{2-} + 2H^+$	+1.24	−0.46
$H_2PO_4^- + H^+$ (2.6 < pH < 6.8)	−1.00	−0.33
$HPO_4^- + 2H^+$ (7.6 < pH < 11.9)	−0.45	0.03

Based on the calculations above, with no CO_2, the predicted adsorbed electrolyte species at each pH on each greigite surface are: i) at pH 4.5 and 6.8, $H_2PO_4^-$ on (001) and H_2O on (111), ii) at $KHCO_3$ pH 8.55, H_2O on (001) and HCO_3^- on (111), and iii) at K_2CO_3 pH 11.2, H_2O on (001) and (111). CO_3^{2-} species is not predicted to adsorb strongly on either (001) or (111) surface at all pHs tested. This is in

contrast to the featureless CV of greigite at K_2CO_3 pH 11.2 where it was assumed that the adsorption of CO_3^{2-} resulted in the featureless CV response. Therefore, this suggests that OH^- ions present in high concentrations at this pH instead may have caused the passivation and featureless CV response on greigite at pH 11.2 K_2CO_3.

On introduction of CO_2, the adsorption of the same species are favoured since the calculated CO_2 binding energy is not favoured on both (001) and (111) surfaces at all pHs. This is in contrast to the differing CV response observed at pH 6.8, 8.55 and 11.2 on introduction of CO_2. This highlights the need to characterise the electrode surface in-situ while considering both the thermodynamic transitions predicted in the Pourbaix diagrams and the DFT calculations.

On mixing of electrolytes (PBS pH 6.8 and K_2CO_3) at pH 9.6, adsorption of H_2O on (001) and HCO_3^- on (111) are favoured over adsorption of CO_3^{2-} or phosphates, which is in agreement with the observed passivation of CV response on addition of K_2CO_3 to PBS pH 6.8 but not vice versa.

Passivation of the greigite surface and its redox reactions due to the adsorption of CO_2 species or formation of iron carbonates and hydroxides as predicted by the Pourbaix diagrams and DFT calculations need to be verified. The following section present spectroscopic evidence performed in-situ to characterise the greigite electrode surface with applied potentials under argon and CO_2 to verify these predictions.

3.5 References

1. Thornber, M. R. Mineralogical and electrochemical stability of the nickel-iron sulphides-pentlandite and violarite. *J. Appl. Electrochem.* **13,** 253–267 (1983).

2. Bura-Nakic, E., Róka, A., Ciglenecki, I. & Inzelt, G. Electrochemical Quartz Crystal Microbalance Study of FeS Particles Attached to Au Surface. *Electroanalysis* **21,** 1699–1708 (2009).

3. Warner, T. E., Rice, N. M. & Taylor, N. An electrochemical study of the oxidative dissolution of synthetic pentlandite in aqueous media. *Hydrometallurgy* **31,** 55–90 (1992).

4. Rickard, D. & Luther, G. W. Chemistry of Iron Sulfides. *Chem. Rev.* **107,** 514–562 (2007).

5. Kelsall, G. H. & Thompson, I. Redox chemistry of H2S oxidation by the British gas Stretford process Part I: Thermodynamics of sulphur-water systems at 298 K. *J. Appl. Electrochem.* **23,** 279–286 (1993).

6. Lu, Y., Dong, J. & Ke, W. Corrosion Evolution of Low Alloy Steel in Deaerated Bicarbonate Solutions. *J. Mater. Sci. Technol.* **31,** 1047–1058 (2015).

7. Marsland, S. D. Ph. D. Thesis, Non-oxidative dissolution of iron sulphide minerals - of relevance to inorganic chemical souring of oil reservoirs. (Imperial College London, 1992).

8. Crundwell, F. K. The mechanism of dissolution of minerals in acidic and alkaline solutions: Part I — A new theory of non-oxidation dissolution. *Hydrometallurgy* **149,** 252–264 (2014).

9. Crundwell, F. K. The mechanism of dissolution of minerals in acidic and alkaline solutions: Part III. Application to oxide, hydroxide and sulfide minerals. *Hydrometallurgy* **149,** 71–81 (2014).

10. Ning, J., Zheng, Y., Brown, B., Young, D. & Nešic, S. A Thermodynamic Model for the Prediction of Mild Steel Corrosion Products in an Aqueous Hydrogen Sulfide Environment. *Corrosion* **71,** 945–960 (2015).

11. Russell, M. J. & Hall, A. J. The emergence of life from iron monosulphide bubbles at a submarine hydrothermal redox and pH front. *J. Geol. Soc. London.* **154,** 377–402 (1997).

12. Di Giovanni, C. *et al.* Low-Cost Nanostructured Iron Sulfide Electrocatalysts for PEM Water Electrolysis. *ACS Catal.* **6,** 2626–2631 (2016).

13. Zhang, R.-R., Wu, X.-M., Zeng, X.-Q., Zou, J.-X. & Ding, W.-J. Electrochemical

Properties of Nanostructure Greigite (Fe3S4) as a Cathode Material in Rechargeable Magnesium Battery. *Chinese J. Inorg. Chem.* **31,** 1351–1356 (2015).

14. Li, T. *et al.* Colloidal synthesis of greigite nanoplates with controlled lateral size for electrochemical applications. *Nanoscale* **7,** 4171–4178 (2015).

15. Hamilton, I. C. & Woods, R. An investigation of surface oxidation of pyrite and pyrrhotite by linear potential sweep voltammetry. *J. Electroanal. Chem. Interfacial Electrochem.* **118,** 327–343 (1981).

16. Hunger, S. & Benning, L. G. Greigite: a true intermediate on the polysulfide pathway to pyrite. *Geochem. Trans.* **8:1,** 1–20 (2007).

17. Bumroongsakulsawat, P. & Kelsall, G. H. Effect of solution pH on CO: Formate formation rates during electrochemical reduction of aqueous CO2 at Sn cathodes. *Electrochim. Acta* **141,** 216–225 (2014).

18. Roldan, A. *et al.* Bio-inspired CO2 conversion by iron sulfide catalysts under sustainable conditions. *Chem. Commun.* **51,** 7501–7504 (2015).

19. Yaguchi, M., Uchida, T., Motobayashi, K. & Osawa, M. Speciation of Adsorbed Phosphate at Gold Electrodes: A Combined Surface-Enhanced Infrared Absorption Spectroscopy and DFT Study. *J. Phys. Chem. Lett.* **7,** 3097–3102 (2016).

20. Eliyan, F. F., Kish, J. R. & Alfantazi, A. Voltammetric Analysis on the Formation of Fe(OH)2 and FeCO3, and on the Reactivity of Passivation of Steel in Carbonate Solutions. *J. Mater. Eng. Perform.* **24,** 2473–2480 (2015).

21. El-Naggar, M. M. Effects of Cl−, NO3− and SO42− anions on the anodic behavior of carbon steel in deaerated 0.50M NaHCO3 solutions. *Appl. Surf. Sci.* **252,** 6179–6194 (2006).

22. Santos-Carballal, D. & Roldan, A. Personal communication. (2016).

Chapter 4 In-situ spectroelectrochemistry of Greigite

4.1 Introduction

In this chapter, in-situ FTIR and XAS techniques were used to monitor the structural changes of a greigite electrode on applying specific external potentials in the same electrolytes used in the previous chapter. Using FTIR allows monitoring of IR-active surface groups present at the nanoparticle interface, while XAS monitors the changes in oxidation states and coordination environment of Fe, both in bulk and at the surface of the particles.

Assignment of the IR bands in these experiments requires comparison to available IR libraries in the literature. However, this can be difficult as the IR-active species need to be differentiated between adsorbed or solution species. Peak positions also often shift under different reaction conditions (e.g. pH and solvation). [1] The peak positions of IR-active species are also sensitive to coordination environment of the species. For example, in the case of the sulfate ion, it can either be uncoordinated near the surface, or bound via monodentate or bidentate bond onto a surface. The various different binding patterns results in different symmetries of the sulfate ion which can be interpreted from the resulting IR spectra.

The XAS experiments were carried out by two students, one of whom is the author of this thesis. We designed the XAS experiments in parallel with the FTIR experiments. For XAS analyses, spectral interpretation was done by comparing to various iron and sulfur standards obtained, as well as comparison to literature. These are provided in the appendix for reference.

The results of in-situ XAS in each electrolyte tested are presented first, followed by the in-situ FTIR results. These spectroscopic results are compared to the predicted redox assignments of greigite based on thermodynamics from the previous chapter as well as DFT calculations to verify the predictions. The chapter will conclude with the impact of introduction of CO_2 on the electrochemical

stability of greigite and its implications on use of greigite electrodes to promote CO_2 reduction.

4.2 In-situ XAS

The XANES spectra of relevant iron compounds on the Fe K-edge are compiled in Figure 4.1, Figure 4.2 and Figure 4.3 for comparison to the results obtained. These include the XANES spectra of hematite (α-Fe_2O_3), magnetite (Fe_3O_4), Fe(II) oxide, ferrihydrite, goethite (α-FeOOH), Fe(III) and Fe(II) sulfate, iron carbonate (siderite, $FeCO_3$), iron phosphate ($FePO_4$) and pyrite (FeS_2). In this thesis, the XANES spectra of various iron and sulfur standards were also recorded for comparison to the XANES data obtained. These are provided in the appendix.

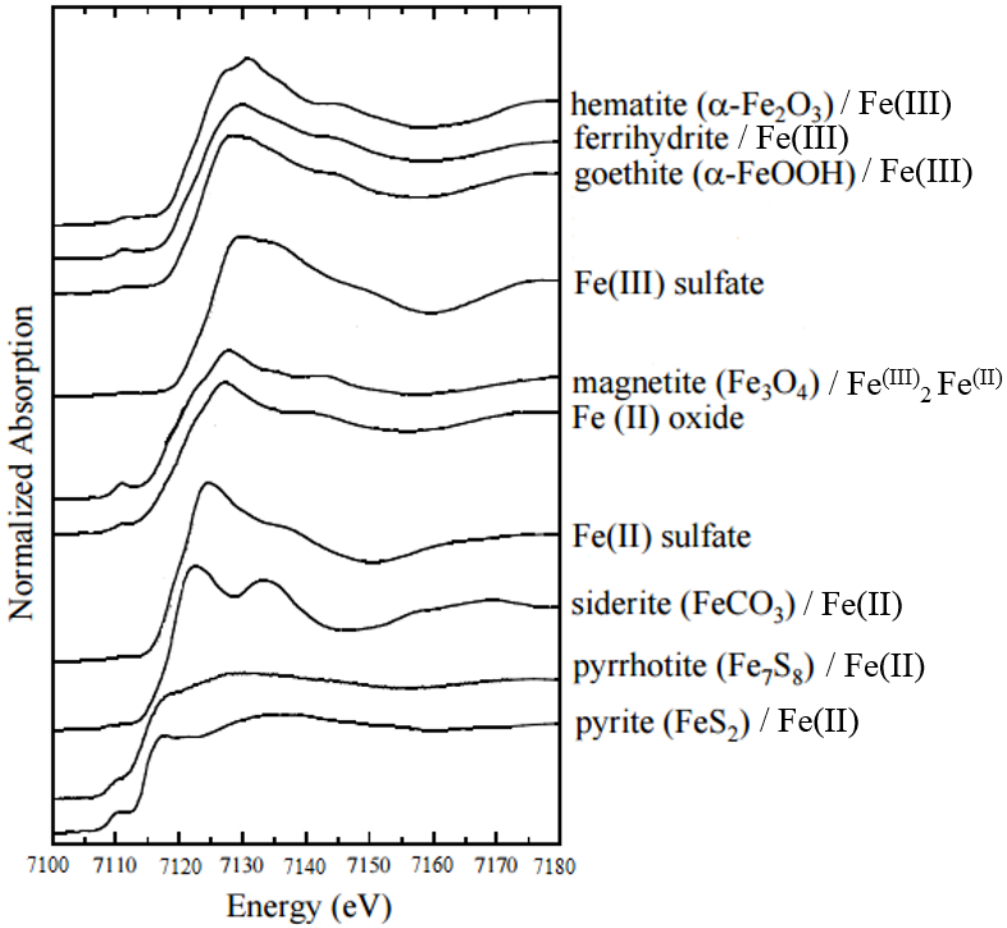

Figure 4.1 Fe K-edge XANES spectra of hematite (α-Fe_2O_3), ferrihydrite, goethite (α-FeOOH), Fe (III) sulfate, magnetite (Fe_3O_4), Fe(II) oxide, Fe(II) sulfate, siderite ($FeCO_3$), pyrrhotite (Fe_7S_8) and pyrite (FeS_2). [2]

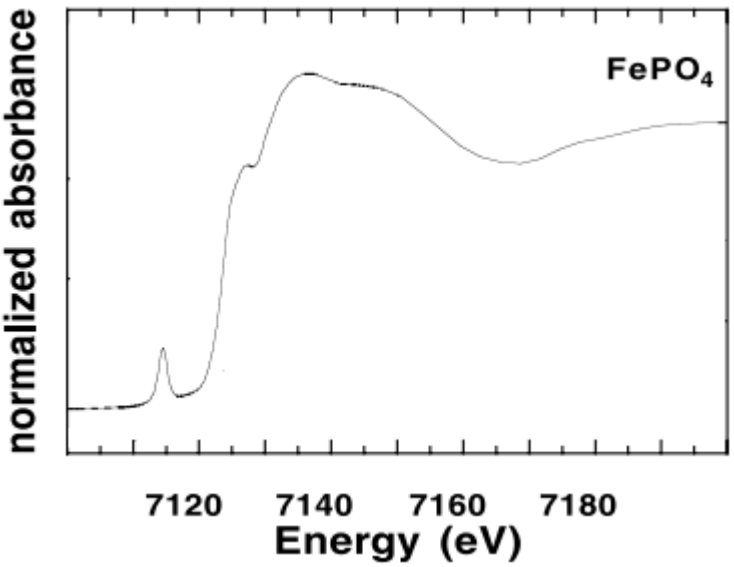

Figure 4.2 Fe K-edge XANES spectrum of iron phosphate, $FePO_4$, where oxidation state of Fe = Fe(II).[3]

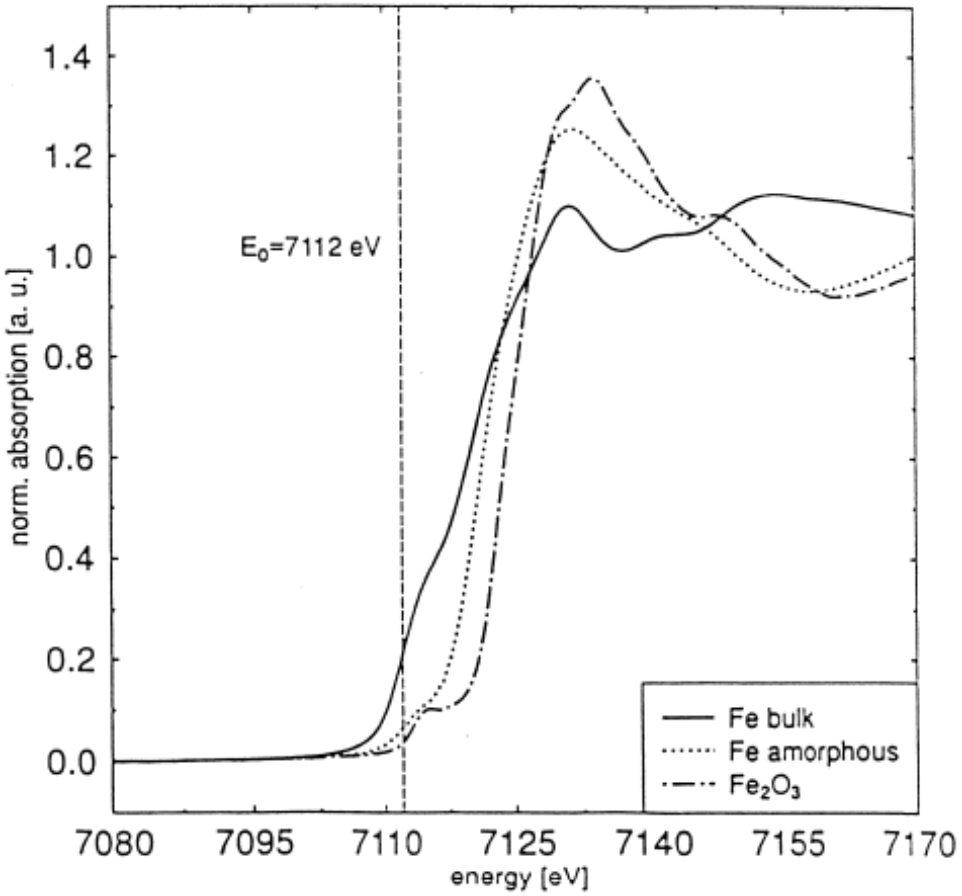

Figure 4.3 Fe K-edge XANES spectra of commercial crystalline iron (Fe bulk, Fe(0)), amorphous iron (Fe(0)) and Fe_2O_3 (where oxidation state of Fe = Fe (III)).[4]

4.2.1 Method

A new electrochemical cell was designed to perform XAS measurements in fluorescence mode on the surface of an electrode. The new cell was built in order to characterise the electrode surface directly using an X-ray photon beam, which could not be achieved using a standard cyclic voltammetry setup. The cell body holds up to 10 cm^3 of electrolyte and is made out of Teflon to prevent electrode contact with conductive walls. At the front of the cell, an inverted cone shaped Teflon ring holds a 40 µm Kapton window held in place with silicon rubber. The window material is thin enough to limit further fluorescence loss since there is significant loss due to an electrolyte layer.

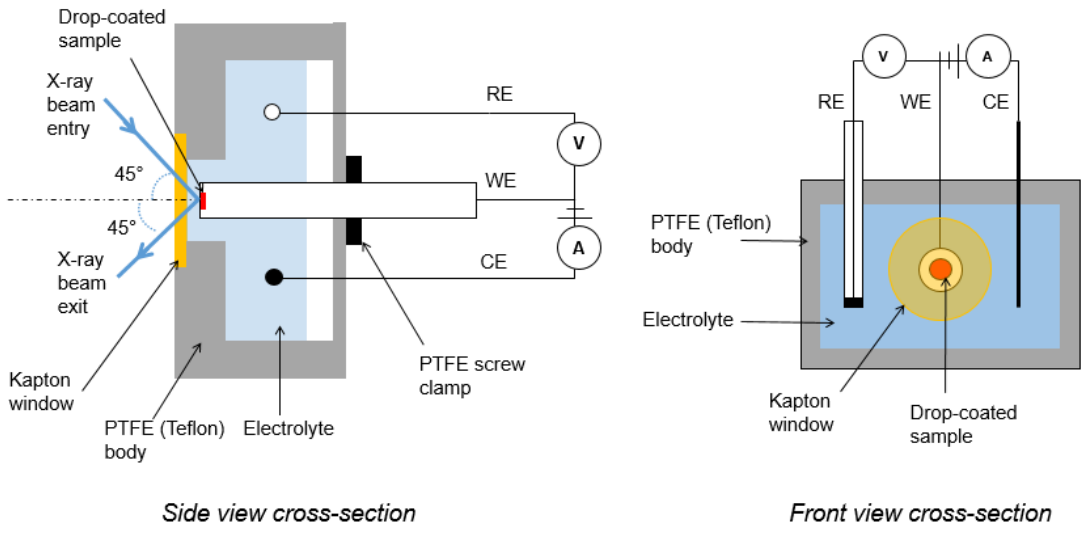

Figure 4.4 Schematic diagram of cross-section of in-situ XAS cell.

The working electrode is a 1 cm diameter carbon rod. The metal sulfide sample dispersed in chloroform was drop coated onto one end of the rod and the rest of the rod was covered with insulating tape to ensure only the sample was in contact with solution. A screw system was used to hold the working electrode horizontally, allowing adjustment of the distance between the Kapton window and the working electrode. The electrode was placed as close as possible to the window at an approximate distance of 0.5 mm. Further setup details are available in reference 5.

Similar to the CV experiments, an AgCl|Ag sat. KCl reference electrode and a platinum wire counter electrode were used. Both the reference and counter electrodes were held perpendicular to the working electrode, which were inserted into the cell via custom made holes on the cell cover. The cover was screwed onto the cell to create an airtight environment. Finally, the cell was held in an aluminium cell holder that can be screwed onto a variety of sample stages in the experimental chamber.

The following external step potentials (multistep amperometry) were applied to the cell: E_1 = −0.25 V, E_2 = −0.8 V, E_3 = −1.0 V, E_4 = +0.4 V and E_5 = −0.5 V. Each potential was held for 1 hour. These potentials were chosen based on the potentials at which the redox features occurred in the CVs recorded in the previous chapter. E_1 was chosen as the potential at which there was no increase in reduction current, E_2 was the potential where the onset of reduction current was recorded on the first negative-going potential sweep, while E_3 is associated with vertex potential chosen in the CV experiments. To mimic the positive-going potential sweep in the CV experiments, a positive potential was chosen for E_4, while E_5 was chosen to mimic the onset of the second scan negative-going potential sweep.

The XANES spectra were acquired on the iron K-edge (7112 eV) for greigite. Each XAS measurement lasted approximately 20 minutes, hence three scans were recorded at each potential step. A k range of 11 $Å^{-1}$ was possible in this time frame. The XAS data was normalized and background subtracted using Horae Athena software. Detailed EXAFS analyses were performed on Excurve Version 9.273. These analyses were published by Dr Islam in a thesis titled “Formation and Electrocatalysis Studies of Nickel and Iron Sulfide Catalysts using in situ XAS”, University College London January 2015. [5] In this chapter, the results are discussed and analysed further in the context of the cyclic voltammetry and in-situ IR results.

4.2.2 Results

4.2.2.1 pH 4.5 and 6.8 under argon

Figure 4.5 and Figure 4.6 show the in-situ XANES spectra of greigite on the Fe K-edge recorded in phosphate buffer solutions pH 4.5 and 6.8 under nitrogen, respectively. The XANES spectra of the dry greigite nanoparticles are included in both sets of the XANES spectra at pH 4.5 and 6.8 for comparison.

On immersion of the greigite electrode in pH 4.5 electrolyte, there was a gradual increase in the white line intensity at *c.a.* 7135 eV which continued on applying potentials of −0.25, −0.80 and −1.00 V (Figure 4.5B). The increase in the white line intensity is characteristic of the coordination of oxygen to Fe. This feature can be seen in Figure 4.1 where the XANES spectra of Fe-O compounds are characterised by a high white line intensity at *c.a.* 7130 eV, while the XANES spectra of Fe-S compounds are characterised by a broad white line intensity at *c.a.* 7115 eV. It is proposed here that the increase in oxygen coordination on greigite is due to the hydration of Fe^{2+} dissolved species forming $[Fe(H_2O)_6]^{2+}$ or the coordination of H_2O at the surface of the greigite nanoparticles. The increase in the white line intensity is not assigned to the formation of Fe-O compounds such as goethite, ferrihydrite or hematite since there is no shoulder at *c.a.* 7145 eV (characteristic of the iron oxides / hydroxides) observed in Figure 4.5 up to potential of −1.00 V. The potential adsorption of phosphate electrolyte species ($H_2PO_4^-$) may also contribute towards the increased oxygen coordination to Fe in the greigite electrode.

On inspection of the edge position of the XANES spectra at pH 4.5 in Figure 4.5C, there was no significant change in the edge position between the immersion of the greigite electrode and applying a potential of −0.25 V. The edge position in the XANES spectra can be used to interpret the average oxidation state of the Fe atoms in the bulk structure of greigite. A positive shift in the edge position denotes an increase in the average oxidation state of Fe atoms, while a negative shift represents a decrease in the average oxidation state of Fe atoms. Since there was no significant change in the edge position at −0.25 V, this suggests that no

change in the oxidation state of Fe or redox process occurred. There is also a pre-edge shoulder feature present at *c.a.* 7120 eV in the XANES spectra in Figure 4.5. This feature is characteristic of coordination between Fe and S and represents the forbidden 1s to 4s transition which is allowed in sulfides when overlap with soft S ligands contributes p character to the Fe 4s orbital. [5] This pre-edge feature gradually became smaller with each potential applied which shows that while considerate Fe-S character remained in the electrode material, Fe-O coordination now also contributes to the XANES spectra.

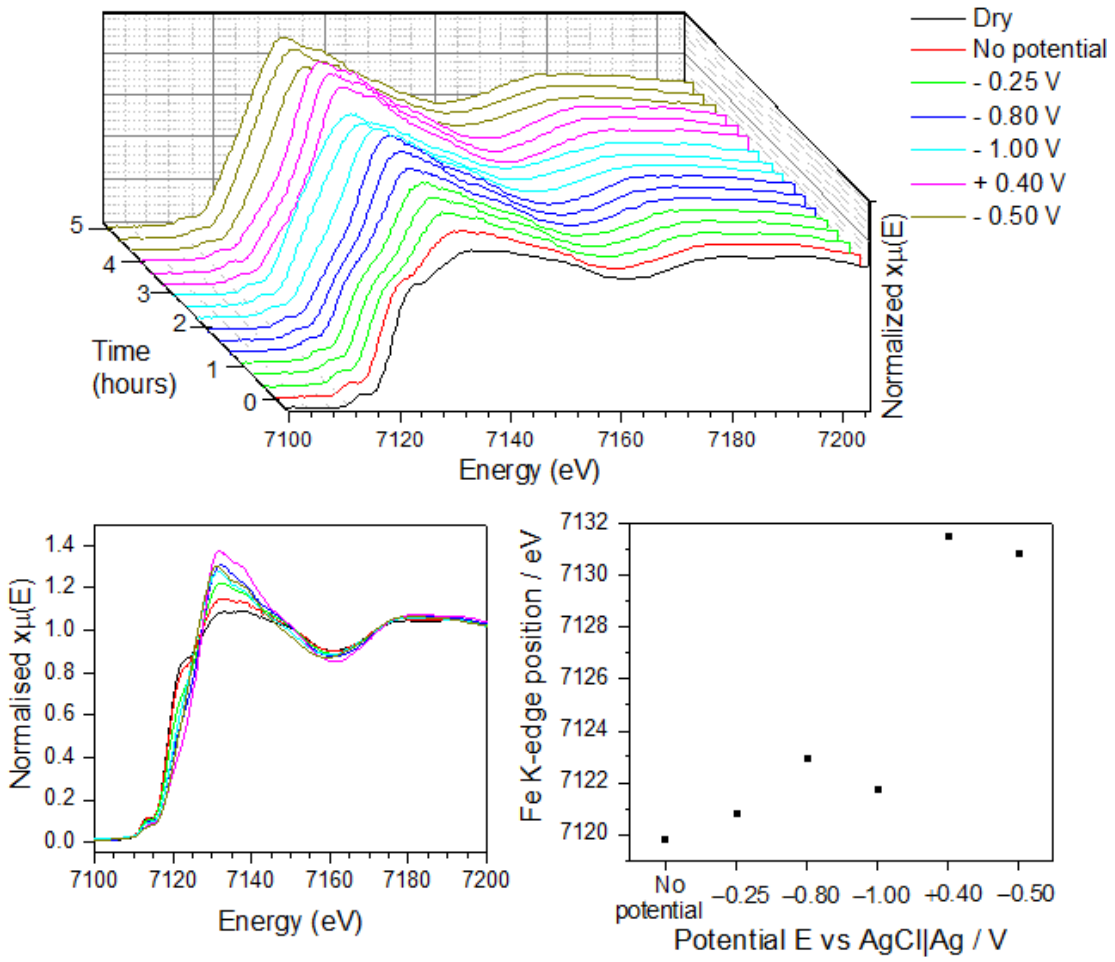

Figure 4.5 In-situ XANES spectra of greigite on Fe K-edge in phosphate buffer solution pH 4.5 under nitrogen: A) stacked spectra with three scans of each potential step, B) merged spectra with last scan of each potential step, and C) edge position of XANES spectra at each potential step.

In contrast to the small changes in the white line intensity observed in the XANES spectra at pH 4.5, at pH 6.8 the white line intensity remained constant on applying −0.25 V and only increased after applying −0.80 V for 40 minutes (up to the

second scan). This implies that the degree of oxygen coordination on Fe via adsorption of H_2O or $H_2PO_4^-$ species on greigite, or the hydration of dissolved Fe^{2+} species is decreased at pH 6.8 which may be attributed to the capping agent present on the greigite surface. At pH 6.8, the amine group (-RNH_2) of the capping agent is neutral and therefore insoluble. Compared to the more acidic pH 4.5, the amine group of the capping agent can be easily protonated in acidic solution and will thus be water soluble. Thus, this may explain the lower degree of oxygen coordination on greigite at pH 6.8 compared to at pH 4.5 as the greigite surface is less exposed at pH 6.8. Regardless of the presence of the capping agent which protected the greigite surface from air-oxidation, the XANES spectra show that the greigite electrode remained unchanged in both pH 4.5 and 6.8 under nitrogen on applying potential of −0.25 V. These observations are consistent with the CVs of greigite at pH 4.5 and 6.8 under argon where no redox features were observed and are also in agreement with the predicted stability of greigite in the Pourbaix diagram in Figure 3.2 at this potential and pHs.

Greigite is predicted to reduce to "FeS" (according to the Pourbaix diagram in Figure 3.2 in chapter 3) between −0.35 and −0.85 V at pH 4.5 and between −0.55 and −1.00 V at pH 6.8. In general, the XANES spectra of iron sulfides (see XANES of Fe_7S_8 and FeS_2 in Figure 4.1) are characterised by a broad XANES edge at *c.a.* 7117 eV. Since the XANES spectra of these iron sulfides are relatively indistinguishable, regardless of the variation in Fe:S ratio, it is difficult to distinguish between greigite and any "FeS" formed in the XANES spectra at both pH 4.5 and 6.8. Therefore, on applying further negative potentials of −0.80 and −1.00 V, the predicted transition of greigite to "FeS" may have occurred at both pHs, but is not distinguishable in the XANES spectra at both pHs. The XANES spectra of greigite in both pH 4.5 and 6.8 on applying −0.80 and −1.00 V, however, recorded a further increase in the white line intensity. The increased white line intensity at both pHs is attributed to an increased coordination of oxygen on Fe which may have resulted from the coordination of OH^- species, generated by water reduction at these potentials, on the greigite surface. The presence of OH^- species may shift the pH near the electrode surface to higher values and potentially favour the formation of iron oxide / hydroxide on the greigite surface.

As previously stated, the XANES spectra of iron oxide / hydroxide are characterised by a high white line intensity and a shoulder at *c.a.* 7147 eV. These characteristic features of iron oxide / hydroxide are observed in the XANES spectra of greigite on applying −0.80 and −1.00 V at pH 6.8 only, which suggests a significant increase in the local pH near the electrode in the pH 6.8 electrolyte. The local pH may have shifted to pH > 7.5 where Fe_3O_4 / $Fe(OH)_2$ is predicted to form at pH > 7.5 in the Pourbaix diagram in Figure 3.1 at potentials < −0.80 V.

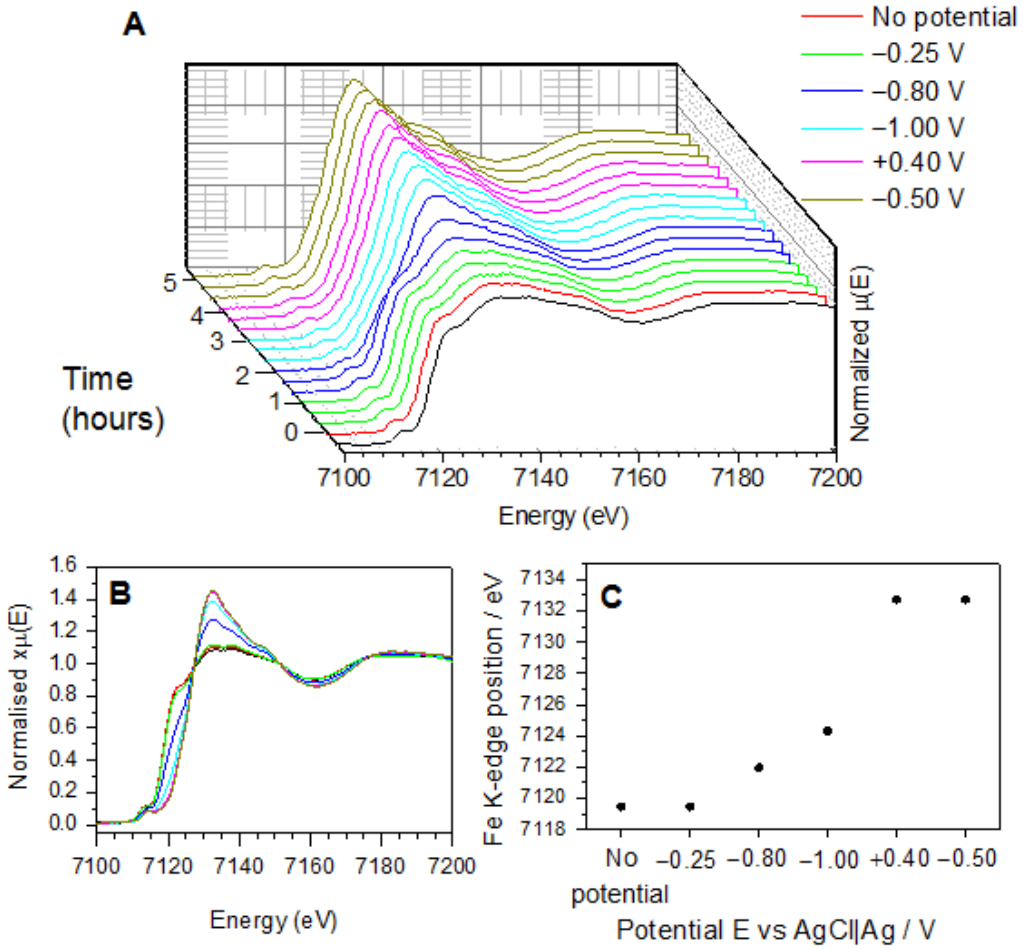

Figure 4.6 In-situ XANES data on Fe K-edge of greigite in phosphate buffer solution pH 6.8 under nitrogen: A) stacked spectra with three scans of each potential step, B) merged spectra with last scan of each potential step, and C) edge position of XANES spectra at each potential step.

One difference between the XANES spectra at pH 4.5 and 6.8 was the shift in the edge position on applying −1.00 V. The edge position at pH 4.5 decreased on applying −1.00 V but it increased at pH 6.8. The negative shift in the edge position at pH 4.5 is proposed to be a result of the formation of iron, which lowered the overall

average oxidation state of Fe atoms in the greigite electrode. This was as predicted in the Pourbaix diagram in Figure 3.2 where FeS is predicted to reduce to metallic Fe at potentials more negative than −0.90 V at pH 4.5. In contrast to the negative shift in the edge position at pH 4.5, there was a gradual increase in the edge position at pH 6.8 on applying −0.80 and −1.00 V which suggest an increase in the average oxidation state of Fe in the greigite electrode. This contrasts the predictions in the Pourbaix diagram in Figure 3.2 where greigite is predicted to reduce to FeS at pH 6.8 at potentials below −0.50 V. The formation of "FeS", which is composed of Fe(II), should lower the overall oxidation state of Fe in the greigite electrode. Therefore, the observed increase in the edge position on applying −0.80 and −1.00 V at pH 6.8 implies that an iron oxide or hydroxide layer may have formed on the surface of the greigite nanoparticles. It is not expected that a bulk transformation of greigite to iron oxide or hydroxide occurred since the shift in the edge position was slow and gradual. The formation of an iron oxide or hydroxide layer on the surface of the greigite nanoparticles was not predicted at these negative potentials in the Pourbaix diagram in Figure 3.2. As the predictions in the Pourbaix diagram are based on bulk transformations and an equilibrated system, a separate analysis is required for the changes in the surface structure, for example changes in unsaturated bonding. DFT calculations have predicted that the formation of a hydroxylated surface of greigite is thermodynamically feasible on adsorption of H_2O or OH^- species.[6] The adsorption process leads to incorporation of oxygen into the surface of greigite, however, it does not oxidise the bulk structure of greigite. Since the greigite electrode was stable on immersion into the electrolyte and on applying −0.25 V at both pHs, the formation of an iron oxide or hydroxide layer on the surface of the greigite nanoparticles on applying −0.80 and −1.00 V at pH 6.8 suggests that it may have been instigated by water reduction occurring at these potentials.

On applying the subsequent positive potential of +0.40 V, according to the Pourbaix diagram in Figure 3.2 in chapter 3, Fe_2O_3 and $Fe(OH)_3$ are predicted to be the stable redox species at both pH 4.5 and 6.8 at this potential. The XANES spectra at +0.40 V at both pH 4.5 and 6.8 resemble the XANES spectra recorded at −1.00 V, but with a further increase in white line intensity and notably an

additional shoulder at *c.a.* 7147 eV at pH 6.8 and at *c.a.* 7135 eV at pH 4.5. These additional features are indicative of the formation of iron oxide or hydroxide such as ferrihydrite, goethite and hematite (see Figure 4.1). The pre-edge shoulder feature at c.a. 7120 eV also gradually decreased over time in the XANES spectra at both pHs which indicate loss of S character and gain of oxide-like character. Thus, it can be deduced that the greigite electrode was oxidised to form iron oxide or hydroxide at both pH 4.5 and 6.8 on applying +0.40 V.

On applying −0.50 V, the white line intensity in the XANES spectra at pH 4.5 decreased, while at pH 6.8 the white line intensity remained constant. At this potential, there was also a decrease in the edge position in the XANES spectra at pH 4.5, which remained constant at pH 6.8. According to the Pourbaix diagram in Figure 3.1, the iron oxide or hydroxide which was formed previously at +0.40V, is predicted to be stable up to −0.50 V at pH 6.8 and only up to 0.00 V at pH 4.5 where it will be reduced to soluble Fe^{2+} species. Thus, the changes in white line intensity and edge position observed in the XANES spectra at both pH 4.5 and 6.8 are in good agreement with the Pourbaix diagrams.

Comparing these observations to the redox assignments of the CVs in chapter 3, the reduction in the white line intensity and the edge position at –1.00 V at pH 4.5 supports the assignment of the reduction of greigite to form Fe(0) in the CV at pH 4.5. At pH 6.8, the increase in the white line intensity and the edge position at –1.00 V show that the iron oxide or hydroxide layer was continuously formed on the greigite electrode up to –1.00 V. Previously, the reduction peaks in the CV of greigite at pH 6.8 was only assigned to the reduction of greigite to FeS. Thus, with the additional evidence for the formation of iron oxide or hydroxide in the XANES spectra at –0.80 and –1.00 V at pH 6.8, the formation of an iron oxide or hydroxide layer needs to be considered in the CV at pH 6.8. Taking into account the formation of an iron oxide or hydroxide layer on the greigite electrode will not be a bulk structure transformation, the most likely pathway for the formation of an iron oxide or hydroxide layer, as suggested by DFT calculations by Santos-Carballal *et al*, will be via adsorption of H_2O and substitution of sulfur by oxygen in the surface of the greigite structure, as depicted in Figure 4.7.[6]

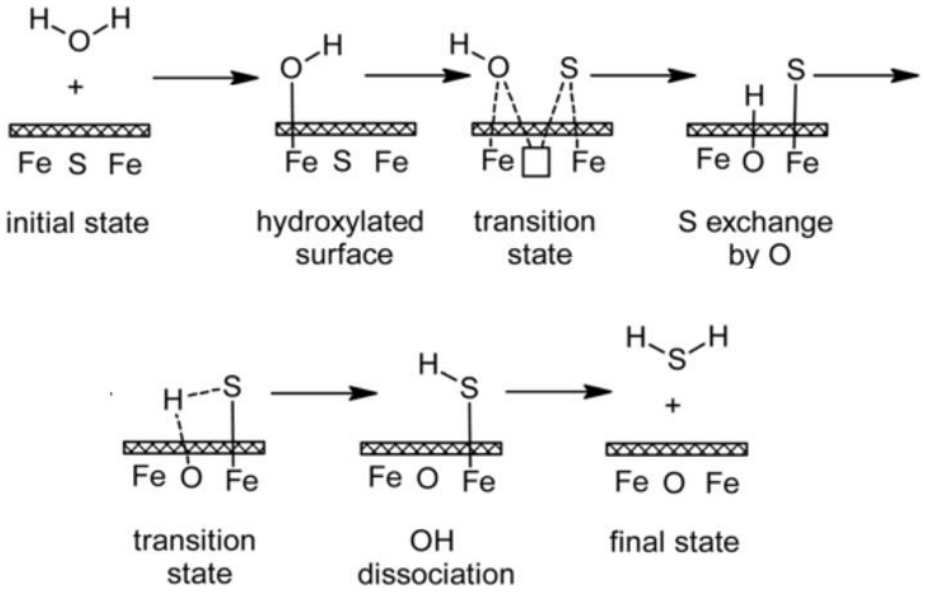

Figure 4.7 Mechanism for the substitution of S by O into the greigite surface via adsorption and dissociation of H_2O. Reprinted with permission from ref 6**. Reprinted with permission.**

Figure 4.7 show the most feasible pathway for the incorporation of OH^- species, generated by water reduction, into the surface of greigite via substitution of sulfur. When OH^- species coordinates onto the surface of greigite, the sulfur atom leaves the surface as H_2S. The final state of the greigite structure consists of a greigite bulk structure with a monolayer of iron oxide or hydroxide on its surface. According to the Pourbaix diagram in Figure 3.1, the iron oxide / hydroxide layer will be reduced to Fe^{2+} soluble species at potentials < –0.40 V. However, the XANES data at pH 6.8 show the iron oxide / hydroxide layer was present up to –1.00 V. This suggests that the local pH near the electrode surface may have been shifted to above pH 8 (where iron oxide / hydroxide remain as the stable redox product) due to water reduction which generate OH^- species. However, further evidence is required for such increase in the local pH.

4.2.2.2 pH 4.5 and 6.8 under CO_2

Figure 4.8 and Figure 4.9 show the XANES spectra of greigite recorded under CO_2 in phosphate buffer solutions at pH 4.3 and 6.5, respectively. On introduction of CO_2, no significant change in the white line intensity and edge position of the XANES spectra at both pHs was observed up to −1.00 V. This is in contrast to the XANES spectra under nitrogen at both pHs, which suggests that on introduction of CO_2 the coordination of oxygen onto Fe, via hydration or adsorption of H_2O, of the greigite electrode was much slower. Thus, the increased stability of the greigite electrode under CO_2 may be attributed to the adsorption of dissolved CO_2 species. The changes in the XANES spectra at pH 4.3 under CO_2 were more defined at −1.00 V, compared to pH 6.5 under CO_2 at the same potential. At this potential, greigite is predicted, in the Pourbaix diagram in Figure 3.2, to reduce to amorphous iron at pH 4.3, but not at pH 6.5. Fe(0) was predicted to form at −0.90 V at pH 4.3, while greigite or FeS should remain stable up to −1.00 V at pH 6.5.

According to the Pourbaix diagrams in Figures 3.2 – 3.5 analysed in the previous chapter, on introduction of CO_2, iron carbonate / siderite may form on the surface of greigite at pH 6.5, but not at pH 4.5. In chapter 3, the presence of iron carbonate was presumed to have caused the current suppression of the CV recorded at pH 6.5 under CO_2. On inspection of the XANES spectra in pH 4.3 and 6.5 under CO_2 in Figure 4.8 and Figure 4.9 and comparison to the XANES spectrum of siderite in Figure 4.1, siderite was not detected at both pH 4.3 and 6.5 under CO_2. This is based on the absence of the characteristic features of the XANES spectrum of siderite at 7123 and 7133 eV. It is evident that the greigite electrode did not undergo a bulk transformation to siderite at pH 6.5, as predicted by the Pourbaix diagrams. However, it is possible that a monolayer of siderite may have formed on the greigite electrode. The XANES technique is sensitive to changes in the surface of the electrode and if a monolayer of siderite was formed, it would be detected. Therefore, since there is no evidence for the formation of siderite in the XANES spectra, the suppression of current in the CV at pH 6.5 under CO_2 may be caused by the adsorption of CO_2 or its dissolved species.

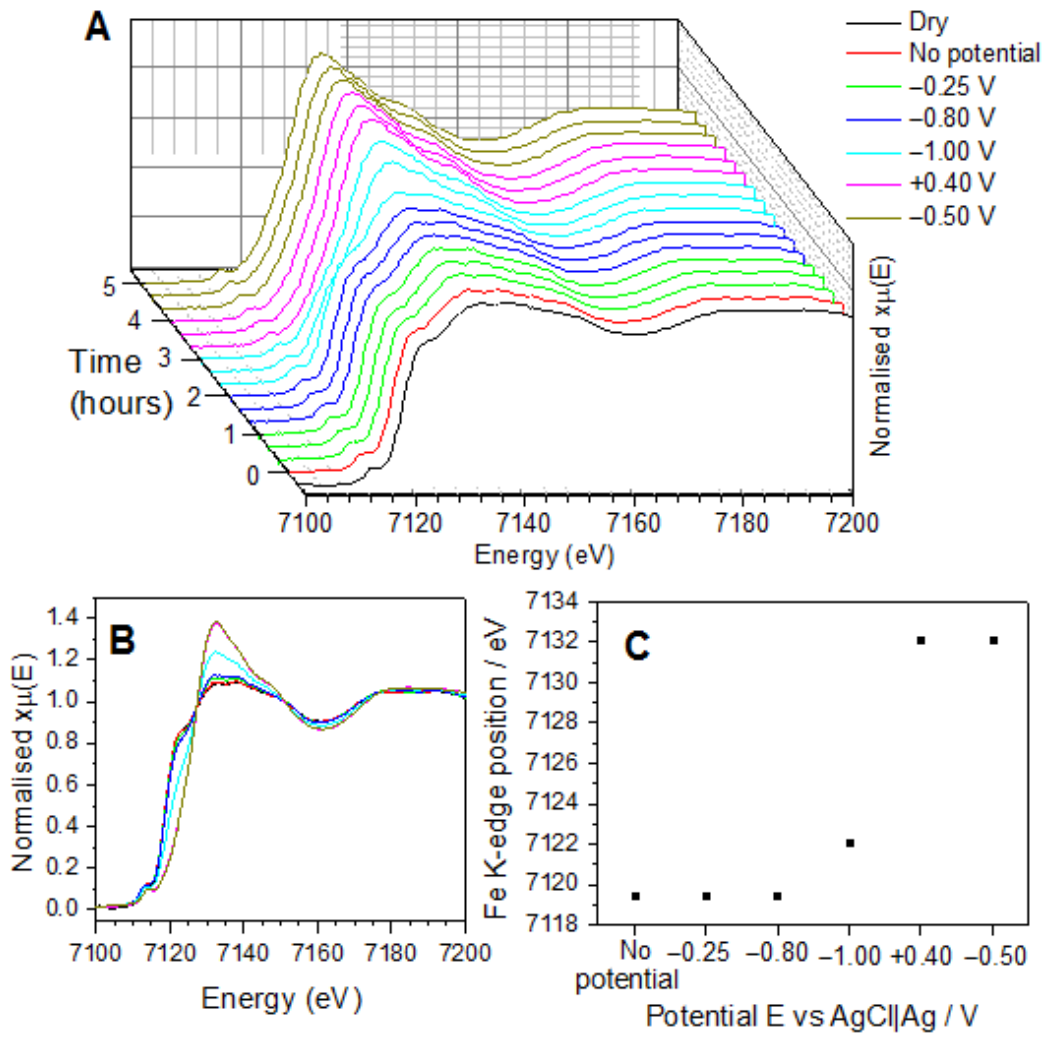

Figure 4.8 In-situ XANES data on Fe K-edge of greigite in phosphate buffer solution pH 4.3 under CO_2: A) stacked spectra with three scans of each potential step, B) merged spectra with last scan of each potential step, and C) edge position of XANES spectra at each potential step.

On applying subsequent potentials of +0.40 and −0.50 V in pH 4.3 and 6.5 under CO_2, a similar trend in the changes to the XANES spectra under nitrogen were observed under CO_2. Thus, the changes to the XANES spectra on applying +0.40 and −0.50 V in pH 4.3 and 6.5 under CO_2 may be attributed to the same reaction under nitrogen which was assigned to the formation of iron oxide or hydroxide.

Overall, the introduction of CO_2 in pH 4.3 and 6.5 slowed down the change in white line intensity and edge position of XANES spectra of the greigite electrode which was observed under the control nitrogen atmosphere up to −1.00 V. The adsorption of CO_2 or its dissolved species may have prevented the competing adsorption of H_2O or even suppressed water reduction on the greigite electrode.

Water reduction produces OH^- species which may coordinate onto the Fe atoms of the greigite electrode and result in an increase in the white line intensity in the XANES spectra of greigite, as observed under the control nitrogen atmosphere. An increased concentration of OH^- species may shift and increase the pH near the electrode surface, which may also favour the formation of iron hydroxides or oxides on the greigite electrode. If water reduction was suppressed under CO_2, due to the adsorption of CO_2 or its dissolved species, such pH shift due to OH^- species may not occur under CO_2 and may hinder the formation of iron hydroxides or oxides on the greigite electrode.

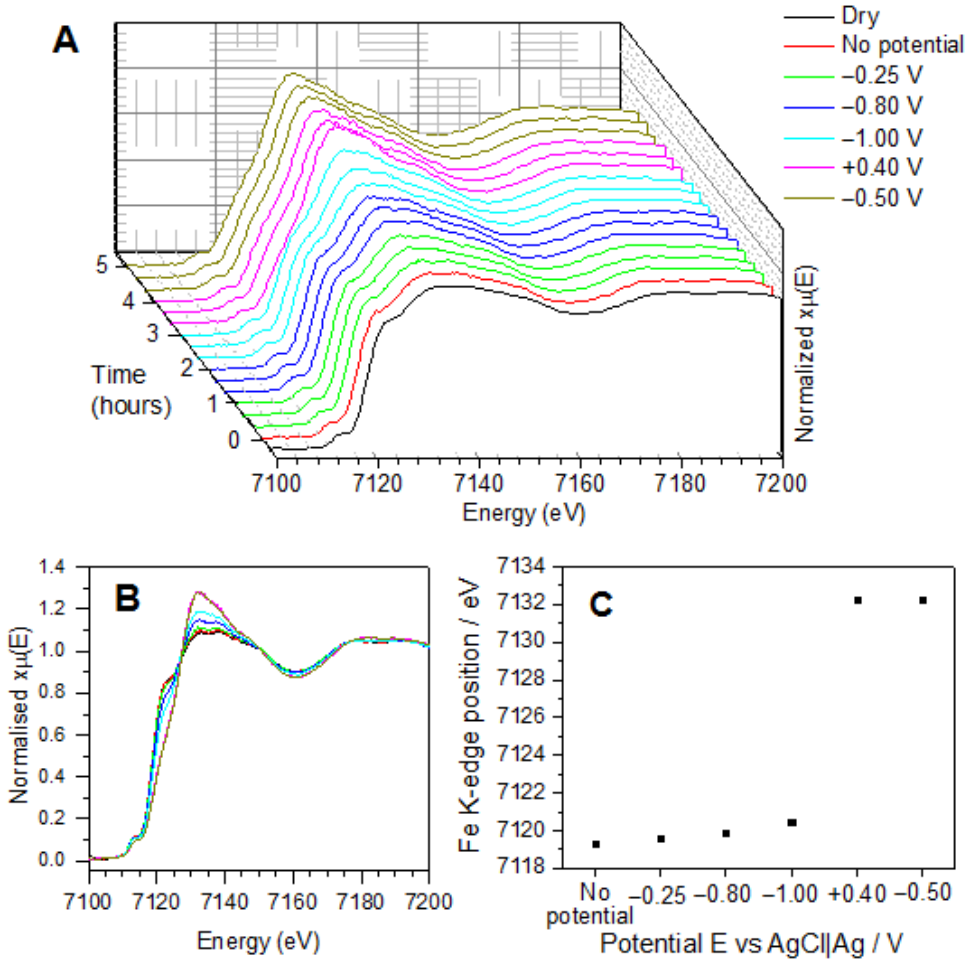

Figure 4.9 In-situ XANES data on Fe K-edge of greigite in phosphate buffer solution pH 6.5 under CO_2: A) stacked spectra with three scans of each potential step, B) merged spectra with last scan of each potential step, and C) edge position of XANES spectra at each potential step.

4.2.2.3 pH 11.2 under nitrogen

Figure 4.10 displays the XANES spectra of greigite recorded in K_2CO_3 pH 11 under nitrogen. Previously in chapter 3, the CV of greigite in K_2CO_3 pH 11 was featureless. This was attributed to the potential presence of a passivating layer such as iron carbonate / siderite, iron oxide or hydroxide. The formation of iron carbonate, oxide or hydroxide may arise from the complexation of soluble Fe^{2+} species (produced via non-oxidative dissolution of greigite) with OH^-, CO_3^{2-} and HCO_3^- species, present in abundance at this high pH, on the surface of greigite.

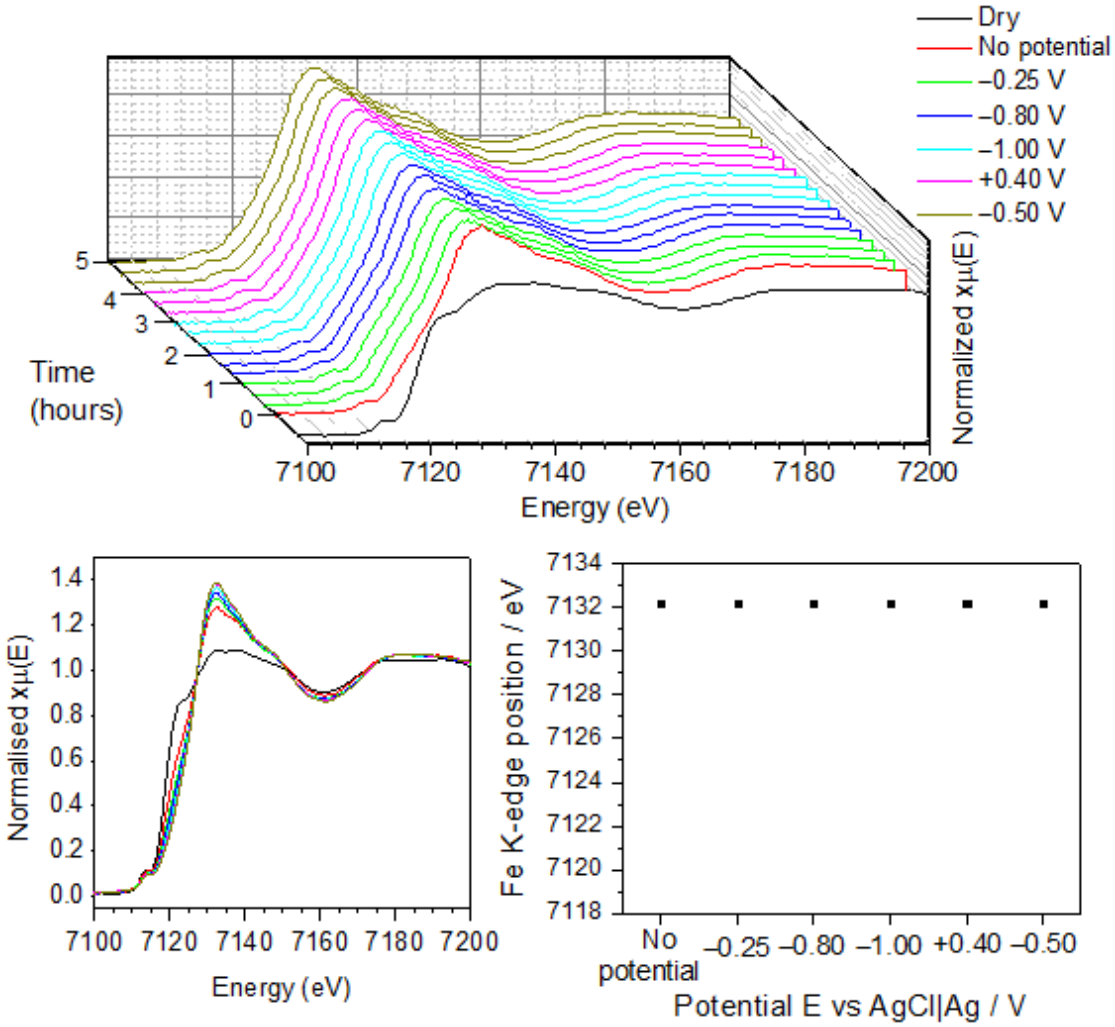

Figure 4.10 In-situ XANES data on Fe K-edge of greigite in K_2CO_3 pH 11.2 under nitrogen: A) stacked spectra with three scans of each potential step, B) merged spectra with last scan of each potential step, and C) edge position of XANES spectra at each potential step.

In contrast to the changes in the XANES spectra observed at pH 4.5 and 6.8 under nitrogen, there was a significant increase in the white line intensity of the XANES spectra at pH 11.2 on immersion of the greigite electrode when no potential was applied. The changes in the XANES spectra at pH 11.2 resemble the XANES spectra of iron oxide / hydroxide (hematite, goethite and ferrihydrite) in Figure 4.1. This suggests that iron oxide / hydroxide was formed on immersion of the greigite electrode in the electrolyte. According to the Pourbaix diagrams in Figures 3.2 and 3.5, at pH 11.2, greigite is predicted to be stable up to −0.70 V. Based on this prediction, it is likely that the greigite electrode did not undergo a bulk transformation to iron oxide or hydroxide, but instead may have formed a core-shell nanoparticle structure with greigite at the core and the newly formed iron oxide / hydroxide as its shell.

At this pH, according to the Pourbaix diagrams in Figures 3.2 and 3.5, iron carbonate is not predicted to form at any of the potential steps applied. There is also no evidence for the formation of iron carbonate (which is characterised by two shoulder features at 7123 and 7133 eV) on inspection of the XANES spectra at pH 11.2. Thus, the proposed passivating layer that may have suppressed the currents in the CV of greigite at this pH in chapter 3 may not be iron carbonate, but instead it may be iron hydroxide or oxide. The transition from greigite to iron hydroxide or oxide is only predicted to occur at potentials more positive than +0.20 V at pH 11.2, according to the Pourbaix diagram in Figure 3.2. The contrasting evidence for the formation of iron hydroxide / oxide in the XANES spectra at pH 11.2 at negative potentials of −0.25, −0.80 and −1.00 V suggests that the changes observed may be confined to the surface of the greigite nanoparticles and do not involve a bulk transformation.

As previously proposed at pH 6.8, the formation of iron hydroxide / oxide on the surface of the greigite electrode, as evidenced by the changes in the XANES spectra at pH 11.2, can be supported by DFT calculations which have predicted that the formation of a hydroxylated surface of greigite is thermodynamically feasible on immersion in a high pH electrolyte.[6] Compared to the changes at pH 6.8, there is a higher concentration of OH^- species present at pH 11.2 which can

coordinate onto Fe atoms of greigite, via the adsorption of H_2O and splitting of H_2O. Thus, this may explain the immediate increase in the white line intensity on immersion of the greigite electrode in pH 11.2 compared to at pH 6.8 where it remained stable until applying potential of −0.80 V. Therefore, the evidence for the formation of iron oxide / hydroxide in the XANES spectra in Figure 4.10 and the DFT calculations support the proposed hypothesis that a passivating iron oxide or hydroxide layer may have caused the featureless CV response of greigite at pH 11.2 in chapter 3.

According to the Pourbaix diagrams in Figures 3.1 and 3.4, once iron oxide / hydroxide is formed at pH 11.2, it will remain stable over a wide potential range (stable at potentials > −1.00 V). Thus, the iron oxide or hydroxide layer will remain on the electrode on applying subsequent potentials of −0.25, −0.80, −1.00, +0.40 and −0.50 V in the XANES spectra. This is in agreement with the observed XANES spectra at pH 11.2, where the XANES spectra remained unchanged on immersion into the electrolyte and throughout the experiment.

The results from the in-situ XANES experiments in this section show that the stability of greigite is significantly affected at high pH and positive potentials which will favour the formation of iron oxide / hydroxide. At pH 4.5 and 6.8, greigite was stable as predicted by the Pourbaix diagrams in chapter 3. However, at high pH (pH 11.2), iron hydroxide / oxide was formed on the surface of the greigite electrode on immersion into the electrolyte which was attributed to the high pH and concentration of OH^- species present. This was in contrast to the thermodynamic prediction in the Pourbaix diagram in Figure 3.2 in chapter 3 where greigite is predicted to remain stable on immersion into the electrolyte within a potential window of +0.20 and −0.70 V. The results at pH 11.2 support the pH 6.8 results at −0.80 and −1.00 V being due to a pH shift above 10, where the white line intensity increased significantly which indicate potential formation of iron hydroxide or oxide due to an increased concentration of OH^- species.

The Pourbaix diagrams in chapter 3 were useful in aiding the assignments of the redox reactions of the CVs of greigite. However, on introduction of CO_2, there was

no evidence for the formation of iron carbonate / siderite in the XANES spectra which was predicted in the Pourbaix diagrams at pH 6.5. The introduction of CO_2 slowed down the change in the white line intensity and edge position of the XANES spectra of the greigite electrode which was observed under the control nitrogen atmosphere. This was proposed to be associated with the adsorption of CO_2 or its dissolved species which may have prevented the competing adsorption of H_2O, the redox reactions of greigite or even suppressed water reduction on the greigite electrode.

4.3 In-situ ATR FTIR

At present, there is no published in-situ IR characterisation work on greigite, specifically. The relevant infrared band assignments reviewed from literature are summarised in Table 4.1. These include: IR bands of i) iron oxides / hydroxides, hematite (Fe_2O_3), iron oxyhydroxide and goethite (α-FeO(OH)), ii) electrolyte species: water, phosphate, sulfate, thiosulfate, CO_3^{2-} and HCO_3^- species, and iii) the capping agent of the greigite nanoparticle. Table 4.1 also includes variation in multiple literature assignments for the same species. Parameters such as pH, concentration, temperature, humidity, pressure and applied potential can affect peak positions which can lead to slight variation in band assignments for similar species. In this thesis, IR spectra of relevant standard samples were recorded for control measurements, as well as for comparison to literature values. These are displayed in Table 4.2 and the standard spectra recorded are attached in the appendix. IR numbers from these tables are referred to when analysing FTIR spectra described later in this chapter.

Table 4.1 IR bands of relevant species.

Species	IR bands / cm^{-1}	Reference
Sulfates / Thiosulfates		
SO_4^{2-}	1100	[7, 8]
HSO_4^-	890, 1050, 1195	[7, 8, 9]
HSO_4^-	876, 1050, 1190	[10]
Hematite-sulfate	975, 1060, 1130	[7]
Goethite-sulfate	975, 1055,1135	[11, 12]
Goethite-sulfate	972, 1052, 1132, 1170	[13]
$S_2O_3^{2-}$	1104	[14]
$S_2O_3^{2-}$	950, 1000, 1120	[15]
Phosphates		
PO_4^{3-}	1005	[1, 16]
HPO_4^{2-}	850, 890, 990, 1075	[1, 16]
$H_2PO_4^-$	875, 940, 1075, 1155	[1, 16]
$H_3PO_4^-$	890, 1005, 1175, 1250	[1, 16]
Goethite-phosphate	1005, 1045, 1100, 1120	[16]
Goethite-phosphate	945, 1044, 1089	[17]
Hematite-phosphate	960, 1040, 1085	[18]
Carbonates / Bicarbonates		
CO_2 (aq)	667, 2342	[19]
CO_3^{2-}	885, 1065, 1383	[20]
CO_3^{2-}	1065, 1389, 1410	[21]
CO_3^{2-}	1385	[19]
HCO_3^-	1011, 1313, 1391, 1657	[21]
HCO_3^-	1010, 1310, 1360, 1605, 1668	[20]
HCO_3^-	1240, 1300, 1360	[19]
Hematite-carbonate	1350, 1500	[22]
Hematite-carbonate monodentate	1067, 1350-1365, 1470-1486	[21]
Hematite-bicarbonate monodentate	1260, 1400	[21]
Hematite-carbonate bidentate	1040-1050, 1300-1330, 1520-1540	[21]
Hematite-bicarbonate bidentate	1010-1020, 1323, 1338, 1410, 1630	[21]
Goethite-carbonate	1335, 1490	[23]
Goethite-bicarbonate	1335, 1410	[20]
Amorphous $Fe(OH)_3$ – carbonate (1 M)	944, 1070, 1336, 1485	[20]
Amorphous $Fe(OH)_3$ – carbonate (0.01 M)	1020, 1135, 1474, 1586, 1674	[20]
Amorphous $Fe(OH)_3$ – bicarbonate (1 M)	950, 1070, 1335, 1487,	[20]

Amorphous $Fe(OH)_3$ – bicarbonate (0.01 M)	1050, 1369, 1477, 1585, 1667	[20]
$FeCO_3$	1460, 1345, 1068, 860	[24]
$FeCO_3$	1400, 865, 740	[25]
Fe sulfide		
Fe-S in pyrrhotite	416	[26]
Fe-S in troilite	425	[26]
Fe oxide		
Fe-O in Fe_3O_4	565	[27]
Fe-O in Fe_2O_3	580	[27]
Fe-O in Fe_2O_3	588	[26]
Adsorbed water		
H_3O^+	~1700	[28, 29]
HOH bending	1630	[29]
Weakly H-bonded -OH	3656	[29]
Strongly H-bonded –OH	~3000	[29]
Bulk water		
Symmetric -OH	3400	[29]
HOH bending	1645	[29]
Translation -OH	200	[30]
Libration -OH	500-800	[31]
Water monomer		
Symmetric –OH	3720	[29]
Antisymmetric -OH	3660	[29]
HOH bending	1595	[29]
Capping agent		
NH_2	3376, 3300, 1593, 795	[32]
=CH	3006	[32]
-CH	2922, 2854	[32]
-C=C	1647	[32]
-CN	1071	[32]
-C-C	722	[32]

Table 4.2 IR bands of standard samples.

Species	IR bands / cm^{-1}
Sulfate / Thiosulfates	
$S_2O_3^{2-}$ (aq)	663, 997, 1116
SO_4^{2-} (aq)	611, 1101
SO_3^{2-} (aq)	935
Na_2SO_3(s)	495, 628, 958, 1118, 1172
$Na_2S_2O_3$ (s)	530, 649, 767, 991, 1014, 1112, 1161, 1616, 1652, 1689
$Na_2SO_4.10H_2O$(s)	486, 611, 1080, 1670
Iron compounds	
$FePO_4.4H_2O$ (s)	524, 1000
Fe(II,III) oxide	545, 879
$FeSO_4.7H_2O$ (s)	430, 536, 975, 1072
Electrolytes	
pH 4 KH_2PO_4	869, 939, 1076, 1155
pH 7 KH_2PO_4 + K_2HPO_4	869, 939, 991, 1076, 1155
pH 8 $KHCO_3$	669, 842, 1008, 1303, 1361, 1620, 1664
pH 11 K_2CO_3	669, 842, 1010, 1305, 1359, 1622, 1656
Capping agent	
In pH 4 phosphate buffer	728, 972, 1058, 1560, 1630, 2837, 2912
In pH 7 phosphate buffer	987, 1076, 1394, 1539, 1635, 2850, 2923
In pH 8 $KHCO_3$	1318, 1497, 2842, 2930
In pH 11 K_2CO_3	966, 1409, 1458, 1629, 2852, 2921

4.3.1 Method

A new electrochemical cell setup was designed for in situ electrochemical-ATR-FTIR analysis. A schematic diagram of the cell is shown in Figure 4.11. This setup is comparable to the in-situ XAS cell where the position of the electrodes are vertical, instead of horizontal, to accommodate the direction of the infrared beam reflected from the ATR prism. This new cell was built in order to characterise the electrode surface directly using the infrared beam, which could not be achieved using a standard three-electrode cell. This electrochemical-ATR-FTIR cell setup is new and has not been reported before in the literature. Here, the material / electrode of interest is pressed directly onto the ATR prism, while simultaneously performing the electrochemical measurements. The setup was designed to investigate the IR groups present near the electrode surface, which is often different from the bulk electrolyte.

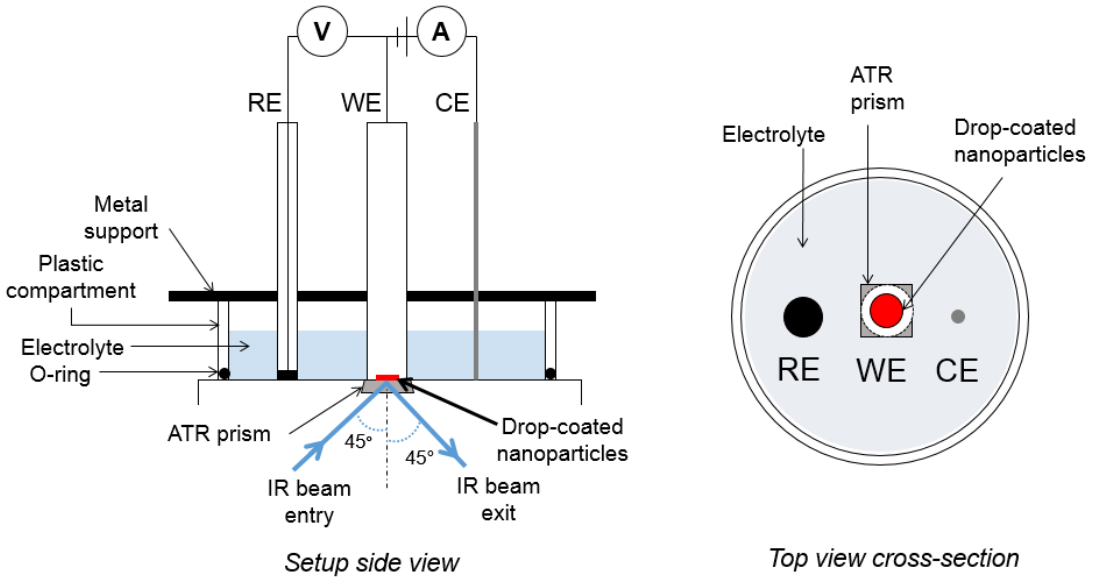

Figure 4.11 Schematic diagram of in-situ ATR-FTIR electrochemical setup with diamond ATR prism. Similar to setup used in CVs with nanoparticles drop coated on BDD WE (Boron doped diamond working electrode), Ag/AgCl RE (reference electrode), Pt CE (counter electrode).

The experiments were performed on a Bruker Tensor 27 spectrometer (Bruker, Coventry, United Kingdom) fitted with a room temperature DLaTGS detector at 4 cm^{-1} resolution and a diamond prism operating with one reflection as the internal

reflection element. In this setup, the working electrode surface was pressed directly on the prism of the ATR. A circular acrylic ring compartment (height: 1 cm) with an O-ring attachment was positioned in the centre of the prism and set in place under a stainless steel metal support. This metal support was also designed to fix all electrodes in position. All electrodes and experimental conditions tested in this in situ measurement are similar to those tested in voltammetry measurements. The electrochemical cell was connected to PalmSens EmStat2 potentiostat (Palm Instruments BV, Netherlands) and measurements were recorded using PSTrace software (ver. 3.0).

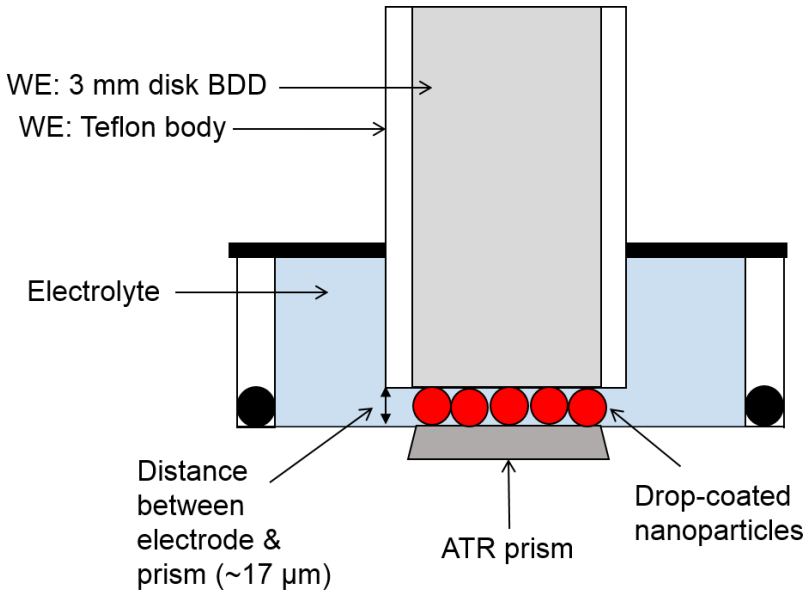

Figure 4.12 Close up of working electrode position on ATR prism. Distance between electrode surface and ATR prism < 10 µm (not to scale).

This technique is comparable to Surface Enhanced Infrared Spectroscopy (SEIRAS) technique where the working electrode material is deposited on the surface of ATR prism. However, in this ATR-FTIR technique, there is an interfacial layer between the electrode surface and ATR prism. The thickness of this interfacial layer has been calculated to be *c.a.* 17 µm.[33] The evanescent wave in the ATR crystal penetrates approximately 2 – 3 µm above the crystal. Thus, the FTIR spectra records the sampling region between the ATR crystal and the electrolyte. The spectra recorded will contain information on gains and losses of IR-active surface groups present in this sampling region. It is also expected that

some nanoparticles will come into contact with the prism, thus giving information on the nanoparticle surface. Therefore, there is a need to account for this interfacial layer when interpreting IR spectra in this thesis.

Prior to starting the measurements, 2 ml of pre-treated desired electrolyte (bubbled with Ar and/or CO_2) was pipetted into the cell. The WE was polished and rinsed thoroughly with distilled water before drop-coating with sample and placing into the cell. Similarly, the CE and RE were rinsed with distilled water and subsequently inserted into the cell.

Similar to in-situ XAS method, the potential steps (E_{step}) applied in this in-situ FTIR measurements are: E_1 = −0.25 V, E_2 = −0.8 V, E_3 = −1.0 V, E_4 = +0.4 V and E_5 = −0.5 V. Each potential step is held for 1 hour. A conditioning step of −0.25 V was applied for 5 seconds before E_1 to equilibrate the system and synchronise data collection.

After setting up the electrochemical cell (with drop-coated WE in direct contact with ATR prism), a background ATR-FTIR spectrum of 100 scans was performed before starting the in situ measurement. All ATR-FTIR spectra collection was performed in 370-4000 cm^{-1} range with 4 cm^{-1} resolution. The sample ATR-FTIR spectrum was set to compose of 50 scans. 60 ATR-FTIR measurements were collected in total with 5 minutes delay between each one. The spectroscopic data were collected in absorbance mode.

Once the background ATR-FTIR spectrum was recorded, the multistep amperometry measurement was initiated and ATR-FTIR measurements commenced after 5 seconds (during which the cell is subjected to the pre-conditioning voltage). Both techniques were synchronised as such so that for each potential step (applied for 1 hour), 12 ATR-FTIR measurements (delayed 5 minutes between each) were collected within this potential step. Several control measurements were also performed where no potentials were applied to the electrochemical cell and ATR-FTIR spectra were collected over 5 hours.

The nature of resulting spectra collected in these in situ measurements are difference spectra. A background ATR-FTIR spectrum, where the sample coated BDD electrode standing in solution with no applied potentials, is the reference spectrum. Thus every ATR-FTIR spectrum collected over time records changes induced by surface reactions on applying potentials relative to the reference spectrum. In general, peaks increasing in absorbance represent a gain in species absorbing at that wavenumber and peaks decreasing in absorbance represent the loss of the species at that wavenumber within the sampling distance of the ATR prism. Thus, changes in absorbance recorded throughout the experiment would assist in understanding surface processes occurring at different stages during the experiment.

4.3.2 IR data analysis and processing

Infrared spectra results were first water vapour-subtracted using MatLab code for water-vapour subtraction developed by Dr Liberty Freeman. The spectrum is then normalized using OriginPro 2015 software where the spectral data is split into wavenumber regions of: 3800 – 2500, 1800 – 750 and 700 – 400 cm^{-1}. Each spectrum within the wavenumber range is normalized against the median absorbance averaged out of the 60 ATR spectra recorded at that wavenumber range. The normalization was done to remove the moving background of the ATR-FTIR spectra overtime due to changes in atmospheric composition within the cell.

4.3.3 Results

4.3.3.1 PBS pH 4.5 and 6.8 under argon

Figure 4.13 and Figure 4.14 show the compilation of in-situ FTIR spectra of greigite recorded in phosphate buffer solutions pH 4.5 and 6.8 under argon, respectively. These two sets of FTIR spectra displayed similar trends on applying each potential step. Therefore, both sets of spectra at pH 4.5 and 6.8 under argon are detailed in parallel in this section. The following IR peaks were observed in both sets of spectra and are assigned as follows:

Table 4.3 IR assignments at pH 4.5 and 6.8 under argon in Figure 4.13 and Figure 4.14. (L is libration vibration, ν is stretching vibration, ν_{sym} is symmetric stretching vibration, ν_{asym} is asymmetric stretching vibration, δ is bending vibration and δ_d is deformation.)

Assignment	IR peaks at pH 4.5 / cm^{-1}	IR peaks at pH 6.8 / cm^{-1}	Reference
H_2O / OH			
L(H_2O)	530	543	31
δ(H_2O)	1627	1639	29
ν_{sym}(OH) (H-bonded)	3002	2987	29
ν_{sym}(OH) (bulk water)	3306	3409	29
$H_2PO_4^-$ species			
ν_{sym}(POH)		898	34
ν_{asym}(POH)	945	939	34
ν_{sym}(PO)	1075	1064, 1087	34
ν_{asym}(PO)	1165	1161	34
HPO_4^{2-} species			
ν(POH)	850	852	34
ν_{sym}(PO)	989	991	34
ν_{asym}(PO)	1075	1064, 1087	34
PO_4^{3-} species			
ν_{asym}(PO)	1014	1014	1,34
δ_d(OPO)	418	420	34

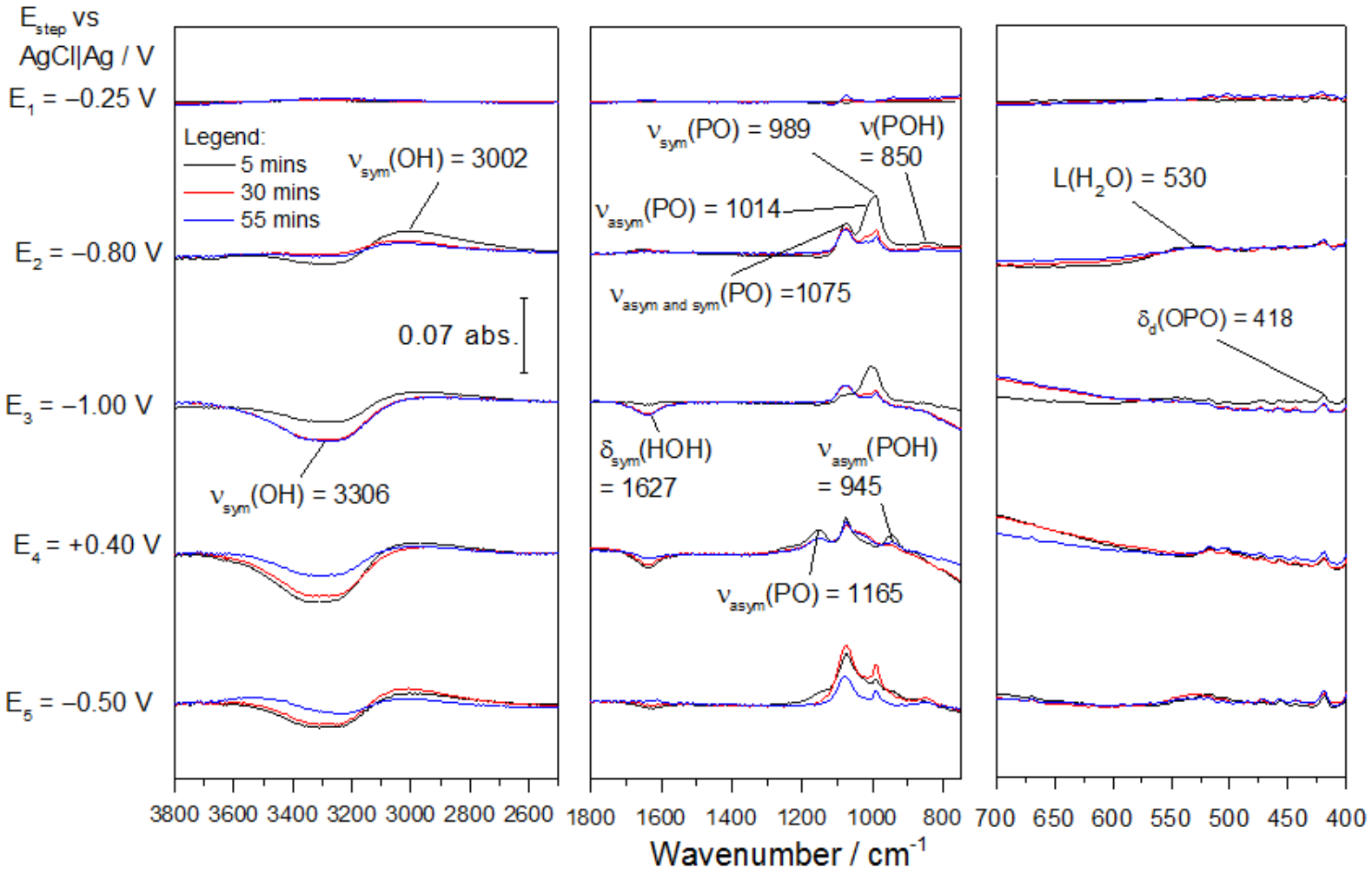

Figure 4.13 In-situ FTIR of greigite in phosphate buffer solution pH 4.5 under argon recorded on applying potential steps of −0.25, −0.80, −1.00, +0.40 and −0.50 V for one hour each step. Spectra displayed at each potential step were recorded at 5, 30 and 55 mins into holding the potential.

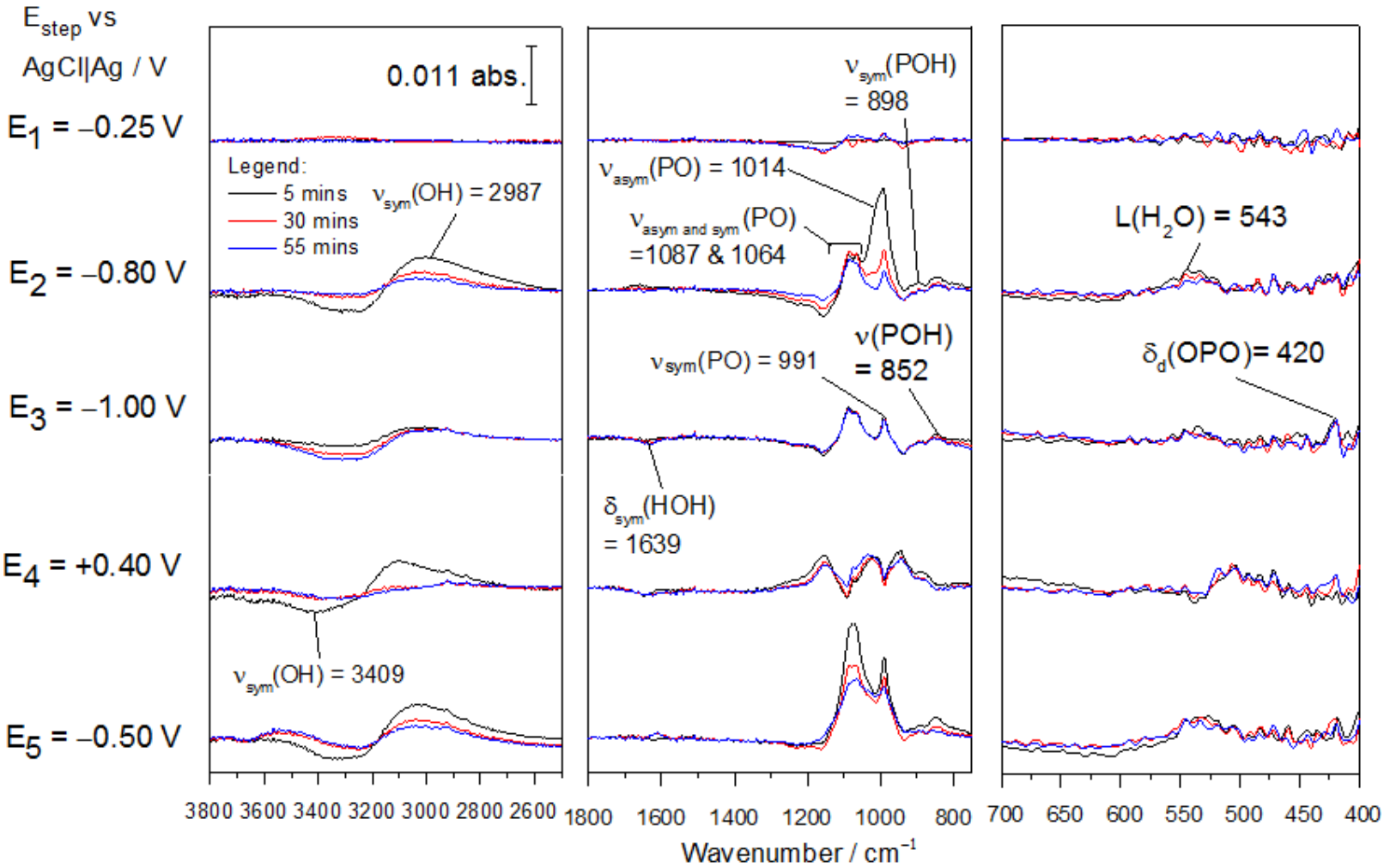

Figure 4.14 In-situ FTIR of greigite in phosphate buffer solution pH 6.8 under argon recorded on applying potential steps of −0.25, −0.80, −1.00, +0.40 and −0.50 V for one hour each step. Spectra displayed at each potential step were recorded at 5, 30 and 55 mins into holding the potential.

At −0.25 V, no significant change in absorbance was recorded at both pH 4.5 and 6.8. Only a small change in absorbance for the ν_{asym}(POH), ν_{sym}(PO) and ν_{asym}(PO) IR bands of $H_2PO_4^-$ species at 945, 1075 and 1165 cm^{-1} was recorded at pH 4.5 (see Figure 4.15) and additionally, at pH 6.8 (see Figure 4.16), a small gain in absorbance for the ν_{sym}(PO) and ν_{asym}(PO) IR bands of HPO_4^{2-} species at 991, 1064 and 1087 cm^{-1} was also observed. These minimal absorbance changes represent equilibration of the phosphate electrolyte species within the interfacial layer between the electrode and the ATR prism. These small changes are in agreement with the XANES spectra recorded at both pH 4.5 and 6.8 under nitrogen in the previous section, where little change in the XANES spectra was observed. Correlating this to the Pourbaix diagram in Figure 3.2, greigite was predicted to be stable at −0.25 V in both pH 4.5 and 6.8. Thus, the minimal change in IR absorbance at both pHs at this potential was expected, indicating no redox reactions occurred, which is consistent with the CVs of greigite at both pH where no redox feature was observed at this potential.

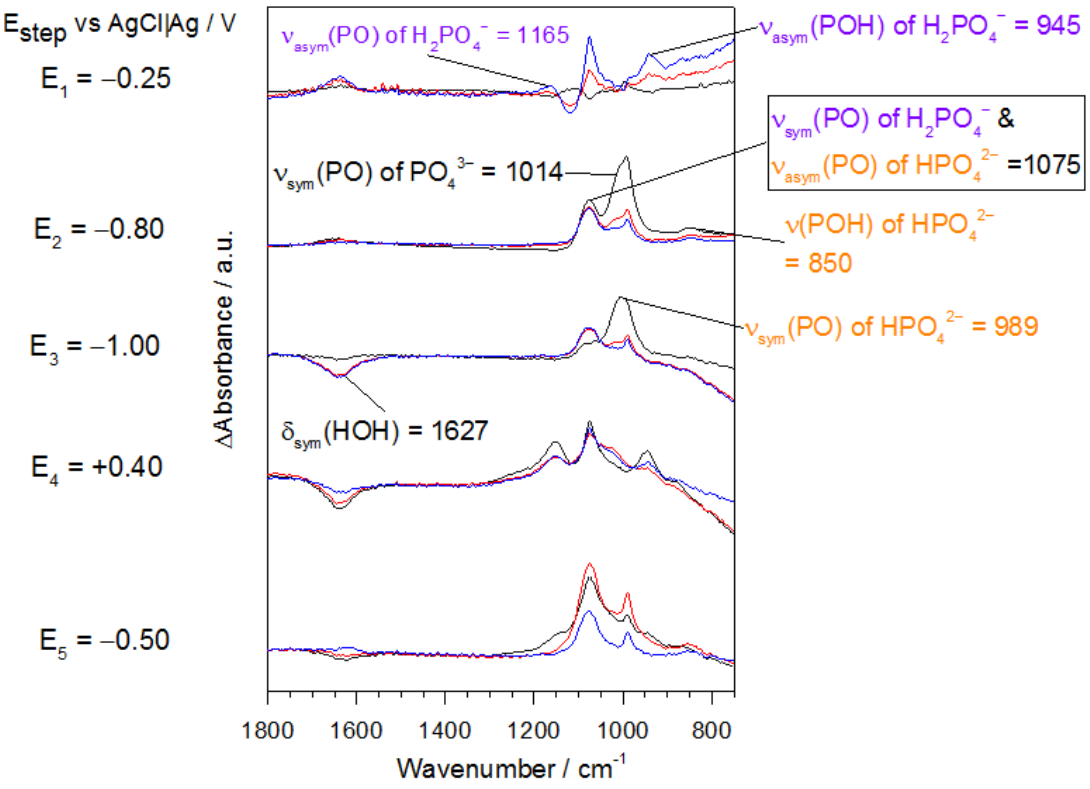

Figure 4.15 Close up of FTIR spectra between 1800 - 750 cm^{-1} of greigite in phosphate buffer solution pH 4.5 under argon. Absorbance axes not to scale. (Black = 5 mins, red = 30 mins, blue = 55 mins).

On applying −0.80 V, a drastic increase in absorbance was recorded at both pHs corresponding to the ν_{sym}(PO) and ν_{asym}(PO) IR bands of HPO_4^{2-} species at 989 and 1075 cm^{-1}. A small shoulder at 1014 cm^{-1} and a small IR peak at *c.a.* 420 cm^{-1} observed at both pHs were assigned to the ν_{sym}(PO) and δ_d(OPO) IR band of PO_4^{3-} species. Compared to the spectral features at −0.25 V at pH 4.5, the IR peaks of $H_2PO_4^-$ species were no longer present on applying −0.80 V at pH 4.5. At pH 6.8, a peak splitting at 1064 and 1087 cm^{-1} was observed which can be attributed to the simultaneous loss of $H_2PO_4^-$ species and gain of HPO_4^{2-} species. The increase in absorbance for the IR bands of HPO_4^{2-} and PO_4^{3-} species at −0.80 V in both pH 4.5 and 6.8 reflects an increase in concentration of both species present within the interfacial layer between the greigite electrode surface and the ATR prism. The increase in concentration of these phosphate species may be a result of a change in the solution pH near the electrode due to water and proton reduction occurring at this potential at both pHs:

$$2H_2O + 2e^- \rightarrow H_2 + 2OH^- \quad (4.1)$$

$$2H^+ + 2e^- \rightarrow H_2 \quad (4.2)$$

$$H_2PO_4^- \rightarrow HPO_4^{2-} + H^+ \quad (4.3)$$

$$HPO_4^{2-} \rightarrow PO_4^{3-} + H^+ \quad (4.4)$$

Water reduction **(4.1)** generates OH^- species which may increase the local pH near the electrode surface. If the local pH was greater than 8, the formation of green rust iron hydroxide is favoured according to the Pourbaix diagram in Figure 3.3. Production of H_2 bubbles on the electrode surface via water **(4.1)** or proton **(4.2)** reduction may also block the surface of the ATR prism and reduce the IR signal corresponding to water molecules present within the sampling region. This was evident at −0.80 V at which there was an absorbance loss for bulk water IR band ν_{sym}(OH) at 3306 cm^{-1} in pH 4.5 and at 3409 cm^{-1} in pH 6.8, and a gain in absorbance for ν_{sym}(OH) of H-bonded OH^- species at *c.a.* 3000 cm^{-1} in both pHs. [21]

The consumption of protons via proton reduction at −0.80 V may shift the equilibrium of **(4.3)** and **(4.4)** and result in the deprotonation of $H_2PO_4^-$ to form HPO_4^- and HPO_4^{2-} to form PO_4^{3-}. The formation of PO_4^{3-} species is evident in the

spectra at −0.80 V in both pHs where the ν_{sym}(PO) IR band of PO_4^{3-} species was present at 1014 cm^{-1}. Reaction **(4.4)** has a pKa of 12.3 which implies that the production of PO_4^{3-} species near the electrode surface will increase the local pH to > 12 on application of −0.80 V. However, this IR peak at 1014 cm^{-1} gradually decreased over time which suggests that PO_4^{3-} species was not continuously formed and the pH increase was not permanent. This sudden increase in local pH > 12 may result in the formation of iron oxide or hydroxide at −0.80 V. This provides support for the characteristic increase in white line intensity in the XANES spectra at both pH 4.5 and 6.8 observed previously at −0.80 V. Separately, the IR bands of HPO_4^{2-} species at c.a. 990 and 1075 cm^{-1} remain present in the spectra at both pHs over time on applying −0.80 V which suggests that the local pH near the electrode surface remained higher than the pH of the bulk electrolyte (local pH near electrode > 7 based on pKa of 7.2 of reaction **(4.3)**).

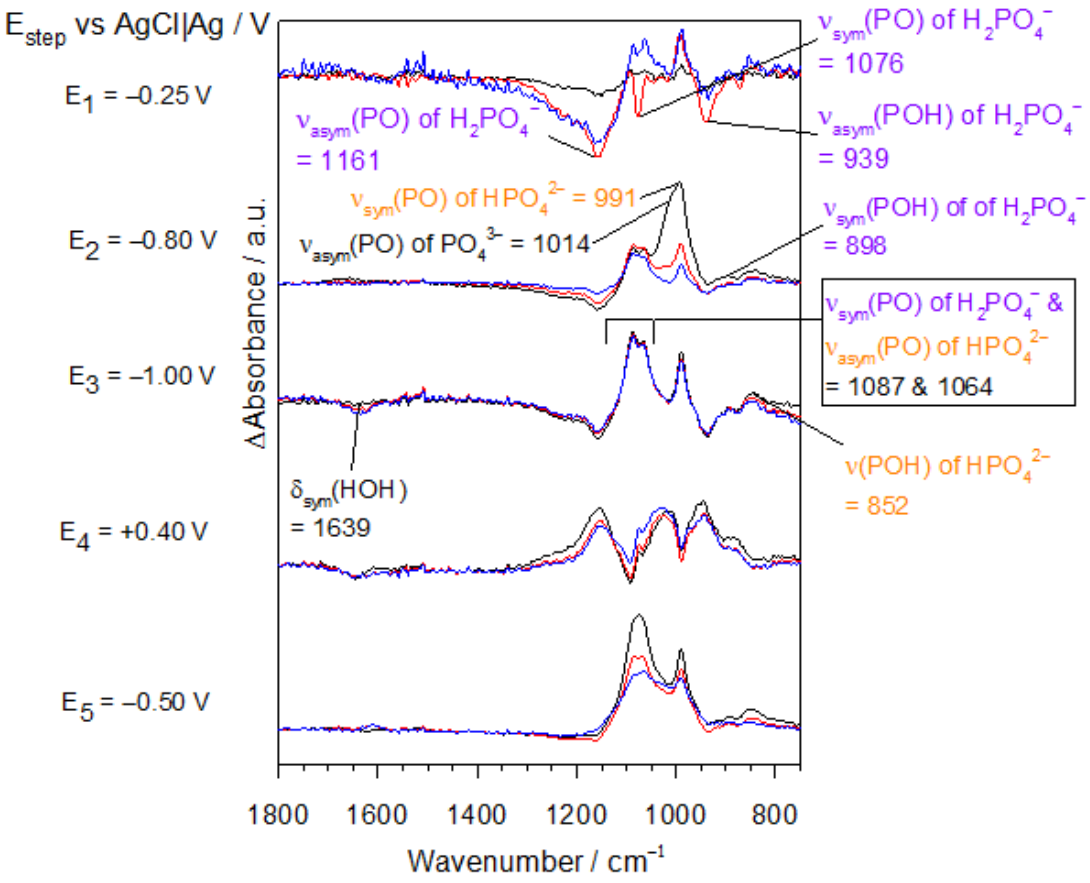

Figure 4.16 Close up of FTIR spectra between 1800 - 750 cm^{-1} of greigite in phosphate buffer solution pH 6.8 under argon. Absorbance axes not to scale. (Black = 5 mins, red = 30 mins, blue = 55 mins).

Overall, the changes in the spectra at both pHs show the phosphate groups present near the electrode surface responding to a change in the solution pH (buffering) caused by water and proton reduction. The changes in absorbance of the phosphate species also provide evidence for the increase in the local pH near the electrode which may lead to the formation of iron oxide or hydroxide on the surface of greigite. If the local pH remained constant and is equal to the bulk solution pH, according to the Pourbaix diagram in Figure 3.2, at −0.80 V, greigite is predicted to reduce to FeS and H_2S at pH 4.5 and to FeS and HS^- at pH 6.8. If the local pH near the electrode increased to pH > 12 due to water and proton reduction in both the pH 4.5 and 6.8 electrolytes, the reduction of greigite to FeS and HS^- species is predicted, while any iron oxide or hydroxide layer formed will remain stable (according to the Pourbaix diagram in Figure 3.1).

The IR stretching vibration of the FeS bond, ν(FeS), of both greigite and FeS occurs at the same characteristic IR position of *c.a.* 420 cm^{-1}. However, lattice vibrations of solid-state materials such as FeS and greigite will not be detectable using this technique since the sampling region is the interfacial electrolyte layer between the electrode and the ATR prism. Regardless of the absence of this Fe-S IR band in the spectra, the detection of Fe-S IR band will not be useful to distinguish between greigite or FeS. This is also comparable to the XANES spectra at pH 4.5 and 6.8 in the previous section where there was also no direct evidence of greigite to FeS transformation. As XANES and IR cannot discriminate between FeS_4 and FeS, the detection of H_2S or HS^- species is essential to verify this reaction assignment.

$$Fe_3S_4 + 2H^+ + 2e^- = 3FeS + H_2S \qquad (4.5)$$
$$Fe_3S_4 + H^+ + e^- = 3FeS + HS^- \qquad (4.6)$$

H_2S possess characteristic IR bands at 1186 and 2580 cm^{-1} corresponding to δ(H_2S) and ν(SH), respectively. In the spectra at pH 4.5 and 6.8, no IR bands were detected at these wavenumber positions. It is most likely that the technique was not sensitive enough to detect small quantities of H_2S or HS^- produced from the reduction of greigite. As the spectra were recorded every 5 minutes, H_2S and HS^-

produced on the electrode surface may also have dispersed away from the sampling region above the ATR prism and remained undetected. The release of H_2S at pH 4.5 or HS^- species at pH 6.8 from the electrode surface is not expected to shift the solution pH near the electrode surface as H_2S is stable at pH < 7 while HS^- species is stable at pH > 7.

On applying a further negative potential of −1.00 V at pH 4.5 and 6.8, similar changes in IR absorbance at −0.80 V were observed at pH 4.5, however, at pH 6.8 the IR bands remained constant with only the IR bands of HPO_4^{2-} species at c.a. 990 and 1075 cm^{-1} present. The $\nu_{sym}(PO)$ of PO_4^{3-} species at 1014 cm^{-1} was absent at pH 6.8. At pH 4.5 at −1.00 V, the broad band at 989 cm^{-1} (overlapping band at 1014 cm^{-1}) decreased over time, following a similar pattern observed at −0.80 V. This suggests that PO_4^{3-} species were produced at pH 4.5, but not at pH 6.8 at −1.00 V and therefore, proton and water reduction must have continued on applying −1.00 V at pH 4.5, but not in pH 6.8. This was evident by the H_2 bubbles generated during the XANES and CV experiments where more bubbles were evident on the electrode surface in pH 4.5 compared to in pH 6.8 electrolyte. Production of H_2 is also evident in the IR spectra at this potential at both pHs where the decrease in absorbances for IR bands of $\delta(H_2O)$ and $\nu_{sym}(OH)$ at *c.a.* 1630 and 3300 cm^{-1} indicate the loss of surface bound and bulk water due to the presence of H_2 bubbles blocking the surface of ATR prism.

With the evidence of an increased local pH near the electrode on applying potentials of −0.80 and −1.00 V, as shown by the changes in the IR absorbances of the phosphates species, due to water and proton reduction in both pHs, it is likely that an iron oxide or hydroxide layer may have formed on the greigite electrode. It is expected that the bulk structure of the electrode remained as greigite / FeS with a layer of iron oxide or hydroxide present. This proposed hypothesis for the formation of an iron oxide or hydroxide layer on the surface of greigite due a shift in pH caused by water and proton reduction is further supported by the changes in the XANES data in both pH 4.5 and 6.8 presented at the beginning of this chapter. In the previous section of the XANES results, there was an increased white line intensity on applying −0.80 and −1.00 V which was

associated with an increase in coordination of oxygen to Fe via hydration of Fe^{2+} dissolved species forming $[Fe(H_2O)_6]^{2+}$ or the coordination of H_2O at the surface of the greigite nanoparticles. However, with the evidence of increased local pH (pH > 12 due to the presence of PO_4^{3-} species) in the IR spectra, it is most likely that the observed increase in white line intensity in the XANES spectra is indeed associated with the formation of an iron oxide or hydroxide layer on the surface of the greigite nanoparticles. Amorphous iron was also proposed to have formed at −1.00 V in pH 4.5 only, based on the decrease in the edge position in the XANES spectra which denotes a lowering of the oxidation state of Fe. The evidence for the formation of iron oxide or hydroxide in the XANES spectra at both pH, and additionally the formation of amorphous iron at pH 4.5, coupled with the presence of the pre-edge feature characteristic of Fe-S bonds, suggest that the transformation of greigite to iron oxide or hydroxide (and amorphous iron at pH 4.5 only) was most likely confined to the greigite surface and is not a bulk transformation of greigite to iron oxide / hydroxide or amorphous iron.

On applying a positive potential of +0.40 V, there was a general decrease in IR absorbance observed at both pH 4.5 and 6.8. The IR bands of HPO_4^{2-} species decreased in absorbance (*c.a.* 989 and 1075 cm^{-1}), while the IR bands of $H_2PO_4^-$ species increased in absorbance (*c.a.* 945, 1075 and 1165 cm^{-1}). The concurrent increase and decrease of HPO_4^{2-} and $H_2PO_4^-$ species suggest it is likely that HPO_4^{2-} species was re-protonated to form $H_2PO_4^-$ species, induced by the application of +0.40 V. Based on the absence of PO_4^{3-} species and the predicted region for water oxidation in the Pourbaix diagram in Figure 3.2, it is unlikely that water oxidation occurred at this potential as the local pH needs to be greater than pH 10 for this to occur. At this point, the local pH within the interfacial layer is likely to be greater than 7.5 but less than 10 (based on HPO_4^{2-} and $H_2PO_4^-$ species present). According to the Pourbaix diagram in Figure 3.2 and 3.3, between pH 7.5 – 10, FeS is predicted to oxidise to Fe_2O_3 or green rust iron hydroxide, any iron oxide or hydroxide layer present will remain stable, iron will oxidise to Fe^{2+} or iron oxide / hydroxide, while any HS^- species present will oxidise to SO_4^{2-} species. However, on inspection of the FTIR data at both pHs, there is no evidence for the formation of Fe_2O_3 and SO_4^{2-} species at +0.40 V at both pHs. It is likely that

the technique was not particularly sensitive to solid-state transformations as only the electrolyte interfacial region between the ATR prism and electrode is probed. SO_4^{2-} species possess a characteristic IR band at *c.a.* 1100 cm^{-1} which may be hidden under the IR bands of $H_2PO_4^-$ species.

On reversing the potential to −0.50 V, a similar increase in absorbance of IR peaks of HPO_4^{2-} species, previously observed at −0.80 and −1.00 V, was recorded. The reproduced changes in absorbance at −0.50 V indicate the reproducibility of the reactions occurring within the interfacial layer, which was the deprotonation of $H_2PO_4^-$ species to form HPO_4^{2-} species due to water and proton reduction. At this potential, FeS and SO_4^{2-} species are the predicted stable redox species. As previously stated, the technique is not sensitive to lattice vibrations of solid-state materials since only the interfacial electrolyte layer between the electrode and ATR prism is probed. Additionally, IR bands of SO_4^{2-} species were not observed and may have been masked by the large increase in absorbance of HPO_4^{2-} species at this potential. It is plausible that the masking of SO_4^{2-} species IR bands indicate the loss of S species may not continue beyond the first potential sweep, but this is dependent on the surface and bulk structure of greigite at each potential applied. This is applicable if the surface was passivated by the formation of iron oxide or hydroxide, which may hinder loss of S as SO_4^{2-} species from the bulk structure, or if there was a complete loss of S from the bulk structure (complete transformation of greigite to Fe_2O_3, as predicted at +0.40 V in the Pourbaix diagram in Figure 3.2).

4.3.3.1.1 Feasibility of local pH changes due to water reduction

The feasibility of the proposed local pH changes due to water reduction occurring, thus stabilising oxides / hydroxides at bulk solution pHs at which they are predicted to be unstable, can be tested by equating the flux of hydroxide ions formed by water reduction at an electrode, forming H_2 at current density j and the diffusional flux of hydroxide ions away from the surface, driven by their surface concentration being greater than that in the bulk solution.

At steady state, the rate of proton production or consumption is equal to the rate of proton diffusion:

For OH^- generating reaction:

$$\frac{j}{2F} = \frac{D_{OH^-}}{\delta}\{[OH^-]_{x=0} - [OH^-]_{x=\delta}\}$$

where j is the current density, F is the Faraday's constant, D_{OH^-} is the diffusion coefficient of hydroxide ions and δ is the diffusion layer thickness.

Determination of electrode pH and PO_4^{3-} concentration:

Ignoring buffering effects:

$$[OH^-]_{x=0} = \frac{j.\delta_N}{2F.D_i} + [OH^-]_{x=\delta} \qquad \text{Eq. 1}$$

Current density, $j = 1 \times 10^{-3}$ A cm^{-2} (approx. order of magnitude from CV)

Diffusion coefficient of hydroxide ions, $D_{OH^-} = 5 \times 10^{-5}$ cm^2 s^{-1} (from reference [35])

Approximate values of diffusion layer thickness, δ, calculated using $\delta = \sqrt{2Dt}$

Time/s	δ/cm	Experimental setup
80	0.09	CV at slow scan rate from 0.00 up to −0.80 V
300	0.17	Time between each IR spectra collected
6000	0.77	Time between each XAS spectrum recorded

Using Eq. 1 to calculate $[OH^-]_{x=0}$ and electrode pH:

Time /s	δ/cm	Δ[OH⁻]/ mol cm^{-3}	$[OH^-]_{x=0}$ = Δ[OH⁻] + $[OH^-]_i$ / mol dm^{-3}	pH
80	0.09	9.27 x 10^{-6}	9.2701 x 10^{-3}	11.96
300	0.17	1.80 x 10^{-5}	1.80001 x 10^{-2}	12.25
6000	0.77	8.02 x 10^{-5}	8.02001 x 10^{-2}	12.90

Change in OH^- concentration: $\Delta[OH] = \frac{j\delta}{2FD}$

Concentration of OH^- at electrode:

$[OH^-]_{x=0} = \Delta[OH^-] + [OH^-]_i$, where $[OH^-]_i = 1 \times 10^{-7}$

Final pH at electrode: pH = 14 – pOH = 14 – (–log[OH^-])

Calculation of concentration of PO_4^{3-}:

pH	Ratio PO_4^{3-}/HPO_4^{2-}	Fraction of PO_4^{3-}	$[PO_4^{3-}]$ / mol dm^{-3}
11.96	0.531	0.347	0.035
12.25	0.708	0.414	0.041
12.90	1.356	0.576	0.058

Using Henderson-Hasselbalch equation:

$$pH = pK_a + \log_{10}\left(\frac{[A^-]}{[HA]}\right)$$

Ratio of PO_4^{3-}/HPO_4^{2-}: $\frac{[A^-]}{[HA]} = e^{(pH-pK_a)}$

Fraction of PO_4^{3-}:

$$\frac{[A^-]}{[HA]+[A^-]} = \frac{Ratio.[HA]}{[HA]+Ratio.[HA]} = \frac{Ratio}{1+Ratio}$$

Concentration of PO_4^{3-}: $[PO_4^{3-}]$ = 0.1 x Fraction of PO_4^{3-}

Therefore, an increase of pH to >11 is certainly feasible at slow CV scan rates (10 mV s^{-1}) and to pH 12 at the longer timescales of the in situ spectroscopy. In other studies[33], changes in absorbance intensity to concentration of solution species were calibrated and the spectral changes observed were consistent with concentration changes in the mM range, as predicted in these calculations.

4.3.3.2 PBS pH 4.5 and 6.8 under CO_2

The in-situ FTIR spectra of greigite in CO_2-saturated pH 4.3 (Figure 4.17) resemble those recorded in pH 4.5 under argon (Figure 4.13), and no new IR bands corresponding to dissolved CO_2 species were present. This is in agreement with the unaffected CV response of greigite in PBS pH 4.5 on introduction of CO_2 detailed in chapter 3. However, one significant difference observed in the spectrum of greigite in pH 4.3 under CO_2 compared to pH 4.5 under argon was the significant loss in IR absorbance at *c.a.* 1635 and 3300 cm^{-1} corresponding to $\delta(H_2O)$ of surface water and $\nu_{sym}(OH)$ of bulk water respectively, which suggests significant water and proton reduction occurring on the greigite electrode. Water and proton reduction will produce H_2 bubbles on the electrode surface which may cover the surface of the ATR prism and reduce the IR signal corresponding to water molecules present within the sampling region.

Similar to the spectra in pH 4.5 under argon, IR bands of $H_2PO_4^-$ species were observed at −0.25 V, while at −0.80 V IR bands of HPO_4^{2-} species were observed in the spectra of CO_2-saturated pH 4.3. The similar pattern of deprotonation of $H_2PO_4^-$ to HPO_4^{2-} species proposed at pH 4.5 under argon, caused by proton reduction occurring at this potential, also occurred in the CO_2-saturated pH 4.3. Thus, it is proposed here the local pH near the electrode under CO_2 will also increase to pH > 7 due to the consumption of protons via proton reduction as well as the increase in concentration of OH^- species generated by water reduction. However, one major difference observed was the absence of the IR band of PO_4^{3-} species at *c.a.* 1010 cm^{-1} in pH 4.3 under CO_2 which was present in pH 4.5 under argon. The absence of PO_4^{3-} species suggests that the introduction of CO_2 may have suppressed proton and water reduction, preventing a significant increase in the local pH near the electrode (to pH > 12). There is also an additional presence of ν_{asym} and ν_{sym} (OCO) IR bands of HCO_3^- species at 1610 and 1361 cm^{-1} arising from the introduction of CO_2.

$$CO_2 + H_2O = HCO_3^- + H^+ \qquad (4.7)$$

Correlating the unchanged spectral features of the IR spectra at pH 4.3 under CO_2 (which was most likely to be pH > 7 due to proton reduction) to the Pourbaix diagram in Figure 3.6, no IR bands corresponding to siderite / iron carbonate were detected, which was as predicted by the Pourbaix diagram in Figure 3.6 (siderite absent at pH 7.5 between 0.00 and −1.00 V).

In the spectra of greigite in pH 6.5 on introduction of CO_2, an IR band at 1396 cm^{-1} assigned to $\nu_{asym}(OCO)$ of CO_3^{2-} species at 1396 cm^{-1} was observed (Figure 4.18).[19–21] In general, the IR spectral features were similar at pH 6.8 under argon and 6.5 with CO_2, including the IR band of PO_4^{3-} species at 1010 cm^{-1}. The presence of PO_4^{3-} species, generated via deprotonation of HPO_4^{2-} caused by water and proton reduction, indicates a shift of local pH to pH > 12. The new IR peak of CO_3^{2-} species was only observed on applying potential of −0.80 and −1.00 V. The presence of CO_3^{2-} species within the interfacial layer near the electrode surface may arise due to further shift in pH caused by water reduction which generate OH^- species, occurring at these potentials (−0.80 and −1.00 V).

$$CO_2 + OH^- = HCO_3^- \qquad (4.8)$$
$$HCO_3^- + OH^- = CO_3^- + H_2O \qquad (4.9)$$

The IR band of PO_4^{3-} species decreased over time on applying −0.80 and was not present at −1.00 V. This suggests that the local pH shift to pH > 12 was temporary, however, the IR bands of HPO_4^{2-} and CO_3^{2-} species remained at −1.00 V. The presence of both species suggest that the local pH near the electrode may be between pH 7 - 12 in the pH 6.5 electrolyte under CO_2. Within this pH range, according to the Pourbaix diagram in Figure 3.5 and 3.6, the formation of siderite is not expected. The formation of $Fe_2(OH)_2CO_3$ and $Fe_2(OH)_{12}CO_3$ were predicted in Figure 3.5 between pH 8 – 12 at −1.00 V, however, these are metastable phases hence not expected to form.

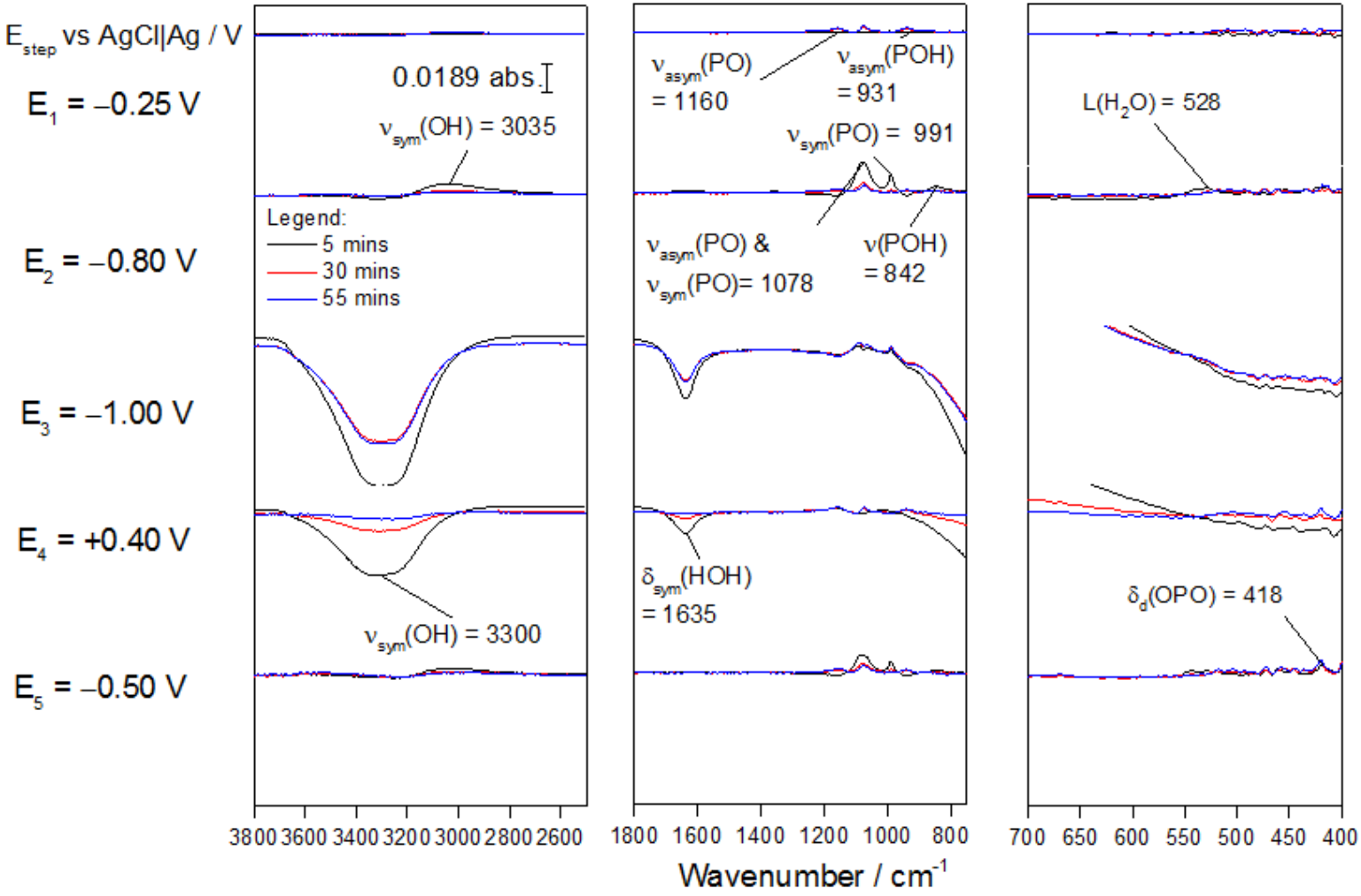

Figure 4.17 In-situ FTIR of greigite in phosphate buffer solution pH 4.3 under CO_2 recorded on applying potential steps of −0.25, −0.80, −1.00, +0.40 and −0.50 V for one hour each step. Spectra displayed at each potential step were recorded at 5, 30 and 55 mins into holding the potential.

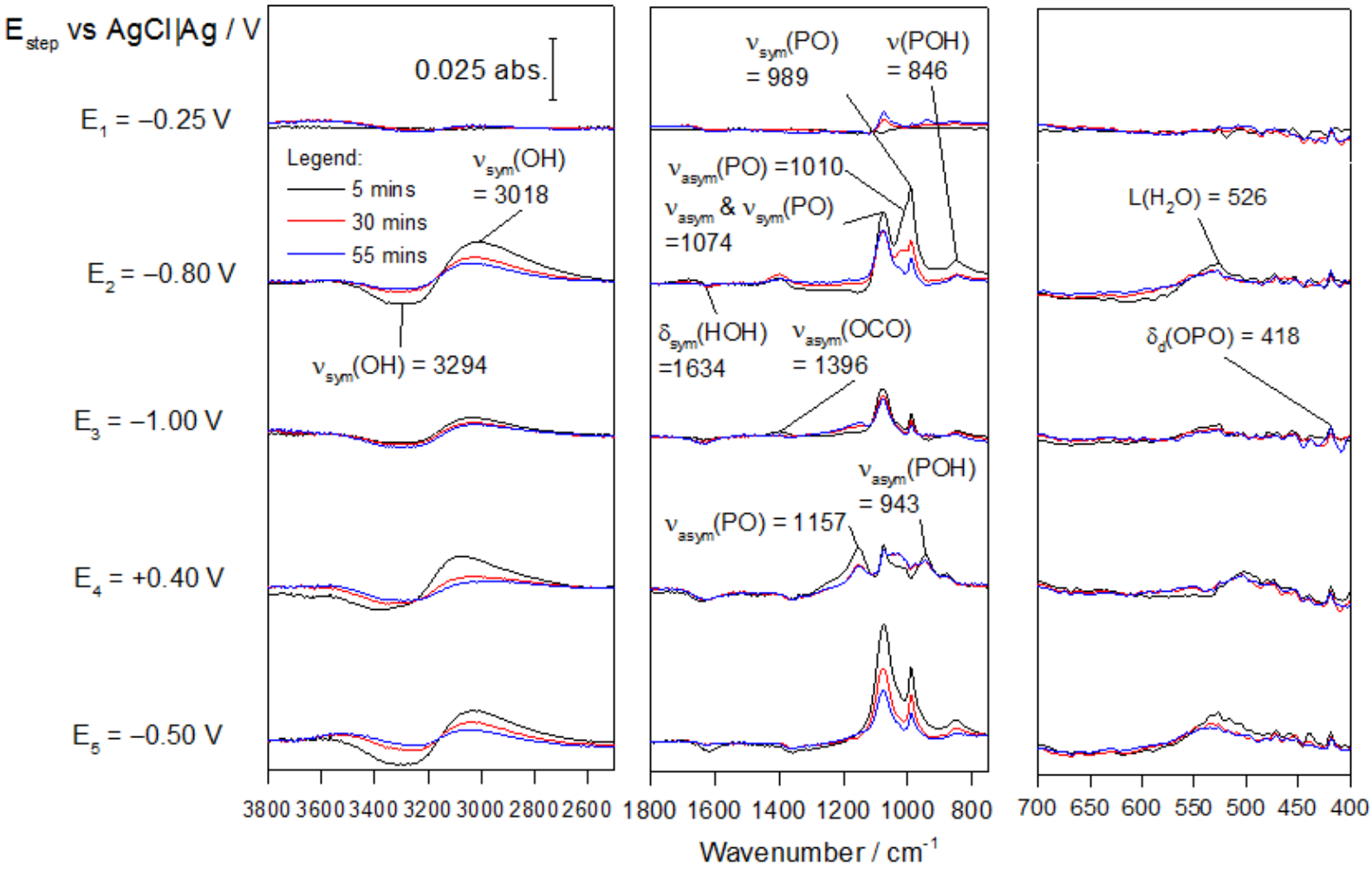

Figure 4.18 In-situ FTIR of greigite in phosphate buffer solution pH 6.5 under CO_2 recorded on applying potential steps of −0.25, −0.80, −1.00, +0.40 and −0.50 V for one hour each step. Spectra displayed at each potential step were recorded at 5, 30 and 55 mins into holding the potential.

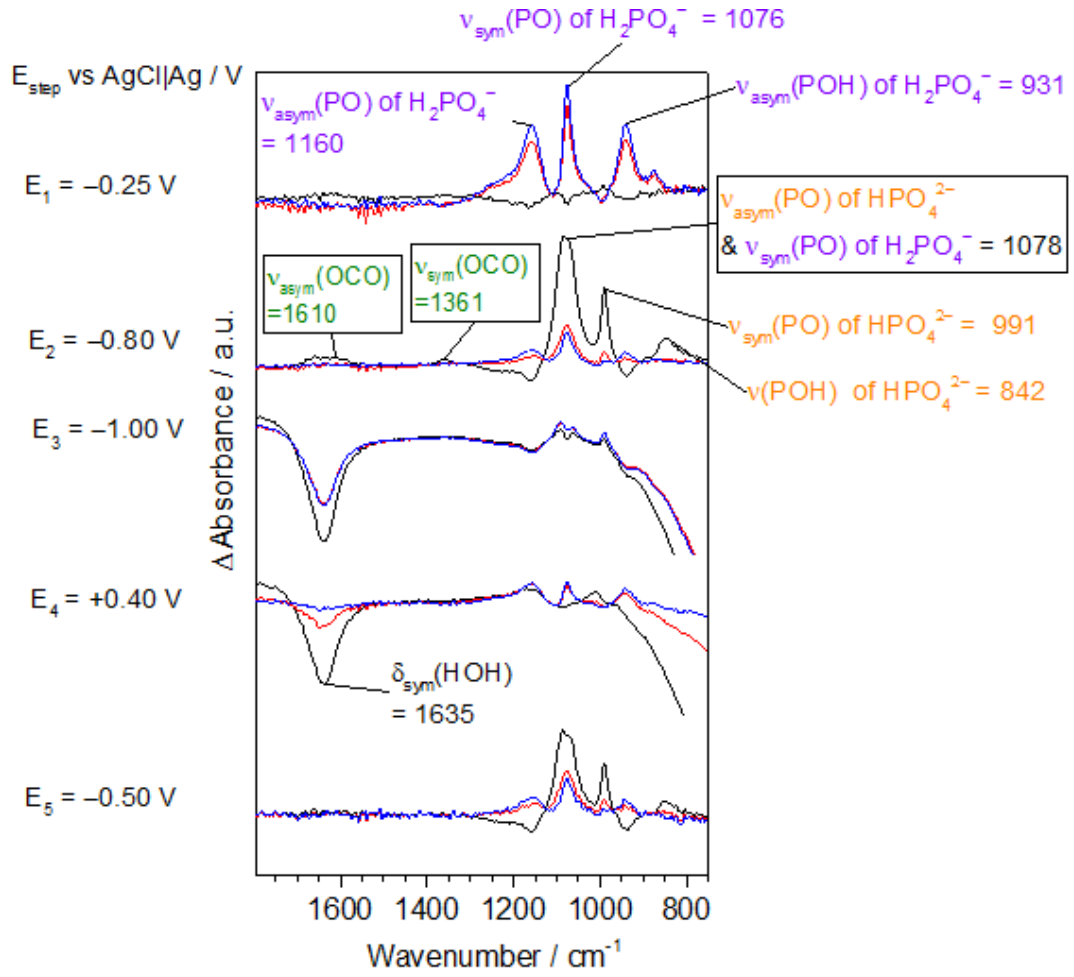

Figure 4.19 Close up of FTIR spectra between 1800 - 750 cm^{-1} of greigite in phosphate buffer solution pH 4.3 under CO_2. Absorbance axes not to scale. (Black = 5 mins, red = 30 mins, blue = 55 mins).

It is important to highlight the evidence of the presence of CO_3^{2-} species observed in pH 6.5 and HCO_3^- species in pH 4.3 under CO_2, which suggests that there is potential for the adsorption of dissolved CO_2 species on the greigite surface. In the previous chapter, the currents in the CVs of greigite at pH 4.5 remained unchanged on introduction of CO_2 while at pH 6.8 the currents were significantly suppressed. These differences may be attributed to the identity of the dissolved CO_2 species adsorbed on the greigite surface, CO_3^{2-} species at pH 6.5 and HCO_3^- species at pH 4.3, as evidenced in the FTIR spectra at both pH. However, according to DFT calculations, the adsorption of HCO_3^- species is favoured over CO_3^{2-} species on greigite surfaces and thus the IR bands of HCO_3^- species were expected to be present at both pHs.[36] It is likely that HCO_3^- species were present in pH 6.5 under CO_2 (but not observed in the FTIR spectra) and were

deprotonated to form CO_3^{2-} species. HCO_3^- species would appear at c.a. 1000, 1360-1390 and 1610-1630 cm^{-1}. The additional presence of the IR bands of CO_3^{2-} species only in the spectra at pH 6.5 suggest a significant increase in the local pH (between 7 and 12), causing the deprotonation of HCO_3^- to CO_3^{2-}. Thus, the suppression of currents in the CV of greigite at this pH may be due to the adsorption of both HCO_3^{2-} and CO_3^{2-} species.

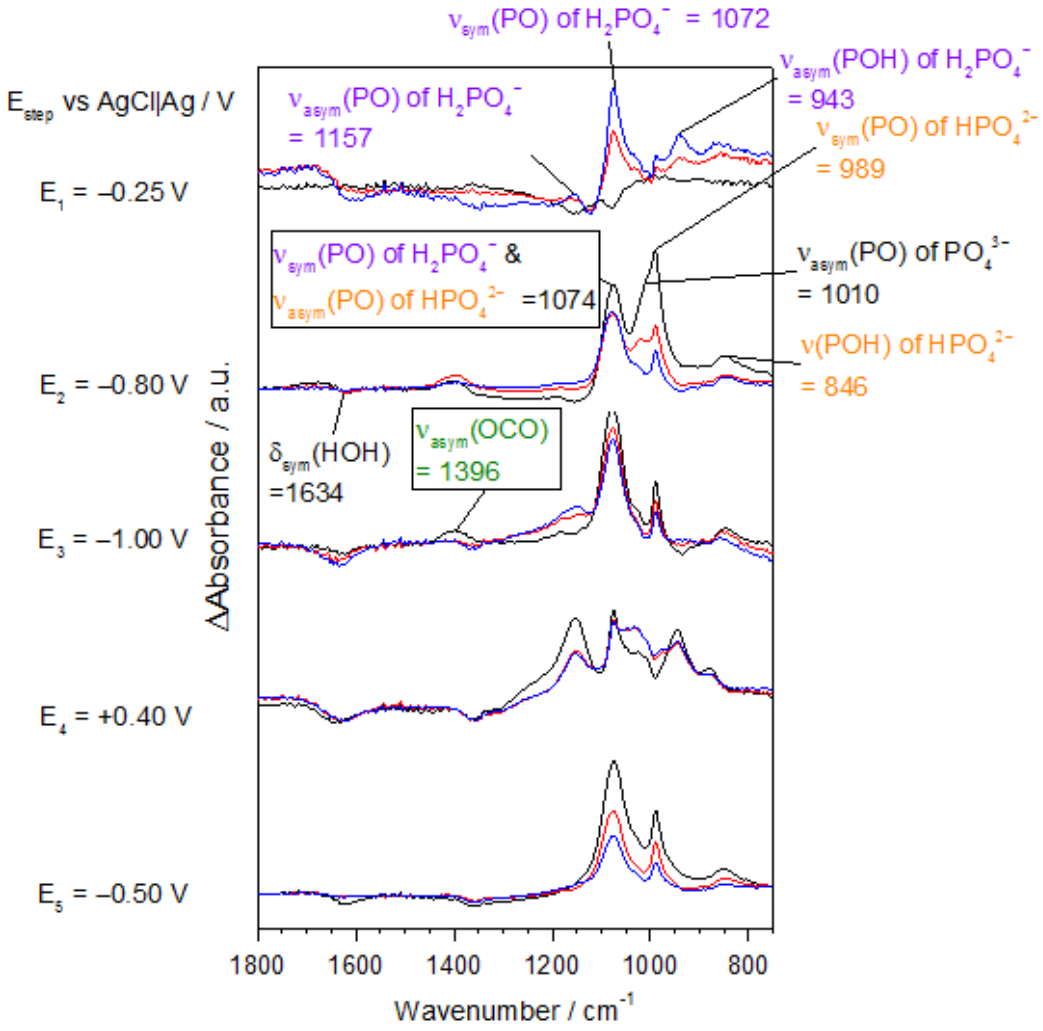

Figure 4.20 Close up of FTIR spectra between 1800 - 750 cm^{-1} of greigite in phosphate buffer solution pH 6.5 under CO_2. Absorbance axes not to scale. (Black = 5 mins, red = 30 mins, blue = 55 mins).

Comparing these observations to the XANES spectra under CO_2 at both pHs, it was previously proposed that the adsorption of CO_2 or its dissolved species may have prevented the competing adsorption of H_2O or even suppressed water reduction on the greigite electrode and slowed down the formation of an iron oxide or

hydroxide layer. The IR evidence for the presence of HCO_3^{2-} and CO_3^{2-} species in pH 6.5 and only HCO_3^{2-} species in pH 4.3 suggest these are the dissolved CO_2 species responsible for the prevention of iron oxide or hydroxide layers forming on greigite. The presence of these dissolved CO_2 species may have suppressed water reduction via adsorption onto the greigite surface, preventing –OH from reacting with the surface by blocking reactive sites / protecting the greigite surface, and prevented the formation of an iron oxide or hydroxide layer.

4.3.3.3 $KHCO_3$ pH 8.55 and K_2CO_3 pH 11.2 under argon

Figure 4.21 and Figure 4.22 show the in-situ FTIR spectra of greigite recorded in $KHCO_3$ pH 8.55 and K_2CO_3 pH 11.2 under argon, respectively. The assignments of the IR bands observed in the FTIR spectra recorded in both electrolytes are detailed in the following table:

Table 4.4 IR assignments at pH 8.55 and 11.2 under argon in Figure 4.21 and Figure 4.22 where ν is stretching vibration, ν_{sym} is symmetric stretching vibration, ν_{asym} is asymmetric stretching vibration and δ is bending vibration.

Assignment	IR peaks at pH 8.55 / cm^{-1}	IR peaks at pH 11.2 / cm^{-1}	Reference
H_2O / OH			
$\delta(H_2O)$	1639		29
ν_{sym}(OH) (H-bonded)	3060	3040	29
ν_{sym}(OH) (bulk water)	3321	3298	29
CO_3^{2-} species			
ν_{asym}(OCO)	1392	1398	20
HCO_3^- species			
ν_{asym}(OCO)		1616	20
ν_{sym}(OCO)	1358	1340	20
ν_{sym}(COH)	1000	1006	20

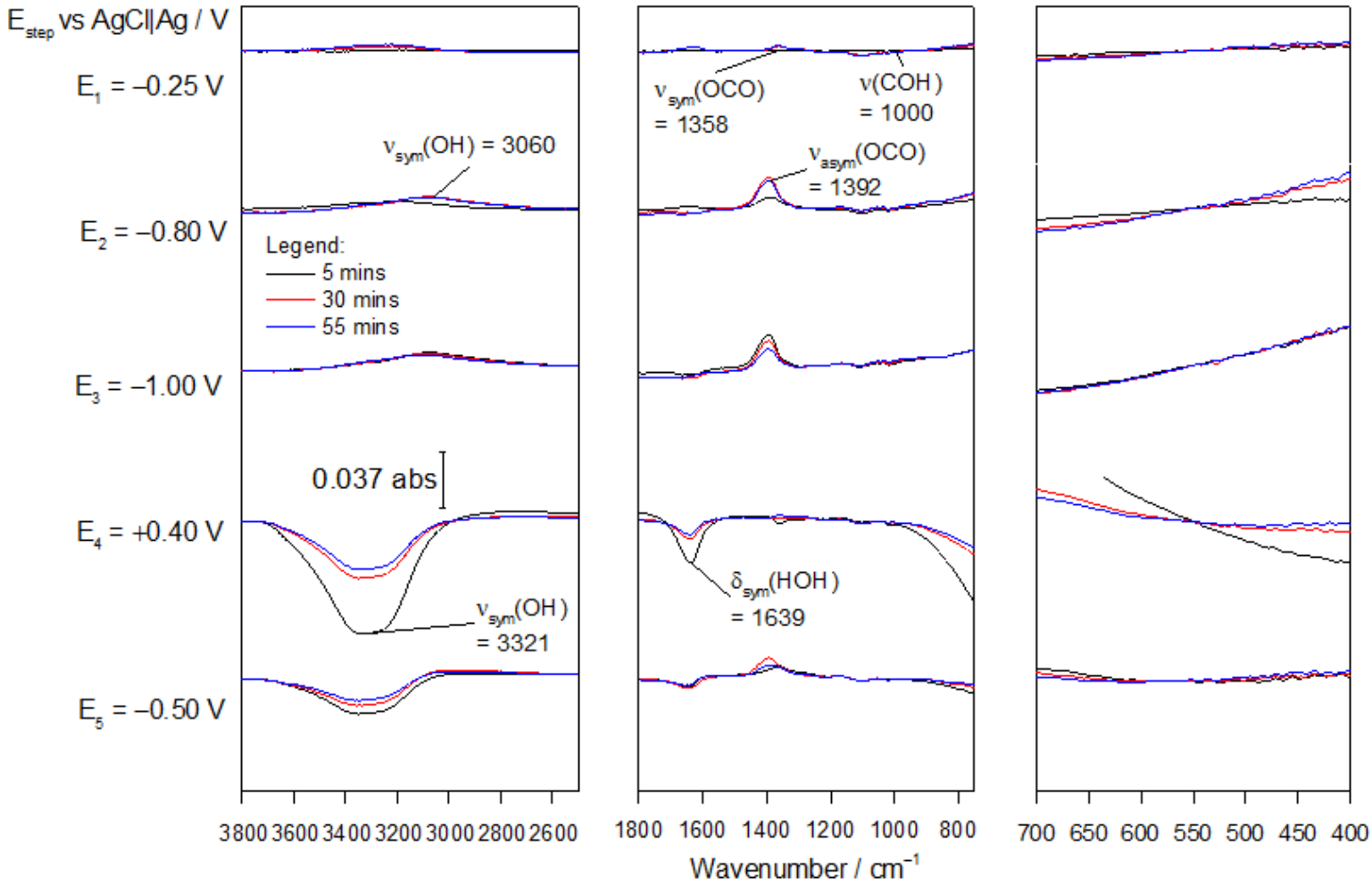

Figure 4.21 In-situ FTIR of greigite in $KHCO_3$ pH 8.55 under argon recorded on applying potential steps of −0.25, −0.80, −1.00, +0.40 and −0.50 V for one hour each step. Spectra displayed at each potential step were recorded at 5, 30 and 55 mins into holding the potential.

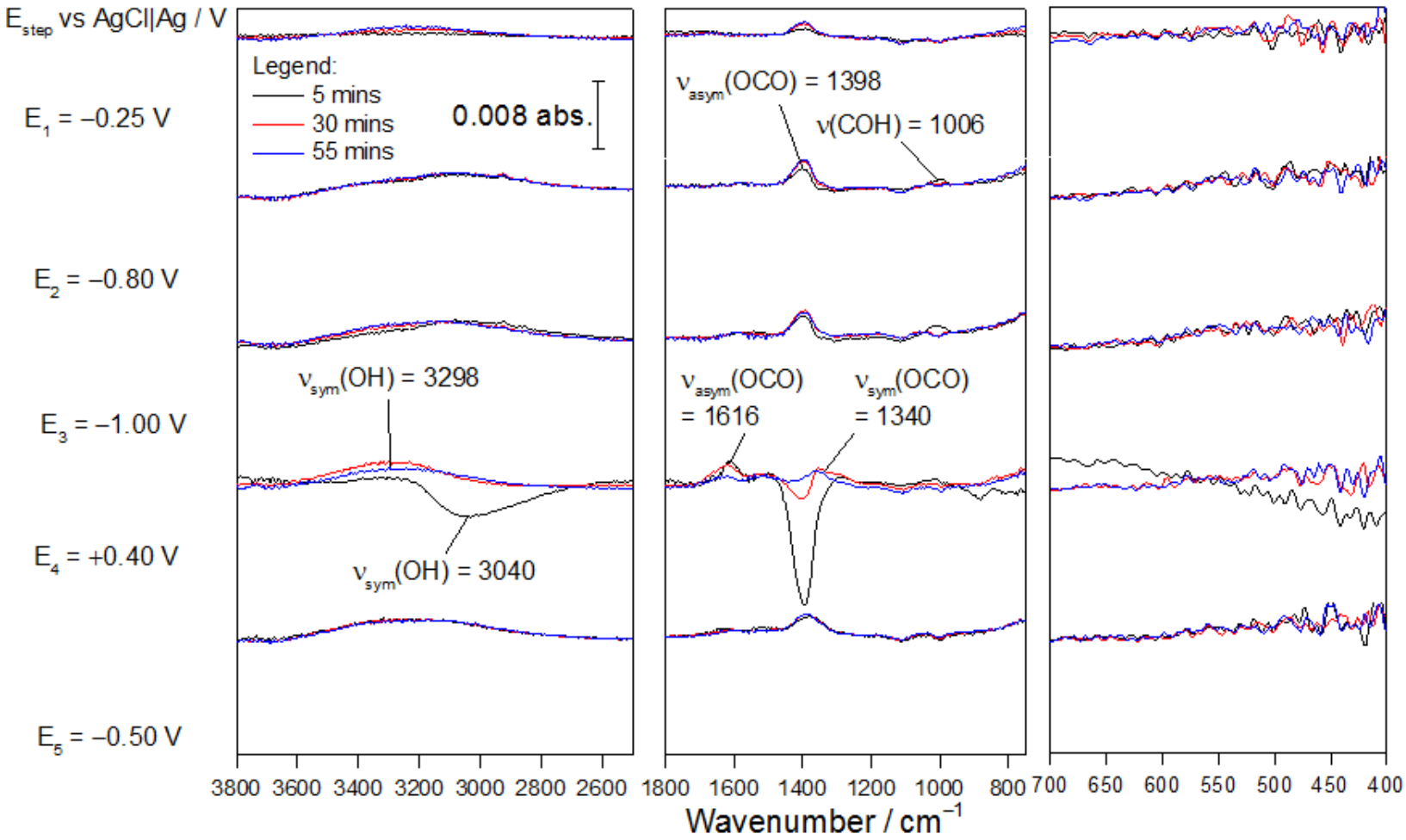

Figure 4.22 In-situ FTIR of greigite in K_2CO_3 pH 11.2 under argon recorded on applying potential steps of –0.25, –0.80, –1.00, +0.40 and –0.50 V for one hour each step. Spectra displayed at each potential step were recorded at 5, 30 and 55 mins into holding the potential.

In general, the spectra at both pHs displayed similar changes related to changes in the IR absorbance of CO_3^{2-} and HCO_3^- species. The presence of the IR bands of CO_3^{2-} species in the FTIR spectra in $KHCO_3$ may be due to a shift in equilibrium between HCO_3^- and CO_3^{2-} species at high pH / low proton concentration. The same reasoning is applied to the presence of HCO_3^- species in FTIR recorded in K_2CO_3. On applying −0.25 V, no significant changes in absorbance were recorded at both pH 8.55 and 11.2. This is in agreement with the conclusions derived based on the Pourbaix diagram in Figure 3.2, where greigite is predicted to be stable up to −0.50 and −0.70 V at pH 8.55 and 11.2, respectively.

On applying further negative potentials of −0.80 and −1.00 V, there was an increase in absorbance recorded for ν_{asym}(OCO) of CO_3^{2-} species at both pHs and additionally, for ν_{sym}(COH) of HCO_3^- species at pH 11.2. According to the Pourbaix diagram in Figure 3.2, at −0.80 and −1.00 V, greigite is predicted to undergo reduction to FeS at both pH 8.55 and 11.2. However, since the technique only probes the interfacial layer between the electrode and the ATR prism, the lattice vibrations of greigite and FeS will not be recorded and thus, the transformation will not be detectable. In contrast to the FTIR spectra of greigite at pH 4.5 and 6.8, no decrease in the ν_{sym}(OH) IR bands of H_2O were observed at both pH 8.55 and 11.2. This suggests that proton and water reduction were supressed, which may be associated with the presence of HCO_3^- and CO_3^{2-} species, as observed in pH 4.3 and 6.5 on introduction of CO_2. No IR bands related to H_2S, HS^- or SO_4^{2-} species were detected, which contradicts with the Pourbaix diagram in Figure 3.4, where HS^- species are predicted to be present at potentials below −0.60 V at both pH 8.55 and 11.2. A plausible explanation for the absence of any dissolved sulfur species at both pHs may be associated with the presence of CO_3^{2-} or HCO_3^- species present, which blocked the surface sites on greigite and prevented the release of dissolved sulfur species. This is consistent with the suppressed redox features in the CVs of greigite in K_2CO_3 pH 11.2 and $KHCO_3$ pH 8.55 compared to the CVs recorded in phosphate electrolytes pH 4.5 and 6.8.

Absorbance loss of ν_{sym}(OH) IR bands of H_2O corresponding to water reduction taking place were only observed on applying a positive potential of +0.40 V, at pH

8.55 only. This may be explained by referring to the Pourbaix diagram in Figure 3.2, where H_2O oxidation to O_2 is predicted at +0.40 V. If oxygen was generated on the electrode surface of greigite, it is most likely that the greigite surface will be oxidised to Fe_2O_3. However, such transformation will not be detected using this technique as the sampling region was the interfacial electrolyte layer between the electrode and ATR prism.

On reversing the potential to −0.50 V, similar spectral features were observed as at −0.80 and −1.00 V, at both pH 8.55 and 11.2. If Fe_2O_3 was present on the greigite electrode, according to the Pourbaix diagram in Figure 3.1, Fe_2O_3 will be stable at this potential at both pHs. If greigite remained on the electrode, it will also be stable according to the Pourbaix diagram in Figure 3.2.

The XANES data of greigite obtained in K_2CO_3 pH 11.2 under argon previously showed that greigite was transformed to a core-shell structure with an iron oxide or hydroxide layer on immersion into the electrolyte. Greigite was predicted to be stable up to −0.80 V at this pH according to the Pourbaix diagram in Figure 3.2. The Pourbaix diagram in Figure 3.2 did not account for possible surface transformation such as the formation of an iron oxide or hydroxide layer on the greigite surface due to high pH. It is possible that at both pH 8.55 and 11.2, the high concentration of OH^- species present near the electrode surface may coordinate onto Fe atoms of greigite and lead to the formation of an iron oxide or hydroxide layer on the greigite surface. With evidence for the suppression of water and proton reduction due to the presence of IR bands of HCO_3^- and CO_3^{2-} species, it seems likely that the local pH within the interfacial layer was high and ideal for the formation of an iron oxide and hydroxide layer on the greigite electrode.

4.3.3.4 $KHCO_3$ pH 8.55 and K_2CO_3 pH 11.2 under CO_2

Upon introduction of CO_2 in $KHCO_3$ and K_2CO_3, the pHs of the electrolytes decreased to pH 7.1 and 10.1, respectively. In the previous chapter, the CV response of greigite in $KHCO_3$ pH 7.1 under CO_2 was suppressed compared to that under argon at pH 8.55. Based on the Pourbaix diagram in Figure 3.6, the formation of siderite / iron carbonate, due to the shift in pH from 8.55 to 7.1, was proposed to have caused the suppression of the CV response. However, on inspection of the FTIR spectra of greigite in $KHCO_3$ pH 7.1, there is no evidence for the formation of siderite. The spectral features of greigite in $KHCO_3$ under argon and CO_2 were similar, with the exception of a significant gain in absorbance on introduction of CO_2 for the $\delta(H_2O)$ of surface water and $\nu_{sym}(OH)$ of bulk water at 1635 and 3344 cm^{-1}, respectively. No new IR peak corresponding to dissolved CO_2 species were detected in FTIR spectra in $KHCO_3$ pH 7.1 under CO_2. This implies that the suppression in current observed in the CV at pH 7.1 was not caused by the formation of siderite or the introduction of CO_2, but perhaps the shift in pH which may increase the competition of adsorption between CO_3^{2-}, HCO_3^-, OH^- species and H_2O. Adsorption of these species may reduce the number of surface sites available for redox reactions.

The trend in similar spectral features under both argon and CO_2 was also observed on introduction of CO_2 in K_2CO_3 pH 10.1. Previously in chapter 3, the CV response of K_2CO_3 showed increased current magnitudes with each scan due to the decrease in pH on introduction of CO_2. The increased redox activity was proposed to be associated with the shift in pH from 11.2 to 10.1, which, according to the Pourbaix diagram in Figure 3.6, may have allowed for the formation of metallic Fe at potentials > −1.00 V. Thus, the additional formation of metallic Fe suggests more redox active species were available compared to in K_2CO_3 at pH 10.1. Additionally, according to the Pourbaix diagram in Figure 3.6, no siderite / iron carbonate is predicted to form in K_2CO_3 at both pH 11.2 and 10.1, and thus should not be expected in the FTIR spectra of greigite in K_2CO_3. No IR bands corresponding to iron carbonate / siderite were detected in both of the FTIR spectra of greigite in K_2CO_3 at pH 11.2 and 10.1, which is in agreement with the

predictions. Similar to the FTIR spectra in $KHCO_3$ under CO_2, no new IR peak corresponding to dissolved CO_2 species were detected in FTIR spectra in K_2CO_3 pH 10.1 under CO_2. The main difference observed between the FTIR spectra in K_2CO_3 under argon and CO_2 is the absence of the absorbance loss for $\nu_{sym}(OH)$ of H_2O at 3055 cm^{-1} under CO_2 at +0.40 V, which suggests water oxidation did not take place under CO_2 in K_2CO_3 at pH 10.1 at this potential, as predicted by the Pourbaix diagram in Figure 3.6. Water oxidation may have been suppressed due to the decrease in pH.

Overall, it seems that the formation of iron carbonate / siderite may not have caused the changes in the CV responses observed in the previous chapter in both K_2CO_3 and $KHCO_3$ but rather the high pH. At high pH such as in K_2CO_3 and $KHCO_3$, the high concentration of OH^- species present may lead to the formation of an iron oxide or hydroxide layer. The XANES data show the presence of iron oxide or hydroxide layer on immersion of the greigite electrode in K_2CO_3. Thus, the passivated redox features observed in the CVs of greigite in K_2CO_3 and $KHCO_3$, compared to the CVs in phosphate electrolytes, may be associated with the presence of the newly formed iron oxide / hydroxide layer. On introduction of CO_2, the pH is lowered in both K_2CO_3 and $KHCO_3$. According to the Pourbaix diagram in Figure 3.1, the iron oxide or hydroxide layer will remain stable on lowering of pH from 11.2 to 10.1. However, for $KHCO_3$, the lowering of pH from 8.55 to 7.1 will result in the reduction of the iron oxide / hydroxide layer to Fe^{2+} soluble species and may result in the depletion of the iron oxide / hydroxide layer. The reduced amount of iron oxide / hydroxide layer available for redox reactions may explain the smaller currents CV on introduction of CO_2, due to the dissolution of the iron oxide / hydroxide layer on lowering of pH to 7.1. Significant dissolution or restructuring of the nanoparticle surfaces may have a significant influence on water structuring at the interface and this is reflected by the increased IR absorbance of water on lowering the pH from 8.55 to 7.1.

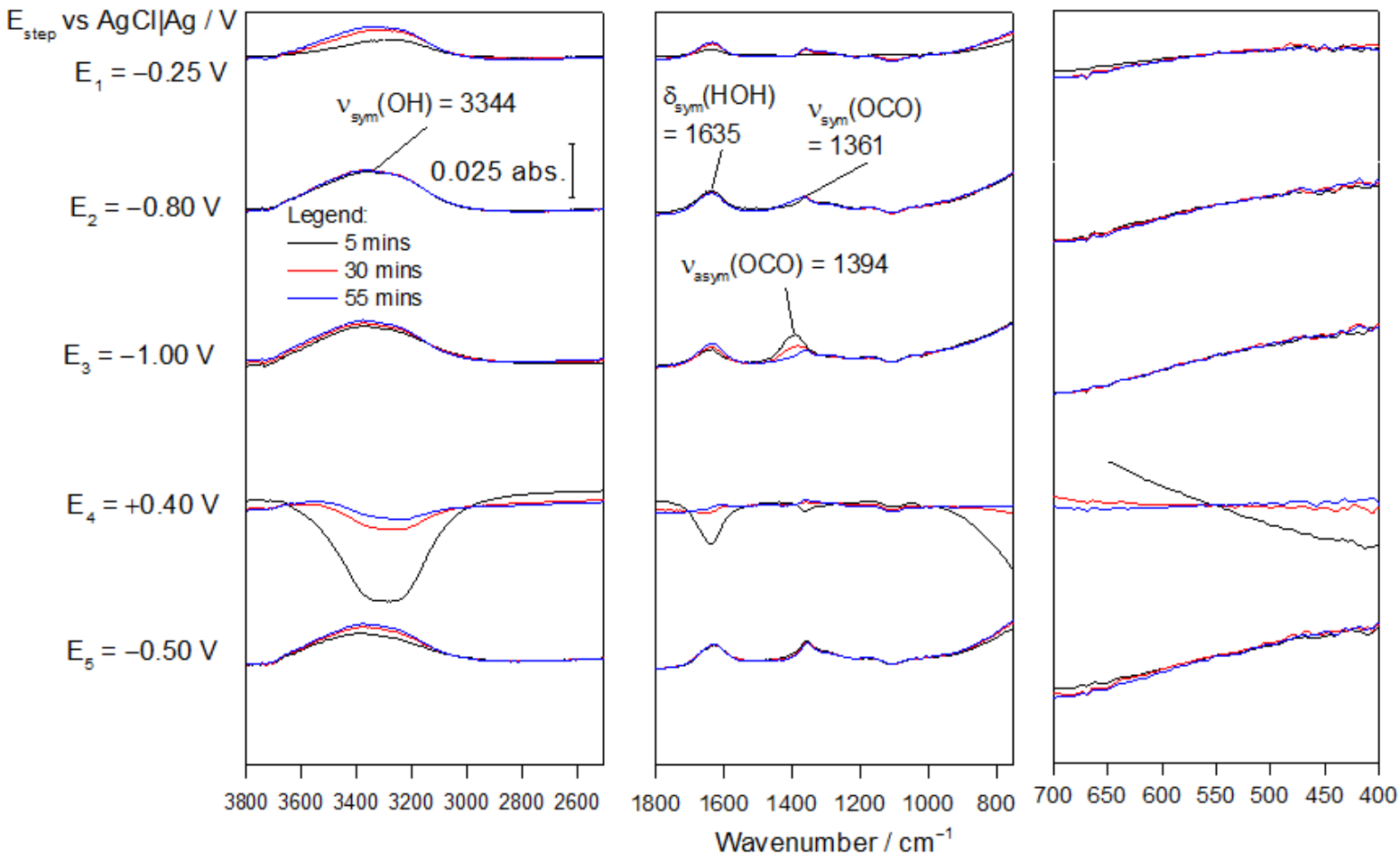

Figure 4.23 In-situ FTIR of greigite in $KHCO_3$ pH 7.1 under CO_2 recorded on applying potential steps of −0.25, −0.80, −1.00, +0.40 and −0.50 V for one hour each step. Spectra displayed at each potential step were recorded at 5, 30 and 55 mins into holding the potential.

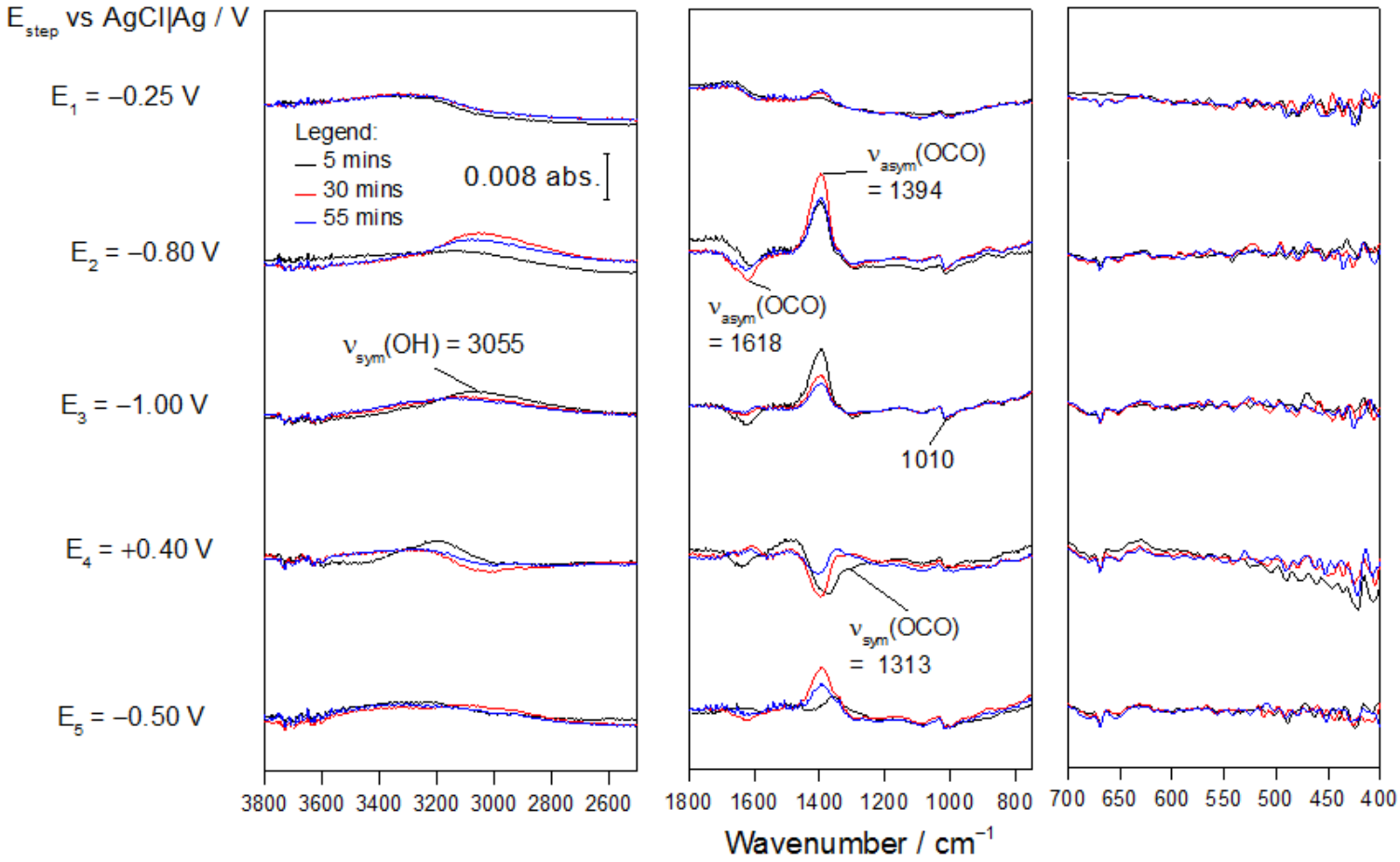

Figure 4.24 In-situ FTIR of greigite in K_2CO_3 pH 10.1 under CO_2 recorded on applying potential steps of −0.25, −0.80, −1.00, +0.40 and −0.50 V for one hour each step. Spectra displayed at each potential step were recorded at 5, 30 and 55 mins into holding the potential.

4.3.3.5 Capping agent

The capping agent, (Z)-octadec-9-enylamine or oleylamine, used in the synthesis of the greigite nanoparticles used in this thesis was investigated for its potential impact, if any, towards the CV response and FTIR of greigite. The CV and FTIR spectra of the capping agent performed in the electrolytes used in this thesis are shown in Figure 4.25 and Figure 4.26, respectively. Oleylamine is used heavily as a solvent in nanoparticle synthesis as it has a suitable boiling point to achieve the crystal structure of nanoparticles desired. However, it was previously speculated that $-NH_2$ or C=C groups present in the oleylamine structure may react with CO_2 on its introduction into the electrolyte. This may interfere with CO_2 reduction and potentially lead to false results for CO_2 reduction feasibility on greigite.

The CV responses of the capping agent drop coated onto an electrode in Figure 4.25 recorded no significant redox feature, compared to the CV of a clean BDD electrode. This suggests that oleylamine did not have any associated redox chemistry and thus, should not affect the CV response of the greigite nanoparticles.

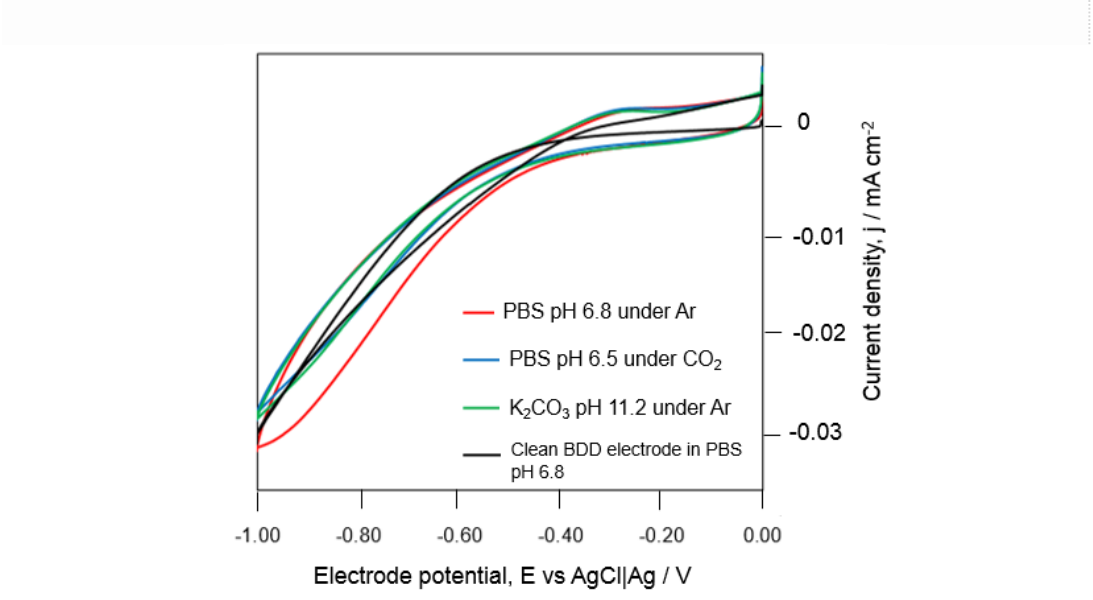

Figure 4.25 Cyclic voltammogram of oleylamine drop coated on a clean BDD recorded in phosphate buffers pH 6.8 under Ar, pH 6.5 under CO_2 and in K_2CO_3 under argon. Scan rate 10 mV s^{-1}.

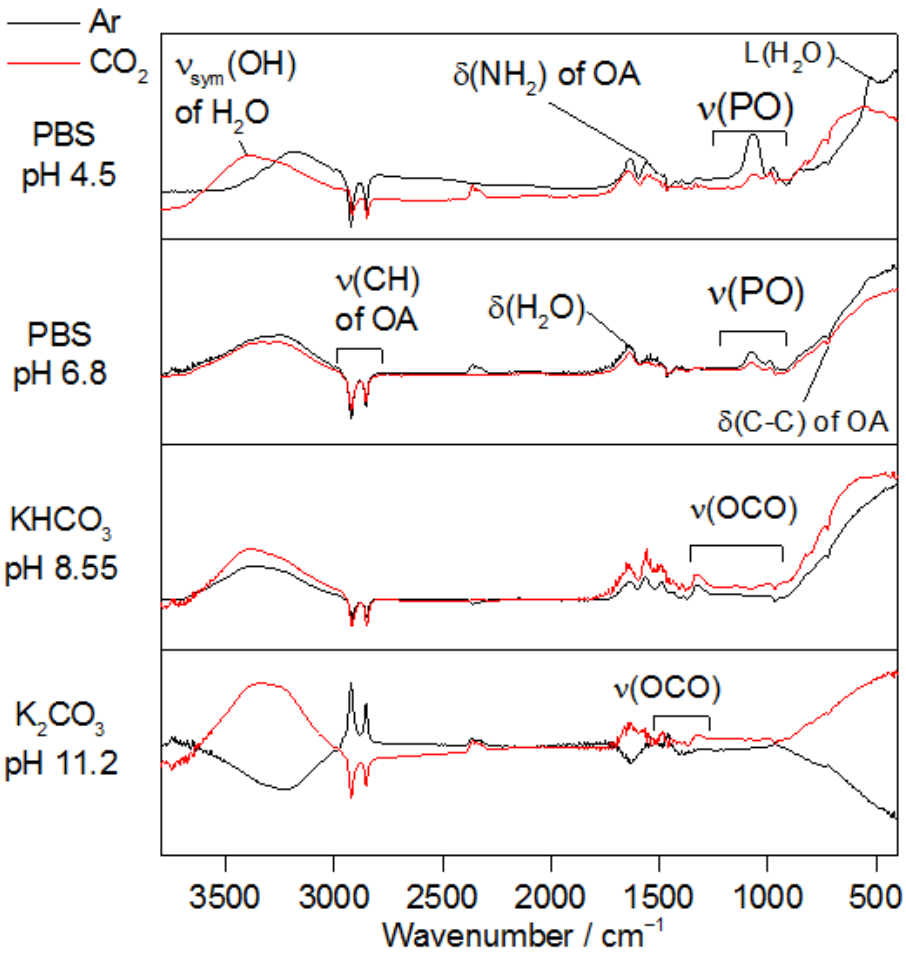

Figure 4.26 FTIR spectra of oleylamine drop coated on a clean BDD electrode in phosphate buffer (PBS) pH 4, 7 and $KHCO_3$ pH 8 and K_2CO_3 pH 11 under argon (black line) and CO_2 (red line) with no applied potentials recorded after 5 hours of electrode immersion in electrolyte. (OA = oleylamine)

The FTIR spectra of oleylamine in each electrolyte tested show the presence IR peaks of oleylamine at 715 cm^{-1} (C-C) and 2924 and 2837 cm^{-1} (C-H), as well as the IR peaks of the electrolyte used. [32] The in-situ FTIR spectra of greigite presented earlier in this chapter did not record significant IR absorbances associated with oleylamine. Thus, it is proposed that oleylamine should not affect the FTIR spectral features of greigite. The introduction of CO_2 also did not affect the spectral features of oleylamine in Figure 4.26 which suggests that no reaction took place between the $-NH_2$ or C=C groups on oleylamine when CO_2 was introduced. Both the CV and FTIR results of oleylamine in this section confirm that the oleylamine capping agent used in the synthesis of greigite should not participate or contribute towards any surface redox reaction on greigite, even when CO_2 is introduced.

4.4 Impact of CO_2 on the structure of greigite and its implications for CO_2 reduction

The in-situ FTIR and XAS results detailed in this chapter can be used to assess the impact of the introduction of CO_2 on the structure of greigite as well as its implications for CO_2 reduction on greigite. CO_2 reduction on the greigite material investigated in this thesis has been reported to be feasible, depending on the experimental conditions.[36]

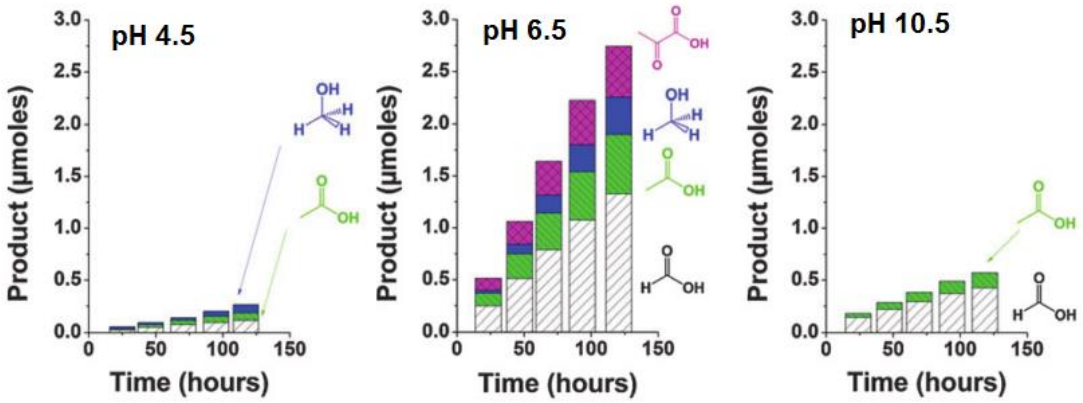

Figure 4.27 Amount of CO_2 reduction products (formic acid, acetic acid, methanol and pyruvic acid) formed over time using greigite electrode in PBS pH 4.5, pH 6.5 and 10.5. [36]

CO_2 reduction on the greigite electrode was reported to be the most optimum in phosphate buffer solution pH 7, which produced formic acid, acetic acid, methanol and pyruvic acid. However, the report only used DFT calculations and assessed the binding energies of CO_2 at each experimental condition to explain the variation in CO_2 reduction efficiency. The work did not consider the possible redox and surface transformations of greigite, the adsorption of electrolyte species and the shift in pH on introduction of CO_2, which may have affected the CO_2 reduction efficiency. Furthermore, no in-situ characterisation on the structure of greigite was performed to verify the predicted changes in surface structure on applying a cyclic potential continuously for CO_2 reduction. Changes in the surface structure of greigite may have determined the efficiency for CO_2 reduction.

Based on the in-situ spectroscopic results obtained in this chapter and cyclic voltammetry results in chapter 3, the following discussion may explain the variation in CO_2 reduction efficiency on the greigite electrode:

i) At pH 4.5, the introduction of CO_2 did not affect the CV response of greigite. The in-situ FTIR results show the presence of HCO_3^- and phosphate electrolyte species, but no IR bands corresponding to the formation of siderite, as predicted by the Pourbaix diagram in Figure 3.6. The in-situ XANES data show greigite was stable on introduction of CO_2 until a more negative potential of −1.00 V was applied. Introduction of CO_2 suppressed water and proton reduction and slowed down but did not halt the transformation of greigite to iron oxide / hydroxide. Thus, the low CO_2 reduction efficiency at this pH may be associated with the presence of iron oxide / hydroxide on greigite, as well as poor adsorption of dissolved CO_2 species compared to the phosphate electrolyte species present near the electrode surface, which may have blocked potential adsorption sites for CO_2 reduction.

ii) At pH 6.5, the CV response of greigite was suppressed on introduction of CO_2, which was initially linked to the potential formation of siderite / iron carbonate, as predicted by the Pourbaix diagram in Figure 3.6 However, there was no evidence for the formation of siderite in both of the FTIR and XAS results at this pH on introduction of CO_2. However, there was evidence for the presence of dissolved CO_2 species (HCO_3^- and CO_3^{2-}) in the FTIR spectra which may have suppressed water and proton reduction at this pH by blocking surface sites for the water reduction reaction. The transformation of greigite to iron oxide / hydroxide was also observed to be halted on introduction of CO_2 at this pH. Thus, the possible adsorption of dissolved CO_2 species (HCO_3^- and CO_3^{2-}) at this pH may have protected the greigite surface which may explain the optimum condition for CO_2 reduction reported.

iii) At pH 10.5, the introduction of CO_2 increased the current magnitudes in the CV of greigite with each scan at this pH. The increased redox activity was attributed to the decrease in pH on introduction of CO_2 and the formation of metallic iron, as predicted by the Pourbaix diagram in Figure 3.6. However, the XANES spectra of greigite show the transformation of greigite to iron oxide / hydroxide on immersion of the electrode in the electrolyte, and the iron oxide / hydroxide structure remained stable throughout the experiment. Thus, the low efficiency of CO_2 reduction at this high pH may be a result of the transformation of greigite to iron oxide / hydroxide, a surface which is not favourable for CO_2 reduction.

The findings in this chapter show the importance of using in-situ techniques to investigate the surface structure of the material investigated. The work in this thesis show that the experimental conditions, including the pH and electrolyte species present, are important when considering CO_2 reduction on the greigite electrode material. Ideally, the electrolyte used should not adsorb strongly on to the greigite electrode material as it may hinder adsorption of dissolved CO_2 species. Electrolyte with close to neutral pH is also recommended, as greigite transforms to iron oxide / hydroxide at high pH. Using an electrolyte with low pH is not recommended, as the competing water and proton reduction will be favoured due to the potential window used (from 0.00 to −1.00 V). Alternatively, non-aqueous electrolytes may be used.

4.4.1 Implications on CO_2 reduction proposed in iron sulphide membrane origin of life theory

The motivation for the work in this thesis was inspired by the potential CO_2 reduction on greigite proposed by the iron sulphide membrane origin of life theory which was detailed in the introduction chapter. There is, however, a clear difference between the work here and the proposed hypothesis, which is the ambient temperature and pressure used in this work, and the high temperature and pressure setting in the hydrothermal vents proposed in the origin of life theory.

Electrolytes of pH 4.5, 6.8, 8.55 and 11.2 were selected in this work to investigate the changes in surface structure of greigite at each pH with applied potentials. This was done to compare the proposed hypothesis where CO_2 reduction would occur on a greigite membrane which exists between acidic (pH 4) and alkaline (pH 11) medium, on each side of the proposed membrane. The theory proposed that the pH gradient which exists across the greigite membrane will catalyse CO_2 reduction on the greigite surface. The results in this work show that the adsorption of dissolved CO_2 species is feasible on the greigite electrode at neutral pH, which lend support to the proposed pH gradient which may catalyse CO_2 reduction on greigite. Based on the transformation of greigite observed in the electrolytes in this chapter, the greigite surface composition might be different on the acid / alkaline sides of the membrane proposed in the theory.

4.5 References

1. Arai, Y. & Sparks, D. L. ATR–FTIR Spectroscopic Investigation on Phosphate Adsorption Mechanisms at the Ferrihydrite–Water Interface. *J. Colloid Interface Sci.* **241,** 317–326 (2001).

2. Takahashi, Y. *et al.* Seasonal changes in Fe species and soluble Fe concentration in the atmosphere in the Northwest Pacific region based on the analysis of aerosols collected in Tsukuba, Japan. *Atmos. Chem. Phys.* **13,** 7695–7710 (2013).

3. Wilke, M., Farges, F., Petit, P. E., Brown, G. E. & Martin, F. Oxidation state and coordination of Fe in minerals: An Fe K-XANES spectroscopic study. *Am. Mineral.* **86,** 714–730 (2001).

4. Kataby, G. *et al.* The adsorption of monolayer coatings on iron nanoparticles: Mössbauer spectroscopy and XANES results. *Thin Solid Films* **333,** 41–49 (1998).

5. Islam, H.-U. Ph. D. Thesis, Formation and Electrocatalysis Studies of Nickel and Iron Sulfide Catalysts using in situ XAS. (University College London, 2015).

6. Santos-Carballal, D., Roldan, A. & de Leeuw, N. H. Early Oxidation Processes on the Greigite Fe_3S_4 (001) Surface by Water: A Density Functional Theory Study. *J. Phys. Chem. C* **120,** 8616–8629 (2016).

7. Hug, S. J. In Situ Fourier Transform Infrared Measurements of Sulfate Adsorption on Hematite in Aqueous Solutions. *J. Colloid Interface Sci.* **188,** 415–422 (1997).

8. Iwasita, T. & Nart, F. C. In situ infrared spectroscopy at electrochemical interfaces. *Prog. Surf. Sci.* **55,** 271–340 (1997).

9. Parry, D., Samant, M., Seki, H. & Philpott, M. In situ Fourier transform infrared spectroelectrochemical study of bisulfate and sulfate adsorption on gold, with and without the underpotential deposition of copper. *Langmuir* 1878–1887 (1993). doi:10.1021/la00031a041

10. Ataka, K. & Osawa, M. In Situ Infrared Study of Water−Sulfate Coadsorption on Gold(111) in Sulfuric Acid Solutions. *Langmuir* **14,** 951–959 (1998).

11. Peak, D., Ford, R. & Sparks, D. An in Situ ATR-FTIR Investigation of Sulfate Bonding Mechanisms on Goethite. *J. Colloid Interface Sci.* **218,** 289–299 (1999).

12. Zhang, G. Y. & Peak, D. Studies of Cd(II)-sulfate interactions at the goethite-

water interface by ATR-FTIR spectroscopy. *Geochim. Cosmochim. Acta* **71,** 2158–2169 (2007).

13. Beattie, D. a, Chapelet, J. K., Gra, M., Skinner, W. M. & Smith, E. In Situ ATR FTIR Studies of SO Adsorption on Goethite in the Presence of Copper Ions In Situ ATR FTIR Studies of SO 4 Adsorption on Goethite in the Presence of Copper Ions. *Environ. Sci. Technol.* **42,** 9191–9196 (2008).

14. Degenhardt, J. & McQuillan, A. J. In Situ ATR-FTIR Spectroscopic Study of Adsorption of Perchlorate, Sulfate, and Thiosulfate Ions onto Chromium(III) Oxide Hydroxide Thin Films. *Langmuir* **15,** 4595–4602 (1999).

15. Chernyshova, I. V. An in situ FTIR study of galena and pyrite oxidation in aqueous solution. *J. Electroanal. Chem.* **558,** 83–98 (2003).

16. Tejedor-Tejedor, M. I. & Anderson, M. A. The protonation of phosphate on the surface of goethite as studied by CIR-FTIR and electrophoretic mobility. *Langmuir* **6,** 602–611 (1990).

17. Luengo, C., Brigante, M., Antelo, J. & Avena, M. Kinetics of phosphate adsorption on goethite: comparing batch adsorption and ATR-IR measurements. *J. Colloid Interface Sci.* **300,** 511–8 (2006).

18. Elzinga, E. J. & Sparks, D. L. Phosphate adsorption onto hematite: an in situ ATR-FTIR investigation of the effects of pH and loading level on the mode of phosphate surface complexation. *J. Colloid Interface Sci.* **308,** 53–70 (2007).

19. Falk, M. & Miller, A. G. Infrared spectrum of carbon dioxide in aqueous solution. *Vib. Spectrosc.* **4,** 105–108 (1992).

20. Su, C. & Suarez, D. L. In Situ Infrared Speciation of Adsorbed Carbonate on Aluminum and Iron Oxides. *Clays Clay Miner.* **45,** 814–825 (1997).

21. Chernyshova, I. V, Ponnurangam, S. & Somasundaran, P. Linking interfacial chemistry of CO2 to surface structures of hydrated metal oxide nanoparticles: hematite. *Phys. Chem. Chem. Phys.* **15,** 6953–64 (2013).

22. Bargar, J. R., Reitmeyer, R. & Davis, J. A. Spectroscopic confirmation of uranium(VI)-carbonato adsorption complexes on hematite. *Environ. Sci. Technol.* **33,** 2481–2484 (1999).

23. Villalobos, M. & Leckie, J. O. Surface Complexation Modeling and FTIR Study of Carbonate Adsorption to Goethite. *J. Colloid Interface Sci.* **235,** 15–32 (2001).

24. Legrand, L., Savoye, S., Chausse, a & Messina, R. Study of oxidation products formed on iron in solutions containing bicarbonate/carbonate.

Electrochim. Acta **46,** 111–117 (2000).

25. Murphy, R., Lammers, K., Smirnov, A., Schoonen, M. A. A. & Strongin, D. R. Ferrihydrite phase transformation in the presence of aqueous sulfide and supercritical CO2. *Chem. Geol.* **271,** 26–30 (2010).

26. Keller, L. P. *et al.* Identification of iron sulphide grains in protoplanetary disks. *Nature* **417,** 148–150 (2002).

27. Allan, K. F., Labib, S. & Holeil, M. Synthesis and characterization of iron sulfide powders and its application for sorption of europium radionuclides. *Desalin. Water Treat.* **3994,** 1–15 (2015).

28. Garcia-Araez, N., Rodriguez, P., Navarro, V., Bakker, H. J. & Koper, M. T. M. Structural effects on water adsorption on gold electrodes. *J. Phys. Chem. C*. 21249–21257 (2011). doi:Doi 10.1021/Jp206539a

29. Osawa, M., Tsushima, M., Mogami, H., Samjeské, G. & Yamakata, A. Structure of Water at the Electrified Platinum–Water Interface: A Study by Surface-Enhanced Infrared Absorption Spectroscopy. *J. Phys. Chem. C* **112,** 4248–4256 (2008).

30. Maréchal, Y. From physics to biology: A journey through science accompanying the hydrogen bond and the water molecule. *J. Mol. Struct.* **880,** 38–43 (2008).

31. Venyaminov SYu & Prendergast, F. G. Water (H2O and D2O) molar absorptivity in the 1000-4000 cm-1 range and quantitative infrared spectroscopy of aqueous solutions. *Anal. Biochem.* **248,** 234–245 (1997).

32. Mourdikoudis, S. & Liz-Marzán, L. M. Oleylamine in Nanoparticle Synthesis. *Chem. Mater.* **25,** 1465–1476 (2013).

33. Lounasvuori, M. M. & Holt, K. B. Acid deprotonation driven by cation migration at biased graphene nanoflake electrodes. *Chem. Commun.* **53,** 2351–2354 (2017).

34. Persson, P. *et al.* Structure and Bonding of Orthophosphate Ions at the Iron Oxide-Aqueous Interface. *J. Colloid Interface Sci.* **177,** 263–275 (1996).

35. Lee, S. H. & Rasaiah, J. C. Proton transfer and the mobilities of the H+ and OH- ions from studies of a dissociating model for water. *J. Chem. Phys.* **135,** (2011).

36. Roldan, A. *et al.* Bio-inspired CO2 conversion by iron sulfide catalysts under sustainable conditions. *Chem. Commun.* **51,** 7501–7504 (2015).

Chapter 5 Electrochemistry of violarite

5.1 Introduction

This chapter details the cyclic voltammetry study performed on the iron-nickel sulfide violarite, $FeNi_2S_4$, which is the nickel analogue of greigite. Violarite has been shown to have a higher Faradaic efficiency for CO_2 reduction compared to greigite, however, no justification was proposed by the published work.[1] Violarite has also been proposed as a catalytic site for CO_2 reduction in the iron sulfide membrane theory.[2] In this thesis, violarite was studied to investigate the effect of nickel incorporated in an iron sulfide material on its structure and redox properties under argon and CO_2. The same technique described in chapter 3 for greigite, cyclic voltammetry, was used to investigate the electrochemistry of violarite.

With the additional presence of nickel in the violarite structure compared to greigite, the Pourbaix diagrams of Fe-Ni-H_2O, Fe-Ni-S-H_2O and Ni-S-O_2-CO_2-H_2O systems need to be considered when analysing the cyclic voltammetry results. Literature on the electrochemical studies of violarite are first reviewed, and followed by the cyclic voltammetry results of violarite. These results will then be compared and correlated with the in-situ FTIR and XAS results of violarite in the next chapter, chapter 6, to assess the validity of the redox assignments.

5.1.1 Pourbaix diagrams

The Pourbaix diagrams that are referred to in this chapter are the Fe-Ni-S-H_2O system (Figure 5.1), the Fe-Ni-H_2O system (Figure 5.2) and the Ni-S-O_2-CO_2-H_2O system (Figure 5.3). Additionally, the Pourbaix diagrams of Fe-H_2O, Fe-H_2S-H_2O, S-H_2O, Fe-CO_2-H_2O and Fe-S-C-H_2O systems previously presented in chapter 3 are also referred to in this chapter. The general reactions that can occur on metal sulfides were discussed in section 3.1.2 in chapter 3. It is presumed that violarite will undergo the same reactions under the same experimental conditions.

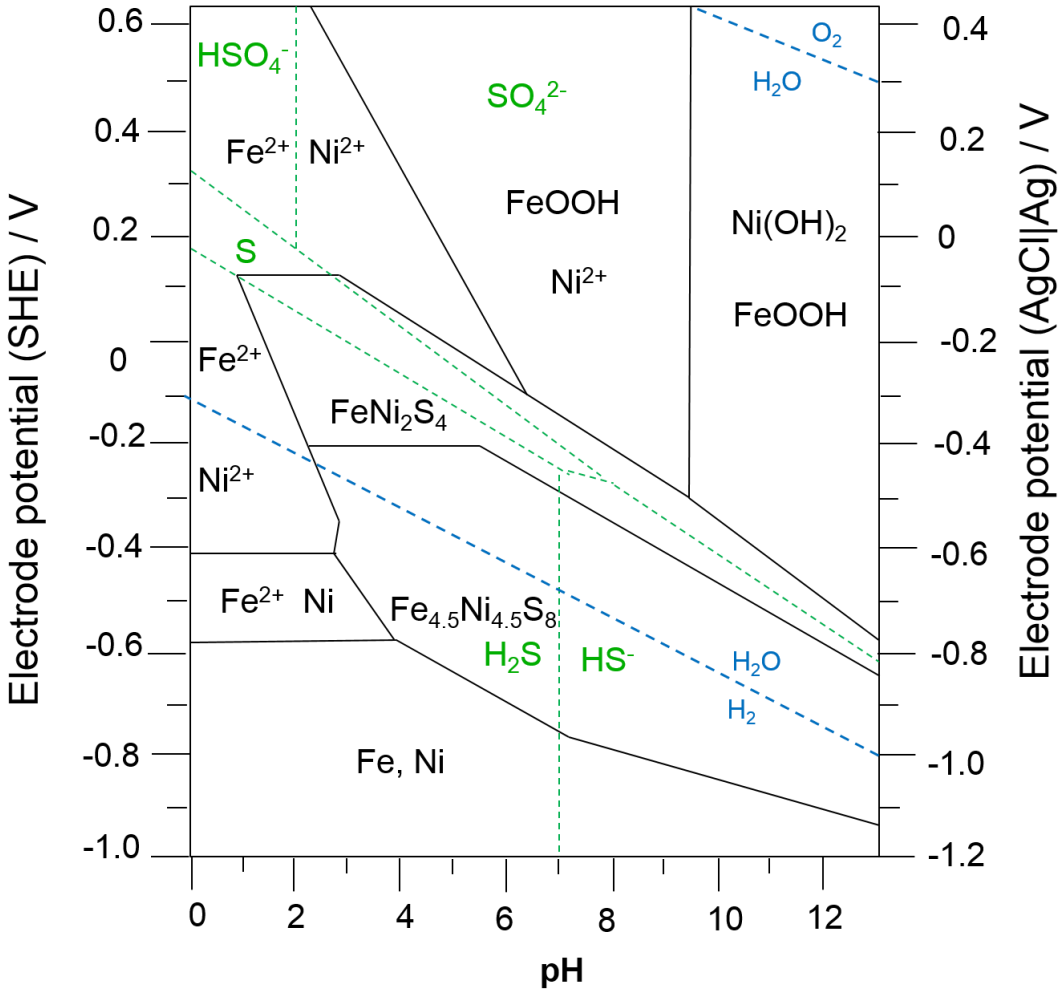

Figure 5.1 Pourbaix diagram for the Fe-Ni-S aqueous system at 298 K. Activities of aqueous sulfur, iron and nickel species = 10^{-6} M. Metastable equilibria: with $Fe_{4.5}Ni_{4.5}S_8$ and $FeNi_2S_4$ as the only metal sulfide phases. H_2S (aq) not consumed. α-FeOOH and $Ni(OH)_2$ as metastable products. Adapted from reference 3.

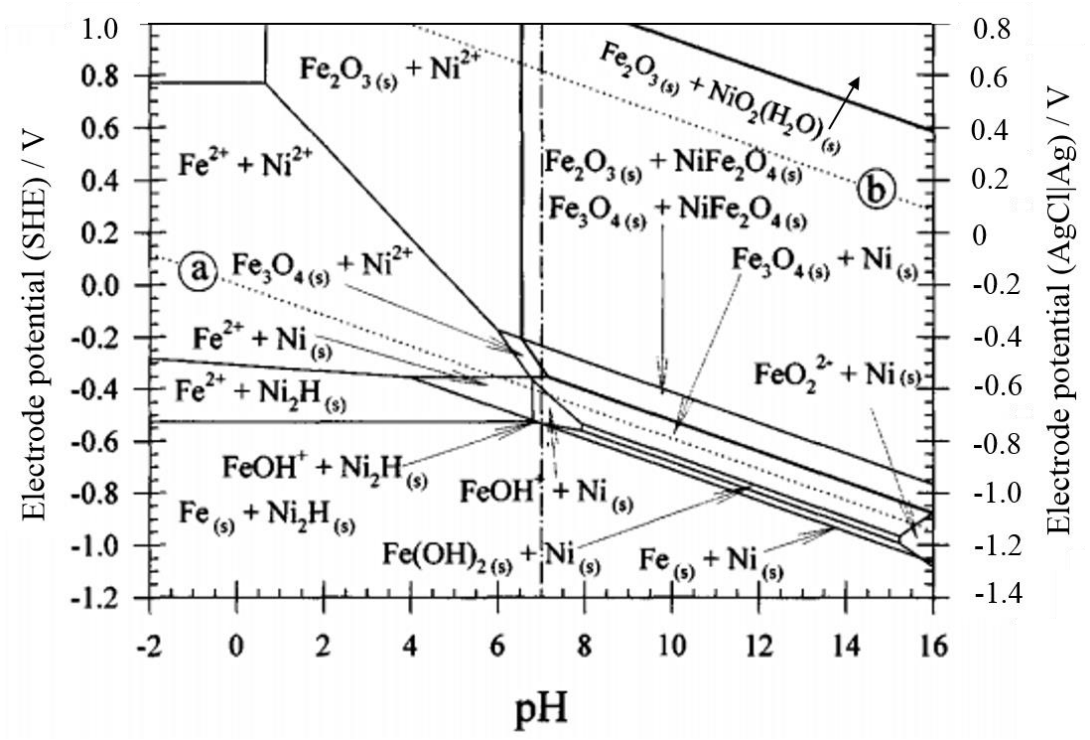

Figure 5.2 Pourbaix diagram of Fe-Ni-H_2O system at 298 K. Concentration of all aqueous species = 10^{-4} M. The molar proportion of Fe:Ni is > 2:1. Line a: H_2O/H_2, b: H_2O/O_2. Adapted from reference 4.

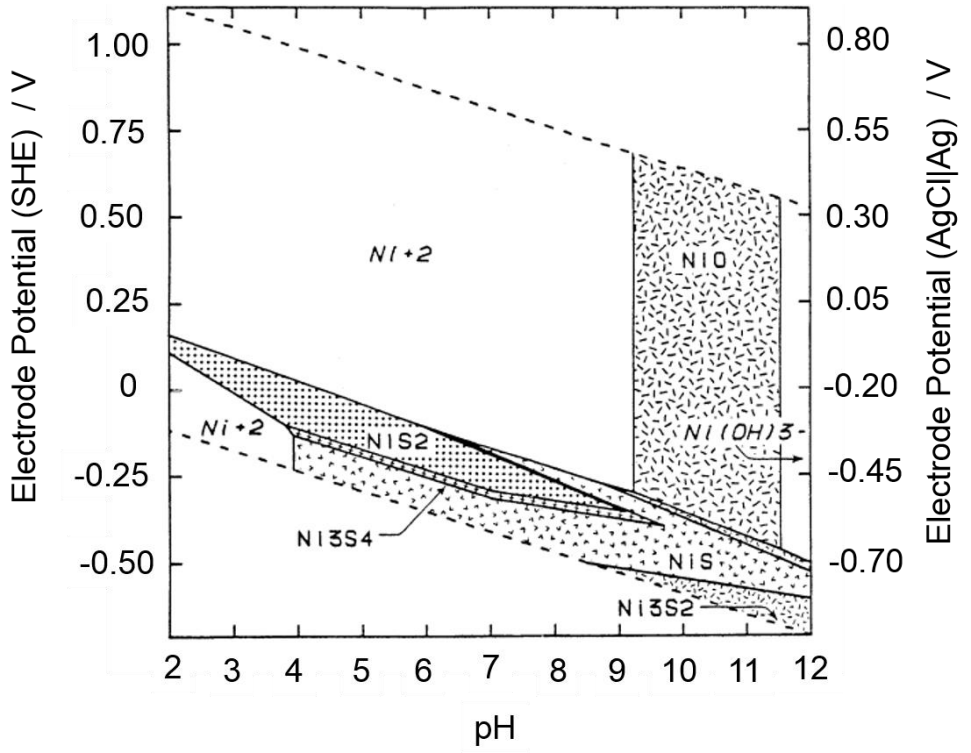

Figure 5.3 Pourbaix diagram of Ni-S-O_2-CO_2-H_2O system, assuming that $\sum Ni = 10^{-6}$ mol kg^{-1} and $\sum S = 10^{-5}$ mol kg^{-1}. Adapted from reference 5.

5.1.2 Literature on electrochemistry of violarite

Thornber *et al*[6] performed cyclic voltammetry on synthetic violarite material in pH 0, 2, 4 and 6 in 0.1 M NaCl. Only results at pH 4 and 6 are of relevance to the investigations in this thesis. The author chose a cyclic potential sweep initiated from 0.0 to –1.0 V, and reversed to +1.0 V and measurements were against SCE (Saturated Calomel Electrode) (+0.241 V vs SHE).

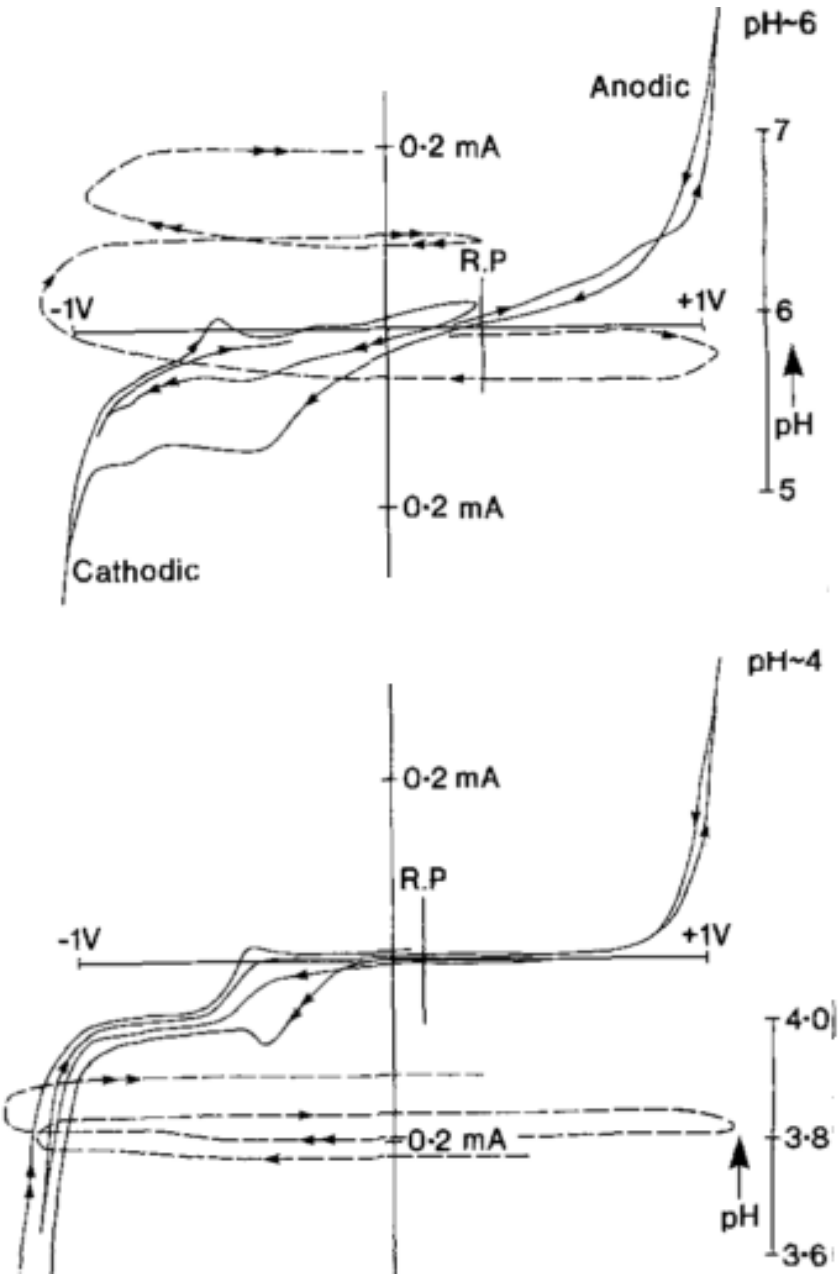

Figure 5.4 CVs of violarite in 0.1 M NaCl at pH 4 and 6. Solid lines = current, dashed lines = pH. [6] Copyright 1983 Chapman and Hall Ltd.

Thornber *et al*[6] proposed the following electrochemical model (with 7 steps) in assigning the redox features observed in the CV of violarite at pH 6:

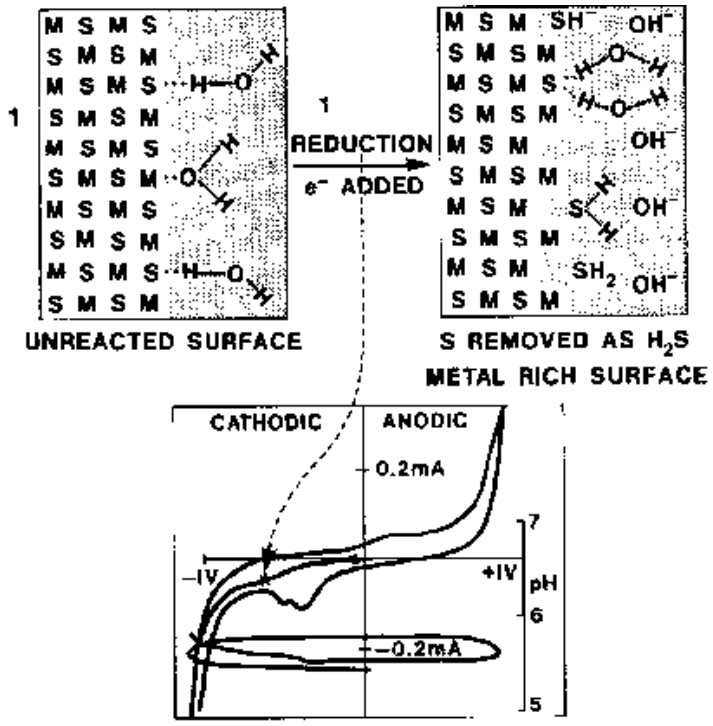

Figure 5.5 First reduction step in the electrochemical model proposed by Thornber *et al* for the CV of violarite at pH 6. [6] **Copyright 1983 Chapman and Hall Ltd.**

The first reduction feature in step 1 in Figure 5.5 at ~ −0.55 V (vs AgCl|Ag) was assigned to the reduction of the violarite surface to a metal−rich surface, producing H_2S which was proposed to have caused an increase in pH (due to OH^- species produced):

$$FeNi_2S_4 + 8H_2O + 2e^- \rightarrow Fe^{2+} + 2Ni^{2+} + 4H_2S + 8OH^- \qquad (5.1)$$

This was followed by a second reduction feature assigned to water reduction (Figure 5.6):

$$2H_2O + 2e^- \rightarrow H_2 + 2OH^- \qquad (5.2)$$

According to the Pourbaix diagram in Figure 5.1, violarite is predicted to be stable between −0.35 V and −0.45 V (vs AgCl|Ag) at pH 6. At the start potential of 0.00 V

(vs SCE) used by Thornber *et al*[6] in the CV of violarite, FeOOH is the predicted stable redox species in an Fe-Ni-S-H_2O system according to the Pourbaix diagram in Figure 5.1. This prediction suggests a bulk transformation of violarite to FeOOH at 0.00 V:

$$FeNi_2S_4 + 18H_2O \rightarrow FeOOH + 2Ni^{2+} + 4SO_4^{2-} + 35H^+ + 31e^- \qquad (5.3)$$

However, Thornber *et al*[6] assumed that the violarite electrode remained unreacted and stable, which is in contrast to the predictions in the Pourbaix diagram. This is a surprising assumption as the violarite electrode may undergo non-oxidative dissolution to form soluble Fe^{2+} and Ni^{2+} species near the electrode surface. If FeOOH was formed on immersion of violarite into the pH 6 electrolyte, the first reduction peak proposed by Thornber *et al*[6] could be associated with the reduction of FeOOH to violarite (reverse of reaction (5.3)), which is predicted to occur between −0.30 and −0.40 V. Hence, the reduction of any iron oxide or hydroxide layer present on the violarite surface may also contribute towards the first reduction feature observed in Figure 5.5.

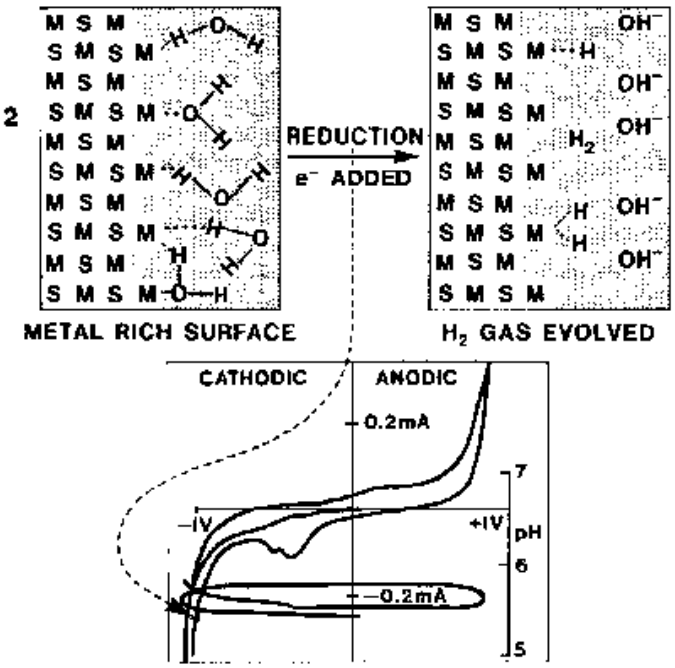

Figure 5.6 Second reduction step in the electrochemical model proposed by Thornber *et al* for CV of violarite at pH 6. [6] **Copyright 1983 Chapman and Hall Ltd.**

At potentials < −0.40 V, violarite is predicted to reduce to pentlandite $Fe_{4.5}Ni_{4.5}S_8$ between −0.40 and −0.90 V, and to metallic Fe and Ni at potentials < −0.90 V. The authors did not consider such transformation in their work. Thus, the transformation of violarite to pentlandite (5.4) may have also contributed to the first reduction feature observed in Figure 5.5. The reduction of pentlandite to metallic Fe and Ni (5.5) may contribute to the second reduction feature observed in the CV of violarite in Figure 5.6.

$$2FeNi_2S_4 + 0.5Ni^{2+} + 2.5FeOOH + 7.5H^+ + 8.5e^- \rightarrow Fe_{4.5}Ni_{4.5}S_8 + 5H_2O \quad (5.4)$$

$$Fe_{4.5}Ni_{4.5}S_8 + 16H^+ + 16e^- \rightarrow 4.5Fe + 4.5Ni + 8H_2S \quad (5.5)$$

On the positive-going potential sweep (reactions 3 and 4 in Figure 5.7), Thornber *et al*[6] proposed that "the metals on and in the surface are oxidised into solution, to leave the surface sulfur-rich". However, no specific reaction equations were proposed. This leaves the current author to assume Thornber *et al*[6] were referring to the oxidation of Fe(0) and Ni(0) to soluble Fe^{2+} and Ni^{2+} species, respectively. According to the Pourbaix diagram in Figure 5.1, the oxidation of Fe(0) and Ni(0) to soluble Fe^{2+} and Ni^{2+} species is not predicted at pH 6. Instead, pentlandite is predicted to form from the oxidation of Fe(0) and Ni(0), in the presence of H_2S (reverse reaction of (5.5)). It is possible that H_2S may be absent near the electrode surface on diffusion away from the electrode, thus the predicted oxidation of Fe(0) and Ni(0) to pentlandite may not occur. In the absence of H_2S near the electrode surface, according to the Pourbaix diagram in Figure 5.2, the oxidation of Fe(0) and Ni(0) to soluble Fe^{2+} and Ni^{2+} species is predicted to occur at ~ −0.55 V in pH 6. This may support the assignment proposed by Thornber *et al*[6] at the reaction step 3 in Figure 5.7. Surprisingly, the authors did not comment on the lack of this redox feature at step 3 when assigning this peak. There was no distinct redox feature for step 3 in Figure 5.7, which seems to suggest a limited amount of Fe(0) and Ni(0) may be present on the surface of the violarite electrode available for oxidation.

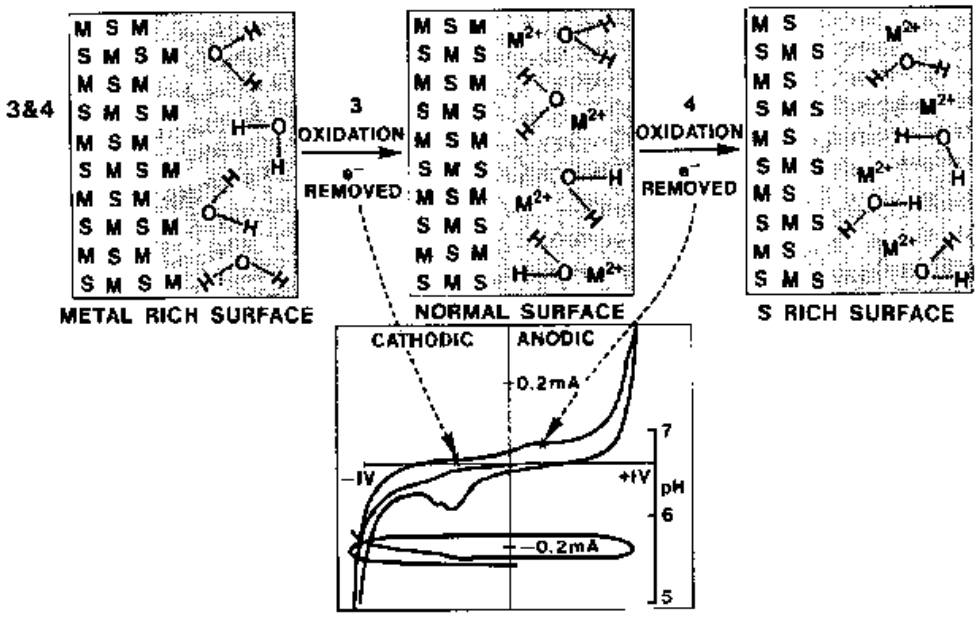

Figure 5.7 Anodic reactions steps 3 and 4 in the electrochemical model proposed by Thornber *et al* for CV of violarite at pH 6. [6] **Copyright 1983 Chapman and Hall Ltd.**

Thornber *et al*[6] claimed that reaction 4 at ~+0.15 V (see Figure 5.7) is where further oxidation of the metal takes place, leaving the surface rich in sulfur, though it is again unclear which metal (Fe or Ni) the authors were referring to. On inspection of the Pourbaix diagrams in Figure 5.1 and Figure 5.2, at this potential ~ +0.15 V at pH 6, FeOOH and Fe_2O_3 are the stable redox species predicted to form. Thornber *et al*[6] did not consider the possible formation of iron oxide or hydroxide on the violarite electrode. According to the Pourbaix diagram in Figure 5.1, violarite may undergo oxidation to form FeOOH or Fe_2O_3 (reaction (5.3)) and produce sulfates. Thornber *et al*[6] proposed the surface to be sulfur-rich, however, based on the Pourbaix diagram in Figure 5.1, it is unlikely that sulfur was present as sulfates are the stable redox species at +0.15 V. Soluble Fe^{2+} species produced on oxidation of Fe(0) in step 3 may also be oxidised to form FeOOH or Fe_2O_3 in step 4. The oxidation of Fe^{2+} to iron oxide Fe_2O_3 or FeOOH is predicted to occur at potentials above −0.40 V in the absence of H_2S. Thus, the anodic reaction step 4 may also be associated with the formation of Fe_2O_3 or FeOOH.

$$2Fe^{2+} + 3H_2O \rightarrow Fe_2O_3 + 6H^+ + 2e^- \qquad (5.6)$$

$$Fe^{2+} + 2H_2O \rightarrow FeOOH + 3H^+ + e^- \quad (5.7)$$

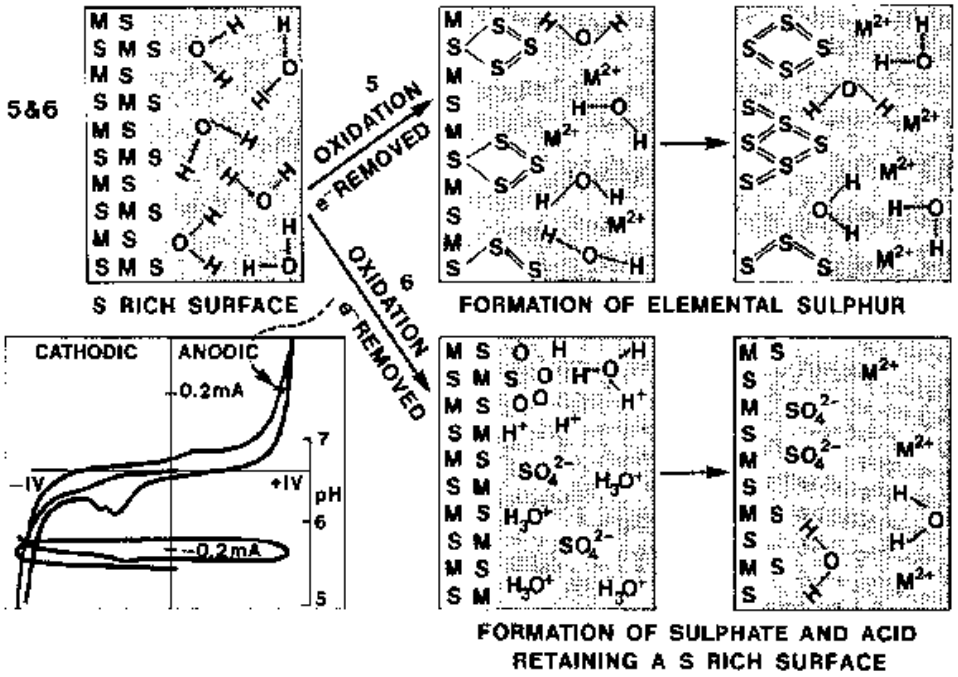

Figure 5.8 Anodic reactions steps 5 and 6 in the electrochemical model proposed by Thornber *et al* for CV of violarite at pH 6. [6] **Copyright 1983 Chapman and Hall Ltd.**

On the positive-going potential sweep up to +0.95 V (Figure 5.8), Thornber *et al* proposed the sulfur-rich surface of violarite will oxidise to form elemental sulfur at pH < 4 (anodic reaction 5) or SO_4^{2-} species at pH > 4 (anodic reaction 6) at ~ +0.85 V. At +0.95 V, SO_4^{2-} species are predicted as the stable redox species between pH 2 to 14 (according to the Pourbaix diagram in Figure 3.3) and elemental sulfur is not predicted to be stable at this positive potential. No explanation was provided by the author as to why the assignment for the oxidation of sulfur was at more positive potentials than predicted, or the stability of elemental sulfur at this potential. The authors also did not consider the potential formation of Fe_2O_3 or FeOOH as predicted by the Pourbaix diagrams in Figure 5.1 and Figure 5.2 at these positive potentials. Thornber *et al*[6] proposed that the formation of a "sulfur layer" on violarite may limit the dissolution of metal atoms. The authors were incorrect to propose the existence of a sulfur layer at this potential of +0.95 V, based on the Pourbaix diagrams in Figure 3.3 and Figure 5.1, where only SO_4^{2-} species are predicted to be stable.

At the end of both oxidation reactions 5 and 6 in Figure 5.8, the authors proposed the surface be rich in sulfur. On the reverse negative-going potential sweep, the authors proposed the reduction of sulfur to H_2S to occur between −0.45 V and −0.55 V (reactions 7 and 1 in Figure 5.9). This is agreeable as the predicted reduction of SO_4^{2-} species to elemental sulfur and H_2S, according to the Pourbaix diagram in Figure 5.1, will not occur due to slow kinetics.

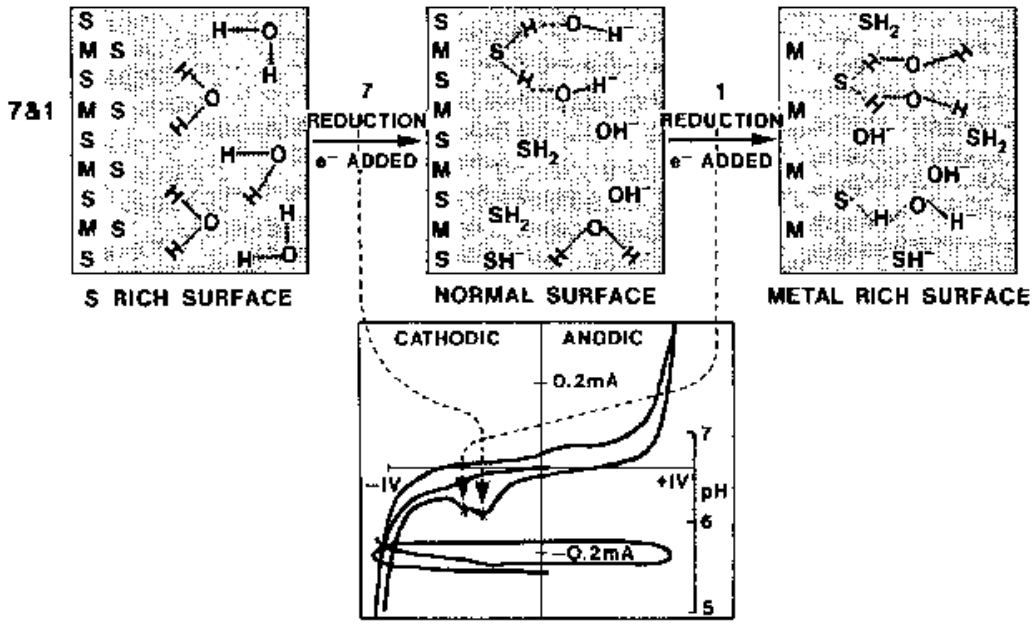

Figure 5.9 Reduction reactions steps 7 and 1 in the electrochemical model proposed by Thornber *et al* for CV of violarite at pH 6. [6] **Copyright 1983 Chapman and Hall Ltd.**

The assignments proposed by Thornber *et al*[6] are entirely dependent on the stability of the violarite electrode in solution. The presumed absence of iron oxide or hydroxide on immersion of the violarite electrode into the solution and applying very positive potentials do not agree with the predicted thermodynamic transitions proposed in the Pourbaix diagrams in Figure 5.1 and Figure 5.2.

Warner *et al*[7] performed a similar cyclic voltammetry experiment using a synthetic violarite electrode in 1M HCl solution (pH = 0) at 373 K. Warner *et al* proposed that the violarite electrode was kinetically inert towards oxidative

dissolution in acidic solution as the measured open circuit potential was recorded as −8 mV (vs SCE).

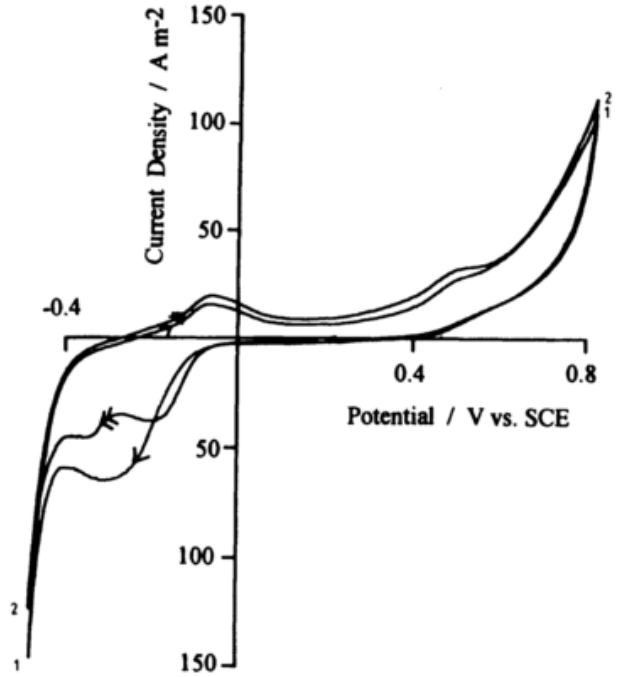

Figure 5.10 CV for violarite electrode performed by Warner *et al* in 1 M HCl, 343 K, scan rate of 4 mV s, RDE. Starting potential sweep is cathodic. [7]

Warner *et al*[7] performed the CV at a starting potential of 0 V to −0.40 V and reversed to +0.80 V. The first reduction feature at ∼−0.30 V was assigned to the reduction of violarite to Fe^{2+}, Ni^{2+} and H_2S, while the reduction peak at −0.40 V was assigned to proton reduction:

$$FeNi_2S_4 + 8H^+ + 2e^- \rightarrow Fe^{2+} + Ni^{2+} + 4H_2S \quad (5.8)$$

$$2H^+ + 2e^- \rightarrow H_2 \quad (5.9)$$

These assignments are in agreement with predictions in the Pourbaix diagram in Figure 5.1, where Fe^{2+}, Ni^{2+} and H_2S are the stable redox species present at this potential (0 V (vs SCE) = −0.241 V (vs SHE)) and pH 0. On the reverse positive-going potential sweep, the anodic peak at −0.10 V was assigned to the oxidation of metal-rich surface, however, no reaction equations were provided by the authors. The current author assumes that Fe(0) and Ni(0) were formed on the previous negative-going potential sweep from the reduction of Fe^{2+} and Ni^{2+}, as

predicted by the Pourbaix diagram in Figure 5.1. However, it is not expected that a bulk transformation to Fe(0) and Ni(0) occurred. Warner *et al*[7] proposed Fe(0) and Ni(0) to form only on the surface of violarite. This is similar to the findings in the previous chapter for the greigite electrode used in this thesis whereby the bulk structure of the electrode remained the same on applying a potential, but the surface is altered. It could be deduced that greigite and violarite may possess similar stabilities within the same potential window used, however, further spectroscopic evidence is required to support this hypothesis. The anodic peak at −0.10 V was assigned to the oxidation of both Fe(0) and Ni(0) to Fe^{2+} and Ni^{2+}. Warner *et al*[7] identified that violarite has a characteristic "prewave" feature in its CV at +0.50 V (vs SCE). The authors proposed this feature to be a secondary oxidation process (assigned to the oxidation of Fe^{2+} to Fe^{3+}), occurring in parallel with the main oxidation of violarite, which was assigned the formation of elemental sulfur. According to the Pourbaix diagram in Figure 5.1, elemental sulfur is not predicted to be stable at potentials > +0.20 V (vs SHE) or > 0.00 V (vs SCE) and instead, HSO_4^- is predicted to be stable above these potentials. Hence, the authors may be incorrect to assign the main oxidation peak at +0.80 V (vs SCE) to the formation of elemental sulfur. Instead, it is proposed here that this oxidation peak is assigned to the oxidation of violarite to Fe^{2+}, Ni^{2+} and HSO_4^-.

$$FeNi_2S_4 + 16H_2O \rightarrow Fe^{2+} + 2Ni^{2+} + 4HSO_4^- + 28H^+ + 30e^- \qquad (5.10)$$

These reactions are, however, dependent on the pH near the electrode to remain constant (pH = 0). Additionally, the Pourbaix diagram in Figure 5.1 is based on reactions at 298 K, thus the stability regions may shift for reactions at 373 K as performed by Warner *et al*[7]. It is expected that the proton reduction which occurred on the initial negative potential sweep may have increased the pH near the electrode and affected the stability of the violarite electrode, however, Warner *et al*[7] did not propose such change in the local pH of the electrode.

On the second negative-going potential sweep, Warner *et al* assigned the reduction peaks to the reduction of violarite and elemental sulfur via the following reactions:

$$FeNi_2S_4 + 8H^+ + 2e^- \rightarrow Fe^{2+} + Ni^{2+} + 4H_2S \quad (5.11)$$

$$S + 2H^+ + 2e^- \rightarrow H_2S \quad (5.12)$$

These reactions are in agreement with the Pourbaix diagram in Figure 5.1 where Fe^{2+}, Ni^{2+} and H_2S are the stable redox species predicted at potentials < +0.40 V (vs SCE).

The suggested stability of violarite at a potential of 0.00 V where FeOOH is predicted to form and the formation of elemental sulfur on the violarite electrode on a positive-going potential sweep are the two common concepts proposed by both Thornber *et al*[6] and Warner *et al*[7]. However, both studies did not characterise the violarite electrode in-situ to verify the stability of the electrode as well as the formation of elemental sulfur. The potential window used in the CV performed by both authors were also wider compared to the potential range used in this work (0.00 and −1.00 V (vs AgCl|Ag)). Therefore, it is not expected that the violarite material used in this thesis would undergo similar formation of elemental of sulfur and only interpretations up to 0.00 V are relevant to thesis.

5.2 Results

5.2.1 PBS pH 4.5 under argon

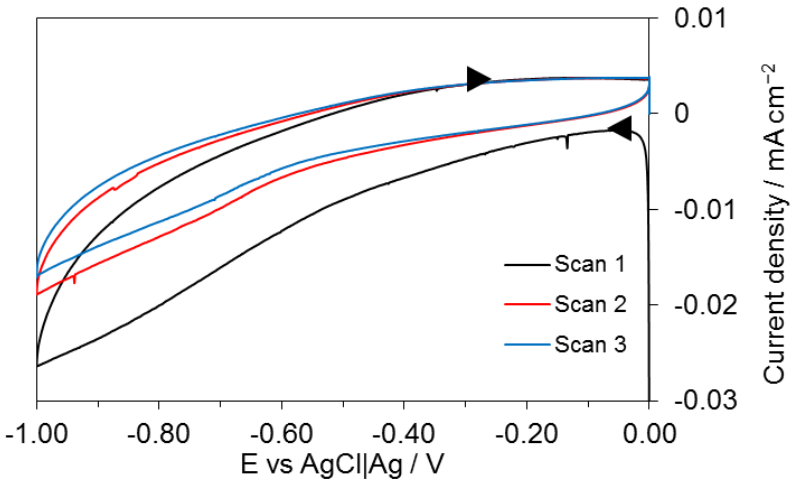

Figure 5.11 First, second and third scan of cyclic voltammogram of violarite in phosphate buffer solution (PBS) pH 4.5 under argon recorded at 10 mV s^{-1}. Potential sweep started at 0.00 V.

Figure 5.11 shows the first three CV scans of violarite in PBS pH 4.5 under argon where all CV scans appeared featureless with a broad reduction current on the initial negative-going potential sweep. This recorded CV is in contrast to the observation by Thornber *et al*[6] where there were two reduction peaks recorded at *c.a.* −0.40 V (vs. SCE) assigned to the reduction of violarite to Fe^{2+}, Ni^{2+} and H_2S (reaction (5.1)) and at *c.a.* −1.00 V (vs. SCE) assigned to proton reduction (reaction (5.2)). According to the Pourbaix diagram in Figure 5.1, at the onset of the negative-going potential sweep (0.00 V) in Figure 5.11 at pH 4.5, violarite is not predicted to be stable and is expected to reduce to Fe^{2+}, Ni^{2+} and H_2S (reaction (5.1)), or oxidise to form FeOOH and SO_4^{2-} (reaction (5.3)). The reduction or oxidation of violarite at 0.00 V will be dependent on the local pH near the electrode surface. It is expected that both water and proton reduction will take place during the negative-going potential sweep and lead to an increase in pH due to the production of OH^- species and the consumption of protons. Thus, with an increase in the local pH near electrode, it is most likely that the formation of FeOOH on the violarite electrode will be favoured at 0.00 V. However, the proposed increase in the local pH and the eventual formation of FeOOH need to

be verified. The Pourbaix diagram in Figure 5.1 predicts a bulk transformation of violarite to FeOOH at 0.00 V at pH 4.5, however, it is expected that the transformation to FeOOH may only be confined to the surface, as was observed for a greigite electrode in the previous chapters.

If FeOOH was present on the violarite electrode on the negative-going potential sweep, it is predicted to be stable up to potentials > −0.20 V, before it is reduced back to violarite at potentials < −0.20 V. However, the re-formation of violarite will depend on the presence of Ni^{2+} and SO_4^{2-} species near the electrode surface (reverse reaction of (5.3)). Subsequently, the reformed violarite is predicted to be stable up to potential of −0.40 V where it will be reduced to pentlandite (reaction (5.4)). Further reduction of pentlandite to metallic Fe and Ni is predicted to occur at −0.80 V (reaction (5.5)). These transformations may have contributed to the broad reduction current observed in the CV in Figure 5.11. The capping agent of the violarite nanoparticles used in this thesis was designed to protect the violarite surface from air-oxidation. If an oxide or hydroxide layer was formed prior to the cyclic voltammetry experiments, a distinct reduction peak would appear in the CV corresponding to the reduction of the iron oxide / hydroxide layer. Since no distinct reduction peak was observed in the CV in Figure 5.11, it seems evident that there was no oxide / hydroxide present on the violarite surface.

On the reverse positive-going potential sweep, no distinct oxidation peak was observed. The featureless positive-going potential sweep resembled the CV of violarite performed by Thornber *et al*[6] at pH 6, which suggests a significant increase in the local pH due to proton and water reduction on the previous negative-going potential sweep. Thornber *et al*[6] assigned the positive-going potential sweep to the oxidation of Fe(0) and Ni(0) produced on the negative-going potential sweep, but no distinct oxidation peak was observed in their study. If the local pH near the violarite electrode surface increased from pH 4.5 to 6 due to water and proton reduction, similar redox transformations are still expected, with the formation of Fe(0) and Ni(0) predicted at ~ −0.90 V.

The subsequent second and third scans in the CV in Figure 5.11 show the same featureless response which suggest the same redox processes occurred. It is unclear why there was no oxidation peak recorded on the positive-going sweep. Thornber *et al*[6] proposed that the violarite electrode is passivated by the formation of elemental sulfur on the positive-going sweep, which may prevent Fe(0) and Ni(0) to undergo redox reactions. However, such formation of elemental sulfur on the violarite electrode requires further evidence.

5.2.2 PBS pH 6.8 under argon

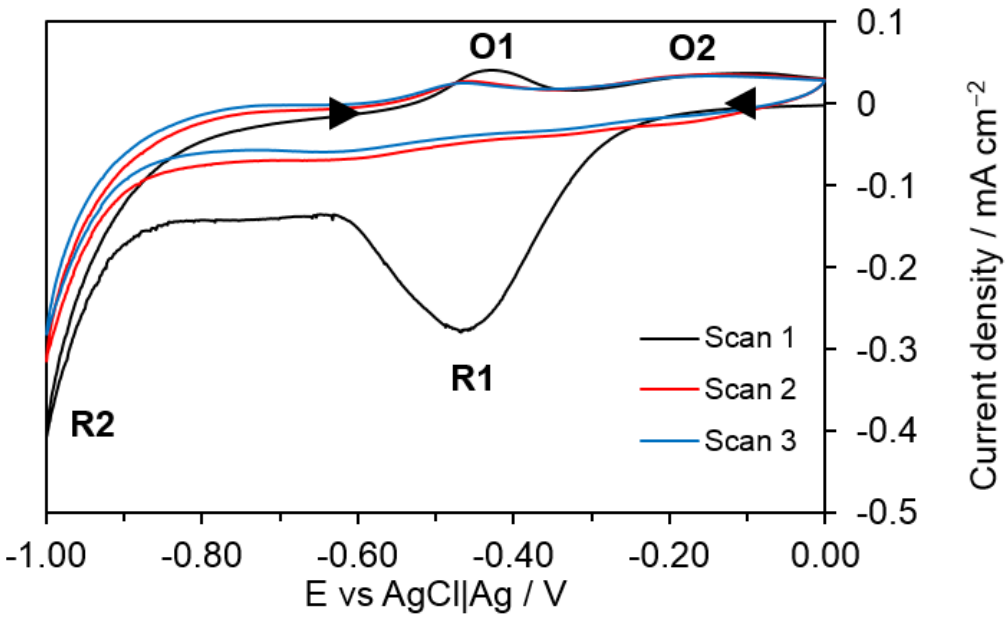

Figure 5.12 First, second and third scan of cyclic voltammogram of violarite in phosphate buffer solution (PBS) pH 6.8 under argon recorded at 10 mV s^{-1}. Potential sweep started at 0.00 V.

The first three scans of the CV of violarite recorded in PBS pH 6.8 under argon are shown in Figure 5.12. In comparison to the CV study reported by Thornber *et al*[6] recorded in pH 6, the redox features were observed at approximately the same potentials. Comparing the currents in the CVs recorded at pH 4.5 (Figure 5.11) and 6.8 (Figure 5.12), the currents at pH 4.5 were one order of magnitude smaller than at pH 6.8. Similar smaller currents were observed by Thornber *et al*[6] on performing CV of violarite at pH 4 compared to pH 6, but was not accounted for

by the authors. The difference in current magnitudes may be associated with the dissolution rate of violarite at various pH conditions.

Assuming that the violarite electrode was stable and did not undergo oxidation to form FeOOH at the start potential, peak R1 (−0.47 V) is assigned to the reduction of violarite to pentlandite (reaction (5.4)), based on the predictions in the Pourbaix diagram in Figure 5.1. If FeOOH was present on the surface of the violarite electrode, the reduction of FeOOH to violarite (reverse of reaction (5.3)) may also contribute to peak R1. Peak R2 at −1.00 V is assigned to water and proton reduction. Further reduction of pentlandite to metallic Fe and Ni is also predicted to occur at this potential (reaction (5.5)). At this point in the CV, the local pH near the electrode surface may increase due to the consumption of protons (proton reduction) as well as the production of OH^- species via water reduction.

On the reverse positive-going potential sweep, two anodic peaks O1 (−0.45 V) and O2 (−0.20 V) were observed. Peak O1 is assigned to the oxidation of Fe(0), Ni(0) and pentlandite back to violarite (reverse reactions of (5.4) and (5.5)), according to the Pourbaix diagram in Figure 5.1. Peak O2 is assigned to the oxidation of H_2S to SO_4^{2-} and the formation of FeOOH (reaction (5.3)).

The second and third scans in the CV in Figure 5.12 show an additional presence of two small reduction peaks at −0.20 and −0.60 V. However, the currents were significantly smaller compared to the first scan. The reduced currents may be a result of the formation of FeOOH on the positive-going potential sweep which may have passivated the violarite surface. In the second and third CV scans, the reduction peak at −0.20 V is assigned to the reduction of SO_4^{2-} to H_2S, while the reduction peak at −0.60 V is assigned to the reduction of violarite to pentlandite, similar to R1 on the first scan. As previously mentioned, the predictions in the Pourbaix diagram in Figure 5.1 are based on bulk transformations but do not consider the reaction kinetics of these transformations, for example the reduction of SO_4^{2-} will be hindered due to slow kinetics under ambient conditions and thus may not occur. Therefore, further evidence is needed to confirm the predicted

reduction of violarite to pentlandite, as well as the formation of FeOOH on the surface of the violarite electrode on immersion into the electrolyte.

5.2.3 PBS pH 4.3 and 6.5 under CO_2

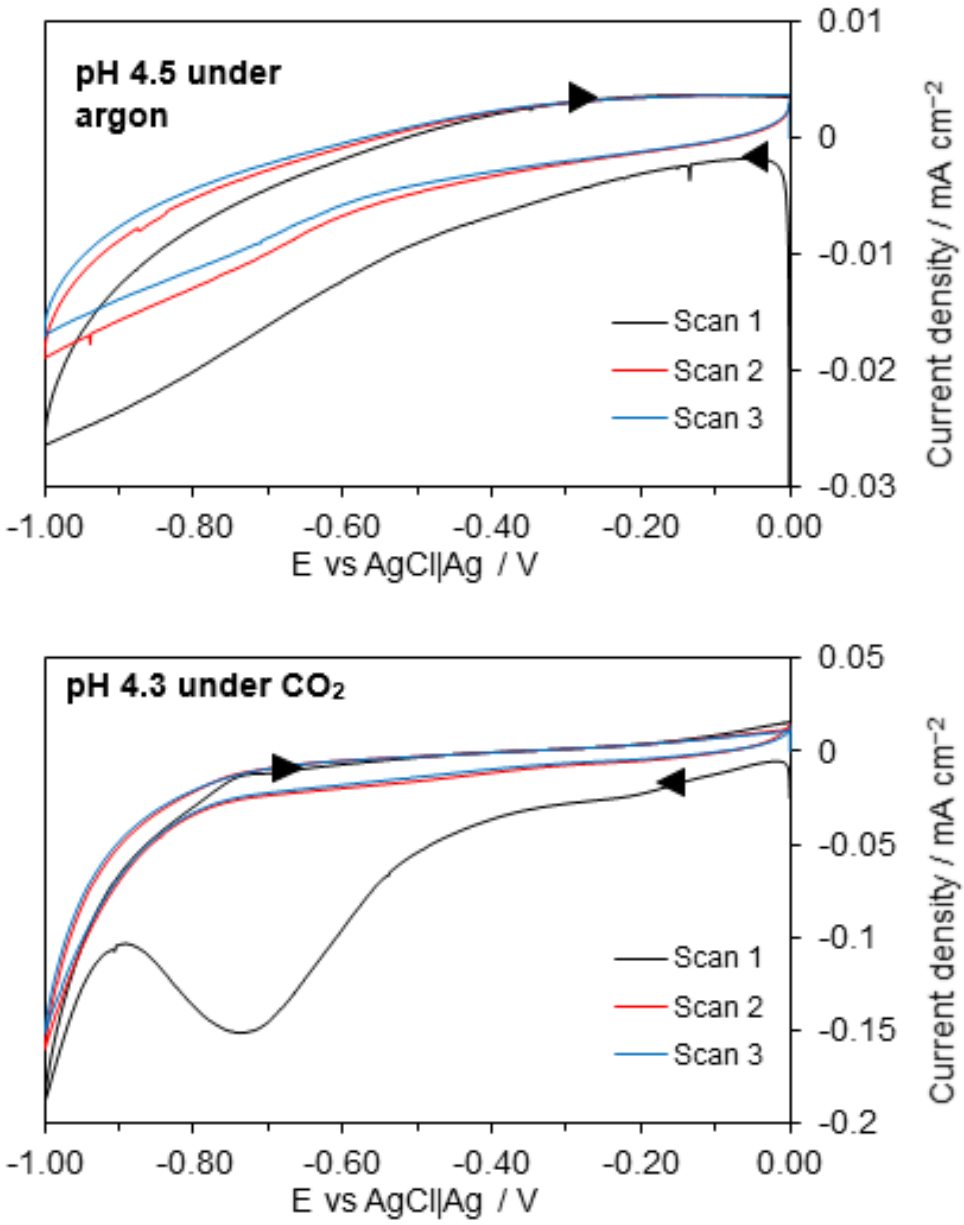

Figure 5.13 CVs of violarite in phosphate buffer solution (PBS) pH 4.5 under argon and 4.3 under CO_2 recorded at 10 mV s^{-1}. Potential sweep started at 0.00 V.

On introduction of CO_2 in PBS pH 4.3 in Figure 5.13, two distinct cathodic peaks were observed at −0.72 and −1.00 V. However, similar to the CV recorded under

argon, no distinct anodic peaks were present. The subsequent scans were also featureless which is comparable to the CV recorded under argon. According to the Pourbaix diagram in Figure 5.3, the formation of metastable nickel carbonate and nickel hydroxycarbonate are not predicted in a Ni-S-O_2-CO_2-H_2O system. At present, there are no Pourbaix diagrams available in literature for the same system without O_2. Therefore, inferring from the predictions in Figure 5.3, it is assumed that for the same system without O_2, the introduction of CO_2 will not favour the formation of nickel carbonate or nickel hydroxycarbonate on the surface of the violarite electrode at any potential and pH. However, it is still important to account for the possible formation of iron carbonate and iron carbonate green rust ($Fe_2(OH)_2CO_3$ and $Fe_6(OH)_{12}CO_3$) on violarite, which were considered in the previous chapters for a greigite electrode.

Iron carbonate is only predicted to form at a narrow pH range (pH 5.5 – 7) and potential range (−0.20 to −0.40 V) as shown in the Pourbaix diagram in Figure 3.5. Iron carbonate green rust is a metastable species compared to iron oxides and hydroxides and thus is not expected to form (see Figure 3.4). In the previous chapters, the introduction of CO_2 suppressed currents in the CV of a greigite electrode and was proposed to hinder water and proton reduction from occurring on greigite. Considering the predictions in the Pourbaix diagrams in Figures 3.5 and 3.6, the suppressed currents were initially attributed to the possible formation of iron carbonate and iron carbonate green rust. However, there was no spectroscopic evidence for the formation of both materials found on the greigite electrode. Therefore, the suppressed currents were later proposed to have resulted from adsorption of dissolved CO_2 species, blocking surface sites on the greigite electrode. It is inferred from this conclusion that the formation of iron carbonate and iron carbonate green rust will also not be favoured on the surface of a violarite electrode. However, further evidence is required.

In contrast to the electrochemical behaviour of greigite, the CV of violarite was not suppressed on the introduction of CO_2. The currents were one order of magnitude larger and distinct redox peaks appeared on the introduction of CO_2 in pH 4.3, while at pH 6.5, the currents were approximately doubled and the redox

features were negatively shifted. However, the current enhancement was only observed on the first scan in the CV of violarite in pH 4.3 and 6.5 under CO_2. The current enhancement observed could be attributed to CO_2 reduction. The subsequent second and third CV scans under CO_2 remained featureless, similar to the CV response under argon at both pHs, which suggests that a passivating layer remained present on the surface. The passivating layer present on the violarite electrode may likely be an iron oxide / hydroxide layer since iron oxide / hydroxide is predicted to form on the violarite electrode at the onset potential of 0.00 V according to the Pourbaix diagram in Figure 5.1. However, further in-situ characterisation of the electrode is needed to verify the nature of the passivating layer present on the electrode surface.

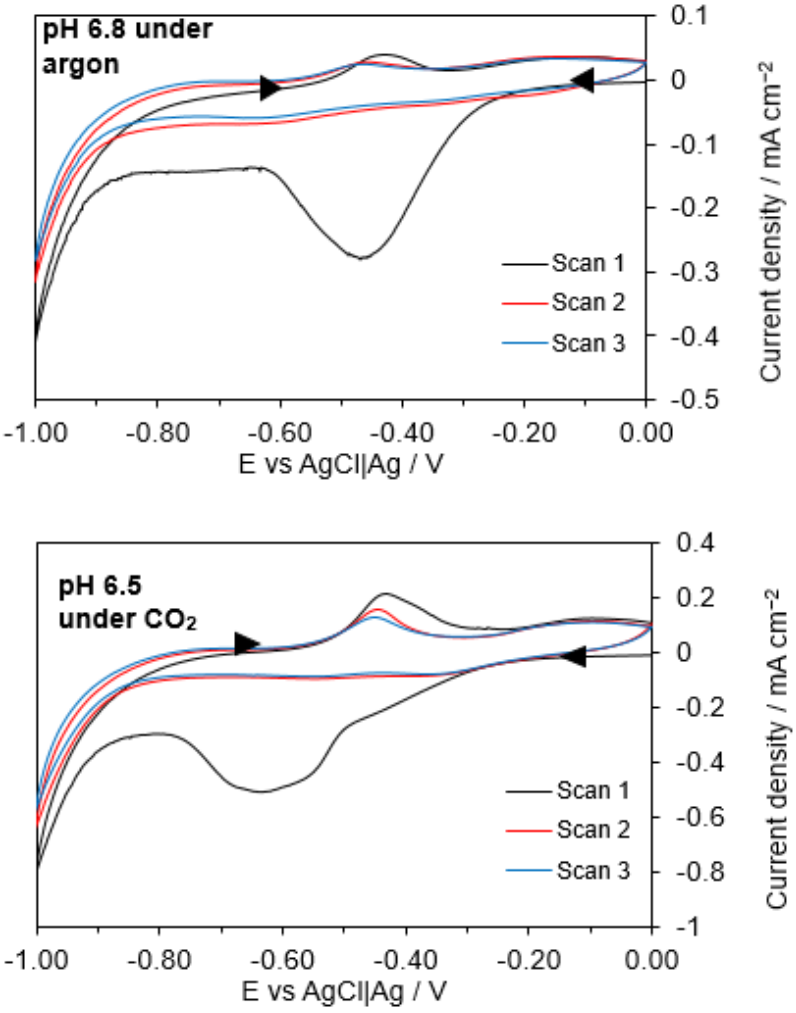

Figure 5.14 CVs of violarite in phosphate buffer solution (PBS) pH 6.8 under argon and 6.5 under CO_2 recorded at 10 mV s^{-1}. Potential sweep started at 0.00 V.

The CV of violarite at pH 6.5 under CO_2 resembled that recorded at pH 6.8 under argon. Thus, it may be deduced that similar redox reactions occurred under both conditions. For pH 4.3 under CO_2, one distinct reduction peak was observed at −0.72 V and is assigned to the reduction of violarite to Fe^{2+}, Ni^{2+} and H_2S (reaction (5.1)) as predicted by the Pourbaix diagram in Figure 5.1.

Yamaguchi *et al*[1] tested for electrochemical CO_2 reduction using a nickel-doped greigite electrode, which was characterised as violarite, and observed increased Faradaic efficiencies for CO_2 reduction as well as an increased H_2 production compared to greigite. The authors, however, did not suggest any reason for the increased Faradaic efficiency for CO_2 reduction and H_2 generation on violarite compared to greigite, other than quoting "the nickel ion centre in the $FeNi_2S_4$ plays an important role in the electrochemical reduction of CO_2 on the surface of FeS deposits".

Comparing the CV response of greigite and violarite in PBS pH 6.8, the redox features of greigite remained present on each subsequent CV scan and the currents also increased with each scan, while for violarite the redox features were suppressed after the first CV scan and the subsequent CV scans appeared featureless. The differences in the CV response of greigite and violarite must be associated with a differing composition / coverage present on each greigite and violarite electrode during the experiment. The presence of Ni in violarite ($FeNi_2S_4$) clearly makes the material more prone to hydrolysis with water compared to greigite (Fe_3S_4). According to the Pourbaix diagram in Figure 5.2 for an Fe-Ni-H_2O system (in the absence of sulfur), Fe_2O_3 and $NiFe_2O_4$ are predicted to be present at the onset potential of 0.00 V. Fe_2O_3 and $NiFe_2O_4$ could be formed via oxidative dissolution of violarite and are predicted to remain stable up to potentials > −0.50 V. Therefore, the additional presence of Fe_2O_3 and $NiFe_2O_4$ may have passivated violarite surface compared to greigite where only FeOOH was predicted to form at the onset potential. Ni was added to increase the reactivity and catalytic activity of an iron sulfide electrode, however, a disadvantage of the addition of Ni could be the lack of stability of the material and the ease of formation of iron and iron-nickel oxides.

5.2.4 $KHCO_3$ pH 8.55 and K_2CO_3 pH 11.2 under argon

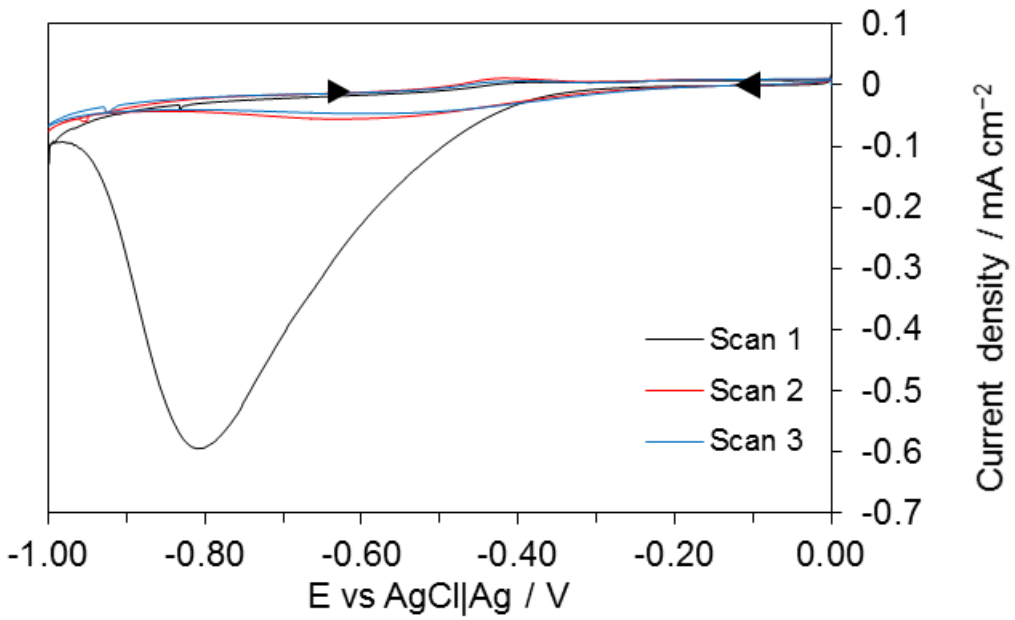

Figure 5.15 First, second and third scan of cyclic voltammogram of violarite in $KHCO_3$ pH 8.55 under argon recorded at 10 mV s^{-1}. Potential sweep started at 0.00 V.

Figure 5.15 and Figure 5.16 show the CVs of violarite recorded in $KHCO_3$ pH 8.55 and K_2CO_3 pH 11.2 electrolyte solutions under argon. The CV response in $KHCO_3$ appeared to be similar to that recorded in PBS pH 6.8, with the cathodic peak shifted by *c.a.* −0.40 V. This negative shift in potential indicates a higher energy barrier was required for the surface reaction to proceed in $KHCO_3$ pH 8.55 compared to in PBS pH 6.8. At pH 6.8, this reduction peak was assigned to the reduction of violarite to pentlandite (reaction (5.4)), based on the predictions in the Pourbaix diagram in Figure 5.1, if FeOOH was absent on immersion of the electrode into the electrolyte. However, if FeOOH was present on the surface of the violarite electrode, the reduction of FeOOH to violarite (reverse of reaction (5.3)) may also contribute to this reduction peak. On inspection of the Pourbaix diagram in Figure 5.1, FeOOH is predicted to be the stable redox species between pH 5 – 9.5 at 0.00 V. Therefore, the reduction peak observed in $KHCO_3$ may be assigned to the reduction of FeOOH to violarite as well as the reduction of violarite to pentlandite. This reduction peak may have been negatively shifted compared to PBS pH 6.8 due to the presence of adsorbed HCO_3^- present on the

electrode surface in $KHCO_3$. However, further evidence is required for such adsorption of HCO_3^- on the violarite electrode. As previously mentioned, the formation of nickel carbonate, nickel hydroxyl carbonate, iron carbonate and iron carbonate green rust are not considered here for both $KHCO_3$ and K_2CO_3 electrolytes as these are metastable phases and are not expected to form on the violarite electrode under these experimental conditions. Similar to the CV in pH 6.8, the subsequent CV scans in $KHCO_3$ show significantly reduced currents compared to the first CV scan which may be attributed to the passivation of the surface by FeOOH produced on the positive-going potential sweep.

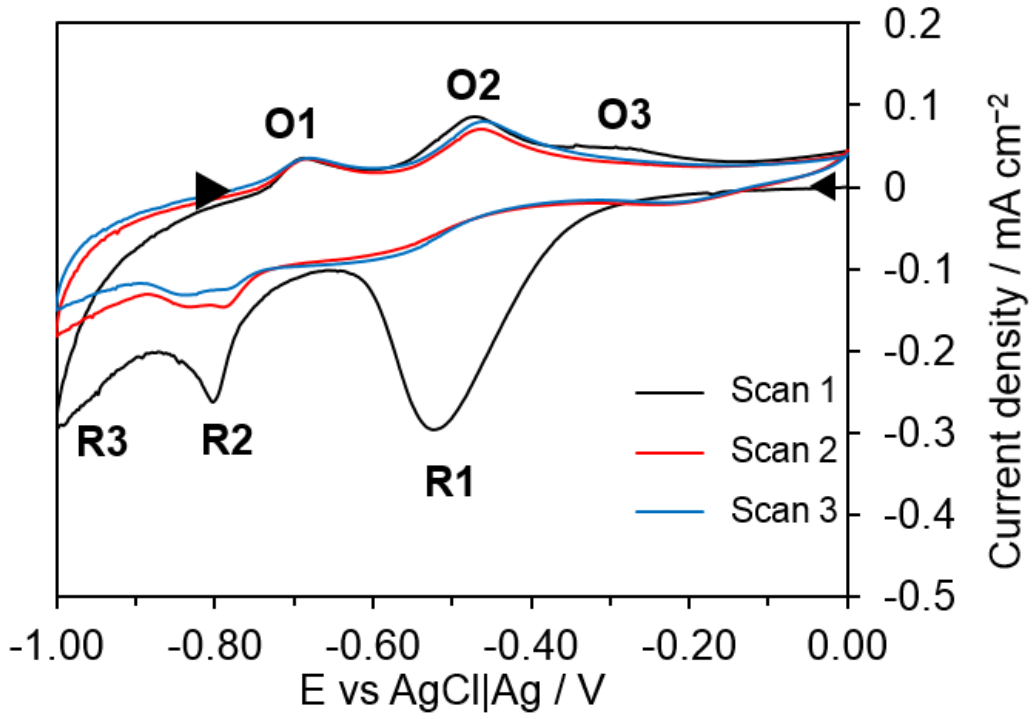

Figure 5.16 First, second and third scan of cyclic voltammogram of violarite in K_2CO_3 pH 11.2 under argon recorded at 10 mV s^{-1}. Potential sweep started at 0.00 V

In contrast to all the CV responses observed for violarite, the CV response in K_2CO_3 pH 11.2 exhibited the most active redox response with three cathodic and three anodic peaks present. According to the Pourbaix diagram in Figure 5.1, FeOOH and $Ni(OH)_2$ are predicted to be the stable redox species at 0.00 V up to *c.a.* −0.75 V, where they will reduce to violarite. Violarite is only predicted to be stable between −0.75 and −0.80 V at this pH and is predicted to be further

reduced to pentlandite at potentials < −0.80 V. Assuming violarite was oxidised to form FeOOH and $Ni(OH)_2$ on immersion into the electrolyte, peak R1 (−0.52 V) is assigned to the reduction of FeOOH and $Ni(OH)_2$ to violarite (reaction (5.13)), peak R2 (−0.80 V) is assigned to the reduction of violarite to pentlandite (reaction (5.14)) and the reduction of SO_4^{2-} to HS^- (reaction (5.15)), while peak R3 (−1.00 V) is assigned to water reduction (reaction (5.16)).

$$FeOOH + 2Ni(OH)_2 + 4SO_4^{2-} + 39H^+ + 31e^- \rightarrow FeNi_2S_4 + 4H_2O \quad (5.13)$$

$$2FeNi_2S_4 + 0.5Ni(OH)_2 + 2.5FeOOH + 8.5H^+ + 8.5e^- \rightarrow Fe_{4.5}Ni_{4.5}S_8 + 6H_2O \quad (5.14)$$

$$SO_4^{2-} + 9H^+ + 8e^- \rightarrow HS^- + 4H_2O \quad (5.15)$$

$$2H_2O + 2e^- \rightarrow H_2 + 2OH^- \quad (5.16)$$

On the reverse positive-going potential sweep, peak O1 (−0.70 V) is assigned to the oxidation of pentlandite to violarite (reverse reaction (5.14)), peak O2 (−0.45 V) is assigned to the oxidation of violarite to FeOOH and $Ni(OH)_2$ (reverse reaction (5.13)), and peak O3 (−0.30 V) is assigned to the oxidation of HS^- to SO_4^{2-} (reverse reaction (5.15)). These predicted transformations, however, will depend on the reaction kinetics. The transformation of violarite to FeOOH and $Ni(OH)_2$ may also be confined to the surface and may not be a bulk transformation, as was observed for greigite electrode in the previous chapter. Subsequent CV scans in K_2CO_3 show a similar CV response compared to the first CV scan which suggests similar redox reactions occurred. This is in contrast to the CVs recorded in PBS pH 4.3 and 6.5 and $KHCO_3$ pH 7.1 where the currents in the subsequent scans were significantly decreased and the violarite was assumed to be passivated by the formation of FeOOH. It is also possible that the solution pH is a significant factor for the redox activity of violarite since more redox features were observed at high pH than at low pH.

5.2.5 $KHCO_3$ pH 7.1 and K_2CO_3 pH 10.1 under CO_2

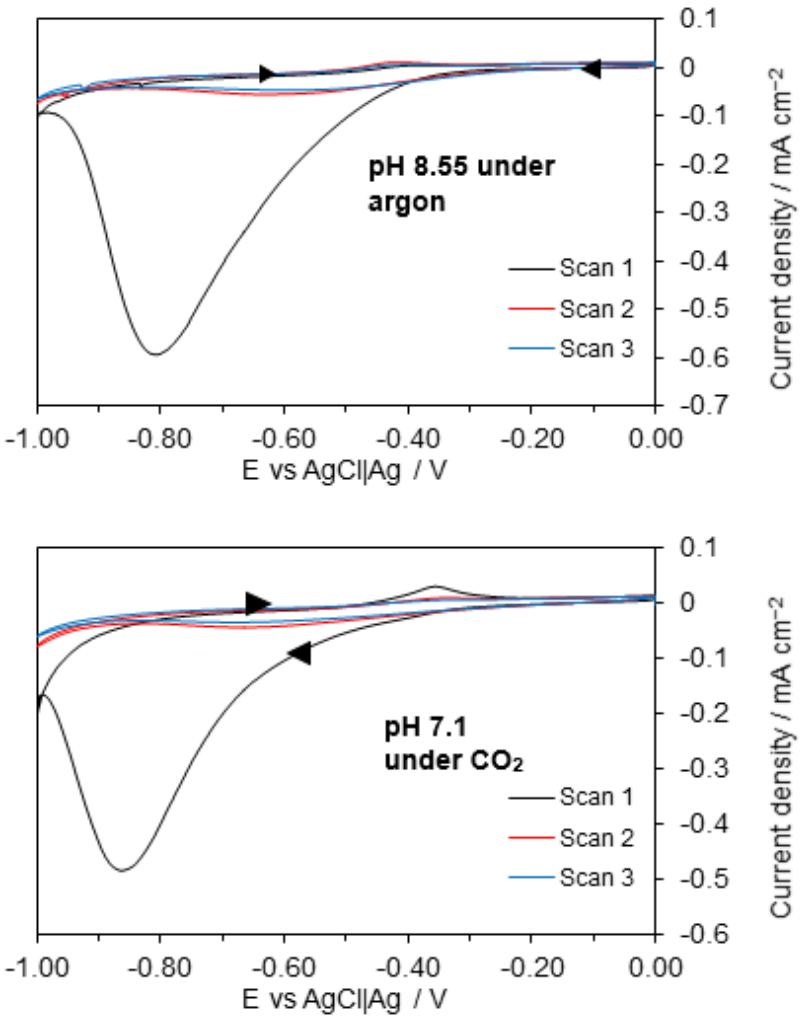

Figure 5.17 CVs of violarite in $KHCO_3$ pH 8.55 under argon and 7.1 under CO_2 recorded at 10 mV s^{-1}. Potential sweep started at 0.00 V.

Figure 5.17 and Figure 5.18 compare the CVs of violarite recorded in $KHCO_3$ and K_2CO_3 under both argon and CO_2. On inspection of the CVs on introduction of CO_2, the CV responses remained approximately similar to those observed under argon. The currents recorded in K_2CO_3 and $KHCO_3$ under CO_2 were not significantly larger compared to CVs under argon. This is in contrast to the observation made in PBS pH 4.3 and 6.5 under CO_2 where the currents were one order of magnitude larger at pH 4.3 and doubled at pH 6.5 under CO_2.

In the CV of violarite in $KHCO_3$ under CO_2, the reduction peak was negatively shifted by *c.a.* 0.05 V, while in K_2CO_3 under CO_2, there was significant noise

recorded in the currents between −0.70 and −1.00 V. Referring to the Pourbaix diagram in Figure 5.1, the pH shift in $KHCO_3$ from 8.55 to 7.1 on the introduction of CO_2 does not involve different redox species, thus similar redox reactions are expected which explains the unchanged CV response on introduction of CO_2 in $KHCO_3$. In contrast, for K_2CO_3, the pH shift from 11.2 to 10.1 will result in moving closer to a different stability region where $Ni(OH)_2$ is no longer predicted to be the stable redox species. This may explain the reduced number of reduction peaks on introduction of CO_2 in K_2CO_3. It is also evident from the noise in currents recorded in K_2CO_3 under CO_2 that there was an increase in H_2 generation. Increased water reduction may have resulted from the absence of $Ni(OH)_2$ which may have blocked surface sites for water reduction.

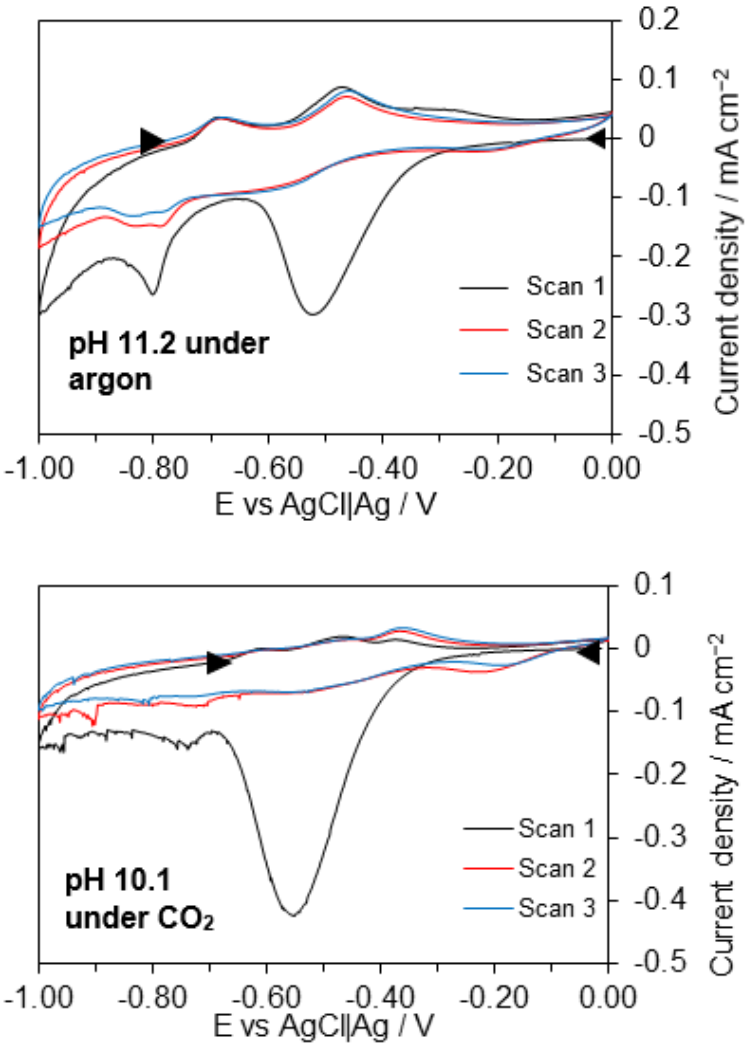

Figure 5.18 CVs of violarite in K_2CO_3 pH 11.2 under argon and 10.1 under CO_2 recorded at 10 mV s^{-1}. Potential sweep started at 0.00 V.

5.2.6 Discussion

Pourbaix diagrams in Figure 5.1 - Figure 5.3 were used to assign the redox features in the CVs of violarite presented in this chapter. At pH 4, the reduction peak was assigned to the reduction of violarite to Fe^{2+}, Ni^{2+} and H_2S. At pH > 4, the reduction peaks were assigned to the reduction of violarite to pentlandite and the reduction of FeOOH or $Ni(OH)_2$ formed on application of 0 V in electrolyte media. The oxidation peaks were assigned to reverse reactions of the reduction processes. In general, violarite exhibited a high redox activity only on the first CV scan, with significantly diminished currents on the subsequent CV scans except in K_2CO_3 pH 11. The reduced currents were attributed to the passivation of the violarite surface by the formation of FeOOH on the positive-going potential sweep. However, further evidence is required to verify the presence of FeOOH. The most redox features were observed in the CV in K_2CO_3 and was attributed to the additional predicted formation of $Ni(OH)_2$ on immersion of the violarite electrode and application of 0 V as well as the high pH.

On introduction of CO_2, the currents increased and were not suppressed, which is the opposite trend compared to the CVs of greigite on introduction of CO_2. The reduction peaks in the CVs of violarite under CO_2 were also slightly negatively shifted. The current enhancement and shift in peak potentials were attributed to CO_2 reduction as well as the adsorption of dissolved CO_2 species on the surface of the violarite electrode. The increased activity under CO_2 is comparable to the study performed by Yamaguchi *et al*,[1] where the authors recorded increased Faradaic efficiencies for a violarite electrode compared to a greigite electrode. It is proposed here that the introduction of CO_2 may have halted the transformation of violarite to FeOOH and $Ni(OH)_2$ on immersion into the electrolyte, leading to increased currents in CVs of violarite under CO_2 on the first CV scan.

The current enhancement recorded in the CVs of violarite on introduction of CO_2 is in contrast with the suppressed currents observed for greigite electrode on introduction of CO_2 detailed in chapter 3. It may be that the cubic Fe-Ni structure of violarite is more catalytic for CO_2 reduction compared to greigite due to lower binding energies of CO_2 and its dissolved species on violarite. DFT calculations by

Varley *et al*[8] show that the substitution of Ni for an Fe atom in an [Fe_4S_4] cubane structure of a CODH enzyme resulted in more thermodynamically favourable binding energies of CO_2 reduction intermediates. The authors proposed that the enhanced CO_2 reduction activity on Ni-containing cubanes was due to the stabilisation of the CO_2 intermediates. The stabilisation of the intermediates is achieved via the breaking of Ni-S and Fe-S bonds within the cubane structure. The authors also acknowledged that while CO_2 reduction is feasible, hydrogen evolution reaction (HER) is also favoured on both [Fe_4S_4] and [$NiFe_3S_4$] cubanes. This is in agreement with the HER observed for both greigite and violarite presented in this thesis.

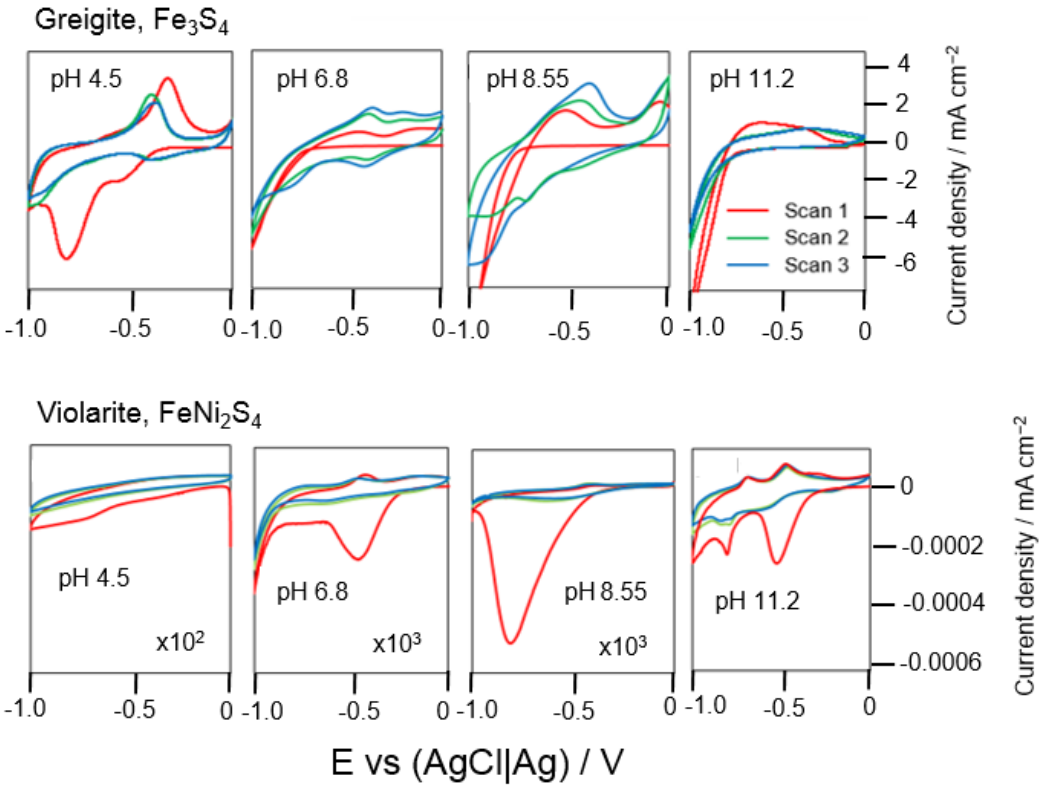

Figure 5.19 Comparison of CV responses of greigite and violarite at pH 4.5, 6.8, 8.55 and 11.2 under argon at scan rate of 10 mVs^{-1}.

The CV responses of violarite at pHs 4.5, 6.8, 8.55 and 11.2 under argon are contrasted with the CV responses of greigite in Figure 5.19 under the same conditions. As previously mentioned, only the first potential sweep showed redox activity for violarite with the subsequent scans appearing featureless. This is in contrast to greigite where redox peaks were still distinct on subsequent potential

sweeps. These differences between the CV responses of violarite and greigite suggest that the incorporation of nickel into an iron sulfide structure has a significant impact on the electrochemical behaviour of violarite, resulting in a passivated CV response compared to greigite. Considering the stability of both violarite and greigite at the starting potential of 0.00 V used in the CV experiments in this thesis, FeOOH and possibly $NiFe_2O_4$ are predicted to be present on the violarite electrode, while greigite is predicted to remain stable. Therefore, this may explain the variation in the CV responses of both violarite and greigite. The next chapter details the spectroscopic data to characterise the violarite electrode surface with applied potentials to verify these predictions and hypothesis.

5.3 References

1. Yamaguchi, A. *et al.* Electrochemical CO2 reduction by Ni-containing iron sulfides: How is CO2 electrochemically reduced at bisulfide-bearing deep-sea hydrothermal precipitates? *Electrochim. Acta* **141,** 311–318 (2014).

2. Russell, M. J., Daniel, R. M., Hall, A. J. & Sherringham, J. A. A hydrothermally precipitated catalytic iron sulphide membrane as a first step toward life. *J. Mol. Evol.* **39,** 231–243 (1994).

3. Warner, T. E., Rice, N. M. & Taylor, N. Thermodynamic stability of pentlandite and violarite and new EH-pH diagrams for the iron-nickel sulphur aqueous system. *Hydrometallurgy* **41,** 107–118 (1996).

4. Thompson, W. T., Kaye, M. H., Bale, C. W. & Pelton, A. D. Pourbaix Diagrams for Multielement Systems. in *Uhlig's Corrosion Handbook* 103–109 (Wiley, Hoboken, 2011). doi:10.1002/9780470872864.ch8

5. Langmuir, D., Chrostowski, P., Vigneault, B. & Chaney, R. Issue Paper on the Environmental Chemistry of Metals. (2005). Available at: https://www.researchgate.net/publication/237330649_ISSUE_PAPER_ON_THE_ENVIRONMENTAL_CHEMISTRY_OF_METALS.

6. Thornber, M. R. Mineralogical and electrochemical stability of the nickel-iron sulphides-pentlandite and violarite. *J. Appl. Electrochem.* **13,** 253–267 (1983).

7. Warner, T. E., Rice, N. M. & Taylor, N. Electrochemical study of oxidative dissolution of synthetic violarite in aqueous media. in *Hydrometallurgy '94: Papers presented at the international symposium `Hydrometallurgy '94' organized by the Institution of Mining and Metallurgy and the Society of Chemical Industry, and held in Cambridge, England, from 11 to 15 July, 1994* 273–287 (Springer Netherlands, 1994). doi:10.1007/978-94-011-1214-7_16

8. Varley, J. B. *et al.* Ni-Fe-S cubanes in CO2 reduction electrocatalysis: A DFT study. *ACS Catal.* **3,** 2640–2643 (2013).

Chapter 6 In-situ spectroelectrochemistry of Violarite

6.1 Introduction

Following the redox assignments of the CVs of violarite in chapter 5, this chapter focuses on monitoring the structural changes of violarite in-situ using similar techniques described in chapter 4, in-situ FTIR and in-situ XAS, to verify the redox assignments of violarite. The IR-active groups present near the electrode surface are monitored via in-situ FTIR, while the oxidation states and coordination environment of Fe and Ni of violarite are analysed using in-situ XAS.

6.2 In-situ XAS

The XANES spectra of reference nickel compounds on the Ni K-edge in Figure 6.1 and Figure 6.2 are used for comparison to the experimental XANES spectra obtained on the Ni K-edge for violarite. These include XANES spectra of Ni, NiS, NiS_2, $2NiCO_3.3Ni(OH)_2.4H_2O$, NiO, $Ni(OH)_2$, Ni carbonate, $NiFe_2O_4$, $NiSO_4.6H_2O$, $Ni(NO_3)_2.6H_2O$. The XANES spectra of Fe compounds on the Fe K-edge presented in chapter 4 will also be referred to in this section to compare with the XANES spectra of violarite on the Fe K-edge. Characteristic differences between the XANES spectra of nickel oxide versus nickel sulfide can be seen in Figure 6.1 and Figure 6.2 where nickel oxide compound is characterised by a sharp white line intensity, while nickel sulfide displayed a broad XANES edge. However, for a number of Ni compounds, the difference is not as significant, for example the XANES spectra of $NiSO_4.6H_2O$, $2NiCO_3.3Ni(OH)_2.4H_2O$ and $Ni(NO_3)_2.6H_2O$ are very similar.

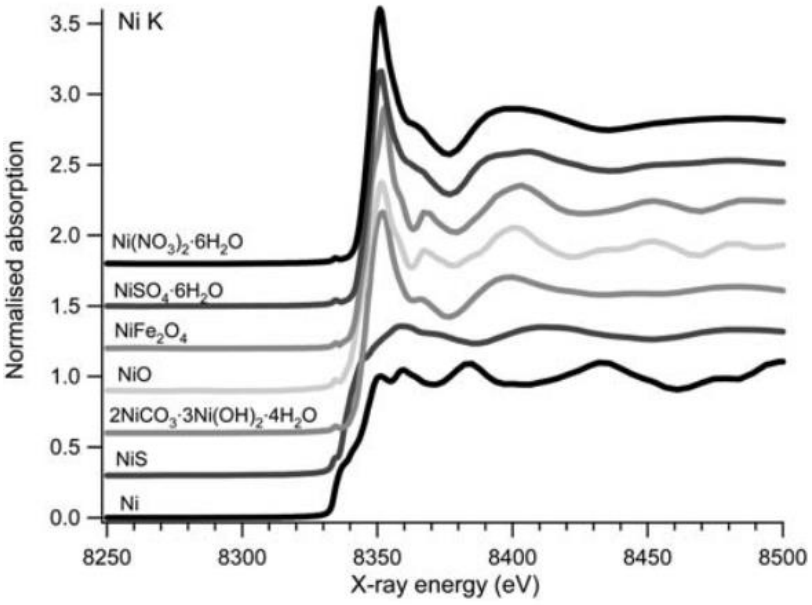

Figure 6.1 Ni K-edge XANES spectra of reference nickel compounds: Ni, NiS, $2NiCO_3.3Ni(OH)_2.4H_2O$, NiO, $NiFe_2O_4$, $NiSO_4.6H_2O$, $Ni(NO_3)_2.6H_2O$. [1]

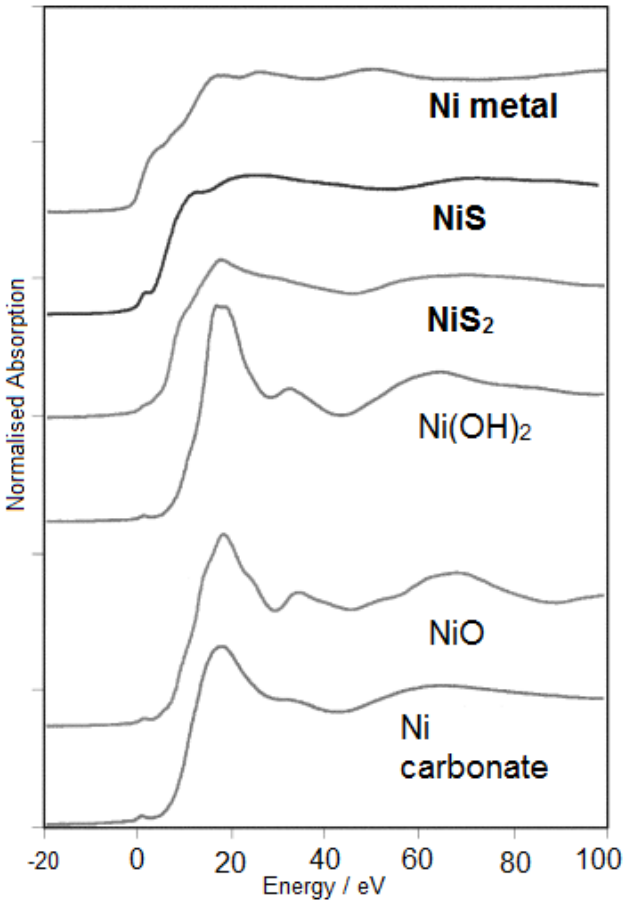

Figure 6.2 Ni K-edge XANES spectra of reference nickel compounds: Ni, NiS, NiS_2, $Ni(OH)_2$, NiO and Ni carbonate.[2]

As previously mentioned in chapter 4, the XAS experiments were carried out by two students, one of whom is the author of this thesis. Detailed XAS analysis were published in the thesis in reference 3. For violarite, the XANES spectra was recorded in PBS pH 6.8 under nitrogen only due to limited access to XAS facilities. Figure 6.3 and Figure 6.4 show the in-situ XANES spectra of violarite on the Fe K-edge and Ni K-edge, respectively, recorded in phosphate buffer solution pH 6.8 under nitrogen.

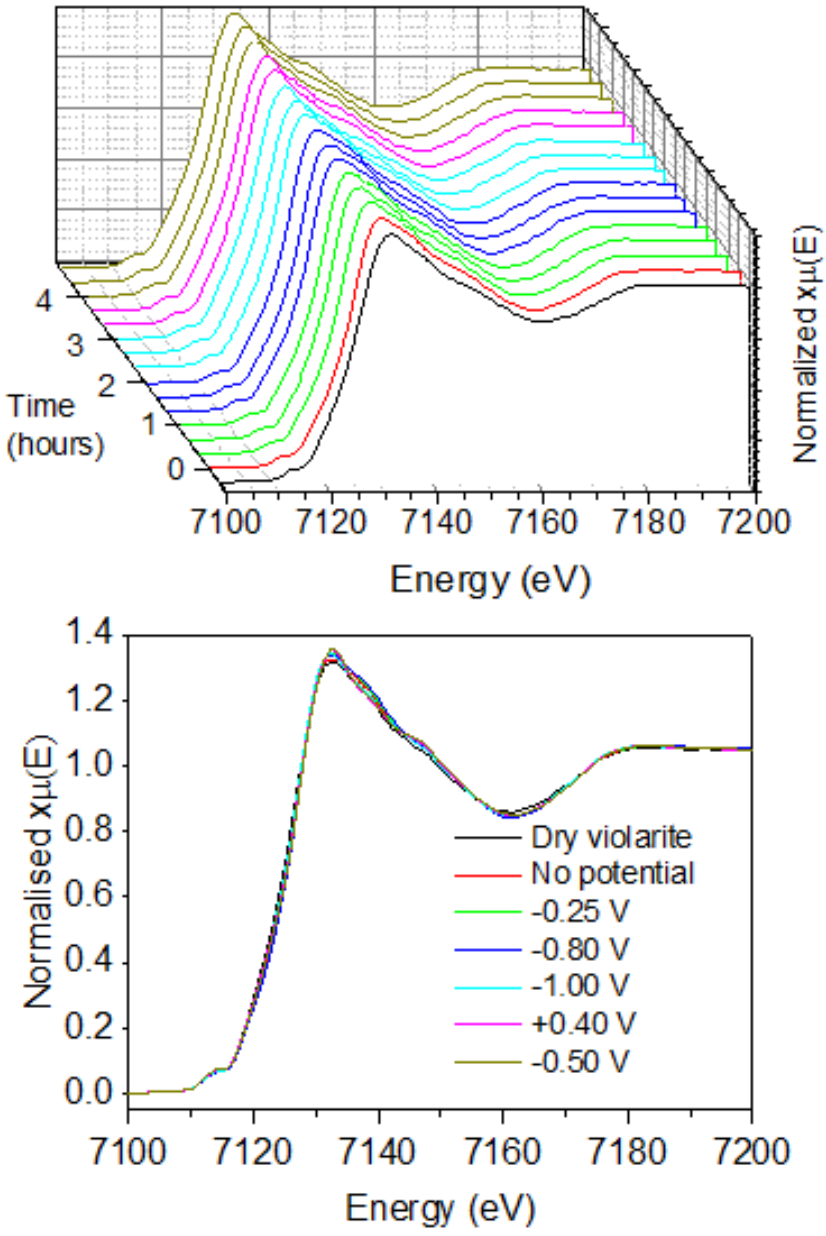

Figure 6.3 In-situ XANES data on Fe K-edge of violarite in phosphate buffer solution pH 6.8 under nitrogen. Top: Stacked spectra with three scans of each potential step. Bottom: merged spectra with last scan of each potential step.

On inspection of the XANES spectra on the Fe K-edge in Figure 6.3, there was very little change observed throughout the experiment. The features in the XANES spectra remained unchanged and were similar to the XANES spectrum of the dry violarite electrode. There was no characteristic "pre-edge" feature of a sulfide character at *c.a.* 7120 eV, which was observed previously in chapter 4 for greigite. The XANES spectra in Figure 6.3 resembled the XANES spectra of greigite at pH 4.5 under argon where the spectral features observed were proposed to be associated with the presence of an iron oxide / hydroxide layer formed on the greigite electrode. This suggests that a high percentage of Fe-O bonds compared to Fe-S bonds were present in the dry violarite sample. According to LCF (linear combination fitting where the XANES spectra are fitted to the XANES spectra of reference compounds), 56% of the Fe centres were consistent with iron oxyhydroxide (FeOOH) structure, while the remaining 44% of the Fe centres were consistent with greigite structure. The ratio was found to remain constant throughout the experiment, which is reflected in the unchanged XANES spectra on the Fe K-edge of the violarite material investigated.

It is unclear why there was no change in the XANES spectra recorded on applying potentials of −0.80 and 1.00 V, where water and proton reduction were expected to occur. In chapter 4, water and proton reduction were proposed to have instigated the formation of iron oxide / hydroxide on a greigite electrode. Inferring from the unchanged XANES spectra at these potentials for violarite, it is clear that the iron oxyhydroxide remained stable and no further transformation occurred. Based on the LCF, the violarite electrode was not fully oxidised and a high percentage of sulfide character still remained (44%). For a Fe-Ni-S-H_2O system, FeOOH is predicted to be stable up to −0.30 V at pH 6.8 according to the Pourbaix diagram in Figure 5.1. FeOOH is predicted to reduce to violarite at −0.30 V, and further reduction of violarite to pentlandite is predicted at −0.50 V. Pentlandite is predicted to be stable up to −1.00 V at pH 6.8. However, the XANES spectra in Figure 6.3 remained unchanged on applying potentials of −0.80 and −1.00 V and there was no obvious characteristic broad edge XANES feature of a sulfide character present. It is most likely that only a small percentage of violarite remained within the electrode and thus the XANES spectral features for the

transformation of FeOOH to violarite and subsequently violarite to pentlandite were masked by the XANES features of FeOOH present in high amounts on the electrode. Since FeOOH remained stable on applying potentials up to −1.00 V as observed in Figure 6.3, it is likely that there was an increase in the local pH near the electrode to pH > 8 where Fe_3O_4 / $Fe(OH)_2$ are predicted to be stable at this potential range (see Pourbaix diagrams in Figures 3.1 and 3.4).

On applying a positive potential of +0.40 V, the XANES spectra remained unchanged which is consistent with the predicted stability of iron oxyhydroxide / oxide as seen in the Pourbaix diagram in Figure 3.1 where it is predicted to be stable at potentials > −0.40 V. At the last potential step applied (−0.50 V), the reduction of this iron oxide / oxyhydroxide layer to Fe^{2+} species was predicted at pH 6.8. However, the XANES spectra remained unchanged which indicates a shift and increase in the local pH near the electrode to pH > 8 where iron oxide / hydroxide are predicted to be stable.

Similar conclusions can be made for the XANES spectra on the Ni K-edge of violarite in Figure 6.4. No characteristic broad edge XANES feature of Ni-S character (see Figure 6.1) was observed in Figure 6.4. Instead, a high white line intensity was recorded at 8350 eV, followed by two shoulder features at 8370 and 8400 eV. These spectral features resembled the XANES spectra of NiO, $Ni(OH)_2$, Fe_2NiO_4 and $NiSO_4.6H_2O$ in Figure 6.1 and Figure 6.2. According to the EXAFS modelling, the XANES spectrum of violarite was calculated to comprise of 26% of Ni-S bonds and 74% of Ni-O bonds. Therefore, the conclusion from the XANES data on both the Fe K-edge and Ni K-edge of the violarite material confirms the presence of an oxide-like character within the violarite material.

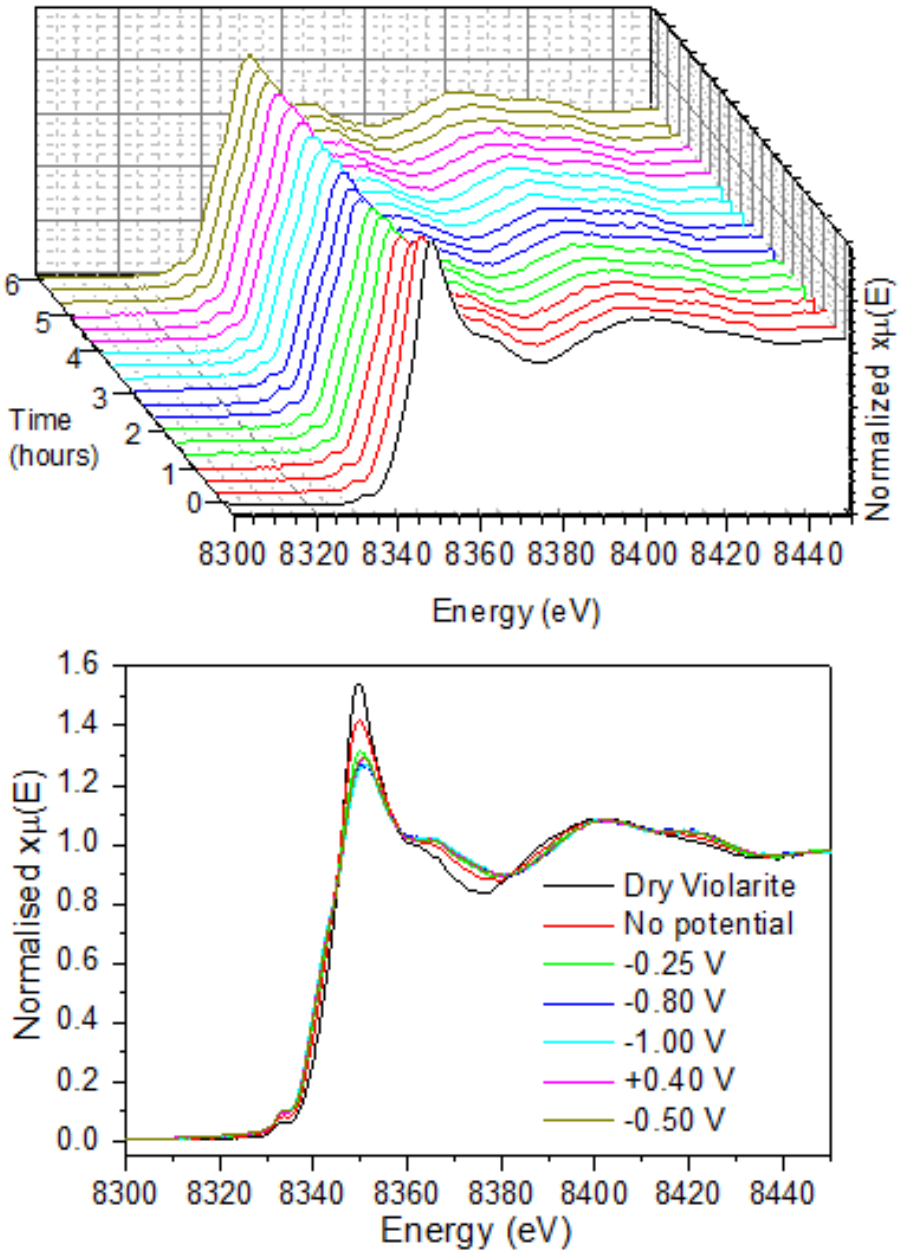

Figure 6.4 In-situ XANES data on Ni K-edge of violarite in phosphate buffer solution pH 6.8 under nitrogen. Top: Stacked spectra with three scans of each potential step. Bottom: merged spectra with last scan of each potential step.

In the XANES spectra on the Ni K-edge of violarite in Figure 6.4, a decrease in the white line intensity was recorded on immersion of the electrode into the electrolyte. This decrease may be associated to the dissolution of the material to Ni^{2+} species, as predicted in the Pourbaix diagram in Figure 5.1. According to the Pourbaix diagram in Figure 5.1, FeOOH and Ni^{2+} species are the stable redox species predicted to be stable up to potential of −0.30 V at pH 6.8. Therefore, the reduction in the white line intensity on immersion of the electrode may be due to

the dissolution of the material to form Ni^{2+} species. Further reduction in the white line intensity on applying −0.25 V suggest further reduction of FeOOH to Fe^{2+} species, as predicted in the Pourbaix diagram in Figure 3.1. According to Figure 5.1, violarite is only predicted to be stable between −0.35 and −0.50 V at pH 6.8, where it is predicted to reduce to pentlandite. However, similar to the XANES spectra on the Fe K-edge, there is no obvious feature of a sulfide character seen in Figure 6.4 for the XANES spectra on the Ni K-edge.

The formation of oxyhydroxide within the violarite material, despite the use of a capping agent during its synthesis which functions to protect the material from air-oxidation, may arise due to the instability of the violarite material itself over time. Violarite is known to be a metastable metal sulfide and therefore, it is not surprising that the transformation to the more thermodynamically stable oxyhydroxide occurred.

Previous published work on violarite showed it is a viable catalyst for CO_2 reduction, even better compared to a greigite surface.[4] The authors applied potentials of −0.5, −0.7, −0.9 and −1.3 V (vs AgCl|Ag) to a violarite electrode in pH 5.5 electrolyte under CO_2 atmosphere and recorded CO_2 reduction products. However, no in-situ characterisation of the violarite surface was performed during the CO_2 reduction experiments. Without any in-situ characterisation of the surface, it is difficult to confirm the nature of the violarite electrode used by the authors and its transformation during catalysis. Thermodynamic transformations of violarite, as predicted in the Pourbaix diagram in Figure 5.1, at the applied potentials used by the authors were not considered in their study. Referring to the Pourbaix diagram in Figure 5.1, at the potentials used by the authors, it is predicted that the violarite electrode will reduce to pentlandite at −0.5 V, remain stable as pentlandite up to −0.7 V, while at potentials of −0.9 and −1.3 V, violarite is predicted to reduce to Fe (0) and Ni (0). However, as previously stated, these transformations are dependent on the reaction kinetics and may not be a bulk transformation. The authors also did not consider the possible pH increase due to H_2 generation which was produced in the study. A pH increase near the electrode surface will favour the transformation of violarite to FeOOH,

as predicted in Figure 5.1. Therefore, the authors may be incorrect to assume that the "violarite" electrode was catalytic for CO_2 reduction, when in fact the catalytic site on the electrode surface may have been a combination of violarite, pentlandite, FeOOH, metallic Fe and Ni present on the surface.

The violarite material used in this thesis was characterised via XRD and was found to match the ICDD (International Centre for Diffraction Data) reference pattern for $FeNi_2S_4$ as shown in Figure 6.5. [5] The material was kept under argon in a sealed sample tube before it was transported to the XAS facility (~ 3 days later) where it was characterised using in-situ XANES. It is clear from the XANES spectra that the material contained oxyhydroxides. This shows the importance for the use of multi characterisation techniques in fully describing the nature of the material studied. The discrepancy between the XRD and XANES data shows that the oxyhydroxides must be amorphous as it was not detected by XRD. The discrepancy may also explain why violarite is not well characterised and understood in literature. Therefore, there is a need to use in-situ IR to determine what is occurring at the interface, since the material is not what was thought.

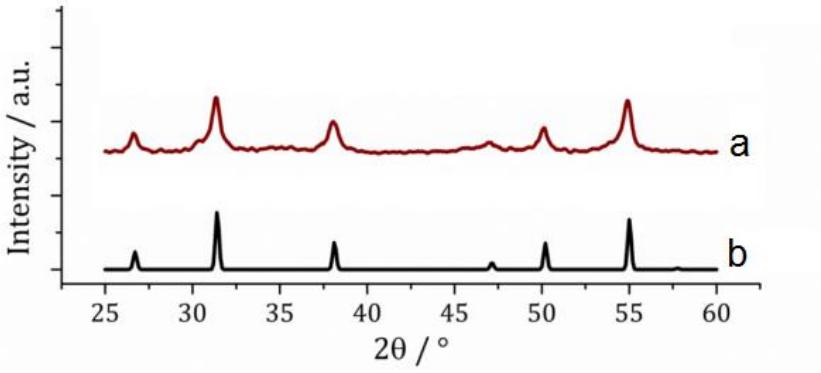

Figure 6.5 XRD patterns for a) synthesised violarite and b) reference pattern for $FeNi_2S_4$ (ICDD card No. 47-1740).[5]

6.3 In-situ ATR-FTIR

To our current knowledge, there is no published in-situ IR characterisation study on violarite. With the additional presence of nickel in the violarite structure compared to greigite, the IR bands of relevant nickel compounds, listed in Table 6.1, need to be considered when interpreting the IR spectra of violarite. These include: the IR bands of nickel hydroxide, nickel oxide and nickel hydroxide carbonate. As violarite consists of Fe, Ni and S, Table 6.1 is used in parallel with the IR data in Tables 4.1 and 4.2 in chapter 4 to analyse the IR spectra of violarite.

Table 6.1 IR bands of relevant species for violarite.

Species	IR bands / cm^{-1}	Reference
Ni hydroxide		
α- & β-NiOH	400	6
δ-NiOH	520	6
δ-NiOH	750	7
$Ni(OH)_2$	436	6
$Ni(OH)_2$	461, 529	8
$Ni(OH)_2$	350	9
Ni oxide		
Ni^{3+}-O	600	6
Ni^{2+}-O	465	6
Ni-O	485	7
Ni-O	450	9
Ni sulfide		
Ni-S in Ni_3S_4	619, 542	10
Ni-S in NiS	652	11
Ni carbonate hydroxide		
C-O in Ni carbonate	1441, 1392, 1061, 823	12
C-O in Ni carbonate	1451, 1397, 1076, 881, 832, 696	13

6.3.1 PBS pH 4.5 and 6.8 under argon

Figure 6.6 and Figure 6.7 show the in-situ FTIR spectra of violarite recorded in phosphate buffer solutions pH 4.5 and 6.8 under argon, respectively. These two sets of spectra displayed similar changes in absorbance at each potential step applied. Thus, both sets of IR spectra at pH 4.5 and 6.8 under argon are discussed in this section. The following IR peaks were observed in both Figure 6.6 and Figure 6.7 and are assigned as follows:

Table 6.2 IR assignments at pH 4.5 and 6.8 under argon for Figure 6.6 and Figure 6.7 where ν is stretching vibration, ν_{sym} is symmetric stretching vibration, ν_{asym} is asymmetric stretching vibration and δ is bending vibration.

Assignment	IR peaks at pH 4.5 / cm^{-1}	IR peaks at pH 6.8 / cm^{-1}	Reference
H_2O / OH			
$\delta(H_2O)$	1643	1631	14
ν_{sym}(OH) (bulk water)	3419	3356	14
$H_2PO_4^-$ species			
ν_{asym}(POH)	945	-	15
HPO_4^{2-} species			
ν_{sym}(PO)	991	987	15
SO_4^{2-} species			
ν_{sym}(SO)	991	987	16–19
ν_{asym}(SO)	-	1043	16–19
ν_{asym}(SO)	1112	1107	16–19

On applying a potential of −0.25 V at both pHs, a decrease in absorbance was recorded at *c.a.* 1100 cm^{-1} assigned to ν_{asym}(SO) of SO_4^{2-} species and a small increase was observed at *c.a.* 990 cm^{-1} which was assigned to ν_{sym}(SO) of SO_4^{2-} species and ν_{sym}(PO) of HPO_4^{2-} species. According to the Pourbaix diagram in Figure 5.1 in chapter 5, at this potential, the oxidation of violarite to FeOOH and SO_4^{2-} is predicted at pH 6.8, while at pH 4.5, violarite is predicted to reduce to Fe^{2+}, Ni^{2+} and H_2S species. However, as previously mentioned in chapter 5, the oxidation of violarite to FeOOH may also be favoured at pH 4.5 if the local pH near the electrode surface increased to a pH greater than 4.5. Such pH increase can be

caused by water and proton reduction (production of OH^- species and the consumption of protons) occurring. At pH 4.5, it is evident that there was an increase in the local pH based on the presence of the IR band of $\nu_{sym}(PO)$ of HPO_4^{2-} species at *c.a.* 990 cm^{-1} which should not be present at pH 4.5, as well as the decrease in absorbance for the IR band $\nu_{sym}(PO)$ of $H_2PO_4^-$ species at c.a. 945 cm^{-1} on applying the subsequent potential step of −0.80 V. The concomitant increase in concentration of HPO_4^{2-} species and decrease in concentration of $H_2PO_4^-$ species give evidence for an increase in the local pH near the electrode due to water and proton reduction occurring at this potential at pH 4.5. The IR bands of $\delta(H_2O)$ of surface water and $\nu_{sym}(OH)$ of bulk water were also recorded at *c.a.* 1640 and 3400 cm^{-1}. The gradual increase in absorbance of the water IR bands suggests increasing adsorption of water / hydration of the nanoparticles on the electrode.

$$FeNi_2S_4 + 8H_2O + 2e^- \rightarrow Fe^{2+} + 2Ni^{2+} + 4H_2S + 8OH^- \quad (6.1)$$

$$FeNi_2S_4 + 18H_2O \rightarrow FeOOH + 2Ni^{2+} + 4SO_4^{2-} + 35H^+ + 31e^- \quad (6.2)$$

$$2H_2O + 2e^- \rightarrow H_2 + 2OH^- \quad (6.3)$$

$$2H^+ + 2e^- \rightarrow H_2 \quad (6.4)$$

$$H_2PO_4^- \rightarrow HPO_4^{2-} + H^+ \quad (6.5)$$

Similar absorbance changes were observed at pH 6.8 in Figure 6.7 with an additional presence of the IR peak at 1043 cm^{-1} assigned to $\nu_{asym}(SO)$ of SO_4^{2-} species. The presence of this additional $\nu_{asym}(SO)$ IR band of SO_4^{2-} species is indicative of the splitting of the triply degenerate IR band at 1100 cm^{-1} into two separate IR peaks, as a result of the coordination of the SO_4^{2-} species via S-O bond onto the metal ions (Fe or Ni) on the electrode (S — O ····· Me, where Me = metal).[16–19] No significant spectral features were observed in the wavenumber region of 700 – 400 cm^{-1} where Fe-O, Ni-O, Fe-S and Ni-S IR peaks were expected at both pHs. This may be due to a lack of sensitivity of this particular ATR technique and setup to detect lattice vibrations of solid-state materials.

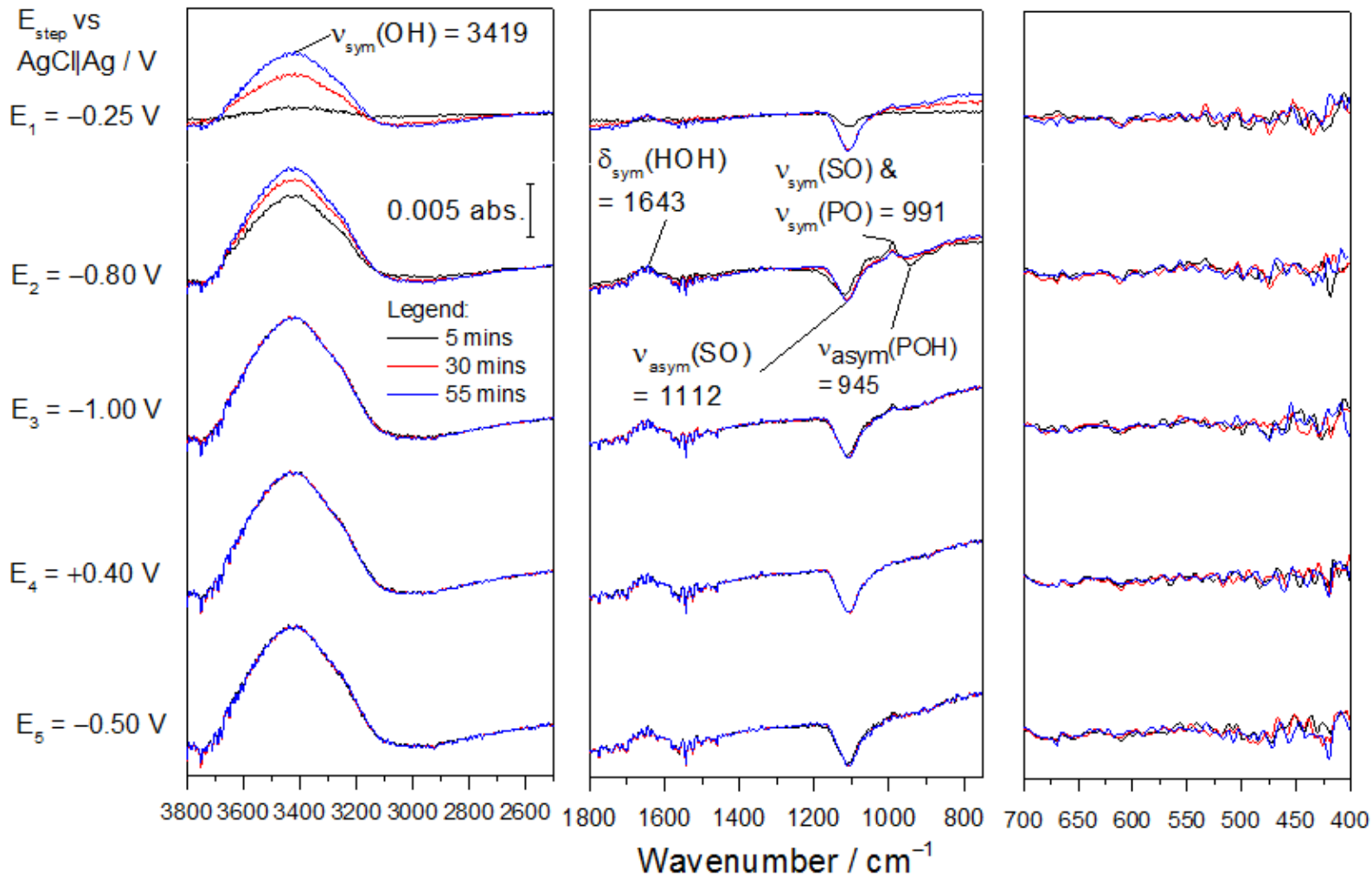

Figure 6.6 In-situ FTIR of violarite in phosphate buffer solution pH 4.5 under argon recorded on applying potential steps of −0.25, −0.80, −1.00, +0.40 and −0.50 V for one hour each step. Spectra displayed at each potential step were recorded at 5, 30 and 55 mins into holding the potential.

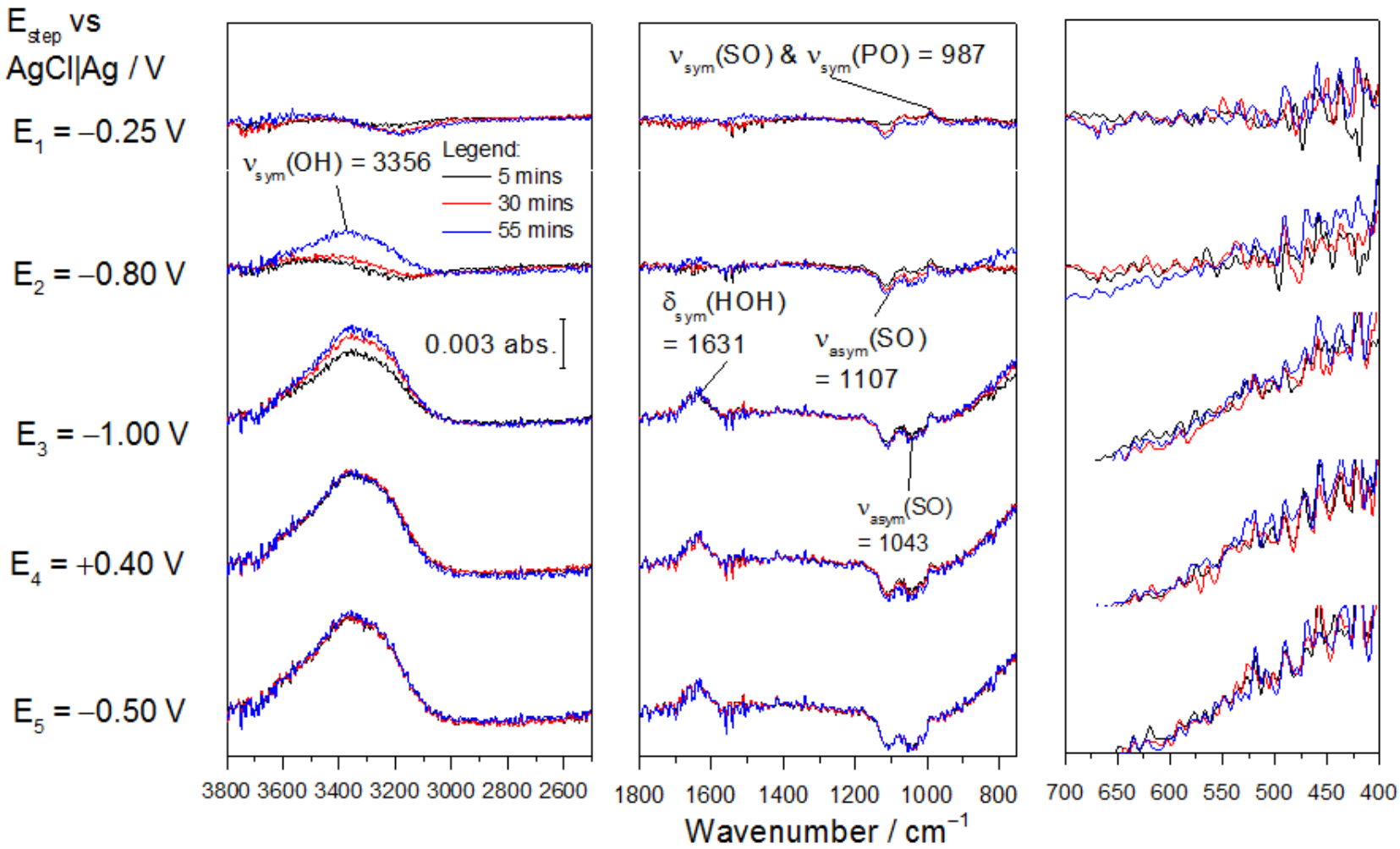

Figure 6.7 In-situ FTIR of violarite in phosphate buffer solution pH 6.8 under argon recorded on applying potential steps of −0.25, −0.80, −1.00, +0.40 and −0.50 V for one hour each step. Spectra displayed at each potential step were recorded at 5, 30 and 55 mins into holding the potential.

On applying subsequent potentials of −0.80, −1.00, +0.40 and −0.50 V, the spectral features remained unchanged at both pHs. The electrode-electrolyte interface also seems to be unaffected by the applied potentials with no significant adsorption or desorption of the phosphate species, opposite to the sharp absorbance changes for phosphates observed for greigite in chapter 4. The IR band of SO_4^{2-} species at *c.a.* 1100 cm^{-1} remained present at all potentials applied at both pHs, even though the reduction of SO_4^{2-} species at potentials < −0.40 V to H_2S at pH 4.5 and to HS^- at pH 6.8 were predicted in the Pourbaix diagram in Figure 5.1. The unchanged spectral features on applying subsequent applied potentials at both pHs indicate that the predicted violarite thermodynamic transformations in the Pourbaix diagram in Figure 5.1 may not have occurred. The predicted formation of FeOOH on immersion of the violarite electrode into the electrolytes may have passivated the electrode surface and prevented further redox reactions from occurring. The presence of FeOOH on the surface of the violarite electrode may also explain the featureless CVs of violarite at these pHs observed in the previous chapter.

6.3.2 PBS pH 4.3 and 6.5 under CO_2

Figure 6.8 and Figure 6.9 show the in-situ IR spectra of violarite in CO_2 saturated PBS pH 4.3 and 6.5, respectively. The two sets of spectra at both pHs did not resemble those recorded under argon discussed in the previous section.

On introduction of CO_2 in pH 4.3, at −0.25 V, a broad IR shoulder was observed centered at *c.a.* 1047 cm^{-1}. This broad IR peak split into multiple distinct IR peaks on applying subsequent potentials of −0.80 and −1.00 V. The IR bands were assigned to HPO_4^{2-} species (ν(POH) at 837 cm^{-1}, ν_{sym}(PO) at 989 cm^{-1} and ν_{asym}(PO) at 1062 / 1090 cm^{-1}) and $H_2PO_4^-$ species (ν_{asym}(POH) at 937 cm^{-1}, ν_{sym}(PO) at 1062 / 1090 cm^{-1} and ν_{asym}(PO) at 1157 cm^{-1}). These phosphate IR spectral features resemble those recorded for greigite in chapter 4. As previously proposed, the simultaneous increase in absorbance of HPO_4^{2-} species and decrease in absorbance of $H_2PO_4^-$ species evidence a change in the local pH near the electrode surface, which most likely was an increase in pH due to water and proton reduction. In contrast to the IR spectra at pH 4.5 under argon, no IR bands corresponding to SO_4^{2-} species were observed in the IR spectra in pH 4.3 under CO_2. The absence of SO_4^{2-} species suggests that the violarite electrode was stable on immersion into the electrolyte and did not undergo transformation to Fe^{2+}, Ni^{2+} and SO_4^{2-} species or to FeOOH and SO_4^{2-} species, depending on the local pH, as predicted in the Pourbaix diagram in Figure 5.1. With the IR evidence of a pH increase, it is most likely that the transformation of violarite to FeOOH, favoured at pH > 4.5, was halted. An additional IR peak at 1338 cm^{-1} assigned to ν_{sym}(OCO) of HCO_3^- species was also present, which was expected on introduction of CO_2, indicating the presence of dissolved CO_2 species within the electrolyte-electrode interface. On applying the subsequent positive potential of +0.40 V, the IR bands of HPO_4^{2-} species were no longer present which suggests that the local pH near the electrode may have decreased back to pH 4.3. Violarite is predicted to oxidise to FeOOH and SO_4^{2-} species at this positive potential, however, no IR bands corresponding to SO_4^{2-} species were recorded. The absence of SO_4^{2-} species suggest no H_2S was present near the electrode for oxidation to SO_4^{2-}. H_2S is predicted to form, according to the Pourbaix diagram in Figure 5.1, on reduction

of violarite to pentlandite on the previous negative applied potentials. The absence of the IR bands of H_2S and SO_4^{2-} species suggest that the reaction kinetics for the reduction of violarite to pentlandite may be slow and the transformation may not have occurred. The IR bands of HPO_4^{2-} species were observed to reform again on applying a final potential step of −0.50 V, which suggest a change in the local pH again due to proton and water reduction occurring.

$$FeNi_2S_4 + 11H^+ + 11e^- \rightarrow Fe_{4.5}Ni_{4.5}S_8 + 5.5H_2S + 4.5NiS \qquad (6.6)$$

These spectral changes can be correlated to the CV of violarite at pH 4.3 under CO_2 where there was a current increase on introduction of CO_2. In the previous CV chapter of violarite, the current increase was proposed to be associated with the reduction of CO_2. With the IR evidence showing significant changes in the IR bands of phosphate species under CO_2 compared to under argon, as well as the presence of HCO_3^- species, it is proposed that the introduction of CO_2 may have increased the redox activity of violarite for water and proton reduction. The adsorption of HCO_3^- species and CO_2 may have prevented the formation of a passivating layer of FeOOH on the violarite electrode on immersion into the electrolyte.

Separately, for the IR spectra of violarite in pH 6.3 under CO_2, IR bands assigned to ν_{asym}(SO) at 1041 and 1110 cm^{-1}, and ν_{sym}(SO) at 991 cm^{-1} of adsorbed SO_4^{2-} species were observed, similar to the spectra under argon. However, the change in absorbance was much larger under CO_2 (max absorbance of 0.013 under CO_2 vs 0.003 under argon). In contrast to the spectra at pH 4.3 under CO_2, no distinct IR bands for phosphate species were recorded but these IR bands may be masked under the IR bands of SO_4^{2-}. Similar to pH 4.3 under CO_2, an additional IR band was present at 1610 cm^{-1} in pH 6.3 assigned to ν_{asym}(OCO) of HCO_3^- species. The IR bands of SO_4^{2-} remained present throughout the experiment which suggests that the adsorbed SO_4^{2-} on the violarite electrode was not reduced to H_2S on applying further negative potentials of −0.80 and −1.00V, contrasting the predicted reduction of SO_4^{2-} to H_2S in the Pourbaix diagram in Figure 5.1. If H_2S

was not produced, this suggests that the reduction of violarite to pentlandite and H_2S may not have occurred.

The CV of violarite at pH 6.8 under argon and 6.5 under CO_2 discussed in the previous chapter showed similar redox features, with the reduction peak negatively shifted under CO_2. The negative shift of the reduction peak potential was initially assigned to adsorption of CO_2 or its dissolved species. Similar to greigite on introduction of CO_2, the Pourbaix diagrams in Figure 3.4 in chapter 3 and Figure 5.3 in chapter 5 did not predict the formation of iron carbonate, iron hydroxide carbonate, nickel carbonate or nickel hydroxide carbonate on violarite at both pH 4.3 and 6.5. Based on the conclusions for the IR spectra of violarite in pH 6.3 under CO_2, the negative shift in the reduction peak potential in pH 6.5 under CO_2 may be due to adsorbed SO_4^{2-} species and HCO_3^- species present on the violarite electrode surface.

Another difference between the IR spectra of violarite in pH 4.3 and 6.5 under CO_2 is the absorbance loss at 3357 cm^{-1} assigned to ν(OH) of bulk water and a gain in absorbance for ν(OH) of H-bonded OH at 2985 cm^{-1} in pH 6.5 on applying potentials of −0.25, −0.80 and −1.00 V. These absorbance changes were not observed at pH 4.5 under both argon and CO_2 and at pH 6.8 under argon. The increase and decrease of these two water IR bands are associated with water reduction taking place. Water reduction will produce OH^- species which should result in an increase in the local pH near the electrode and induce a change in the phosphate ion speciation near the electrode surface. However, no significant phosphate IR bands were observed in pH 6.5 under CO_2. As previously stated, the IR bands of phosphates may be masked under the large IR bands of the adsorbed SO_4^{2-} species.

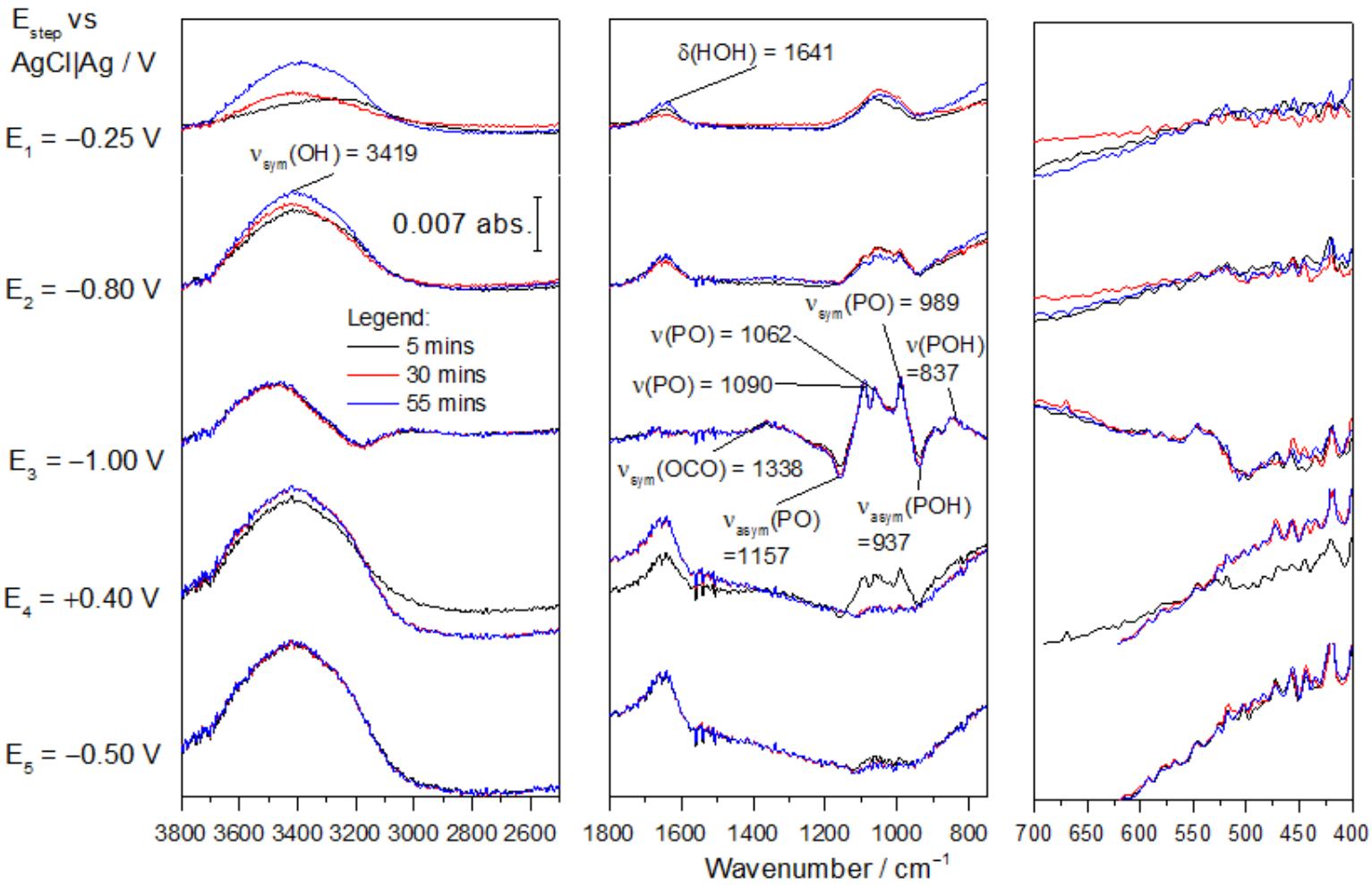

Figure 6.8 In-situ FTIR spectra of violarite in phosphate buffer solution pH 4.3 under CO_2 recorded on applying potential steps of −0.25, −0.80, −1.00, +0.40 and −0.50 V for one hour each step. Spectra displayed at each potential step were recorded at 5, 30 and 55 mins into holding the potential.

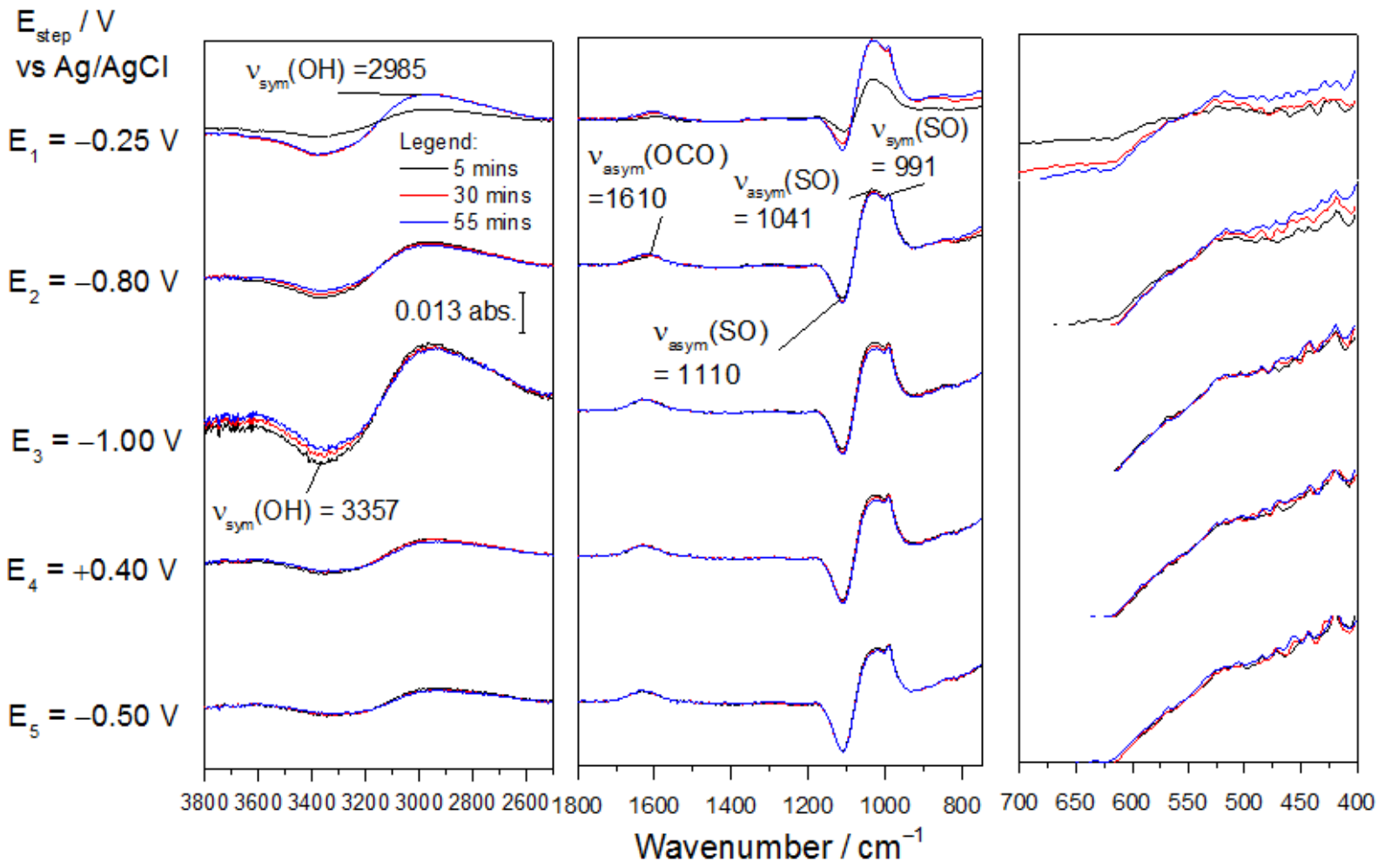

Figure 6.9 In-situ FTIR spectra of violarite in phosphate buffer solution pH 6.5 under CO_2 recorded on applying potential steps of –0.25, –0.80, –1.00, +0.40 and –0.50 V for one hour each step. Spectra displayed at each potential step were recorded at 5, 30 and 55 mins into holding the potential.

6.3.3 $KHCO_3$ pH 8.55 and K_2CO_3 pH 11.2 under argon

The in-situ FTIR spectra of violarite recorded in $KHCO_3$ pH 8.55 and K_2CO_3 pH 11.2 under argon are shown in Figure 6.10 and Figure 6.11. The IR spectra at pH 8.55 and 11.2 are clearly very different. Table 6.3 lists the assignments of the IR bands recorded in both spectra at pH 8.55 and 11.2.

Table 6.3 IR assignments at pH 8.55 and 11.2 under argon in Figure 6.10 and Figure 6.11 where ν is stretching vibration, ν_{sym} is symmetric stretching vibration, ν_{asym} is asymmetric stretching vibration and δ is bending vibration.

Assignment	IR peaks at pH 8.55 / cm^{-1}	IR peaks at pH 11.2 / cm^{-1}	Reference
H_2O / OH			
δ(H_2O)	-	1641	14
ν_{sym}(OH) (H-bonded)		-	14
ν_{sym}(OH) (bulk water)	3201, 3365	3444	14
CO_3^{2-} species			
δ(CO_3^{2-})	842	-	
ν_{asym}(OCO)	1400	1407	20
ν_{asym}(OCO)	1460	1471	
HCO_3^- species			
ν_{sym}(COH)	1012	-	20
ν_{sym}(OCO)	1303	-	20
ν_{sym}(OCO)	1357	-	20
ν_{asym}(OCO)	1616	-	20
SO_4^{2-} species			
ν_{asym}(SO)	1103	1105	16–19

In the spectra at $KHCO_3$ pH 8.55, on applying potential of −0.25 V, there was a small decrease in absorbance at peak 1103 cm^{-1} assigned to SO_4^{2-} species. Similar to the IR spectra at pH 4.5 and 6.8, this IR peak of SO_4^{2-} remained present throughout the experiment. The presence of this IR peak suggest that the transformation of violarite to FeOOH and SO_4^{2-} species occurred, as predicted in the Pourbaix diagram in Figure 5.1. However, the presence of this IR peak throughout the experiment suggests that it was not reduced to HS^- at further negative potentials of −0.80 and −1.00 V, as predicted by the Pourbaix diagram in Figure 5.1. No significant IR peaks were visible in the lower wavenumber region

of 700 – 400 cm^{-1} where the Fe-O IR band of FeOOH is expected. As previously stated, this may be due to the lack of sensitivity of the technique in detecting solid state materials present within the electrolyte-electrode interface. On applying further negative potentials of −0.80 and −1.00 V, a decrease in absorbance of IR bands of HCO_3^- (ν_{sym}(COH) at 1012 cm^{-1}, ν_{sym}(OCO) at 1303 and 1357 cm^{-1}, and ν_{asym}(OCO) at 1616 cm^{-1}), CO_3^{2-} species ($\delta(CO_3^{2-})$ at 842 cm^{-1}, ν_{asym}(OCO) at 1400 and 1460 cm^{-1}) and ν_{sym}(OH) of bulk water at 3201 cm^{-1} were observed. The presence of the IR bands of CO_3^{2-} species in the FTIR spectra in $KHCO_3$ may be due to a shift in equilibrium between HCO_3^- and CO_3^{2-} species due to water reduction which generates OH^- species.

$$CO_2 + OH^- = HCO_3^- \qquad (6.7)$$
$$HCO_3^- + OH^- = CO_3^- + H_2O \qquad (6.8)$$

The decrease in absorbance for ν_{sym}(OH) of bulk water at 3201 cm^{-1} evidenced the loss of water molecules within the electrode-electrolyte interface due to water reduction and generation of H_2 on the electrode surface. According to the Pourbaix diagram in Figure 5.1, violarite is predicted to reduce to pentlandite at both pHs at these potentials. However, no Fe-S / Ni-S IR bands were observed in the lower wavenumber region of the IR spectra at both pHs. The technique may not be sensitive enough to detect the lattice vibrations of violarite or pentlandite. The absence of the IR band of HS^- species at these potentials suggest that the reduction of violarite to pentlandite may be kinetically slow and may not have occurred.

On reversing the potential to +0.40 V, only the IR peaks of CO_3^{2-} and SO_4^{2-} remained present but were recorded as absorbance loss. The IR peaks of HCO_3^- were absent which suggests that the absorbance loss of HCO_3^- at −0.80 and −1.00 V was regained at this potential. This suggests that CO_3^{2-} species were protonated to HCO_3^- species at this potential. The IR peak at 3356 cm^{-1} assigned to ν_{sym}(OH) of bulk water evidence the regain in water molecules within the ATR sampling region whose IR signal may have been blocked by H_2 generation occurring at the negative potentials of −0.80 and −1.00 V. At this potential, according to the Pourbaix diagram, FeOOH is predicted to form via the oxidation of violarite at pH

8.55. However, no significant IR peaks associated with these oxides were observed.

Comparing these IR observations to the CV of violarite at $KHCO_3$ pH 8.55, the presence of HCO_3^-, CO_3^{2-} and SO_4^{2-} species near the electrode surface may have caused the negative shift in the reduction peak potential by *c.a.* −0.40 V compared to the CV of violarite in PBS pH 4.5 and 6.8. It was initially proposed in chapter 5 that the negative shift in the reduction peak may have been caused by the presence of adsorbed HCO_3^- species present near the electrode surface in $KHCO_3$. With the IR evidence for the presence of adsorbed HCO_3^-, CO_3^{2-} species, it can be concluded that the negative shift was caused by the adsorption of these species.

In contrast to the distinct spectral features observed in $KHCO_3$ pH 8.55, very few and small changes were observed in the spectra of violarite recorded in K_2CO_3 pH 11.2. The IR bands present were assigned to CO_3^{2-} species (ν_{asym}(OCO) at 1407 and 1471 cm^{-1}), SO_4^{2-} species (ν_{asym}(SO) at 1105 cm^{-1}) and H_2O ($\delta(H_2O)$ at 1641 cm^{-1} and ν_{sym}(OH) at 3444 cm^{-1}). The spectra in K_2CO_3 pH 11.2 resemble those recorded in PBS pH 4.5 and 6.8 where very little spectral features were recorded, indicating the violarite surface was passivated. Previously in chapter 4, greigite was found to transform to iron oxide / hydroxide on immersion into K_2CO_3 pH 11.2. The formation of the iron oxide / hydroxide was associated with the high pH and high concentration of OH^- present in K_2CO_3. According to the Pourbaix diagram in Figure 5.1, FeOOH, $Ni(OH)_2$ and SO_4^{2-} species are predicted to form on immersion of the electrode in pH 11.2 and remain stable up to −0.70 V. Therefore, it may be deduced that the formation of FeOOH and $Ni(OH)_2$ on the violarite electrode may have passivated the surface and prevented the redox reactions of violarite as well as water and proton reduction from occurring. Violarite is predicted to reform at −0.70 V and reduced to pentlandite at −0.85 V. However, these transformations seem unlikely to occur since no IR band of HS^- species were detected in the spectra.

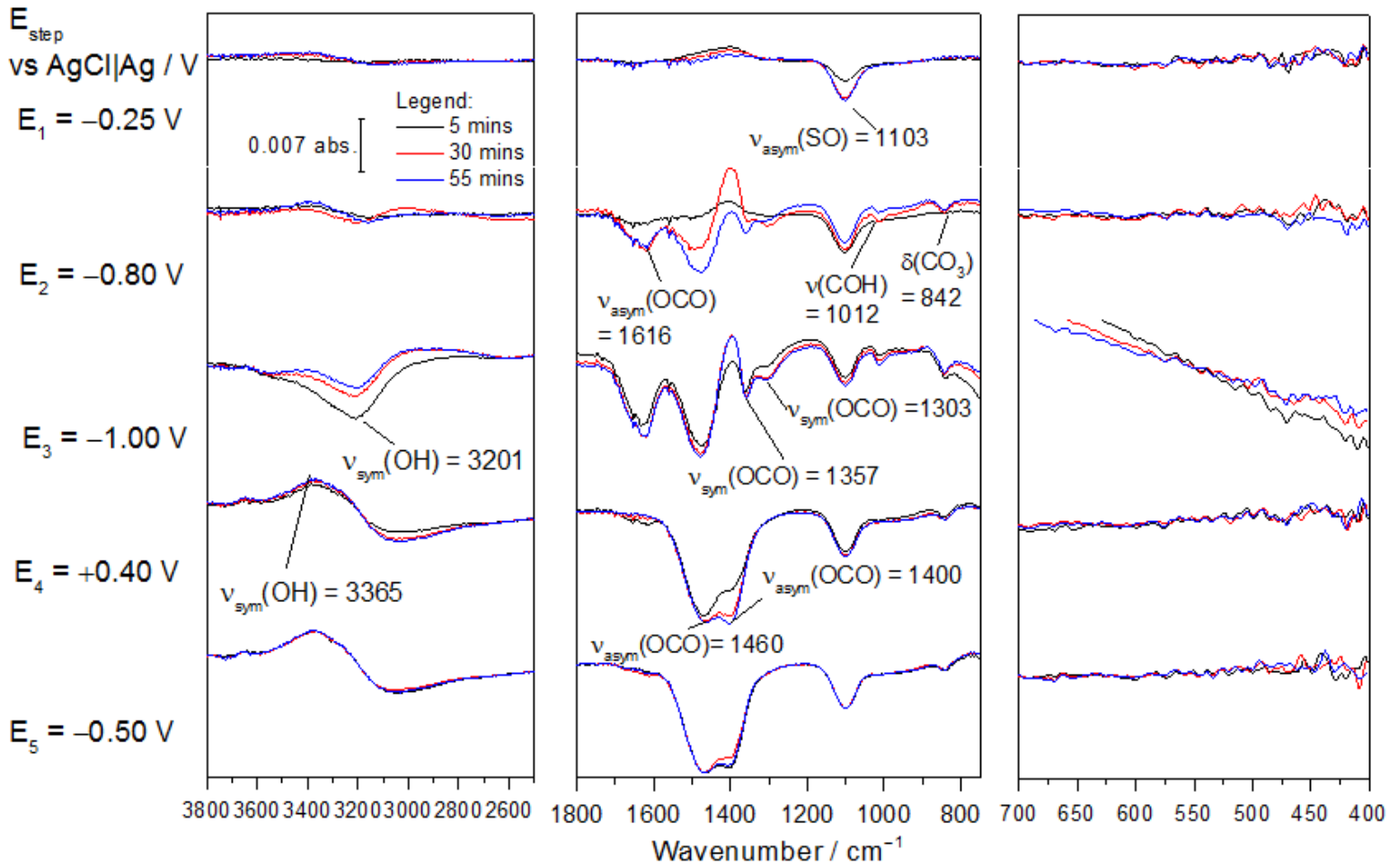

Figure 6.10 In-situ FTIR of violarite in $KHCO_3$ pH 8.55 under argon recorded on applying potential steps of –0.25, –0.80, –1.00, +0.40 and –0.50 V for one hour each step. Spectra displayed at each potential step were recorded at 5, 30 and 55 mins into holding the potential.

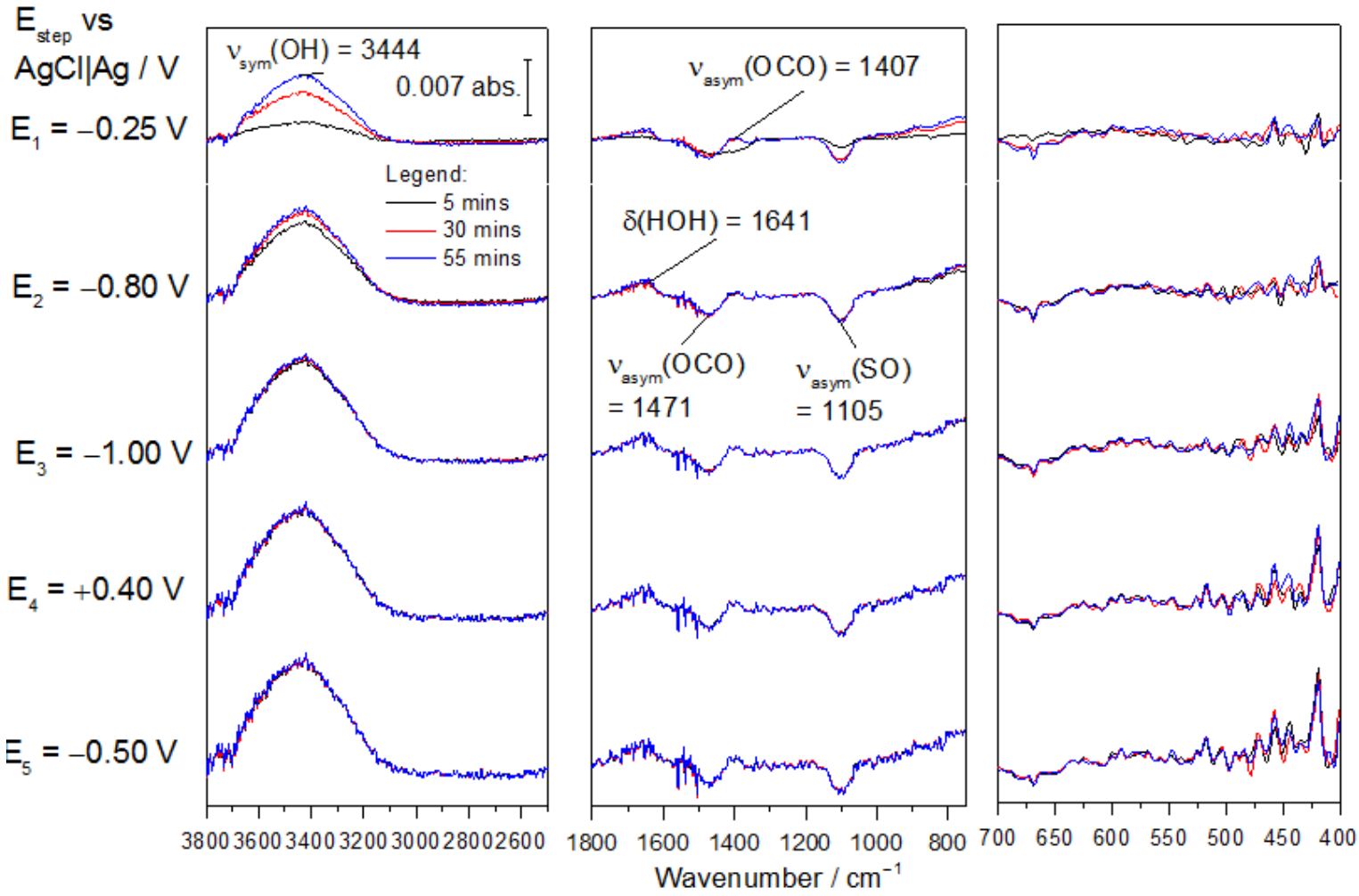

Figure 6.11 In-situ FTIR of violarite in K_2CO_3 pH 11.2 under argon recorded on applying potential steps of −0.25, −0.80, −1.00, +0.40 and −0.50 V for one hour each step. Spectra displayed at each potential step were recorded at 5, 30 and 55 mins into holding the potential.

Previously in chapter 5, the CV of violarite in K_2CO_3 pH 11.2 featured the most redox peaks compared to the CV of violarite recorded at other pHs. The reduction peaks were assigned to the reduction of FeOOH and $Ni(OH)_2$ to violarite, the reduction of violarite to pentlandite, the reduction of SO_4^{2-} to HS^- and water reduction. The oxidation peaks were assigned to the reverse reaction of the reduction peaks. Out of these predicted transformations, only the reduction of violarite and SO_4^{2-} produce the IR-active HS^- species. The formation of FeOOH, $Ni(OH)_2$, violarite and pentlandite will not be detected by IR spectroscopy due to the lack of sensitivity of the technique for lattice vibrations of solid state-materials. Based on the absence of IR peak for HS^- species in the spectra in K_2CO_3, it is most likely that FeOOH and $Ni(OH)_2$ remained on the surface of the electrode and prevented further reduction of violarite. Therefore, the redox peaks observed in the CV of violarite in K_2CO_3 must be associated with the redox reactions of FeOOH and $Ni(OH)_2$.

6.3.4 $KHCO_3$ pH 7.1 and K_2CO_3 pH 10.1 under CO_2

On introduction of CO_2 in $KHCO_3$ and K_2CO_3, the pHs of the electrolytes decreased to pH 7.1 and 10.1, respectively. In $KHCO_3$ pH 7.1 under CO_2 (Figure 6.12), no distinct IR bands of HCO_3^- and CO_3^{2-} species, previously observed under argon, were present, with the exception of ν_{sym}(OCO) of CO_3^{2-} species at 1357 cm^{-1}. The absence of the IR bands of HCO_3^- and CO_3^{2-} species suggests that these species were not adsorbed onto the electrode. The adsorption of CO_2 may have blocked the adsorption of HCO_3^- and CO_3^{2-} species on the electrode surface. A recurring trend was also observed where the IR band at 1093 cm^{-1} assigned to ν_{sym}(SO) of SO_4^{2-} remained constant at all potential steps applied, which suggests that no further reduction of violarite occurred once FeOOH was formed on the surface of the electrode.

In K_2CO_3 pH 10.1 under CO_2 (Figure 6.13), the spectra resembled that recorded under Ar, with the additional IR bands of HCO_3^- (ν_{sym}(OCO) at 1357 cm^{-1}) and CO_3^{2-} (ν_{asym}(OCO) at 1463 cm^{-1}) species present. The main difference between the IR spectra of violarite in $KHCO_3$ pH 7.1 and K_2CO_3 10.1 under CO_2 is the substantial loss in absorbance of ν_{sym}(OH) of bulk water at 3269 cm^{-1} on applying

potential of −1.00 V which occurred at pH 10.1 only. ¹⁴¹⁴The absorbance loss is associated with loss of IR signal due to H_2 generated via water and proton reduction occurring at this potential.

Comparing these IR observations to the CVs of violarite at both pHs discussed in the previous chapter, the CV of violarite in $KHCO_3$ under CO_2 resemble that recorded under argon but the reduction peak was negative shifted by *c.a.* 0.05 V, while in K_2CO_3 under CO_2, there was significant noise recorded in the currents between −0.70 and −1.00 V. The negative shift of the reduction peak potential in $KHCO_3$ under CO_2 could be associated with the adsorption of CO_2 since the IR spectra did not show any IR bands of HCO_3^- and CO_3^{2-} species, which was in contrast to the spectra under argon. For K_2CO_3 under CO_2, the IR evidence for the loss of water due to water and proton reduction is in agreement with the noisy currents observed in the CV of violarite in K_2CO_3 on introduction of CO_2 associated with increased H_2 generation.

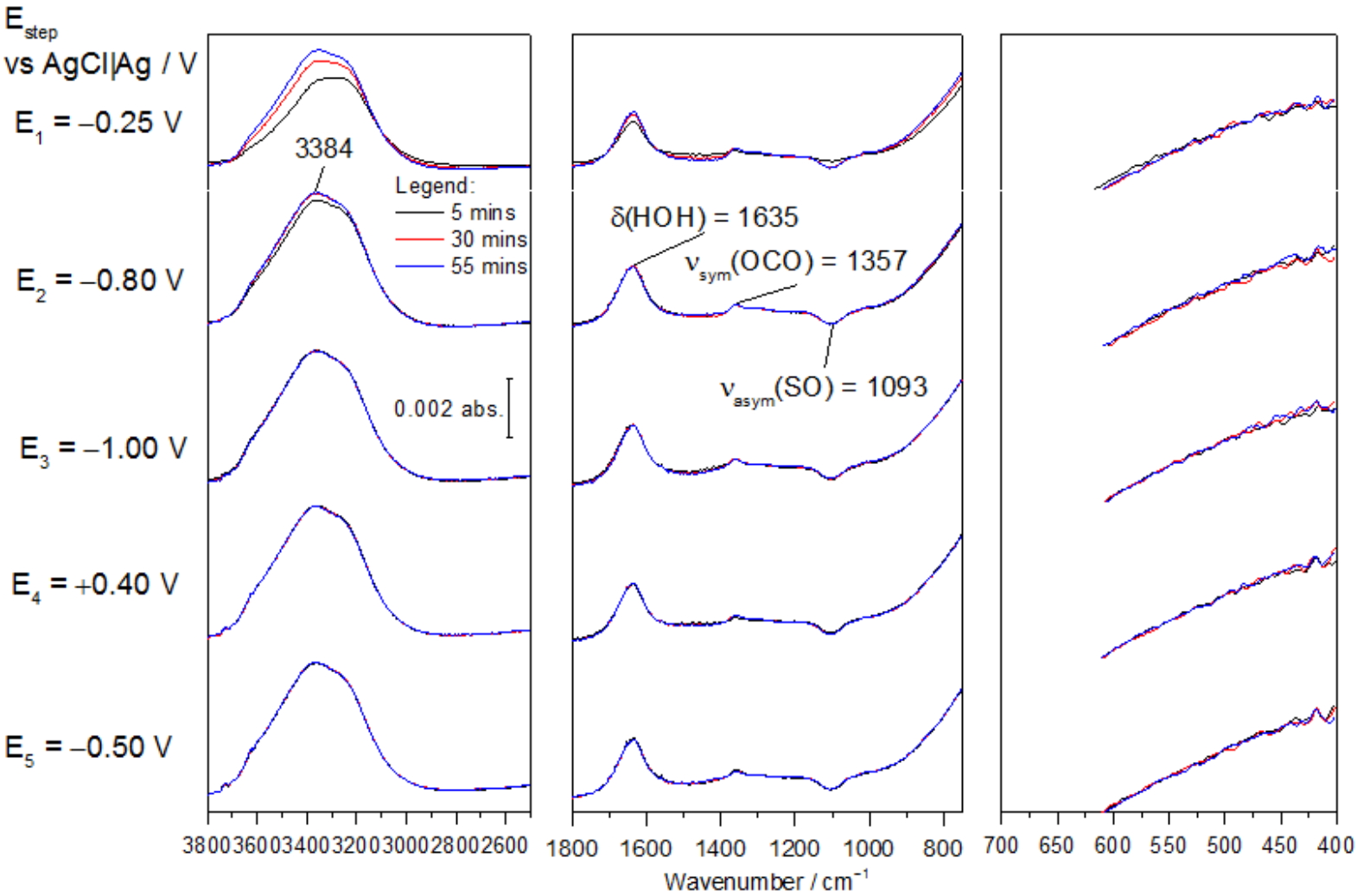

Figure 6.12 In-situ FTIR of violarite in $KHCO_3$ pH 7.1 under CO_2 recorded on applying potential steps of −0.25, −0.80, −1.00, +0.40 and −0.50 V for one hour each step. Spectra displayed at each potential step were recorded at 5, 30 and 55 mins into holding the potential.

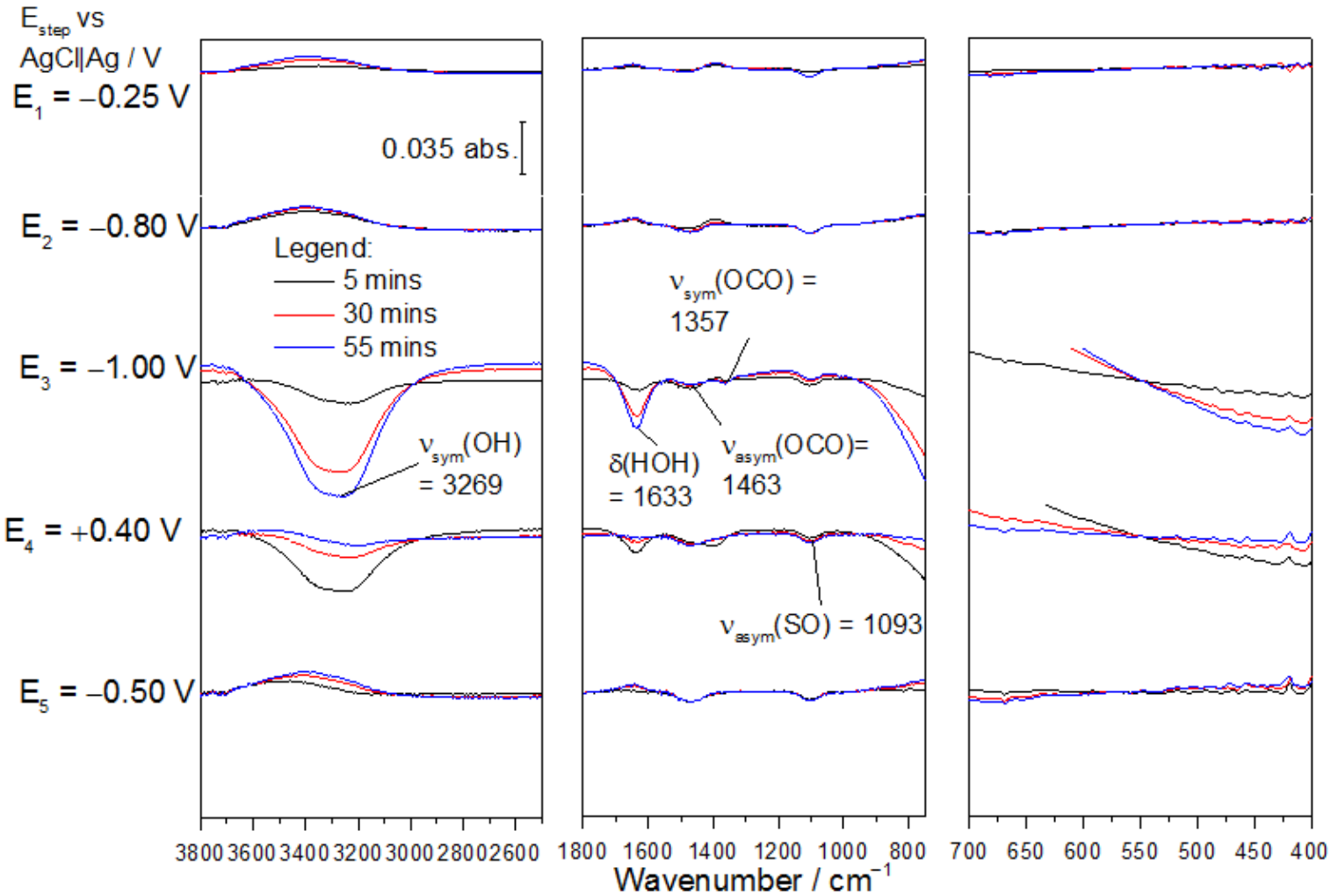

Figure 6.13 In-situ FTIR of violarite in K_2CO_3 pH 10.1 under CO_2 recorded on applying potential steps of −0.25, −0.80, −1.00, +0.40 and −0.50 V for one hour each step. Spectra displayed at each potential step were recorded at 5, 30 and 55 mins into holding the potential.

6.4 Discussion

The in-situ IR spectra of violarite showed loss of SO_4^{2-} species at all pHs tested under both argon and CO_2. The loss of SO_4^{2-} species is indicative of the transformation of violarite to FeOOH and SO_4^{2-} species on immersion of the electrode into the electrolyte and application of potentials in range 0 to −1.00 V. The Pourbaix diagram in Figure 5.1 predicted FeOOH and SO_4^{2-} to be the stable redox species at potentials > −0.40 V. However, the ν_{asym}(SO) IR band of SO_4^{2-} at *c.a.* 1100 cm^{-1} was present at all of the potential steps applied (−0.25, −0.80, −1.00, +0.40 and −0.50 V) at all pHs. The maximum absorbance of this IR band of SO_4^{2-} was found to remain constant throughout the experiment. This suggests that the SO_4^{2-} species lost were not regained any point during the experiment. SO_4^{2-} species were expected to be present on oxidation of H_2S or HS^- on applying potential of +0.40 V, as predicted by the Pourbaix diagram in Figure 5.1. It is likely that due to the absence of H_2S or HS^- within the interfacial layer, SO_4^{2-} species were not reproduced at +0.40 V. No significant IR bands of H_2S or HS^- were recorded at all pHs tested, which further suggests that the predicted reduction of violarite of pentlandite may not have occurred (predicted at −0.40 V at pH 4.5, −0.50 V at pH 6.8, −0.60 V at pH 8.55 and −0.75 V at pH 11.2). It is proposed that the presence of FeOOH on the violarite electrode and the high stability of FeOOH within the potential window used may have hindered the redox reactions of violarite. The proposed formation of FeOOH and its stability at each potential step applied is evident in the XANES spectra of violarite at pH 6.8 under argon shown at the beginning of this chapter. In comparison to the IR spectral features for greigite in chapter 4 under argon, no distinct phosphate IR bands were observed in the spectra of violarite under argon. The absence of the IR phosphate bands under argon for violarite suggests that no significant water and proton reduction occurred on the violarite electrode. It is likely that water and proton reduction was hindered due to the formation of FeOOH on the surface of violarite.

On introduction of CO_2, the IR spectra of violarite showed suppressed loss of absorbance of the "free" SO_4^{2-} at PBS pH 4.3, $KHCO_3$ pH 7.1 and K_2CO_3 pH 10.1, while at PBS pH 6.5, IR bands indicative of adsorbed of SO_4^{2-} were recorded. The

suppression of the loss of SO_4^{2-} on introduction of CO_2 suggests that the adsorption of CO_2 or its dissolved species (IR spectra show presence of HCO_3^-) may have hindered the formation of FeOOH and the subsequent loss of SO_4^{2-} on the violarite electrode. The IR bands of phosphate species were observed in PBS pH 4.3 and may also have been present in PBS pH 6.5, but were masked under the IR bands of adsorbed SO_4^{2-}. The presence of phosphate IR bands is indicative of a change in the local pH near the electrode, most likely induced by water or proton reduction. However, the loss of absorbance of water IR band was only observed at PBS pH 6.5 but not at pH 4.3. It may be that the adsorption of CO_2 and HCO_3^- on violarite at pH 4.3 suppressed water and proton reduction. For the IR spectra of violarite in $KHCO_3$ and K_2CO_3 under CO_2, H_2 evolution was evident in K_2CO_3 but was not observed in $KHCO_3$. This was surprising as it was expected that H_2 would be generated in $KHCO_3$ pH 7.1 as well, similar to the spectra in PBS pH 6.5. It may be that the adsorption of CO_2 prevented water and proton reduction in $KHCO_3$ pH 7.1.

Overall, the introduction of CO_2 suppressed the transformation of violarite to FeOOH based on the suppressed loss of SO_4^{2-}. Introduction of CO_2 also increased H_2 generation on the violarite electrode, echoing the observations made by Yamaguchi *et al*.[4] This may be due to the adsorption of CO_2 on violarite. Comparing these observations to greigite in chapter 4, the absorbance loss of IR bands of SO_4^{2-} was not observed in the IR spectra of greigite. These differences show that greigite was more stable than violarite on immersion of the electrodes into the electrolytes. The relative stability of greigite and violarite on immersion into the electrolytes were in agreement with the predictions in the Pourbaix diagrams discussed in chapters 3 and 5, where greigite remains stable and violarite is transformed to FeOOH on immersion into the electrolyte. However, on applying further negative potentials, iron oxyhydroxide was detected on the greigite electrode which was not predicted by the Pourbaix diagrams. Similarly for violarite, the Pourbaix diagrams did not predict FeOOH to remain stable at further negative potentials. On introduction of CO_2, the Pourbaix diagrams predicted the formation of iron carbonate on greigite, but there was no spectroscopic evidence for this. The Pourbaix diagrams also did not predict the

halted formation of FeOOH on both greigite and violarite on introduction of CO_2, which were evident in the spectroscopic data. The combined use of in-situ FTIR and XAS techniques in this thesis show that it is inadequate to use Pourbaix diagrams in assigning redox features observed in the CVs of greigite and violarite. This is because reactions such as water reduction can result in significant changes in the interfacial pH. The in-situ spectroscopic evidence for the presence of oxides / hydroxides on greigite and violarite show the importance of fully characterising the material of interest in-situ to confirm and assign the redox peaks observed in the CVs. For example, XRD will not provide any information on amorphous oxide phases.

Violarite has shown potential for applications in CO_2 reduction based on the increased currents on introduction of CO_2 and the suppression of FeOOH formation. The redox activity of violarite was especially enhanced on introduction of CO_2 in PBS pH 6.5 and K_2CO_3 pH 10.1. However, violarite is more prone to hydrolysis compared to greigite on immersion into the electrolyte. The formation of FeOOH on both greigite and violarite passivates the surface. However, CO_2 reduction is still possible on both greigite and violarite, provided that FeOOH is prevented from forming. This can be done by choosing a holding potential where greigite and violarite are predicted to be stable. A cyclic potential sweep is not favourable for CO_2 reduction as the formation of FeOOH may be favoured and hinder CO_2 reduction.

The results for violarite in this chapter lend support for the iron sulphide membrane theory where violarite was proposed to be catalytic for CO_2 reduction. However, in a deep-sea ocean setting, it is very likely that FeOOH will be present on the surface of violarite produced during hydrolysis of violarite. The removal of FeOOH from the surface of violarite will be essential for effective CO_2 reduction on violarite. The membrane, proposed by Russell and Hall in the iron sulphide membrane theory,[21] may assist in removing the FeOOH formed on violarite and greigite since one side of the membrane is in acidic media and also if the membrane was constantly regenerated / precipitated to prevent passivation.

6.5 References

1. Tirez, K. *et al.* Speciation and fractionation of nickel in airborne particulate matter: comparison between selective leaching and XAS spectroscopy. *J. Anal. At. Spectrom.* **26,** 517–527 (2011).

2. Goodarzi, F. & Huggins, F. Speciation of nickel in Canadian subbituminous and bituminous feed coals, and their ash by-products. *J. Environ. Monit.* **6,** 787–791 (2004).

3. Islam, H.-U. Ph. D. Thesis, Formation and Electrocatalysis Studies of Nickel and Iron Sulfide Catalysts using in situ XAS. (University College London, 2015).

4. Yamaguchi, A. *et al.* Electrochemical CO2 reduction by Ni-containing iron sulfides: How is CO2 electrochemically reduced at bisulfide-bearing deep-sea hydrothermal precipitates? *Electrochim. Acta* **141,** 311–318 (2014).

5. Roffey, A. Ph. D. Thesis, Dithiocarbamate Complexes as Single Source Precursors to Metal Sulfide Nanoparticles for Applications in Catalysis. (University College London, 2014).

6. Ren, Y. *et al.* The coloration and degradation mechanisms of electrochromic nickel oxide. *Sol. Energy Mater. Sol. Cells* **116,** 83–88 (2013).

7. Surca, A., Orel, B., Pihlar, B. & Bukovec, P. Optical, spectroelectrochemical and structural properties of sol-gel derived Ni-oxide electrochromic film. *J. Electroanal. Chem.* **408,** 83–100 (1996).

8. Hou, L. *et al.* Electrochemically induced transformation of NiS nanoparticles into Ni(OH)2 in KOH aqueous solution toward electrochemical capacitors. *Electrochim. Acta* **56,** 7454–7459 (2011).

9. Kober, F. P. Analysis of the Charge-Discharge Characteristics of Nickel-Oxide Electrodes by Infrared Spectroscopy. *J. Electrochem. Soc.* **112,** 1064–1067 (1965).

10. Yin, P. *et al.* Shape and phase evolution of nickel sulfide nano / microcrystallines via a facile way. *J. Alloys Compd.* **620,** 42–47 (2015).

11. Fazli, Y., Pourmortazavi, S. M., Kohsari, I., Karimi, M. S. & Tajdari, M. Synthesis, characterization and photocatalytic property of nickel sulfide nanoparticles. *J. Mater. Sci. Mater. Electron.* 1–8 (2016). doi:10.1007/s10854-016-4683-2

12. Rincke, C., Bette, S., Dinnebier, R. E. & Voigt, W. Nickel Bicarbonate Revealed as a Basic Carbonate. *Eur. J. Inorg. Chem.* 5913–5920 (2015).

doi:10.1002/ejic.201501094

13. Jia, Y., Luo, T., Yu, X.-Y., Liu, J.-H. & Huang, X.-J. Surfactant-free preparation of nickel carbonate hydroxide in aqueous solution and its toxic ion-exchange properties. *New J. Chem.* **37,** 534–539 (2013).

14. Osawa, M., Tsushima, M., Mogami, H., Samjeské, G. & Yamakata, A. Structure of Water at the Electrified Platinum–Water Interface: A Study by Surface-Enhanced Infrared Absorption Spectroscopy. *J. Phys. Chem. C* **112,** 4248–4256 (2008).

15. Persson, P. *et al.* Structure and Bonding of Orthophosphate Ions at the Iron Oxide-Aqueous Interface. *J. Colloid Interface Sci.* **177,** 263–275 (1996).

16. Hug, S. J. In Situ Fourier Transform Infrared Measurements of Sulfate Adsorption on Hematite in Aqueous Solutions. *J. Colloid Interface Sci.* **188,** 415–422 (1997).

17. Peak, D., Ford, R. & Sparks, D. An in Situ ATR-FTIR Investigation of Sulfate Bonding Mechanisms on Goethite. *J. Colloid Interface Sci.* **218,** 289–299 (1999).

18. Zhang, G. Y. & Peak, D. Studies of Cd(II)-sulfate interactions at the goethite-water interface by ATR-FTIR spectroscopy. *Geochim. Cosmochim. Acta* **71,** 2158–2169 (2007).

19. Beattie, D. a, Chapelet, J. K., Gra, M., Skinner, W. M. & Smith, E. In Situ ATR FTIR Studies of SO Adsorption on Goethite in the Presence of Copper Ions In Situ ATR FTIR Studies of SO 4 Adsorption on Goethite in the Presence of Copper Ions. *Environ. Sci. Technol.* **42,** 9191–9196 (2008).

20. Su, C. & Suarez, D. L. In Situ Infrared Speciation of Adsorbed Carbonate on Aluminum and Iron Oxides. *Clays Clay Miner.* **45,** 814–825 (1997).

21. Russell, M. J., Daniel, R. M., Hall, A. J. & Sherringham, J. A. A hydrothermally precipitated catalytic iron sulphide membrane as a first step toward life. *J. Mol. Evol.* **39,** 231–243 (1994).

Chapter 7
Electrochemistry of pyrrhotite and pentlandite

7.1 Introduction

In this chapter, the cyclic voltammetry studies performed on the iron sulfide pyrrhotite (Fe_7S_8) and iron-nickel sulfide pentlandite ($(Fe,Ni)_9S_8$) are presented and discussed. These two metal sulfides were chosen for further CV studies to compare and contrast their electrochemical behaviour with the CV responses of greigite and violarite, based on the variation of Fe:S ratio in pyrrhotite and greigite, and of the Fe:Ni ratio in pentlandite in violarite. The effect of the differing stoichiometries of pyrrhotite vs greigite and pentlandite vs violarite on their CV responses are explored. In general, it is expected that the CV response of pyrrhotite will resemble greigite and the CV response of pentlandite will resemble violarite. The effect of the introduction of CO_2 on the CV responses of pyrrhotite and pentlandite is also explored and discussed. Similar to the analysis in the CVs of greigite and violarite, Pourbaix diagrams of relevant systems will be considered when assigning the redox features in the CVs of pyrrhotite and pentlandite.

7.1.1 Pourbaix diagrams

The Pourbaix diagrams that are referred to on analysing the CVs of pyrrhotite are the Pourbaix diagram of Fe-S-H_2O system (Figure 7.1) and the Pourbaix diagrams presented in chapter 3: Fe-H_2O, S-H_2O, Fe-CO_2-H_2O, Fe-S-C-H_2O systems. Additionally, for pentlandite, the Pourbaix diagrams presented in chapter 5: Fe-Ni-S-H_2O, Fe-Ni-H_2O and the Ni-S-O_2-CO_2-H_2O systems are referred to.

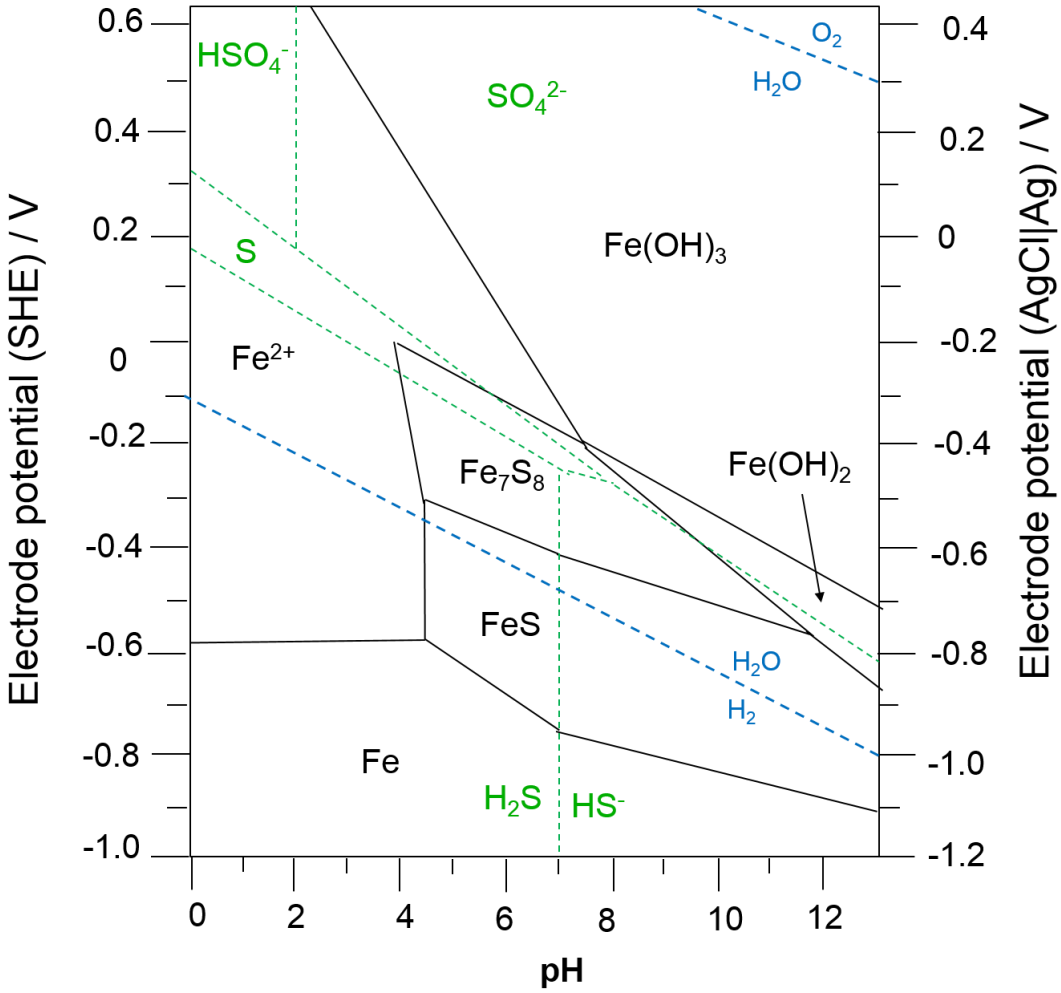

Figure 7.1 Pourbaix diagram for the Fe-S-H_2O system at 298 K, considering $Fe(OH)_3$ as the solid iron oxide phase and excluding pyrite FeS_2. Dissolved Fe(II)/Fe(III) activities of 10^{-3}. Dissolved sulphur species activities of 10^{-3}. Adapted from reference 1.

7.1.2 Literature on the electrochemistry of pyrrhotite

Almeida and Giannetti performed a CV of ground natural pyrrhotite incorporated in a carbon paste working electrode in pH 4.5 acetic acid-sodium acetate electrolyte. [2] The potential range used was between +0.922 V and −0.6 V (vs. SHE) and the CV reported is shown in Figure 7.2 where the CV was initiated from the open circuit potential.[2]

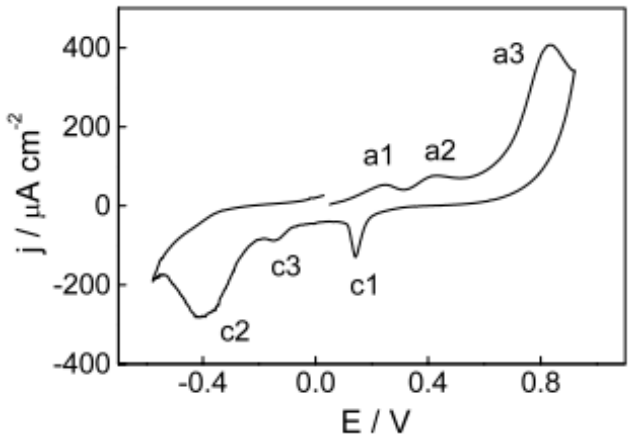

Figure 7.2 Cyclic voltammogram of pyrrhotite carbon paste electrode (vs. SHE) performed at a scan rate 20 mVs^{-1} with electrolyte of pH 4.5. ($E_i = E_{ocp}$, $E_{\lambda a}$ = +0.922 V, $E_{\lambda c}$ = −0.6 V). Reprinted with permission from Elsevier. [2] Copyright 2003 Elsevier B.V.

The authors assumed the pyrrhotite electrode as an iron-deficient iron sulfide with the formula $Fe_{(1-x)}S$ and proposed the formation of elemental sulfur (7.1) at the anodic peak a1 at *c.a.* +0.25 V. [2]

$$Fe_{(1-x)}S \rightarrow (1-x)Fe^{2+} + S + 2(1-x)e^{-} \qquad (7.1)$$

According to the Pourbaix diagram in Figure 7.1, Fe^{2+} and SO_4^{2-} are the predicted stable redox species at this potential and pH. The authors further suggested an accumulation of the sulfur layers formed on the pyrrhotite electrode and proposed that the accumulated sulfur layers would result in an increasing difficulty for Fe^{2+} ions to diffuse.[2] However, no spectroscopic evidence was

provided to verify the presence of elemental sulfur on the pyrrhotite electrode ex-situ or in-situ.

Peak a2 was assigned to the oxidation of Fe^{2+} while peak a3 was assigned to the oxidation of thiosulfate $S_2O_3^{2-}$ to sulfate. The assignment of Fe^{2+} oxidation to peak a2 is not supported by the Pourbaix diagram in Figure 7.1. The authors also proposed the formation of $S_2O_3^{2-}$ from the oxidation of elemental sulfur and pyrrhotite itself. However, it is unlikely that $S_2O_3^{2-}$ was present as it is a metastable species compared to sulfate.

$$2S + 3H_2O \rightarrow S_2O_3^{2-} + 6H^+ + 4e^- \quad (7.2)$$

$$2FeS + 3H_2O \rightarrow S_2O_3^{2-} + 2Fe^{2+} + 6H^+ + 8e^- \quad (7.3)$$

$$S_2O_3^{2-} + 5H_2O \rightarrow 2SO_4^{2-} + 10H^+ + 8e^- \quad (7.4)$$

The authors proposed these assignments based on a study by Paul *et al.*[3] However, based on the predictions in the Pourbaix diagram in Figure 7.1, the assignments of the oxidation peaks by the authors may be incorrect. It is proposed here that peak a1 is assigned to the formation of sulfur, peak a2 is assigned to the formation of sulfate, while peak a3 is assigned to the formation of $Fe(OH)_3$. The authors did not assign the reduction peaks but instead, quoted that these reduction peaks are commonly assigned in the literature to the reduction of FeOOH to Fe^{2+} at peak c1, and the reduction of sulfur and its intermediates at peaks c2 and c3. Based on the Pourbaix diagram in Figure 7.1, it is proposed here that peak c1 is assigned to the reduction of $Fe(OH)_3$ to Fe^{2+}, peak c3 to the reduction of S to H_2S and peak c2 to further reduction of pyrrhotite to "FeS".

$$Fe(OH)_3 + 3H^+ + e^- \rightarrow Fe^{2+} + 3H_2O \quad (7.5)$$

$$S + 2H^+ + 2e^- \rightarrow H_2S \quad (7.6)$$

$$Fe_7S_8 + 2H^+ + 2e^- \rightarrow 7FeS + H_2S \quad (7.7)$$

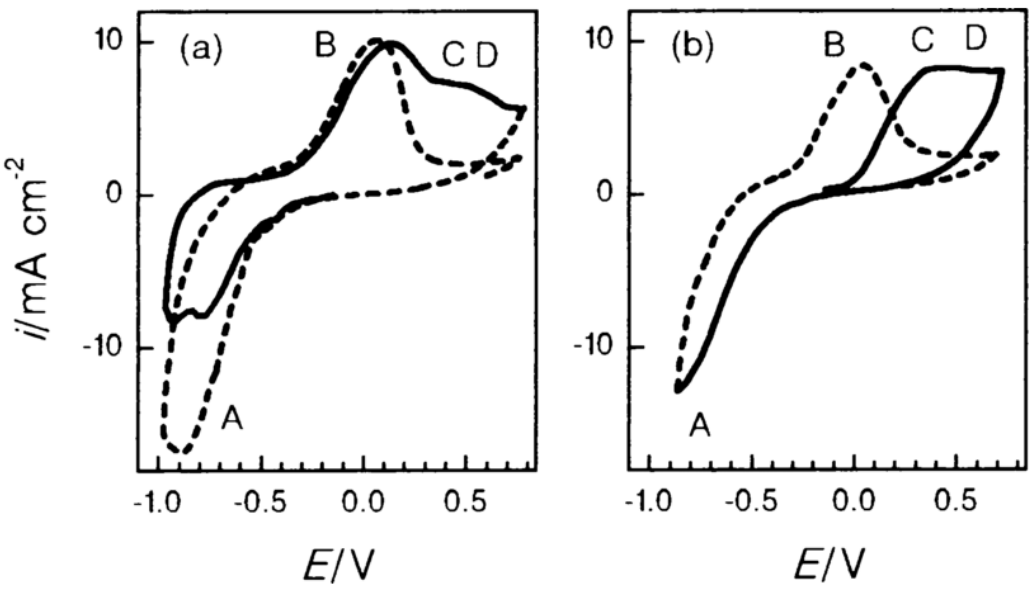

Figure 7.3 CV of natural pyrrhotite in 0.05 M $Na_2B_4O_7$ pH 9, pre-etched in HCl, where the scan was initiated from the OCP a) in the positive-going direction and b) negative-going direction. Solid line: first scan, dashed line: second scan. T = 20°C and scan rate of 5 mV s^{-1}.[4] Reproduced with permission.

In a separate study, Mikhlin used a natural pyrrhotite electrode (of composition $FeS_{1.11}$) pre-treated in 1 M HCl for 1 hour before performing the CV in $Na_2B_4O_7$ pH 9 as shown in Figure 7.3.[4] The author assigned peak A to the reduction of the electrode surface producing H_2S:

$$FeS_{1.11} + 0.22H^+ + 0.22e^- \rightarrow FeS + 0.11H_2S \qquad (7.8)$$

In contrast to the assignments by Almeida *et al*,[2] Mikhlin assigned the anodic peaks (B, C and D) to the complex formation of polysulfide layers on the electrode surface.[4] However, no spectroscopic evidence for the presence of polysulfides was provided. Polysulfides are metastable species compared to elemental sulfur and sulfate species and therefore are not predicted to form, as shown in the Pourbaix diagram in Figure 7.1.

Hamilton and Woods performed similar CV experiments using a natural pyrrhotite electrode in pH 9.2 and 13 electrolytes (Figure 7.4). Both CVs possessed approximately similar redox features, except for the sharp increase in the anodic current at 0 V at pH 13.

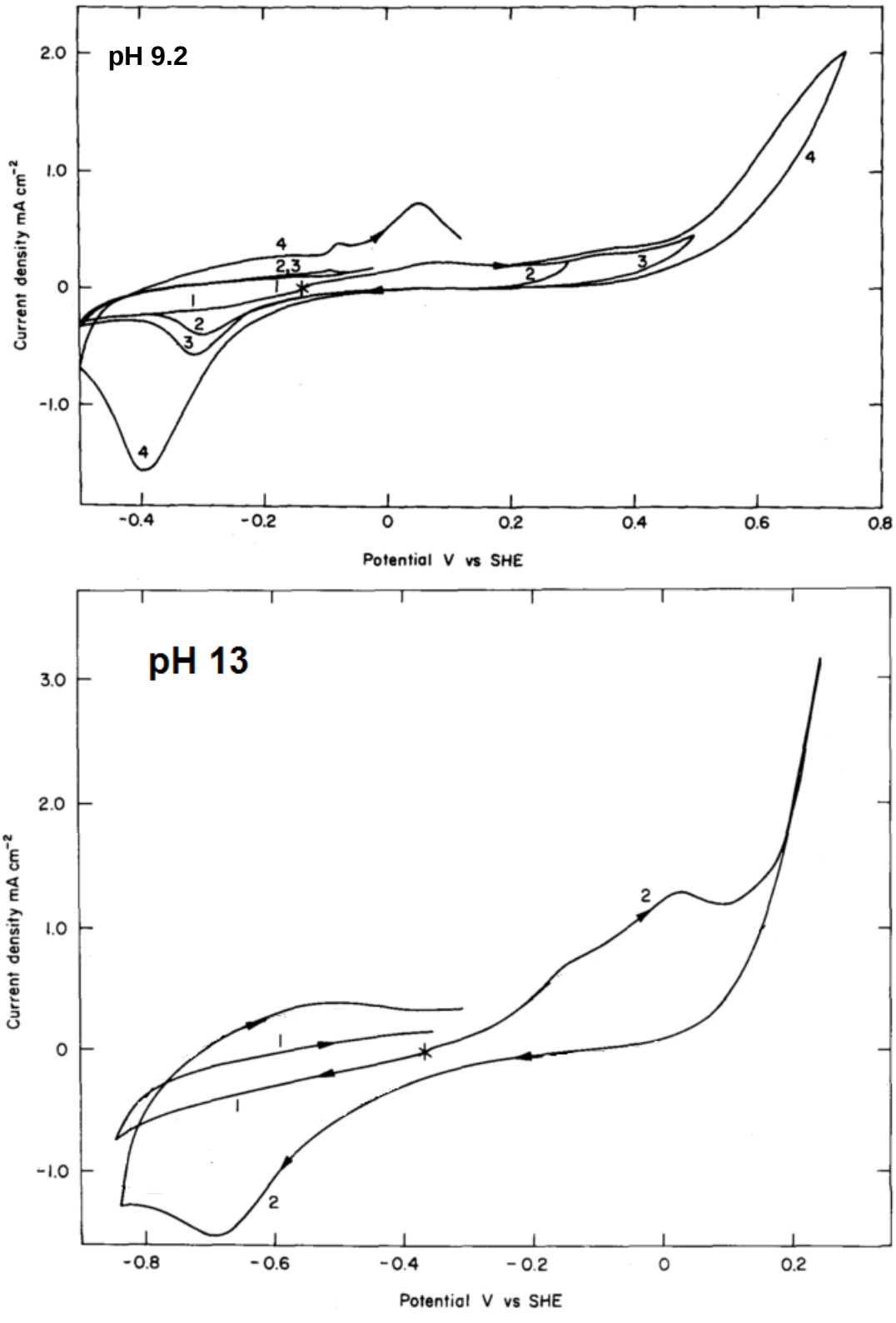

Figure 7.4 CV of natural pyrrhotite in pH 9.2 (0.05 M $Na_2B_4O_7$) and pH 13 (0.1 M NaOH). Scan rate of 20 mV s^{-1}. The CVs at pH 9.2 were reversed at different upper potential limits.[7] Reproduced with permission.

The authors assigned the anodic currents to the oxidation of FeS to $Fe(OH)_3$, elemental sulfur and SO_4^{2-}, while the cathodic peaks were assigned to the reduction of $Fe(OH)_3$ to $Fe(OH)_2$ and FeS. The anodic current at 0 V at pH 13 increased steeply compared to at pH 9.2 and the authors proposed that the increased current at pH 13 was due to the nucleation of $Fe(OH)_3$ formed from the oxidation of FeS / pyrrhotite. According to the Pourbaix diagram in Figure 7.1, elemental sulfur is not predicted to be stable at both pH 9.2 and 13. Thus, the anodic currents must instead be associated to the oxidation of "FeS" / pyrrhotite electrode to SO_4^{2-} and not elemental sulfur. The assignment of the formation of $Fe(OH)_3$ on the positive-going sweep is in agreement with the Pourbaix diagram in Figure 7.1, where it is predicted to be the stable redox species at potentials > −0.50 V (vs AgCl|Ag) at pH 9.2 and at potentials > −0.7 V (vs AgCl|Ag) at pH 13. The authors also proposed that the formation of $Fe(OH)_3$ may have inhibited further oxidation of the pyrrhotite / FeS electrode based on the smaller cathodic currents on the negative-going sweep compared to the anodic currents on the positive-going sweep. Due to the potential limits of the negative-going potential sweep used by the authors, it is not surprising that the authors assumed that $Fe(OH)_3$ remained present on the electrode in the negative-going sweep and was not stripped off the electrode, resulting in small cathodic currents for the reduction of sulfates to HS^-. The potential limits of −0.5 V at pH 9.2 and −0.8 V at pH 13 vs SHE are just within the limit of the predicted stability region of $Fe(OH)_3$ (see Figure 7.1).

The potential range used by the authors in this section is clearly much wider and more positive, up to +0.8 V (vs SCE) compared to that used in this thesis. Only interpretations up to 0.00 V (vs AgCl|Ag) will be considered on assigning the redox features in the CVs of pyrrhotite.

7.1.3 Literature on the electrochemistry of pentlandite

Warner *et al* performed a CV on a natural pentlandite electrode in 1 M HCl and the CV response recorded is shown in Figure 7.5. [5] The CV shows the effect of increasing the positive-going potential limit on the negative-going sweep. Warner *et al* proposed that it was impossible to reduce pentlandite in aqueous electrolyte due to the competing water reduction reaction and assigned the cathodic currents below 0 V (vs SCE) to the reduction of elemental sulfur to H_2S and below −0.4 V (vs SCE) to proton reduction. One important observation in the CV of pentlandite is that the cathodic currents between 0 to −0.3 V (vs SCE) were not observed until the positive-going potential limit was extended beyond +0.2 V (vs SCE).

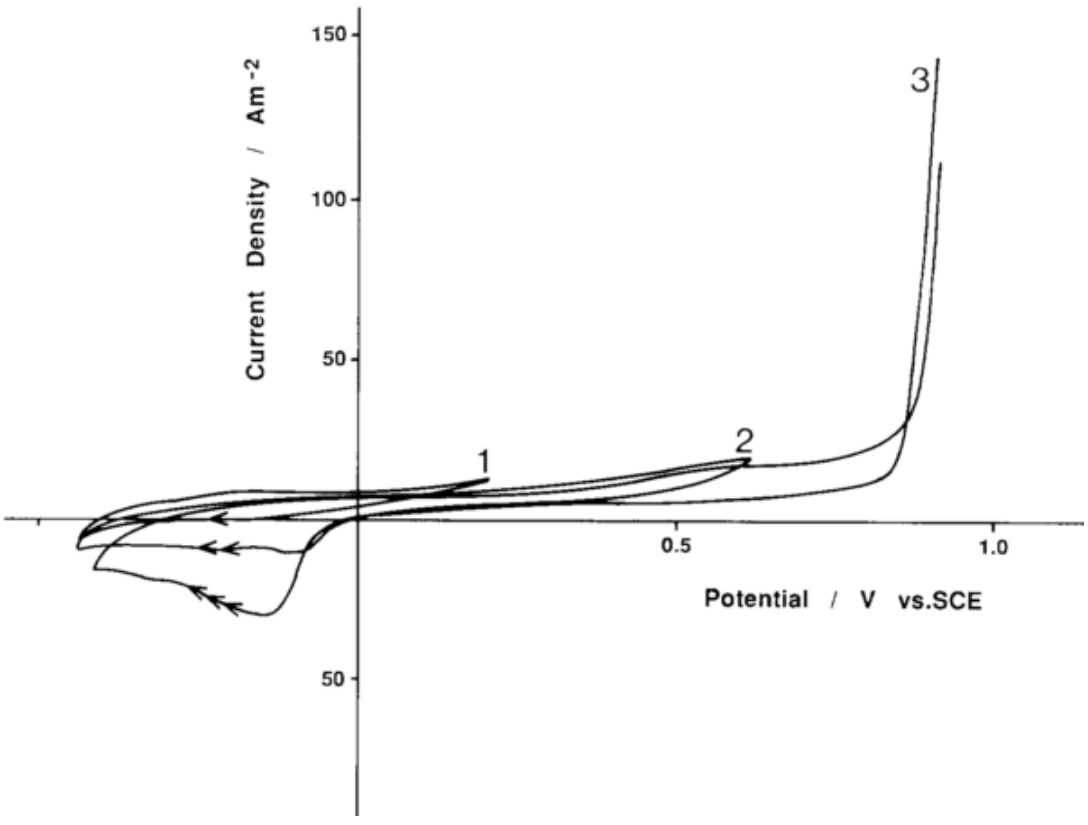

Figure 7.5 CV of natural pentlandite electrode in 1 M HCl pH 1 at 343 K with a sweep rate of 5 mV s^{-1} , 20 Hz RDE. The initial scan is negative-going.[5] Reproduced with permission.

The authors characterised the electrode ex-situ and did not detect elemental sulfur. However, the pentlandite surface was found to be extensively etched. Referring to the Pourbaix diagram in Figure 5.1 in chapter 5, at pH 1, Fe^{2+} and Ni^{2+} are the predicted stable redox species at potentials above −0.40 V. The transformation of pentlandite to Fe^{2+} and Ni^{2+} will constitute as an oxidation process. The oxidative dissolution of pentlandite to Fe^{2+} and Ni^{2+} may explain the etching of the pentlandite electrode.

$$Fe_{4.5}Ni_{4.5}S_8 \rightarrow 4.5Ni^{2+} + 4.5Fe^{2+} + 8S + 18e^- \quad (7.9)$$

$$Fe_{4.5}Ni_{4.5}S_8 + 32H_2O \rightarrow 4.5Ni^{2+} + 4.5Fe^{2+} + 8SO_4^{2-} + 64H^+ + 66e^- \quad (7.10)$$

In another study, Khan and Kelebek investigated and compared the CV responses (vs SCE) of natural and synthetic pentlandite electrodes in pH 9.2 0.05 M $Na_2B_4O_7$ electrolyte as shown in Figure 7.6. [6] The authors assigned the anodic peak to the formation of $Fe(OH)_3$ and $Ni(OH)_2$ as well as elemental sulfur and sulfate. The cathodic peaks were proposed to be associated with the reduction of $Fe(OH)_3$ and $Ni(OH)_2$. The authors suggested that the small currents of the reduction peak was due to the soluble nature of some of the oxidation products formed at the anodic peak, but the authors did not specify which products. The current author assumes that the cathodic peak was assigned to the reduction of elemental sulfur and sulfates to HS^-, and that the formation of $Fe(OH)_3$ and $Ni(OH)_2$ on the electrode on the positive-going sweep may have inhibited this reaction.

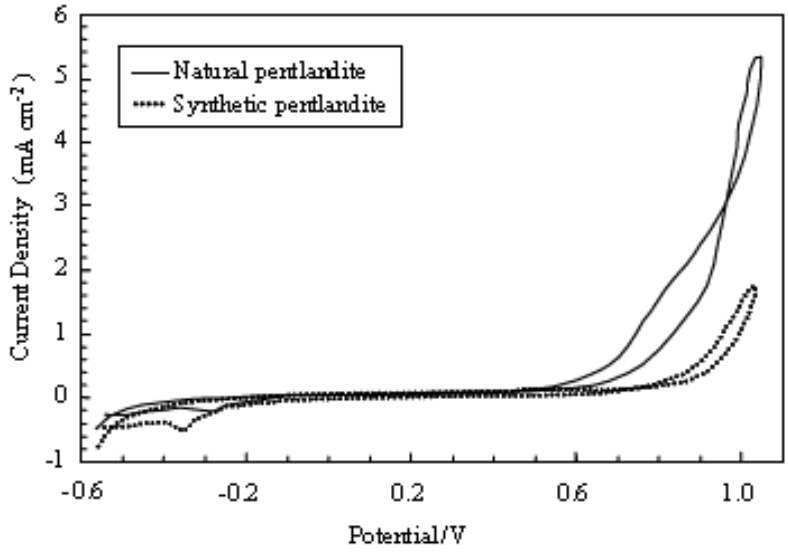

Figure 7.6 CVs of natural and synthetic pentlandite recorded in pH 9.2 electrolyte at scan rate of 10 mV s^{-1} (vs SCE). [6] Reprinted with permission from CRC Press Taylor & Francis Group. Copyright 2011 CRC Press Taylor & Francis Group.

According to the Pourbaix diagram in Figure 5.1 in chapter 5, at pH 9.2, FeOOH and Ni^{2+} are the predicted stable redox species present at potentials > −0.50 V (vs AgCl|Ag). However, on comparison of the Pourbaix diagrams in Figure 5.1 and 3.1, it is also likely that $Fe(OH)_3$ was formed, as suggested by the authors, in place of FeOOH as both are Fe^{3+} containing compounds. It is also possible that $Ni(OH)_2$ may have formed on the electrode on the positive-going potential sweep as the stability regions of Ni^{2+} and $Ni(OH)_2$ coincide at this pH. At potentials < −0.50 V (vs AgCl|Ag), these metal oxides are predicted to reduce to violarite and subsequently to pentlandite. However, these transformations may be kinetically slow and may not occur.

$$FeOOH + 2Ni^{2+} + 4SO_4^{2-} + 35H^+ + 31e^- \rightarrow FeNi_2S_4 + 18H_2O \quad (7.11)$$

$$FeOOH + 2Ni(OH)_2 + 4SO_4^{2-} + 39H^+ + 31e^- \rightarrow FeNi_2S_4 + 22H_2O \quad (7.12)$$

$$FeNi_2S_4 + 2.5FeOOH + 0.5Ni(OH)_2 + 8.5H^+ + 8.5e^- \rightarrow Fe_{4.5}Ni_{4.5}S_8 + 6H_2O \quad (7.13)$$

Similar to the discussion for pyrrhotite, the potential range used by the authors in this section is wider and more positive, up to +1.0 V (vs SCE) compared to that used in this thesis and only interpretations up to 0.00 V (vs AgCl|Ag) will be considered when analysing the CVs of pentlandite.

7.2 Results

7.2.1 Pyrrhotite, Fe_7S_8

7.2.1.1 PBS pH 6.8 under argon and pH 6.5 under CO_2

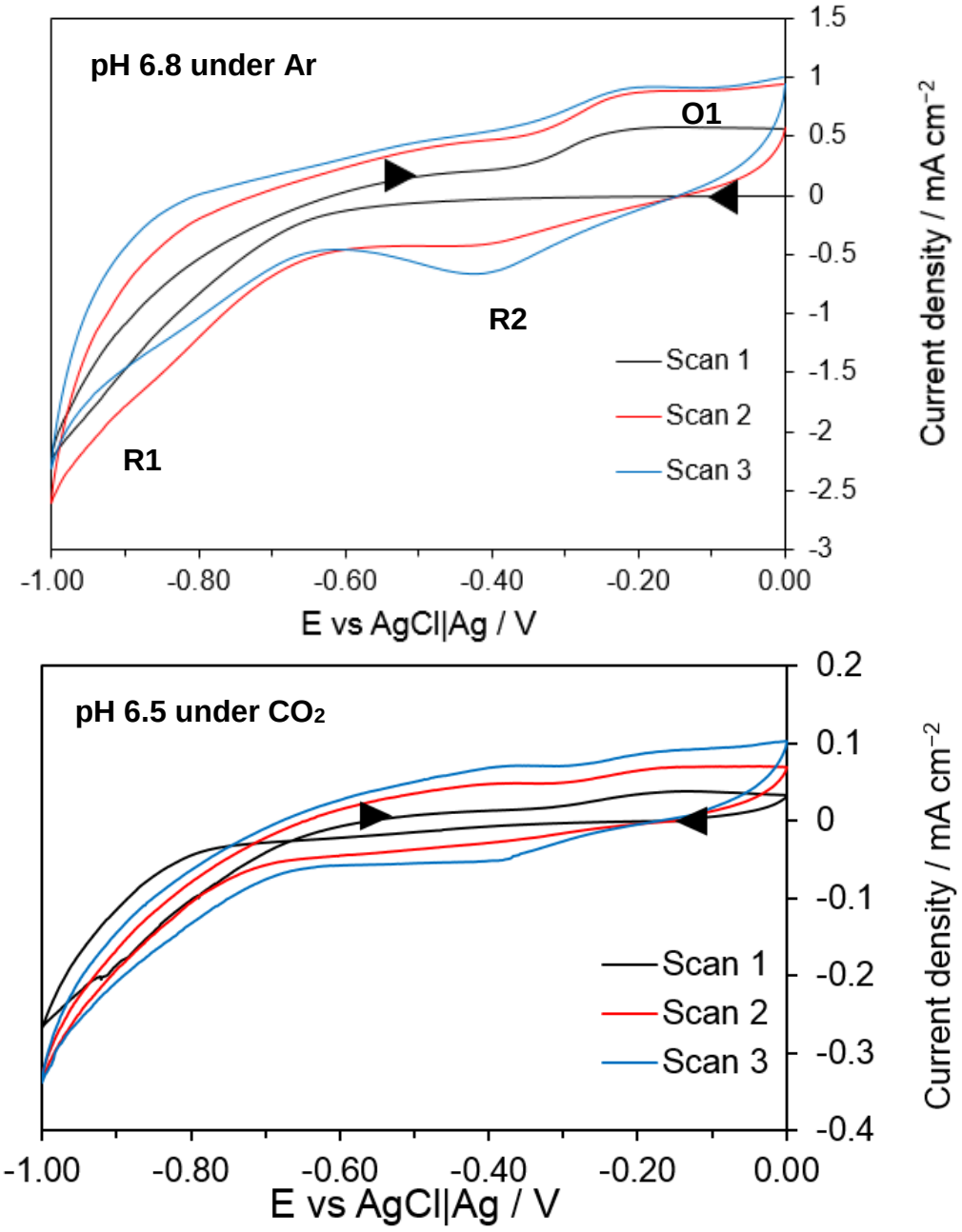

Figure 7.7 CVs of pyrrhotite in phosphate buffer solution pH 6.8 under argon and pH 6.5 under CO_2. Scan rate 10 mV s^{-1}, start potential 0.00 V.

The CVs of pyrrhotite, Fe_7S_8, in phosphate buffer solutions pH 6.8 under argon and pH 6.5 under CO_2 are shown in Figure 7.7. In the first CV scan under argon, the current appears to be close to zero up to the potential of −0.60 V on negative-going potential sweep. This is similar to the observation made in the CV of greigite in chapter 3 in PBS pH 6.8 under argon. According to the Pourbaix diagram in Figure 7.1, between 0 to −0.30 V at pH 6.8, $Fe(OH)_3$ is the predicted stable redox species before it is reduced to Fe^{2+} **(7.5)**, while pyrrhotite is only predicted to be stable between −0.40 and −0.65 V before it is reduced to FeS at −0.65 V **(7.7)**. The featureless current trace up to −0.60 V suggest that pyrrhotite was stable than predicted by the Pourbaix diagram in Figure 7.1 and that $Fe(OH)_3$ may not have formed on the surface of the electrode since there was no reduction peak at *c.a.* −0.40 V on the negative-going potential sweep where the reduction of $Fe(OH)_3$ to Fe^{2+} is predicted to occur. Therefore, the reduction peak R1 in Figure 7.7 is assigned to the reduction of pyrrhotite and water reduction. On the positive-going sweep of the first CV scan of pyrrhotite in PBS pH 6.8 under argon, a broad anodic peak O1 at *c.a.* −0.20 V was observed and is assigned to the oxidation of pyrrhotite to Fe^{2+} and SO_4^{2-} **(7.14)**, and the formation of $Fe(OH)_3$ (reverse of **(7.5)**), based on the Pourbaix diagram in Figure 7.7. The oxidation of pyrrhotite at peak O1 may also produce elemental sulfur **(7.15)**.

$$Fe_7S_8 + 32H_2O \rightarrow 7Fe^{2+} + 8SO_4^{2-} + 64H^+ + 62e^- \quad (7.14)$$

$$Fe_7S_8 \rightarrow 7Fe^{2+} + 8S + 14e^- \quad (7.15)$$

If water reduction occurred on the first negative-going potential sweep, this may increase the local pH near the electrode surface. The assignments above remain true if the local pH was below pH 7.5. Above pH 7.5, $Fe(OH)_2$ is predicted to form from the oxidation of pyrrhotite, and is subsequently oxidised to $Fe(OH)_3$. However, it is most likely that the main oxidation product of pyrrhotite was $Fe(OH)_3$ and not $Fe(OH)_2$ based on the size of the stability regions of both oxides in the Pourbaix diagram in Figure 7.1.

$$Fe_7S_8 + 46H_2O \rightarrow 7Fe(OH)_2 + 8SO_4^{2-} + 78H^+ + 62e^- \quad (7.16)$$

$$Fe(OH)_2 + H_2O \rightarrow Fe(OH)_3 + H^+ + e^- \quad (7.17)$$

At the beginning of the second CV scan of pyrrhotite under argon, $Fe(OH)_3$ and SO_4^{2-} are likely to be present near the electrode. Based on the Pourbaix diagram in Figure 7.1, the reduction peak R2 is assigned to the reduction of $Fe(OH)_3$ to pyrrhotite and $Fe(OH)_2$ (reverse reaction of **(7.16)** and **(7.17)**), and the reduction of SO_4^{2-} to elemental sulfur and H_2S. The broad anodic peaks on the positive-going potential sweep of the second CV scan of pyrrhotite under argon are assigned to the oxidation of $Fe(OH)_2$, elemental sulfur and SO_4^{2-}. There was an increase in current with each subsequent CV scan after the first CV scan of pyrrhotite under argon. This suggests an accumulation of $Fe(OH)_3$ / $Fe(OH)_2$ on the surface of the pyrrhotite electrode.

On introduction of CO_2 in PBS pH 6.5, the currents in the CV of pyrrhotite were comparably suppressed compared to the CV response under argon. This is a similar observation made for the greigite electrode in chapter 3 on introduction of CO_2. The formation of $Fe(CO)_3$ and carbonate green rust ($Fe_2(OH)_2(CO)_3$ and $Fe_6(OH)_{12}CO_3$), predicted by the Pourbaix diagrams Figures 3.4 and 3.5 in chapter 3 at this pH, were ruled out as the cause for the current passivation based on the absence of spectroscopic evidence for these compounds. Inferring from this conclusion, it is assumed that $Fe(CO)_3$ and carbonate green rust ($Fe_2(OH)_2(CO)_3$ and $Fe_6(OH)_{12}CO_3$) are not expected to form on the surface of the pyrrhotite electrode. Therefore, the passivated CV response of pyrrhotite may have been caused by the adsorption of CO_2 or its dissolved species (HCO_3^- / CO_3^{2-}).

The assignments of the redox features in this section are comparable to the assignments proposed by Almeida and Gianetti [2] and Hamilton and Woods, even if the potential window used here did not go above 0.00 V. [7] The potential window used in this work (between 0.00 and −1.00 V) was selected to investigate potential for CO_2 reduction compared to greigite in chapter 3. The introduction of CO_2 clearly affected the CV response of pyrrhotite, similar to greigite. Comparing the anodic currents of pyrrhotite and greigite, there are differences in the peak height of the anodic peaks towards the end of the positive-going potential sweep where the anodic currents increased further in pyrrhotite and decreased in

greigite. These differences may be associated with the different ratio of elemental sulfur and sulfates produced in different amounts based on the stoichiometries of pyrrhotite and greigite.

7.2.1.2 K_2CO_3 pH 11.2 under argon and pH 10.1 under CO_2

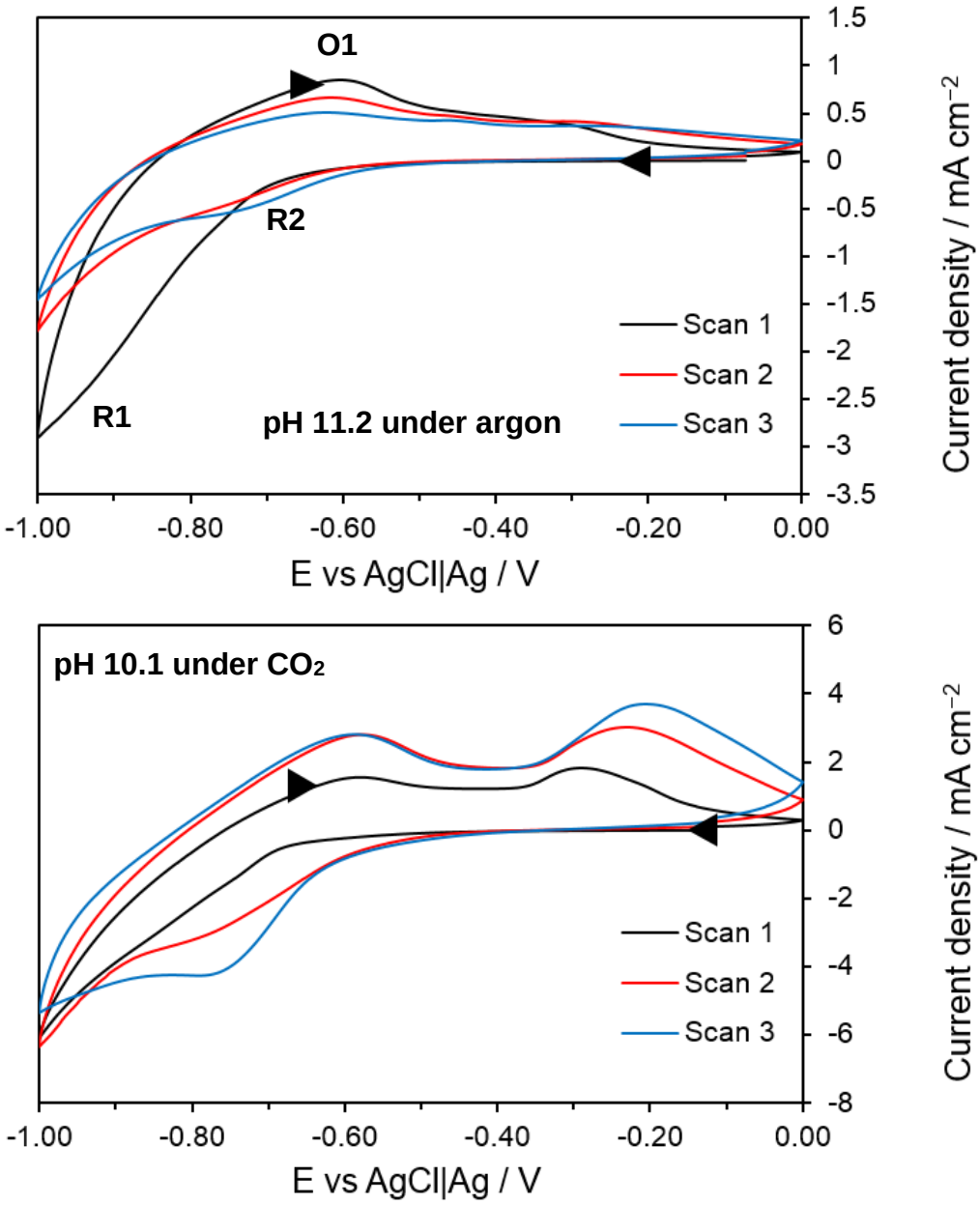

Figure 7.8 CVs of pyrrhotite in K_2CO_3 pH 11.2 under argon and pH 10.1 under CO_2. Scan rate 10 mV s^{-1}, start potential 0.00 V.

Figure 7.8 CVs of pyrrhotite in K2CO3 pH 11.2 under argon and pH 10.1 under CO2. Scan rate 10 mV $s^{-1,}$ start potential 0.00 V.Figure 7.8 display the CVs of pyrrhotite in K_2CO_3 pH 11.2 under argon and pH 10.2 under CO_2. Similar to the CV reseponse in PBS pH 6.8, the CV response of pyrrhotite in K_2CO_3 resembled

that of greigite. According to the Pourbaix diagram in Figure 7.1, $Fe(OH)_3$ is predicted to form at the onset potential of 0.00 V and will be oxidised to $Fe(OH)_2$ at −0.6 V. At this pH, pyrrhotite is only predicted to be stable within a narrow potential range between −0.75 and −0.78 V before it is reduced to FeS. A bulk transformation of the pyrrhotite electrode to $Fe(OH)_3$ at the onset potential is, however, not expected to occur as was observed for greigite in chapter 3 where there was spectroscopic evidence of sulfur character remaining within the electrode. It is also likely that due to the high pH, OH^- species may adsorb onto the pyrrhotite electrode and instigate the formation of $Fe(OH)_3$. Based on these predictions, peak R1 is assigned to the reduction of $Fe(OH)_3$, pyrrhotite and water reduction.

$$Fe_7S_8 + H^+ + 2e^- \rightarrow 7FeS + HS^- \qquad (7.18)$$

On the positive-going potential sweep, broad anodic currents were observed and peak O1 is assigned to the oxidation of $Fe(OH)_2$ to $Fe(OH)_3$, the oxidation of HS^- to SO_4^{2-} and the oxidation of FeS to $Fe(OH)_2$. Since $Fe(OH)_3$ is predicted to be stable at potentials > −0.6 V, the absence of distinct anodic peaks on the positive-going potential sweep was expected. The subsequent CV scans of pyrrhotite resemble the first CV scan with an additonal reduction peak R2 present, assigned to the reduction of SO_4^{2-} to HS^-.

On introduction of CO_2 in K_2CO_3, the CV of pyrrhotite featured two distinct anodic peaks at *c.a.* −0.20 and −0.60 V. A similar effect was observed previously in the CV of greigite in K_2CO_3 on introduction of CO_2 where the anodic peaks became more distinct. The shift in pH on introduction of CO_2 in K_2CO_3 from pH 11.2 to pH 10.1 may have caused the change in the CV response of pyrrhotite. At this pH, pyrrrhotite is predicted to be stable between −0.65 and −0.75 V. The oxidation of pyrrhotite to $Fe(OH)_2$ may have contributed to the anodic peak at −0.60 V and this process may have lead to increased amounts of $Fe(OH)_3$ formed at −0.20 V. Hamilton and Woods suggested that increased anodic currents on the positive-going potential sweep is indicative of an accumulation of $Fe(OH)_3$ on the electrode surface.[7] The adsorption of CO_2 and its dissolved species (HCO_3^-/CO_3^{2-}) on the

pyrrhotite electrode may have hindered a complete passivation of the pyrrhotite electrode surface by OH^- species present in the high pH electrolyte, enabling the oxidation of pyrrhotite to $Fe(OH)_2$ to take place.

7.2.2 Pentlandite

7.2.2.1 PBS pH 6.8 under argon and pH 6.5 under CO_2

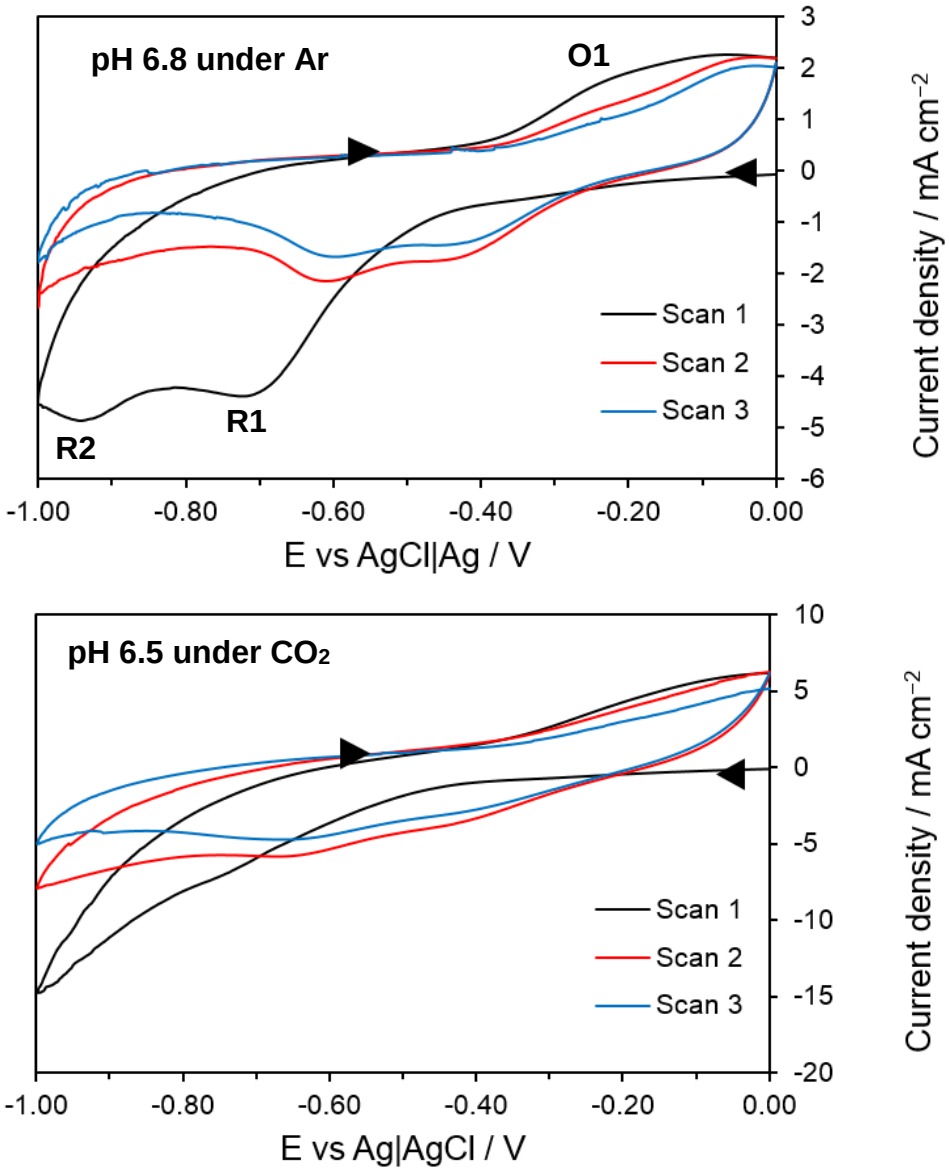

Figure 7.9 CVs of pentlandite in phosphate buffer solution pH 6.8 under argon and pH 6.5 under CO_2. Scan rate 10 mV s^{-1}, start potential 0.00 V.

Figure 7.9 contrasts the CVs of pentlandite in PBS pH 6.8 under argon and pH 6.5 under CO_2. In the CV under argon, the current trace on the negative-going potential sweep in the first CV scan appeared featureless up to −0.40 V where two

reduction peaks R1 and R2 were recorded at *c.a.* −0.70 and −0.90 V. According to the Pourbaix diagram in Figure 5.1 in chapter 5, FeOOH and Ni^{2+} are the predicted stable redox species at the onset potential of 0.00 V at pH 6.8 (produced via (5.3)). Subsequent reduction of FeOOH and Ni^{2+} to violarite (7.20) is predicted at potentials < −0.40 V and the reduction of violarite to pentlandite (7.21) at potentials < −0.50 V. However, these reactions may not proceed due to slow kinetics. If the pentlandite electrode was stable and FeOOH did not form at the onset potential of 0.00 V, pentlandite is predicted to reduce to Fe(0), Ni(0) and H_2S at −1.00 V (7.22).

$$Fe_{4.5}Ni_{4.5}S_8 + 41H_2O \rightarrow 4.5FeOOH + 4.5Ni^{2+} + 8SO_4^{2-} + 77.5H^+ + 70.5e^- \quad (7.19)$$

$$FeOOH + 2Ni^{2+} + 4SO_4^{2-} + 35H^+ + 31e^- \rightarrow FeNi_2S_4 + 18H_2O \quad (7.20)$$

$$2FeNi_2S_4 + 0.5Ni^{2+} + 2.5FeOOH + 7.5H^+ + 8.5e^- \rightarrow Fe_{4.5}Ni_{4.5}S_8 + 5H_2O \quad (7.21)$$

$$Fe_{4.5}Ni_{4.5}S_8 + 16H_2O + 16e^- \rightarrow 4.5Fe + 4.5Ni + 8H_2S \quad (7.22)$$

Based on the predictions above, peaks R1 and R2 are assigned to the reduction of pentlandite (7.22) and water reduction. On the positive-going potential sweep in the first CV scan under argon, a broad anodic peak at *c.a.* −0.30 V was recorded and is assigned to the formation of FeOOH and SO_4^{2-}. Referring to the Pourbaix diagram in Figure 3.1, Fe_2O_3 / $Fe(OH)_3$ may also have been formed in place of FeOOH. The subsequent CV scans of pentlandite recorded two reduction peaks at *c.a.* −0.40 and −0.60 V which are assigned to the reduction of FeOOH / Fe_2O_3 / $Fe(OH)_3$ to Fe^{2+} and the reduction of SO_4^{2-} to elemental sulfur / H_2S. The reduction of Fe_2O_3 / $Fe(OH)_3$ to Fe^{2+} is predicted at pH 6.8 at potentials < −0.40 V in the Pourbaix diagram in Figure 3.1 in chapter 3, if there are no Ni^{2+} and SO_4^{2-} species present near the electrode surface. The reduction of FeOOH / Fe_2O_3 / $Fe(OH)_3$ to pentlandite was not assigned to these reduction peaks as it is unlikely

to occur as the sulfates required may have been consumed and reduced to elemental sulfur / H_2S. The assignments of the redox features in the CV of pentlandite in this thesis agree with the results reported by Khan and Kelebek and Warner where the formation of an oxide is expected on the positive-going potential sweep close to 0.00 V. [5,6] However, in this work, the CVs of pentlandite were recorded up to −1.00 V, a negative-potential limit which the authors did not explore.

On introduction of CO_2 in PBS pH 6.5, current enhancement was observed in the CV response of pentlandite. This is a similar observation made in chapter 5 for the CV of violarite in PBS pH 6.5 on introduction of CO_2. Based on the Pourbaix diagrams of Ni-S-O_2-CO_2-H_2O (Figure 5.3) and Fe-S-C-H_2O (Figure 3.5) systems, it was concluded that iron carbonate, carbonate green rust, nickel carbonate or nickel hydroxycarbonate are not predicted to form on the violarite electrode on introduction of CO_2 and the current enhancement observed for violarite could be attributed to CO_2 reduction. Therefore, inferring from this conclusion, the current enhancement observed for pentlandite could also be associated with the reduction of CO_2. The two distinct reduction peaks recorded under argon were suppressed which suggests that the reduction of pentlandite and water reduction were suppressed as a result of the introduction of CO_2. The adsorption of CO_2 or its dissolved species on the pentlandite electrode may have blocked surface sites and hindered redox reactions from occurring.

7.2.2.2 K_2CO_3 pH 11.2 under argon and pH 10.1 under CO_2

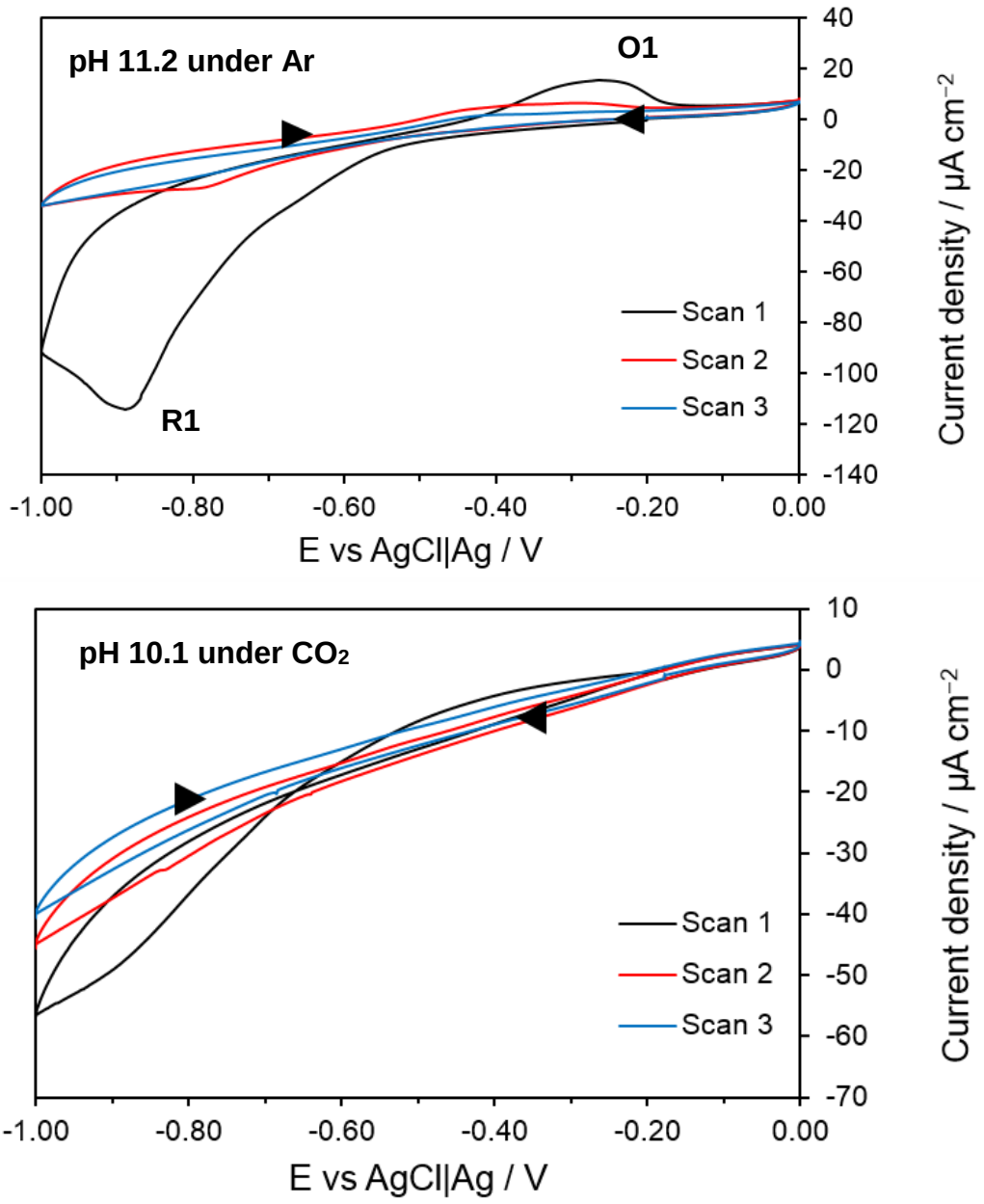

Figure 7.10 CVs of pentlandite in K_2CO_3 pH 11.2 under argon and pH 10.1 under CO_2. Scan rate 10 mV s^{-1}, start potential 0.00 V.

Figure 7.10 shows the CVs of pentlandite in K_2CO_3 pH 11.2 under argon and pH 10.1 under CO_2. The currents were significantly smaller compared to the CVs recorded in PBS pH 6.8 under argon and pH 6.5 under CO_2 which suggests a passivated electrode surface. The passivation of the electrode surface may be caused by a high concentration of OH^- species present near the electrode. According to the Pourbaix diagram in Figure 5.1 in chapter 5, at pH 11.2, FeOOH

and $Ni(OH)_2$ are the stable redox species predicted at the onset potential of 0.00 V. The formation of FeOOH and $Ni(OH)_2$ will result in the oxidation of pentlandite. Both FeOOH and $Ni(OH)_2$ are predicted to remain stable up to potentials > −0.65 V.

$$Fe_{4.5}Ni_{4.5}S_8 + 6H_2O \rightarrow 0.5Ni(OH)_2 + 2.5FeOOH + 2FeNi_2S_4 + 8.5H^+ + 8.5e^- \quad (7.23)$$

At potentials below −0.65 V, FeOOH and $Ni(OH)_2$ are predicted to reduce to violarite and subsequently to pentlandite. However, these reactions may be slow and may not occur. Instead, it is proposed here that the reduction peak R1 is assigned to the reduction of FeOOH to Fe_3O_4 or $Fe(OH)_2$ and the reduction of $Ni(OH)_2$ to Ni, as predicted by the Pourbaix diagrams in Figure 3.1 in chapter 3 and Figure 5.2 in chapter 5. On the positive-going potential sweep, only one small oxidation peak O1 at *c.a.* −0.30 V was recorded. Peak O1 is assigned to the oxidation of Fe_3O_4 / $Fe(OH)_2$ to FeOOH / Fe_2O_3 / $Fe(OH)_3$ and the oxidation of any remaining pentlandite (7.23). The subsequent CV scans of pentlandite revealed significantly reduced currents but similar redox features were still present.

On introduction of CO_2 in K_2CO_3, the CV response of pentlandite was featureless compared to that under argon. No significant redox features were present. According to the Pourbaix diagram in Figure 5.1 in chapter 5, the pH shift from pH 11.2 to pH 10.1 on introduction of CO_2 in K_2CO_3 approaches the region where FeOOH and Ni^{2+} are the predicted stable redox species at the onset potential of 0.00 V, in place of FeOOH and $Ni(OH)_2$ at pH 11.2. The featureless CV response of pentlandite on introduction of CO_2 suggest that there was no metal oxide available for reduction on the negative-going potential sweep. The adsorption of CO_2 and its dissolved species on the pentlandite electrode may have blocked surface sites preventing the formation of FeOOH and $Ni(OH)_2$.

The results in this work echoes the conclusion made by Warner *et al* [5] who proposed that pentlandite is impossible to reduce at a very low pH (pH 1). The

results in this work add further experimental evidence to the existing knowledge that pentlandite also cannot be reduced at high pHs (pH 10-11).

7.3 Discussion

The CVs of pyrrhotite Fe_7S_8 were found to slightly vary from the CV response of greigite Fe_3S_4 and the same was true for the CVs of pentlandite $(Fe,Ni)_9S_8$ vs the CV response of violarite $FeNi_2S_4$.

Both pyrrhotite and greigite were found to be comparably stable on the negative-potential sweep of the first CV scan. There was no reduction peak indicating the presence and reduction of FeOOH which was predicted in the Pourbaix diagrams to form at the onset potential of 0.00 V. The results also show that both materials were protected from air-oxidation by the capping agent used in their synthesis. Similar suppression of currents on introduction of CO_2 previously observed in greigite was also found in pyrrhotite. Differences in the CV responses of greigite and pyrrhotite were found in the anodic currents in the positive-going potential sweep. The anodic currents in the CV of pyrrhotite in PBS pH 6.8 were found to decrease on approaching the final potential of 0.00 V, while in contrast, the anodic currents of greigite were found to increase. These differences may be due to the differing stoichiometries of pyrrhotite and greigite resulting in different amounts of elemental sulfur and sulfates produced.

For pentlandite and violarite, the trend in the CV responses were similar where the currents in the subsequent CV scans were significantly suppressed compared to the first CV scan. The current suppression was attributed to the formation of FeOOH and $Ni(OH)_2$ passivating the surface. On introduction of CO_2, current enhancement was observed in both the CVs of pentlandite and violarite in PBS pH 6.8 which was attributed to CO_2 reduction, while in K_2CO_3 the reduction peaks were no longer present which suggests a halt in the formation of FeOOH and $Ni(OH)_2$ possibly due to adsorption of CO_2 and its dissolved species. Differences in the CV response of pentlandite and violarite: i) the CV of pentlandite in K_2CO_3 did not show much redox features compared to violarite, which suggests pentlandite was impossible to reduce at high pH, and ii) the onset of the reduction

current in the CV of pentlandite was more negative (by −0.20 V) compared to the CV of violarite in PBS pH 6.8 which may be related to the relative stability of each material.

The findings in this chapter show that while both iron and iron-nickel sulfides have potential for CO_2 reduction, it is clear that different surfaces exist on the iron and iron-nickel sulfides which may affect the redox responses and the CO_2 reduction efficiency. For example, the formation and the presence of FeOOH on iron sulfides, and similarly, the formation and the presence of FeOOH and $Ni(OH)_2$ on iron-nickel sulfides are dependent on the pH conditions and potential range used. It is also important to consider the stability (pH and potential range) of the metal oxides potentially present on the iron and iron-nickel sulfide electrodes when performing catalysis work.

The use of Pourbaix diagrams on predicting the formation of FeOOH on iron sulfides and FeOOH and $Ni(OH)_2$ on iron-nickel sulfides aided in assigning the redox features in the CVs of greigite, pyrrhotite, violarite and pentlandite. However, it is clear that in-situ characterisation of the electrode is essential on verifying the predicted thermodynamic transitions. In chapters 4 and 6, the formation of FeOOH on greigite and violarite, and additionally of $Ni(OH)_2$ on violarite, at negative potentials (below −0.80 V) were not predicted by the Pourbaix diagrams. Water reduction reaction was found to instigate the formation of FeOOH on these materials, however, on introduction of CO_2, the formation of FeOOH was halted. It is believed that the same transformations would also occur on both pyrrhotite and pentlandite, however, further in-situ characterisation should be done on both pyrrhotite and pentlandite to verify this prediction.

7.4 References

1. Marsland, S. D. Ph. D. Thesis, Non-oxidative dissolution of iron sulphide minerals - of relevance to inorganic chemical souring of oil reservoirs. (Imperial College London, 1992).

2. Almeida, C. M. V. . & Giannetti, B. F. The electrochemical behavior of pyrite–pyrrhotite mixtures. *J. Electroanal. Chem.* **553,** 27–34 (2003).

3. Paul, R. L., Nicol, M. J., Diggle, J. W. & Saunders, A. P. The electrochemical behaviour of galena (lead sulphide) — I. Anodic dissolution. *Electrochim. Acta* **23,** 625–633 (1978).

4. Mikhlin, Y. Reactivity of pyrrhotite surfaces: An electrochemical study. *Phys. Chem. Chem. Phys.* **2,** 5672–5677 (2000).

5. Warner, T. E., Rice, N. M. & Taylor, N. An electrochemical study of the oxidative dissolution of synthetic pentlandite in aqueous media. *Hydrometallurgy* **31,** 55–90 (1992).

6. Khan, A., Kelebek, S. & Hall, G. Electrochemical aspects of pyrrhotite and pentlandite in relation to their flotation with xanthate . Part-I: Cyclic voltammetry and rest potential measurements. *J. Appl. Electrochem.* **34,** 849–856 (2004).

7. Hamilton, I. C. & Woods, R. An investigation of surface oxidation of pyrite and pyrrhotite by linear potential sweep voltammetry. *J. Electroanal. Chem. Interfacial Electrochem.* **118,** 327–343 (1981).

Chapter 8
Concluding Remarks

This project set out to determine the stability of the iron (-nickel) sulfides under conditions where CO_2 reduction has been demonstrated to take place. Of particular interest in this work is the stability of iron sulfide greigite, (Fe_3S_4) and iron nickel sulfide violarite, ($FeNi_2S_4$) in aqueous solutions under ambient conditions. Both metal sulfides have been shown to reduce CO_2 on application of low electrode potentials (up to −1.3 V vs AgCl|Ag). However, at such low electrode potentials, metal sulfides are predicted to undergo reductive decomposition and competing reactions such as water reduction may also take place. Previous electrochemical studies on these materials have proposed various redox transformations on application of an applied electrode potential, however, there is a lack of surface characterisation of the electrodes in-situ to verify the proposed redox assignments and transformations in all of the published studies.[3–16]

The work in this thesis offers a new insight into the stability and potential thermodynamic transformations of the iron and iron-nickel sulfides in aqueous solutions, on application of an applied electrode potential under the conditions relevant for CO_2 reduction, by using newly designed electrochemical cells which are suitable for in-situ characterisation of the electrodes. Use of in-situ IR allows the monitoring of the IR-active surface groups present in the interfacial electrode / electrolyte layer, while in-situ XAS enables the monitoring of changes in the oxidation state and coordination environment of the Fe or Ni atoms in the bulk structure of these metal sulfides. Additionally, the novel synthesis of the iron and iron-nickel sulfides used in this project, by using a protective capping agent to protect the nanoparticles from aerial oxidation, removed the necessary requirement to pre-treat the materials before performing experiments, in order to remove any oxide layers which often form on metal sulfides on exposure to air. To the best of our knowledge, this is the first time in-situ characterisation of greigite and violarite in aqueous solutions has been attempted.

8.1 Effect of the introduction of CO_2 on the electrochemical behaviour of iron and iron-nickel sulfides

Cyclic voltammetry was the main technique used to record the electrochemical responses of the iron and iron-nickel sulfides studied. Pourbaix diagrams from the literature were then used to preliminarily assign the redox features recorded for each material. A systematic pH study was performed where the CVs of greigite and violarite were recorded in electrolytes of PBS pH 4.5, PBS pH 6.8, $KHCO_3$ pH 8.55 and K_2CO_3 pH 11.2 under both argon and CO_2. To the best of our knowledge, this is the first time an experimental pH CV study has been performed for greigite and violarite under both argon and CO_2.

Under argon atmosphere, the XANES data showed that iron hydroxide / oxyhydroxide formed on the greigite electrode on applying negative potentials of −0.80 and −1.00 V. This result contradicted the thermodynamic predictions in the Pourbaix diagrams in the literature where iron hydroxide / oxyhydroxide are not expected to form at these negative potentials. Separately, the IR results showed that on applying −0.80 and −1.00 V, the phosphate speciation within the interfacial layer changed drastically, indicating a significant increase in the local pH near the electrode. The increase in the local pH evidences water reduction occurring on the surface of the electrode. It is proposed in this project that the OH^- species generated by water reduction caused a pH increase near the electrode surface, and thus the formation of iron hydroxide / oxyhydroxide was favoured at these negative potentials, instigated by water reduction. This proposal is further supported by DFT calculations where insertion of OH^- species, produced via water reduction, is thermodynamically feasible, but such transformation occurs only on the surface of greigite and does not affect the bulk structure.

The introduction of CO_2 resulted in the suppression of currents in the CVs of greigite. Across all the pH conditions tested, the XANES spectroscopic data showed a halt in the formation of iron hydroxide / oxyhydroxide at negative potentials. Additionally, there was no evidence for the formation of iron

carbonate or carbonate green rust (such as $Fe_2(OH)_2CO_3$ and $Fe_6(OH)_{12}CO_3$) on the greigite which could have contributed to the current suppression under CO_2. The halt in the formation of iron hydroxide / oxyhydroxide suggests a suppression of water reduction under CO_2 which may be caused by the adsorption of CO_2 or its dissolved species. Based on the evidence of the presence of HCO_3^- species in the IR data, the current suppression under CO_2 was proposed to be a result of the adsorption of HCO_3^- species on the greigite surface. The adsorption of HCO_3^- species may have blocked the surface of greigite, preventing the formation of iron hydroxide / oxyhydroxides.

The evidence for the structural changes of greigite obtained in this project represents new information for the surface transformations of greigite in aqueous solutions. These results were correlated to the published CO_2 reduction study on greigite where pH 7 was found to be the optimum condition.

8.2 Effect of the presence of Ni in iron sulfides on their electrochemical behaviour and CO_2 reduction

It is clear from the findings in this project that different surfaces exist on the iron and iron-nickel sulfides which may affect the redox responses and the CO_2 reduction efficiency. The CVs of iron nickel sulfides violarite and pentlandite were comparably featureless compared to the iron sulfides greigite and pyrrhotite. This was attributed to the formation of FeOOH and $Ni(OH)_2$ on the surface of the iron-nickel sulfides. The IR data of violarite showed loss of SO_4^{2-} species which is indicative of the transformation of violarite to FeOOH and SO_4^{2-} species on immersion of the electrode into the electrolyte, as predicted by the Pourbaix diagrams. The XANES data showed the FeOOH and $Ni(OH)_2$ present on the violarite surface remained stable throughout the experiment, and no further structural transformations were observed. It is proposed that the presence of FeOOH on the violarite electrode and the high stability of FeOOH within the potential window used may have hindered the redox reactions of violarite. There was also no change in the speciation of the phosphate species in the IR data collected which suggested that no water reduction occurred on violarite.

However, on introduction of CO_2, current enhancement was observed for iron-nickel sulfides which was an opposite trend observed for the current suppression in the CVs of the iron sulfides. Unfortunately, due to limited access to XAS facilities, the XANES data of violarite under CO_2 was not recorded. However, based on the Pourbaix diagrams, the formation of iron carbonate, carbonate green rust, nickel carbonate and nickel hydroxide carbonate is not predicted on a violarite surface in the presence of CO_2. Thus, the current enhancement could be a result of CO_2 reduction itself. Separately, the IR data showed suppressed loss of SO_4^{2-} species which suggests that the adsorption of CO_2 or its dissolved species may have hindered the formation of FeOOH and the subsequent loss of SO_4^{2-} on the violarite electrode. There was also evidence for water reduction occurring on the violarite electrode based on the loss of water IR bands.

The results in this thesis echoes the observations made by Yamaguchi *et al*[2] in which a violarite electrode was shown to be catalytic for CO_2 and water reduction. However, further work is still required

8.3 Effect of the variation in stoichiometries (Fe:S and Fe:Ni) of iron and iron-nickel sulfides on their electrochemical behaviour under argon and CO_2

The project went further to explore the effect of the variation in Fe:S and Fe:Ni ratios on the electrochemical behaviour of iron and iron-nickel sulfides and on the CO_2 reduction efficiencies. This was done by comparing the CVs of pyrrhotite vs greigite and the CVs of pentlandite vs violarite.

The general features of the CVs of greigite vs pyrrhotite and pentlandite vs violarite appeared similar. However, on the positive-going potential sweep in the CV of pyrrhotite, clear differences compared to greigite were observed. The anodic currents in the CV of pyrrhotite were found to decrease on approaching the final potential of 0.00 V, while in contrast, the anodic currents of greigite were found to increase. These differences may be due to the differing stoichiometries of pyrrhotite and greigite resulting in different amounts of elemental sulfur and

sulfates produced. Comparing the CVs of violarite vs pentlandite, the onset of the reduction in pentlandite was more negative (by −0.20 V) compared to the CV of violarite in PBS pH 6.8 which may be related to the relative stability of each material, and pentlandite seemed impossible to reduce at high pH as the CV of pentlandite in K_2CO_3 did not show many redox features compared to violarite. The introduction of CO_2 suppressed the currents in the CVs of pyrrhotite (similar to the effect seen in greigite), while the currents were enhanced in the CVs of pentlandite (as seen in violarite). Based on the similar trend of the CV responses on introduction of CO_2, pyrrhotite and pentlandite may have the potential for CO_2 reduction and this should be explored further.

The similarities in the CV features of greigite vs pyrrhotite and pentlandite vs violarite were expected. However, the minor differences observed between greigite and pyrrhotite and between violarite and pentlandite serve as a preliminary assessment that the variation in stoichiometries of Fe:S and Fe:Ni resulted in a variation in the redox responses, which could be another future research avenue for consideration.

8.4 Significance for CO_2 reduction applications and origin of life theories

The work in this thesis was motivated by the proposed potential CO_2 reduction on greigite and violarite by the iron sulphide membrane origin of life theory. There is, however, a clear difference between the work here and the proposed hypothesis, which is the contrasting ambient conditions used in this work, and the high temperature and pressure setting in the hydrothermal vents proposed in the theory. Under the ambient conditions used in this project, the formation of hydroxides and oxyhydroxides was detected in both greigite and violarite. This suggests that in the proposed origin of life theory, the greigite and violarite membranes must be continually refreshed to prevent passivation of the surface by hydroxides / oxyhydroxides which may hinder CO_2 reduction. Future studies could consider implementing high pressure and high temperature conditions to explore this further.

It is clear from the results presented in this thesis that it is important to consider the stabilities of the iron sulfides and iron-nickel sulfides in the electrolyte media used for future CO_2 reduction applications. Water reduction was found to be a dominating competitive reaction at negative potentials under argon control atmosphere, which favoured the formation of hydroxides / oxyhydroxides on these metal sulfides. However, since water reduction was found to be halted on the introduction of CO_2, these metal sulfides are still good candidates for CO_2 reduction in aqueous solutions. Future studies should consider applying a holding potential, instead of a cyclic potential which may potentially passivate the catalytic surface due to the formation of hydroxides / oxyhydroxides.

8.5 Future Work

The in-situ spectroelectrochemistry techniques used in this thesis aided in investigating the changes occurring on the surface and bulk structure of the iron and iron-nickel sulfides studied. However, further investigation is still needed to verify the reactions occurring on these materials as the redox features were linked to a number of possible redox reactions. CO_2 adsorption on the iron and iron-nickel sulfides seemed plausible from the findings in this thesis based on the evidence for the presence of adsorbed HCO_3^- species and the variation in the redox responses on introduction of CO_2. Successful CO_2 reduction was reported on the iron sulfide greigite used in this thesis.[1] Similar CO_2 reduction experiments should be carried out using violarite to assess the impact of nickel incorporation in the iron sulfide structure on the feasibility of CO_2 reduction on violarite.

Separately, there was no evidence for the formation of H_2S or HS^- species which was expected on reduction of iron and iron-nickel sulfides at the negative electrode potentials used in this project. It may be that the amount of H_2S or HS^- species were under the detection limit of the techniques used in this project. The absence of H_2S or HS^- species further confirms that the transformations of the iron and iron-nickel sulfides are not bulk transformations, but rather, are confined to the surface of the electrode. The cell volume in the electrochemical cells could be reduced to increase the detection limit for H_2S or HS^- species.

Further characterisation by recording the in-situ XANES on the sulfur K-edge of the iron and iron-nickel sulfides should be considered under similar conditions. This would allow monitoring of the changes in the oxidation states and coordination environment of the sulfur component of the iron and iron-nickel sulfides.

Due to the differences in the electrochemical equipment between the CV and in-situ spectroscopic techniques, there was a limitation in linking the data obtained from all the techniques with regards to the reaction kinetics and thus, only qualitative analyses were detailed in this project. It may be beneficial to use a similar time scale and method of applying potentials in all of the techniques, for example performing CV instead of multi-step amperometry in the in-situ spectroelectrochemistry techniques. A slower scan rate for the CVs may reveal further thermodynamic and redox transformations which were undetected in this work. The acquisition of spectroscopic data could also be done quicker to follow the structural changes more closely, as exposure of the iron and iron-nickel sulfides to the electrolyte clearly show the formation of oxyhydroxides / hydroxides on immersion in some cases. Separately, the formation of oxyhydroxides / hydroxides on metal sulfides on exposure to air often require an additional step to purify the metal sulfide surface. The formation of aerial-oxidation products can be prevented by preparing pristine surfaces of these metal sulfide nanoparticles by performing reductive dissolution of surface phases on FeS_x in acidic solutions. Carefully de-oxygenated solutions of any specified pH can then be substituted for that acidic solution, without exposing the electrode to air. Additionally, for future quantitative analysis of CV responses, the nature of the ohmic contact of the nanoparticles on the electrode surface could be determined through impedance measurements.

The use of in-situ ATR-FTIR in this work did not detect IR bands of solid state materials which were expected to be produced, for example oxides, oxyhydroxides and carbonates. Additionally, the IR bands of electrolyte species such as phosphates dominated several IR spectra and are found within the same wavenumber region as sulfate species which are the key evidence for the

formation of oxides / oxyhydroxides on these metal sulfides. Use of electrolytes which do not possess similar IR bands with sulfates would simplify IR spectra interpretations.

The findings in this thesis highlight the importance of using multiple characterisation techniques in-situ on materials deemed catalytic. Both greigite and violarite were cited as potential catalyst for CO_2 reduction. However, both metal sulfides were found to be passivated by oxyhydroxide / oxides over time under control argon atmosphere. This transformation was halted under CO_2, however, may still pose significant setback for CO_2 reduction applications. The CO_2 reduction efficiency may drop due to formation of oxyhydroxide / oxide passivating the iron (-nickel) sulfides. The presence of nickel in an iron sulfide structure such as violarite was proposed to enhance the catalytic activity of iron sulfides. The results in this thesis show current enhancement on introduction of CO_2 on iron-nickel sulfides which suggests potential for CO_2 reduction. However, iron-nickel sulfides suffer from facile formation of hydroxides / oxyhydroxides on the surface on exposure to air, compared to iron sulfides. Another research avenue which should be explored for both iron and iron-nickel sulfides is the potential as a hydrogen evolution / water reduction catalyst.

8.6 References

1. Roldan, A. *et al.* Bio-inspired CO2 conversion by iron sulfide catalysts under sustainable conditions. *Chem. Commun.* **51,** 7501–7504 (2015).

2. Yamaguchi, A. *et al.* Electrochemical CO2 reduction by Ni-containing iron sulfides: How is CO2 electrochemically reduced at bisulfide-bearing deep-sea hydrothermal precipitates? *Electrochim. Acta* **141,** 311–318 (2014).

3. Thornber, M. R. Mineralogical and electrochemical stability of the nickel-iron sulphides-pentlandite and violarite. *J. Appl. Electrochem.* **13,** 253–267 (1983).

4. Hamilton, I. C. & Woods, R. An investigation of surface oxidation of pyrite and pyrrhotite by linear potential sweep voltammetry. *J. Electroanal. Chem. Interfacial Electrochem.* **118,** 327–343 (1981).

5. Bura-Nakic, E., Róka, A., Ciglenecki, I. & Inzelt, G. Electrochemical Quartz

Crystal Microbalance Study of FeS Particles Attached to Au Surface. *Electroanalysis* **21,** 1699–1708 (2009).

6. Di Giovanni, C. *et al.* Low-Cost Nanostructured Iron Sulfide Electrocatalysts for PEM Water Electrolysis. *ACS Catal.* **6,** 2626–2631 (2016).

7. Hunger, S. & Benning, L. G. Greigite: a true intermediate on the polysulfide pathway to pyrite. *Geochem. Trans.* **8:1,** 1–20 (2007).

8. Khan, A., Kelebek, S. & Hall, G. Electrochemical aspects of pyrrhotite and pentlandite in relation to their flotation with xanthate . Part-I: Cyclic voltammetry and rest potential measurements. *J. Appl. Electrochem.* **34,** 849–856 (2004).

9. Mikhlin, Y. Reactivity of pyrrhotite surfaces: An electrochemical study. *Phys. Chem. Chem. Phys.* **2,** 5672–5677 (2000).

10. Belzile, N., Chen, Y.-W., Cai, M.-F. & Li, Y. A review on pyrrhotite oxidation. *J. Geochemical Explor.* **84,** 65–76 (2004).

11. Mikhlin, Y. L., Kuklinskii, A. V, Pashkov, G. L. & Asanov, I. P. Pyrrhotite Electrooxidation in Acid Solutions. *Russ. J. Electrochem.* **37,** 1277–1282 (2001).

12. Ghahremaninezhad, A., Asselin, E. & Dixon, D. G. In Situ Electrochemical Analysis of Surface Layers on a Pyrrhotite Electrode in Hydrochloric Acid Solution. *J. Electrochem. Soc.* **157,** C248–C257 (2010).

13. Cruz, R., González, I. & Monroy, M. Electrochemical characterization of pyrrhotite reactivity under simulated weathering conditions. *Appl. Geochemistry* **20,** 109–121 (2005).

14. Li, Y. *et al.* Synergistic Interaction between Electricigens and Natural Pyrrhotite to Produce Active Oxygen Radicals. *Geomicrobiol. J.* **29,** 264–273 (2012).

15. Marape, G. & Vermaak, M. K. G. Fundamentals of pentlandite mineralogy and its effect on its electrochemical behaviour. *Miner. Eng.* **32,** 60–67 (2012).

16. Deng, J. *et al.* Electrochemistry of Pentlandite in the Absence and Presence of Sodium Sulfide. *Chiang Mai J. Sci.* **39,** 336–345 (2012).

Appendix 1 Synthesis of iron (-nickel) sulfides

Iron-nickel sulfide nanoparticles were synthesised via solvothermal decomposition method and characterised via XRD (X-ray Diffraction), TEM (Transmission Electron Microscopy) and HRTEM (High-Resolution Transmission Electron Microscopy) by Dr Anna Roffey and Dr Nathan Hollingsworth. Below is a brief description of the synthesis of the nanoparticles used in this work. The reader is referred to the thesis entitled *Dithiocarbamate Complexes as Single Source Precursors to Metal Sulfide Nanoparticles for Applications in Catalysis* (Roffey A, University College London, 2014) for further details on the synthesis and characterisation of the nanoparticles.

Equipment:

The main equipment consisted of a three-necked-round-bottomed flask attached to a condenser connected to a Schlenk line providing a flow of nitrogen. The flask sits in a heating mantle on a stirring plate and a temperature probe is inserted through a rubber septum into the reaction mixture. This decomposition setup is used for the synthesis of all the nanoparticles used in this thesis where the setup was kept under nitrogen atmosphere at all times.

Greigite Fe_3S_4:

In the reaction flask, $Fe(S_2CN^iBu_2)_3$ (0.1 mmol, 0.0669 g) and $(Et_2NCS_2)_2$ (0.2 mmol, 0.0593 g) precursors were dissolved in 20 mL of OA. The mixture was heated to 230°C for 1 hour. The XRD pattern of the resulting nanoparticles is shown below.

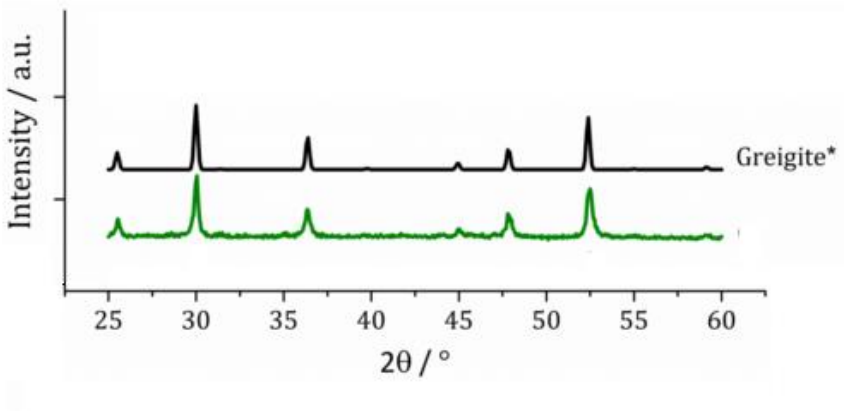

Figure A. 1 XRD patterns of synthetic greigite (green) and reference pattern for Fe_3S_4 (ICDD card No.16-0713) in black.

Violarite $FeNi_2S_4$:

In the reaction flask, $Fe(^iBu_2NCS_2)_3$ (2.5 mM) and $Ni(^iBu_2NCS_2)_2$ (2.5 mM) precursors were heated in 20 mL of OA for 1 hr at 240° C. The XRD pattern of the resulting nanoparticles is shown below.

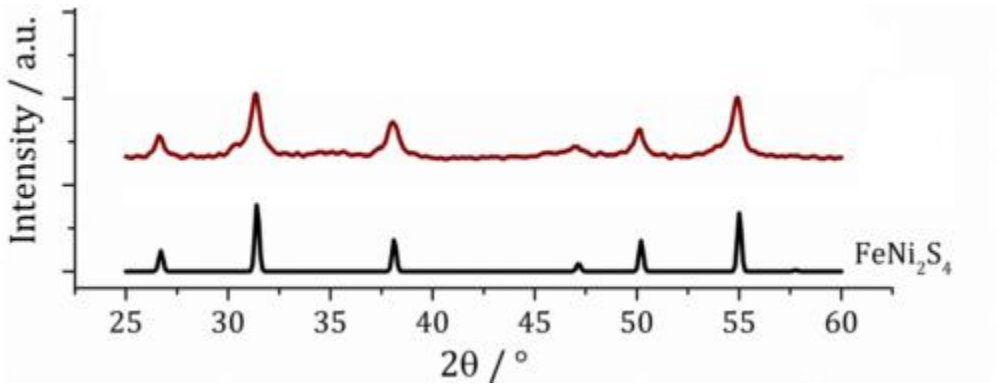

Figure A. 2 XRD patterns of synthetic violarite (brown) and reference pattern for $FeNi_2S_4$ (ICDD card No. 47-1740) in black.

Pyrrhotite Fe_7S_8:

In the reaction flask, $Fe(S_2CN^iBu_2)_3$ (5 mM) precursor was decomposed in 20 mL of OA at 230 °C for 1 hr. The XRD pattern of the resulting nanoparticles is shown below.

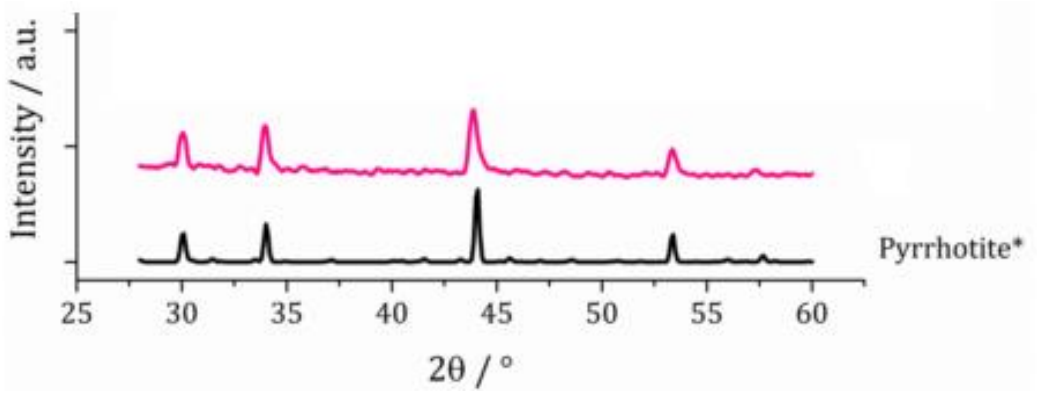

Figure A. 3 XRD patterns of synthetic pyrrhotite (pink) and reference pattern for Fe_7S_8 (ICDD card No. 29-0723) in black.

Pentlandite $(Fe,Ni)_9S_8$:

In the reaction flask, $Fe(^iBu_2NCS_2)_3$ (2.5 mM) and $Ni(^iBu_2NCS_2)_2$ (2.5 mM) precursors were heated in 20 mL of OA for 1 hr at 280° C. The XRD pattern of the resulting nanoparticles is shown below.

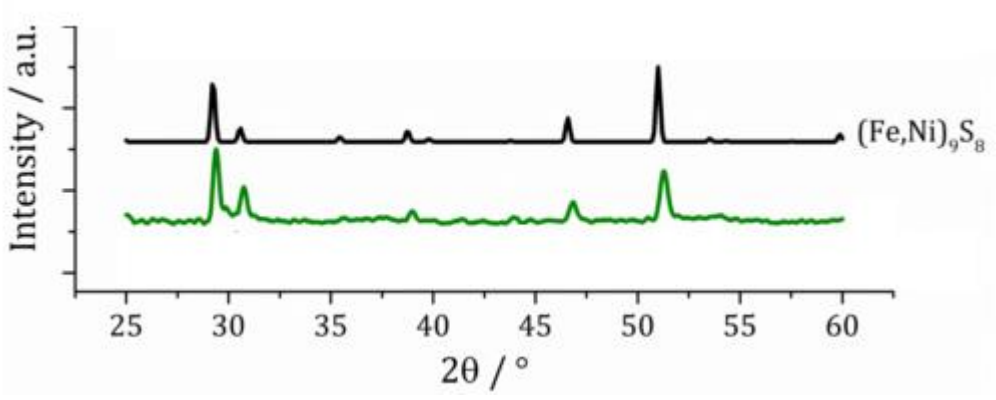

Figure A. 4 XRD patterns of synthetic pentlandite (green) and reference pattern for $(Fe,Ni)_9S_8$ (ICDD card No.75-2024) in black.

Appendix 2 Standard IR absorbance spectra for Table 4.2

The IR absorbance spectra of the following standards were recorded. Solid samples were placed directly onto the cleaned ATR prism, and the pressure handle was lowered to improve contact between the sample and prism. For liquid samples, 0.1 g of the solid samples were dissolved in 2 ml of Millipore pure water and the solution was contained within an acrylic compartment placed on the ATR prism.

The following preparation were carried out for each spectrum:

$S_2O_3^{2-}$(aq): 0.1 g of $Na_2S_2O_3$(s) dissolved in 2 ml of Millipore pure water.
SO_4^{2-}(aq): 0.1 g of $Na_2SO_4.10H_2O$(s) dissolved in 2 ml of Millipore pure water.
SO_3^{2-}(aq): 0.1 g of Na_2SO_3 (s) dissolved in 2 ml of Millipore pure water.
Na_2SO_3(s), $Na_2S_2O_3$(s) and $Na_2SO_4.10H_2O$(s): 0.02 g of the sample was placed directly onto the cleaned ATR prism
OA in PBS pH 4, pH 7, $KHCO_3$ pH8, K_2CO_3 pH 11: 1µ l of OA was drop-coated onto the ATR prism and 2 ml of electrolyte was layered above the coating
$FeSO_4.7H_2O$(s), $FePO_4.4H_2O$(s), Fe(II.III) oxide(s): 0.02 g of the sample was placed directly onto the cleaned ATR prism

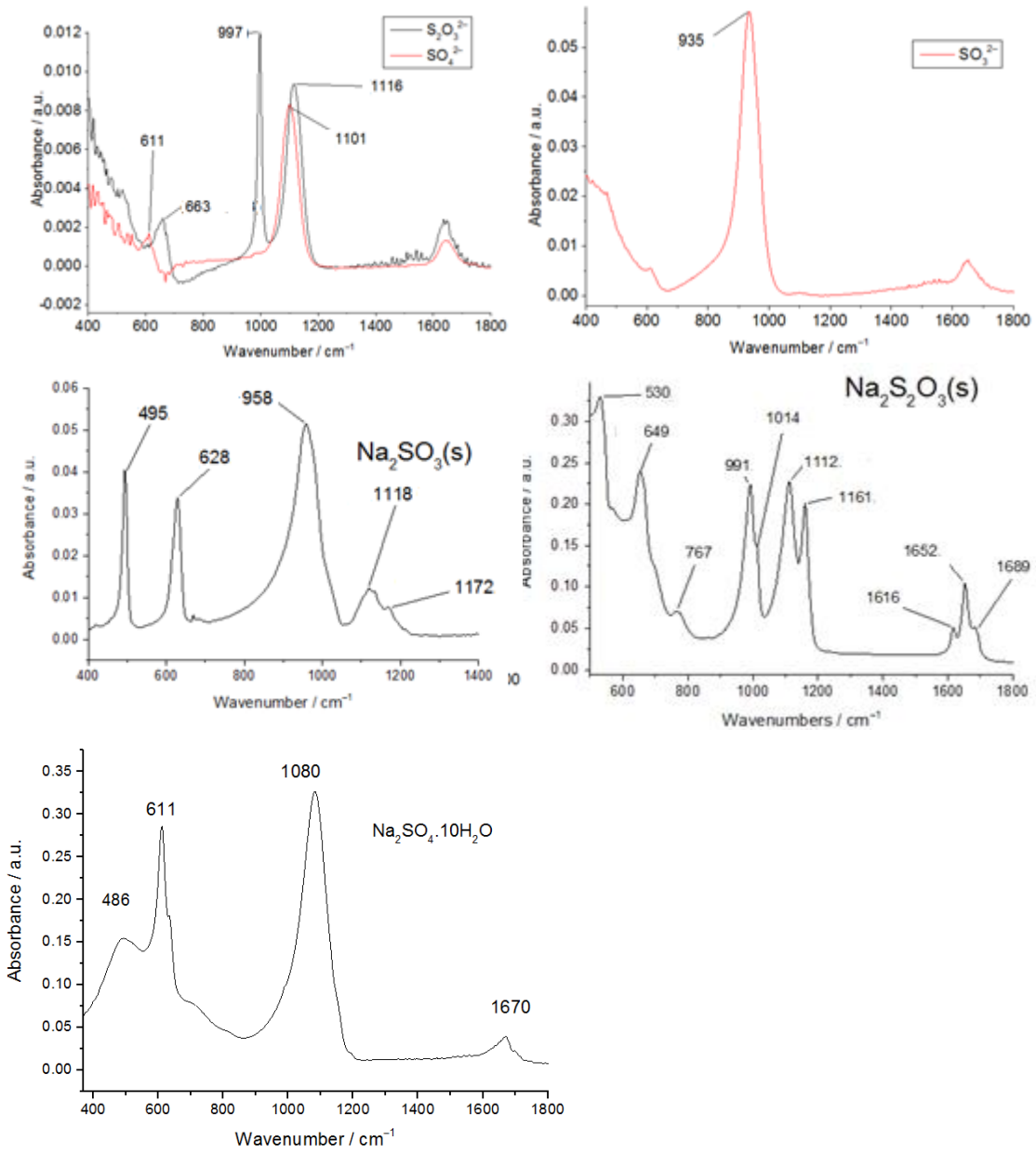

Figure A.5 FTIR absorbance spectra of $S_2O_3^{2-}$, SO_4^{2-}, SO_3^{2-}, Na_2SO_3, $Na_2S_2O_3$ and $Na_2SO_4.10H_2O$.

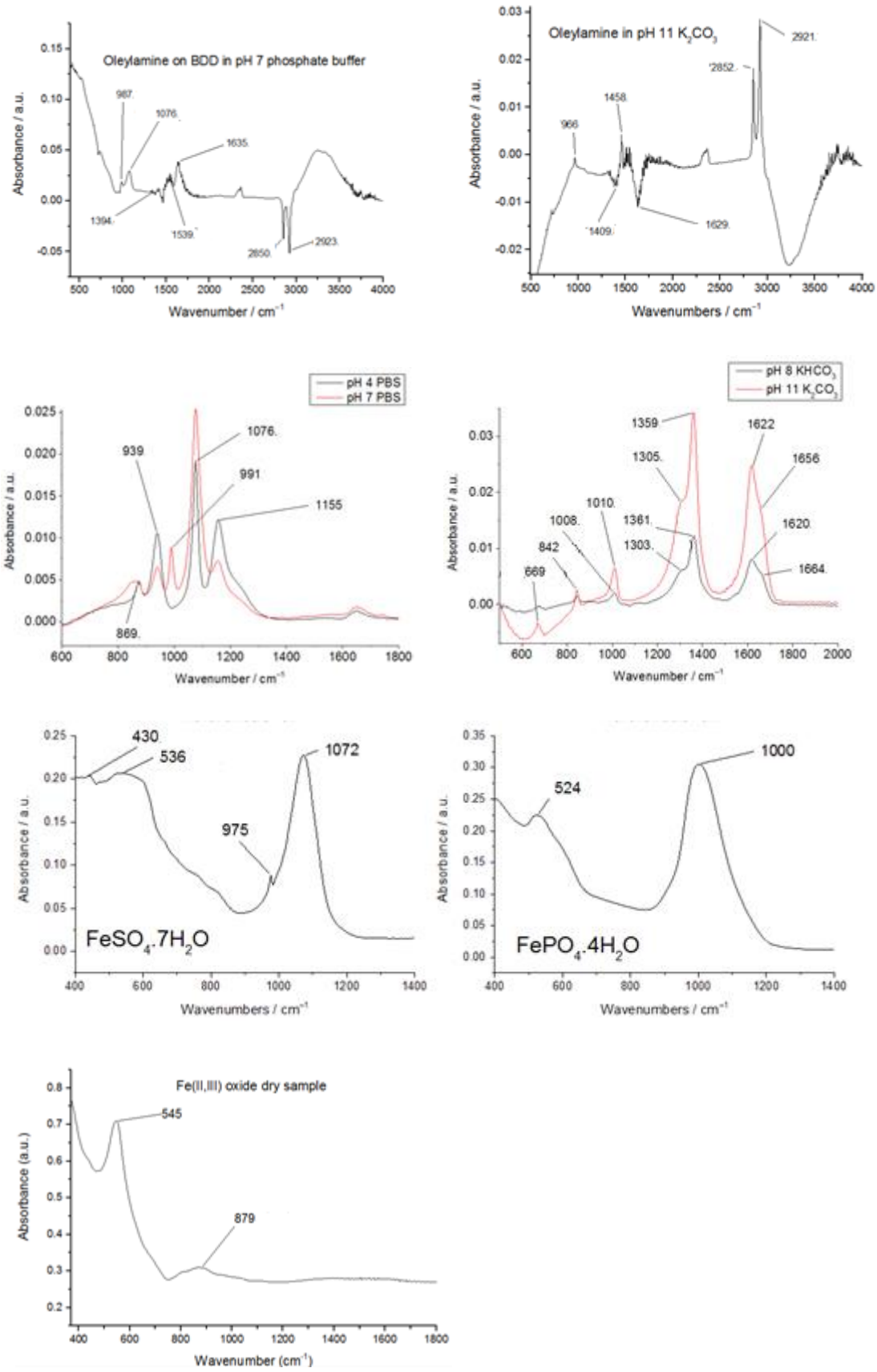

Figure A.6 FTIR absorbance spectra of OA in PBS pH 4, pH 7, $KHCO_3$ pH8, K_2CO_3 pH 11, $FeSO_4.7H_2O$, $FePO_4.4H_2O$, Fe(II.III) oxide.

Appendix 3 Reproducibility of CVs

Greigite

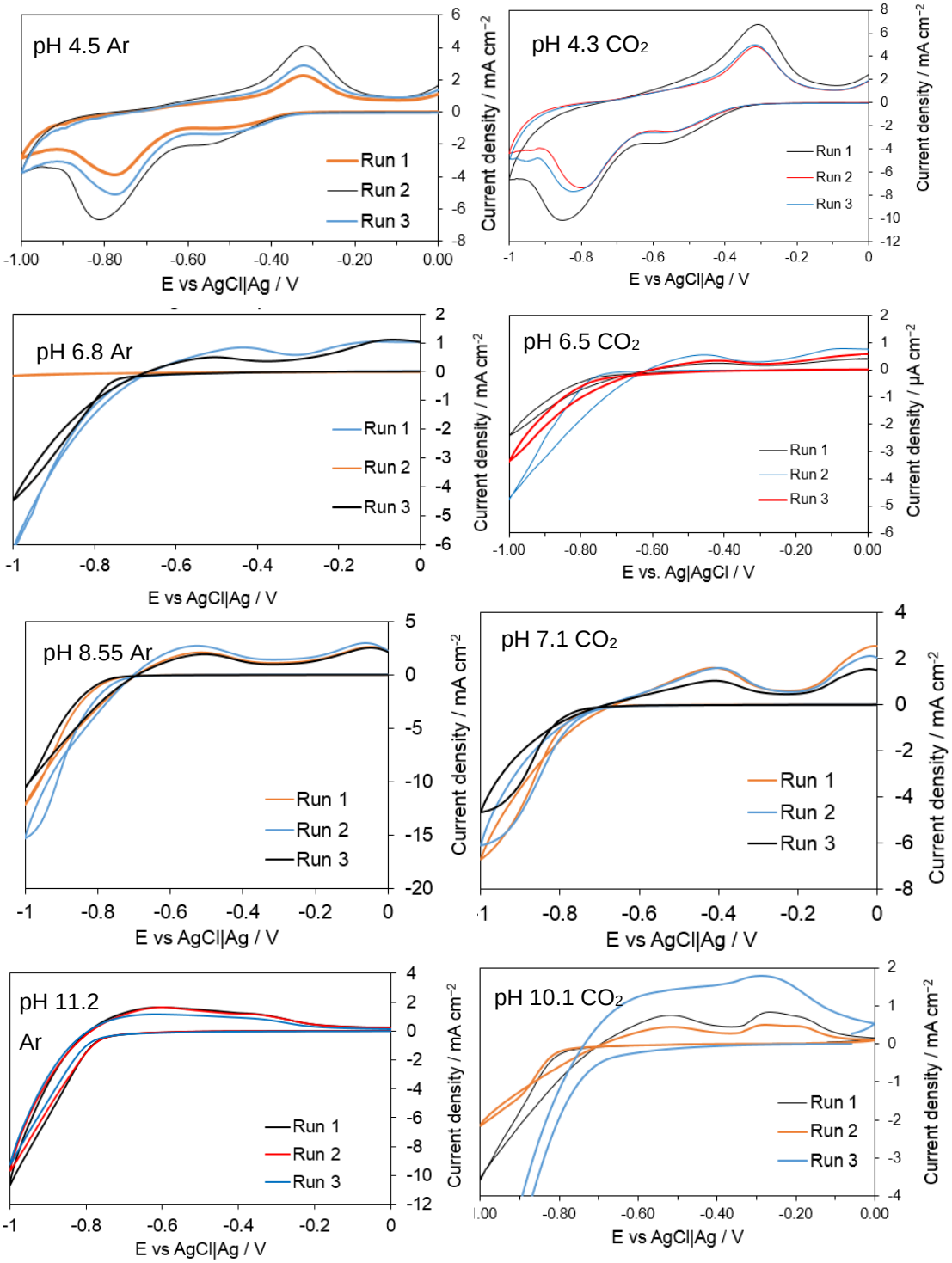

FIgure A. 7 First CV scan of greigite repeated three times in PBS pH 4.5, PBS pH 6.8, $KHCO_3$ pH 8.55 and K_2CO_3 pH 11.2, under both argon and CO_2.

Violarite

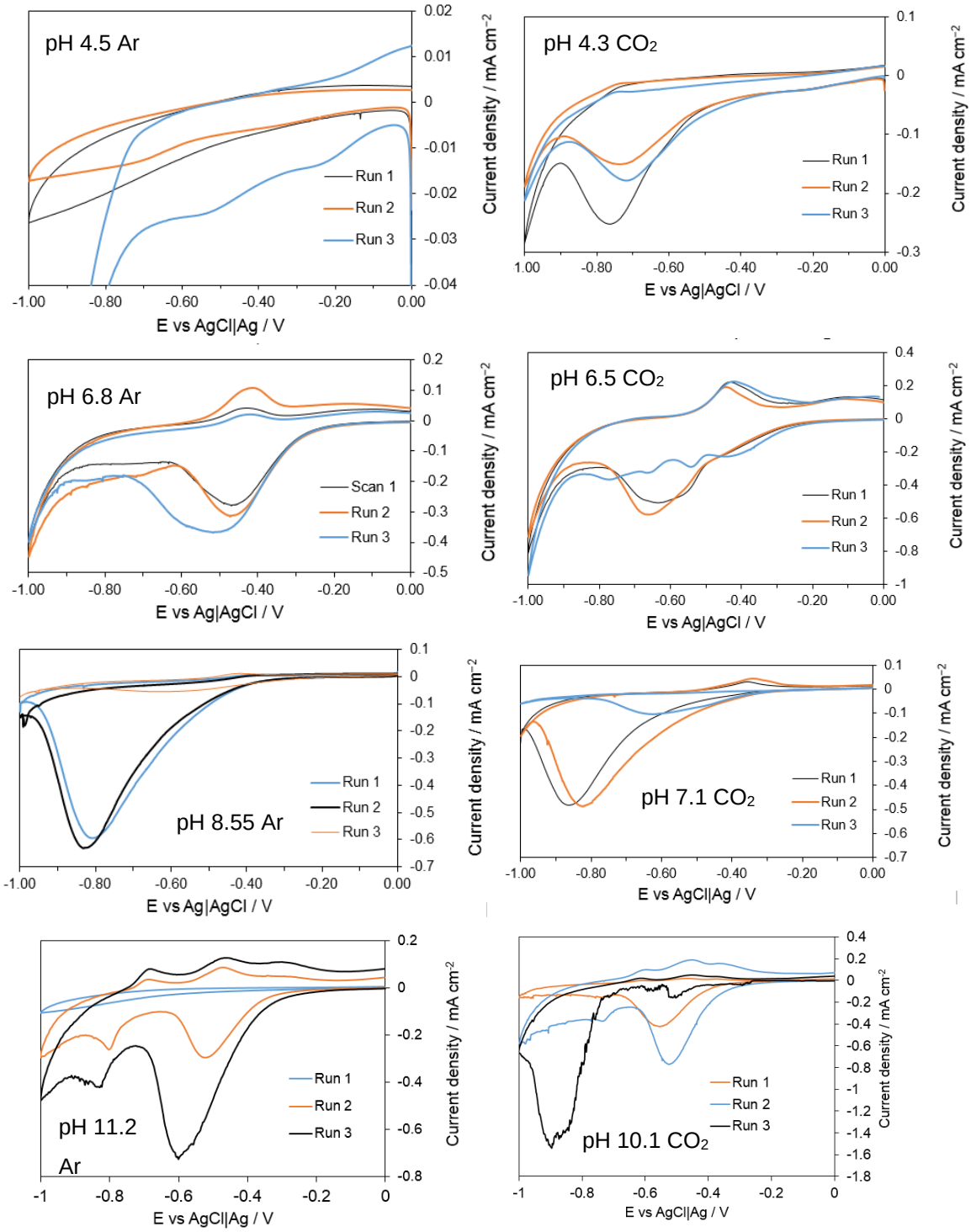

FIgure A. 8 First CV scan of violarite repeated three times in PBS pH 4.5, PBS pH 6.8, $KHCO_3$ pH 8.55 and K_2CO_3 pH 11.2, under both argon and CO_2.

Pyrrhotite

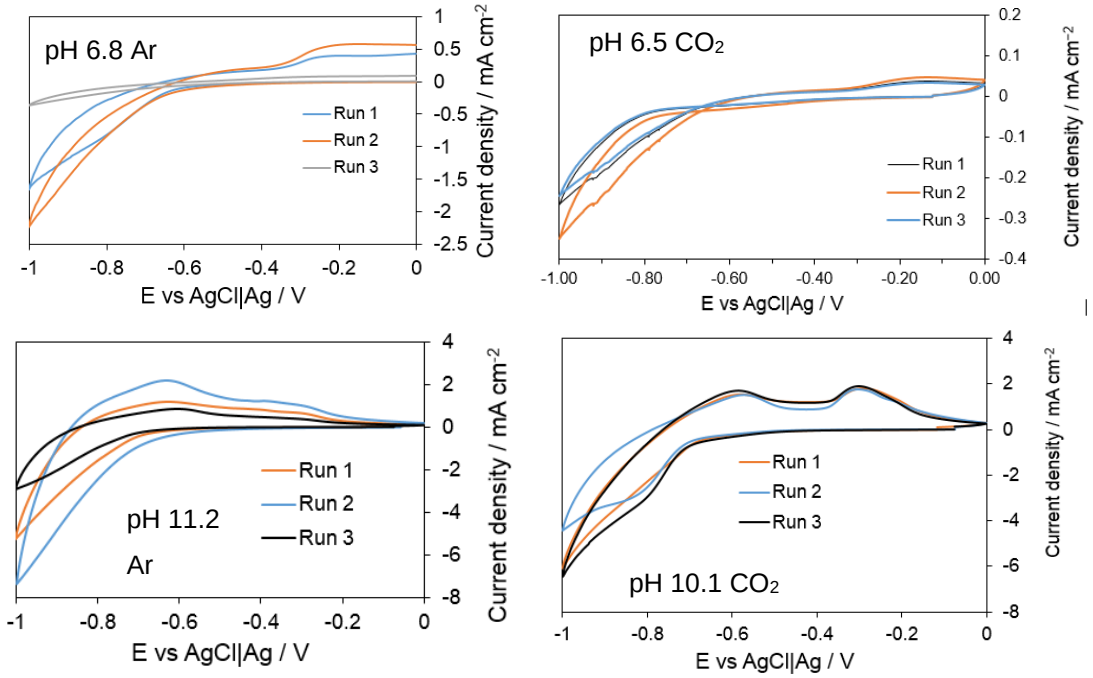

FIgure A. 9 First CV scan of pyrrhotite repeated three times in PBS pH 6.8 and K_2CO_3 pH 11.2, under both argon and CO_2.

Pentlandite

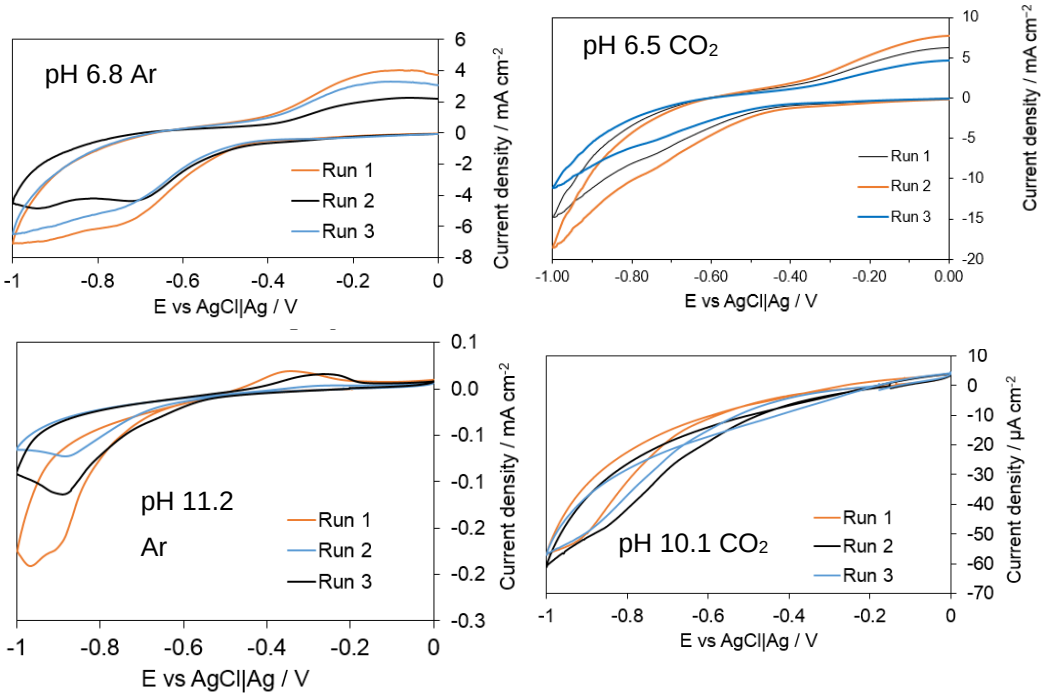

FIgure A. 10 First CV scan of pentlandite repeated three times in PBS pH 6.8 and K_2CO_3 pH 11.2, under both argon and CO_2.

Appendix 4 XAS of iron and sulfur standards

XAS of standard samples used to analyse XAS of iron (-nickel) sulfides were published in thesis of Dr Husn-Ubayda Islam titled "Formation and Electrocatalysis Studies of Nickel and Iron Sulfide Catalysts using in-situ XAS" University College London 2016.

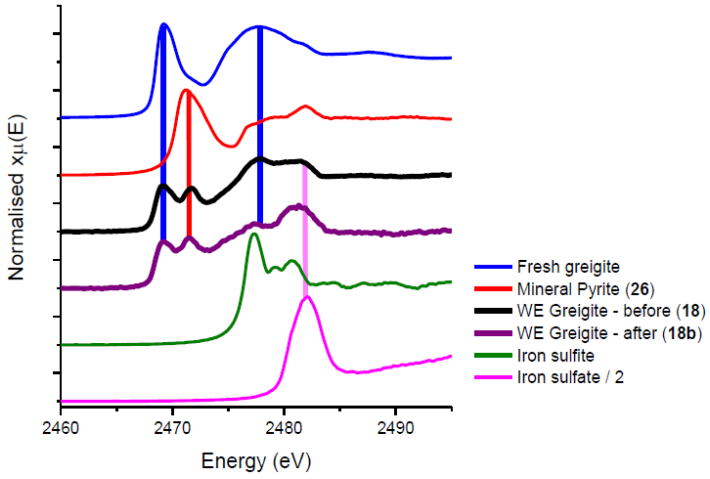

Figure A.11 XANES of iron standards used.

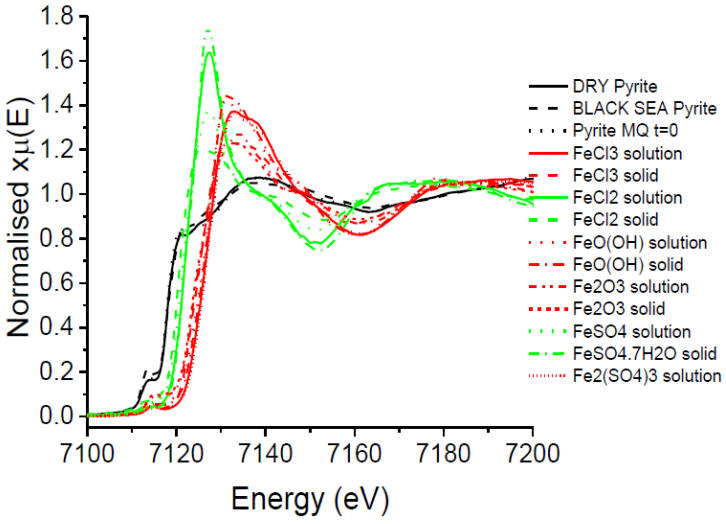

Figure A.12 XANES of iron standards used

Appendix 5 In-situ XAS spectra of greigite on Fe K-edge in pH 4 under Ar and CO_2, pH 7 under Ar and CO_2, pH 11 under Ar.

In-situ XAS spectra of greigite on Fe K-edge were performed by two students, one of whom is the author of this thesis. The data were published in thesis of Dr Husn-Ubayda Islam titled "Formation and Electrocatalysis Studies of Nickel and Iron Sulfide Catalysts using in-situ XAS" University College London 2016.

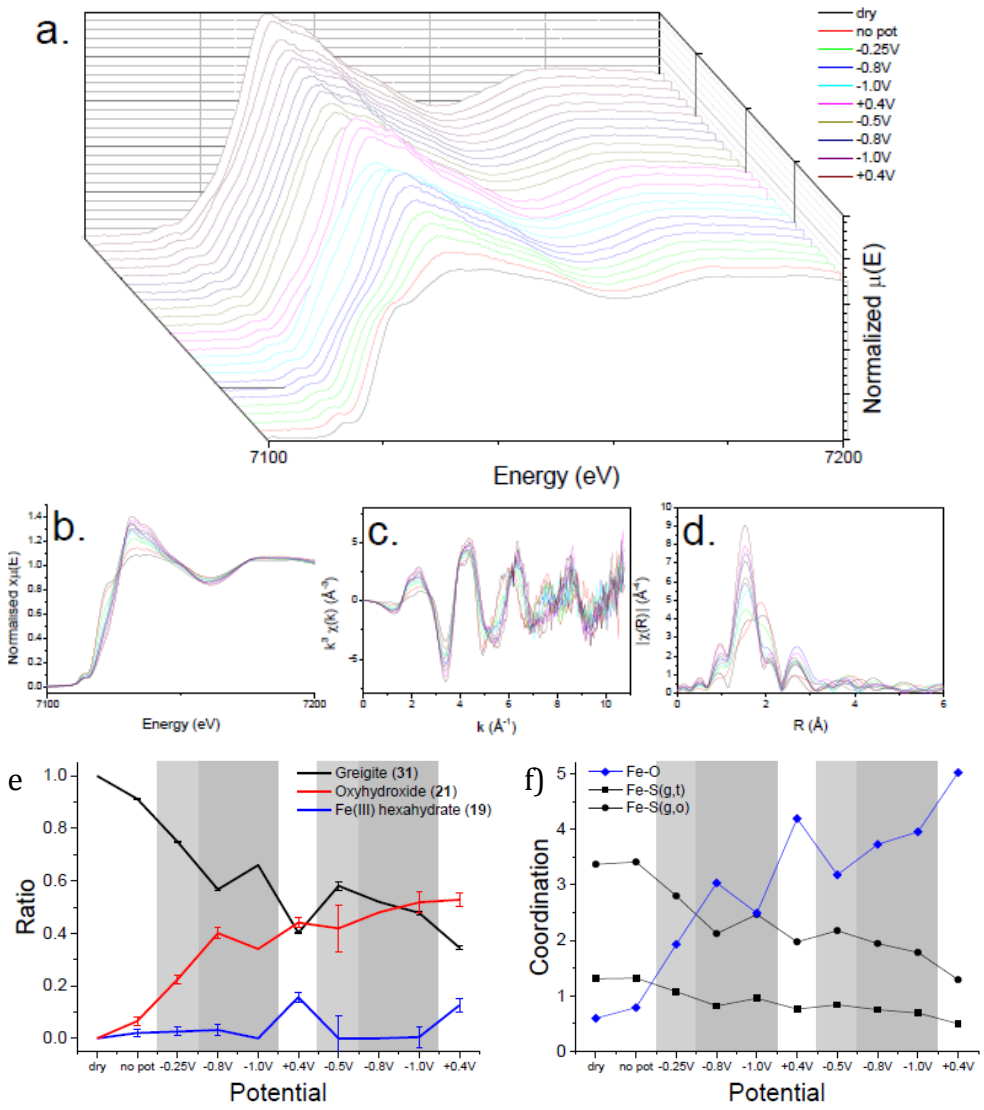

Figure A.13 In-situ XAS data on Fe K-edge of greigite in pH 4 under Ar a. in situ XANES spectra during two CV loops of carbon loaded greigite in a pH 4.5 buffer solution bubbled with N_2, and merged b. XANES spectra, c. EXAFS, d. Fourier Transform (FT) at each potential in the loop, e) Linear combination fitting and f) coordination numbers derived from EXAFS modelling of carbon loaded greigite in a pH 4.5 buffer solution bubbled with N_2 at each potential in the loop.

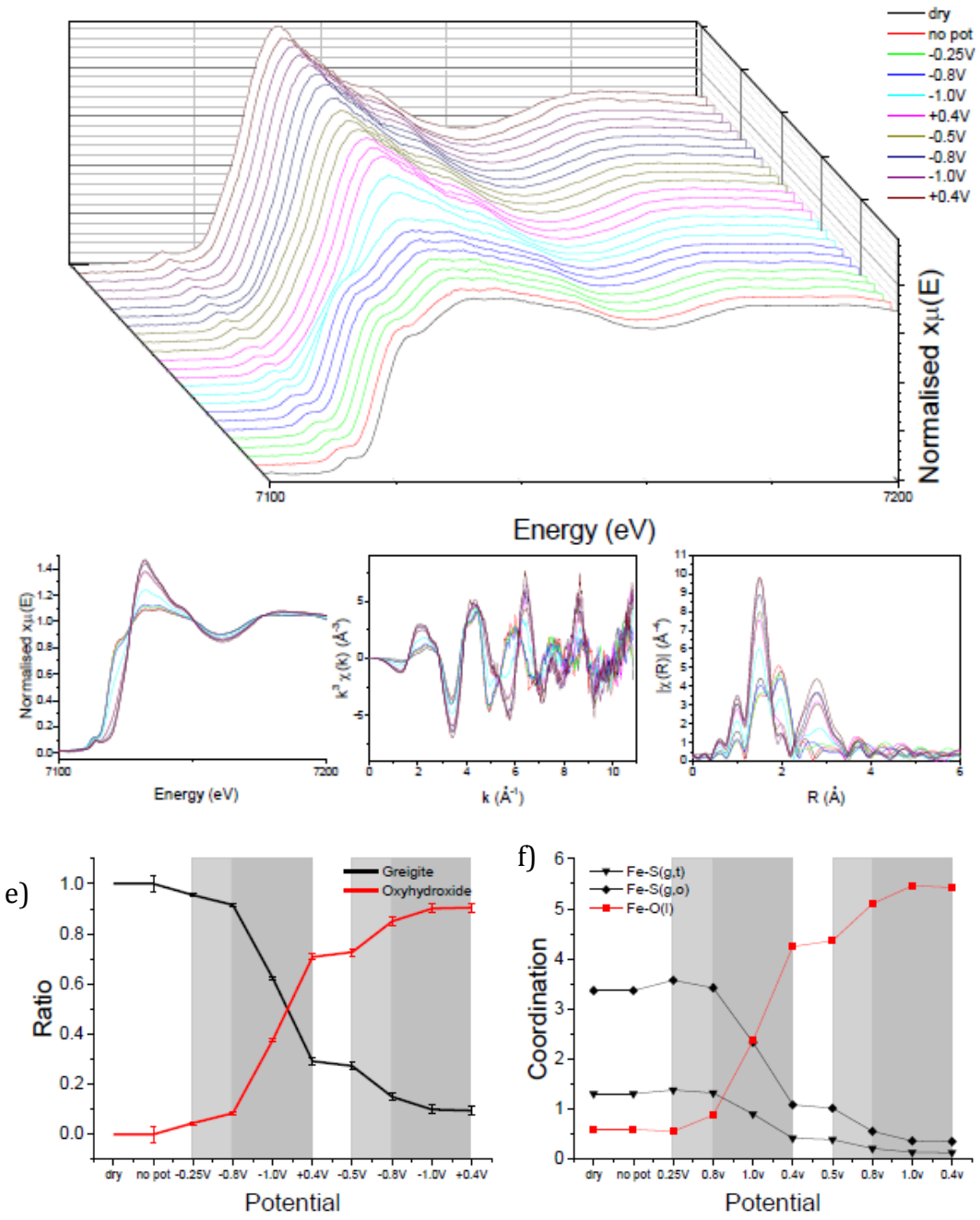

Figure A.14 In-situ XAS data on Fe K-edge of greigite in pH 4 under CO_2 a. in situ XANES spectra during two CV loops of carbon loaded greigite in a pH 4.5 buffer solution bubbled with CO_2, and merged b. XANES spectra, c. EXAFS, d. FT at each potential in the loop, e) Linear combination fitting and f) coordination numbers derived from EXAFS modelling of carbon loaded greigite in a pH 4.5 buffer solution bubbled with CO_2 at each potential in the loop.

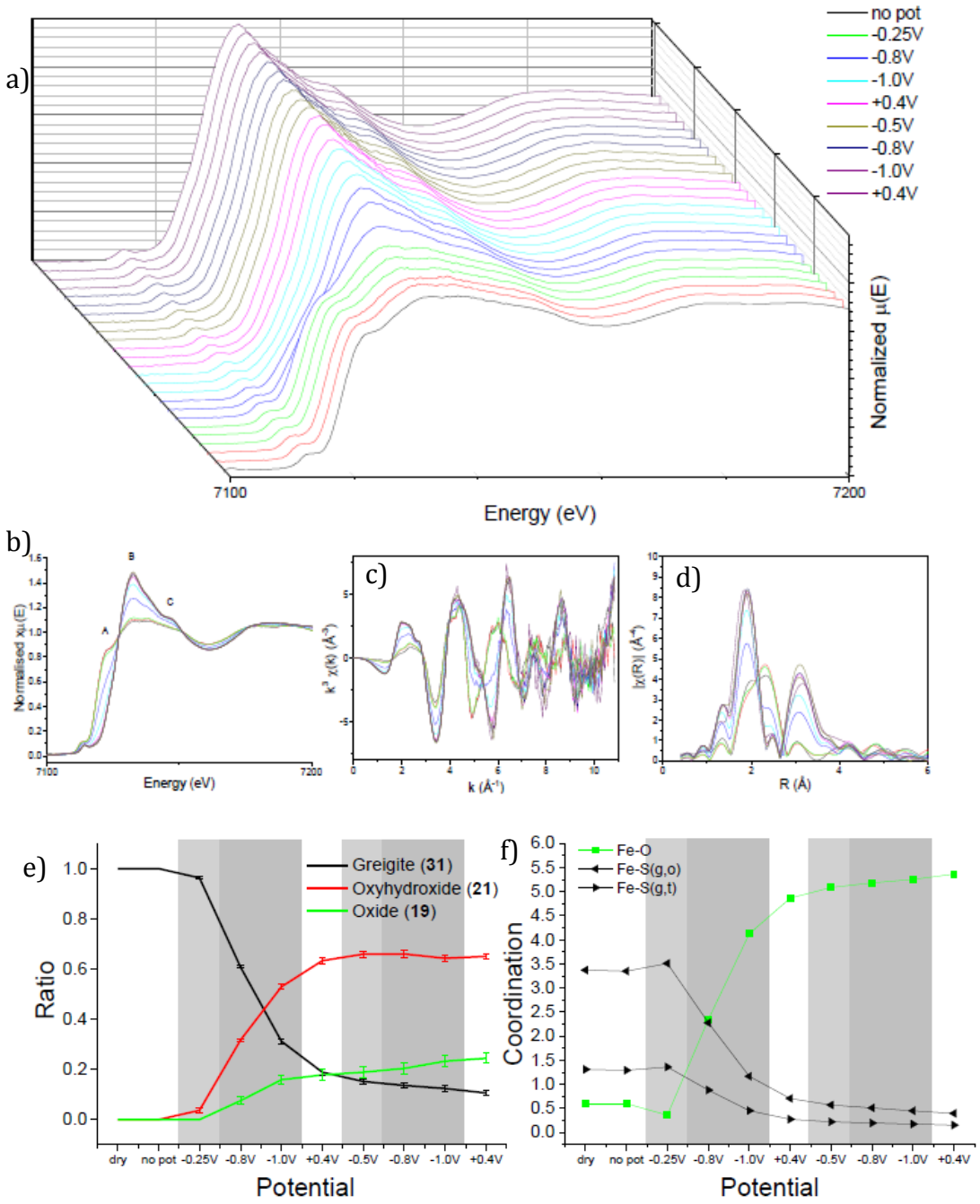

Figure A. 15 In-situ XAS data on Fe K-edge of greigite in pH 7 under N_2: a. in situ XANES spectra during two CV loops of carbon loaded greigite in a pH 7 buffer solution bubbled with N_2, and merged b. XANES spectra, c. EXAFS, d. FT at each potential in the loop, e) Linear combination fitting and f) coordination numbers derived from EXAFS modelling of carbon loaded greigite in a pH 7 buffer solution bubbled with N_2 at each potential in the loop.

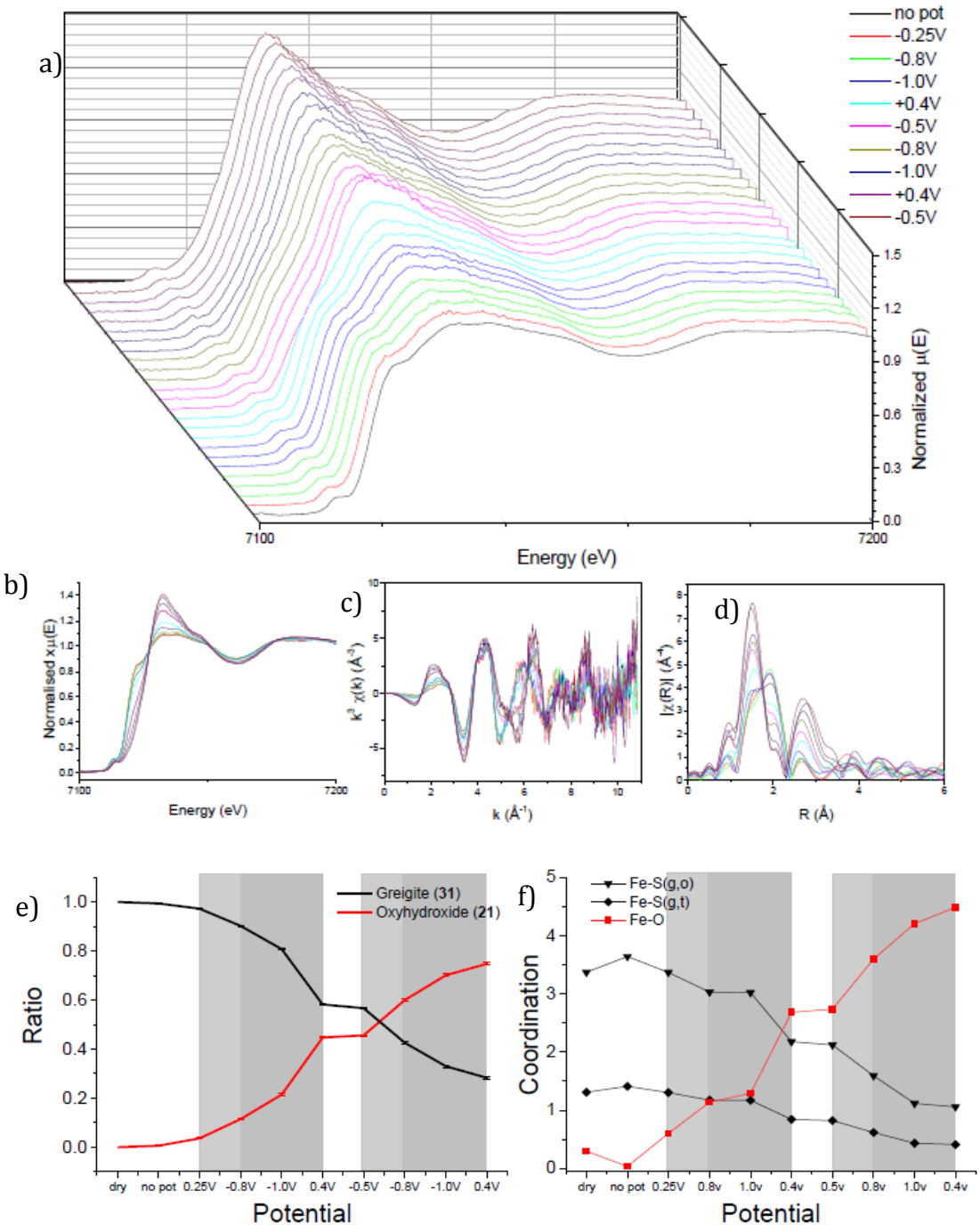

Figure A.16 In-situ XAS data on Fe K-edge of greigite in pH 7 under CO_2: a. in situ XANES spectra during two CV loops of carbon loaded greigite in a pH 7 buffer solution bubbled with CO_2, and merged b. XANES spectra, c. EXAFS, d. FT at each potential in the loop, e) Linear combination fitting and f) coordination numbers derived from EXAFS modelling of carbon loaded greigite in a pH 7 buffer solution bubbled with CO_2 at each potential in the loop.

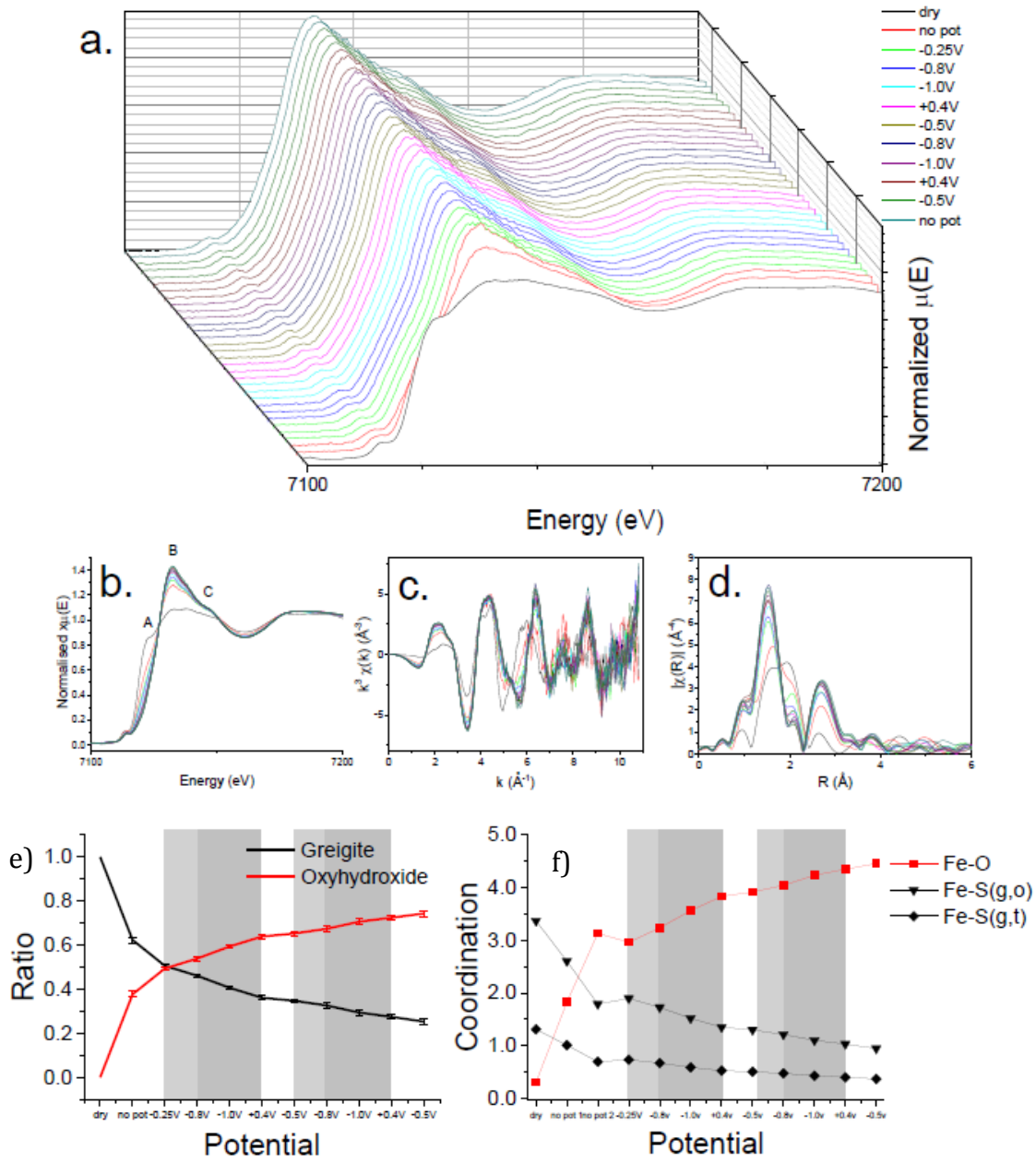

Figure A.17 In-situ XAS data on Fe K-edge of greigite in pH 11 under N_2: a. in situ XANES spectra during two CV loops of carbon loaded greigite in a pH 11 K_2CO_3 solution bubbled with N_2, and merged b. XANES spectra, c. EXAFS, d. FT at each potential in the loop, e) Linear combination fitting and f) coordination numbers derived from EXAFS modelling of carbon loaded greigite in a pH 11 K_2CO_3 bubbled with N_2 at each potential in the loop.

Appendix 6 In-situ XAS spectra of violarite on Fe K-edge and Ni K-edge pH 7 under Ar.

In-situ XAS spectra of violarite on Fe and Ni K-edge were performed by two students, one of whom is the author of this thesis. The data were published in thesis of Dr Husn-Ubayda Islam titled "Formation and Electrocatalysis Studies of Nickel and Iron Sulfide Catalysts using in-situ XAS" University College London 2016.

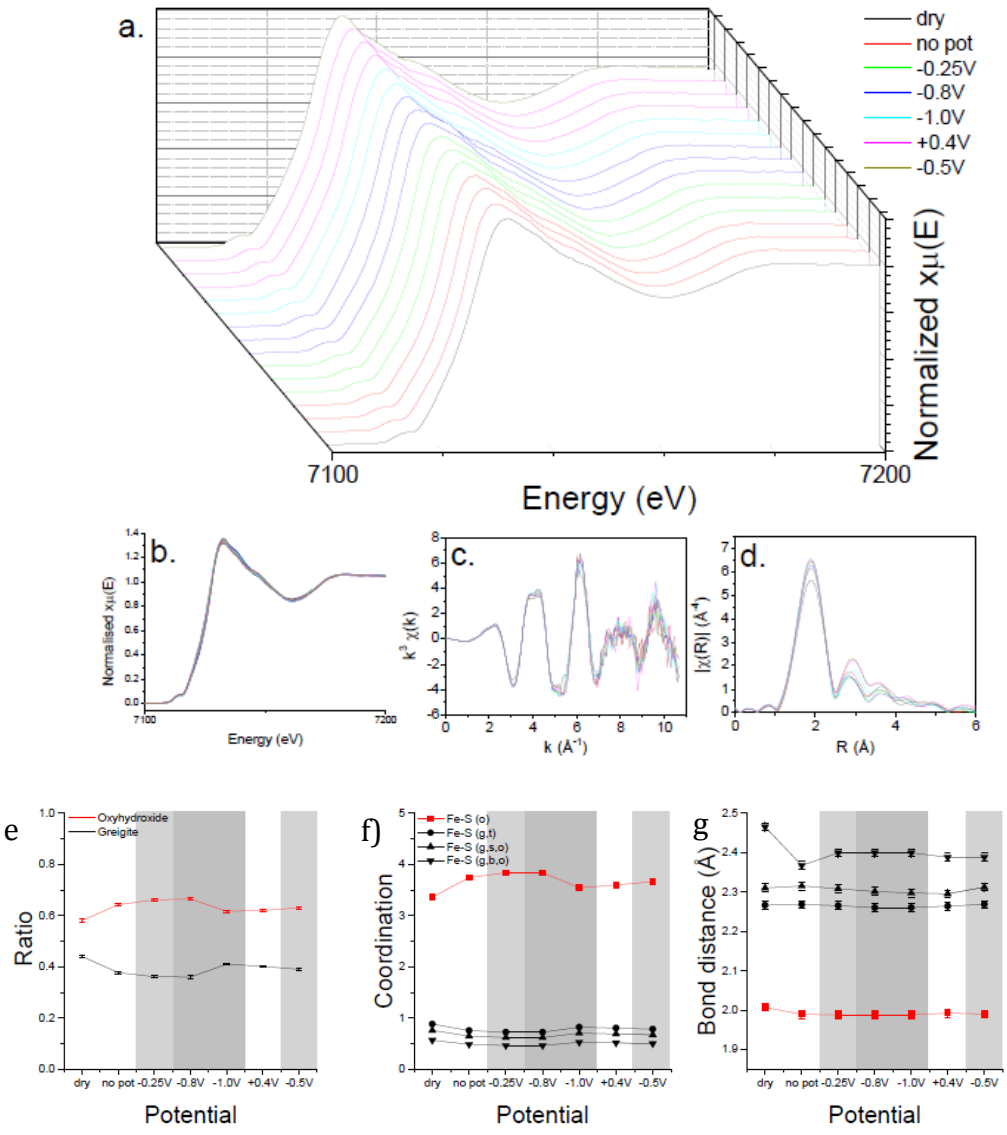

Figure A. 18 In-situ XAS data on Fe K-edge of violarite in pH 7 under: a. in situ XANES spectra during CV of violarite in a pH 7 phosphate buffer solution bubbled with N_2, and merged b. XANES spectra, c. EXAFS, d. FT at each potential in the CV, e) Linear combination fitting, f) coordination numbers and g) bond distances derived from EXAFS modelling on Fe K-edge of violarite in a pH 7 bubbled with N_2 at each potential in the loop.

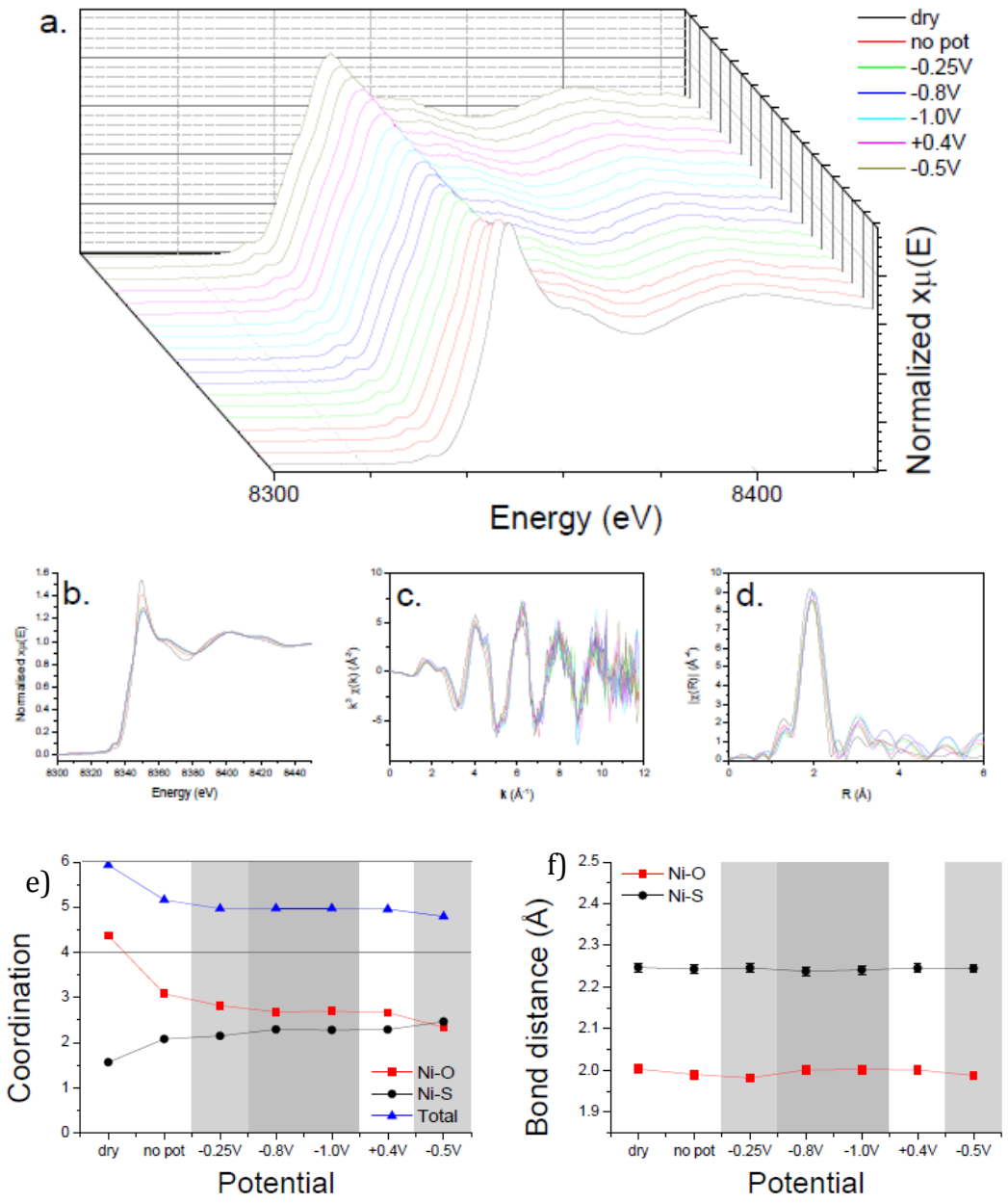

Figure A. 19 In-situ XAS data on Ni K-edge of violarite in pH 7 under: a. in situ XANES spectra during CV of violarite in a pH 7 phosphate buffer solution bubbled with N_2, and merged b. XANES spectra, c. EXAFS, d. FT at each potential in the CV, e) Coordination numbers and f) bond distances derived from EXAFS modelling of violarite on Ni K-edge in a pH 7 bubbled with N_2 at each potential in the loop.

Appendix 7 Thermodynamics calculations of FeS_2/CO_2 coupled reactions

$$FeS_2 + H^+ + 2e^- \rightleftarrows FeS + H_2S$$

$$E_{FeS_2/FeS}\ (\mathrm{SHE})\ /\ \mathrm{V} = -0.1938 - 0.0592\,pH - 0.0296\log(H_2S)$$

$$\mathrm{E} = -0.5780 \ @\ \mathrm{pH}\ 7$$

$$CO_2(g) + 8H^+ + 8e^- \rightleftarrows CH_4 + 2H_2O$$

$$E_{CO_2/CH_4}(\mathrm{SHE})\ /\ \mathrm{V} = 0.1694 - 0.0592\,pH + 0.0074\log p_{CO_2} - 0.0074\log p_{CH_4}$$

$$\mathrm{E} = -0.2447 \ @\ \mathrm{pH}\ 7$$

$$CO_2(g) + H^+ + 2e^- \rightleftarrows HCOO^-$$

$$E_{CO2/HCO_2^-}(\mathrm{SHE})\ /\ \mathrm{V} = -0.2248 - 0.0296\,pH + 0.0296\log p_{CO_2} - 0.0296\log(HCOO^-)$$

$$\mathrm{E} = -0.4319 \ @\ \mathrm{pH}\ 7$$

$$2H^+ + 2e^- \rightleftarrows H_2$$

$$\mathrm{E} = -0.4141 \ @\ \mathrm{pH}\ 7$$

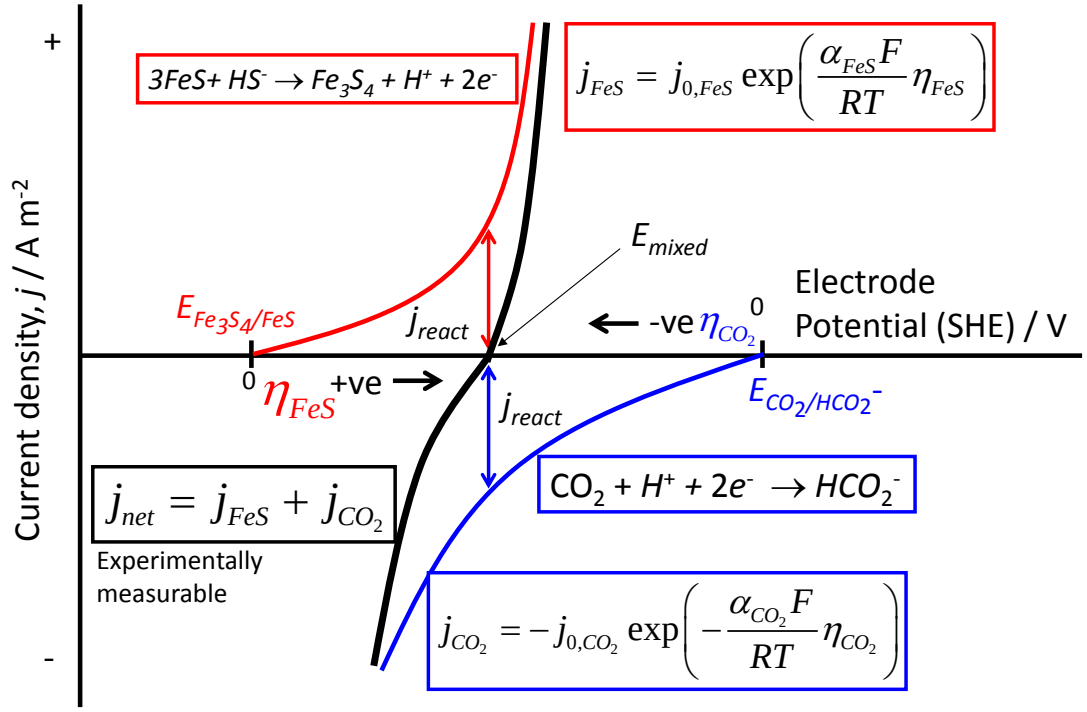

Figure A. 20 Calculated thermodynamic constraints of spontaneous coupled reaction of FeS/CO_2. The blue line shows the potential range for CO_2/HCO_2^-, the red line shows the potential range for Fe_3S_4/FeS and the black line shows the resulting mixed potential range for the coupling of FeS/CO_2.

Appendix 8 OCP (Open circuit potential) measurements of greigite

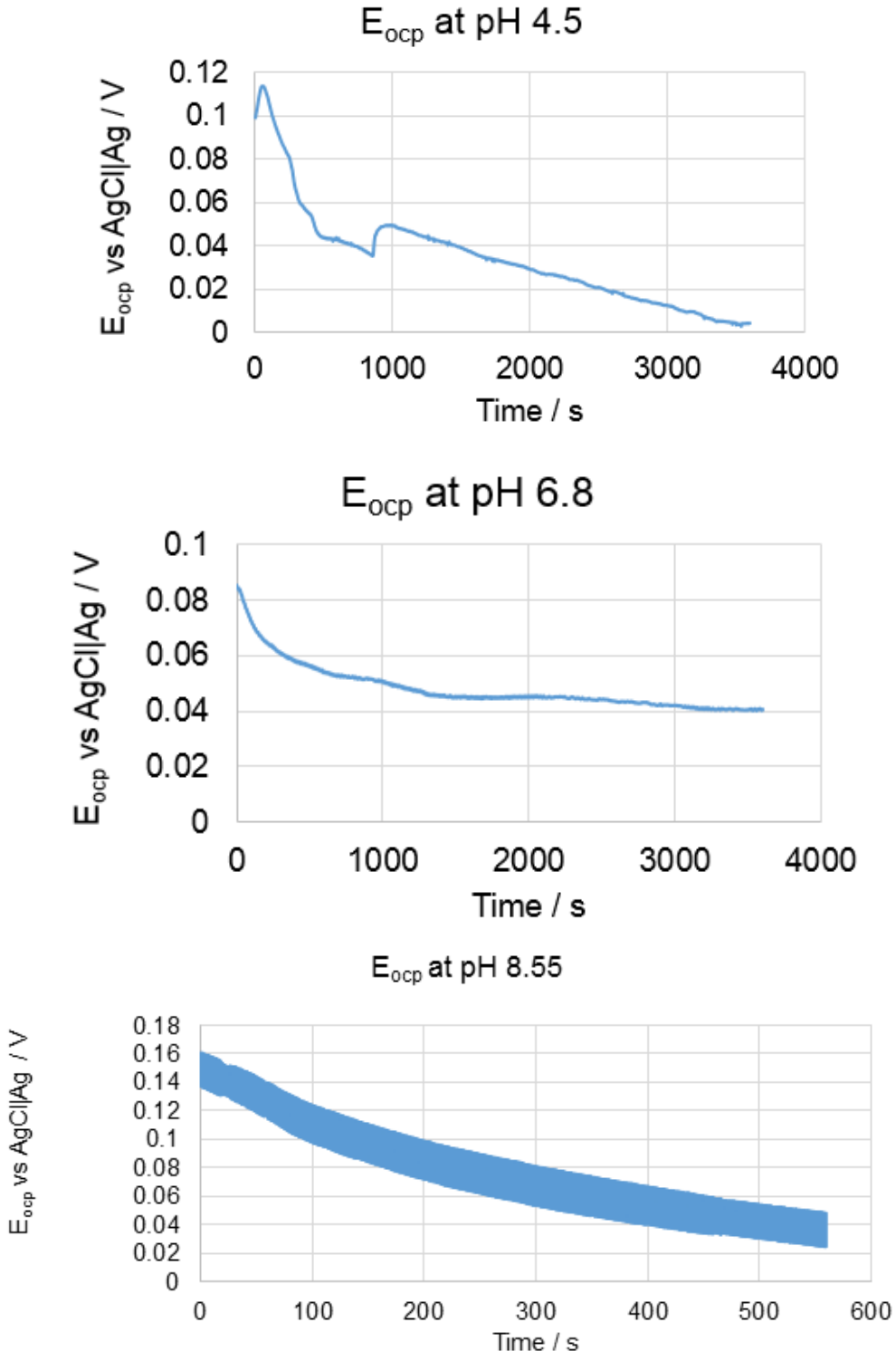

Figure A. 21 OCP measurements of greigite electrode in PBS pH 4.5, PBS pH 6.8 and $KHCO_3$ pH 8.55 under argon.

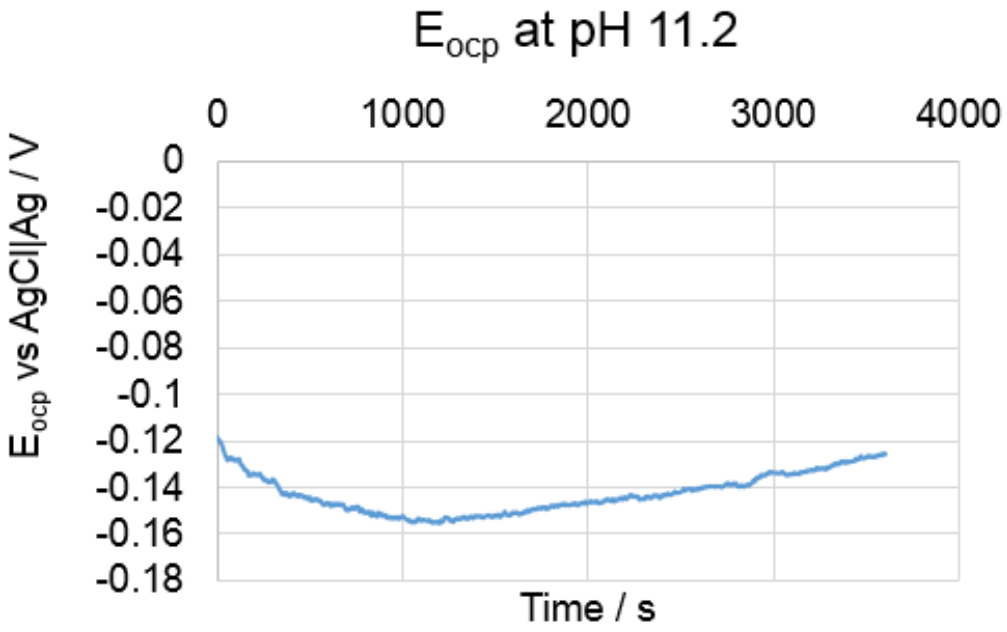

Figure A. 22 OCP measurements of greigite electrode in K_2CO_3 pH 11.2 under argon.

Figures A.21 and A.22 show the OCP measurements of greigite recorded in PBS pH 4.5, 6.8, $KHCO_3$ pH 8.1 and K_2CO_3 pH 11.2. The open circuit potential values of greigite recorded above are within the stability region as shown in the Pourbaix diagram in Figure 3.2 for an Fe-H_2S-H_2O system. The consensus with the Pourbaix diagram in Figure 3.2 suggest that the greigite electrode was stable.

However, on comparison with the Pourbaix diagram in Figure 3.3 for an Fe-S-H_2O system, these open circuit potential values are well above the stability region of greigite. The higher than predicted value of the OCP measurements falls within the stability region for iron oxides in Figure 3.3. However, the XAS measurements clearly showed that greigite was stable on immersion into the electrolyte with no applied electrode potential. These values may instead represent a floating potential of carbon electrodes as the oleylamine coating on the nanoparticles may have prevented sufficient contact between the greigite and the underlying electrode for the potential to be defined by that redox couple.

Appendix 9 Reproducibility of FTIR spectra

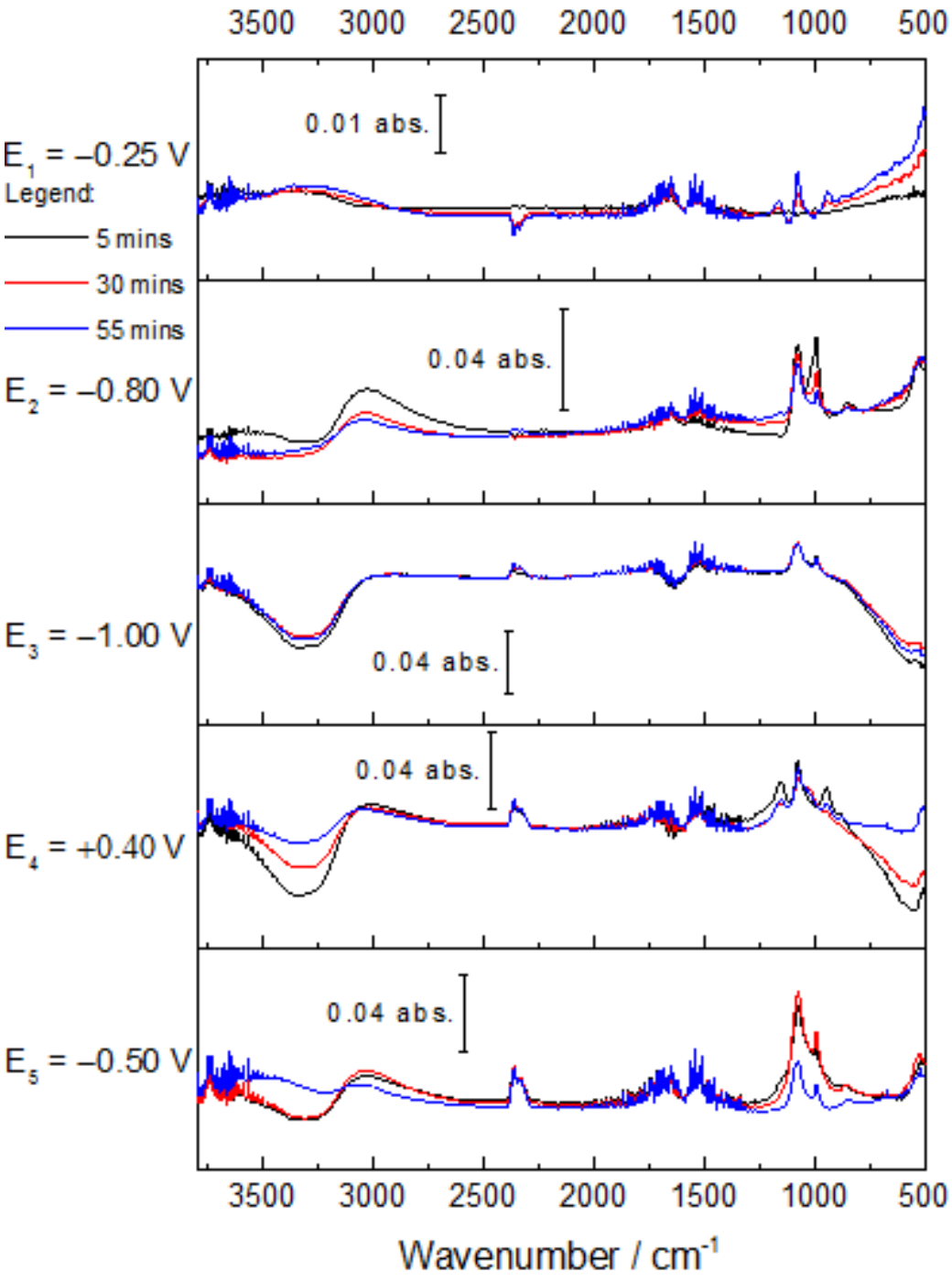

Figure A. 23 First repeat measurement of in-situ FTIR spectra of greigite in phosphate buffer solution pH 4.5 under argon, recorded on applying potentials of −0.25, −0.80, −1.00, + 0.40 and −0.50 V for one hour each step. Spectra displayed at each potential step were recorded at 5, 30 and 55 mins into holding the potential.

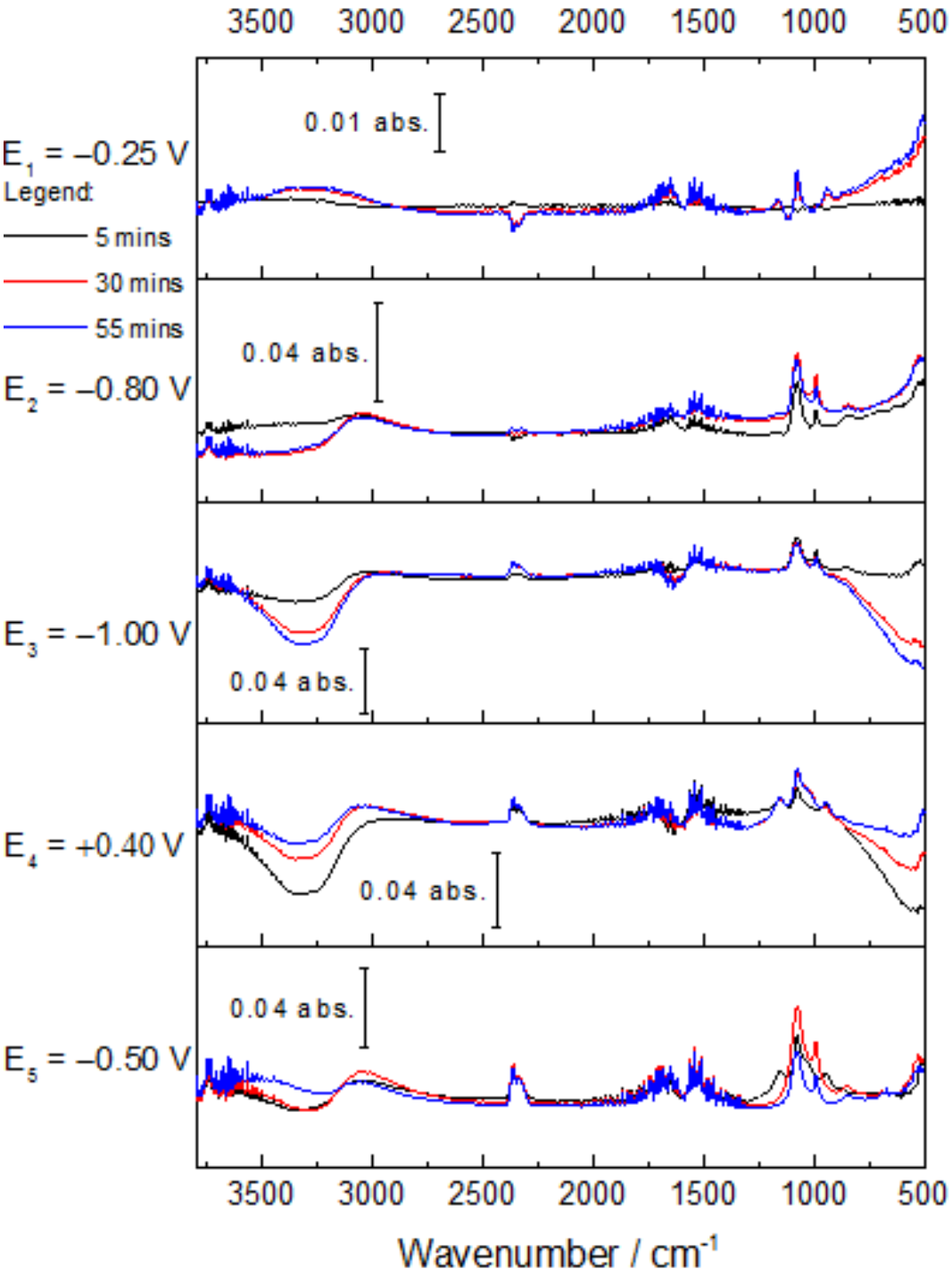

Figure A. 24 Second repeat measurement of in-situ FTIR spectra of greigite in phosphate buffer solution pH 4.5 under argon, recorded on applying potentials of −0.25, −0.80, −1.00, + 0.40 and −0.50 V for one hour each step. Spectra displayed at each potential step were recorded at 5, 30 and 55 mins into holding the potential.

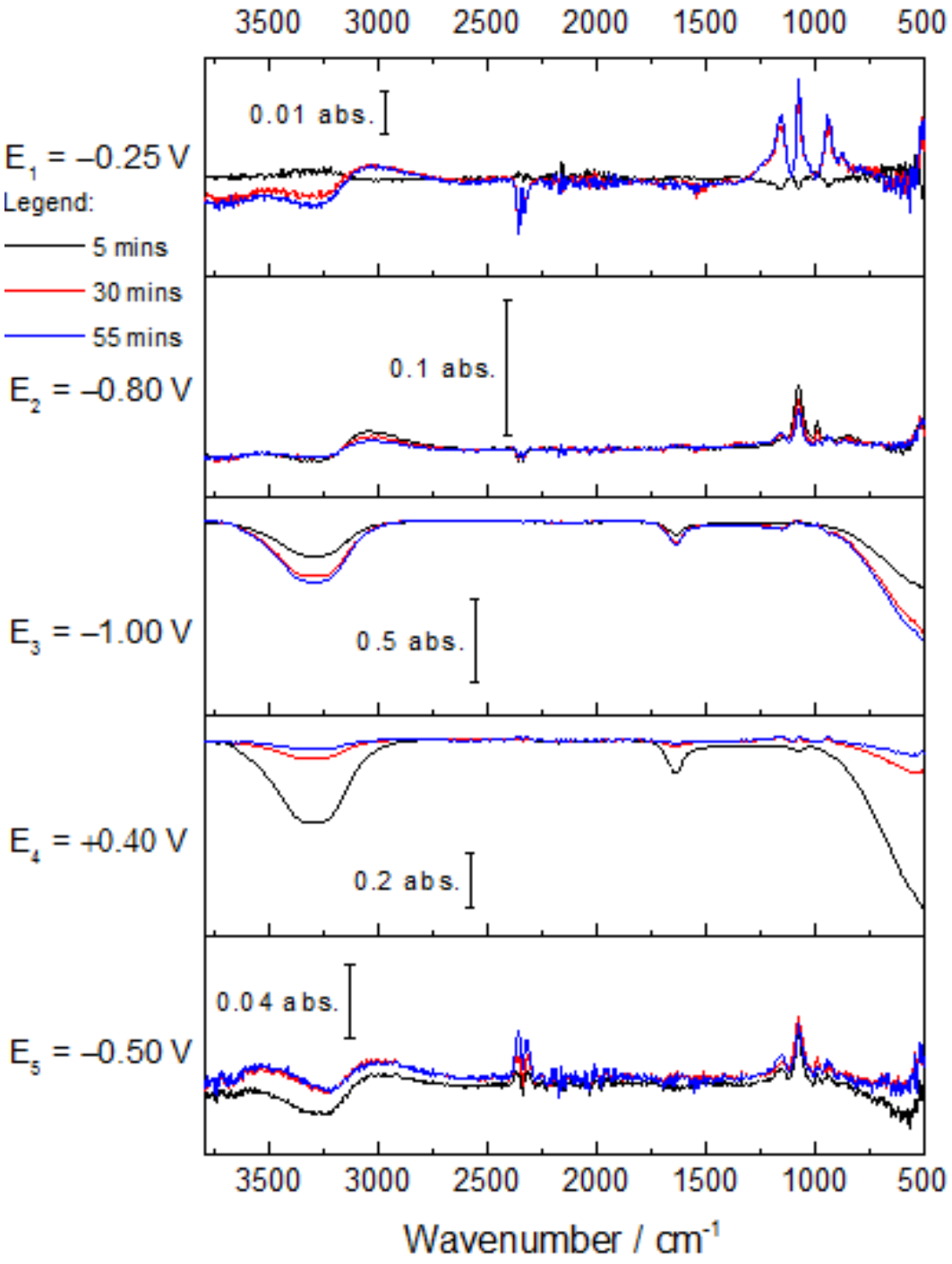

Figure A. 25 First repeat measurement of in-situ FTIR spectra of greigite in phosphate buffer solution pH 4.3 under CO_2, recorded on applying potentials of −0.25, −0.80, −1.00, + 0.40 and −0.50 V for one hour each step. Spectra displayed at each potential step were recorded at 5, 30 and 55 mins into holding the potential.

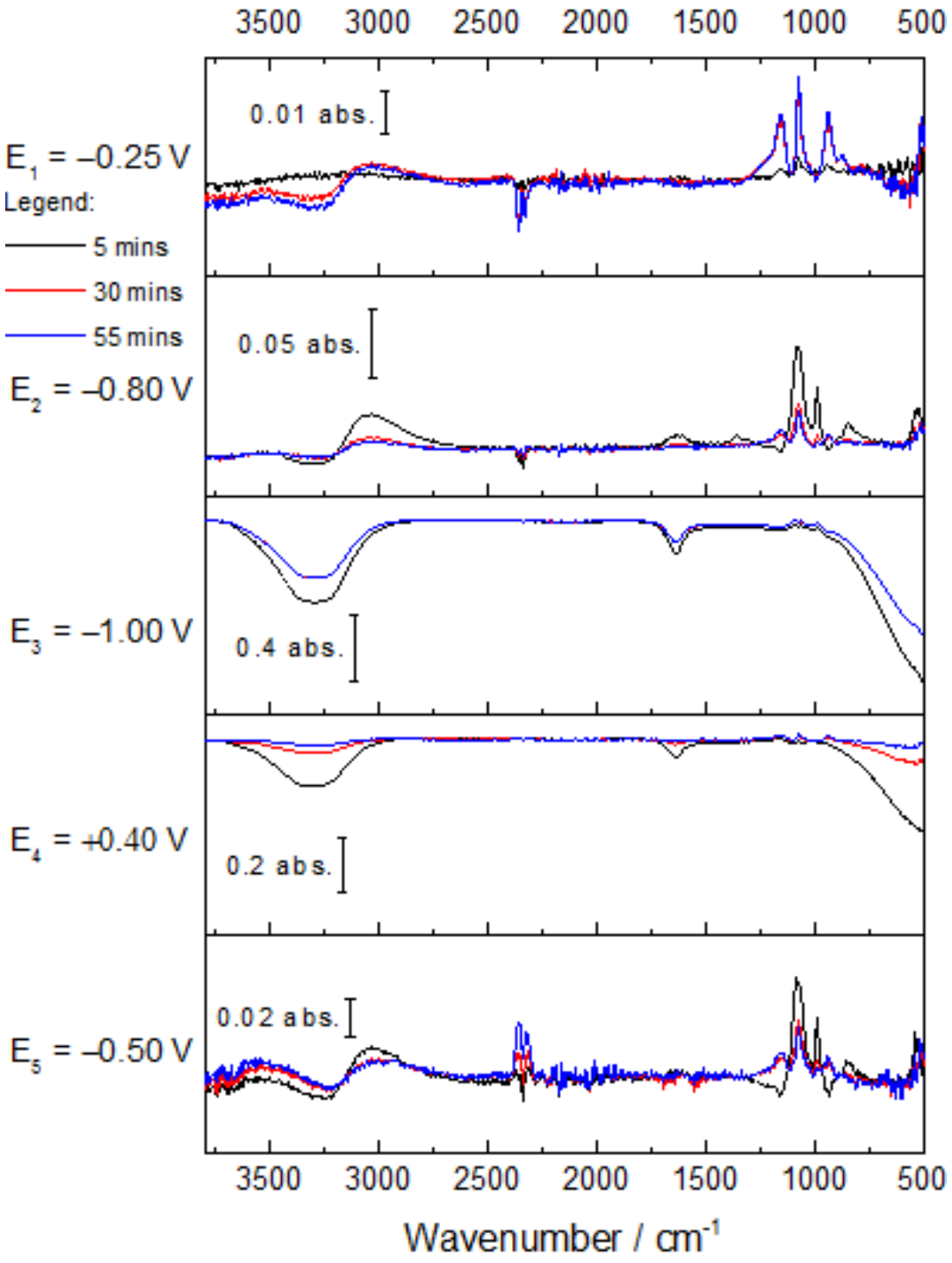

Figure A. 26 Second repeat measurement of in-situ FTIR spectra of greigite in phosphate buffer solution pH 4.3 under CO_2, recorded on applying potentials of −0.25, −0.80, −1.00, + 0.40 and −0.50 V for one hour each step. Spectra displayed at each potential step were recorded at 5, 30 and 55 mins into holding the potential.

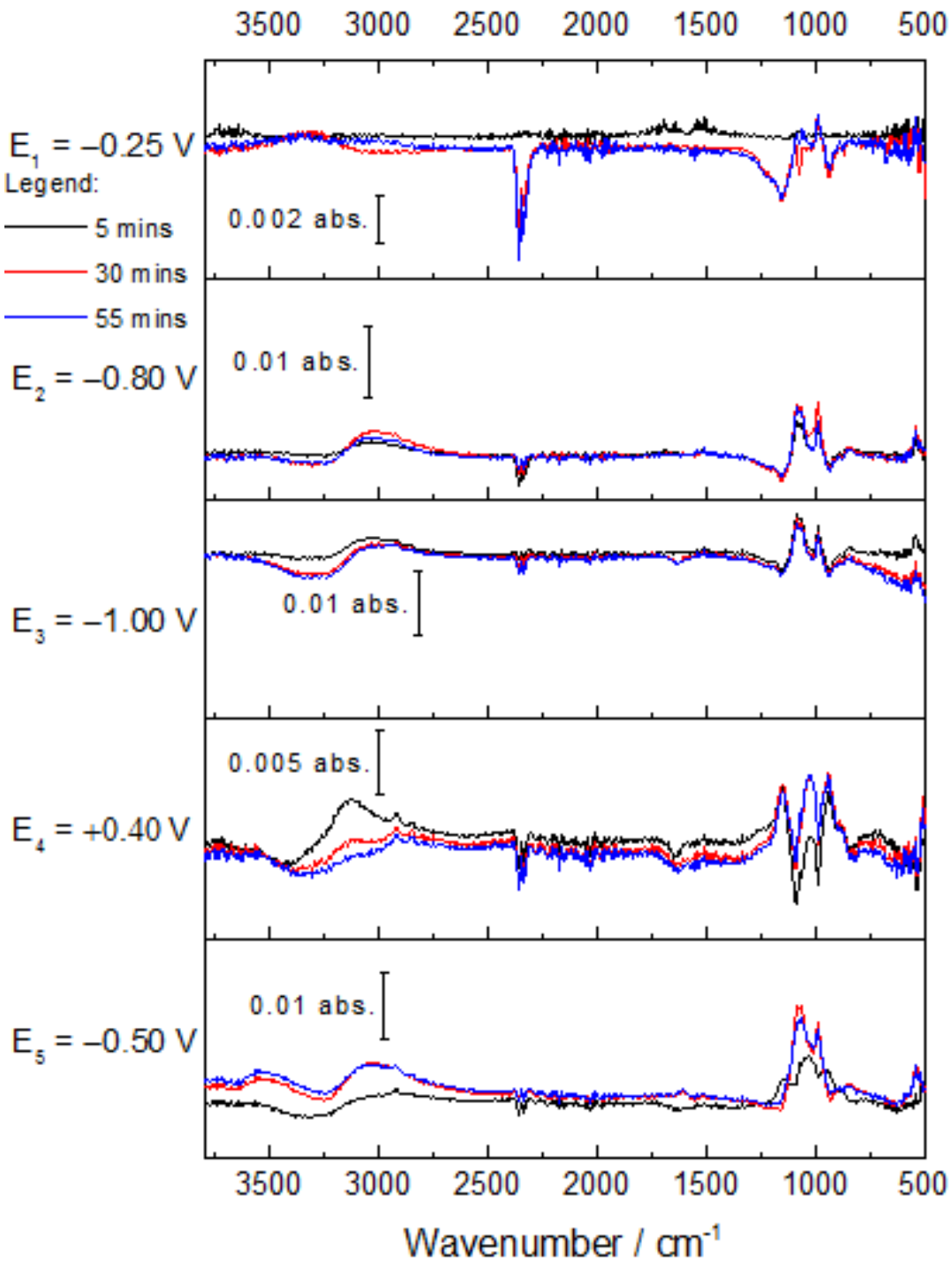

Figure A. 27 First repeat measurement of in-situ FTIR spectra of greigite in phosphate buffer solution pH 6.8 under argon, recorded on applying potentials of −0.25, −0.80, −1.00, + 0.40 and −0.50 V for one hour each step. Spectra displayed at each potential step were recorded at 5, 30 and 55 mins into holding the potential.

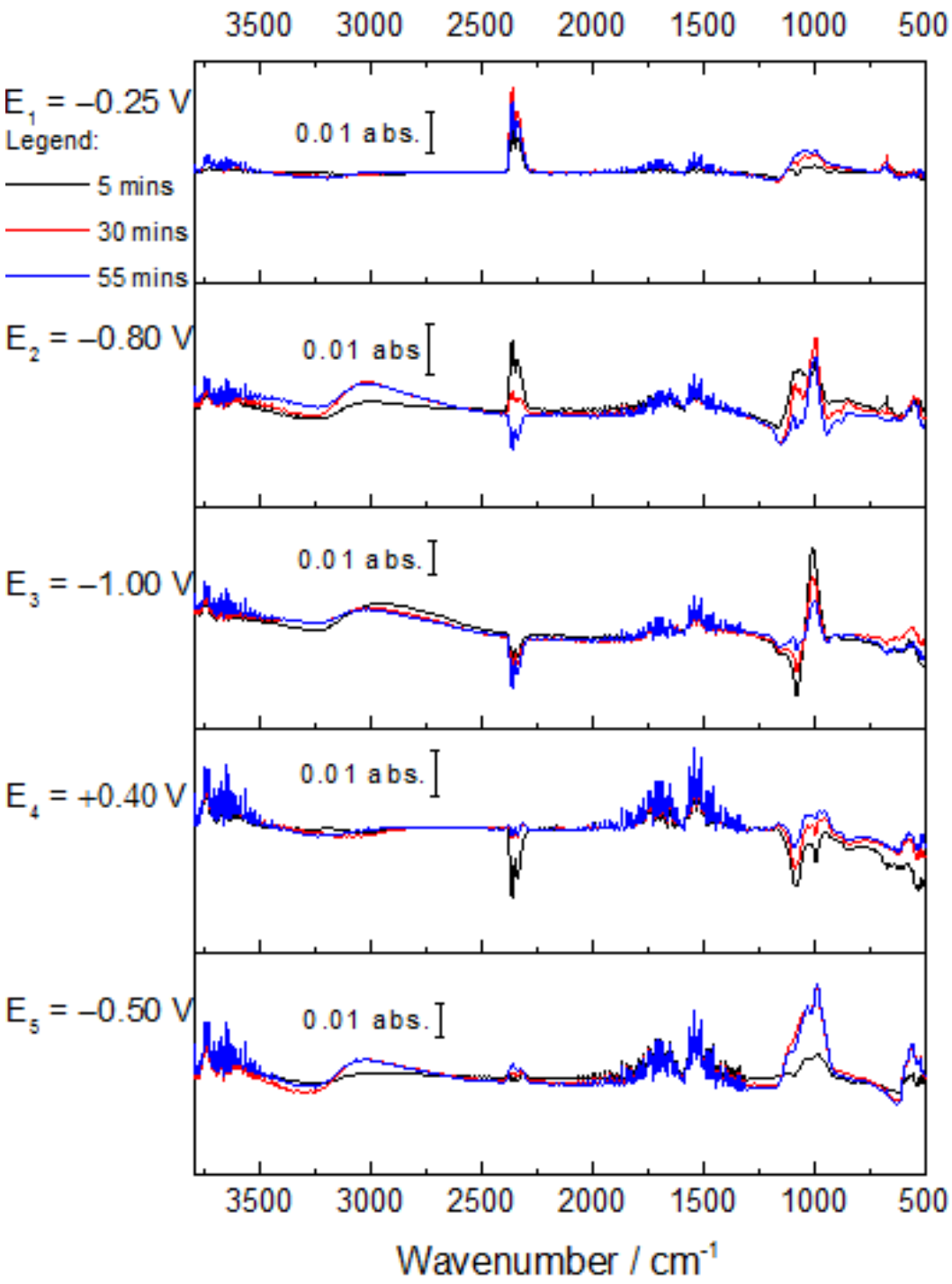

Figure A. 28 Second repeat measurement of in-situ FTIR spectra of greigite in phosphate buffer solution pH 6.8 under argon, recorded on applying potentials of −0.25, −0.80, −1.00, + 0.40 and −0.50 V for one hour each step. Spectra displayed at each potential step were recorded at 5, 30 and 55 mins into holding the potential.

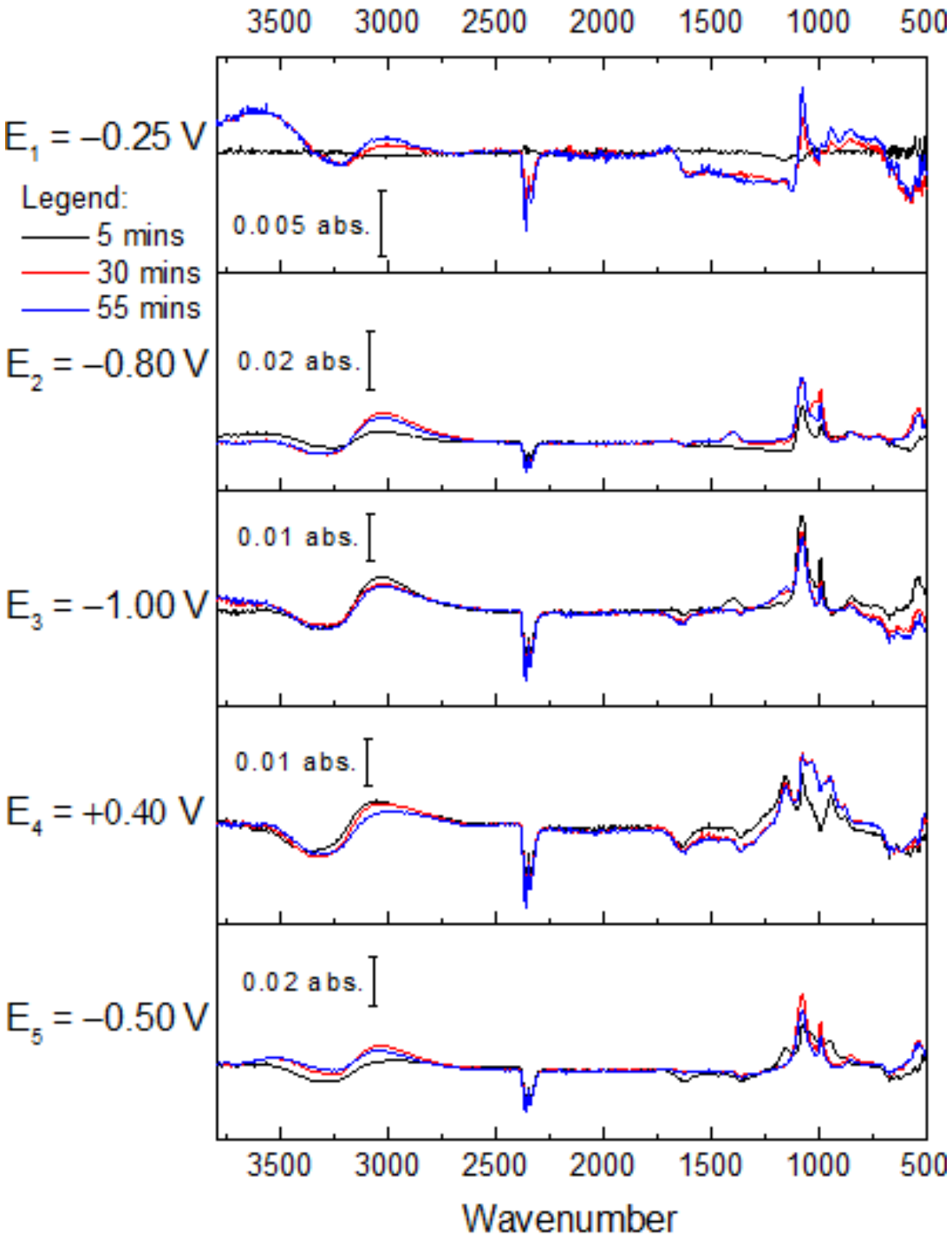

Figure A. 29 First repeat measurement of in-situ FTIR spectra of greigite in phosphate buffer solution pH 6.5 under CO_2, recorded on applying potentials of −0.25, −0.80, −1.00, + 0.40 and −0.50 V for one hour each step. Spectra displayed at each potential step were recorded at 5, 30 and 55 mins into holding the potential

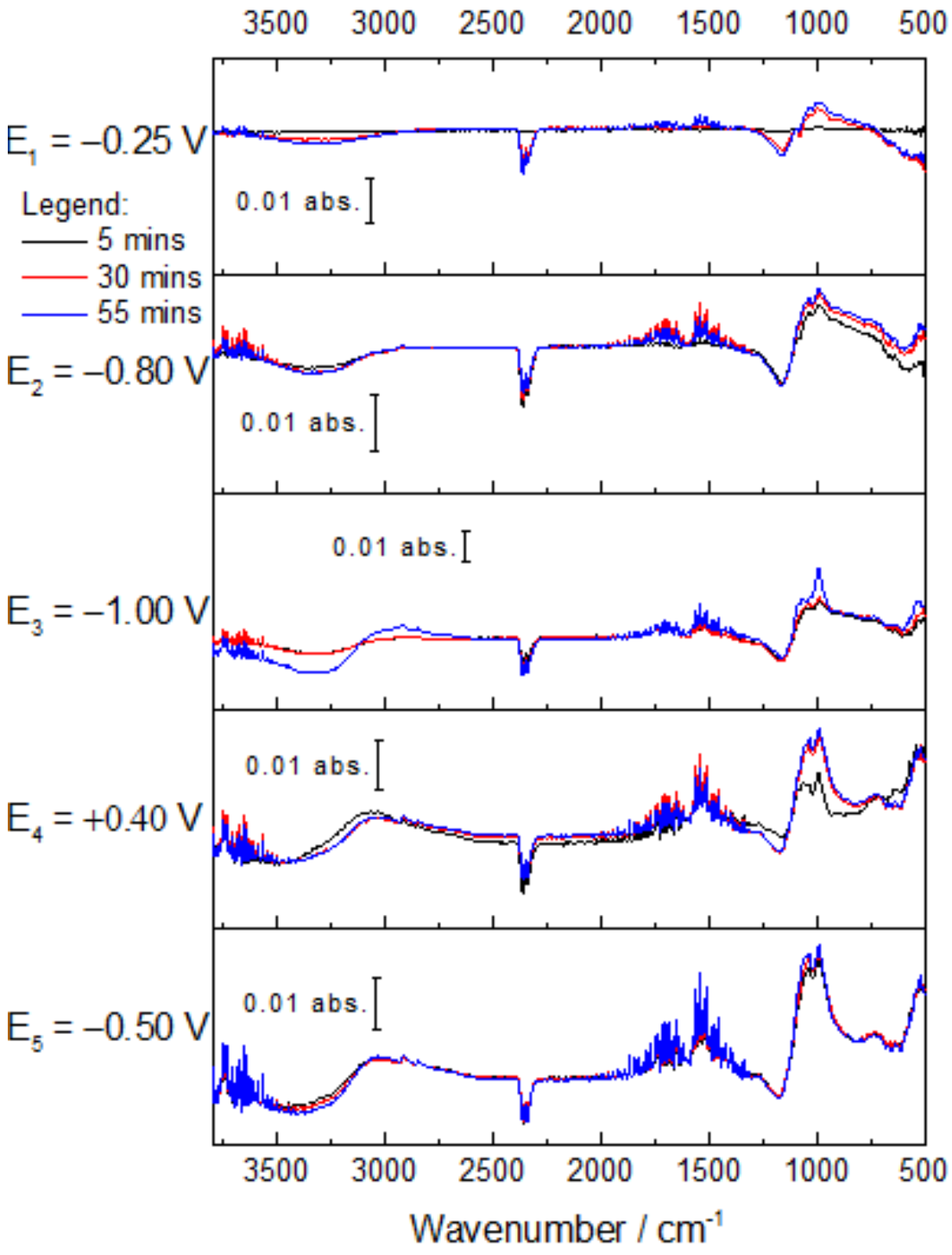

Figure A. 30 Second repeat measurement of in-situ FTIR spectra of greigite in phosphate buffer solution pH 6.5 under CO_2, recorded on applying potentials of −0.25, −0.80, −1.00, + 0.40 and −0.50 V for one hour each step. Spectra displayed at each potential step were recorded at 5, 30 and 55 mins into holding the potential.

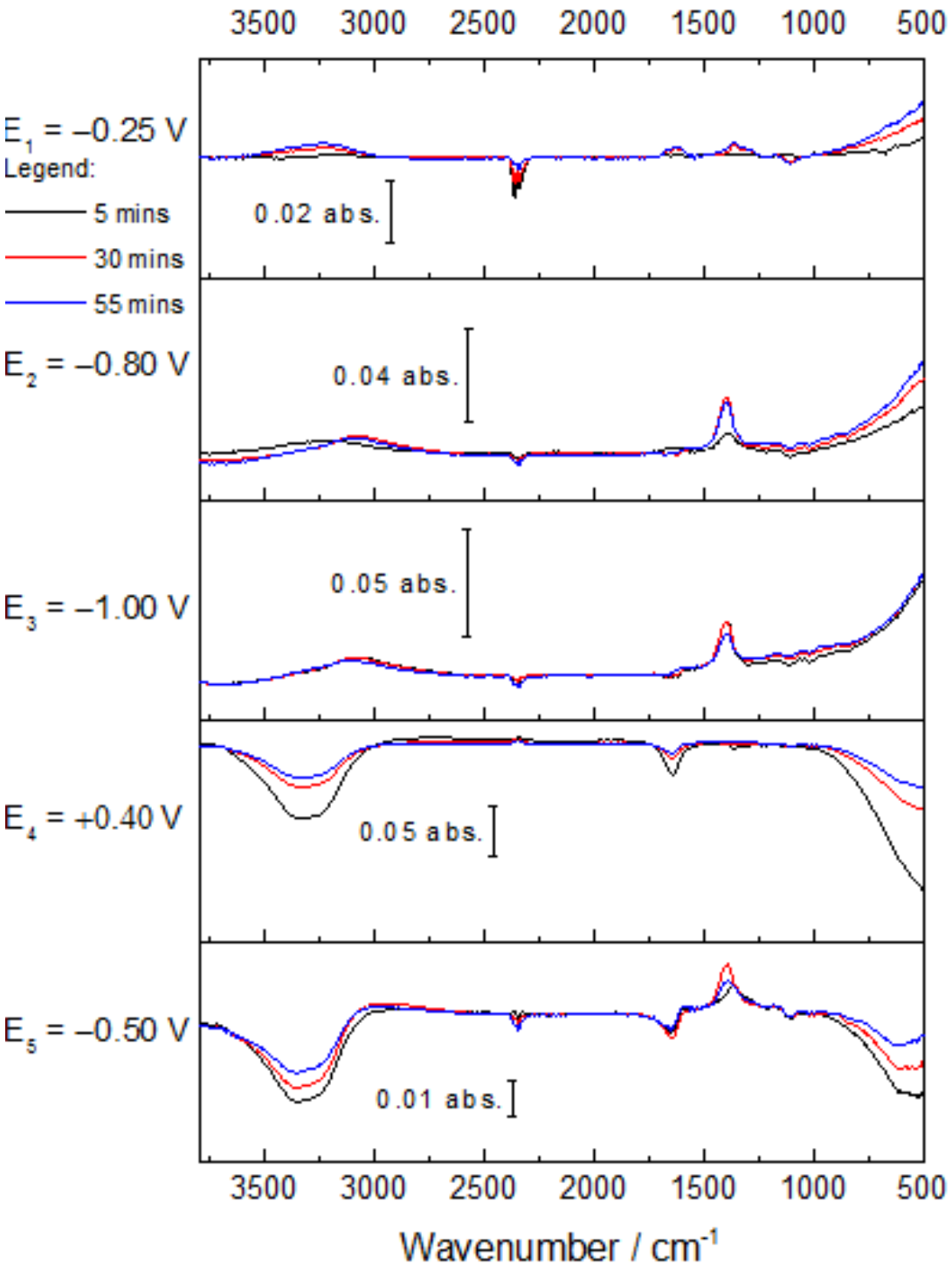

Figure A. 31 First repeat measurement of in-situ FTIR spectra of greigite in $KHCO_3$ solution pH 8.55 under argon, recorded on applying potentials of −0.25, −0.80, −1.00, + 0.40 and −0.50 V for one hour each step. Spectra displayed at each potential step were recorded at 5, 30 and 55 mins into holding the potential.

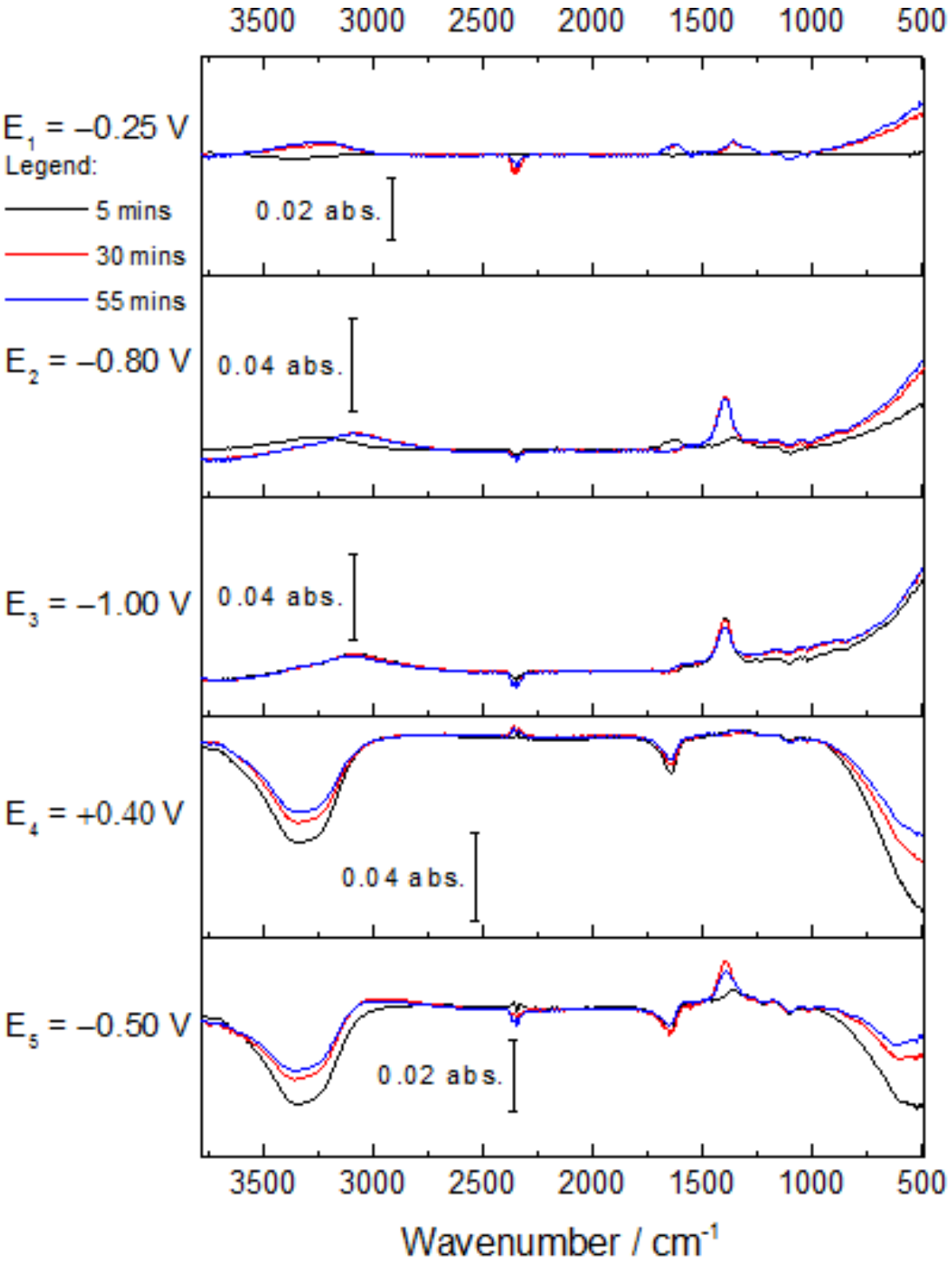

Figure A. 32 Second repeat measurement of in-situ FTIR spectra of greigite in $KHCO_3$ solution pH 8.55 under argon, recorded on applying potentials of −0.25, −0.80, −1.00, + 0.40 and −0.50 V for one hour each step. Spectra displayed at each potential step were recorded at 5, 30 and 55 mins into holding the potential.

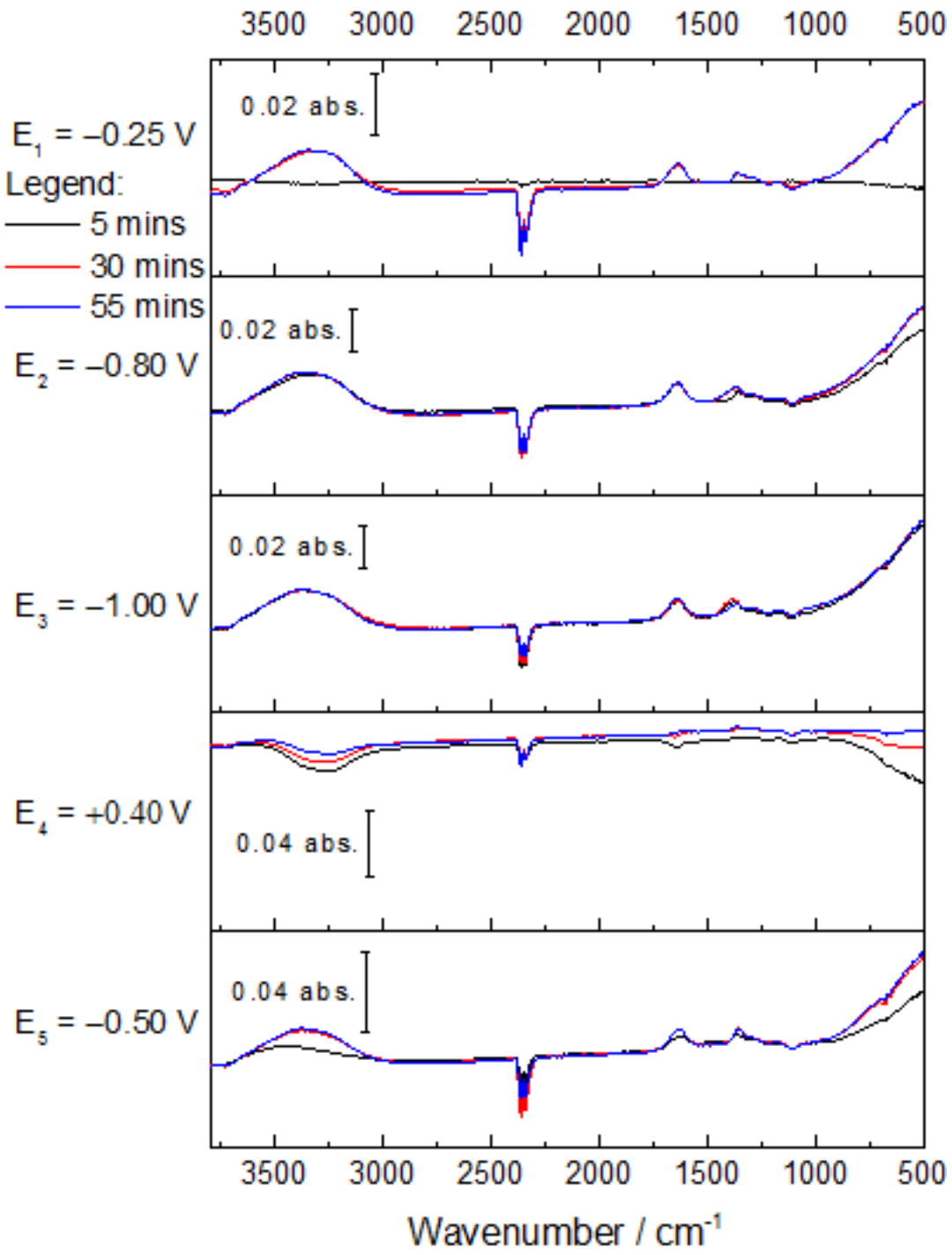

Figure A. 33 First repeat measurement of in-situ FTIR spectra of greigite in $KHCO_3$ solution pH 7.1 under CO_2, recorded on applying potentials of −0.25, −0.80, −1.00, + 0.40 and −0.50 V for one hour each step. Spectra displayed at each potential step were recorded at 5, 30 and 55 mins into holding the potential.

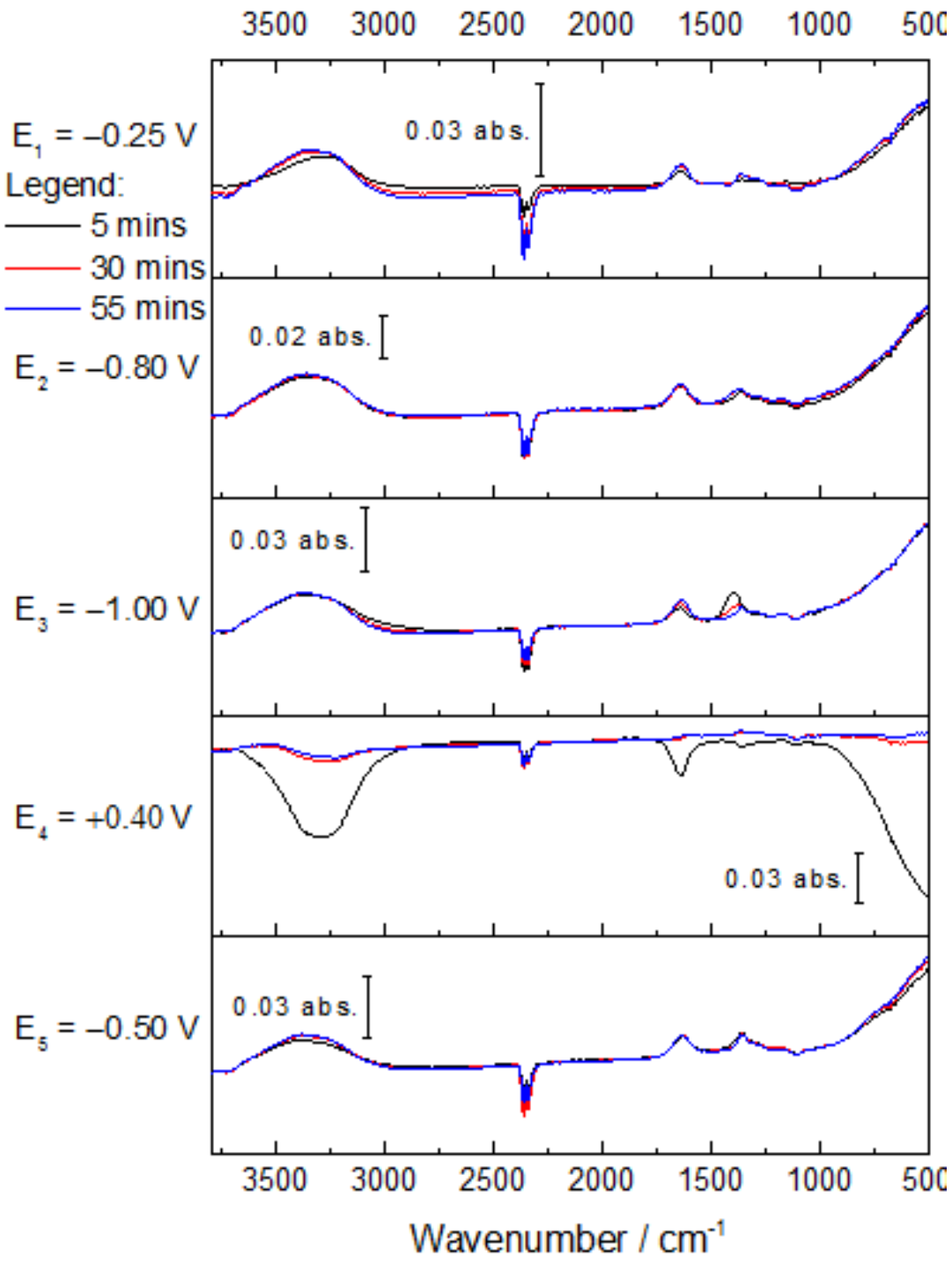

Figure A. 34 Second repeat measurement of in-situ FTIR spectra of greigite in $KHCO_3$ solution pH 7.1 under CO_2, recorded on applying potentials of −0.25, −0.80, −1.00, + 0.40 and −0.50 V for one hour each step. Spectra displayed at each potential step were recorded at 5, 30 and 55 mins into holding the potential.

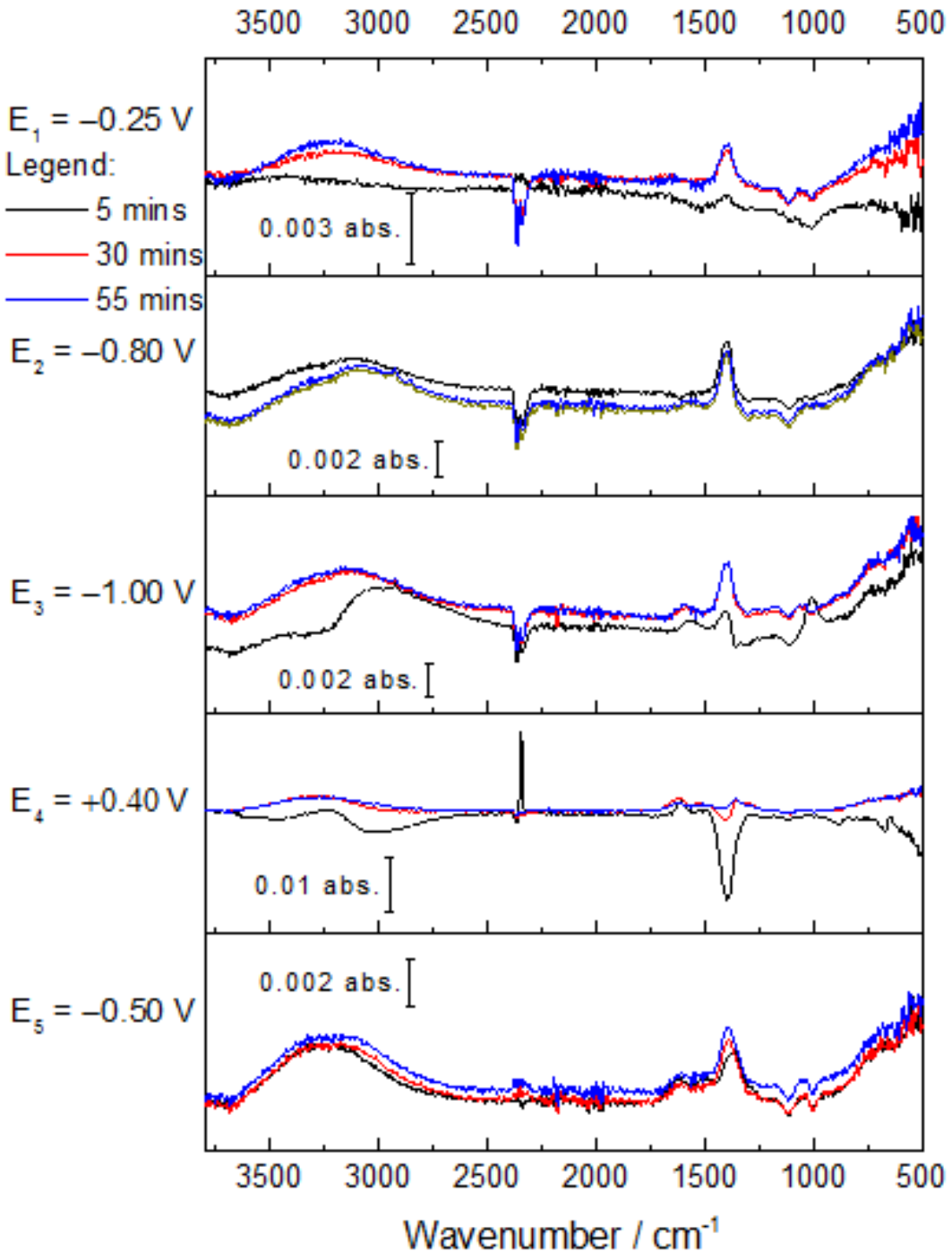

Figure A. 35 First repeat measurement of in-situ FTIR spectra of greigite in K_2CO_3 solution pH 11.2 under argon, recorded on applying potentials of −0.25, −0.80, −1.00, + 0.40 and −0.50 V for one hour each step. Spectra displayed at each potential step were recorded at 5, 30 and 55 mins into holding the potential.

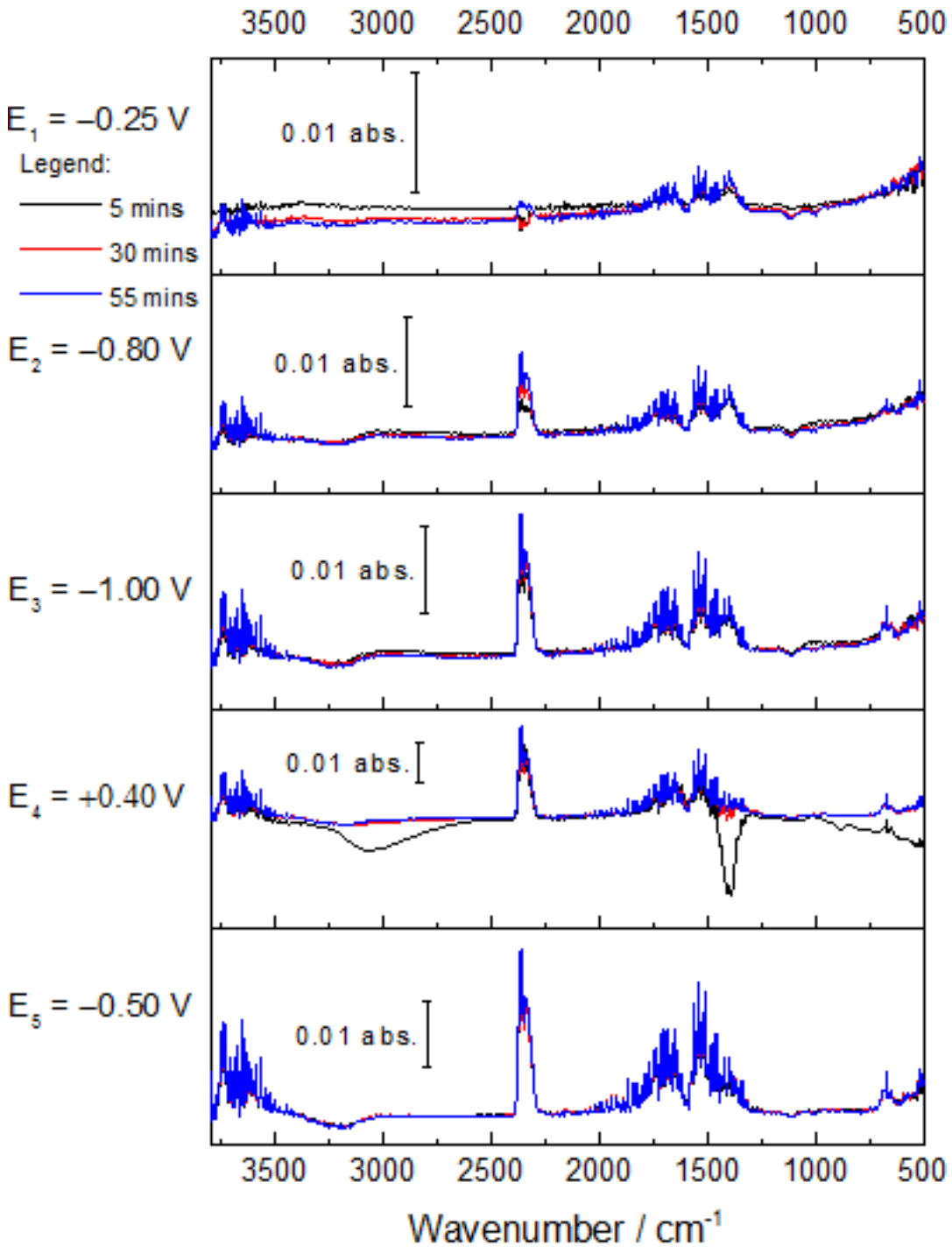

Figure A. 36 Second repeat measurement of in-situ FTIR spectra of greigite in K_2CO_3 solution pH 11.2 under argon, recorded on applying potentials of −0.25, −0.80, −1.00, + 0.40 and −0.50 V for one hour each step. Spectra displayed at each potential step were recorded at 5, 30 and 55 mins into holding the potential.

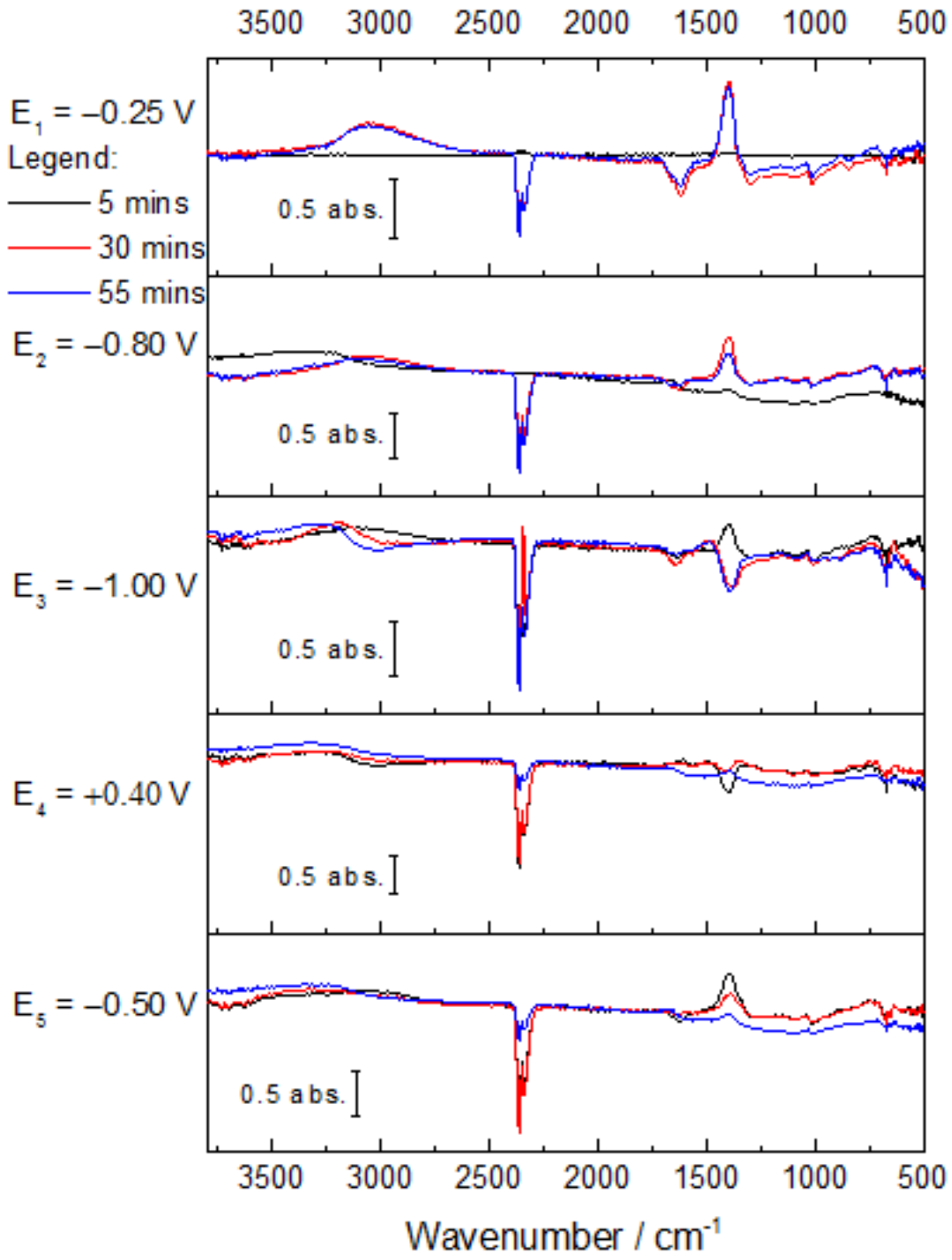

Figure A. 37 First repeat measurement of in-situ FTIR spectra of greigite in K_2CO_3 solution pH 10.1 under CO_2, recorded on applying potentials of −0.25, −0.80, −1.00, + 0.40 and −0.50 V for one hour each step. Spectra displayed at each potential step were recorded at 5, 30 and 55 mins into holding the potential.

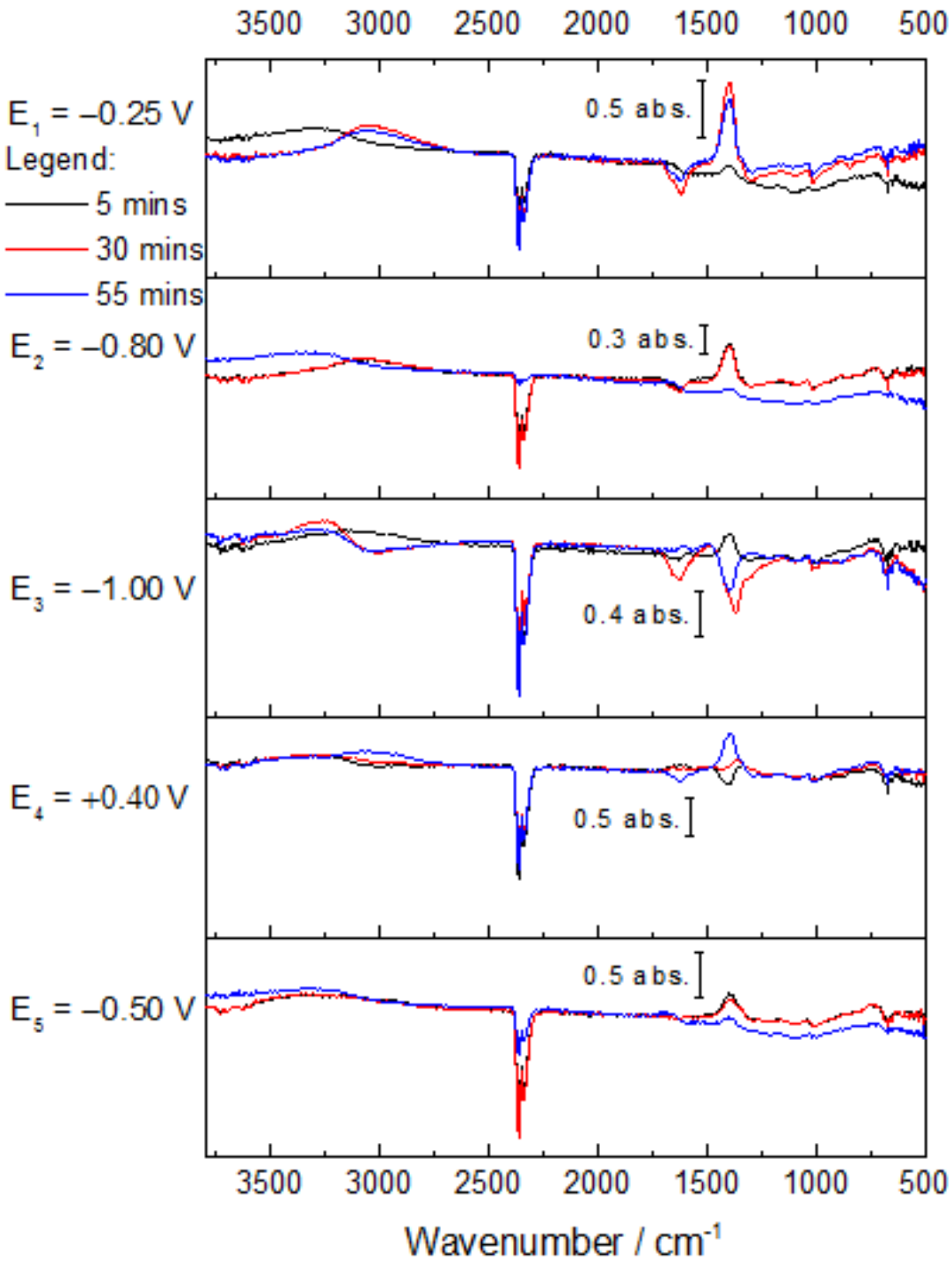

Figure A. 38 Second repeat measurement of in-situ FTIR spectra of greigite in K_2CO_3 solution pH 10.1 under CO_2, recorded on applying potentials of −0.25, −0.80, −1.00, + 0.40 and −0.50 V for one hour each step. Spectra displayed at each potential step were recorded at 5, 30 and 55 mins into holding the potential.

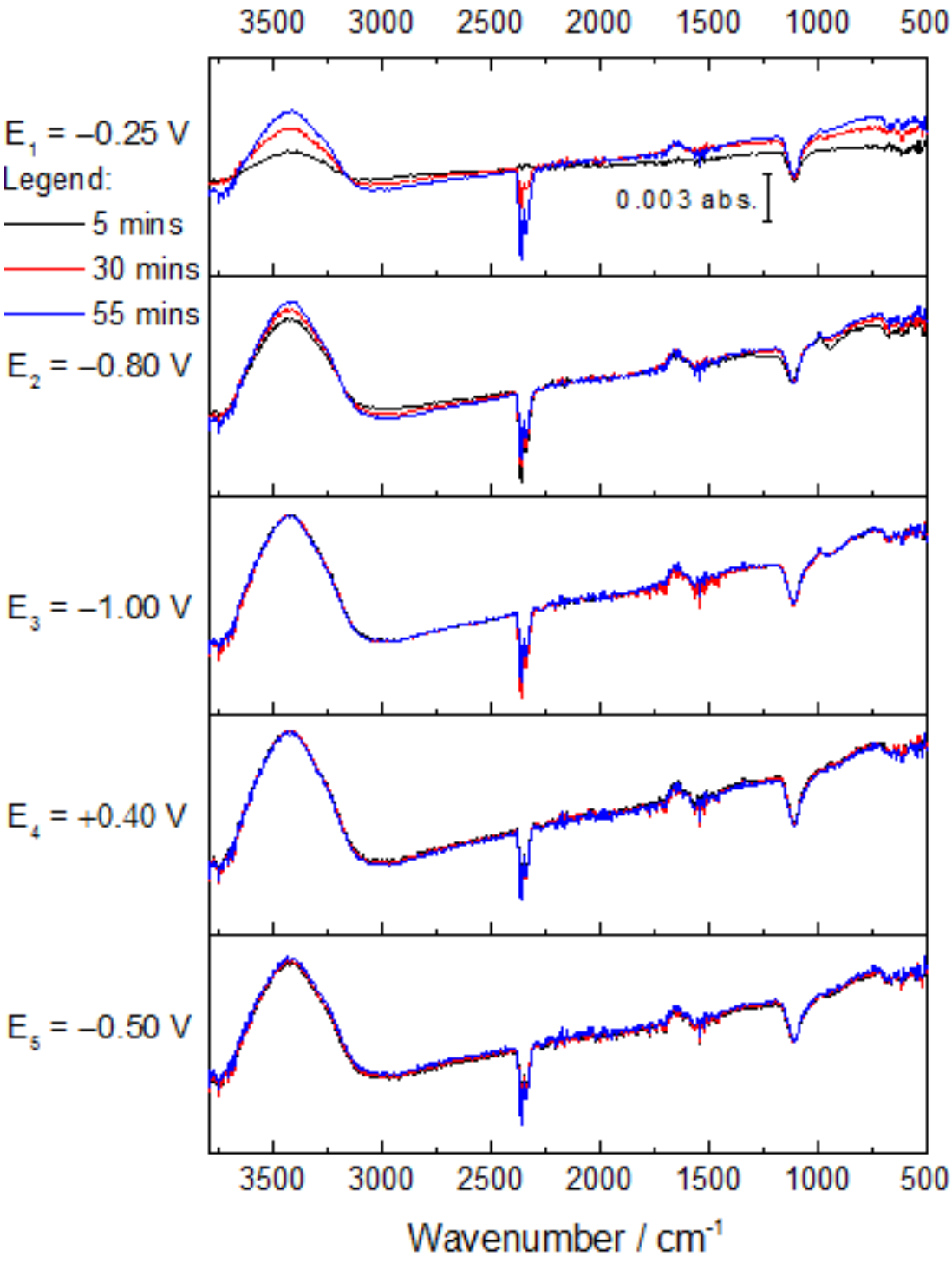

Figure A. 39 First repeat measurement of in-situ FTIR spectra of violarite in phosphate buffer solution pH 4.5 under argon, recorded on applying potentials of −0.25, −0.80, −1.00, + 0.40 and −0.50 V for one hour each step. Spectra displayed at each potential step were recorded at 5, 30 and 55 mins into holding the potential.

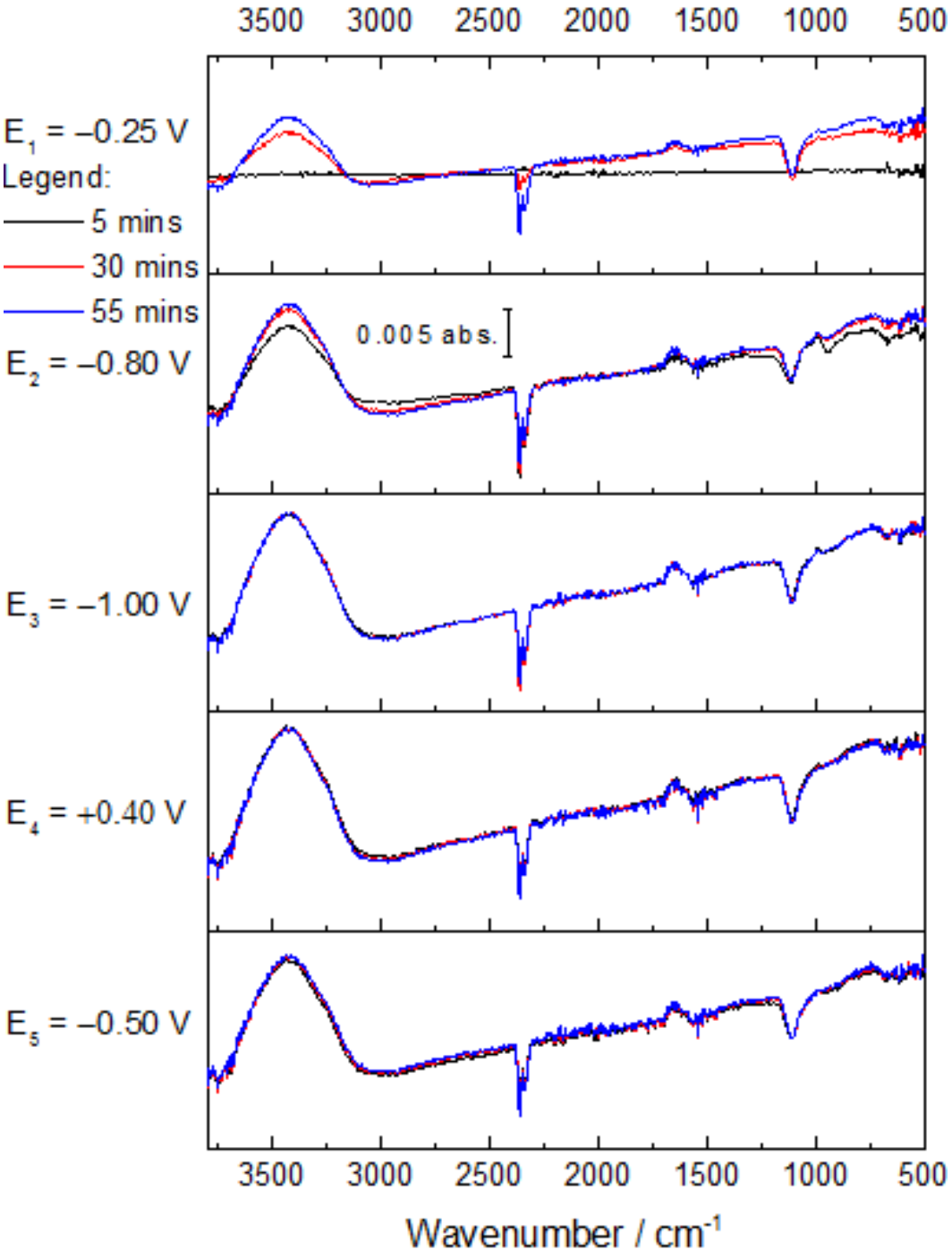

Figure A. 40 Second repeat measurement of in-situ FTIR spectra of violarite in phosphate buffer solution pH 4.5 under argon, recorded on applying potentials of −0.25, −0.80, −1.00, + 0.40 and −0.50 V for one hour each step. Spectra displayed at each potential step were recorded at 5, 30 and 55 mins into holding the potential.

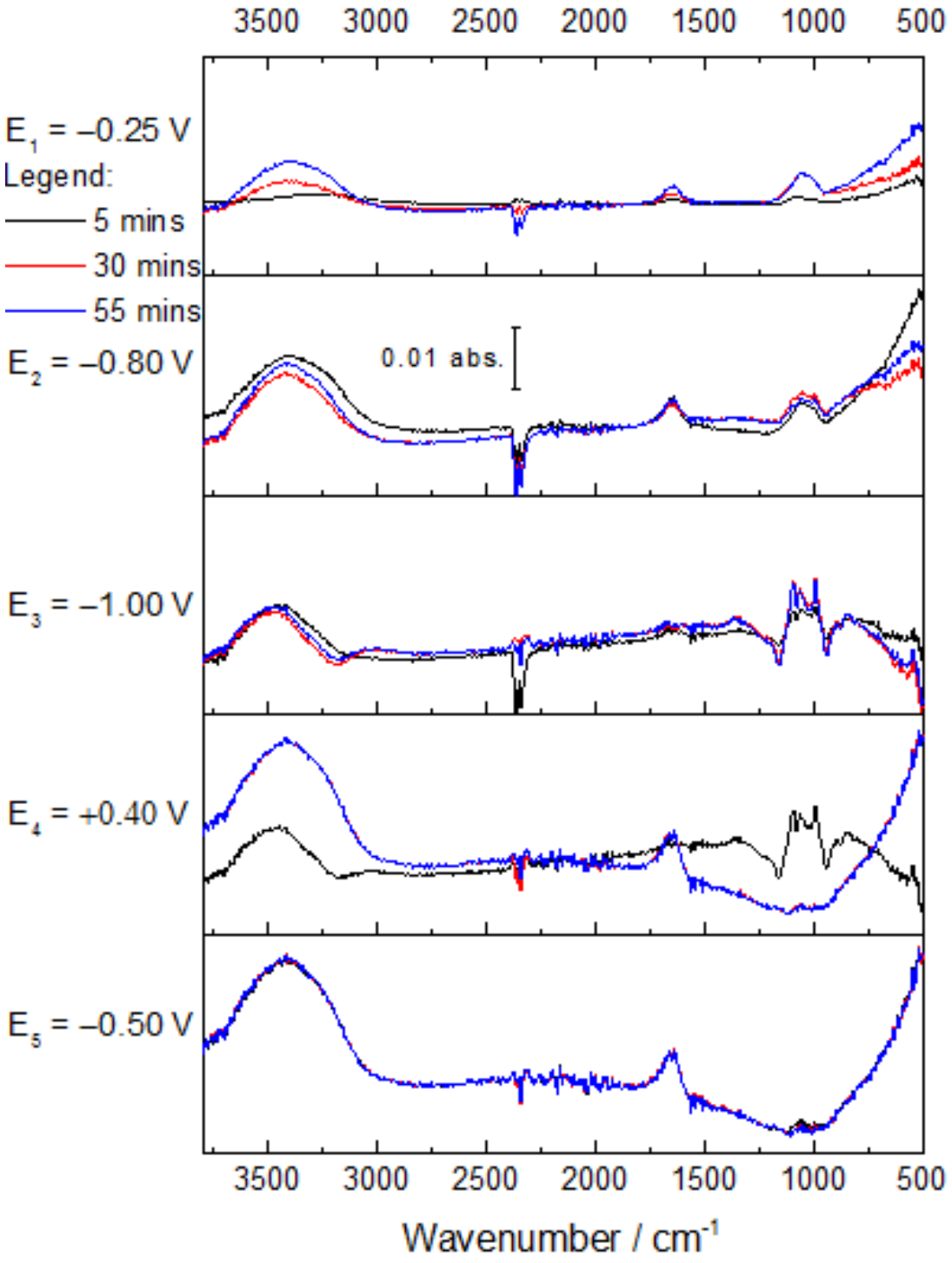

Figure A. 41 First repeat measurement of in-situ FTIR spectra of violarite in phosphate buffer solution pH 4.3 under CO_2, recorded on applying potentials of −0.25, −0.80, −1.00, + 0.40 and −0.50 V for one hour each step. Spectra displayed at each potential step were recorded at 5, 30 and 55 mins into holding the potential.

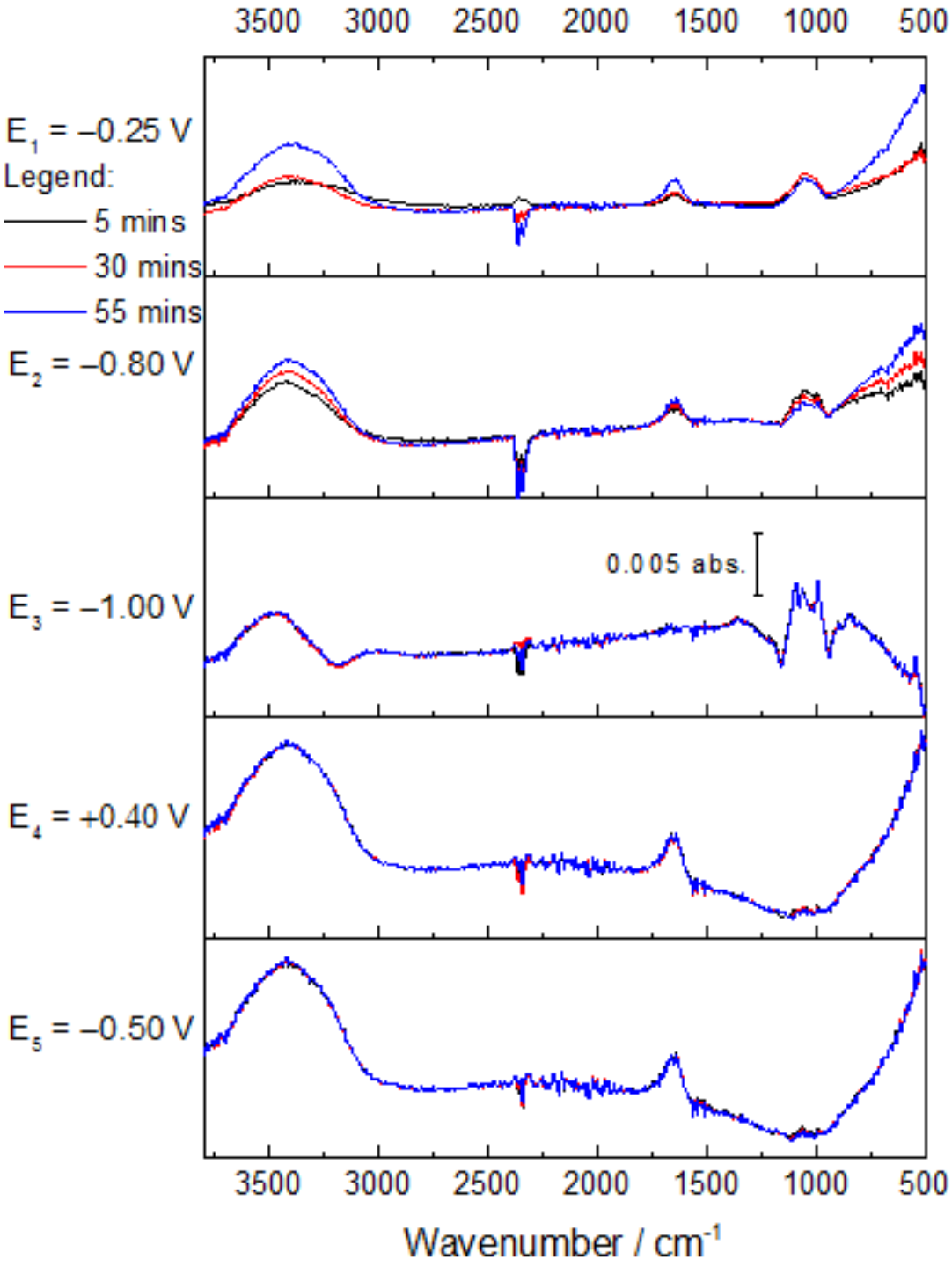

Figure A. 42 Second repeat measurement of in-situ FTIR spectra of violarite in phosphate buffer solution pH 4.3 under CO_2, recorded on applying potentials of −0.25, −0.80, −1.00, + 0.40 and −0.50 V for one hour each step. Spectra displayed at each potential step were recorded at 5, 30 and 55 mins into holding the potential.

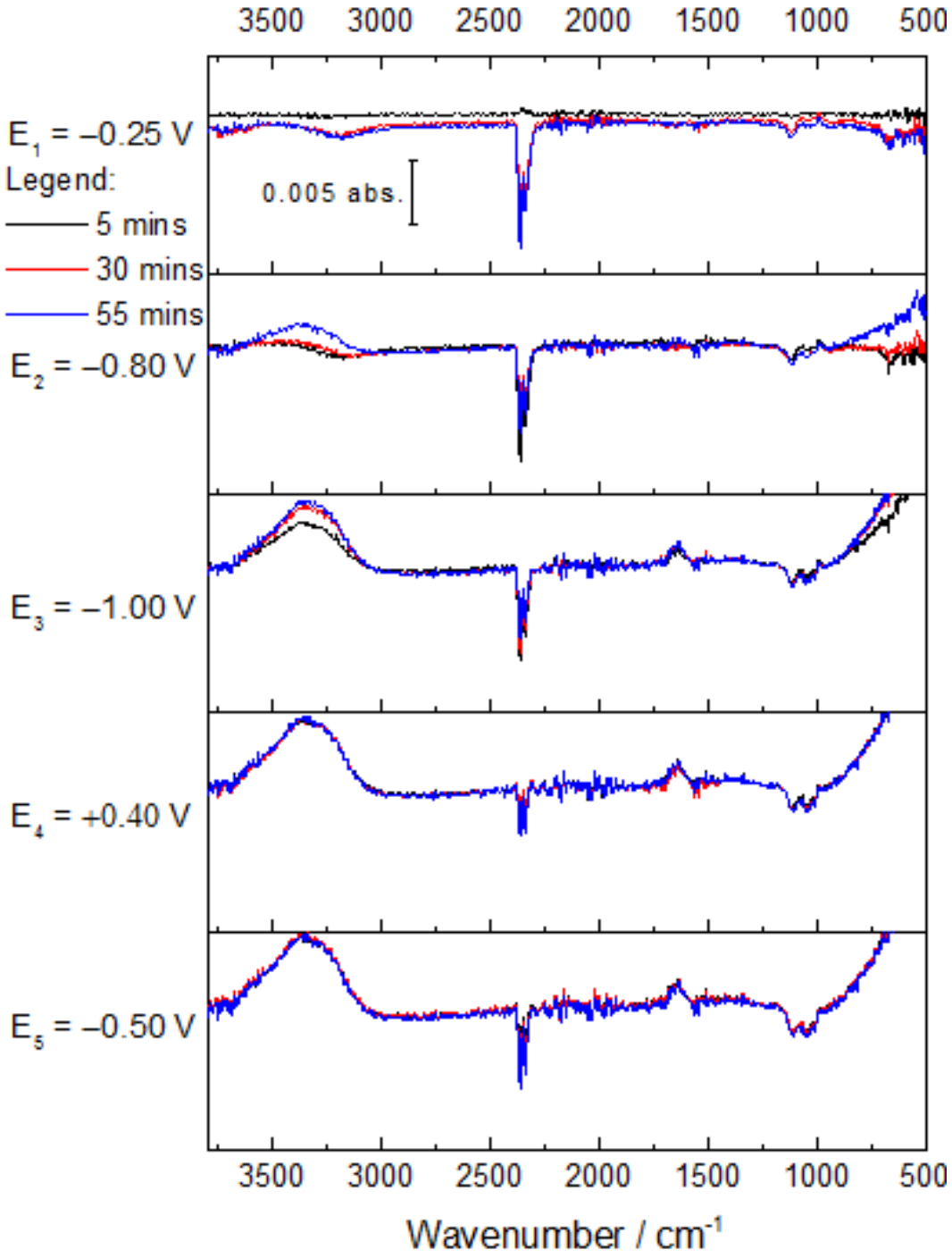

Figure A. 43 First repeat measurement of in-situ FTIR spectra of violarite in phosphate buffer solution pH 6.8 under argon, recorded on applying potentials of −0.25, −0.80, −1.00, + 0.40 and −0.50 V for one hour each step. Spectra displayed at each potential step were recorded at 5, 30 and 55 mins into holding the potential.

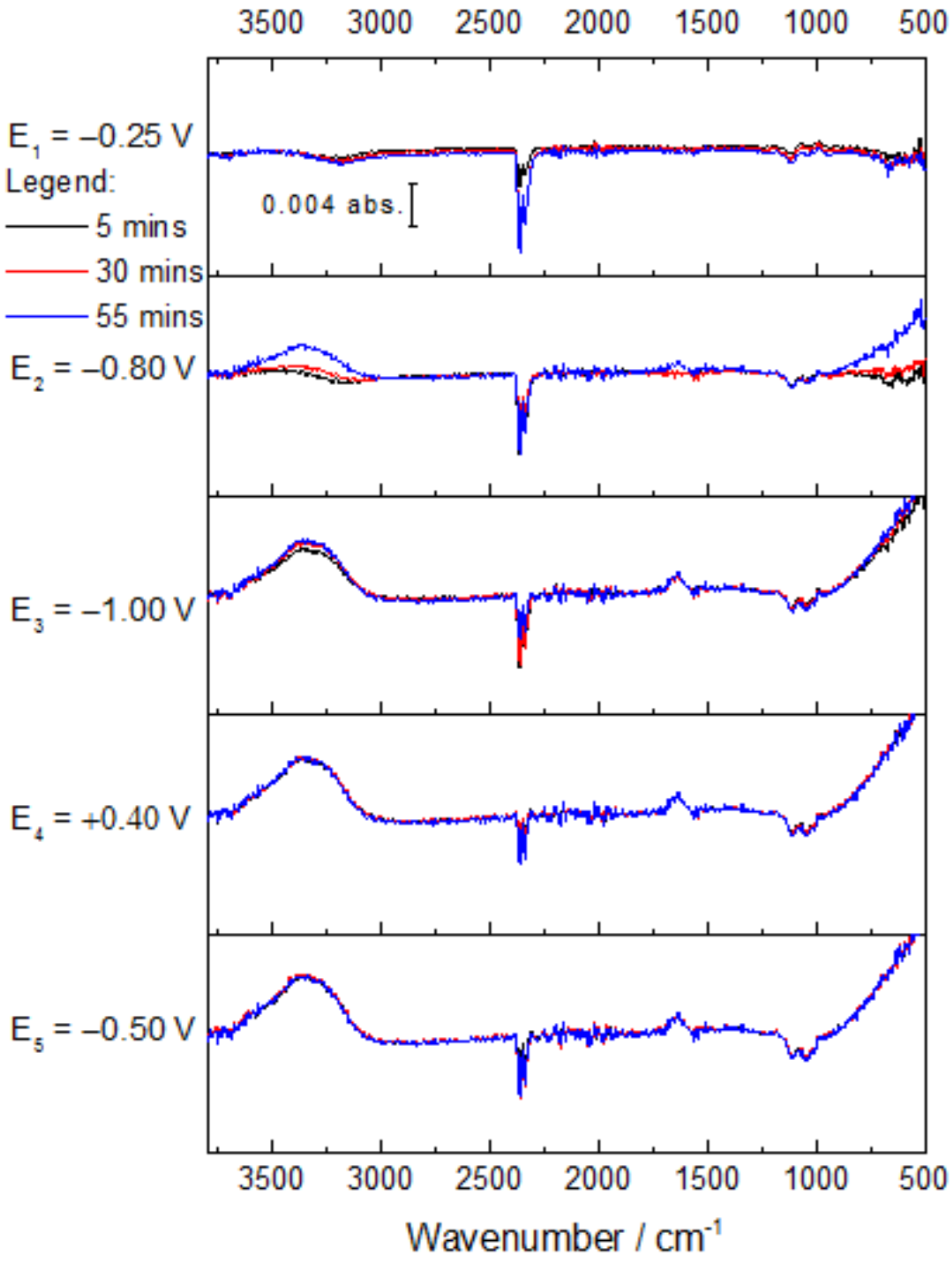

Figure A. 44 Second repeat measurement of in-situ FTIR spectra of violarite in phosphate buffer solution pH 6.8 under argon, recorded on applying potentials of −0.25, −0.80, −1.00, + 0.40 and −0.50 V for one hour each step. Spectra displayed at each potential step were recorded at 5, 30 and 55 mins into holding the potential.

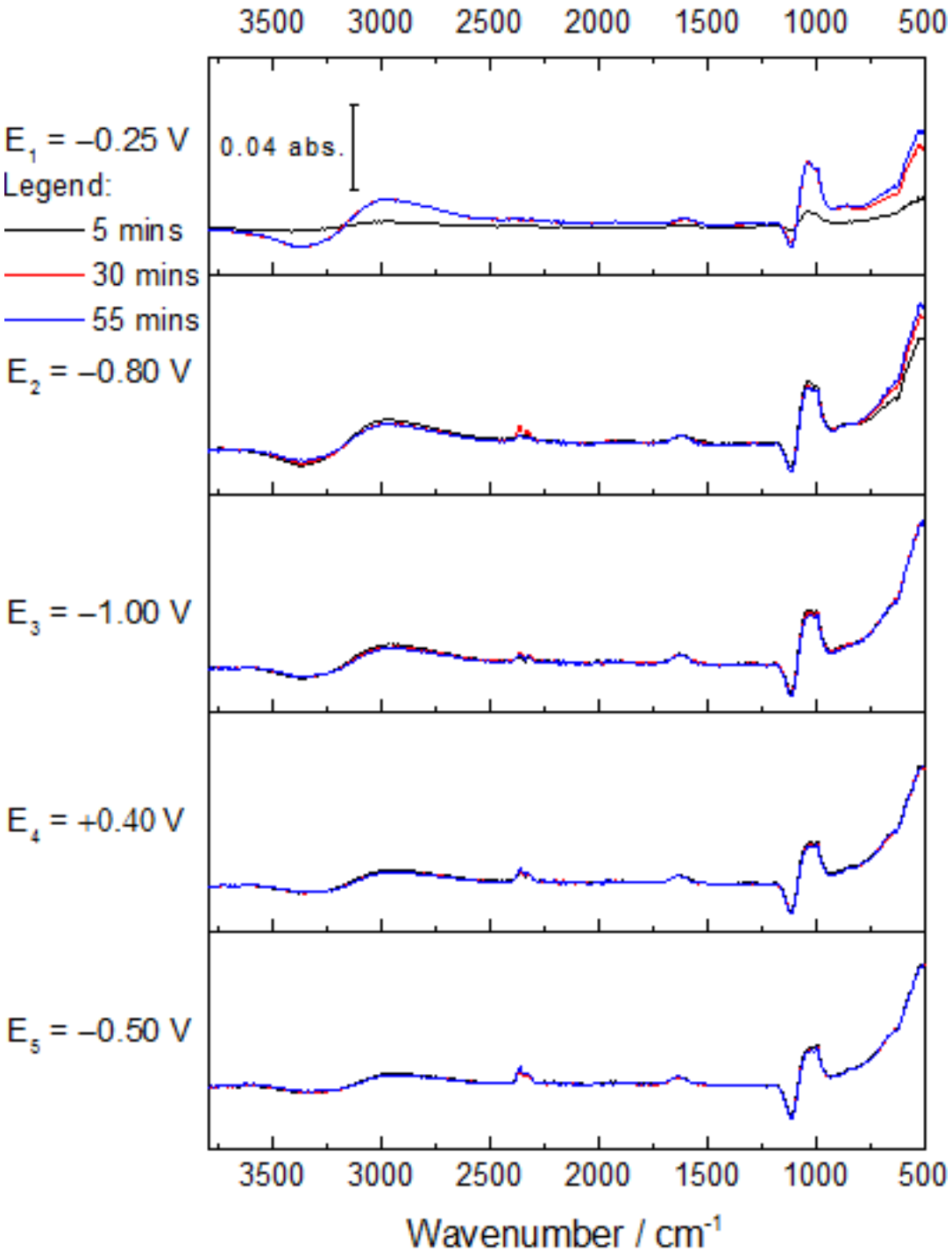

Figure A. 45 First repeat measurement of in-situ FTIR spectra of violarite in phosphate buffer solution pH 6.5 under CO_2, recorded on applying potentials of −0.25, −0.80, −1.00, + 0.40 and −0.50 V for one hour each step. Spectra displayed at each potential step were recorded at 5, 30 and 55 mins into holding the potential.

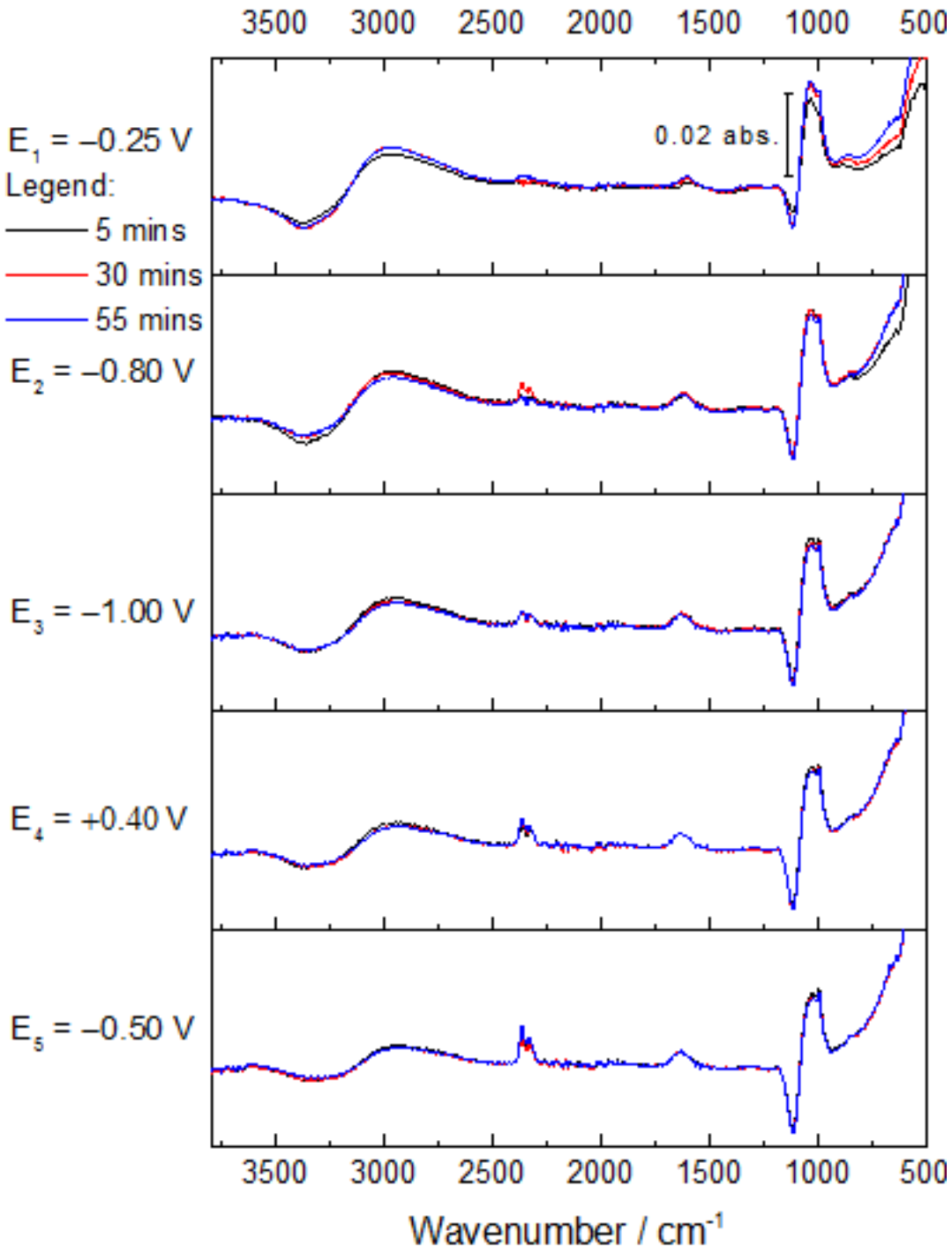

Figure A. 46 Second repeat measurement of in-situ FTIR spectra of violarite in phosphate buffer solution pH 6.5 under CO_2, recorded on applying potentials of −0.25, −0.80, −1.00, + 0.40 and −0.50 V for one hour each step. Spectra displayed at each potential step were recorded at 5, 30 and 55 mins into holding the potential.

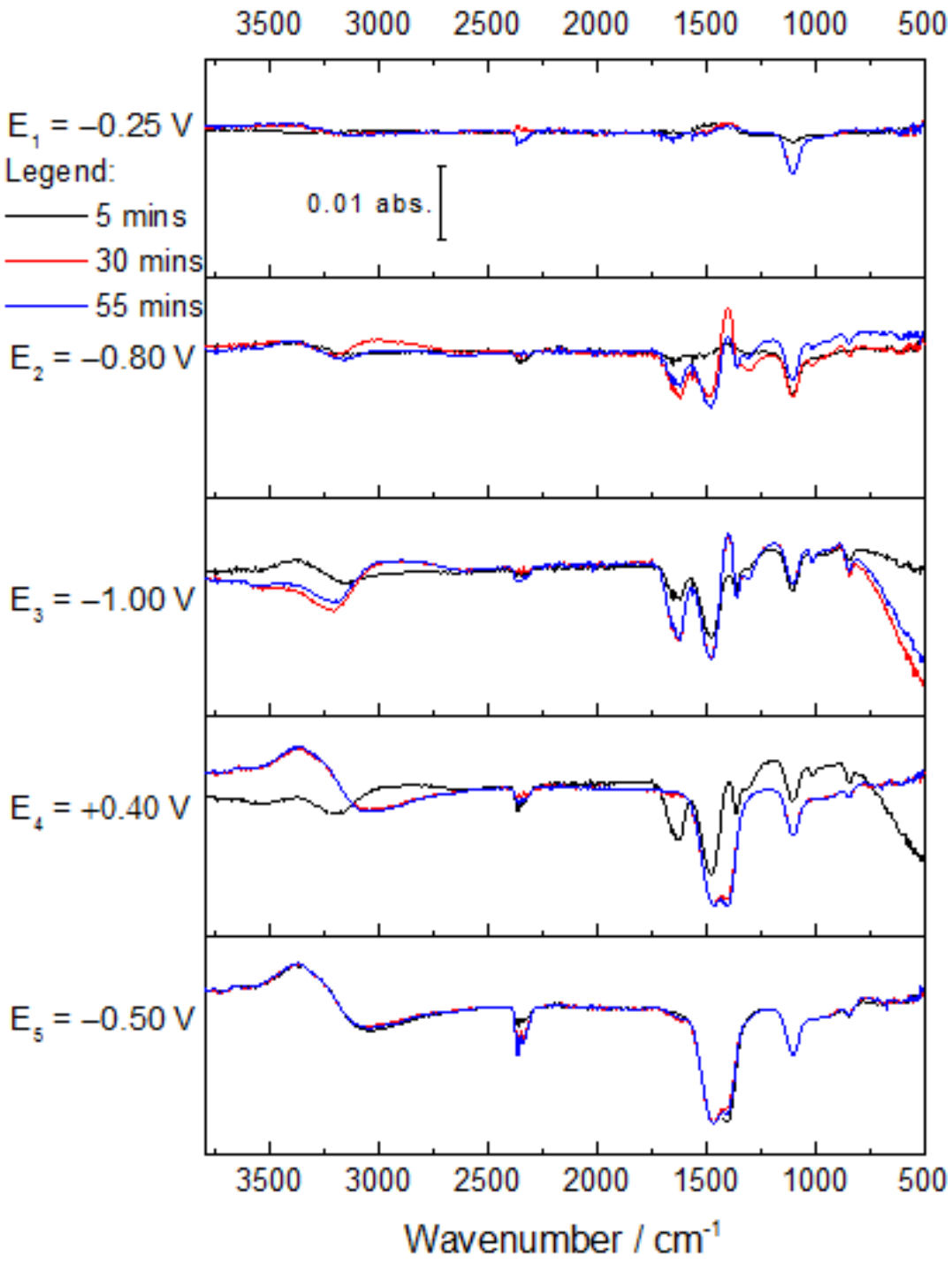

Figure A. 47 First repeat measurement of in-situ FTIR spectra of violarite in $KHCO_3$ solution pH 8.55 under argon, recorded on applying potentials of −0.25, −0.80, −1.00, + 0.40 and −0.50 V for one hour each step. Spectra displayed at each potential step were recorded at 5, 30 and 55 mins into holding the potential.

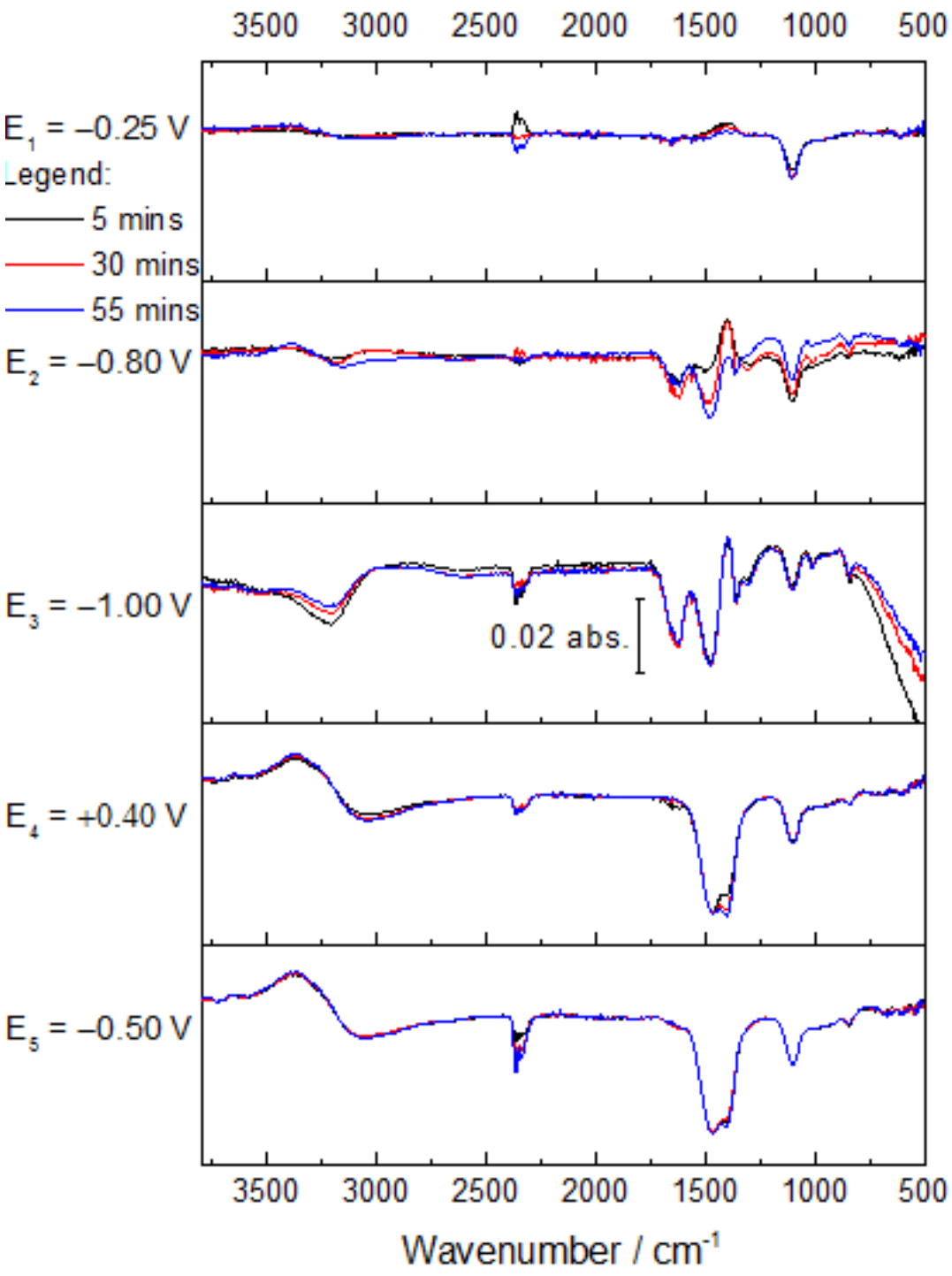

Figure A. 48 Second repeat measurement of in-situ FTIR spectra of violarite in $KHCO_3$ solution pH 8.55 under argon, recorded on applying potentials of −0.25, −0.80, −1.00, + 0.40 and −0.50 V for one hour each step. Spectra displayed at each potential step were recorded at 5, 30 and 55 mins into holding the potential.

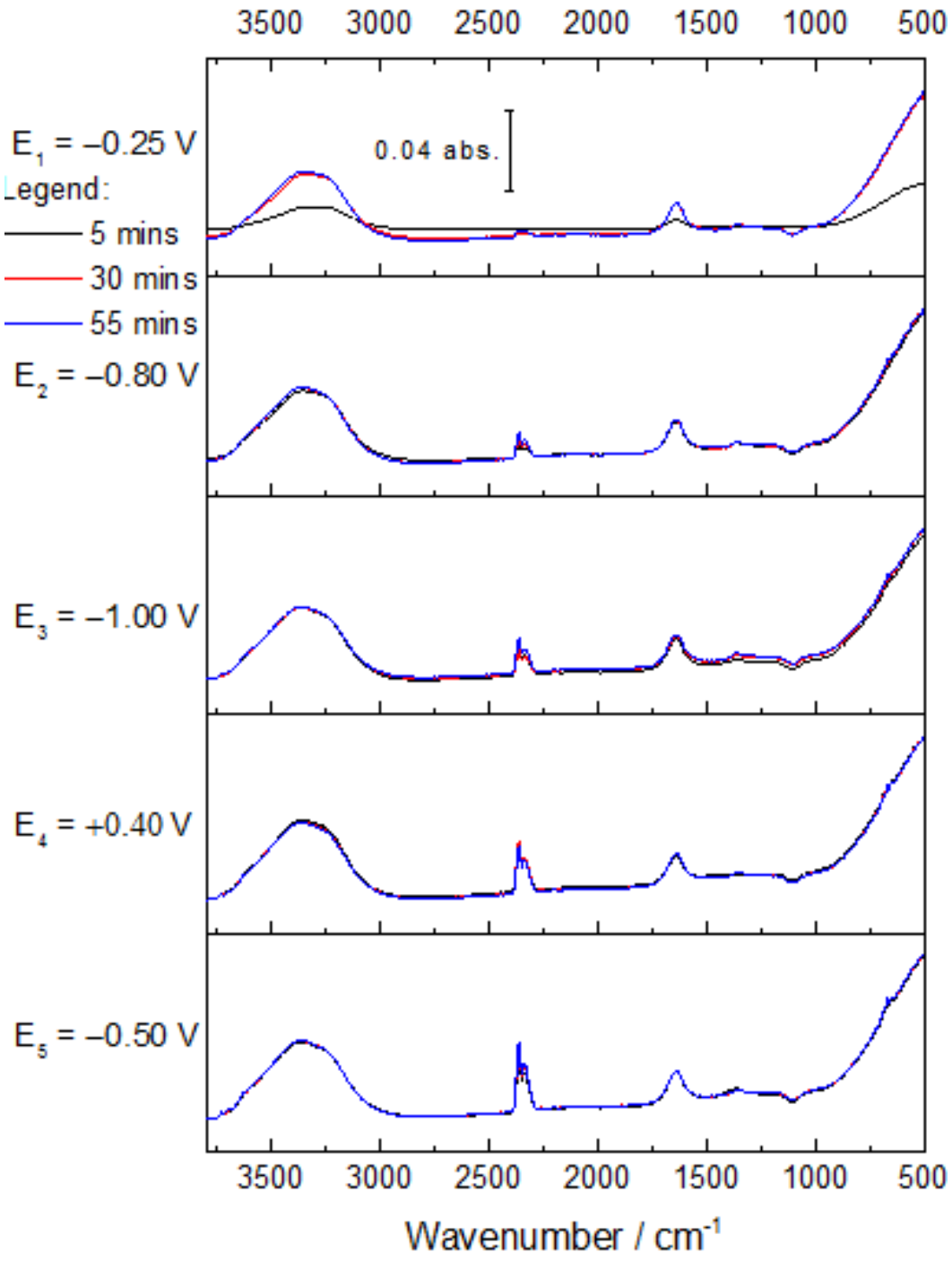

Figure A. 49 First repeat measurement of in-situ FTIR spectra of violarite in $KHCO_3$ solution pH 7.1 under CO_2, recorded on applying potentials of −0.25, −0.80, −1.00, + 0.40 and −0.50 V for one hour each step. Spectra displayed at each potential step were recorded at 5, 30 and 55 mins into holding the potential.

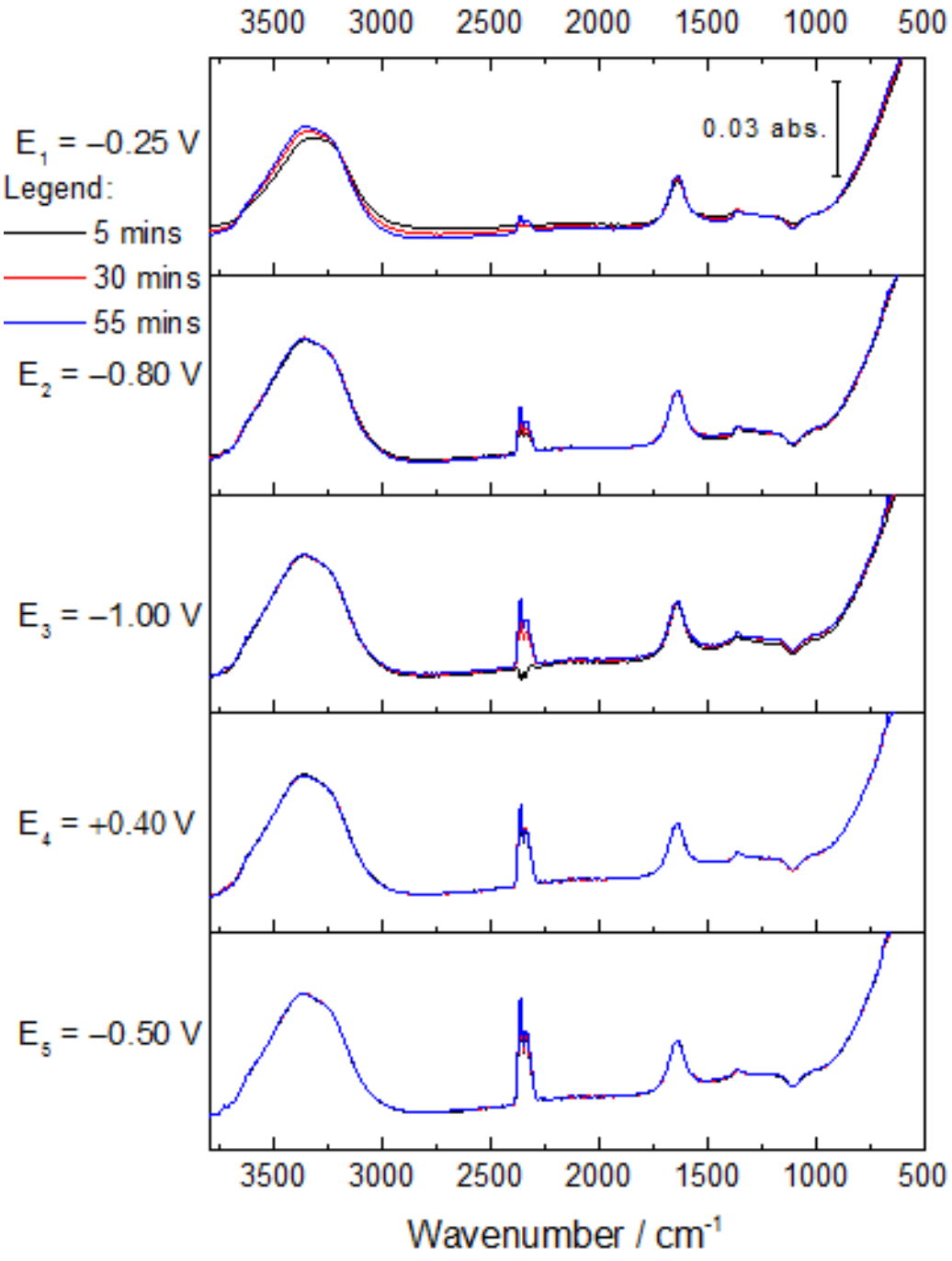

Figure A. 50 Second repeat measurement of in-situ FTIR spectra of violarite in $KHCO_3$ solution pH 7.1 under CO_2, recorded on applying potentials of −0.25, −0.80, −1.00, + 0.40 and −0.50 V for one hour each step. Spectra displayed at each potential step were recorded at 5, 30 and 55 mins into holding the potential.

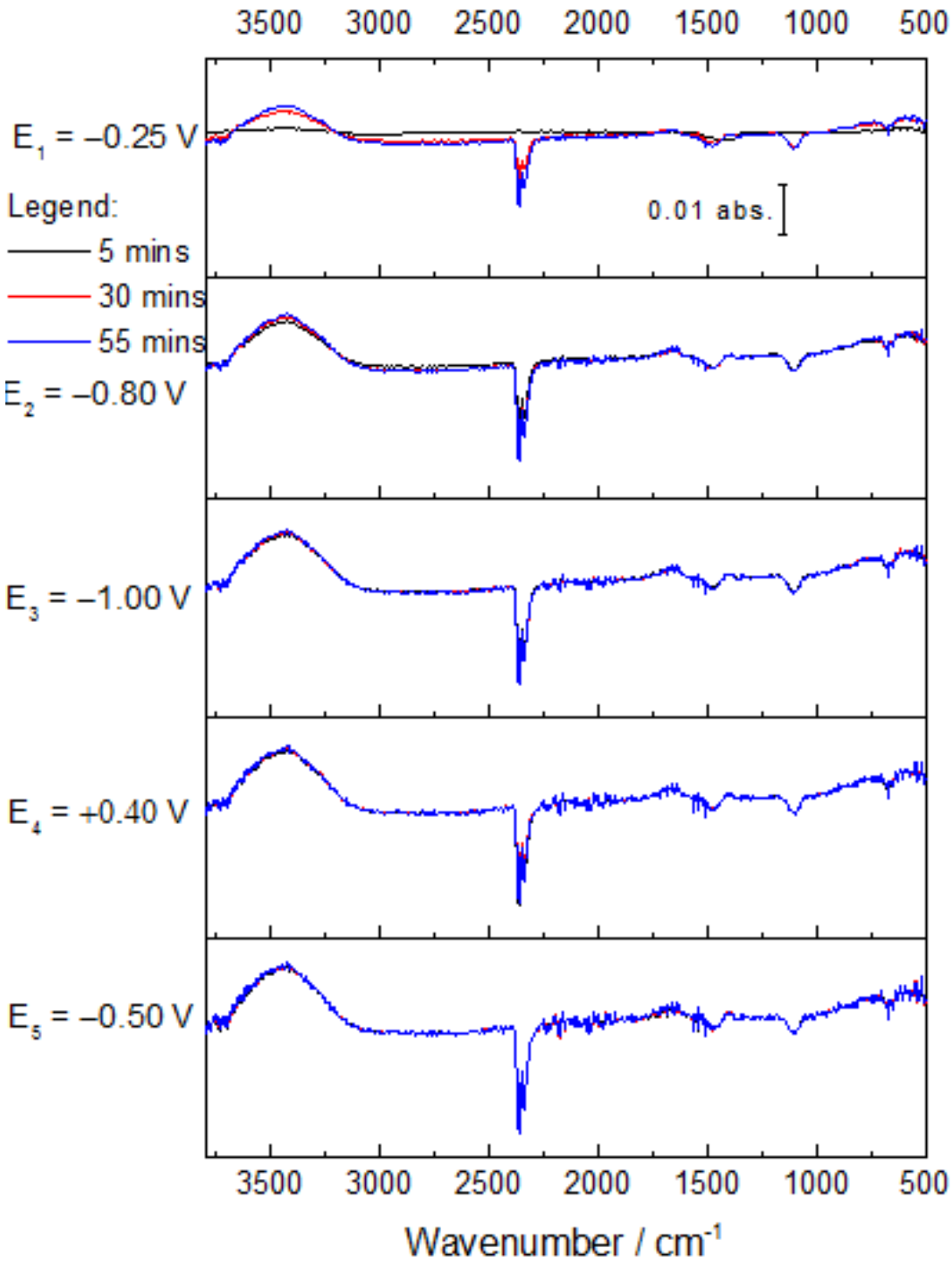

Figure A. 51 First repeat measurement of in-situ FTIR spectra of violarite in K_2CO_3 solution pH 11.2 under argon, recorded on applying potentials of −0.25, −0.80, −1.00, + 0.40 and −0.50 V for one hour each step. Spectra displayed at each potential step were recorded at 5, 30 and 55 mins into holding the potential.

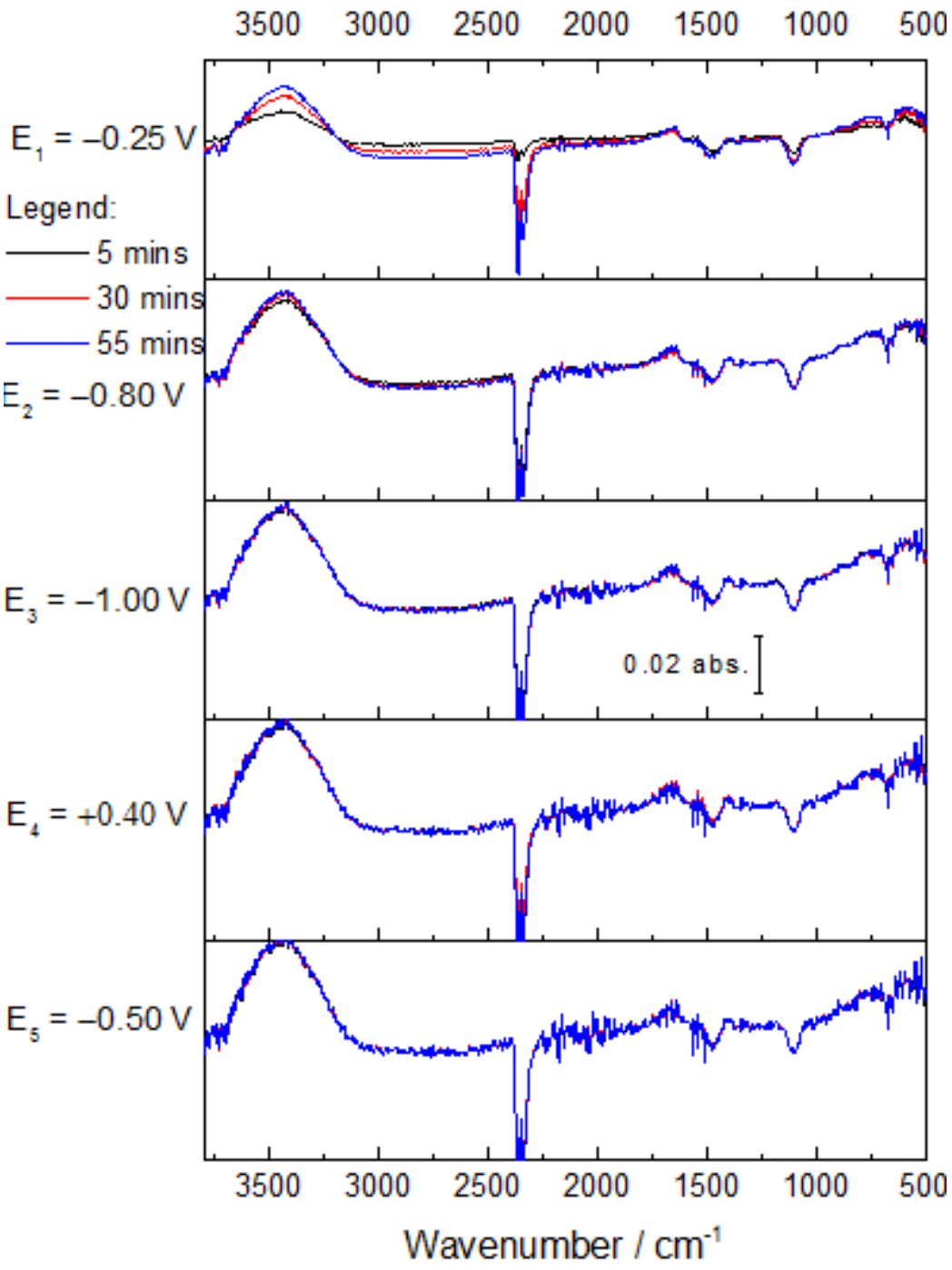

Figure A. 52 Second repeat measurement of in-situ FTIR spectra of violarite in K_2CO_3 solution pH 11.2 under argon, recorded on applying potentials of −0.25, −0.80, −1.00, + 0.40 and −0.50 V for one hour each step. Spectra displayed at each potential step were recorded at 5, 30 and 55 mins into holding the potential.

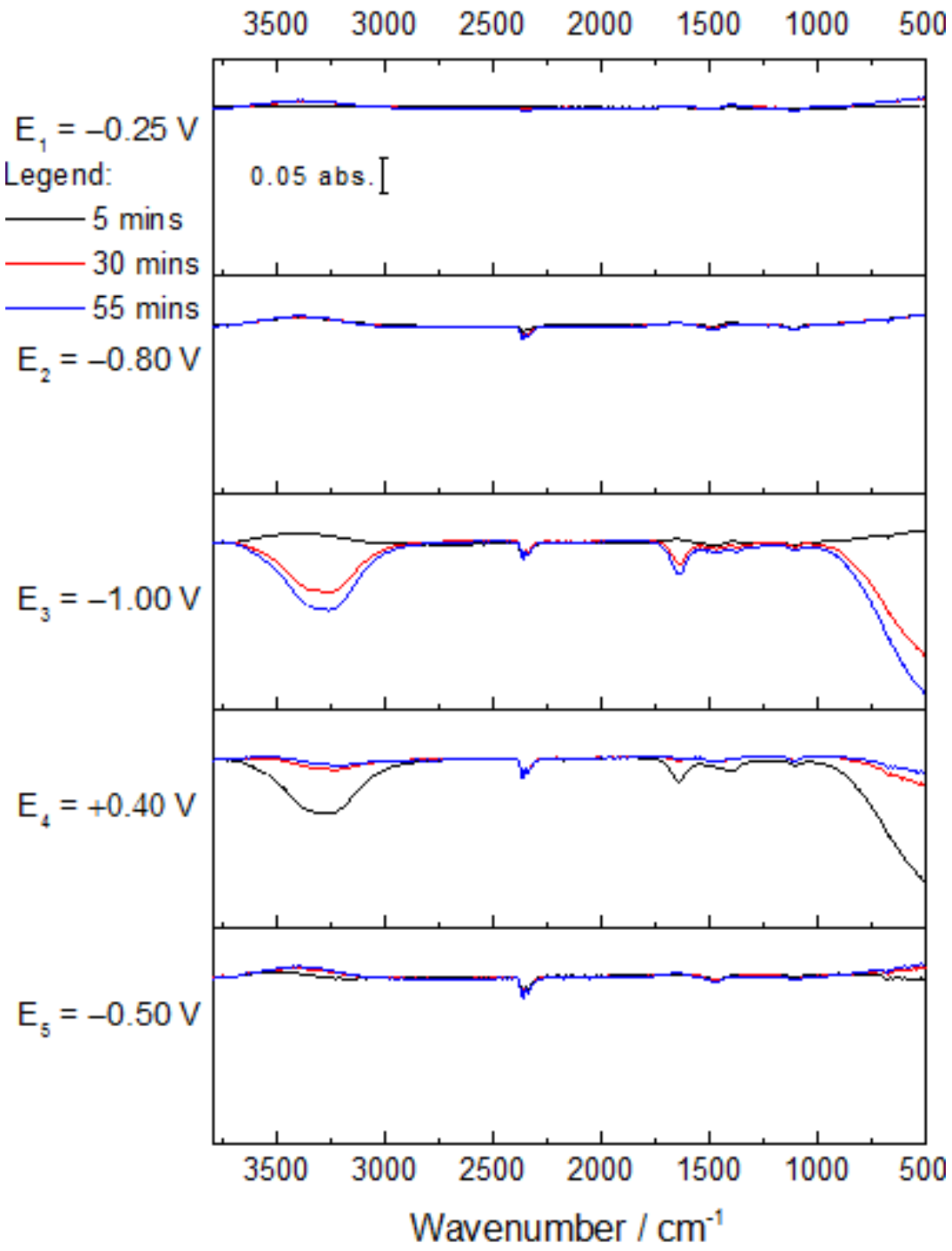

Figure A. 53 First repeat measurement of in-situ FTIR spectra of violarite in K_2CO_3 solution pH 10.1 under CO_2, recorded on applying potentials of −0.25, −0.80, −1.00, + 0.40 and −0.50 V for one hour each step. Spectra displayed at each potential step were recorded at 5, 30 and 55 mins into holding the potential.

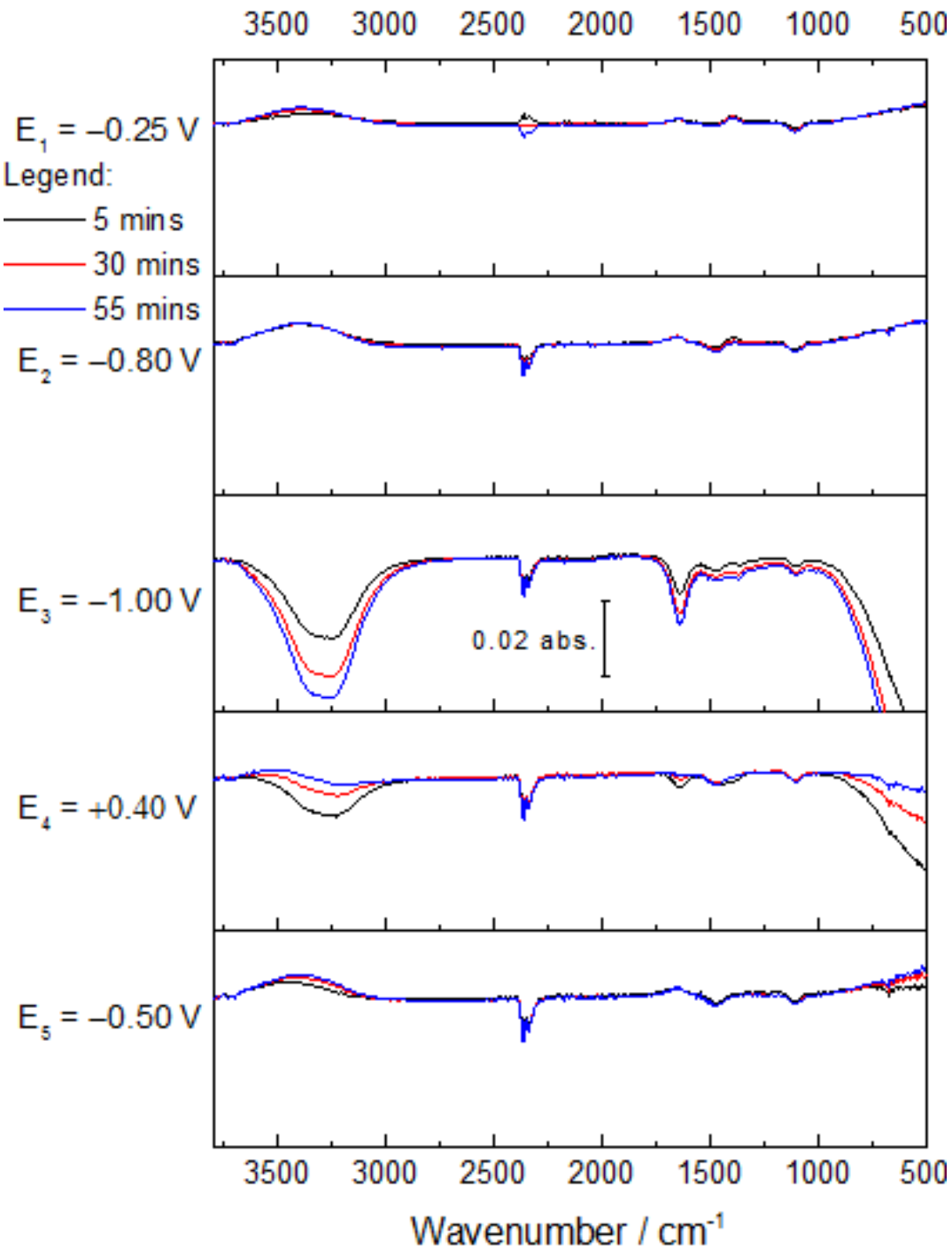

Figure A. 54 Second repeat measurement of in-situ FTIR spectra of violarite in K_2CO_3 solution pH 10.1 under CO_2, recorded on applying potentials of −0.25, −0.80, −1.00, + 0.40 and −0.50 V for one hour each step. Spectra displayed at each potential step were recorded at 5, 30 and 55 mins into holding the potential.